ORGANISATION EUROPÉENNE POUR LA RECHERCHE NUCLÉAIRE
CERN EUROPEAN ORGANIZATION FOR NUCLEAR RESEARCH

CERN–2002–001
10 June 2002
SPS + LHC Division

Proceedings

ECLOUD'02

CERN, Geneva, 15–18 April 2002

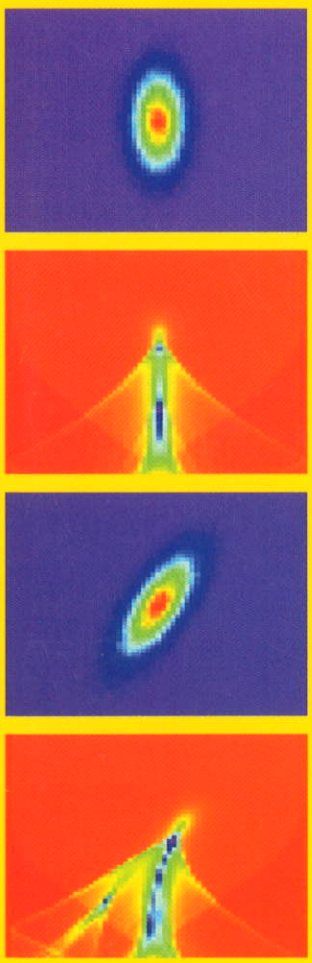

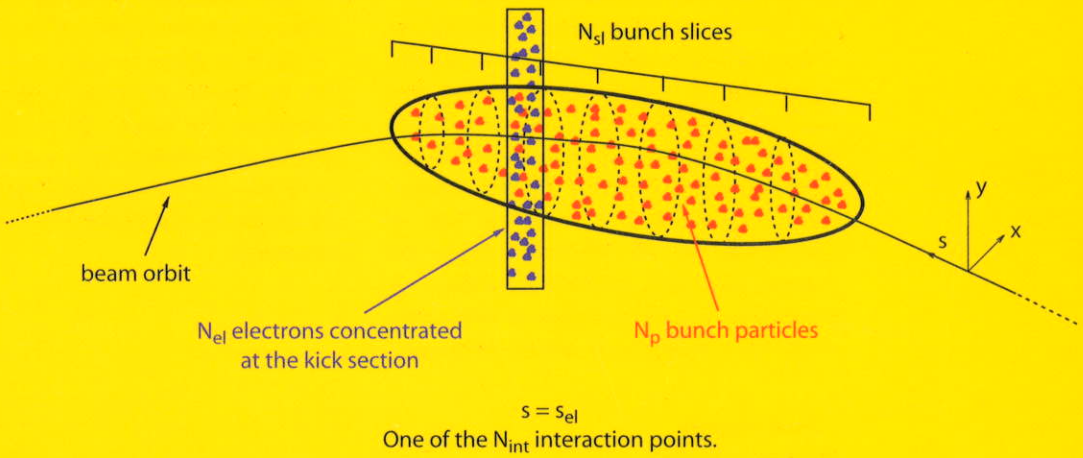

$s = s_{el}$
One of the N_{int} interaction points.

Mini-Workshop on Electron-Cloud Simulations for Proton and Positron Beams

Editors:
G. Rumolo
F. Zimmermann

Geneva, 2002

ISSN 0007-8328
ISBN 92-9083-193-6

CERN–2002–001
10 June 2002
SPS + LHC Division

ORGANISATION EUROPÉENNE POUR LA RECHERCHE NUCLÉAIRE
CERN EUROPEAN ORGANIZATION FOR NUCLEAR RESEARCH

ECLOUD'02: MINI-WORKSHOP ON ELECTRON-CLOUD SIMULATIONS FOR PROTON AND POSITRON BEAMS

CERN, Geneva, Switzerland
15–18 April 2002

PROCEEDINGS

Editors: G. Rumolo and F. Zimmermann

GENEVA
2002

CERN Scientific Information Service–650–June 2002

Abstract

This report contains the Proceedings of the Mini-Workshop on Electron-Cloud Simulations for Proton and Positron Beams (ECLOUD'02) held at CERN from 15 to 18 April 2002. The ECLOUD'02 workshop brought together the international experts on electron-cloud modelling, measurements, and observations, who discussed the following issues: (1) simulations of electron-cloud build-up, decay time, and minimum size of clearing gap; (2) effective transverse and longitudinal wake fields induced by the cloud; (3) simulations and analytical treatments of transverse instabilities driven by the electrons; (4) coherent tune shift and incoherent tune spread; (5) simulation of potential remedies; (6) plasma approaches to the electron-beam interactions; (7) synergies between electron cloud, regular impedance, space-charge and/or beam–beam interaction; and (8) observations at existing storage rings, predictions for future accelerators, and possible cures. Among the highlights of the workshop are the prediction of a 'blow-out' regime reached with high bunch charges and close spacing (S. Heifets), the generalization of the wake-field formalism and transverse-mode coupling calculation to the case of the electron-cloud wake depending on the longitudinal location of the driving charge (E. Perevedentsev), the detailed experimental results and simulations from KEKB (H. Fukuma, K. Ohmi, S.S. Win), the discussion of the SPS instability (K. Cornelis), the impressive number of different and sophisticated electron-cloud measurements in the SPS (M. Jimenez), the first application of plasma-modelling tools to the electron-cloud problem (T. Katsouleas), the large horizontal single-bunch wake field computed for a combined-function magnet (G. Rumolo), the calculation of the dynamic pressure in the LHC interaction regions due to the electron cloud (A. Rossi), and the proposal to affect the electron cloud using microwaves (F. Caspers). The latter could already be tested experimentally soon after the workshop (F.-J. Decker). Collaborations between the various laboratories were established, or revived, and a common R&D programme was agreed upon, which will be coordinated by a group of selected contact persons. A condensed overview of the primary achievements is provided by the summary reports at the end of these proceedings.

Preface

A Mini-Workshop on Electron-Cloud Simulations for Proton and Positron Beams (ECLOUD'02) was held at CERN from 15 to 18 April 2002. The workshop was organized by members of the Accelerator Physics group in the CERN SL Division, with the help of an international organizing committee, comprising representatives from BNL, CERN, DESY, FNAL, KEK and SLAC. The ECLOUD'02 workshop received an enthusiastic response from the international accelerator-physics community as reflected by more than 60 participants from 17 different institutes, which underlines a growing consensus that electron-cloud effects have to be fully understood and mastered, since they may otherwise become a performance limit for many next-generation, high-intensity rings. Participants included several members from the CERN SL Operation group, PS Experimental Areas group, and the LHC Vacuum group. Also SLAC, KEK, and BNL displayed a strong interest with six, five, and three participants, respectively.

Beam-induced multipacting, instabilities and beam blow-up driven by the accumulated electrons have been observed at many accelerators around the world, for example at CERN with the LHC proton beam in the SPS and in the PS, at the SLAC and KEK B factories, at the Los Alamos PSR, at the Beijing Electron–Positron Collider, etc. The pressure increase caused by the electron cloud, its impact on beam diagnostics, and, for the LHC, the heat load on the beam screen and cold bore are further primary concerns. Simulations for future linear colliders and intense proton drivers suggest that in these machines electrons in the vacuum chamber may reach densities higher by up to a factor 10–100 than in existing machines.

The electron cloud induces betatron tune shifts, tune spread, and transverse single- and multibunch instabilities. A variety of theoretical and simulation approaches have addressed these possibilities. A number of simulation codes have also been developed, using different approximations and including different physics. ECLOUD'02 has reviewed the present analytical, simulation and modelling approaches to the electron-cloud problem, determined the important outstanding questions, and developed a strategy for further R&D. Reports on the current status of experimental observations world-wide served as a motivation and benchmark for the simulation studies.

In this spirit, experimental work carried out at many different laboratories (KEK, SLAC, CERN, LANL, BNL, LBNL, IHEP, ANL) was reported in the two opening sessions (I+II) of the workshop on Monday 15 April. The second session also included results from laboratory measurements of secondary emission and of electron energy spectra, which are an invaluable input for the electron-cloud modelling. Tuesday's sessions (III+IV) were entirely devoted to the simulations of the electron-cloud build-up and of the associated beam instabilities. They included presentations of the physics models which form the basis of the existing simulation codes, discussions of simulation results, and comparisons of simulations and observations. In particular, several reports on the simulation of single-bunch instabilities driven by the electron cloud, e.g., by K. Ohmi (KEK), G. Rumolo (CERN), Y. Cai (SLAC), and J. Xing (IHEP), and on theoretical studies by S. Heifets (SLAC), E. Metral (CERN) and E. Perevedentsev (BINP) demonstrated the recent fast progress in the field.

Wednesday's two sessions (V+VI) concentrated on plasma physics approaches and on future research and development as well as possible remedies to the electron-cloud problems, respectively. A highlight was the presentation by T. Katsouleas (University of Southern California) who applied the sophisticated and well bench-marked plasma simulation codes which were developed at USC/UCLA to the electron cloud in the CERN SPS, and who also pointed out

the importance of cloud image forces. A further intensified collaboration with the USC group is foreseen. Another interesting simulation result is the surprising strength of the horizontal wake field in a combined-function magnet, presented by G. Rumolo (CERN).

During the workshop, F. Caspers (CERN) drew attention to the possible interaction of microwaves with the electrons. At the banquet, he proposed an experimental study of trapped modes near the PEP-II collimators and their effect on the electron cloud. This experiment was indeed performed by F.-J. Decker soon after the workshop, on May 16. Its encouraging results have been posted on the workshop web site. F. Caspers stressed that rf waves could intentionally be fed into the vacuum chamber as a possible means to either suppress the cloud or to enhance surface conditioning.

The workshop was summarized in Session VII on Thursday morning by R. Macek (LANL), O. Gröbner (CERN), M. Furman (LBNL), A. Wolski (LBNL), R. Assmann (CERN), and W. Chou (FNAL), who highlighted the necessity of strengthening the international collaboration on electron-cloud effects. With this goal in mind, a few key contact persons were selected from different institutes, who agreed to coordinate the future worldwide activities related to laboratory measurements (F.-J. Decker, SLAC; F. Ruggiero, CERN; S. Kato, KEK), theoretical approaches (A. Chao, SLAC; M. Furman, LBNL; S. Heifets, SLAC), and simulation-code comparisons (F. Zimmermann, CERN).

The ECLOUD'02 programme, presentations, and papers are posted on the workshop web site `http://wwwslap.cern.ch/collective/ecloud02`

The proceedings are structured according to the seven workshop sessions:

- Session I: Experimental Observations at Existing Accelerators and Concerns for Future Machines (chair R. Macek, secretary G. Arduini).
- Session II: Further Observations, Laboratory Measurements, and Modelling (chair O. Gröbner, secretary M. Jimenez).
- Session III: Simulations of Electron-Cloud Build-Up (chair M. Furman, secretary G. Rumolo).
- Session IV: Simulations of Electron-Cloud Instabilities (chair T. Raubenheimer, secretary F. Zimmermann).
- Session V: Specific Comparisons and Plasma Approaches (chair T. Katsouleas, secretary R. Assmann).
- Session VI: Discussions of Future Studies, Collaborations, and Possible Solutions (chair W. Chou, secretary O. Brüning).
- Session VII: Summary Talks (chair S. Myers, secretary F. Ruggiero).

These proceedings have been published in paper and electronic form. The paper copy is in black and white; the electronic version contains colour pictures. Electronic copies can be retrieved through: `http://wwwslap.cern.ch/collective/ecloud02/proceedings`
In addition, workshop participants were encouraged to submit their contributions to a special ECLOUD'02 conference edition of Physical Review Special Topics - Accelerators and Beams.

The compilation of these proceedings would not have been possible without the help of the chairmen, scientific secretaries, and speakers of all the sessions. In particular, we would like to thank all the participants for their stimulating contributions.

Geneva, 10 June 2002

F. Ruggiero, G. Rumolo, J. Thomashausen, and F. Zimmermann

List of ECLOUD'02 Participants

Name	Institute	Email address
Gianluigi Arduini	CERN	gianluigi.arduini@cern.ch
Ralph Assmann	CERN	ralph.assmann@cern.ch
Vincent Baglin	CERN	vincent.baglin@cern.ch
Michael Blaskiewicz	BNL	mmb@bnl.gov
Daniel Brandt	CERN	daniel.brandt@cern.ch
Reinhard Brinkmann	DESY	reinhard.brinkmann@desy.de
Maura Brunetti	EPFL	maura.brunetti@epfl.ch
Oliver Bruning	CERN	oliver.bruning@cern.ch
Yunhai Cai	SLAC	yunhai@slac.stanford.edu
Fritz Caspers	CERN	fritz.caspers@cern.ch
Alex Chao	SLAC	achao@slac.stanford.edu
Weiren Chou	FNAL	chou@fnal.gov
Roberto Cimino	CERN	roberto.cimino@cern.ch
Paul Collier	CERN	paul.collier@cern.ch
Ian Collins	CERN	ian.collins@cern.ch
Karel Cornelis	CERN	karel.cornelis@cern.ch
Franz-Josef Decker	SLAC	decker@slac.stanford.edu
Renato Fedele	INFN	renato.fedele@na.infn.it
Wolfram Fischer	BNL	wolfram.fischer@bnl.gov
Hitoshi Fukuma	KEK	fukuma@post.kek.jp
Miguel Furman	LBNL	mafurman@lbl.gov
Jacques Gareyte	CERN	jacques.gareyte@cern.ch
Massimo Giovannozzi	CERN	massimo.giovannozzi@cern.ch
Oswald Grobner	CERN	oswald.grobner@cern.ch
Katherine Harkay	ANL	harkay@aps.anl.gov
Samuel Heifets	SLAC	heifets@slac.stanford.edu
Noel Hilleret	CERN	noel.hilleret@cern.ch
Ubaldo Iriso	CERN	ubaldo.iriso@cern.ch
Miguel Jimenez	CERN	jose.miguel.jimenez@cern.ch
John Jowett	CERN	john.jowett@cern.ch
Dobrin Kaltchev	TRIUMF	kaltchev@triumf.ca
Tom Katsouleas	USC	katsoule@usc.edu
Jean Michel Laurent	CERN	j-michel.laurent@cern.ch
Robert Macek	LANL	macek@lanl.gov
Elias Metral	CERN	elias.metral@cern.ch
Steve Myers	CERN	steve.myers@cern.ch
Kazuhito Ohmi	KEK	ohmi@post.kek.jp
Evgueni Perevedentsev	BINP	perevedent@inp.nsk.su
Mauro Pivi	LBNL	mpivi@lbl.gov
Alain Poncet	CERN	alain.poncet@cern.ch
Tor Raubenheimer	SLAC	tor@slac.stanford.edu
Marc Ross	SLAC	mcrec@slac.stanford.edu
Adriana Rossi	CERN	adriana.rossi@cern.ch
Francesco Ruggiero	CERN	francesco.ruggiero@cern.ch
Giovanni Rumolo	CERN	giovanni.rumolo@cern.ch
Hans Schamel	Uni Bayreuth	hans.schamel@uni-bayreuth.de
Horst Schoenauer	CERN	horst.schonauer@cern.ch
Takeshi Toyama	KEK	takeshi.toyama@kek.jp
Luc Vos	CERN	lucien.vos@cern.ch
Lanfa Wang	KEK	wanglf@post.kek.jp
Rainer Wanzenberg	DESY	rainer.wanzenberg@desy.de
Jie Wei	BNL	wei1@bnl.gov
Su Su Win	KEK	susuwin@post.kek.jp
Jorg Wenninger	CERN	jorg.wenninger@cern.ch
Andy Wolski	LBNL	awolski@lbl.gov
Jun Xing	IHEP	xingj@mail.ihep.ac.cn
Pavel Zenkevich	ITEP & GSI	zenkevich@vitep3.itep.ru
Frank Zimmermann	CERN	frank.zimmermann@cern.ch

CONTENTS

ELECTRON CLOUD EFFECTS AT KEKB

H. Fukuma† for the KEKB Group, KEK, Tsukuba, Japan

Abstract

This paper describes a review of an experimental study of electron cloud effects at the KEKB LER.

1 INTRODUCTION

Vertical beam blow-up has been observed in the KEKB low energy positron ring (LER) since early operation period [1]. The beam size as a function of beam current started to increase at a threshold beam current and was almost doubled at 300 mA under typical operating conditions. Thus the blow-up was one of the most serious problems limiting the luminosity of KEKB.

The main characteristics of the blow-up observed in early operation period are summarized as: 1) the blow-up was a single beam and a multi-bunch effect; 2) the blow-up has a threshold intensity which was determined roughly by (bunch current)/(bunch spacing); 3) no dipole oscillation has been observed when the vertical chromaticity is enough high; 4) the blow-up was almost independent of betatron tunes; 5) the blow-up did not depend on the positions of the vertical masks, which are among the main impedance sources; 6) the blow-up did not depend on the vacuum pressure, especially for hydrogen, in the arc; and 7) no blow-up was observed in the horizontal plane.

A model to explain the blow-up was proposed by F. Zimmermann and K. Ohmi [2]. In their model the blow-up is explained as a single-bunch instability of a positron bunch due to a large number of electrons, i.e. "electron cloud", generated by photoemission or secondary emission. The instability will occur only in multi-bunch operation since the electron cloud is built up by the successive passage of the bunches. The coherent dipole oscillation of positrons along the bunch caused by the “wake” force due to the electron cloud appears as either regular or strong head-tail instability. A beam size blow-up will be observed as a result of the head-tail oscillation of the instability.

Many small permanent magnets, called “C-yokes”, were attached to vacuum ducts to sweep out the electrons from November 1999 to July 2000. The C-yokes were replaced to solenoid magnets in September 2000 because a simulation showed that the solenoid magnets were more effective than C-yokes to suppress the buildup of the electron cloud [6]. The effect of the solenoids on the blow-up was confirmed by the measurements of the vertical beam size by an interferometer and a gated camera and by the measurement of the luminosity. Then more solenoids were installed in the ring. The number of the solenoids installed so far amount to about 8600. As the result the measurement by the interferometer in February 2002 showed no beam size blow-up up to 1300mA in regular operation condition for the physics experiment.

†hitoshi.fukuma@kek.jp

Table 1 : Main parameters of the KEKB LER

Beam energy (GeV)	3.5
Circumference (m)	3016
rf bucket spacing (ns)	2
Bunch length (mm)	4
Bunch spacing (ns)	8
Number of bunch	1200
Beam current (mA)	1400
Particles / bunch (10^{10})	7
Emittance ε_x/ ε_y(10^{-8}m)	1.8 / 0.036
Average beta function (m)	15
Critical energy (keV)	5.8
Vacuum chamber	copper (round)
Chamber radius (mm)	47

The electron cloud can cause not only the beam blow-up but also a tune shift along the train and a coupled bunch instability, which are both observed in the KEKB LER.

This paper describes an experimental study of the electron cloud effects at the KEKB LER[3,4]. As a reference main parameters of the KEKB LER in present operation condition are listed in Table 1.

2 CLOUD BUILDUP

2.1 Electron measurement

An electron yield was measured by retarded field analysers (RFA's) [5] which are located at 1.2m and 8.0m downstream from a bend. Figure 1 shows the electron current measured by the RFA's. A simulation by K. Ohmi gives an electron current of 10μA and 1μA at the upstream- and downstream-RFA respectively. Thus the measurement is roughly consistent with the simulation.

Energy distribution of the electrons was also measured by the RFA. Measured energy distribution (Fig. 2 (a)) is well reproduced by a simulation [6] (Fig. 2 (b)).

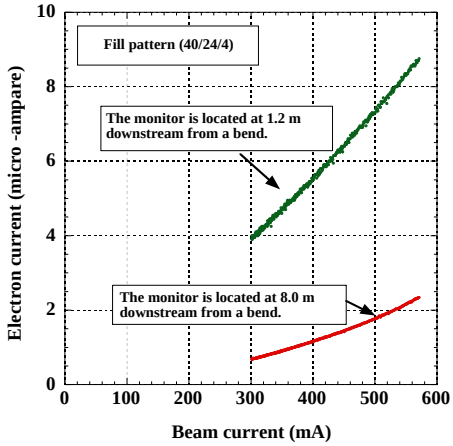

Figure 1 : Electron current measured by the retarded field analysers.

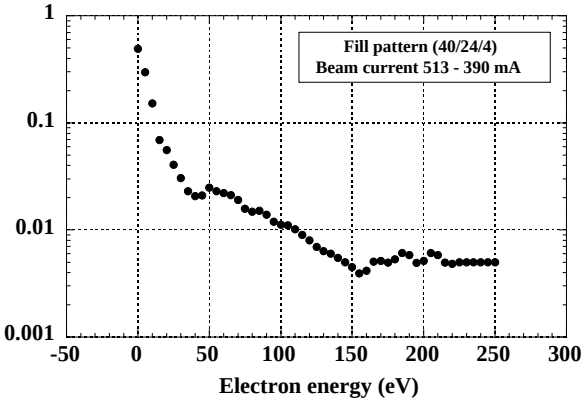

Figure 2 (a) : Energy distribution of the electrons measured by the retarded field analyser.

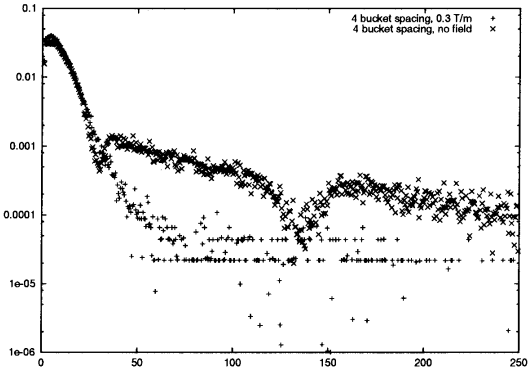

Figure 2 (b) : Energy distribution of the electrons by the simulation [6].

2.2 Tune shift and build-up time

Fig. 3 (a) shows a tune shift along the bunch train normalised by the charge density of the beam. The tune shift was measured by a gated tune meter [7]. As shown by K. Ohmi et al. the tune shift is a good measure of the density of the electron cloud [8]. The saturated tune shift is consistent with the result of the simulation which is indicated by a dotted line [9]. Build-up time of the tune shift, as seen in Fig. 3 (a), is about 20 bunches which is also consistent with the build-up time of the electron cloud density obtained by the simulation [9] ; see Fig. 3 (b).

2.3 Decay time

To measure the decay time of the electron cloud a test bunch was injected at the end of a train with variable distance between the last bunch of the train and the test bunch, then the tune shift and the vertical beam size was measured. Fig. 4 (a) and (b) show the tune shift [7] and the vertical beam size respectively. The decay time was 28ns

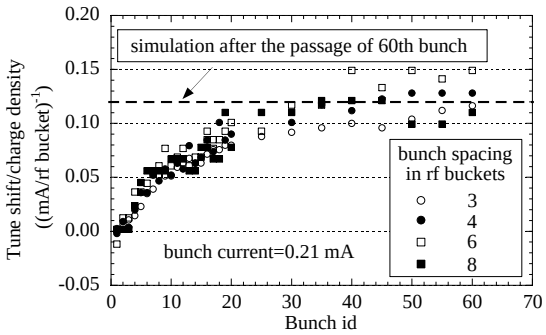

Figure 3 (a) : Vertical betatron tune shift along the train for four different bunch spacing, 3, 4, 6 and 8 rf buckets. The tune shift is normalised by the charge density of the beam (i.e. bunch current/bunch spacing in the unit of rf bucket) [3].

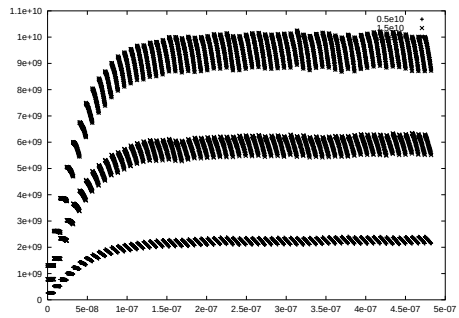

Figure 3 (b) : Simulation result of the cloud build-up [9]. The horizontal axis is the time in ns and the vertical axis is the number of the electrons / meter in m^{-1}.

from the data of the tune shift. For the vertical beam size the blow-up was disappeared when the test bunch was injected 24ns after from the end of the train. Two measurements are roughly consistent with each other.

Fig. 5 (a) shows the result of an another experiment which also indicates the decay time of the electron cloud [3]. Two trains which were separated by 64ns were injected in the ring, then the vertical beam size of each bunch was measured by the gated camera [10]. While the blow-up started at about 7th bunch in the first train, second bunch already blew-up in the second train. The result is supported by a simulation [6] as shown in Fig. 5 (b).

While the data in Fig. 4 suggest the decay time of about 30ns, the data in Fig. 5 (a) suggest the decay time longer than 64ns. It seems that there are two components which govern the decay time [11].

2.4 Change of vertical tune shift

Fig. 6 compares the tune shift in July 2000 and April

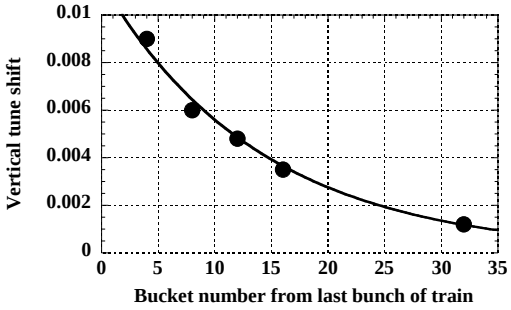

Figure 4 (a) : Vertical tune shift of the test bunch as a function of the distance between the last bunch of the train and the test bunch. The train consisted of 32 bunches. Bunch spacing was 4 rf buckets. Bunch current was 0.8mA.

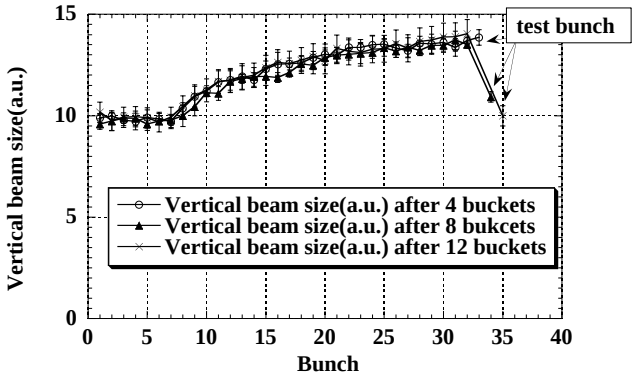

Figure 4 (b) : Vertical beam size of the test bunch as a function of the distance between the last bunch of the train and the test bunch. The train consisted of 32 bunches. Bunch spacing was 4 rf buckets.

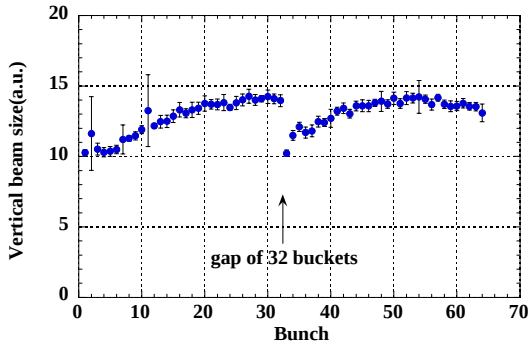

Figure 5 (a) : Beam sizes over two trains measured by the fast gated camera. Train-to-train gap which is not shown in the Figure, is 32 rf buckets [3].

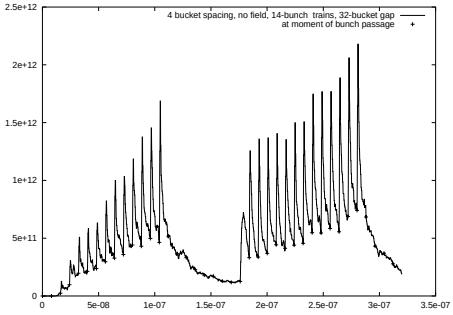

Figure 5 (b) : Simulated electron density near the beam per cubic meters as a function of time in sec in a field free region [6].

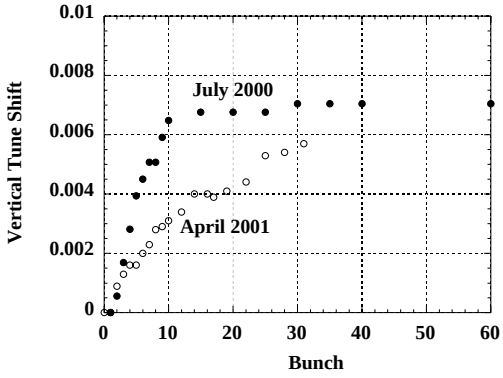

Figure 6 : Vertical tune shift along the train in July 2000 and April 2001.

2001. The data in July 2000 was taken after removing all C-yokes and before the installation of the solenoids. The data in July 2001 was taken when all solenoids were turned off. The build-up time in April 2001 is larger than that in July 2000. The result may suggest conditioning effects which cause the decrease of the cloud density.

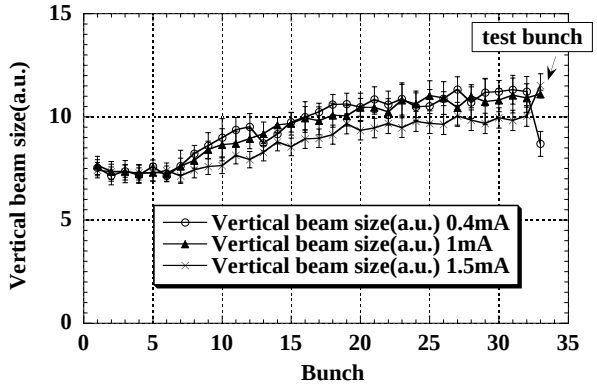

Figure 7 : Vertical beam size of the test bunch as a function of the bunch current. The test bunch was injected after the train apart from 4 rf buckets. Bunch spacing of the train was 4 rf buckets.

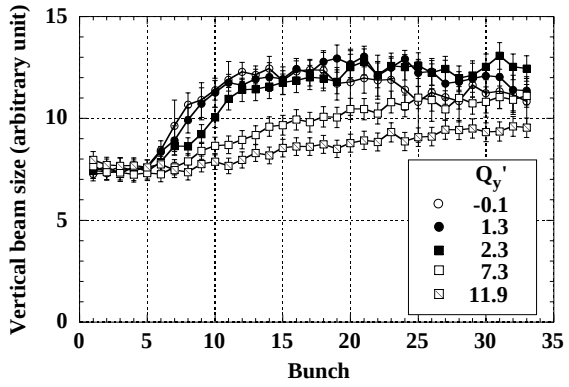

Figure 8 : Beam size along the train observed by the fast gated camera in various chromaticities. Diffraction effect is not corrected [3].

3 BEAM BLOW-UP

3.1 Single bunch characteristics

A test bunch was injected immediately behind a train to prove the single bunch nature of the blow-up. The beam size of the test bunch was measured at several bunch currents of the test bunch. Fig. 7 shows the result in which the beam size of the test bunch increased when its bunch current increased. The measurement demonstrates that the blow-up is a single bunch effect.

3.2 Effect of chromaticity

The effect of the vertical chromaticity on the blow-up was measured by the fast gated camera. If the blow-up is caused by the head-tail instability it should be sensitive to the chromaticity. Fig. 8 shows that the blow-up along the train became weaker when the chromaticity was increased [3].

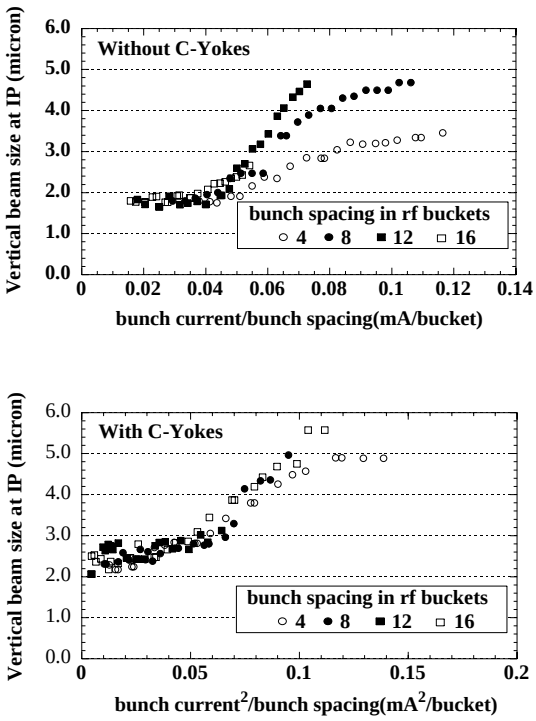

Figure 9 : Blow-up of the beam size in various bunch spacing without and with C-Yokes [3].

According to a calculation based on the transverse mode coupling instability (TMCI) theory, the dependence of the threshold cloud density on the vertical chromaticity is rather weak, i.e. it increases 17 % if the chromaticity increases by 10 [13]. It is not clear that the observation is consistent with the result of the TMCI theory.

3.3 Threshold intensity of blow-up

The average beam size at various bunch spacing was measured by the interferometer [12] as a function of the beam current [3]. As shown in Fig. 9, without C-yokes the threshold intensity $I_{b,th}$ was proportional to the bunch spacing s_b while with C-yokes $I_{b,th}$ was proportional to square root of s_b. According to a model of the single bunch instability caused by the electron cloud $I_{b,th}$ is proportional to s_b for the head-tail instability and the TMCI and is proportional to the square root of s_b for the beam break-up instability [14]. After these experiments the blow-up at bunch spacing of 3 and 4 rf buckets was measured in July 2001 when the solenoids were turned on. The results showed the scaling of $I_{b,th} \propto s_b$. The reason why the scaling changed after the installation of C-Yokes is not understood yet.

3.4 Bunch by bunch luminosity

A bunch by bunch luminosity was measured by the "zero-degree luminosity monitor" [15]. In a beam-fill the luminosity of first several bunches was higher than that of remaining bunches, while in other beam-fill it showed almost flat behaviour. It may be difficult to separate the single beam blow-up from the beam-beam blow-up because during collision the beam size is intentionally controlled by automatic programs and/or operators to obtain the high luminosity.

4 COUPLED BUNCH INSTABILITY

The coupled bunch instability is observed in LER [16]. As shown in Fig. 10, totally different mode spectra were observed with and without solenoid field, which strongly suggests that the instability is caused by the electron cloud as usual wake fields are not affected by weak solenoid field. In Fig. 10 peaks of the mode spectra in horizontal and vertical planes appeared at almost same position when the solenoids were turned off. A simulation shows that the observed mode spectra, especially position of the peaks, are well reproduced if the electrons are produced uniformly on the chamber wall [17]. Almost equal horizontal and vertical tune shift along the train, shown in Fig. 19, also suggests the transverse distribution of the electron cloud is round [18]. Growth rates of the instability shown in Fig. 11 are roughly consistent with the simulation [17].

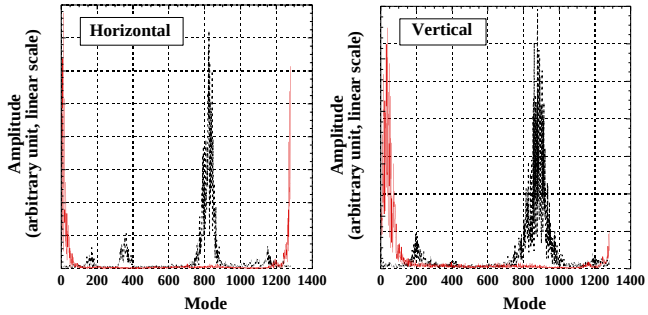

Figure 10 : Observed mode spectrum of the coupled bunch instability with and without solenoids at 600mA. Red-solid (black-broken) lines are the data taken when the solenoids were turned on (off).

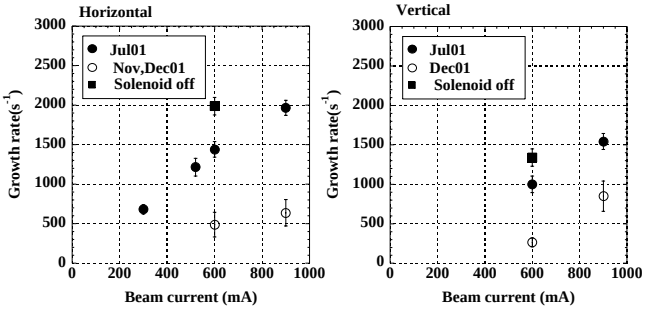

Figure 11 : Measured growth rates of the coupled bunch instability. Closed and open circles indicate the data were taken with the solenoids being turned on. The data shown by closed squares were taken in July 2001.

5 EFFECT OF SOLENOID

5.1 Solenoid system

Since September 2000 the solenoids to sweep out the electrons have been installed in LER [4]. Parameters of solenoid system are shown in Tables 2 and 3. There are two kind of solenoids, one is a bobbin-type solenoid and the other a bobbinless-type solenoid. The length of the bobbin-type solenoid is from 150 to 650 mm depending on the length of available free space for winding. The bobbinless-

Table 2 : Parameters of solenoids.

Type	Length (mm)	Diameter (mm)	Turns	Bz (center) @ 5A (Gauss)
Bobbin	150 - 650	148	250(typ.)	45
Bobbinless	40	220	190, 200	48
Bobbinless	40	250	200	43
Bobbinless	40	300	200	37

Table 3 : Parameters of power supply for the solenoids.

	KEKB corrector P.S.	TRISTAN corrector P.S.
Current(A)	5	3
Units	616	40

Table 4 : Installation history of the solenoids. Second and third columns show the number of the installed solenoids.

Date	Bobbinless	Bobbin	Location
2000. 9.	0	2783	Arc section straight section (Cu chamber)
2001. 1.	1950	0	Arc section (Bellows+NEG)
2001. 4.	254	10	Straight section of Fuji andTsukuba (Bellows, Cu chamber)
2001. 9.	3411	43	Straight section (Bellows, Cu chamber) Arc section (NEG,IP, Bellows+NEG)
2002. 1.	119	0	Arc section (Between Quad and Sext)
Total	5734	2836	

Figure 12 : Solenoids in a NEG pump and bellows section (upper) and in a NEG section (lower). Long solenoids are the bobbin-type solenoids and short solenoids the bobbinless-type solenoids.

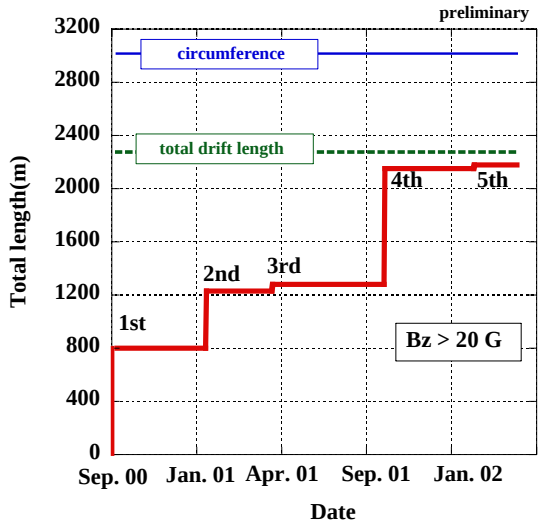

Figure 13 : Length of the regions covered by the solenoids. "1st" to "5th" mean the installation stages of the solenoids.

type solenoid has a length of 40mm and mainly located on bellows and both sides of NEG pumps and ion pumps to cover regions in which the bobbin-type solenoids can not be wound. The magnetic field along the beam line at the centre of a solenoid is about 45 Gauss. Pictures of the solenoids are shown in Fig. 12. The power supplies for the correctors of the KEKB rings are partly diverted to those for the solenoids. And several power supplies for the correctors of the TRISTAN collider are also used.

The solenoids were installed in LER five times as shown in Table 4. First (in 2000.9), 2nd (in 2001.1) and 4th (in

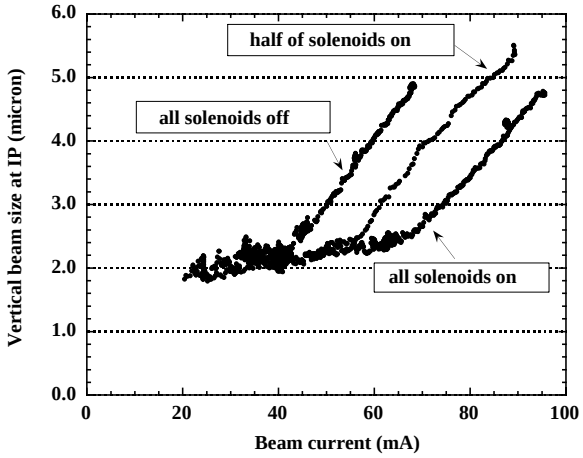

Figure 14 : Vertical beam size as a function of the beam current measured by the interferometer. In the measurement two trains were injected on opposite sides in the ring. Each train contained 60 bunches. Bunch spacing was 4 rf buckets. [4].

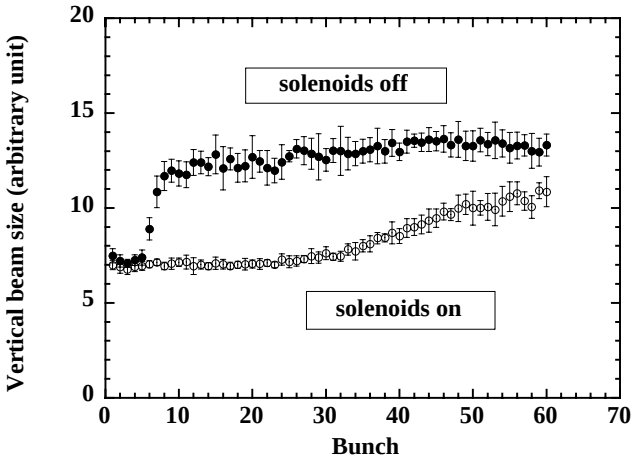

Figure 15 : Vertical beam size along the train taken by the gated camera with and without the solenoids. The train consisted of 60 bunches. Bunch spacing was 4 rf buckets. Bunch current was 0.67 mA [4].

2001.9) installations are major installations. Fig. 13 shows a very rough estimation of the length covered by the solenoid field larger than 20 Gauss. Now about 75% of the circumference are covered by the solenoids.

5.2 Beam blow-up

The effect of the solenoids on the beam blow-up was confirmed by the measurement of the vertical beam size of a single beam. Fig. 14 shows the beam size as a function of beam current in a short train after 1st installation of the solenoids [4]. Turning on the solenoids, the threshold current increased from 40 mA to 70 mA. Fig. 15 shows the beam size along the train measured by the gated camera after 1st installation of the solenoids [4]. The blow-up started at 7th bunch when the solenoids were turned off while it started at 30th bunch when the solenoids were turned on.

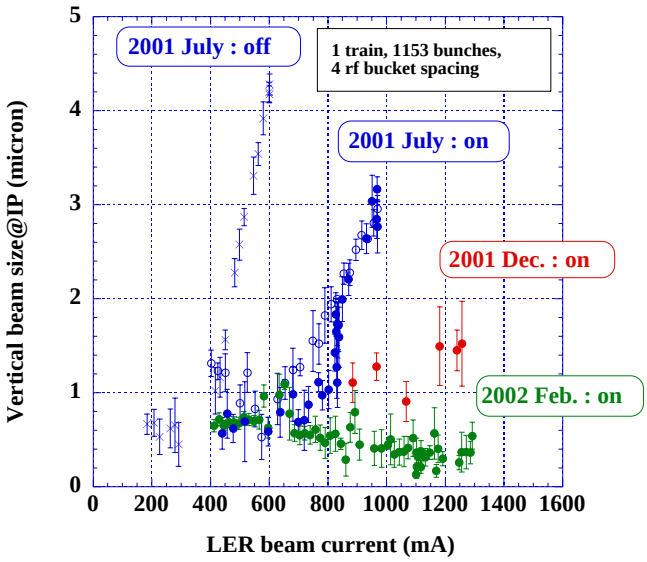

Figure 16 : Effect of solenoids on the vertical beam size for a long train measured by the interferometer. "On/off" means the solenoids were turned on/off.

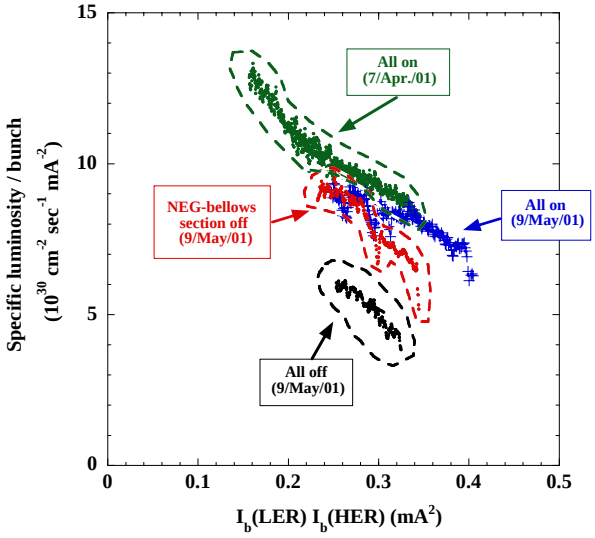

Figure 17 : Effect of solenoids on the luminosity after 3rd installation of the solenoids.

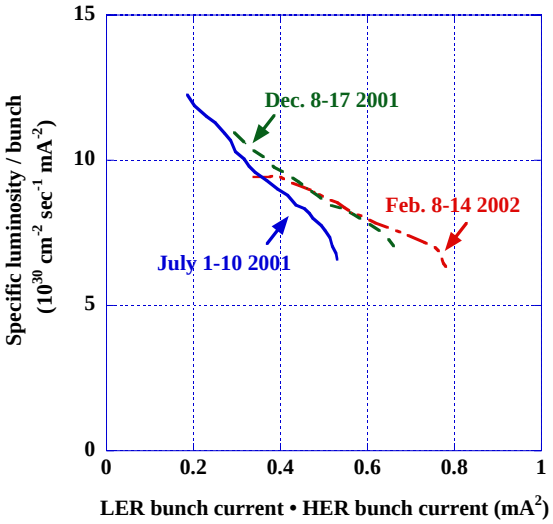

Figure 18 : Effect of solenoids on the luminosity after 3rd, 4th and 5th installations of the solenoids.

Fig. 16 shows the beam size in a long train for the physics experiment after several installation stages of the solenoids. For every additional installations of the solenoids the threshold current of the blow-up increased and finally the blow-up disappeared in the measurement in February 2002.

5.3 Luminosity

The effect of the solenoids was also confirmed by the luminosity measurement. Fig. 17 shows the specific luminosity as a function of the bunch current product of HER and LER after 3rd installation of the solenoids. When all solenoids were turned off the specific luminosity decreased by 40%. Fig. 18 shows the specific luminosity after 3rd, 4th and 5th installations of the solenoids. In Fig. 18 an envelope curve of the specific luminosity taken for a week is plotted for each data set because the specific luminosity is affected by the beam tuning. As seen in Fig. 18 the specific luminosity was improved after 4th installation of the solenoids. It seems that the specific luminosity was slightly improved above $0.6 mA^2$ after 5th installation of the solenoids though the luminosity drop above $0.6 mA^2$ in Dec. 2001 might be caused by the beam tuning.

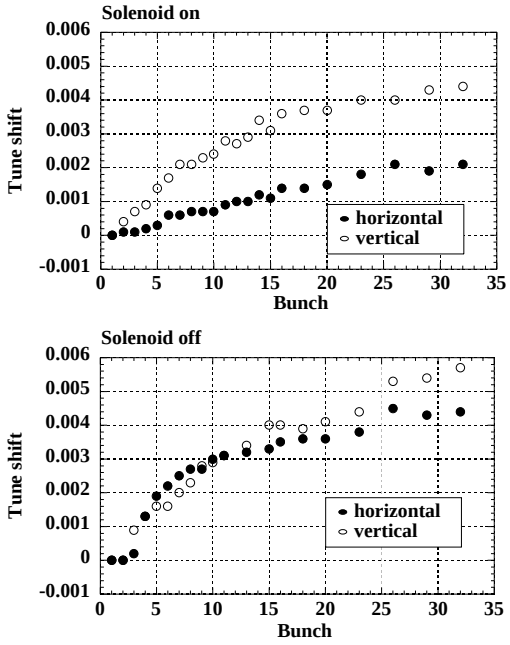

Figure 19 : The effect of the solenoids on the horizontal and vertical tune shift along the train. Bunch current was 0.31 mA [18].

5.4 Tune shift and coupled bunch luminosity

The tune shift along the train decreased when the solenoids were turned on. Fig. 19 compares the tune shift with and without solenoid field [18].

The mode spectrum of the coupled bunch instability was changed with and without solenoid field as described in section 4. The effect of the solenoids on the growth rate of the coupled bunch instability was also observed as shown in Fig. 11. The mode spectrum and the growth rate when the solenoids are turned on are studied by a simulation. The mode spectrum can be explained by the simulation assuming the effective solenoid field of 5 to 20 Gauss [17]. The growth rate obtained by the simulation is roughly consistent with the measurement [17].

6 OPEN QUESTIONS

Several open questions remain about the electron cloud effects at KEKB.

1) Beam blow-up has been observed in the vertical plane and not observed in the horizontal plane. A calculation based on the TMCI theory gives almost same horizontal and vertical threshold cloud density of the TMCI, i.e. 2.0 x 10^{-12}m^{-3} horizontally and 2.3 x 10^{-12}m^{-3} vertically [13]. The threshold cloud density in the vertical plane may be reduced by the focusing of the electron cloud during the bunch passage as pointed out in [13].

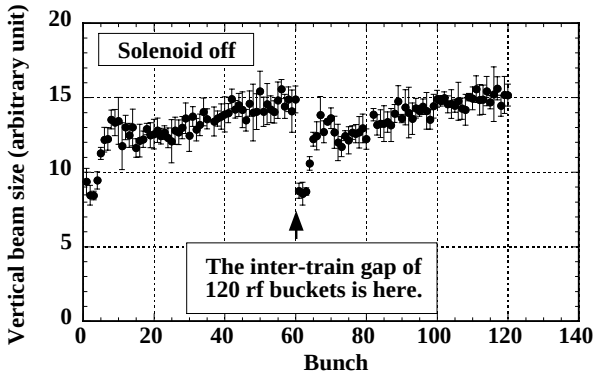

Figure 20 : Beam sizes over two trains measured by the fast gated camera. Train-to-train gap which is not shown in the Figure, is 120 rf buckets.

2) The decay time of the cloud density seems very long. Fig. 20 shows the vertical beam size of two trains injected 240ns apart from each other. The 4th bunch of the second train already blew-up while that of the 1st train did not, which indicates very long decay time of the cloud density. The electron cloud may be trapped in quadrupole and sextupole field as L. Wang et al. recently pointed out [19]. But no experimental evidence of such trapping is observed yet. A large puzzle is that the experiments described in subsection 2.3 imply a short decay time of the cloud density.

3) Very slow blow-up along the train was observed after 1st installation of the solenoids. This slow blow-up is not explained by simulations yet.

4) Conditioning effect for the cloud density is not clear. Change of the build-up time of the tune shift and the fact that the luminosity did not immediately improve after the installation of the solenoids but after several weeks of beam operation may suggest the decrease of the cloud density due to the conditioning by the beam. But the conditioning effect is not confirmed by a measurement of the electron yield yet.

5) Transverse distribution of the electron cloud may not concentrate near an illumination point by the direct synchrotron radiation but be round when the solenoids are turned off. Mode spectrum of the coupled bunch instability and almost equal horizontal and vertical tune shifts support this hypothesis. A measurement of the cloud distribution around the chamber wall will be welcome.

7 SUMMARY

Cloud build-up studied by the measurements of the electron yield, the energy distribution, the tune shift along the train, the build-up time of the tune shift and the beam blow-up along the train is well explained by the simulations.

Observations such as single bunch characteristics of the blow-up and the scaling of the threshold beam current of the blow-up on the bunch spacing are consistent with the single bunch head-tail instability model. It is unclear whether the chromaticity dependence of the beam blow-up and no horizontal blow-up are well explained by the TMCI theory or not.

Mode spectrum of the coupled bunch instability can be explained by the simulation assuming a uniform production of the electrons on the chamber wall. Growth rate is roughly consistent with the simulation.

Effect of the weak solenoid field on the electron cloud effects was confirmed by the measurements of the beam blow-up, the luminosity, the tune shift and the coupled bunch instability.

Several questions about the absence of a horizontal blow-up, the decay time of the cloud, very slow blow-up along the train, the conditioning effect and the transverse distribution of the electron cloud still remain to be studied.

8 ACKNOWREDGEMENTS

The experimental study of the electron cloud effects at KEKB has been carried out by many people of the KEKB group. Many thanks are extended to them. The author especially thanks S. Kurokawa and K. Oide for their support to attend this workshop. The discussions with T. Ieiri, K. Ohmi, K. Oide, E. Perevedentsev, Y. Suetsugu and F. Zimmermann were very stimulating to understand the electron cloud effects.

9 REFERENCES

[1] K. Akai et al., “COMMISSIONING OF THE KEKB B-FACTORY”, PAC’99, New York, Particle Accelerator Vol.1, 288-292(1999).

[2] K. Ohmi and F. Zimmermann, “Head-Tail Instability Caused by Electron Clouds in Positron Storage Rings”, Phys.Rev.Lett.85:3821- 3824(2000).

[3] H. Fukuma et al., “OBSERVATION OF VERTICAL BEAM BLOW-UP IN KEKB LOW ENERGY RING”, 1122, EPAC2000, Vienna, June 2000.

[4] H. Fukuma et al., “STUDY OF VERTICAL BEAM BLOWUP IN KEKB LOW ENERGY RING”, HEAC2001, Tsukuba, March 2001.

[5] Y. Ohnishi et al., “DETECTION OF PHOTOELECTRON CLOUD IN POSITRON RING AT KEKB", HEAC2001, Tsukuba, March 2001.

[6] F. Zimmermann, “Electron Cloud at the KEKB Low Energy Ring: Simulations of Central Cloud Density, Bunch Filling Patterns, Magnetic Fields, and Lost Electrons”, CERN-SL-2000-017 (AP) (May, 2000).

[7] T. Ieiri et al., "MEASUREMENT OF BETATRON TUNE ALONG BUNCH TRAIN IN THE KEKB LOW ENERGY RING", HEAC2001, Tsukuba, March 2001.

[8] K. Ohmi et al., "STUDY OF COHERENT TUNE SHIFT CAUSED BY ELECTRON CLOUD", APAC01, Beijing, September, 2001.

[9] F. Zimmermann, “Electron-Cloud Studies for the Low Energy Ring of KEKB”, CERN SL-Note-2000-004 AP (2000).

[10] J. Flanagan et al., “High-Speed Gated Camera Observations of Transverse Beam Size Along Bunch Train at the KEKB LER”, 1119, EPAC2000, Vienna, June 2000.

[11] K. Oide, private communications.

[12] T. Mitsuhashi et al., “OPTICAL DIAGNOSTIC SYSTEM FOR THE KEK B-FACTORY”, 1783, EPAC2000, Vienna, June 2000.

[13] K. Ohmi et al., "Wake-field and fast head-tail instability caused by an electron cloud", Phys. Rev. E 65, 016502 (2002).

[14] F. Zimmermann, "THE ELECTRON CLOUD INSTABILITY: SUMMARY OF MEASUREMENTS AND UNDERSTANDING", 666, PAC2001, Chicago, June 2001.

[15] T. Uehara, private communications.

[16] S. S. Win et al., "OBSERVATION OF TRANSVERSE COUPLED BUNCH INSTABILITY AT KEKB", APAC01, Beijing, September, 2001.

[17] S. S. Win et al., "Effect of Electron Cloud on the Bunch Oscillations in KEKB LER ", in these proceedings.

[18] T. Ieiri, private communications.

[19] L. Wang et al., "3D Particle in Cell Program for Electron Cloud", in these proceedings.

THE ELECTRON CLOUD INSTABILITY IN THE SPS

K. Cornelis, CERN, Geneva, Switzerland

ABSTRACT

The beam-induced electron multi-pacting, which is created by the LHC beam in the SPS, occurs mainly in the dipoles. It creates a vertical electron ribbon, which is responsible for strong transverse instabilities. In the horizontal plane a coupled bunch mode instability could be identified. Tune shift measurements and mode number analyses can tell us something on the electron cloud density and the electron survival time. In the vertical plane a single bunch head-tail like instability occurs. A method is described by which we can estimate an equivalent impedance, created by the electron cloud.

1 OBSERVATIONS

In the SPS the e-cloud is mainly created in the dipoles. This can be seen from the vacuum pressure rise in the ion pumps and vacuum gauges, which is only observed in the arcs and not in the straight sections. The instability starts somewhere from bunch number 15 to bunch number 30, depending on the bunch intensity. For high bunch intensities the instability starts earlier in the batch.

The characteristics of the instability are quit different in both planes. In fig. 1 and 2 for example, one can see a snapshot over one turn of the position of the first 48 bunches in the batch. In fig. 1, which is the horizontal plane, the instability starts after some 400 nsec i.e. 16 bunches and it looks like slow wave over more than 20 bunches. In the vertical plane, the instability starts also after ~16 bunches but there is no apparent phase correlation between subsequent bunches.

The two dimensional plots in fig. 3 summarise the main observations on the instability in both horizontal and vertical plane. The first two pictures on the top show the oscillation amplitude as function of bunch number and turn number. One can see that the horizontal oscillation sets on after only 50 turns, whereas in the vertical plane it takes about 500 turns. These pictures were taken for a bunch intensity of 3 10^{10}, just above the threshold. For bunch intensity twice as high, 6 10^{10}, the horizontal rise time stays the same (50 turns), but the vertical rise time reduces to 100 turns.

The second row of plots shows the tune as a function of the bunch number. In the horizontal plane one can see a second distinct tune line appearing as from bunch number ~16, i.e. the bunches which are sitting in the cloud. The second line is 0.03 higher in tune than the first one.

In the vertical plane the tune line widens for the bunches that are sitting in the cloud. Detailed spectra show several synchrotron sidebands around the main tune line.

The two bottom pictures show a two dimensional FFT. It shows the betatron tunes in one dimension and the frequency of the oscillation inside the batch. These plots confirm what is suggested by the snapshots in fig. 1 and 2. The horizontal instability shows up like a low frequency inside the batch, i.e. a coupled bunch instability of low order. The vertical mode spectrum looks like a white spectrum, covering the whole frequency range, suggesting a non-correlated motion between the bunches. In the vertical plane the motion looks like a single bunch instability.

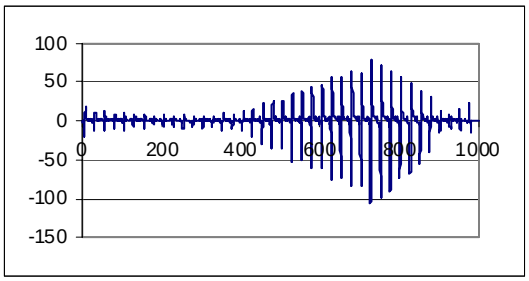

Fig. 1: snapshot of the horizontal position of the first 48 bunches in the batch when the instability is present.

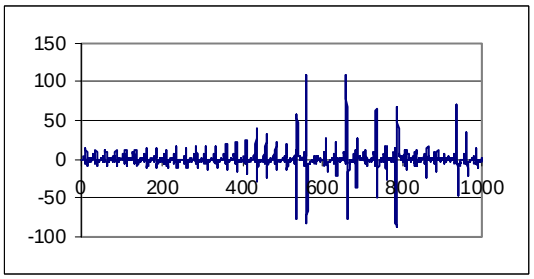

Fig. 1: snapshot of the vertical motion of the first 48 bunches in the batch when the instability is present.

We can summarise the observations as follows:

- In the Horizontal plane the e-cloud provokes a fast growing coupled bunch instability of low order. Growth rate is ~50turn. Does not change with intensity.
- In the vertical plane the instability looks like single bunch instability Growth rate: ~500 turns just above threshold going to ~100 turns at two times the threshold.

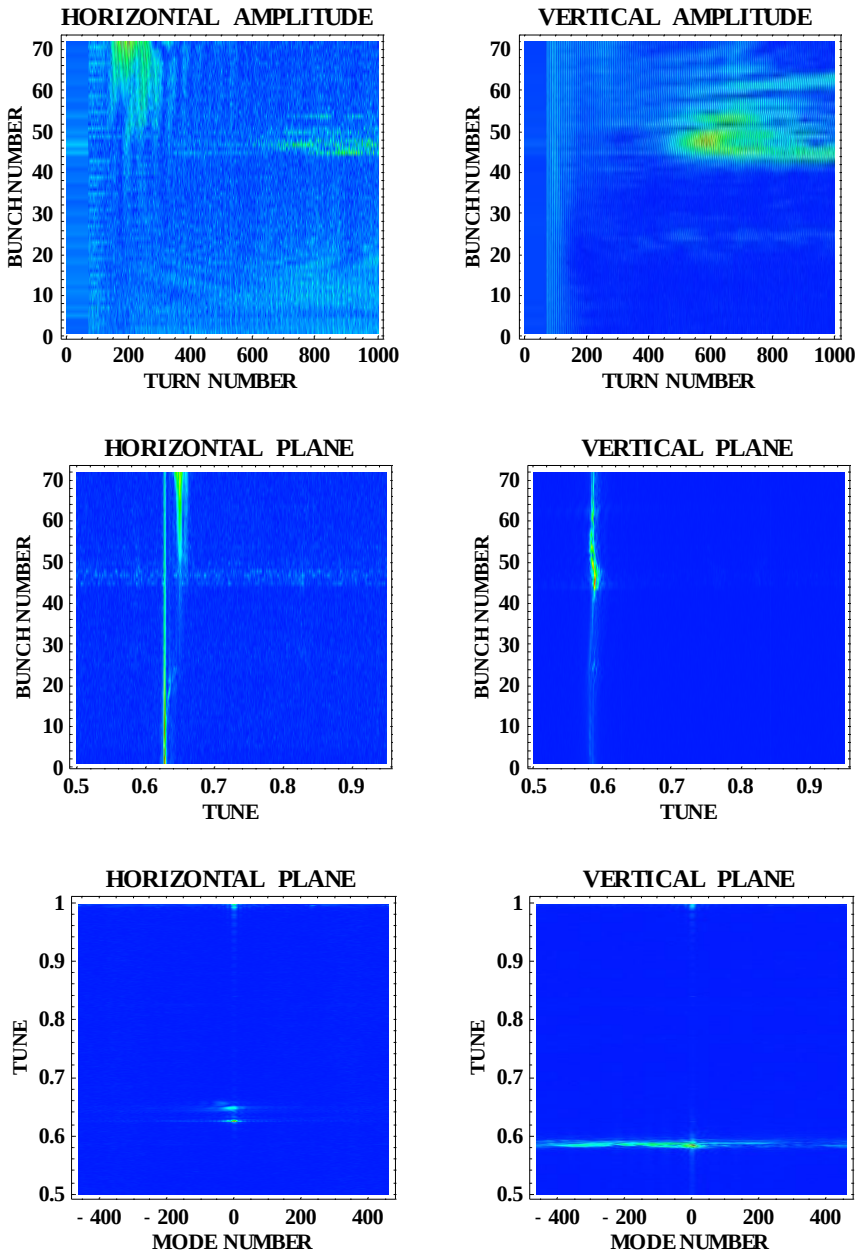

Fig. 3 Two-dimensional plots showing the main characteristics of horizontal and vertical instabilities. The top row shows the oscillation amplitude as function of turns and bunch number. The middle shows the tune versus bunch number and the bottom shows the mode number inside the batch.

1 THE HORIZONTAL INSTABILITY

The difference between horizontal and vertical behaviour comes from the fact that the electron cloud is created in the dipoles. The combination of a vertical magnetic field and the flat vacuum chamber makes that the electrons are mainly bouncing up and down, spiralling around the magnetic field lines, creating a vertical ribbon at the position of the bunches. It is this behaviour, which creates a coupling mechanism between subsequent, bunches in the horizontal plane. When a bunch passes at a different horizontal position than the previous ones, it will go off-centre through the electron cloud and experience a force proportional to the displacement (fig. 4).

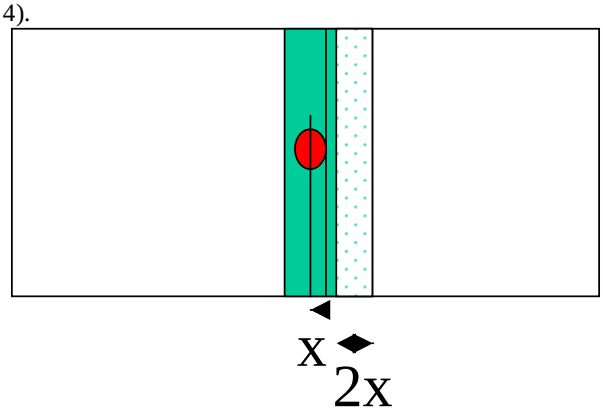

Fig. 4: the force on a bunch displaced by x is equal to force from a slice of the ribbon with thickness 2x (the light green part). The forces in dark green part cancel out because of symmetry.

In a linear approximation the horizontal force of the e/cloud can be expressed as:

$$F = -\rho e.(X_{n+1}-X_n)/2\varepsilon_0$$

With ρ the electron density, Xn the horizontal position of the nth bunch.
The behaviour of the 72 bunches in a batch can be expressed in the following set of coupled oscillators:

$$X_1'' + \omega_\beta^2 X_1 = 0$$
$$\vdots$$
$$X_n'' + \omega_\beta^2 X_n = 0$$
$$X_{n+1}'' + \omega_\beta^2 X_{n+1} = -k(X_{n+1} - X_n)$$
$$\vdots$$
$$X_{72}'' + \omega_\beta^2 X_{72} = -k(X_{72} - X_{71})$$

ω_β being the betatron frequency. The first n bunches see no electron cloud and they behave like uncoupled oscillators. As from the n+1th bunch there is a coupling via the electron cloud with the previous bunch. This degenerate system gives two eigen-frequencies (Ω) given by:

$$(\Omega^2-\omega_\beta^2)^n(\Omega^2-\omega_\beta^2-k)^{72} = 0$$

One mode is the unperturbed betatron frequency. This is the mode where all bunches move in phase with the cloud. The second mode has a slightly higher frequency and it corresponds to the modes where bunches move with a different phase.
The corresponding tune shift can be calculated from the force exercised by the cloud:

$$dP/dx = dt\ dF/dx = \rho e.ds/\varepsilon_0 c$$

P is the transverse momentum, s de longitudinal coordinate and c the speed of light. The normalised kick can be written as:

$$k = dP/dsdxP = \rho e/\varepsilon_0 cP$$

Expressing P in eV/c this becomes for the SPS energy of 26GeV:

$$k = \rho/\varepsilon_0 26\ 10^9$$

The corresponding tune shift is then:

$$\Delta Q = \rho\{\beta\}L/\ \varepsilon_0 26\ 10^9$$

with L the total length of the dipoles in the SPS.

3 THE VERTICAL PLANE

In the vertical plane things look quit different. During the bunch passage, the electrons are accelerated in the vertical plane towards the centre of the bunch. Some electrons are even trapped inside the bunch leading to an increased electron density inside the bunch [1]. Fig. 5 and 6 show the different behaviour of the electron phase space during the bunch passage. In the horizontal plane (fig.5), the dynamics is completely dominated by the magnetic field creating a cyclotron motion. The bunch passage has no influence on the phase space density. In the vertical plane however (fig 6) there is a build up of electron density inside the bunch. This phenomenon creates a coupling between the head and the tail of the bunch. When the tail passes at a different vertical position as the head, it will experience a force from the displaced electron density. This creates the same coupling

mechanism as a wake field, leading to head tail instability. However, there are two major differences with the normal wake field: the longitudinal dependence of the force can not be written as a greens function and the frequency content of the “electron-wake” changes with the bunch intensity. For higher bunch currents the electrons impinge much faster (fig 7)

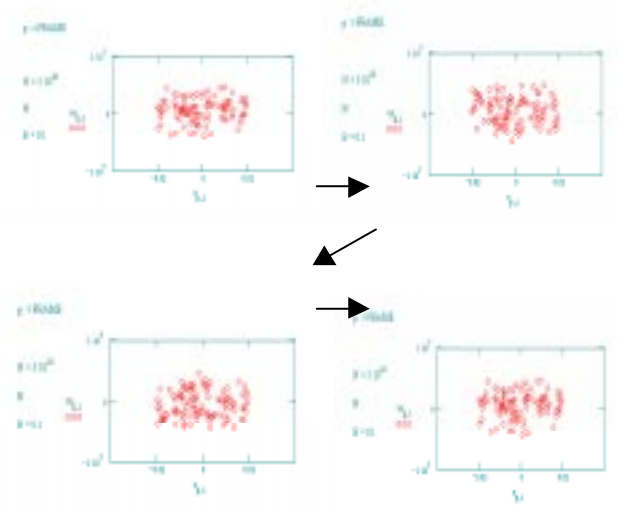

Fig. 5: Evolution of the electron phase space during the bunch passage in the horizontal plane.

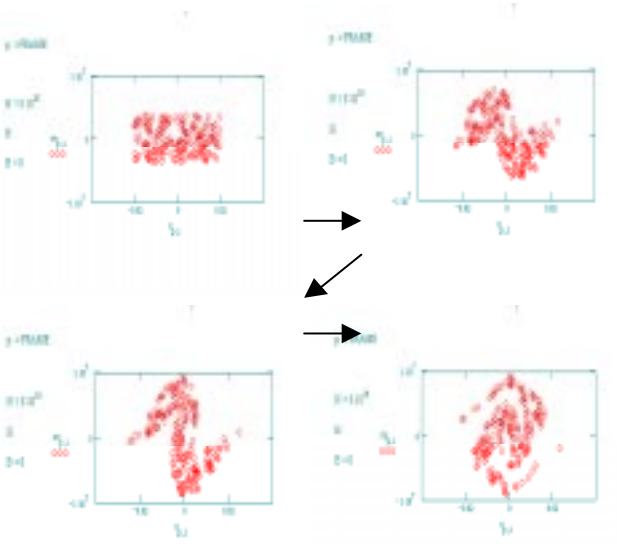

Fig. 6: Evolution of the electron phase space during the bunch passage in the vertical plane.

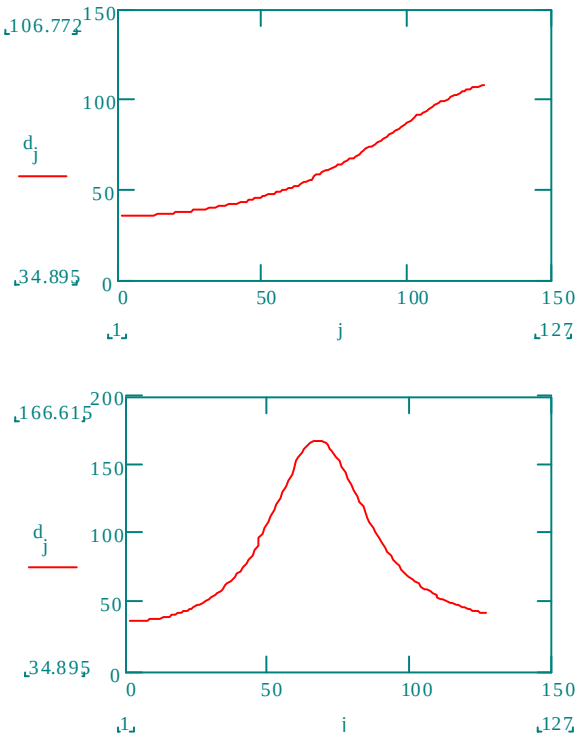

Fig. 7: Evolution of the vertical electron cloud density during the bunch passing. The top is for a bunch intensity of 2.5 10^{10}, the bottom for 8 10^{10}.

If there is something like an equivalent vertical impedance, created by the electron cloud, can we measure it? For this one has to measure de effect of the impedance on an individual bunch inside the cloud. A technique, which can be used, is to look at the betatron phase evolution over one synchrotron period (fig 8) after a vertical kick [2].

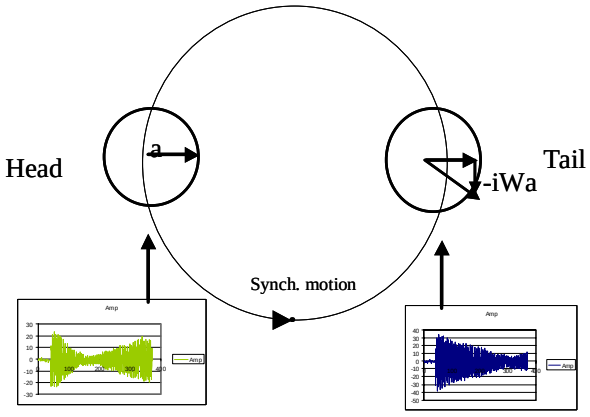

Fig. 8: The wake field W creates a phase advance for the tail depending on the position of the head. Following the phase evolution of head and tail over a synchrotron period can give details about W.

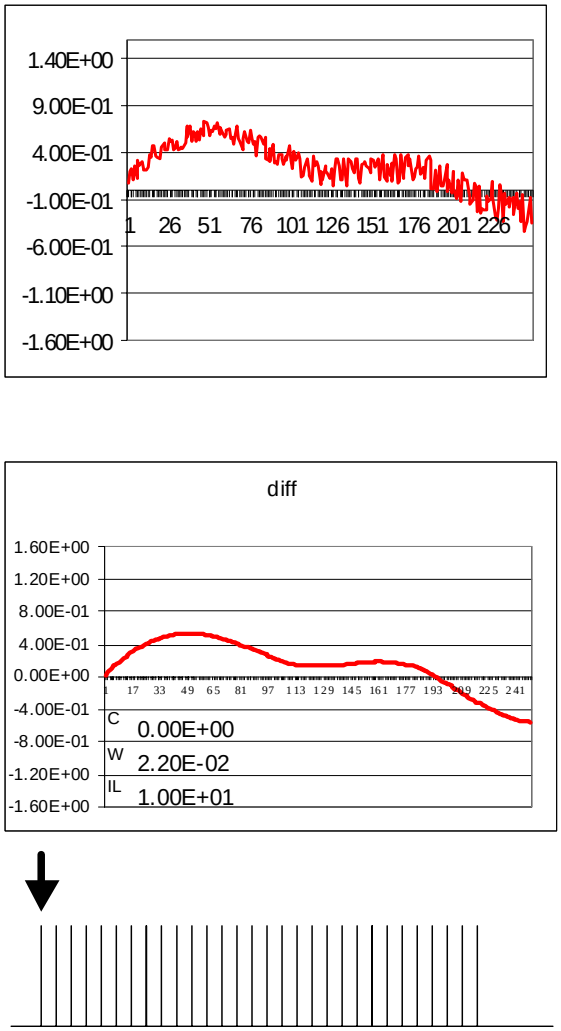

Fig 9: Calculated (bottom) and measured (top) head-tail phase advance difference for the first bunch.

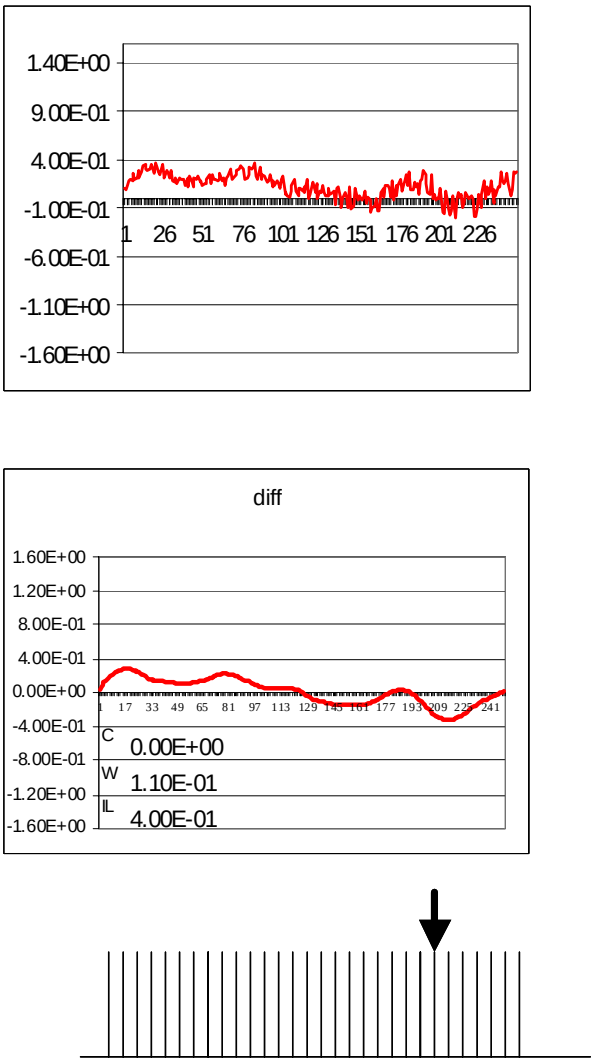

Fig 10: Calculated (bottom) and measured (top) head-tail phase advance difference for a bunch. Sitting in the e-cloud

In fig. 9 de result of such a phase measurement is presented. What is shown is de evolution of the phase difference between head and tail over one synchrotron period and this for the first bunch of the train. The bottom picture shows a calculation of this phase difference using a long wake field, i.e. longer than the bunch.
In fig 10 de same measurement is shown, but for a bunch sitting in the cloud. In order to be able to recalculate the measured data a wake field is needed with a shorter interaction length (0.3 t0 0.5 times the bunch length). This leads to a picture of the wake field as shown in fig 11.

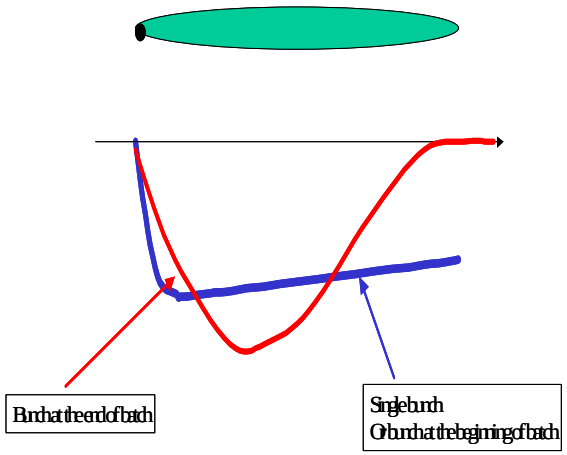

Fig 11: Picture of the equivalent wake field, created by the electrons (red), compared to the machine impedance (bleu).

4 CONCLUSIONS

- In the SPS the electron cloud is created in the dipoles.
- It results in a fast, horizontal coupled bunch instability of low order that can be cured by the existing feedback.
- The vertical instability is of single bunch nature (higher head tail mode). The growth rate depends on intensity.
- The equivalent short wake, created by the electrons could be measured.

REFERENCES

[1] G. Rumolo, *Theory and simulation of electron-cloud instabilities*, proceedings of the 11th Chamonix workshop, CERN, 2001.

[2] K. Cornelis, *SPS measurements of electron cloud impedance*, proceedings of the 11th Chamonix workshop, CERN, 2001.

Electron Cloud with LHC-type beams in the SPS: a review of three years of measurements

J.M. Jimenez, G. Arduini, P. Collier, G. Ferioli, B. Henrist, N. Hilleret, L. Jensen, K. Weiss, F. Zimmermann
CERN, Geneva - Switzerland

Abstract

In August 1999, high bunch intensities LHC-type beams were injected for the first time in the SPS inducing strong vacuum pressure rises, perturbations on the electrostatic pick ups and beam instabilities. Evidences of the electron cloud phenomenon as the mechanism responsible for these instabilities are reviewed. This paper present also the results obtained with several detectors installed in the SPS machine to improve the understanding of the electron cloud mechanism and refine the simulations. The spatial distributions of the electrons in the cloud are shown in presence of and without a dipole magnetic field. The effects of the beam intensity and filling pattern on the behaviour of the electron cloud are presented. The scrubbing effect is studied using an in-situ measurement of the secondary electron yields. Finally, the potential limitations due to the electron cloud in the SPS and the issues for the LHC are discussed. Possible remedies will be presented, i.e. nitrogen and argon glow discharges or new filling schemes. A table of contents located at the end of this paper gives detailed information on the subjects covered.

1 Introduction

Pressure rises in presence of LHC-type[1] beams were highlighted in August 1999 [1]. Fig.1 shows that the pressures increase only in presence of the LHC type beams. With the fixed target SPS[2] proton beams, the pressures recover with a time constant consistent with the effective pumping speed. Pressure increases by a factor of 50 to 60 were recorded in the arcs and in the long straight sections. The maximum pressure measured was 10^{-5} Pa for a proton bunch intensity of 5.8×10^{10} p/b and a duty cycle close to 62%. The average static pressure in the SPS was 10^{-7} Pa.

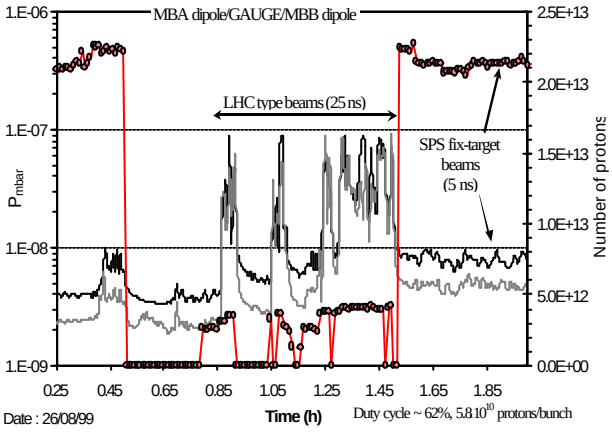

Fig. 1: Pressure rises versus time, 5.6×10^{10} p/bunch, single batch (81 bunches), duty cycle 62 %.

Below a given threshold (4.0×10^{10} p/b in August 99 in field free regions), no pressure rise was observed and a biased pick-up collector shielded from the beam by a metallic grid detected no signal. Above the threshold of the electron cloud, pressures raise and with a single batch, the shielded pick-ups detected peaks of current separated by 23 μs which corresponds to the revolution time in the SPS. Fig.2 shows the signal detected at 7.5×10^{10} p/b.

The transverse feedback system ("damper") used in the SPS to damp injection oscillations and to stabilize the beam against transverse coupled bunch instabilities was also strongly perturbed [2]. The vertical position signal induced by a single batch showed a drift of the signal starting half through the 2-μs batch (Fig.3). This drift is due to electrons hitting the pick-up electrode. The threshold intensity of this phenomenon, around 4.0×10^{10} p/b, was increased up to 7.0×10^{10} p/b by applying a longitudinal solenoid magnet field of 100 Gauss (10^{-2} T) giving a clear indication that electrons, in the vacuum chamber, were at the origin of the effect.

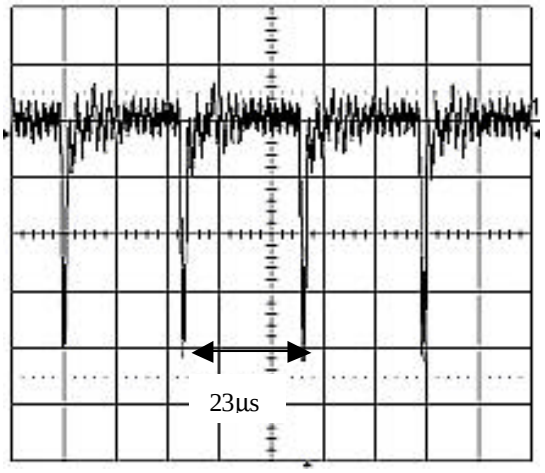

Fig.2: Structure of the current collected by the pick-up with a proton bunch intensity of 7.5×10^{10} (bias +45V)

[1] 3-4 batches of 72 bunches separated by 225 ns, 25 ns bunch spacing, $1.1\text{-}1.7 \times 10^{11}$ p/b (81 bunches in 1999), bunch length: 4 ns.

[2] 2 trains of 2100 bunches separated by 1 ms, 5 ns bunch spacing, $1.0\text{-}2.0 \times 10^{10}$ p/b

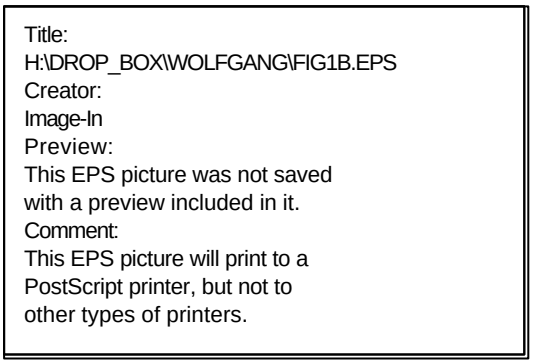

Fig.3: Vertical damper pick-up signal perturbed by electron cloud effect (6.8x10^{10} p/bunch) [2].

In the SPS or in the LHC, electrons created at the vacuum chamber wall, will be accelerated by the proton bunches up to 200 eV and will need less than 5ns to cross the chamber[3]. A significant fraction of the electrons will be lost with the nominal spacing of 25ns, except the electrons with an energy below 10eV, which will survive and be kicked up to several keV by the following bunches. This non resonant single pass mechanism may lead to an electron cloud build up if the maximum secondary electron yield (SEY) δ_{max} of the chamber wall is larger than a critical value, typically around 1.3 [3][4]. The critical value is 1.15 [5] if the contribution of the reflected electrons is taken into account in the secondary electron yield coefficient (SEY). Then, the electron cloud is amplified at each bunch passage and reaches a saturation value determined by the space charge repulsion with implications for the beam stability, emittance growth [6] and heat load on the LHC cryogenic system [7][8].

The observed threshold bunch intensity has a weak dependence on the residual gas pressure, contrary to ion effects and is in agreement with electron cloud simulations. Measurements showed that for bunch intensities above 7.0x10^{10} p/bunch, the weak solenoid field becomes insufficient in view of the keV energies acquired by the electrons near the beam axis.

An issue for the vacuum system of the SPS, as the LHC injector, is to avoid any emittance growth due to the gas density since this emittance will be preserved in the LHC leading to a degradation of the luminosity. The emittance growth due to a residual pressure (N_2 equivalent) is given by:

$$\frac{\partial e}{\partial t} = 1.2\ 10^{-3} \langle b \rangle \frac{P(Pa)}{g} \quad [9]$$

where g is the relativistic factor. For a b of 40 m and an average pressure below 10^{-6} Pa, the emittance growth due to the beam-gas interaction is negligible[4].

The electron cloud can drive multi [10][11] and single bunch instabilities [12][13][14][15][16], and it can also induce coherent and incoherent tune shifts. Electrons near the beam are thought to be responsible for the single bunch instability. A broadband pick-up at the SPS has allowed the detection of motion inside the bunch, and to fit for the period of the effective wakefield [17]. The result is consistent with the estimated electron oscillation wavelength, and with the proposed instability model based on a head-tail interaction [13][14][16].

Beam instabilities induced by the electron cloud will not be covered in this paper, which aims to resume the observations in the SPS, to crosscheck and give inputs to refine the simulations and to validate the scrubbing scenario proposed for the LHC.

2 Measurable and Set-ups description

Table 1 shows the different types of detectors, which were used to study the electron cloud phenomena and to measure the beam effects.

	Field free region	Dipole field region
Electron cloud phenomena		
e⁻ cloud activity (intensity)	Electrons energy analyser, strip detectors	
e⁻ cloud build-up	Pick-ups	-
Energy distribution of the electrons	Electrons energy analysers	
	Electrostatic energy analyser	-
	Retarding field detector	-
Spatial distribution of the electrons	Strip detectors (16 channels)	
Secondary electron yield measurements (δ)	Secondary Electron Yield (δ) set-up	
Surface treatment to cure e⁻ cloud	Pressure, pick-ups	-
Beam effects		
Bunch intensity	Pressures, strip detectors	
Filling pattern		
Batch length		
Missing bunches		
Bunch spacing		
Bunch length		
Batch spacing		
Filling factor		
Scrubbing	Secondary Electron Yield (δ) set-up, pressures	

Table 1: *Different types of detectors and the corresponding measurable parameters.*

2.1 Pressure gauges and pick-ups

The majority of the electrons from the cloud will be lost on the vacuum chamber walls inducing pressure rises by the electron stimulated desorption (ESD) phenomenon. In the SPS, the pressure rises are a direct signature of the electron cloud activity and therefore, the 70 pressure gauges installed all around the SPS ring give an indication of the electron cloud activity. This simple technique is sensitive to a small variation of the beam parameters, i.e. 5% of variation of the bunch intensity above the electron cloud threshold is measurable. Nevertheless, variations of less than 10 seconds duration of the beam parameters cannot be studied due to the time constant imposed by the conductance of the vacuum chambers. Real pumping speed should also be taken into account when comparing $\Delta P/P$ at different locations in the SPS ring.

The electron cloud build up in the field free regions is studied using pick-up buttons screened from the beam by a grounded grid. A fraction of the electrons from the cloud are collected by a current integrator or measured using a scope. The 20 mm diameter buttons allow low RC time constant and therefore a single bunch can be seen using a scope (see Fig.4).

[3] SPS dipoles chambers: MBA: h=34.5mm/l=152mm, MBB: h=48.5mm/l=129mm, drift ID=ϕ156mm

[4] Injection cycle for the LHC: ~15 seconds.

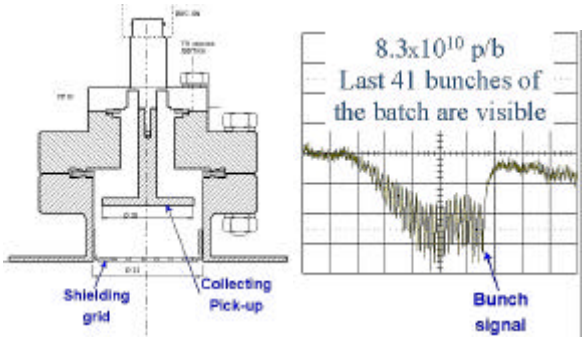

Fig.4: Drawing of a shielded pick up and a typical signal (-) obtained in presence of the electron cloud.

2.2 Strip detector: Spatial distribution of the electrons

Preliminary measurement on the electron cloud indicates different behaviours in presence or not of a dipole magnetic field and simulations predicted the appearance of two strips above a given bunch intensity: 5.5×10^{10} p/bunch.

To confirm these simulations and study the spatial distribution, a 16 copper strips detector was installed in the SPS. The copper strips, deposited on a MACOR™ substrate in the longitudinal plane, allow the collection of a fraction of the electrons from the cloud. The strips, which remain under vacuum, are separated from the beam by the vacuum chamber wall in which hundreds of holes (ϕ 2mm) are drilled with a total transparency of 7.5 % to avoid the extinction of the multipacting by an excessive collection of electrons. The distribution of the holes was calculated to minimize the interference with the strips arrangement. The resulting sensibility shows a fluctuation of the transparency below 20%. The signal collected by each channel is measured individually using a current integrator with a minimum integrating time of 2 ms (~100 turns in the SPS). The detection limit of the current integrator is about 10^{-8} A for each individual channel. Fig.5 shows the signal of the electron cloud following a controlled beam bump of 8mm.

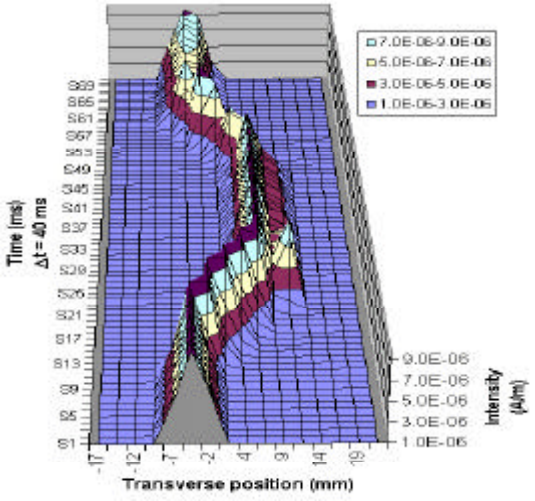

Fig.5: Signal of the electron cloud following a controlled beam bump of 8 mm.

3 Main results - Beam effects

3.1 Bunch intensity

Pressures in the SPS do not vary up to a threshold bunch intensity above which the pressures increase with the bunch intensity (Fig.6 and Fig.7). The amplitudes of the negative current signals measured on the pick-ups also increase with the bunch intensity (Fig.8a and Fig.8b). In August 1999, the threshold in the long straight section (field free region) was about 4.3×10^{10} p/b and increased up to 6.4×10^{10} p/b in April 2000 after several days of operation with high bunch intensity LHC-type beams. In the arc, the dipole magnetic field affects the behaviour of the pressure versus the bunch intensity (Fig.7). In presence of a dipole magnetic field, the measurements give consistently a lower threshold value, between 3.0 and 4.0×10^{10} p/b and higher-pressure rises.

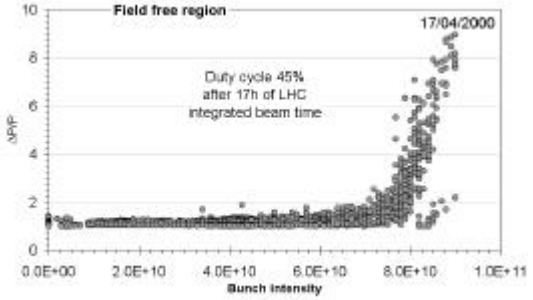

Fig.6: Pressure rise versus bunch intensity in a field free region. Static pressure 10^{-6} Pa, MBB-type aperture.

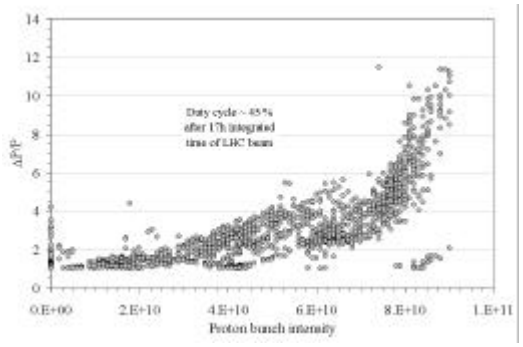

Fig.7: Pressure rise versus proton bunch intensity in a dipole region (arcs). Static pressure 10^{-6} Pa, MBB-type aperture.

The difference observed between the field free and the dipole regions has not been understood but cannot be attributed to systematic errors since the gauges are not influenced by the dipole magnetic field. One explanation could come from the simulations [7] which showed that, in a dipole magnetic field, the electrons are confined in the vertical plane. The number of electrons and their distribution in energy in the cloud will depend on the bunch intensity and therefore, in a dipole field, the impinged surface will depend on the bunch intensity. The entire vacuum chamber will not be bombarded and recontamination should be expected.

In the SPS and in presence of a strong electron cloud activity, the pressure limitations were mainly coming from the arcs (dipole field regions).

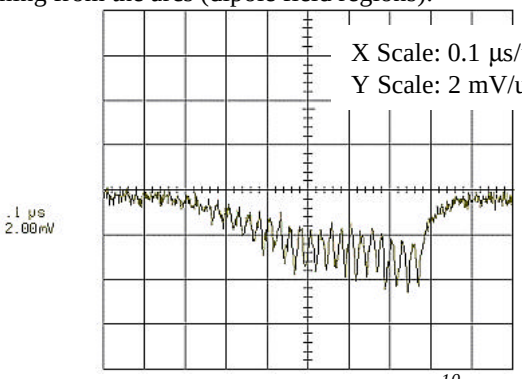

8a) Pick-up signal, bunch intensity of $6.9_{x}10^{10}$ p/b

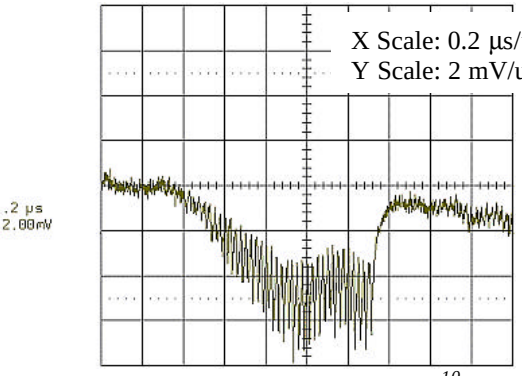

8b) Pick-up signal, bunch intensity of $8.3_{x}10^{10}$ p/b

Fig.8: Pick-up signals showing the effect of an increase of the bunch intensity

3.2 Filling pattern – Electron Cloud build up

3.2.1 Batch length – Electron cloud build up

The initial results obtained in the SPS [1] showed that the number of bunches needed to build up the electron cloud decreased when the bunch intensity increased. As an example, 32 bunches were needed at $6.5x10^{10}$ p/b, only 20 bunches at $7.9x10^{10}$ p/b (see Fig.9 and Fig.10). These results were confirmed also by observations on pick-ups (see Fig.8a and Fig.8b) which showed that the number of detectable bunches on the pick up signal increased with the bunch intensity.

3.2.2 Missing bunches

The batch of 72 bunches is made out of 6 trains of 12 bunches (Fig.11) and allowed the suppression of one of these trains. During the measurements, the 3rd and the 4th train were removed. The results showed that the pick up signals were affected by the 12 missing bunches (Fig.12) and the pressure rises decreased by a factor 8 (Fig.13). The pick-ups showed that the 4th missing train is more efficient than the 3rd one (Fig.12a and Fig.12b). No difference in the pressure rises could be seen between the two missing trains (Fig.13).

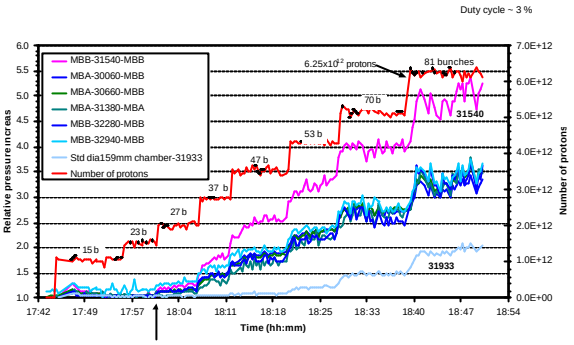

Fig.9: Relative pressure increase DP/P versus number of bunches at $7.7x10^{10}$ protons per bunch.

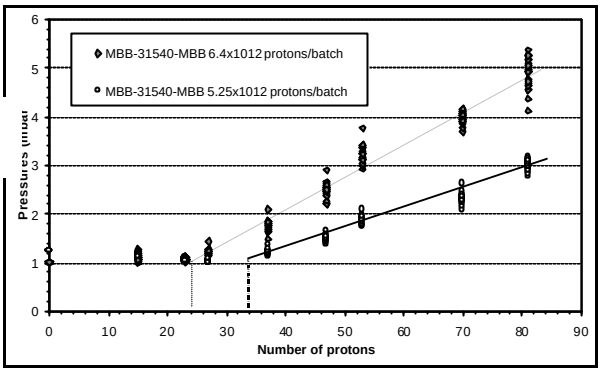

Fig.10: Relative pressure increase DP/P versus number of bunches in the batch (81 bunches) at $6.5x10^{10}$ and $7.7x10^{10}$ p/bunch.

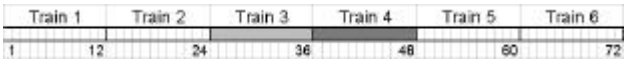

Fig.11: Filling pattern with 72 bunches made out of 6 trains of 12 bunches each.

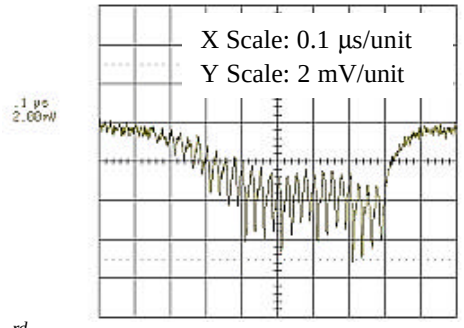

12a) 3rd missing train (12 missing bunches)

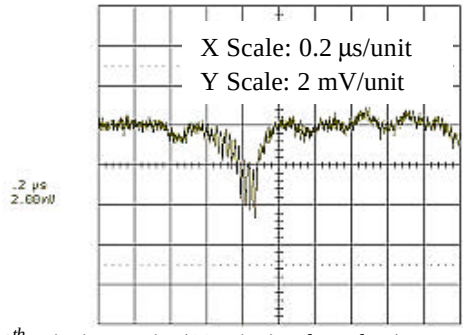

12b) 4th missing train (12 missing bunches)

Fig.12: Pick-up signals with 12 missing bunches.

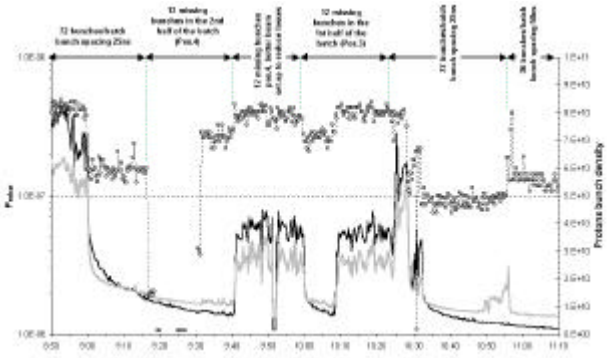

Fig.13: Pressures behaviour versus time with 12 missing bunches in 3rd and 4th positions.

3.2.3 Bunch spacing

The nominal LHC bunch intensity (10^{11} p/bunch) was achieved using the 50 ns bunch spacing and 36 bunches per batch instead of the nominal 72 bunches per batch. The resulting electron cloud activity was 10 times below as compared to the level measured with 5_x10^{10} p/b and 72 bunches per batch.

The electron cloud effect was also observed both by the strip detector and by the pressure gauges with the SPS fixed target beam with 5ns spacing. The presence of the electron cloud was only observed in specific conditions during the ramp from 26 to 450 Ge V where the beam is squeezed in all dimensions and therefore the bunch density is maximized. In normal operation, the bunch intensity is much below the threshold and this explains why the electron cloud is not observed in the SPS with the fixed target-type beams.

Using the nominal LHC bunch spacing, i.e. 25ns, the maximum intensity achieved in 2001 with a single batch was $8.0x10^{10}$ p/bunch. With 3 batches, the maximum bunch intensity achieved was $5.5x10^{10}$ p/bunch. Above these intensities, the pressure interlock was reached and the beam dumped. In addition, the strong electron cloud activity induced strong beam oscillations, which could not be damped by the RF damper [18].

The origin of the pressure limitations will be discussed in the paragraph on beam scrubbing.

3.2.4 Bunch length

Qualitative measurements on the effect of the bunch length on the electron cloud were made using the strip detector. Fig.14 shows an enhancement of the electron cloud activity when the bunch length was decreased from 5ns down to 2ns. As the transverse emittance remained stable, this is easily understandable since in these conditions, a decrease of the bunch length result in an increase of the bunch density leading to a stronger electron cloud activity [19].

3.2.5 Filling factor - Batch spacing

Three to four batches of 72 bunches will be injected into the SPS, ramped from 26 GeV to 450 GeV and then injected into the LHC. The standard LHC 8 bucket spacing [225ns] showed that the electron cloud did not disappear between two successive batches. All this was evidenced by pick up measurements with 2, 3 and 4 successive batches (see Fig.15). The pick-ups even showed that the build up of the 2nd, 3rd or 4th batch profits from the cloud created left behind by the previous batch resulting in a faster build up.

Other batch spacing have been studied to reduce the electron cloud effect, i.e. 21 bucket [550 ns] and ¼ of the SPS evolution time [5.25 μs] instead of the standard 8 buckets spacing [225 ns]. Results obtained on the pick ups (see Fig.16) showed that a batch spacing bigger than 550 ns [21 bucket spacing] is required to decouple the effect of two successive batches on the electron could build up. Fig.17, obtained using the strip detector, shows no difference between the two batch spacings 225ns and 550ns on the total electron cloud activity.

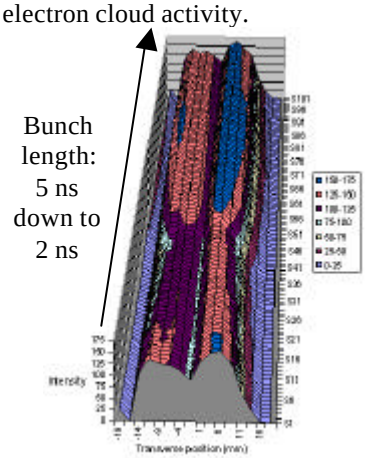

Fig.14: Effect of the bunch length on the electron cloud activity. Results obtained with the strip detector.

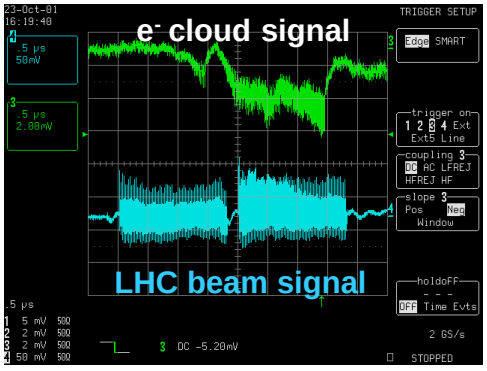

15a) 2 batches of 72 bunches [225ns batch spacing]

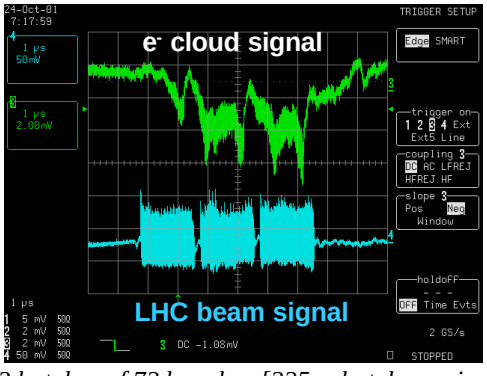

15b) 3 batches of 72 bunches [225ns batch spacing]

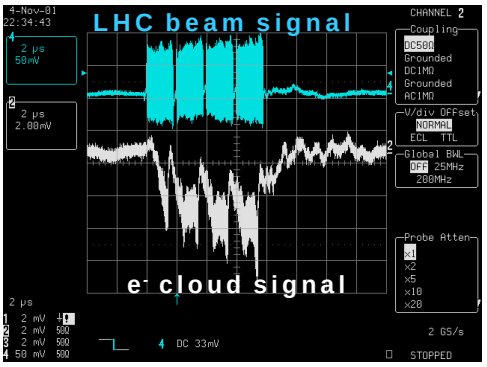

15c) 4 batches of 72 bunches [225ns batch spacing]

Fig.15: Pick up signals with a multi-batch injection [nominal 225 ns LHC batch spacing].

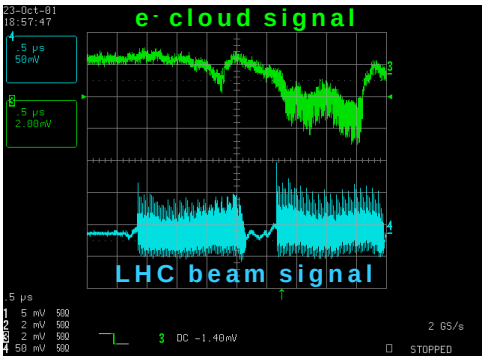

16a) 2 batches [550 ns spacing]

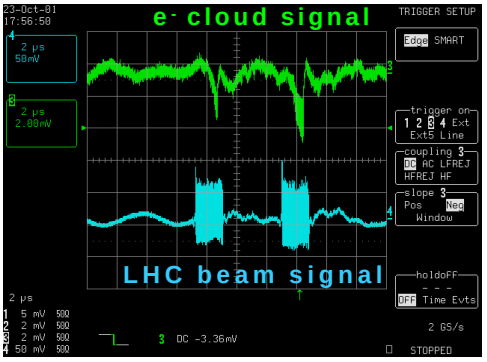

16b) 2 batches [5.25 ms spacing]

Fig.16: Pick up signals of the electron cloud build up with two different batch spacing [550 ns and 5.25ms].

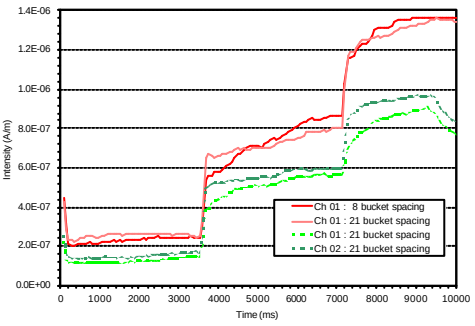

Fig.17: Results obtained using the strip detector, showing no difference between the two batch spacing [225 ns and 550 ns] on the total electron cloud activity.

Fig.18 obtained with the strip detector shows the increase of the electron cloud activity after injecting the 2nd and 3rd batch. The two strips (or bands) visible in Fig.18 will be discussed later on in the paragraph on dipole field effects.

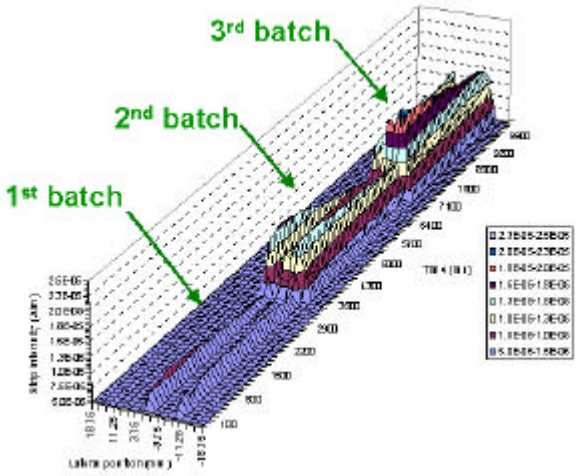

Fig.18: Electron cloud activity measured using the strip detector with a multi-batch injection in a dipole field.

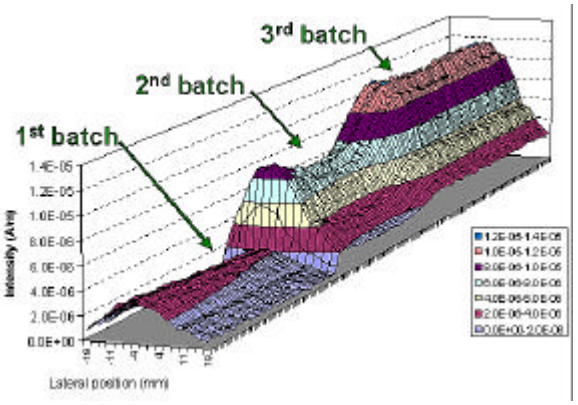

Fig.19: Electron cloud activity measured using the strip detector with a multi batch injection in a field free region.

Above the threshold in the field free regions, the strip detector can also be used to visualise the electron cloud in a field free region. Fig.19 gives a 3D view with 3-batch injection. As for the dipole regions, the electron cloud activity increased after the 2nd and 3rd batch injection. The non-isotropic angular acceptance of the strip detector resulted in a non-flat distribution. A flat distribution is expected in the field free regions.

4 Effect of a dipole magnetic field

The simulations made for the LHC [5] pointed out the strong effect of a dipole magnetic field on the electron cloud. A longitudinal magnetic field has been successfully used in *B* factories, e.g. KEKB, PEPII [20][21][22] and SPS [2] to reduce the electron cloud activity. A transverse dipole field will force the electrons to follow a cyclotron motion depending mainly on the beam potential and on their lateral position before being kicked by the beam. This cyclotron motion will, also influence all the detectors

including the strip detector used to study the electron cloud in a dipole field. The effect of the dipole field on the electron cloud behaviour and the limitations of the different detectors used will be discussed.

4.1 Appearance of two strips at high intensities

Above a given threshold, which is related to the energy of the δ_{max} (secondary electron yield) of the chamber wall and to the energy of the electrons, simulations predicted the appearance of two strips in the cloud in a dipole field (see Fig.20). The distance between the two strips will increase with the beam potential and does not depend on the magnetic field strength. If the bunch dimensions are assumed to remain constant (bunch length, transverse emittance), the bunch potential varies as the bunch intensity. The minor variations observed with the strip detector with the magnetic field strength arise from the dependence of the acceptance of this detector on the magnetic field. This dependence is mainly due to the diameter of the holes (ϕ 2mm), which at a field of B= 10^{-2} T is close to the Larmor radius of the high-energy electrons (> 200 eV).

The increase of the width of the electron cloud when decreasing the magnetic field strength is not yet understood (Fig.21) and will be studied in the future with a higher resolution strip detector.

Fig.22 shows the position of the two strips at two different bunch intensities.

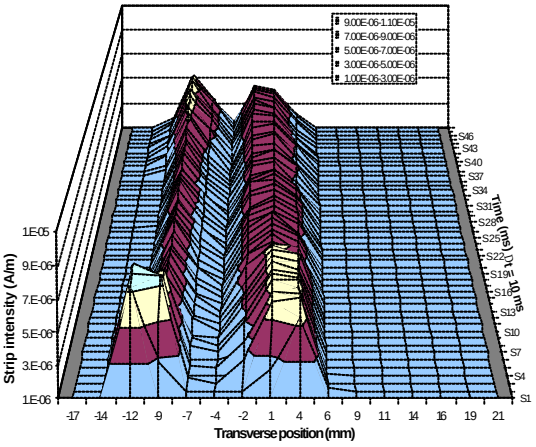

Fig.20: Appearance of two strips in a dipole field above a threshold, in this case: 6.0_x10^{10} p/bunch.

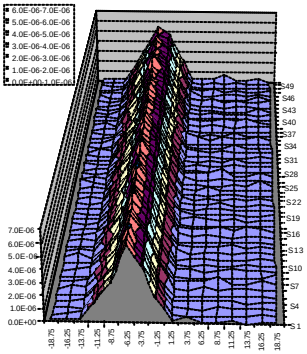

21a) Dipole field of 0.2 T

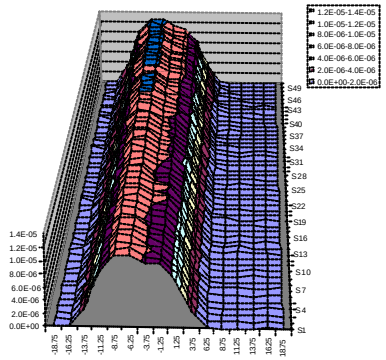

21b) Dipole field of 2_x10^{-2} T

Fig.21: Effect of the magnetic field strength on the electron cloud (5.0_x10^{10} p/bunch, single batch)

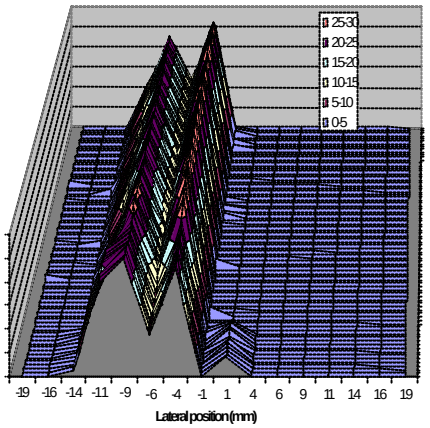

22a) Position of the two strips at 5.0_x10^{10} p/bunch

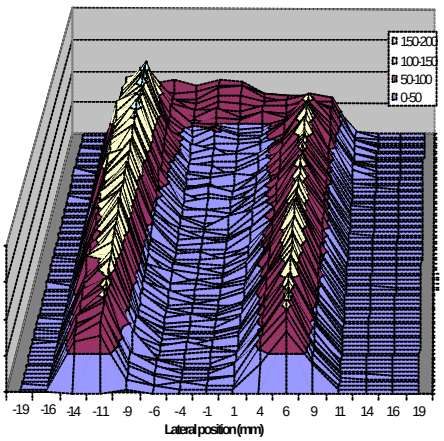

22b) Position of the two strips at 8.6_x10^{10} p/bunch

Fig.22: Position of the two strips depending on the bunch intensity.

4.2 Threshold of the dipole field effect

The strip detector showed that weak dipole field strength has a strong effect on the electron cloud. The strip detector used at bunch intensities below the threshold for the field free regions showed that a dipole field of 20 to 30 Gauss is required to trigger the electron cloud (see Fig.23 and Fig.24).

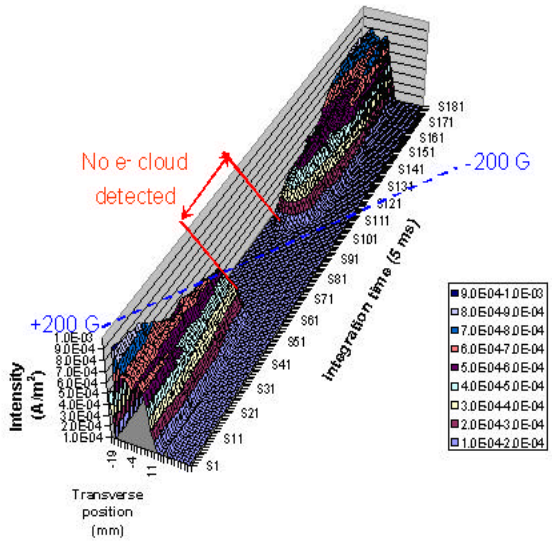

Fig.23: 3D view showing the disappearance of the electron cloud below 20 Gauss ($2x10^{-3}$ T).

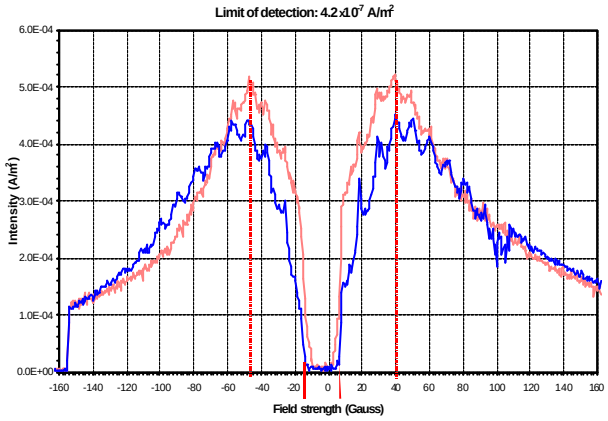

Fig.24: Intensities collected by two different strips as a function of the dipole field strength.

5 Beam scrubbing

In the SPS, the pressure rises (ΔP/P) are a direct signature of the electron bombardment. The beam scrubbing (or the scrubbing) effect characterises a decrease of these pressures rises. This decrease of ΔP/P results from both a cleaning of the surface (gas desorbed by the electron bombardment and pumped) and a reduction of the electron cloud activity as a result of the decrease of secondary electron yield (δ) of the inner chamber walls.

The scrubbing effect was studied in details to quantify the scrubbing time required in the SPS, after a shutdown, before being able to inject the LHC. Another objective of these measurements is to validate the "scrubbing scenario" proposed for the LHC. This scenario is based on the decrease of the SEY (δ) with the subsequent reduction of the heat load in the LHC cryogenic circuit.

In addition to the variation of the ΔP/P of the 70 gauges around the SPS, the scrubbing effect was quantified using a set up which allowed an in-situ measurement of the secondary electron yield (δ) of a copper sample exposed to the bombardment of the electrons from the cloud (see Fig.25). After receiving a controlled dose, the copper sample was rotated towards the electron gun to measure the SEY. When required, the sample was masked from the beam to avoid any exposure with non-optimal beam conditions.

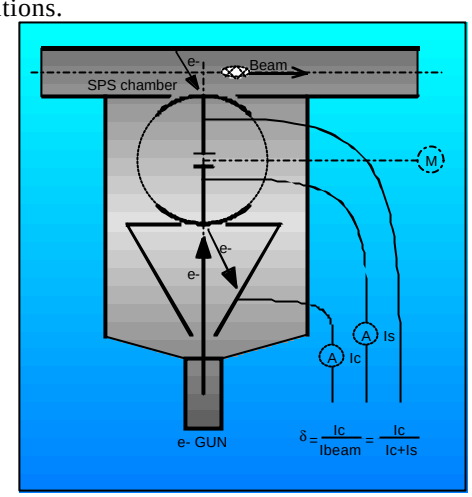

Fig.25: Schematic view of the in-situ SEY detector installed in the SPS

First measurements presented in 2000 [1][23] were made with a total integrated LHC beam time of about 60 hours. The decrease of the pressure rises was significant both in the field free and in the dipole field regions [23] (see Fig.26). An increase of the threshold bunch intensity was observed indicating a decrease of the SEY (δ) since the reduction of the outgassing rate by the electron stimulated desorption (ESD) can not explain this shift.

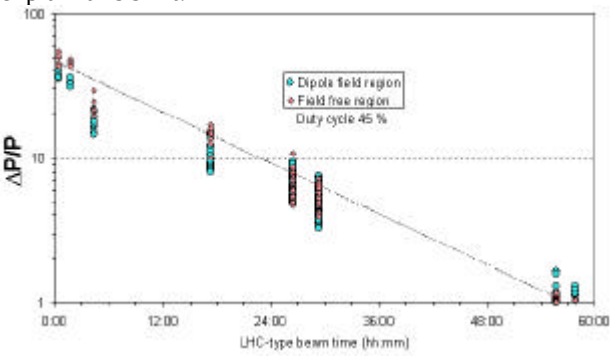

Fig.26: Pressure decrease observed both in the dipole and field free region with the LHC beam time in 2000.

The measurements have shown that the pressure rise decrease by a factor of 30 after about 2.5 integrated days of LHC-type beams. The beam scrubbing efficiency depends on the electron cloud activity and therefore on the bunch intensity. The higher the bunch intensity, the higher is the scrubbing effect. The beam time in Fig.26 corresponds to the cumulated time in presence of LHC-type beams with bunch intensities higher than $5.0x10^{10}$, which corresponded to the threshold of the electron cloud in the field free regions. Fig.26 shows a clear evidence

of a cleaning effect and no pressure increase can be seen after 60 hours of LHC-type beams.

The measurements have shown that the scrubbing effect is effective up to the bunch intensity used for the commissioning. If a beam with higher bunch intensity is injected, the pressure will increase. This observation is consistent with the displacement of the electron strips in the magnets when the bunch intensity increases.

Results obtained in 2001 were less encouraging in terms of pressure decrease versus LHC-beam time. The reduced scrubbing observed could be explained by the lower bunch intensities injected in the SPS in 2001 as compared to 2000 (Fig.27). In winter 2000-2001, the whole SPS was vented to air during about 5 months for an installation of the pumping port shielding[5][24]. Fig.28 shows a smaller threshold after venting which implies a higher electron cloud activity for the same bunch intensity. Measurements made in the Laboratory (Fig.29)[25] confirmed that a venting to air resets the SEY (δ) of a sample submitted to an electron beam scrubbing.

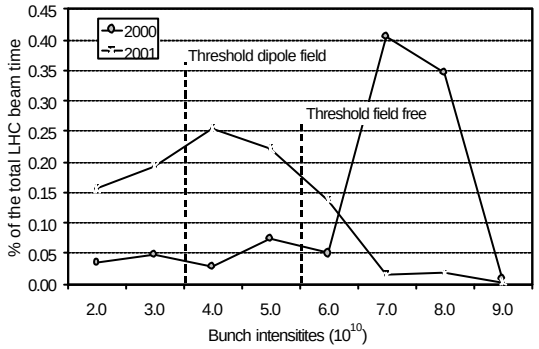

Fig.27: Distribution of the bunch intensities in 2000 and 2001

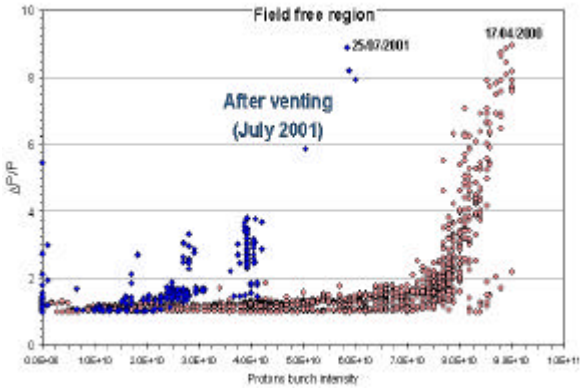

Fig.28: Threshold of the electron cloud in 2000 and in 2001 after a long venting to air of the SPS machine.

[5] Installed between all magnets to decrease the impedance of the SPS machine

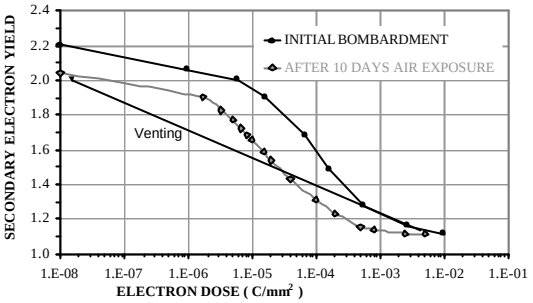

Fig.29: Measurements made in the laboratory showing the scrubbing effect with electron dose and the reset induced by a venting to air.

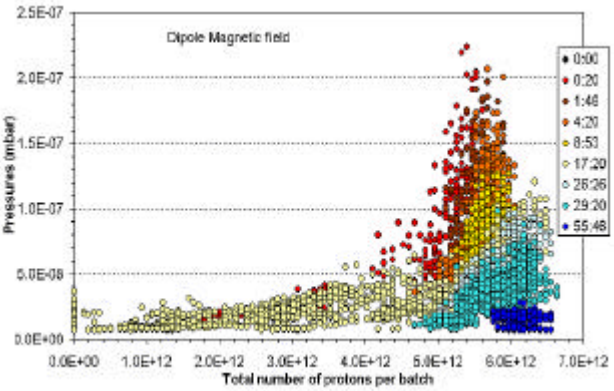

Fig.30: Threshold increasing with the LHC beam time.

The increase of the threshold of the electron cloud, as shown in Fig.30 is a clear indication of a decrease of the SEY. More recent measurements made in 2001 in the SPS with the in-situ SEY detector gave evidence of the decrease of the SEY with the LHC-Type beam time (Fig.31).

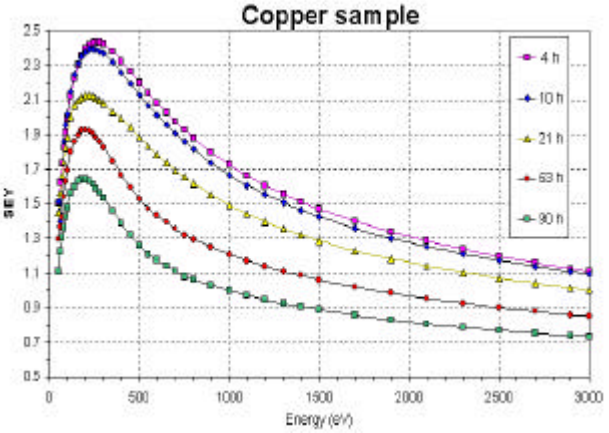

Fig.31: Decrease of the SEY of a copper sample exposed to the bombardment of the electrons from the cloud in the SPS as a function of the LHC-beam time.

Even with the relatively low bunch intensities injected in the SPS in 2001 (see Fig.27), the decrease of the SEY (δ_{max} and $E[\delta_{max}]$) is significant (see Fig.32). The value of the δ_{max} decreased from 2.4 down to 1.6 after less than 100 hours. More relevant is the evolution of the integral of the curve above a δ of 1.3, which is considered as the threshold of the

multipacting effect [3][4][5]. Fig.33 shows that the reservoir of secondary electrons decreased by more than 80% after about 100 hour of LHC beam time.

All the results presented above gave evidence of the scrubbing effect in the SPS. The lower efficiency observed in 2001 can be explained by the statically lower bunch intensities and therefore, the lower energies of the electrons impinging on the inner wall of the vacuum chambers.

All the results presented above gave evidence of the scrubbing effect in the SPS. The lower efficiency observed in 2001 can be explained by the statically lower bunch intensities and therefore, the lower energies of the electrons impinging on the inner wall of the vacuum chambers.

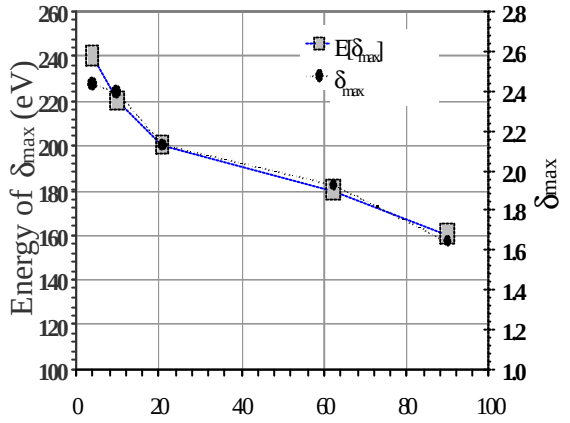

Fig.32: Decrease of the d_{max} and $E[d_{max}]$) with the LHC beam time

An important issue for the scrubbing is obviously the existence of the electron cloud effect. The higher the bunch intensity, the higher the electron cloud activity and the higher will be the scrubbing effect. Operating the SPS and the LHC below the electron cloud threshold will never be a solution since the SEY (δ_{max}) will remain high i.e. 2.3-2.4 for a copper sample.

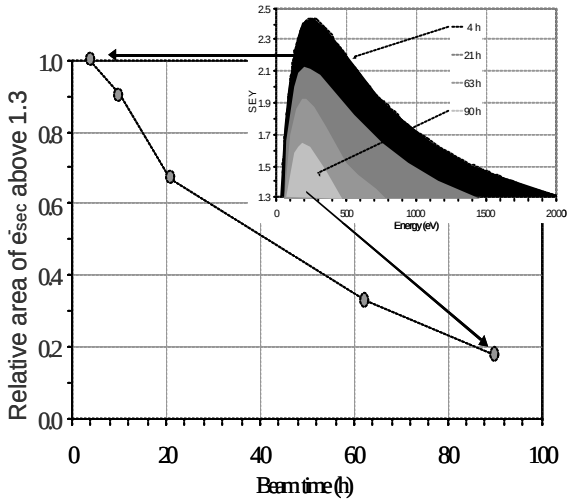

Fig.33: Decrease of the reservoir of secondary electrons with the LHC-beam time

5.1.1 Nitrogen discharge - Memory effect

No difference in the pressure rises nor in an increase of the scrubbing effect could be seen between the non treated vacuum chambers and the two chambers treated with a N_2 discharge.

Nevertheless, the chambers treated with a N_2 discharge and submitted to a beam scrubbing showed a faster conditioning compared to the non-treated chambers after an exposure to air and pressure rises were 4 times smaller.

More recent measurements were made to study the effect of an Ar/O_2 discharge and of a N_2 discharge followed by a 300°C bake out. These results confirmed that the N_2 discharge even after the bake out at 300°C during 24h had a behaviour identical to the non treated chambers. On the other hand, the Ar/O_2 discharge gave satisfactory results. The $\Delta P/P$ measured was 2.5 times smaller than the one measured on the identical non-treated chambers (see Fig.34).

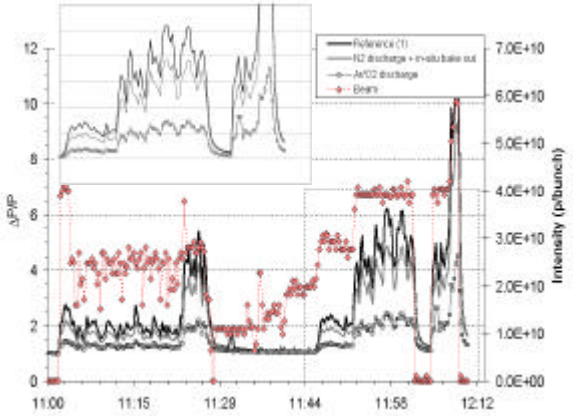

Fig.34: DP/P measured in dipole regions and in field free regions. Effect of an Ar/O_2 discharge and N_2 discharge followed by a 300°C bake out. Static pressure 10^{-6} Pa, MBB-type aperture.

6 Conclusions - Discussions

All the measurements confirmed the electron cloud as the mechanism being responsible for the pressure rises in the SPS: pick-ups measured an electron current signal, pressure rises occurred only in the presence of LHC-type beams and the strip detector gave a 3D view of the cloud. In addition, the behaviour of pressure rises versus bunch intensity is consistent with observations made in *B* factories, i.e. KEKb, PEPII [20][21][22]. As for KEKB, a small longitudinal magnetic field (10^{-2} T) partly cured the limitations induced by the electron cloud.

The electron cloud is a threshold mechanism, which depends on the existence or not of a dipole field. In presence of a dipole field, the threshold was around $2.0\text{-}3.0\times10^{10}$ p/bunch[6] and it was $5.5\text{-}6.0\times10^{10}$ p/bunch[5] for the field free regions. The threshold mechanism was confirmed by the measurements using the strip detector with bunch intensities between 3.0

[6] Nominal bunch length of 4 ns

and 5.5×10^{10} p/bunch. In presence of a dipole field, the electron cloud was observed and it disappeared immediately after suppressing the dipole field.

The beneficial effect of a 50 ns bunch spacing was evidenced. The nominal LHC bunch intensity (10^{11} p/bunch) was achieved with a single batch and the observed electron cloud activity was 10 times below the level expected. But the used of a higher bunch spacing will require an increase of the bunch intensity to keep constant the luminosity.

All the other parameters of the filling pattern were tested and showed a low efficiency in suppressing the electron cloud. Missing bunches did not suppress the electron cloud but decreased its intensity by a factor of 8. This is consistent with other measurements which showed that the electron cloud would need much more time to decay. Increasing the batch spacing would be effective only with a batch spacing higher than 550 ns which would lead to an unacceptable decrease of the LHC luminosity.

The cleaning effect or "scrubbing" was evidenced in the SPS using pressure gauges, pick-ups and in-situ SEY detector. In the SPS, the scrubbing effect results from the bombardment of the electrons from the cloud on the inner chamber wall. The higher the electron cloud activity, the higher will be the scrubbing efficiency. The measurements showed that, in less than three days of scrubbing in 2002, the pressure rises in presence of LHC-type beams become negligible in the SPS. This effect was visible both in the field free and in the dipole field regions with bunch intensities above 6.0×10^{10} p/bunch. A recontamination by the non-bombarded surface could explain the lower efficiency in the dipole regions due to the existence of two strips. All the measurements have shown an increase of the threshold bunch intensity, a decrease of the SEY (δ) from 2.3 down to 1.6 after 100 hours of LHC-beam time and a decrease by a factor 30 of the relative pressure increase $\Delta P/P$.

Operating any machine limited by the electron cloud below its threshold, in particular the SPS and the LHC, will never be a solution since the SEY (δ_{max}) will not decrease and will stay at 2.3 for a copper surface.

To reduce the scrubbing time, chambers treated by N_2 and Ar/O_2 discharges were installed in the SPS. In the first cycle of experiments no difference between the non-treated chambers and the two chambers submitted to a N_2 glow discharge have been observed. After an air exposure, only the treated chamber (N_2 discharge) seems to have a memory of the scrubbing effect. The in-situ bake out at 300°C did not improve the efficiency of this treatment. The Ar/O_2 discharge was more efficient; a reduction of the $\Delta P/P$ by a factor of 2.5 was measured.

The measurements in the SPS also confirmed that a venting to air will reset the scrubbing effect, i.e. the SEY (δ_{max}) value will increase back to its initial value 2.3.

7 Issues for the LHC machine

Contrary to the SPS machine which is limited by the pressure rises and beam instabilities in presence of a strong electron cloud activity, the LHC will be mainly limited by the heat load on the cryogenic system. Different parameters of the filling pattern could be used to decrease the heat load but measurements showed that the cloud was never suppressed. In addition, the bunch intensities should be increased above the nominal value (1.1×10^{11} p/bunch) to reach the nominal luminosity.

However, the strip detector gave issues for the design of the beam screen as the expected position of the electron cloud strips at nominal intensity coincides with the position of the pumping holes in the beam screen (Fig.35).

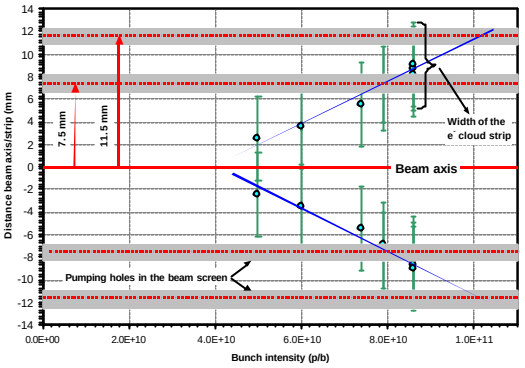

Fig.35: Measured position and width of the two strips on the SPS and their expected position at the nominal LHC-bunch intensity. The expected position is in coincidence with the position of the pumping holes in the initial design of the beam screen.

To avoid that the beam screen no longer ensures the interception of the heat load and that a non-negligible fraction of the electrons from the cloud impinge directly the cold bore, the position of the holes has been reviewed and an additional screen is being studied (see Fig.36).

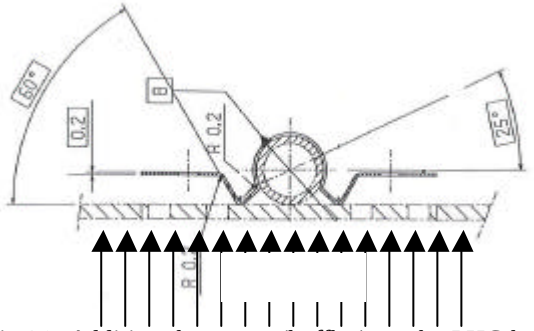

Fig.36: Additional screens (baffles) on the LHC beam screen to intercept the electrons from the cloud to reduce the heat load to the cold bore (1.9 K) [26].

8 Acknowledgements

Many thanks to the Operation crew of both SPS and PS machines for their collaboration and also to K.Cornelis, O. Gröbner, J-M. Laurent, F. Ruggiero and P. Strubin for their helpful discussions.

References

[1] G. Arduini and al., "Electron Cloud: SPS Observations with LHC-Type Beams", Proceedings of the Workshop on LEP-SPS Performance-Chamonix X, 119-122 (2000)

[2] W. Hofle, "Observation of the Electron Cloud Effect on Pick up Signals in the SPS", Proceedings of the Workshop on LEP-SPS Performance-Chamonix X (2000)

[3] O. Brüning and al. "Electron Cloud and Beam Scrubbing in the LHC", CERN LHC Project Report 290 (April 1999), Proc. Particle Accelerator Conference (PAC99), New York, 29 March - 2 April 1999, edited by A. Luccio and and W. MacKay (IEEE, New York, 1999), pp. 2629-2631

[4] O. Grobner, "Beam Induced Multipacting", 10th International Conference on High Energy Accelerators, Protvino, July 1977.

[5] F. Zimmermann, "Electron Cloud Simulations: An Update", Proceedings of the Workshop on SPS Performance-Chamonix XI, (2001)

[6] G. Arduini, "Observations in the SPS: Beam Emittance, Instabilities", Proceedings of the Workshop on LEP-SPS Performance-Chamonix X, (2000)

[7] F. Zimermann and al., "Electron Cloud Effect in the CERN SPS and LHC", Proceedings of the Workshop on LEP-SPS Performance-Chamonix X, (2000)

[8] M. Furman and M. Pivi, " Updated Electron-Cloud Simulation Results for the LHC", IEEE PAC 2001 Chicago (2001)

[9] M.V. Mokhov and al., Handbook of Accelerator Physics and Engineering, edited by A.W. Chao and M. Tigner, World Scientific, p216 (1999)

[10] K. Ohmi, "Beam and Photoelectron Interactions in Positron Storage Rings", Phys. Rev. Lett. 75, 1526 (1995)

[11] K. Ohmi, "Weak-Strong Simulation of Beam Photoelectron Instability in a Proton Storage Ring", PAC97 Vancouver (1997)

[12] F. Zimmermann, "Electron Cloud Studies for the Low Energy Ring of KEKB", CERN SL Note 2000-04 AP (2000)

[13] K. Ohmi, and al., "Head-Tail Instability caused by Electron Cloud in Positron Storage Rings", Phys. Rev. Lett. 85, 3821 (2000)

[14] K. Ohmi and al., "Study of the Fast Head-Tail Instability caused by Electron Cloud", HEACC'01 Tsukuba (2001)

[15] G. Rumolo and al., "Theory and Simulation of Electron Cloud Instability", Chamonix XI, CERN-SL-2000-007 DI (2001)

[16] G. Rumolo and al., "Simulation of Single Bunch Instabilities Driven by Electron Cloud in the SPS", PAC'01 Chicago (2001)

[17] K. Cornelis, "SPS Measurements of Electron Cloud Impedance", Chamonix XI, CERN-SL-2001-003-DI

[18] W. Hoefle, (private comm.)

[19] G. Arduini and al., "Transverse behaviour of the LHC Proton Beam in the SPS: An update", PAC 2001 Chicago (2001)

[20] K. Oide, "Observation and Cure of the Electron Cloud Effect at the KEKB Low Energy Ring", Chamonix XI (2001)

[21] H. Fukuma and al. "Observation of Vertical Beam Blow-up in KEKB Low Energy Ring", EPAC 2000 Vienna (2000)

[22] H. Fukuma and al., "Study of Vertical Beam Blow-up in KEKB Low Energy Ring", HEACC 2001 Tsukuba (2001)

[23] J.M. Jimenez and al., "Electron cloud: observations with LHC-type beams in the SPS", EPAC2000 Vienna.

[24] P. Collier and al., "Reducing the SPS Machine Impedance", EPAC 2002 Paris (2002) to be published

[25] N. Hilleret and al., "The variation of the secondary electron emission with surface modifications", 2Stream Instabilities Workshop Geneva 2002 to be published.

[26] N. Kos, P. Cruikshank, CERN LHC Vacuum Group (Private comm.)

Table of contents

ELECTRON-CLOUD EFFECTS IN HIGH-INTENSITY PROTON ACCELERATORS*

Jie Wei†, Brookhaven National Laboratory, Upton, New York 11973, USA
Robert J. Macek, Los Alamos National Laboratory, New Mexico 87545, USA

Abstract

One of the primary concerns in the design and operation of high-intensity proton synchrotrons and accumulators is the electron cloud and associated beam loss and instabilities. Electron-cloud effects are observed at high-intensity proton machines like the Los Alamos National Laboratory's PSR and the CERN SPS, and investigated experimentally and theoretically. In the design of next-generation high-intensity proton accelerators like the Spallation Neutron Source ring, emphasis is made in minimizing electron production and in enhancing Landau damping. This paper reviews the present understanding of the electron-cloud effects and presents mitigation measures.

1 INTRODUCTION

Electron-cloud effects are important, but incompletely understood dynamical phenomena. Effects that can severely limit the performance of high-intensity proton synchrotrons include trailing-edge tune-shift and resonance crossing, electron-proton instability, emittance growth and beam loss, increases in vacuum pressure, heating of the vacuum pipe, and interference with beam diagnostics. The following are examples of hadron rings where electron-cloud effects are observed: Proton Storage Ring (PSR) at the Los Alamos National Laboratory (LANL), where a strong, fast transverse-instability occurs both for coasting and bunched beam when a threshold intensity is exceeded [1]; the CERN PS and SPS, where a large number of electrons are produced by beam-induced multipacting when the machine's parameters are configured for LHC injection [2, 3]; and, BNL's Relativistic Heavy Ion Collider (RHIC) where the vacuum pressure dramatically increases when the beams are injection with halved nominal bunch-spacing. The electron-cloud effects can limit the performance of the next-generation high-intensity proton rings, such as the Spallation Neutron Source (SNS) accumulator ring [4], the Large Hadron Collider (LHC) [5], and neutrino-factory proton-drivers.

This paper attempts to summarize the present understanding of the electron-cloud effects pertaining to high-intensity proton synchrotrons and accumulators. Section 2 describes some typical phenomena. Section 3 identifies the main sources of electron generation including stripping injection, proton grazing at the collimator surfaces, beam-induced multipacting, and gas ionization. The effects of the electron cloud on the proton beam are discussed in Sections 4 and 5. Preventive methods are described in Section 6. Finally, a summary is given in Section 7.

2 PHENOMENA

In the recently commissioned Relativistic Heavy Ion Collider (RHIC) [6], vacuum-pressure rises were observed during high-intensity operation of both gold- and proton-beams. As shown in Figure 1, beam injection with halved bunch spacing resulted in a much higher vacuum pressure than the normal value [7, 8]. The pressure rise occurred when the total beam intensity in the ring is only 60% of the nominal intensity. The dominant mechanism is suspected to be due to the electron cloud [7].

A fast, vertical instability was observed at Brookhaven's AGS Booster when the proton beam was debunched. After the beam was injected, the beam suffered a 10% slow loss over about 1 ms followed by a 60% fast loss over tens of micro-seconds. Accompanying the fast beam-loss was instability in the vertical direction. The threshold could vary by a factor of 2, from a peak current of 2.7 A to 5.3

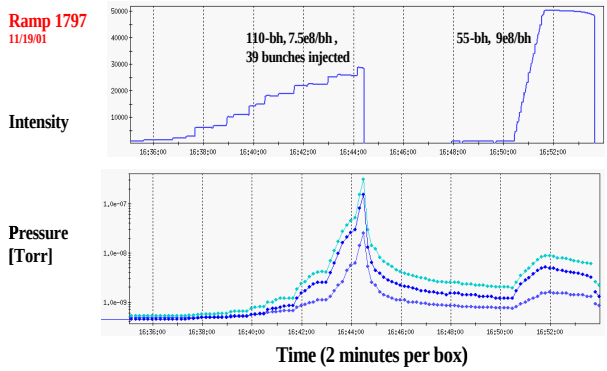

Figure 1: Vacuum-pressure rise in RHIC during gold-beam injection (courtesy S. Y. Zhang and the RHIC crew). The top curve indicates the total beam intensity as a function of time, and the bottom curves indicate the corresponding vacuum pressure at one location (BO11) of the ring. The horizontal scale is 2 minutes per box. The right-hand side shows the nominal operation when 55 bunches, each containing 9×10^8 gold ions, are injected into the ring. The left-hand side shows that when the bunch spacing is reduced by half, the vacuum pressure increases dramatically even when only 39 bunches, each containing 7.5×10^8 gold ions, are injected.

* Work performed under the auspices of the US Department of Energy
† wei1@bnl.gov

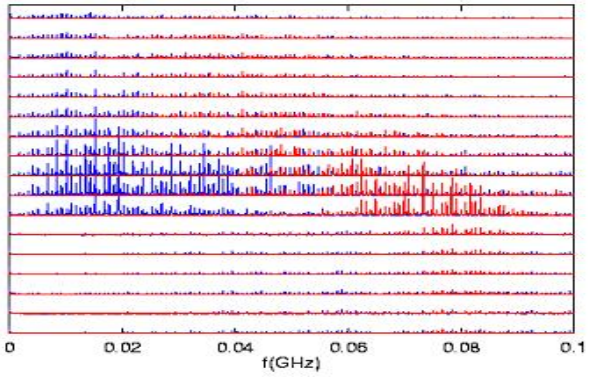

Figure 2: Beam-Position-Monitor (BPM) difference signal of a debunched proton-beam measured in the AGS Booster indicating an instability in the vertical direction (courtesy M. Blaskiewicz). The vertical axis is the spectral amplitude of the BPM's sum (blue) and difference (red) signals. Every trace is 12 μs apart. The horizontal and vertical tunes are 4.8 and 4.95, respectively.

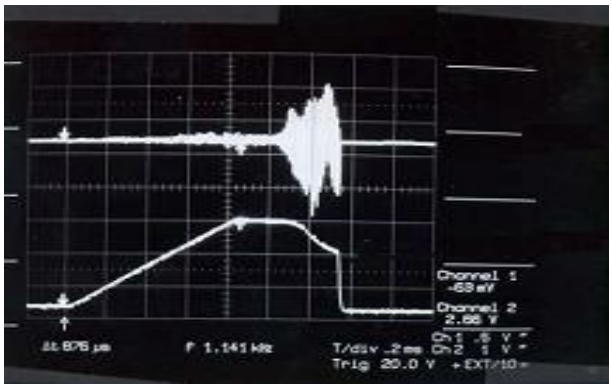

Figure 3: Fast instability observed at PSR. The top curve is the vertical difference signal of the BPM, and the bottom curve is from the beam-loss monitor. The horizontal scale is 0.2 ms per box. The total beam charge is 4.2 μC. The RF voltage is 13.5 kV.

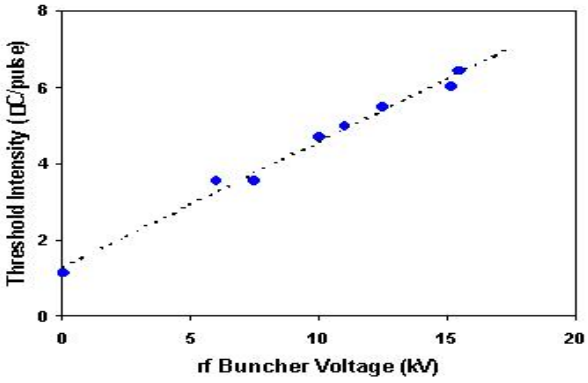

Figure 4: Intensity threshold of the transverse instability as a function of the RF voltage at the PSR.

A, depending on the vertical betatron tune. As shown in Figure 2, the characteristic frequency of instability was between 80 and 100 MHz. Possible mechanisms included the trapping of electrons when the proton beam-gap was eliminated [9].

In the LANL PSR, a strong, fast transverse-instability occurred both for coasting and bunched beams when a threshold intensity was exceeded [10]. The phenomenon limited the ring's achievable intensity. Depending on the lattice optics (e.g., sextupole and skew-quadrupole settings), the instability could be in either horizontal or vertical direction. As shown in Figure 3, the instability growth-time was about 75 μs (or 200 turns). The frequency spectrum was from 70 to 200 MHz corresponding to the bounce frequency of the electrons. The threshold intensity was linearly proportional to the RF voltage applied to the beam (Figure 4). A large number of electrons was measured on the beam vacuum-pipe, with a time structure closely correlated to the passage of the proton beam.

3 ELECTRON GENERATION

We classify electron production into the following categories: (1) electrons generated at the stripping foil in the injection region; (2) electrons generated at the surfaces of collimators and vacuum pipe due to the impact of lost protons; (3) electrons produced by beam-induced multipacting from the vacuum-pipe wall; and, (4) electrons produced around the ring from residual-gas ionization.

Figure 5 shows the distribution of electron-density flux measured at the PSR using the electron detector developed at the Argonne National Laboratory [11]. The quantity f_e is defined as the ratio of the number of electrons striking the vacuum pipe within one turn to the number of stored protons in the ring, scaled from the area of the detector surface. The electron density is high at the injection region where the H^- beam is stripped of its electrons, and high at the extraction region due to limited aperture.

3.1 Injection Region

Multi-turn charge-exchange injection is often preferred for high-intensity rings to enhance the phase-space density of the accumulated beam. The charge-exchange process is performed with a stripping-foil typically of density from 200 to 400 μg/cm^2 (about 1μm thick). Near the injection stripping-foil, a high concentration of electrons is expected with a broad energy-spectrum. With a H^- beam, the stripped electrons carry twice the current of the injecting H^- beam with a kinetic energy of $m_e c^2(\gamma - 1)$, where γ is the relativistic factor of the H^- beam. The injecting- and circulating-beams impacting on the foil produce secondary emission of electrons at low energy (tens of eV). Although the yield is low (0.006 for a 800-MeV proton incident on carbon material), the effect is proportional to the number of traversals of the foil. The injecting- and circulating-beam also produce knock-on electrons at a high energy (up to several MeV). The stripping-foil, operating at

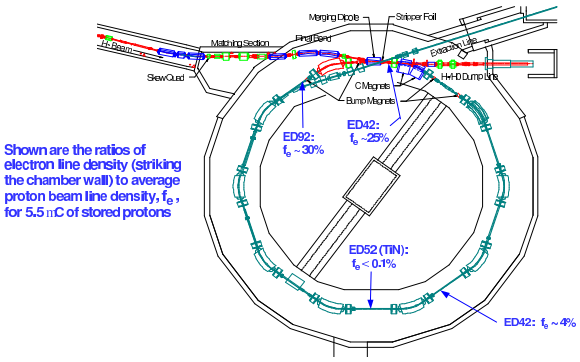

Figure 5: Distribution of the electron flux measured on the wall of the vacuum pipe at the PSR. The circumference of the ring is 90.2 m. The kinetic energy of the proton beam is 800 MeV. The flux ratio f_e, varying around the ring, is about 30% downstream of the extraction septum, about 25% downstream of the injection stripping-foil, about 4% in section 4, and within the noise level in the TiN-coated section 5.

a high temperature around 2000 K, emits thermionic electrons at low energy. All these electrons may backscatter from the stripped-electron collector and the surrounding surfaces [12]. As an example, Table 1 lists the sources of production, yield, and energy-range of the electrons at the PSR's injection region [13].

Figure 6 illustrates the collection of stripped-electrons at the SNS accumulator ring. The electrons are guided by a magnetic field and collected by a water-cooled device of heat-resistant material. The electron collector uses a carbon material attached to a water-cooled copper plate [14]. Selecting a low charge-state material for the collector also reduces the number of backscattered electrons. Figure 7 shows the temperature distribution at the electron collector when the stripped-electron beam of 3 kW power strikes the surface of about 1 cm^2 area.

Table 1: Estimated yield and kinetic energy of the electrons produced by the injected H$^-$ beam at the PSR. The yield is defined as the ratio of total number of electrons produced during the accumulation period per injected H$^-$ particle. The average number of foil traversal is about 50. The kinetic energy of the injecting beam is 800 MeV. The average H$^-$ beam current is 100μA (courtesy M. Plum).

Source	Yield	Kinetic energy
Stripped e^-	2.0	430 keV
Secondary e^-	1.0	up to 20 eV
Knock-on e^-	0.4	up to 2.4 MeV
Thermionic e^-	< 0.002	$\sim$0.24 eV
Ionization	0.02	up to 2.4 MeV

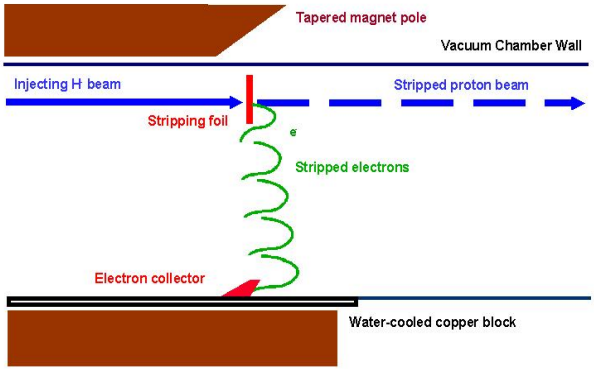

Figure 6: Collection of stripped electrons during the injection of H$^-$ beam at the SNS accumulator ring.

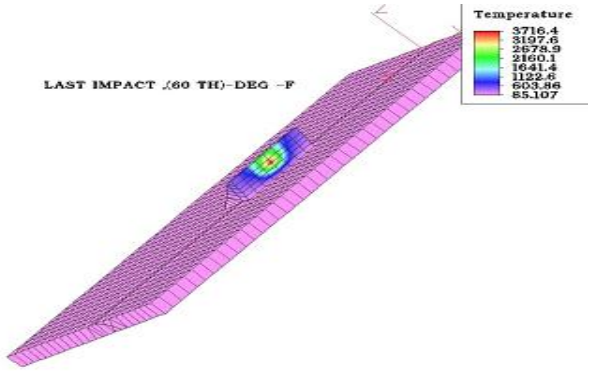

Figure 7: Temperature (F) distribution at the stripped-electron collector at the SNS ring in units of Fahrenheit (or $5F/9 + 255.37$ K, Courtesy C. J. Liaw and J. Brodowski).

3.2 *Collimation Region*

The region near the scrapers and collimators is susceptible to a high beam-loss and, potentially, is another location of high electron-concentration. Protons incident on the collimator surfaces produce secondary electrons. Depending on the energy of the beam and the incident angle, the secondary electron-to-proton yield can greatly exceed 1 when the incident beam is nearly parallel to the surface (i.e., grazing angle $\theta_g \approx \pi/2$). Experiments were performed with different ions at the Brookhaven's Tandem accelerator to verify the angular dependence of electron yield [15]. As shown in Figure 8, the proton-induced yield Y_{ep} has a $1/\cos\theta_g$ dependence on the angle θ_g, similar to the electron-induced secondary-emission yield as predicted by the Seiler model based on experimental fits [16, 17, 18, 7]

$$Y_{ep} = \frac{1.11 Y_{ep}^{max} \left\{ 1 - \exp\left[-2.3 \left(\frac{E_k}{E_k^{max}} \right)^{1.35} \right] \right\}}{\left(\frac{E_k}{E_k^{max}} \right)^{0.35} \cos\theta_g} \quad (1)$$

where E_k is the kinetic energy of the primary proton, and the proton energy that corresponds to the maximum yield, E_k^{max}, is about 0.7 MeV. A serrated surface with triangular

teeth greatly reduced the generation of secondary-emission electrons. However, at the beam energy around 1 GeV the proton stopping-length is long (about one meter). A serrated surface may be ineffective since protons incident on the front edge of the teeth may easily escape from the collimator body. The SNS ring uses a two-stage collimation system so that the beam halo is likely to be incident on the front edge of the secondary collimators consisting of layers of stainless-steel blocks, stainless-steel balls, borated water, and lead shield. Figure 9 shows one of three secondary collimators [19]. The primary scraper consists of four adjustable, thin tantalum-blades spaced at 45 degree angles, and shielded for radioactivation containment.

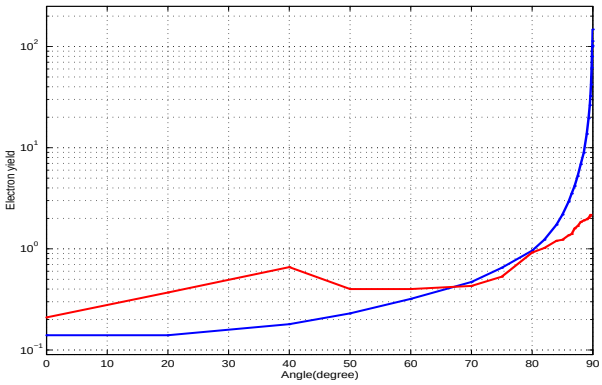

Figure 8: Proton-induced secondary-emission yields of electrons as functions of the incident angle for 28-MeV protons striking a flat (blue) and a serrated (red) stainless-steel surface (courtesy P. Thieberger).

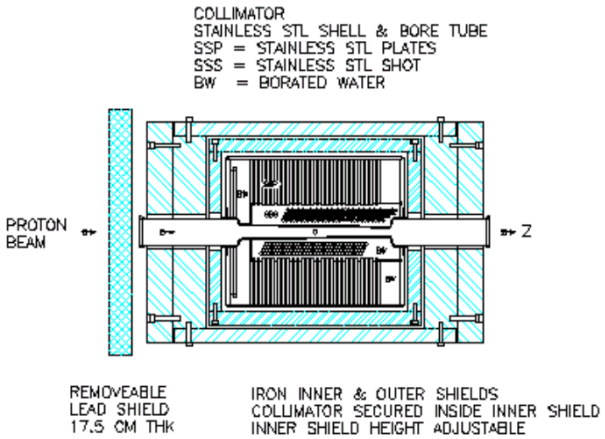

Figure 9: Schematics of one of SNS ring's secondary collimators showing layers of material for radio-activation containment (courtesy H. Ludewig and N. Simos). The effective length is about 1.5 m. The collimator is designed to withstand an average beam power of up to 10 kW at 1 GeV kinetic energy.

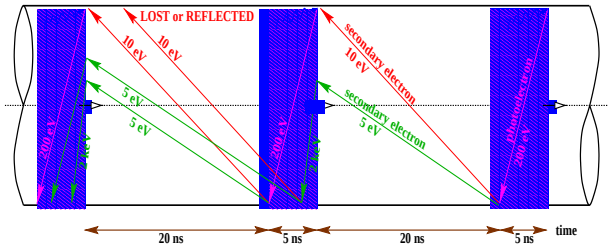

Figure 10: Electron build-up at the CERN LHC as an example of multibunch, beam-induced electron multipacting (courtesy F. Ruggiero). The time between successive bunches is 25 ns. The energy gain due to the bunch passage is about 200 eV.

3.3 *Beam-induced Multipacting*

Beam-induced multipacting is believed to be the leading source of sustained electron-production. Depending on the beam parameters, one of the two multipacting models applies: multibunch passage multipacting [20, 21, 22, 23, 24], or single-bunch, trailing-edge multipacting [1, 25].

The phenomena of multibunch, beam-induced multipacting were observed at the CERN PS and SPS when the machines' parameters were configured for LHC injection. The electron-cloud buildup was sensitive to the intensity, spacing, and length of the proton bunches, and to the secondary-emission yield (SEY) of electrons from the beam-pipe surfaces.

As shown in Figure 10, the multibunch multipacting occurs if the transit time of the electrons crossing the vacuum pipe is comparable to the time between successive bunches, and if the electrons gain enough energy to produce more than one secondary-electrons when they hits the vacuum-pipe wall [20]. The multipacting parameter ζ_m is defined as the ratio between the transit time of the electrons crossing the vacuum pipe to the time between successive bunches

$$\zeta_m = \frac{2b}{s_b}\frac{\beta}{\beta_e} \tag{2}$$

where b is the radius of the vacuum pipe, s_b is the distance between the subsequent bunches, β is the velocity of the proton normalized by the speed of light c, and $\beta_e c$ is the average velocity of the electrons. Here, β_e is related to the energy gained by the electron from the passage of the proton bunch

$$\Delta E_e = m_e c^2 \left[\sqrt{\left(\frac{2r_e N_0}{\beta b}\right)^2 + 1} - 1\right] \tag{3}$$

where $r_e = e^2/4\pi\epsilon_0 m_e c^2$ is the classical radius of electron, and N_0 is the number of protons in the bunch. When the electron motion is non-relativistic, i.e.,

$$\frac{2r_e N_0}{\beta b} \ll 1 \tag{4}$$

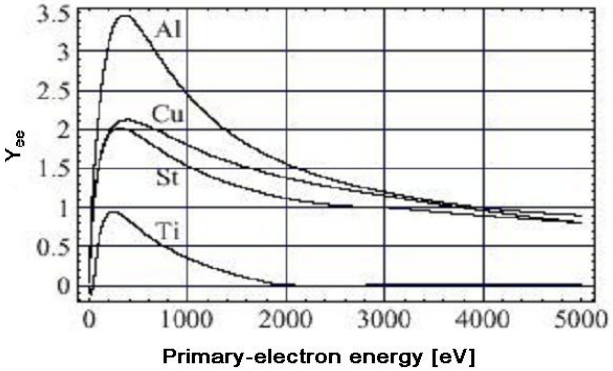

Figure 11: Secondary-electron yield Y_{ee} as a function of the primary-electron energy for a perpendicular incidence and for technical surfaces representative of vacuum pipes (courtesy N. Hilleret and O. Gröbner).

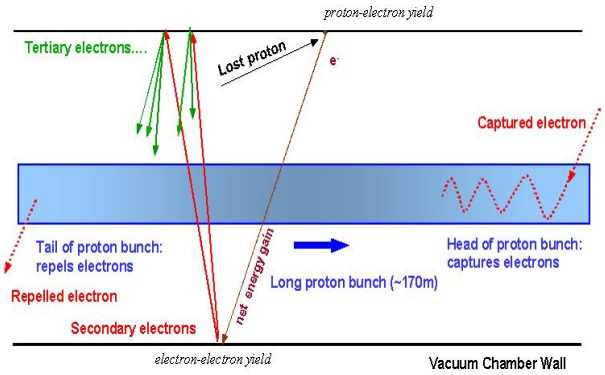

Figure 12: Beam-induced electron multipacting at the trailing edge of a long proton-bunch. The transit time of the electrons across the beam pipe is much shorter than the passage time of the proton bunch.

Eqs. 2 and 3 can be approximated as [20]

$$\zeta_m \approx \frac{\beta^2 b^2}{r_e N_0 s_b} \tag{5}$$

and

$$\Delta E_e \approx 2 m_e c^2 \left(\frac{r_e N_0}{\beta b}\right)^2 \tag{6}$$

The condition for proper multibunch multipacting is given by

$$\zeta_m = 1 \tag{7}$$

The energy gained by an electron must be such that the electron-induced secondary-emission yield (SEY) satisfies

$$\alpha_e Y_{ee} > 1 \tag{8}$$

where $\alpha_e \leq 1$ is the electron survival-rate in the bunch gap [7]. Figure 11 shows the typical electron-induced SEY (Y_{ee}) as a function of the primary-electron energy for a perpendicular incidence.

Multibunch electron multipacting may occur for almost any value of ζ_m [26]. The exact resonance condition is met if $\zeta_m = 1$. If $\zeta_m > 1$, the primary electrons interact with more than one proton bunch; If $\zeta_m \leq 1$, part of the primary electrons are lost before the next bunch arrives, leaving behind less-energetic secondary particles (PS, SPS). On the other hand, if $\zeta_m \ll 1$, the electron cloud is usually dominated by single-bunch multipacting. In fact, since here the transit time of the electrons across the vacuum chamber is typically much shorter than the passage time of the proton bunch, the energy gained by the electrons is much lower than that predicted by the multibunch multipacting model (Eqs. 3 and 6).

Single-bunch, trailing-edge multipacting starts to dominate if the bunch length is long enough to sustain multiple passes of electrons. As shown in Figure 12, electrons are attracted towards the rising edge of the proton bunch. At the trailing edge of the proton bunch, electrons are released and yet still accelerated by the bunch to multipact. The number of electrons grows exponentially at the trailing edge of the proton bunch, as observed at the PSR (Figure 13) [10]. The electron-cloud buildup due to this single-bunch mechanism is expected to have a weak dependence on bunch spacing, the vacuum-pressure level, and the amount of residual protons in the beam gap. On the other hand, it depends critically on the length of the proton bunch and the variations in its longitudinal density.

Similar to the multibunch parameter ζ_m (Eq. 5), single-bunch multipacting parameter ζ_s can be defined as the ratio between the transit time of the electrons crossing the vacuum pipe to the passage time of half of the proton bunch

$$\zeta_s = \frac{b}{s_b B_f} \frac{\beta}{\beta_e} \tag{9}$$

where the effective length of the proton bunch is $s_b B_f$, bunching factor B_f ($B_f \leq 1$) is defined as the ratio between the average and peak line-density of the proton

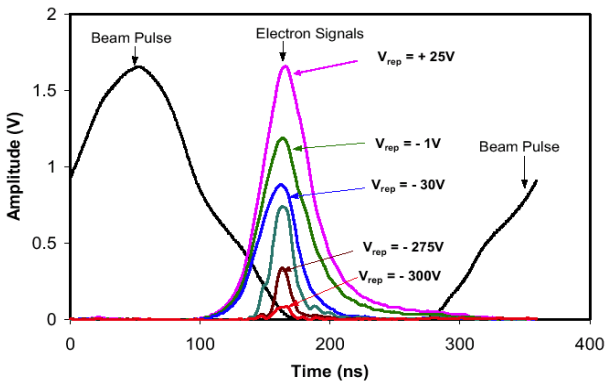

Figure 13: Electron signals measured at the PSR as a function of time relative to the proton-beam pulse during a single revolution. The repeller voltage, V_{rep}, is varied to select the electrons striking the detector according to their energy.

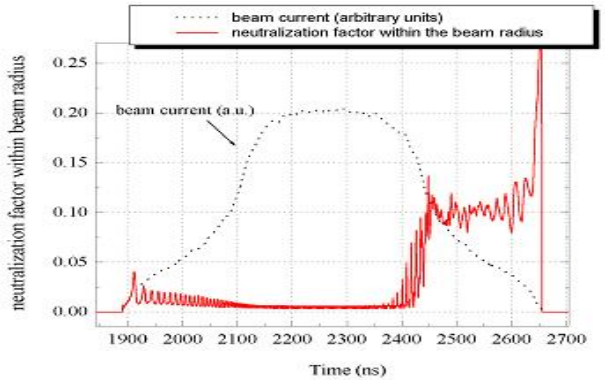

Figure 14: Computer simulation of electron generation in the SNS accumulator ring (courtesy M. Pivi and M. Furman). The neutralization factor is defined as the density ratio between the electron and proton within the proton beam-radius. The beam intensity is 2×10^{14} per bunch. The peak secondary-emission yield is assumed to be 2. The full bunch-length is about 700 ns.

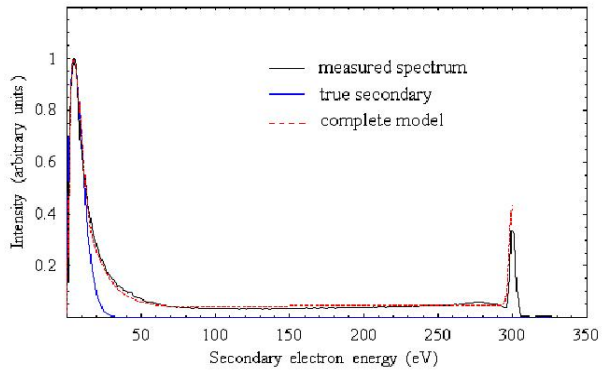

Figure 15: Secondary-emission energy-spectrum used for simulations (Hilleret fit Cu) for a 300 eV incident-electron beam. The rediffused and reflected components are included in the model (courtesy M. Pivi and M. Furman).

beam, and

$$\zeta_s > \zeta_m \tag{10}$$

To obtain an order-of-magnitude estimate, assume that the beam charge is uniformly distributed in the transverse directions in the vacuum chamber. The average velocity of electron in the non-relativistic limit is given by

$$\beta_e \approx \sqrt{\frac{r_e N_0}{s_b B_f}} \ll 1 \tag{11}$$

Eq. 9 thus becomes

$$\zeta_s \approx \frac{\beta b}{\sqrt{r_e N_0 s_b B_f}} \tag{12}$$

The energy gained by an electron is approximately

$$\Delta E_e \approx 4 m_e c^2 \beta b \sqrt{\frac{r_e N_0}{s_b^3 B_f^3}} \tag{13}$$

Single-bunch multipacting occurs if the condition

$$\zeta_s \ll 1 \tag{14}$$

is satisfied, and if the energy gained by an electron is such that

$$Y_{ee} > 1 \tag{15}$$

As an example, consider the SNS ring parameters: $N_0 = 2\times10^{14}$, $s_b = 248$ m, $B_f \approx 0.5$, $b \approx 0.1$ m, and $\beta = 0.875$. The single-bunch multipacting parameter is $\zeta_s \approx 0.01 \ll 1$. The characteristic energy gain is approximately $\Delta E_e \approx 97$ eV. Single-bunch, trailing-edge multipacting is expected to occur, as shown by the computer-simulation results shown in Figure 14 [27].

The actual multipacting process may be a combination of the single- and multibunch multipacting. Figure 15 shows the measured secondary-emission spectrum used for simulation consisting of true-secondary, backscattered, and rediffused electrons [28]. Uncertainties remain in key parameters describing the interactions of low-energy (< 20 eV) electrons with the accelerator surfaces.

3.4 Ionization

The rate of electron production by gas ionization is linearly proportional to the proton current I, the vacuum pressure P, and the ionization cross-section σ_{ion} [26, 7]. The rate of electron line-density increase per unit length of circumference is given by the relation

$$\frac{d^2\lambda_e}{dtds} = \frac{\rho_m \beta I \sigma_{ion} P}{e} \tag{16}$$

where P is in units of Torr (1 Torr = 133.3 Pascal). At the room temperature of 300 K, the molecular density ρ_m is about 3.3×10^{22} m^{-3}. For the SNS ring at a pressure of 10^{-8} Torr, a total of 2.6×10^9 electrons is produced per turn when the proton accumulation reaches 2×10^{14}. This is much fewer than the electrons produced at the bunch trailing-edge when multipacting occurs. The effect of photoemission usually is negligible for medium-energy protons due to lack of synchrotron radiation.

Various computer-simulation programs were developed to model the process of electron generation [30, 31, 21]. Simulated mechanisms included space-charge fields of both protons (or e^+) and electrons, vacuum pipe and the image charges, external magnetic-fields, gas ionization, secondary emission, and photoemission. Recent developments incorporated trailing-edge multipacting, rediffusion, backscattering, and proton-induced secondary emission with refined angular dependence of the incident particle [27, 32, 29]. Particle-in-cell (PIC) algorithms were also developed to model detailed electron-generation processes [33].

4 ELECTRON NEUTRALIZATION AND TUNE SHIFT

4.1 *Electron Bounce-frequency*

The electron motion is characterized by the electron bounce-frequency

$$\omega_e \approx c\sqrt{2\pi r_e n_p} \tag{17}$$

where n_p is the volume density of the proton beam. Figure 16 shows the frequency spectra of the BPM's vertical difference-signal measured at the PSR for two beam intensities. The peak spectrum for the 6.1 mC beam-intensity centers around 200 MHz, corresponding to the electron bounce-frequency. When the intensity is reduced by a factor of two by injecting every other pulse, the mean frequency of the peak spectrum shifts downwards by a factor of about 0.7.

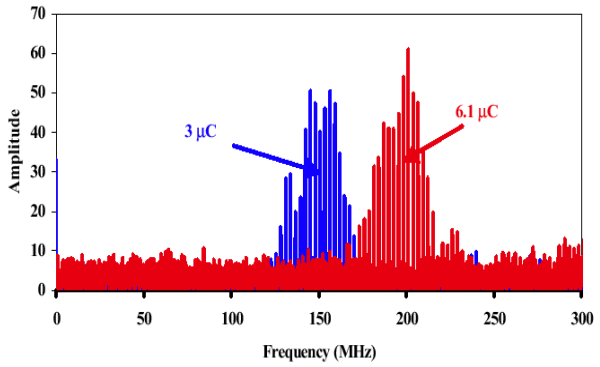

Figure 16: Frequency-spectrum of BPM's vertical difference-signal for two beam intensities measured at the PSR. The lines in the peaks are the betatron side-bands.

4.2 *Neutralization Tune-shift*

In high-intensity synchrotrons, proton tune-shifts can be attributed to various mechanisms: space charge, chromaticity, kinematic nonlinearity, magnetic nonlinearity, and magnetic fringe field. The dominant contribution is usually from space charge at the injection energy. Beam loss is often caused by resonance crossing associated with an excessive amount of tune spread in the beam. Figure 17 shows the spread of tune shift of a 2 MW proton-beam in the absence of electron cloud at the SNS accumulator ring.

An electron cloud tends to neutralize the positive charge of the proton beam. Compared to the space-charge tune-shift between the protons, the tune shift produced by the electron cloud is enhanced by a factor γ^2 due to absence of the compensating electric and magnetic forces in the laboratory frame. With the electron cloud, the space-charge

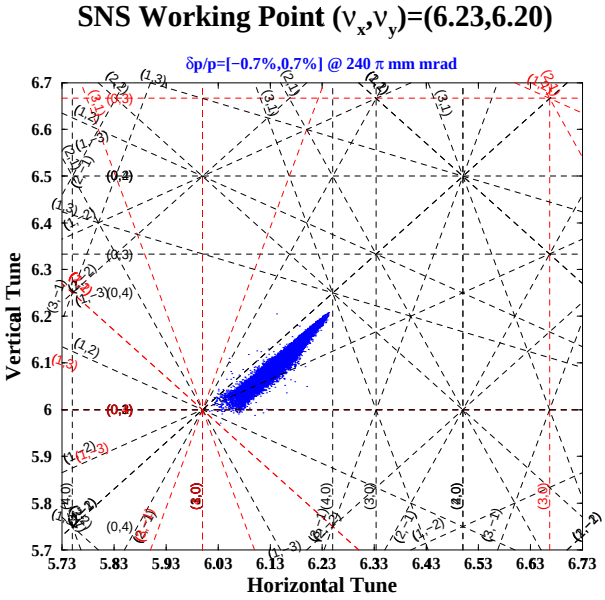

Figure 17: Spread of tune shift of a 2 MW proton beam in the SNS accumulator ring. The computer-simulation results are obtained with the Unified-Accelerator-Libraries (UAL) package [35]. Structure resonances are indicated in red.

tune-shift becomes

$$\Delta\nu_{x,y} = -\frac{f_{sc}N_0 r_0 R_0}{2\pi B_f \nu_{x,y,0}\beta^2\gamma}\left[\frac{1}{\sigma_{x,y}(\sigma_x+\sigma_y)}\left(\frac{1}{\gamma^2}-\eta_e\right) + A^e_{im}\left(\gamma^{-2}-\eta_e\right) + A^m_{im}\right] \tag{18}$$

where $r_0 = e^2/4\pi\epsilon_0 m_0 c^2$ is the classical radius of proton, R_0 is the average radius of circumference, $\nu_{x,0}$ and $\nu_{y,0}$ are the base transverse tunes, and σ_x and σ_y are the horizontal- and vertical-rms beam sizes. The bunch's form-factor f_{sc} is equal to $1/2$ for an uniform distribution, and to 1 for a Gaussian distribution. The neutralization factor (η_e), defined as the electron-to-proton density ratio in the laboratory frame, represents the contribution of electron cloud at a low energy (typically up to several hundreds eV). The contribution from the electric and magnetic images of the beam are represented by the Laslett tune-shifts A^e_{im} and A^m_{im}, respectively. The electric fields due to both the direct space-charge and the image charge are reduced by the neutralization [34]. For both incoherent and coherent space-charge tune-shifts, the relative contribution of the electron cloud to the direct space-charge and electric image is $-\gamma^2\eta_e$.

4.3 *Trailing-edge "Pacman" Effect*

With the trailing-edge electron-multipacting model, protons at the trailing edge of the bunch experience, on average, a high concentration of electrons. Electron neutralization increases the transverse tunes and possibly increases the tune spread of the beam. When the beam is stored in the

ring for an extended time, the bunch may continuously lose its trailing-edge particles upon resonance crossing. Here, we call it trailing-edge Pacman effect.

Figure 14 shows the structure of electron neutralization inside the proton bunch at the SNS accumulator ring, predicted from a computer simulation [27]. With a 2-MW beam in the SNS ring, the peak tune-shift due to space charge is about -0.2. The neutralization level is about 10% ($\eta_e \approx 0.1$) inside the proton beam for trailing-edge particles at 50% of the peak longitudinal-density, as shown in Figure 14. The tune shift due to the electron cloud is about $+0.04$. Given the same space-charge tune-spread at injection, this effect becomes more important for injection at a higher energy.

5 ELECTRON-PROTON INSTABILITIES

Experimental observations of electron-cloud instabilities are distinctively different for "short bunches" stored at energies above the transition energy, where multibunch multipacting is expected to be important (PS, SPS, and B-factories), and "long bunches" stored at energies far below the transition energy, where single-bunch, trailing-edge multipacting is expected to be dominant (PSR and SNS).

5.1 Coasting-beam and Long-bunch Regime

During the 1970s, coupled oscillations associated with electron trapping and multipacting occurred during high-intensity coasting-beam operation at the CERN ISR [37, 38, 20]. The problem was alleviated by installing additional clearing electrodes around the ring. Since 1988, a fast, vertical instability accompanied by beam loss, both with bunched and unbunched beams, was attributed to coupled electron-proton oscillations [39, 10]. At the BNL AGS Booster, an intense proton-beam became vertically unstable when it was debunched.

The threshold of electron-proton instability is associated with the amount of Landau damping caused by the beam momentum-spread [40, 38, 41, 42]. Figure 4 shows the measured dependence of the threshold intensity on RF voltage for a given length of injected bunch. The threshold scaling is different from that of transverse instability due to conventional coupling-impedance, where the threshold intensity is proportional to the RF voltage squared. The linear dependence of the threshold results from the dependence of the instability's frequency on the beam intensity [32]. In fact, at the electron bounce-frequency, ω_e, the transverse frequency-spread is mostly contributed by the momentum slip, i.e.,

$$\frac{\omega_e}{\omega_0} \gg \nu_{x,y}; \quad |\eta|\omega_e \gg \xi_{x,y}\omega_0 \tag{19}$$

where ω_0 is the angular revolution frequency, η is the momentum-slip factor, $\nu_{x,y}$ are the transverse tunes, and $\xi_{x,y}$ are the chromaticities. The threshold for the transverse stability is

$$|Z_{\perp x,y}| \leq F_\perp \frac{4|\eta|E_s}{\sqrt{\pi}e^2\omega_0 a\langle\beta_\perp\rangle}\sqrt{\frac{B_f R_0 r_e}{N_0}}\left(\frac{\Delta p}{p}\right)_{FWHM} \tag{20}$$

where $\left(\frac{\Delta p}{p}\right)_{FWHM}$ is the full-width, half-maximum momentum spread of the beam, E_s is the total energy of the proton, $F_\perp$ is the form factor, and a is the average beam radius. With a given coupling-impedance, the threshold intensity is linearly proportional to the momentum-spread squared, and is insensitive to the machine chromaticity. Also, the scaling behavior is extended from bunched beams to a coasting beam as the RF voltage is lowered.

Several theoretical approaches were used to study instabilities of the coupled electron-proton motion. Centroid models of rigid beams provided estimates of the unstable dipole-modes and their scaling with intensity for coasting-beams. They offered plausible predictions for the threshold intensities of the instability, given the uncertainties in parameters such as average neutralization [42, 39, 43]. However, estimates of growth rates and behavior beyond threshold showed poor agreement with observations. The centroid models were extended to bunched beams to better describe the trailing-edge electron concentration, the instability threshold, and the structure and growth rates above the threshold [32]. Another approach was to develop fully kinetic simulations based on self-consistent solutions of the Maxwell-Vlasov equations for coasting beams in a smooth-focusing approximation [44].

5.2 Short-bunch Regime

The short-bunch regime included instabilities that occurred at most lepton (e^+) rings (KEK photon factory, B-factory KEKB, and BEPC), as well as proton rings (PS and SPS) when the beams were prepared for collider uses [26]. Coupled-bunch, transverse instabilities were observed at the KEK PF [45, 30] and BEPC [46], and at the SPS (horizontal direction) with the LHC proton test-beams [47]. The electron cloud coupled the motion of subsequent bunches similar to a multibunch wake field. With computer simulations, the effective wake fields were computed to predict the multibunch growth-rates.

Single-bunch, transverse (strong and regular head-tail, fast blow-up) instabilities were identified first at the KEK B-factory and then at the CERN SPS (vertical direction) and PS with the LHC proton test-beams. The electron cloud coupled the head and tail of the bunch similar to a short-range wake-field. A broadband-resonator model was used to describe the coupling impedance, with the resonator frequency at the electron bounce-frequency [48]. Such single-bunch instabilities were often sensitive to the chromaticity.

Theoretically, beam break-up treatment [49, 50] and two-particle model [51] were used to obtain the threshold and growth time of the instability, assuming that the electron production saturated near the neutralization den-

sity. Transverse mode-coupling (TMCI) calculation using simulated wake-field was further used [52]. The instability threshold was found to be linearly proportional to the average electron-density (i.e., N_0/s_b). Recently, particle-in-cell (PIC) simulations based on strong-strong models were performed [53, 54].

6 PREVENTIVE MEASURES

Control of the electron-cloud effects involves suppressing electron generation and enhancing Landau damping. The number of multipacting-electrons can be effectively reduced by surface treatment of the vacuum pipe. Electrons in the injection region need to be guided to the collectors with a low backscattering yield [12]. A beam-in-gap kicker can ensure a clean beam-gap [55, 56, 57]. Vacuum ports can be screened, and steps in the vacuum pipe can be tapered to reduce peaked electric fields causing electron emission. A good vacuum can reduce electrons from gas ionization. Solenoids can be wound in straight sections to reduce multipacting [58, 59]. Electrodes can be installed around the ring to clear the electron cloud and to isolate areas of high electron-concentration. Electron detectors need to be installed at locations susceptible of high electron-concentration to monitor the electron production (Figure 18).

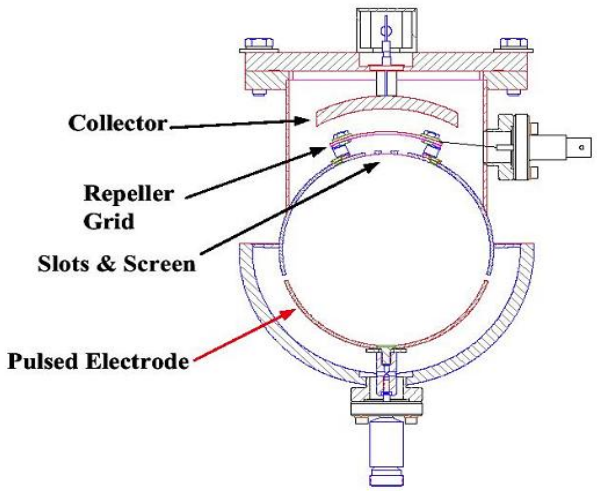

Figure 18: Electron sweeping detector developed at the LANL PSR (courtesy A. Browman).

Enhancement of Landau damping starts with the design of the machine. A large vacuum-pipe aperture is needed, especially at locations of high dispersion to allow further increase in momentum spread. A large RF voltage is required to provide sufficient momentum acceptance. Longitudinal painting can be used to expand the momentum spread of the injecting beam. Inductive inserts can be used to compensate for the space-charge effect, effectively increasing RF focusing [60]. Landau-damping octupoles (KEK PF and BEPC) has been shown to raise the stability threshold. Lattice sextupole families (BEPC, SPS, KEKB, and SNS) can be used for chromatic adjustments, to either improve momentum acceptance [61] or enhance damping. Finally, a fast, wide-band feedback system can be implemented to damp instabilities.

6.1 Surface Treatment

Surface coating of TiN was shown to effectively suppress the electron flux by a factor of more than 100 at a coated section of the PSR (Figure 5). The thickness of the coating, typically about 100 nm, is chosen to withstand the bombardment of the electrons during the lifetime of the machine operation. For critical elements, e.g., the ferrite of the extraction kicker inside the vacuum pipe (SNS), the pattern and thickness of the coating are chosen to avoid eddy-current heating and to prevent changes in material property. Planned, long-term bombardment with cold electrons further reduces the secondary-emission yield. Evidence of this "surface scrubbing" was seen at the SPS, KEKB, and PSR. The memory of the scrubbing may be preserved by a glow discharge in nitrogen [62].

6.2 Clearing Electrodes

Clearing electrodes were shown to suppress the electron multipacting at the CERN ISR. At the SNS accumulator ring, the BPMs around the ring are designed to be also used as clearing electrodes, capable of applying a voltage of up to ± 1 kV (Figure 19). Such a voltage overcomes the energy gain due to the proton bunch (Eq. 13). A dedicated clearing-electrode is implemented inside the stripping-foil assembly at the injection region.

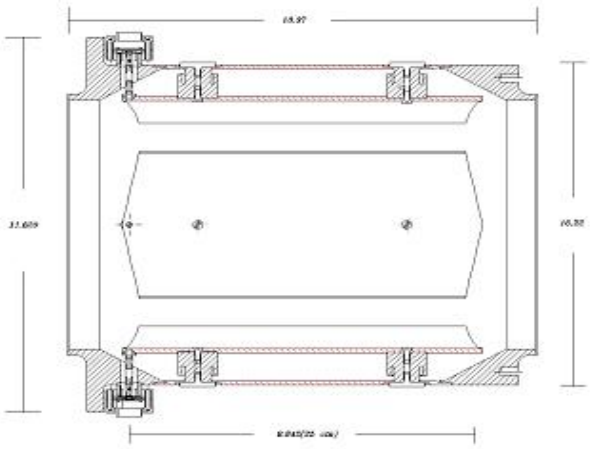

Figure 19: Schematics of the floating-ground BPM designed for the SNS accumulator ring (courtesy P. Cameron). A voltage of about ± 1 kV can be applied for the clearing of the electron cloud.

6.3 Solenoids

Weak solenoids were shown to effectively improve machine operation under the electron-cloud at KEKB and

PEP-II. In a short test-section at the PSR, a weak solenoid is found to suppress the electron flux (f_e) by a factor of about 50. For future high-intensity synchrotrons, such solenoids can also be used at straight sections, like the collimation section, to suppress electron generation. The solenoid field B_ϕ needs to be strong enough so that the radius r_ϕ of electron motion is small compared with the vacuum-pipe radius [7]

$$r_\phi = \frac{m_e v_e}{e B_\phi} \ll b \tag{21}$$

Effects on the proton beam can be minimized by alternating the polarities of the solenoids according to the betatron phase ϕ_x and ϕ_y [63]. Skew quadrupoles can further be used to correct coupling according to the relation

$$-\sum_{sq} \frac{\sqrt{\beta_x \beta_y}}{f_{sq}} \begin{bmatrix} \cos\Delta\phi \\ \sin\Delta\phi \end{bmatrix} = \sum_{sol} g_\phi \theta_\phi \begin{bmatrix} \cos(\Delta\phi + \omega_\phi) \\ \sin(\Delta\phi + \omega_\phi) \end{bmatrix} \tag{22}$$

where $\Delta\phi \equiv \phi_x - \phi_y$,

$$g_\phi = \sqrt{\gamma_x \beta_y + \gamma_y \beta_x + 2(1 - \alpha_x \alpha_y)} \tag{23}$$

$$\tan(\omega_\phi) = \frac{\beta_x + \beta_y}{\alpha_x \beta_y - \alpha_y \beta_x}, \quad \theta_\phi = \frac{B_\phi L_\phi}{B_0 \rho} \tag{24}$$

f_{sq} is the focal length of the skew quadrupole, L_ϕ is the length of the solenoid, $B_0\rho$ is the rigidity of the proton beam, and $\alpha_{x,y}$, $\beta_{x,y}$, and $\gamma_{x,y}$ are Courant-Snyder lattice functions.

7 SUMMARY

Electron-cloud effects are of primary concern to the operation of high-intensity proton synchrotrons and accumulator rings. During the last decade, significant progress has been made in the studies of both electron generation and electron-proton dynamics. However, quantitative understanding is still lacking, especially in the prediction of instability threshold and growth rates.

Some open, challenging tasks include: (1) establishing a coupling-impedance model for the electron cloud when trailing-edge multipacting is dominant; (2) identifying the leading instability drive in the presence of a strong space-charge force in the proton beam; (3) predicting the detailed distribution of electron neutralization inside the proton bunch; (4) a self-consistent treatment of electron production and electron-proton interaction; (5) fully reproducing the experimental observations in high-intensity rings like the PSR; and (6) predicting the electron-cloud effects for next-generation high-intensity machines like the SNS accumulator ring and the JAERI/KEK Joint Project synchrotrons [64].

8 ACKNOWLEDGEMENTS

We thank A. Aleksandrov, M. Blaskiewicz, J. Brodowski, A. Browman, F. Caspers, A. Chao, P. Cameron, V. Danilov, D. Davino, A. Fedotov, W. Fischer, D. Fitzgerald, M. Furman, O. Gröbner, S. Henderson, H. Hahn, H. Hseuh, Y. Y. Lee, H. Ludewig, N. Malitsky, R. McCrady, W. Meng, S. Peggs, M. Pivi, D. Raparia, F. Ruggiero, H. Schonauer, N. Simos, T. Spickermann, P. Thieberger, T. S. Wang, S.Y. Zhang, F. Zimmermann, and B. Zotter for many enlightening discussions, information, and assistances.

9 REFERENCES

[1] R. Macek, Workshop on Two-Stream Instabilities, Sante Fe (1999).

[2] E. Mètral, R. Cappi, M. Giovannozzi, G. Mètral, F. Zimmermann, Proc. 2001 Particle Accelerator Conference, Chicago (2001), p. 682.

[3] G. Arduini, V. Baglin, O. Bruening, R. Cappi, F. Caspers, P. Collier, I.R. Collins, K. Cornelis, R. Garoby, O. Groebner, B. Henrist, N. Hilleret, W. Hoefle, J.M. Jimenez, J-M. Laurent, T. Linnecar, E. Mercier, M. Pivi, F. Ruggiero, G. Rumolo, C. Scheuerlein, J.'Tuckmantel, L. Vos, F. Zimmermann, *Electron-cloud effects in the CERN SPS and LHC*, Proc. 2000 European Particle Accelerator Conference, Vienna (2000), p. 1611.

[4] J. Wei, D. T. Abell, J. Beebe-Wang, M. Blaskiewicz, P. R. Cameron, N. Catalan-Lasheras, G. Danby, A. V. Fedotov, C. Gardner, J. Jackson, Y. Y. Lee, H. Ludewig, N. Malitsky, W. Meng, Y. Papaphilippou, D. Raparia, N. Tsoupas, W. T. Weng, R. L. Witkover, S. Y. Zhang, *Low-loss design for the high-intensity accumulator ring of the Spallation Neutron Source*, Phys. Rev. ST-AB, **3** (1999), p. 080101.

[5] *The LHC Conceptual Design Report*, CERN/AC/95-05(LHC), CERN (1995).

[6] *The Relativistic Heavy Ion Collider Design Manual*, Brookhaven National Laboratory (1994).

[7] S. Y. Zhang, Private communications.

[8] W. Fischer, talk presented at the Workshop ECLOUD'02, CERN (2002).

[9] M. Blaskiewicz, AIP Conference Proceedings **496**, edited by T. Roser and S.Y. Zhang (AIP, N.Y. 1999), p. 321.

[10] R. J. Macek, A. Browman, D. Fitzgerald, R. McCrady, F. Merrill, M. Plum, T. Spickermann, T.S. Wang, J. Griffin, K.Y. Ng, D. Wildman, K. Harkay, R. Kustom, R. Rosenberg, *Electron proton two-stream instability at the PSR*, Proc. 2001 Particle Accelerator Conference, Chicago (2001), p. 688.

[11] R.Rosenberg and K.Harkay, Nucl. Instrum. Methods, **A 453** (2000), p. 507.

[12] T. Tabata, R. Ito, and S. Okabe, Nucl. Instrum. Methods, **94** 1971, p. 509.

[13] M. Plum, *Electric fields, electron production, and electron motion at the stripper foil in the Los Alamos Proton Storage Ring*, Proc. 1995 Particle Accelerator Conference, Dallas (1995), p. 3403.

[14] J. Brodowski, private communications (2002).

[15] P. Thieberger, A. L. Hanson, D. B. Steski, V. Zajic, S. Y. Zhang, H. Ludewig, Phys. Rev., **A61** (1999), p. 042901.

[16] J. Shou, *Transport theory for kinetic emission of secondary electron from solids*, Phys. Rev., **B27** (1980), p. 2141.

[17] H. Seiler, J. Appl. Phys., **54** (1983), p. R1.

[18] J.E. Borovsky, D.J. McComas, and B.L. Barraclough, *The secondary-electron yield measured for 5-24 MeV protons on aluminum-oxide and gold target*, Nucl. Instrum. Methods, **B30** 1988, p. 191.

[19] H. Ludewig, N. Simos, J. Walker, P. Thieberger, A. Aronson, J. Wei, *Collimator system for the SNS accumulator ring*, Proc. 1999 Particle Accelerator Conference, New York (1999), p. 548.

[20] O. Gröbner, HEACC'77, Protvino (1977), p. 277.

[21] F. Zimmermann, *A simulation study of electron-cloud instability and beam-induced multipacting in the LHC*, LHC Project-Report 95, and SLAC-PUB-7425 (1997).

[22] M. A. Furman and G. R. Lambertson, *The electron cloud effect in the arcs of the PEP-II positron ring*, KEK Proceedings 97-17, p. 170, (Proc. MBI97 workshop, KEK, Y.H. Chin, ed.) (1997).

[23] O. Gröbner, *Beam induced multipacting*, Proc. 1997 Particle Accelerator Conference, Vancouver (1997), p. 3589.

[24] F. Ruggiero, G. Rumolo, F. Zimmermann, *Simulation of the electron-cloud build up and its consequences on heat load, beam stability and diagnostics*, Phys. Rev. ST-AB **2** (2001), p. 012801, Erratum-ibid. (2001), p. 029901.

[25] V. Danilov, et al., *Multipacting on the trailing edge of proton beam bunches in the PSR and SNS*, AIP Conference Proceeding 496, edited by T. Roser and S.Y. Zhang (AIP, N.Y. 1999), p. 315.

[26] F. Zimmermann, *The electron cloud instability: summary of measurements and understanding*, Proc. 2001 Particle Accelerator Conference, Chicago (2001), p. 666.

[27] M. Pivi, M. Furman, Proc. Workshop on Electron-Cloud Simulations for Proton and Positron Beams, CERN (2002, to be published).

[28] R. Kirby et al, SLAC-PUB-8212, Stanford University (2000).

[29] V. Danilov, A. Aleksandrov, J. Wei, M. Blaskiewicz, *Calculations of the electron accumulation in the SNS storage ring*, Proc. 2001 Particle Accelerator Conference, Chicago (2001), p. 1749.

[30] K. Ohmi, *Beam and photoelectron interactions in positron storage rings*, Phys. Rev. Lett. 75 (1995), p. 1526.

[31] M. A. Furman et al, KEK Proc. 97-17 (1997), p. 170.

[32] M. Blaskiewicz, *Implications of the PSR instability for the SNS*, Proc. 2000 European Particle Accelerator Conference, Vienna (2000), p. 1110.

[33] L. F. Wang, H. Fukuma, K. Ohmi, Y. Suetsugu, *3D simulation of photoelectron cloud*, Proc. 2001 Particle Accelerator Conference, Chicago (2001), p. 701.

[34] B. Zotter, in *Handbook of Accelerator Physics and Engineering: a Compilation of Formulae and Data*, edited by A. Chao and M. Tigner, World Scientific, Singapore (1998), p. 112.

[35] N. Malitsky, J. Smith, J. Wei, R. Talman, Proc. 1999 Particle Accelerator Conference, New York, edited by A. Luccio and W. MacKay (1999), p. 2713.

[36] L. J. Laslett, *Workshop on Injection and Extraction*, BNL Report 7534 (1963), p. 324.

[37] H. Hereward, Workshop on Injection and Extraction, CERN Report 71-15 (1971).

[38] E. Keil and B. Zotter, *Laudau-damping of coupled electron-proton oscillations*, Workshop on Injection and Extraction, CERN Report CERN-ISR-TH-71-58 (1971).

[39] D. Neuffer, *Observations of a fast transverse instability in the PSR*, Nucl. Instrum. Methods, **A321** (1992), p. 1.

[40] L.D. Landau, J. Physics USSR, **10** (1946), p. 25.

[41] P. R. Zenkevich and D. G. Koshkarev, *Coupling resonances of the transverse oscillations of two circular beams*, Institute of Theoretical and Experimental Physics (Moscow) Report 1060 (1970); Particle Accelerators **3** (1972), p. 1.

[42] L. J. Laslett, A. M. Sessler, D. Möhl, *Transverse two-stream instability in the presence of strong species-species and image forces*, Nucl. Instrum. Methods, **121** (1974), p. 517.

[43] T.S. Wang, P.J. Channell, R. Macek, R.C. Davidson, *Transverse electron-proton two-stream instability in a bunched beam*, Proc. 2001 Particle Accelerator Conference, Chicago (2001), p. 704.

[44] R.C. Davidson, H. Qin, P.J. Channell, Phys. Rev. ST-AB, **2** (2001), p. 074401.

[45] M. Izawa, Y. Sato, and T. Toyomasu, *The vertical instability in a positron bunched beam*, Phys. Rev. Lett. 74 (1995), p. 5044.

[46] Z.Y. Guo et al., *Study of the beam-photoelectron instability in BEPC*, KEK-PREPRINT-98-23, Proc. 1st Asian Particle Accelerator Conference, Tsukuba (1998).

[47] G. Arduini, K. Cornelis, W. Hoefle, G. Rumolo, F. Zimmermann, *Transverse behavior of the LHC proton beam in the SPS: an update*, Proc. 2001 Particle Accelerator Conference, Chicago (2001), p. 1883.

[48] K. Ohmi et al, Proc. 2001 High Energy Accelerator Conference, Tsukuba (2001).

[49] T. Raubenheimer et al, Phys. Rev. **E52** (1995), p. 5487.

[50] F. Zimmermann, *Electron-cloud studies for the low energy ring of KEKB*, CERN-SL-NOTE-2000-004 AP (2000).

[51] K. Ohmi and F. Zimmermann, *Head-tail instability caused by electron cloud in positron storage rings*, Phys. Rev. Letters, **85**, p. 3821.

[52] K. Ohmi, F. Zimmermann, E. Perevedentsev, *Wake field and fast head-tail instability caused by an electron cloud*, Phys. Rev., **E 65** (2002), p. 016502.

[53] G. Rumolo, F. Zimmermann, *Simulation of single bunch instabilities driven by electron cloud in the SPS*, Proc. 2001 Particle Accelerator Conference, Chicago (2001), p. 1889.

[54] K. Ohmi, *Particle-in-cell simulation of beam-electron cloud interactions*, Proc. 2001 Particle Accelerator Conference, Chicago (2001), p. 1895.

[55] R. Nawrocky et al, Proc. 1993 Particle Accelerator Conferences, Washington, D.C. (1993), p. 2145.

[56] R. L. Witkover, P. R. Cameron, T. J. Shea, R. C. Connolly and M. Kesselman, Proc. 1999 Particle Accelerator Conference, New York, edited by A. Luccio and W. MacKay (1999), p. 2150.

[57] N. Catalan-Lasheras, Y. Y. Lee, H. Ludewig, N. Simos, J. Wei, *Optimization of the collimation system for the Spallation Neutron Source accumulator ring*, Phys. Rev. ST-AB, **4** (2001), p. 010101.

[58] Y. Funakoshi, K. Akai, N. Akasaka, K. Bane , A. Enomoto, J. Flanagan, H. Fukuma, K. Furukawa, J. Haba, S. Hiramatsu, K. Hosoyama, T. Ieiri, N. Iida, T. Kamitani, S. Kato, M. Kikuchi, E. Kikutani, H. Koiso, S.I. Kurokawa, M. Masuzawa, T. Matsumoto, S. Michizono, T. Mimashi, T. T. Nakamura, Y. Ogawa, K. Ohmi, Y. Ohnishi, S. Ohsawa, N. Ohuchi, K. Oide, E. A. Perevedentsev, K. Satoh, M. Suetake, Y. Suetsugu, T. Suwada, F. Takasaki, M. Tawada, M. Tejima, M. Tobiyama, N. Yamamoto, M. Yoshida, S. Yoshimoto, M. Yoshioka, C. H. Yu, F. Zimmermann, *KEKB performance*, Proc. 2000 European Particle Accelerator Conference, Vienna (2000), p. 28.

[59] S.-I. Kurokawa, *B-factory commissioning and first result*, Proc. 2001 Particle Accelerator Conference, Chicago (2001), p. 6.

[60] K. Y. Ng, D. Wildman, M. Popovic, A. Browman, D. Fitzgerald, R. Macek, M. Plum, T. Spickermann, *Recent experience with inductive insert at PSR*, Proc. 2001 Particle Accelerator Conference, Chicago (2001), p. 2890.

[61] N. Tsoupas, C. Gardner, Y. Y. Lee, Y. Papaphilippou, J. Wei, *Chromatic correction and optical compensation in the SNS accumulator ring using sextupoles*, Proc. 2000 European Particle Accelerator Conference, Vienna (2000), p. 1581.

[62] J. M. Jimenez, Chamonix XI, CERN-SL-2001-003-DI (2001).

[63] S. Peggs, *Coupling and decoupling in storage rings*, IEEE Transactions, **NS-30** (1983), p. 2460.

[64] *Accelerator Technical Design Report for High-Intensity Proton Accelerator Facility Project*, Japan Atomic Energy Reserach Institute (JAERI) and High Energy Accelerator Research Organization (KEK) (2002).

ELECTRON CLOUD IN LINEAR COLLIDER DAMPING RINGS*

A. Wolski, LBNL, Berkeley, CA 94720, USA

Abstract

The positron damping rings for a future linear collider will operate at energies and with beam currents where electron cloud effects could be a significant problem. Both coupled-bunch and single-bunch instabilities would adversely affect damping ring performance, by limiting the stored current, or by increasing the transverse bunch size; either effect would reduce the luminosity of the collider. Recent work has estimated, for TESLA and the NLC, the thresholds and growth rates of instabilities driven by the electron cloud, with results from simulation and analytical investigation in reasonable agreement. We review the results, which strongly suggest that serious consideration needs to be given to ways in which the effects of electron cloud can be mitigated.

1 DAMPING RINGS

The damping rings for a linear collider are designed to reduce the 6-D emittance of the beams from the sources, before acceleration in the main linacs. Luminosity requirements and main linac parameters drive the storage ring parameters; in particular, the damping rings are designed for high currents and moderate energies, and they are therefore susceptible to various instabilities. Observations of electron cloud effects at other storage rings operating in broadly comparable parameter regimes have led to concerns that positron damping rings will be limited by instabilities driven by the electron cloud. Here we present estimates suggesting that electron cloud could indeed be a problem, and that attention should be given to strategies for preventing the cloud build-up. We consider damping rings for the NLC [1] and TESLA [2], since these are the most mature designs for future linear collider damping rings.

Some relevant parameters for the NLC Main Damping Ring (MDR), NLC Positron Pre-Damping Ring (PDR), and the TESLA Positron Damping Ring are compared with those of some operating positron storage rings in Table 1. In TESLA, the long bunch train, and the bunch-by-bunch injection/extraction in the rings, leads to the need for a very large damping ring circumference of 17 km, compared to the few hundred meters of the NLC damping rings. A specific feature of the TESLA design is that the beam is fully coupled in the long straight sections, to overcome space-charge effects.

Some simulations of electron cloud in the NLC have been performed, aimed mainly at determining the cloud density and distribution under various conditions, although initial estimates of the long-range wake field have also been made. The results of these simulations are reported elsewhere [3]; here, we use simple analytic models to estimate the likely severity of the instabilities driven by the electron cloud. Our aim in this approach is to try and develop an understanding of the dependence of the various instability modes on the significant parameters. As a simple check, we apply the models to some operating positron storage rings, to see whether the expectations are consistent with observations.

2 OUTLINE OF MODELS

We are concerned with the instabilities driven by the electron cloud, rather than with the production of the cloud. Although the damping rings include antechambers to allow the absorption of synchrotron radiation at photon stops, the secondary electron yield of the vacuum chamber walls can lead to a build-up of the cloud from a small number of seed electrons, produced e.g. from residual gas ionization. Although the rate of electron production may be small, simulations suggest that the saturation density of the cloud may be estimated using the neutralization condition:

$$n_0 = \frac{N_b}{\pi b^2 s_b}$$

Table 1: Parameters of NLC and TESLA damping rings compared to some other positron storage rings.

	NLC MDR	NLC PDR	TESLA	KEK-B LER	PEP-II LER	DAΦNE	HERA-e
Energy /GeV	1.98	1.98	5	3.5	3.1	0.51	12
Circumference /m	300	231	17000	3000	2200	98	6300
Bunch charge /10^{10}	0.75	0.75	2	3.3	9	5.4	3
Betatron tunes	27, 11	11, 5.5	76, 41	46, 46	20, 20	5, 5	50
Synchrotron tune	0.0035	0.011	0.066	0.015	0.03	0.01	50
RMS beam sizes /μm	200, 20	150, 230	60, 80	420, 60	1400, 200	1700, 95	110, 11
Bunch length /mm	3.6	5.2	6.0	4	13	25	5
Mom^m compaction	0.3×10^{-3}	2×10^{-3}	0.1×10^{-3}	0.2×10^{-3}	0.1×10^{-3}	0.03	0.5×10^{-3}
Bunch separation /m	0.42	0.42	6.0	2.4	2.5	1.6	29
Beam pipe radius /mm	16	36	50	47	45/25	35	20/40

*Work supported by the US DOE under contract DE-AC03-76SF00098

where n_0 is the cloud density at saturation, N_b the number of positrons per bunch, πb^2 the cross-sectional area of the vacuum chamber, and s_b the bunch separation. We further assume that the distribution of the cloud is Gaussian, with width equal to that of the beam. Although these assumptions neglect the complicated dynamics of the cloud, we feel they are sufficient for our purposes of estimating whether a storage ring is operating in a regime where electron cloud effects will be significant.

The electron cloud will couple the dynamics of particles in the beam over both a short range (i.e. within a bunch) and a long range (i.e. between bunches). Although the effects are in some ways similar to electromagnetic transverse wake fields arising, for example, in cavities in the vacuum chamber, there are important differences. In the case of an electromagnetic wake, the field seen by a particle at the tail of a bunch is simply the sum of the fields generated by the preceding particles, so the wake may be represented by a Green's function. Since the electrons in the electron cloud are electrically charged, the wake from particles at the head of a bunch is affected by all subsequent particles, which also contribute their own wake. This means that the wake cannot be strictly represented by a Green's function. Nevertheless, one may consider the electrons in the cloud to oscillate in the field of a bunch (over a short range) or of the beam (over a long range), in which case the effect of the cloud is similar to that of a broad-band resonator. To allow us to apply standard methods to arrive at estimates of thresholds and growth rates, we shall model the wake of the cloud by that of a broad-band resonator. This is the approach taken, for example, by Ohmi, Zimmermann and Perevedentsev [4] and by Heifets [5,6]; much of our analysis follows their work.

3 SHORT-RANGE WAKE

We can first attempt to apply the standard head-tail theory. We write the wake function in units of m^{-2} for $z<0$ as:

$$W_1(z) = \frac{cR_s}{Q}\exp\left(-\frac{\omega_c z}{2cQ}\right)\sin\left(\frac{\omega_c z}{c}\right) \qquad (1)$$

where the amplitude is given by [4]:

$$\frac{cR_s}{Q} = \frac{\gamma\omega_b^2\omega_c}{\lambda_b r_e c^3}C \qquad (2)$$

Here, C is the circumference, and ω_b and ω_c are the oscillation frequencies of the bunch particles in the cloud, and the cloud particles in the bunch respectively, given by:

$$\omega_b^2 = \frac{\lambda_c r_e c^2}{\gamma(\sigma_x+\sigma_y)\sigma_y} \qquad \omega_c^2 = \frac{\lambda_b r_e c^2}{(\sigma_x+\sigma_y)\sigma_y}$$

where λ_b and λ_c are the line densities of particles in the bunch and the cloud, respectively, and r_e is the classical electron radius. The quality factor Q characterizes the decoherence of the oscillations in the electron cloud initiated by a transverse displacement of particles in the beam. This factor may be estimated analytically [6], or fitted from simulation. One generally finds that Q is of the order 5, but the results of the single bunch instability estimate are insensitive to the exact value. Relevant quantities for NLC MDR and TESLA are given in Table 2.

Table 2: Short-range wake parameters.

Quantity	NLC MDR	TESLA
Cloud density /m^{-3}	2.2×10^{13}	4.2×10^{11}
Cloud frequency /s^{-1}	1.0×10^{12}	2.1×10^{11}
Bunch frequency /s^{-1}	2.8×10^{6}	1.6×10^{5}
Wake amplitude /m^{-2}	1.5×10^{8}	9.6×10^{6}
Quality factor	5	5

The frequencies of the synchrotron sidebands (in units of the synchrotron frequency) to the betatron frequency are given by the eigenvalues of the matrix:

$$M_{ll'} = l\delta_{ll'} - \mathrm{i}\frac{N_b r_e c^2}{4\pi\gamma C\omega_\beta\omega_s}\frac{\mathrm{i}^{l-l'}}{\sqrt{ll'}}\int_{-\infty}^{\infty}\mathrm{d}\omega Z_1(\omega)\left(\frac{\omega\sigma_z}{\sqrt{2}c}\right)^{l+l'}\exp\left(-\frac{\omega^2\sigma_z^2}{c^2}\right)$$

where Z_1 is the impedance associated with the wake field (1), σ_z is the bunch length, and ω_β and ω_s are the betatron and synchrotron frequencies respectively. We have assumed that the bunch has a Gaussian distribution in longitudinal phase space, the chromaticity is zero, and we consider only the lowest radial mode.

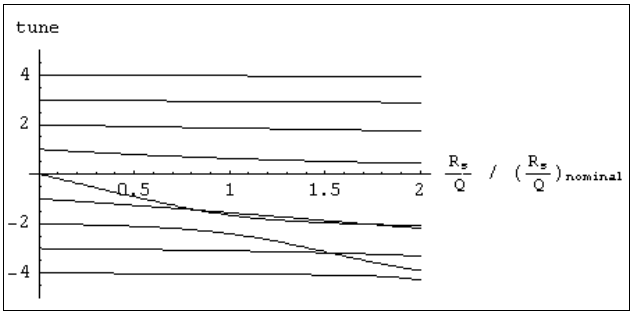

Figure 1: Synchrotron sideband tunes as a function of the electron cloud impedance, for the NLC MDR.

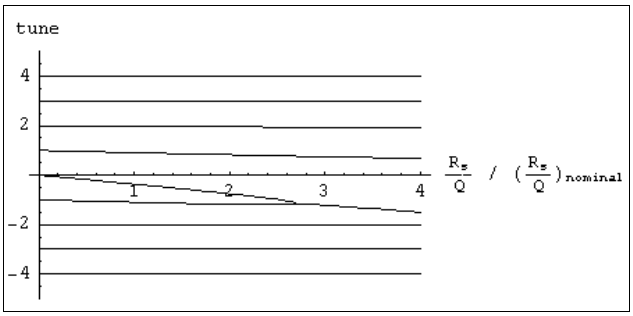

Figure 2: Synchrotron sideband tunes as a function of the electron cloud impedance, for the TESLA damping ring.

We have also assumed that the electron cloud distribution is Gaussian, with the same transverse widths as the bunch. Ohmi et al [4] find that with a larger cloud

having the same central density, the wake force is increased; with a cloud ten times larger than the beam, for example, the wake force is doubled. Other simulations suggest that the field of the bunch can have the effect of reducing the width, but increasing the density on the beam axis by more than an order of magnitude [9]. In either case, our results for the instability threshold will be rather optimistic.

The tunes for some of the low-order synchrotron sidebands are shown in Figure 1 for the NLC MDR, and Figure 2 for TESLA (treating the beam as fully coupled through the entire lattice, and with the cloud density defined by a vacuum chamber radius of 50 mm).

In each case, the tune is shown as a function of the amplitude of the impedance, in units of the nominal impedance expected from (2). The coupling of a pair of modes indicates a complex value for the frequency of the sideband, and hence identifies the head-tail threshold. Given the approximations in the model, the graphs should be read only as being indicative of the proximity of the nominal operating conditions to the head-tail threshold; thus although it appears that TESLA could operate some way below the threshold, this should not be regarded as any kind of safety margin.

A feature of the tune shifts in the case of the NLC, is the narrow range over which the modes couple, before separating. This arises from the fact that the cloud frequency is large compared to the characteristic bunch frequency c/σ_z, i.e. electrons in the cloud perform many oscillations in the bunch during one bunch passage. In this situation it may be more appropriate to use a coasting beam model for the instability, rather than the head-tail theory. Kernel et al [7], reproducing earlier results by Ruth and Wang [8], have described a relevant model. The instability threshold bunch population is given by:

$$N_{th} = 4\sqrt{\frac{3}{2}}\frac{\gamma C \alpha \sigma_\delta \sigma_z \omega_q}{r_e c^2 \beta_y \left|Z_{eff}\right|}$$

where the effective impedance Z_{eff} is given by:

$$Z_{eff} = \frac{\sum_{p=-\infty}^{\infty} Z_1(\omega_p)\exp\left(-(\omega_p-\omega_q)^2\sigma_z^2/c^2\right)}{\sum_{p=-\infty}^{\infty}\exp\left(-(\omega_p-\omega_q)^2\sigma_z^2/c^2\right)}$$

$\omega_p = p\omega_0 + \omega_\beta$, and ω_q is chosen to maximize the real part of Z_{eff}. For the NLC MDR, we find that this gives a population of just under 10^{10} particles, again indicating that the nominal parameters place the ring close to the threshold.

As we have already mentioned, the above analysis assumes that the electron cloud distribution has the same widths as the bunch, and that the thresholds with a realistic distribution will be somewhat lower. Also, the density enhancement that takes place during the bunch passage will lead to an incoherent tune shift that may be estimated by:

$$\Delta\nu_{x,y} = K_b \frac{\omega_b^2}{\omega_0^2 \nu_{x,y}}$$

where K_b is an enhancement factor ~10. For the NLC, the incoherent tune shift is of the order 0.2 (including an enhancement factor of 10), while for TESLA this approximation yields a value larger by an order of magnitude compared to the case of the NLC.

A further consideration for TESLA is the effect of electron cloud in the long straight sections, where there are no synchrotron oscillations. Here, the instability may resemble beam break-up, which is characterized by the parameter

$$\mathrm{Y} = \frac{N_b r_e \beta_y}{4\gamma}\frac{cR_s}{Q}$$

with the linear growth rate for the dipole mode given by

$$\frac{1}{\tau} = \frac{c}{C}\mathrm{Y}$$

For TESLA, the linear growth time τ is about 5 μs. This includes a large enhancement factor of 30, arising from the large bunch size in the straights. The growth time is short compared to the transit time for one of the long straight sections (about 25 μs), which means that beam break-up is indeed a possible instability mode.

4 LONG-RANGE WAKE

Although the density of the electron cloud decreases rapidly between bunches, as low energy electrons are absorbed on impact with the walls of the vacuum chamber, the cloud density can remain sufficiently high between bunch passages to couple the dynamics of one bunch to the next. We continue to use simple models to give rough estimates, to try and understand the dependence on various parameters. We neglect the fluctuation in the cloud density during bunch passages. Further, we assume that the electrons oscillate in the mean field of the beam; if the oscillation period is large compared with the bunch separation, this is likely to be a reasonable approximation. Note that we are concerned with electrons at relatively large amplitudes that perform slow oscillations in the beam; the short-range wake arises principally from electrons close to the beam, that perform rapid oscillations in the field of a single bunch.

We can write the equation of motion of an electron in the field of the beam:

$$\ddot{y} = -\frac{k^2}{y} \qquad k^2 = \frac{2N_b r_e c^2}{s_b}$$

where y is the transverse displacement of an electron with respect to the beam. With the initial conditions $y(0)=a$, $\dot{y}(0)=0$, this has the solution:

$$\sqrt{\ln\left(\frac{a}{y}\right)} = \mathrm{Erf}^{-1}\left(\sqrt{\frac{2}{\pi}}\frac{k}{a}t\right)$$

Solving for $y(\pi/2\omega)=0$ where ω is the frequency of oscillation, we find:

$$\omega = \sqrt{\frac{\pi}{2}}\frac{k}{a}$$

Note that the frequency of oscillation is inversely proportional to the amplitude. The frequency spread will lead to a rapid decoherence of the oscillations.

As for the short-range wake, we assume that the wake field resulting from the electron cloud may be modeled as a broad-band resonator. We write the resonant frequency as:

$$\omega_c = \sqrt{\frac{\pi}{2}}\frac{k}{r_{\min}} \qquad (3)$$

where $r_{\min}=2N_b r_e s_b/b$ is the maximum distance from the beam at which electrons receive sufficient energy in a single bunch passage to reach the wall before the next bunch arrives. With bunches of zero length, electrons closer to the beam than $r_{\min}$ cannot contribute to coherent oscillations in the cloud coupling one bunch to the next; with long bunches, the more complicated dynamics means that some electrons close to the bunch will survive a bunch passage, and our model will tend to underestimate the wake field.

To estimate the amplitude of the wake field, we consider the kick given to electrons in the cloud on the nominal beam orbit, by a bunch with some displacement from the orbit. This leads to:

$$\frac{cR_s}{Q} = \frac{n_0 s_b}{N_b}\frac{\omega_c}{c}C \qquad (4)$$

Decoherence of the oscillations leads to a damping of the wake field characterized by a quality factor $Q \approx 5$. Some parameters for the long-range wake are given in Table 3.

Table 2: Long-range wake parameters.

Quantity	NLC MDR	TESLA
Cloud frequency /s^{-1}	3.4×10^9	1.2×10^8
Wake amplitude /m^{-2}	4.2×10^6	8.7×10^5
Quality factor	5	5

For M equally spaced bunches the frequencies Ω_μ of the different modes are given by:

$$\Omega_\mu - \omega_\beta = \frac{N_b r_e c}{2\gamma\omega_\beta}\sum_{k=0}^{\infty} W_1(ks_b)\mathrm{e}^{2\pi ik(\mu+\nu_y)/M}$$

The real part of Ω_μ gives the coherent tune shift, and the imaginary part gives the growth rate of the amplitude of the mode.

Simulations of the long-range wake have been performed for the NLC MDR using the code POSINST [10], which also simulates the build-up of the electron cloud. A comparison between the expected wake with frequency given by (3) and amplitude given by (4), and the results from the simulations, are shown in Figure 3. Note that we use two different values for the cloud density: one given by the neutralization condition, and the other from the simulation. Although the agreement is not exact, it appears that our estimates are of the right order, and we might expect the growth rates that we calculate to be indicative of those to be found in the real machine under the appropriate conditions.

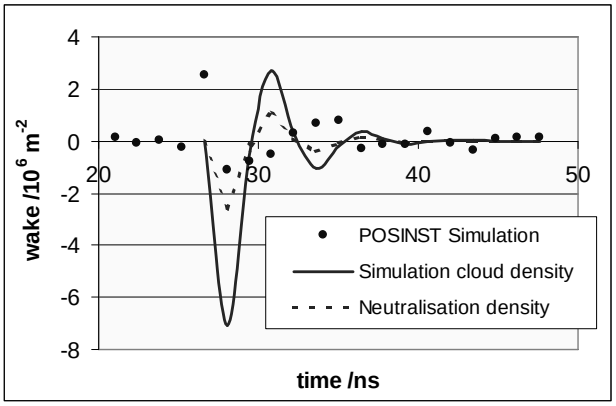

Figure 3: Wake field in NLC MDR from simple analytical model compared with simulation. The points show the simulated wake at successive bunches; the wake is generated by a displaced bunch at 25 ns. (Simulation by M. Pivi)

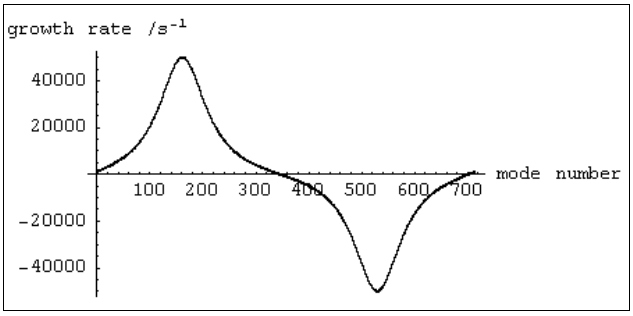

Figure 4: Coupled bunch growth rates in the NLC MDR.

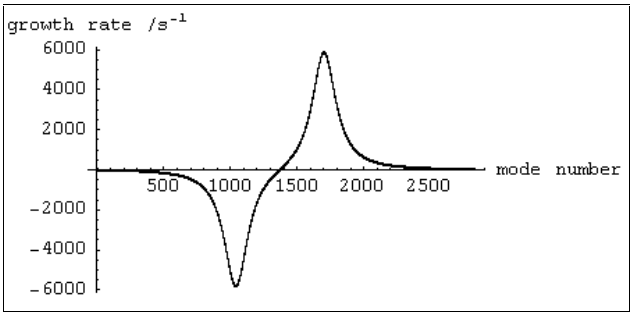

Figure 5: Coupled bunch growth rates in the TESLA damping ring.

The harmonic number of the NLC MDR is 714. The bunches are arranged in three trains of 192 bunches with every RF bucket within a train filled, and a gap of around 65 ns between the trains. This structure makes it difficult to calculate exactly the modes and their growth rates for a given impedance; for simplicity, we assume that the ring

is completely filled with 714 bunches. This is likely to give a pessimistic estimate for the growth rates, which are shown in Figure 4. The fastest growth time is 20 μs. TESLA is a simpler case, since the ring is completely filled with 2830 bunches; the growth rates are shown in Figure 5. The fastest growth time in this case is around 170 μs.

We note that the coherent tune shifts induced by the long-range wake are small, of the order 10^{-3} in both the case of the NLC MDR and the TESLA damping ring.

5 MACHINE COMPARISONS

We have applied the simple models described in the previous sections to the positron storage rings for which the parameters are given in Table 1. In Table 4, we give for each machine the incoherent tune shift, the head-tail threshold impedance divided by the nominal expected impedance, and the fastest coupled bunch growth time. We do not include the density enhancement of the cloud during a single bunch passage, predicted by simulations, so the estimates of incoherent tune shift and head-tail threshold are likely to be rather optimistic.

Table 4: Electron cloud instability thresholds and growth times for some positron storage rings.

	Incoherent Tune Shift	Single Bunch Threshold /Nominal	Coupled Bunch Growth Time /μs
NLC MDR	0.019	0.8	20
NLC PDR	0.003	10	370
TESLA	0.06	2.6	170
KEK-B	0.02	3	180
PEP-II	0.16	0.6	16
DAΦNE	0.007	6	20
HERA-e	0.006	20	1750

Of the operating storage rings, electron cloud effects have been observed at KEK-B and PEP-II, but not at DAΦNE or the HERA electron ring. Given that the feedback system for DAΦNE is capable of damping growth times of the order 20 μs, the results from our simple instability models are in broad agreement with whether electron cloud effects are observed or not. For the damping rings, it appears that the NLC MDR and TESLA are likely to suffer from electron cloud effects, while the NLC PDR may not.

6 CONCLUSIONS

The simple models we have used do not take into account the full complexity of the electron cloud production, dynamics, and interaction with the beam. Nevertheless, the results we obtain are in qualitative agreement with the results of simulations, in the cases where comparisons have been made. The formulae we have used indicate the dependence of the instabilities on beam parameters. The damping rings operate in regimes (high current, small beam size, moderate energy and, in the case of TESLA, large circumference) where electron cloud is likely to be a performance limitation.

More detailed studies, based on a variety of simulations, are needed to give a full understanding, and are in progress. The effects of magnetic fields are known to be important, and have not been included at all in the above analysis. At present, it is expected that use will need to be made of methods to prevent the build-up of electron cloud, e.g. by coating the vacuum chamber with a material that has a low secondary emission yield.

7 ACKNOWLEDGEMENTS

The author would like to thank Miguel Furman, Mauro Pivi, Sam Heifets, Tor Raubenheimer and Frank Zimmermann for useful comments and discussions.

8 REFERENCES

[1] The NLC Collaboration, "2001 Report on The Next Linear Collider", SLAC-R-571.
[2] TESLA Technical Design Report, DESY 2001-011, March 2001.
[3] M. Pivi, "Electron-Cloud Updated Simulation Results for the PSR, Recent Results for the SNS and for the NLC Damping Ring", these proceedings.
[4] K. Ohmi, F. Zimmermann, E. Perevedentsev, "Study of the Fast Head-Tail Instability Caused by Electron Cloud", CERN-SL-2001-011 AP.
[5] S. Heifets, "Qualitative Analysis of the e-Cloud Formation", SLAC-PUB-9105, January 2002.
[6] S. Heifets, "Wake Field of the Electron Cloud", SLAC-PUB-9025, November 2001.
[7] P. Kernel, R. Nagaoka, J.-L. Revol and G. Besnier, "High Current Single Bunch Instabilities at the ESRF: A New Approach", proceedings EPAC 2002.
[8] R.D. Ruth and J.M. Wang, "Vertical Fast Blow-Up in Single Bunch", IEEE Transactions on Nuclear Science, 1981.
[9] T. Raubenheimer, private communication.
[10] M. Furman, code POSINST (undocumented).

Electron-Cloud Effects in the LHC *

F. Zimmermann, CERN, Geneva, Switzerland

Abstract

We describe the simulated electron-cloud build up inside the vacuum chamber of the Large Hadron Collider (LHC) and its possible impact on the machine performance. The predictions are based on computer simulation programmes which have been calibrated against laboratory measurements of surface properties as well as against observations in existing accelerators (SPS, PS, KEKB). For the LHC, the major concern is the electron heat load inside the cold magnets. Various possible countermeasures are also discussed.

1 INTRODUCTION

There are four electron-cloud effects which could affect the performance of the LHC: (1) the head load deposited on the beam screen in the LHC arcs, (2) the heat load passing through the pumping slots onto the cold bore of the superconducting magnets, (3) the beam instability at injection into the LHC, and (4) the vacuum pressure rise and electron-induced gas desorption in the LHC straight sections. The last aspect is considered in a separate presentation [1] and will not be discussed here. In this report, we will describe the first three, then outline the LHC recipe for combatting the electron cloud, and finally comment on a future luminosity upgrade.

2 ELECTRON BUILD UP

The electron cloud is generated by either of three production mechanisms or a combination thereof.

In the LHC at injection primary electrons are produced by residual gas ionization. The design hydrogen density is 10^{15} molecules/m^3 and the CO density 1.3×10^{14} molecules/m^3 [3]. (For comparison, a pressure of 1 nTorr at 300 K corresponds to 3×10^{13} molecules/m^3). The ionization cross sections for hydrogen and CO molecules are about 0.16 and 1.5 Mbarn, respectively [4]. Then, for a beam current of 0.7 A, the typical production rate of primary electrons due to ionization is of the order $d^2\lambda_e/(ds\,dt) \approx 2 \times 10^{11}$ e$^-$ m^{-1}s^{-1}.

At 7 TeV the largest source of primary electrons is synchrotron radiation and photo-emission. Assuming a bending radius of $\rho \approx 1$ km, $\gamma = 10^6$ and a photoelectron yield $Y^* \approx 0.1$, about one photo-electron is emitted per positron or proton and per meter. For these numbers, and taking a beam current of about 0.7 A, we find an electron production rate of $d^2\lambda_e/(ds\,dt) \approx 5 \times 10^{15}$ e$^-$ m^{-1}s^{-1}, *i.e.*, the number of photoelectrons is 4 orders of magnitude higher than that from ionization.

Finally, the third production mechanism of electrons is secondary emission or beam-induced multipacting. This can lead to an exponential increase in the electron density during the passage of a bunch train. The secondary electrons themselves consist of two components: (1) secondaries, and (2) elastically reflected and rediffused electrons.

The true secondary electrons have an initial energy of a few eV, the elastic electrons an energy equal to the energy of the incident electron, the rediffused an energy somewhere in between. Our latest simulations [6] distinguish between the true and the elastically reflected electrons. Both components are represented based on measurements and parametrizations for LHC vacuum chamber prototypes [5]. For small incident energies (a few eV), the probability of elastic reflection is 30–50%, depending on the surface conditioning.

In simulations of the electron-cloud build up in the LHC [6] the elastic reflection is modelled as follows. Whenever a (macro-)electron hits the wall, we change the charge attributed to that macro-electron according to the total secondary emission yield at this value of incident energy. We then determine randomly whether the secondary (macro-)electron is elastically reflected or a true secondary. If it is elastically reflected, we preserve the absolute momentum of the macro-particle and invert its momentum component normal to the wall.

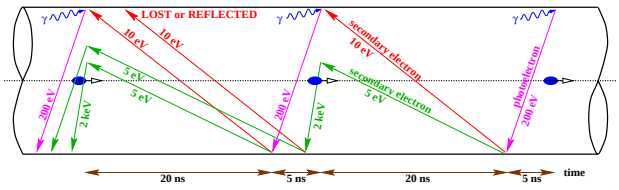

Figure 1: Schematic of electron-cloud build up in the LHC.

Figure 1 illustrates how the number of electrons is amplified during the passage of an LHC bunch train. The LHC bunches are spaced by 25 ns. For nominal bunch current, a photoelectron created on the wall while the head of a bunch is passing is accelerated to about 200 eV by the beam field and reaches the other side of the wall about 5 ns later, well before the next bunch arrives. The electron energy is high enough to produce a significant number of secondaries, which move slowly across the chamber and can be accelerated by the following bunch.

For a bunch current that is about five times lower, the

* LHC electron-cloud studies are performed in collaboration with G. Rumolo, G. Arduini, V. Baglin, S. Berg, O. Bruning, F. Caspers, A. Chao, R. Cimino, I. Collins, K. Cornelis, H. Fukuma, M. Furman, O. Grobner, S. Heifets, N. Hilleret, M. Jimenez, K. Ohmi, E. Perevedentsev, M. Pivi, A. Rossi, F. Ruggiero, G. Stupakov, L. Wang, and many others.

velocity gained by the photoelectrons would also be five times slower, and in this case they would need about 25 ns to traverse the chamber. This corresponds to the so-called multipacting condition [2]

$$n_{\min} \equiv \frac{h_y^2}{N_b r_e L_{\rm sep}} = 1\,, \qquad (1)$$

where h_y denotes the vertical half aperture, $L_{\rm sep}$ the bunch spacing, N_b the bunch population, and r_e the classical electron radius. However, in order to obtain a fast growth rate it is neither sufficient nor necessary to be close to the condition $n_{\min} = 1$, and strong electron-cloud effects are indeed observed for $n_{\min} \gg 1$ as well as for $n_{\min} \ll 1$.

Table 1 lists parameters for the three CERN machines which must accommodate an LHC type beam with 7.48 m bunch spacing. For the LHC two sets of parameters are listed, referring to the initial and final surface conditions, *i.e.*, before and after surface scrubbing due to electron bombardement with a dose larger than 10 mC/mm^2. The measured photoelectron yield per absorbed photon, Y^*, is 10% and 5%, respectively. The photon reflectivity R also diminishes after the scrubbing. The primary electron creation rates per proton and meter, $d\lambda_e/ds$, quoted for SPS and PS correspond to gas ionization with a cross section of 2 Mbarn and to a CO pressure of 50 nTorr and 10 nTorr, respectively. For the two LHC cases the numbers $d\lambda_e/ds$ correspond to a photo-electron yield per adsorbed photon of $Y_e = 0.05$ and $Y_{pe} = 0.025$.

Table 1: Simulation parameters for LHC, SPS, and PS.

symbol	LHC (init.)	LHC (fin.)	SPS	PS
E [GeV]	7000	7000	26	26
N_b	10^{11}	10^{11}	10^{11}	10^{11}
σ_x [mm]	0.3	0.3	3.0	2.4
σ_y [mm]	0.3	0.3	2.3	1.3
σ_z [cm]	7.7	7.7	30	30
$\beta_{x,y}$ [m]	80	80	40	15
L_{sep} [m]	7.48	7.48	7.48	7.48
h_x [mm]	22	22	70	70
h_y [mm]	18	18	22.5	35
$\delta_{\max}$	1.9	1.1	1.9	1.9
$\epsilon_{\max}$ [eV]	262	318	300	300
R [%]	10	5	100	100
$d\lambda_e/ds$ [10^{-6} m^{-1}]	1230	615	0.25	0.05

Figure 2 shows the simulation of electron-cloud build up in an LHC dipole magnet for a maximum secondary emission yield of $\delta_{\max} = 1.5$, and various different bunch populations. For $N_b \geq 4 \times 10^{10}$, the number of electrons increases rapidly.

Figures 3 and 4 illustrate that the energy distribution of electrons incident on the wall and, as a consequence, also

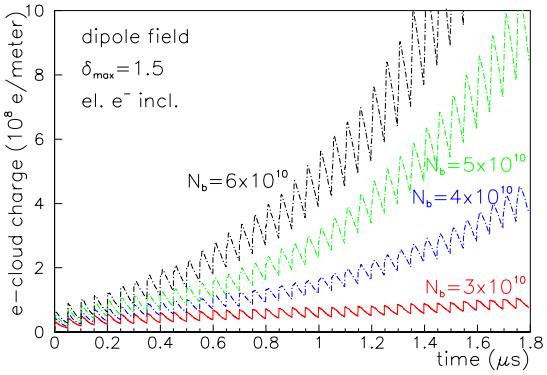

Figure 2: Simulated evolution of electron line density in units of m^{-1} vs. time during the passage of a 72-bunch LHC batch through an LHC dipole chamber for $\delta_{\max} = 1.5$.

the electron-cloud build up strongly depend on the dimension of the vacuum chamber.

The apertures of an SPS dipole magnet, a special SPS calorimeter chamber, and the LHC arcs are compared in Fig. 5. The SPS dipole has almost the same vertical dimension as the beam screen in the LHC arc. Thus in the SPS we can study the electron multipacting under conditions which are close to those expected at the LHC.

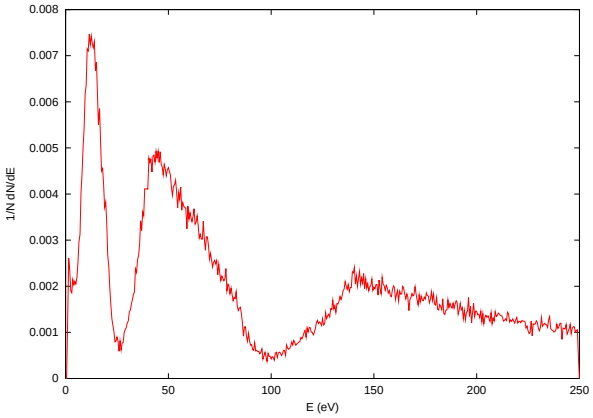

Figure 3: Energy distribution of electrons incident on LHC chamber wall for a round chamber radius $r = 158$ mm.

In Fig. 6 we show the simulated evolution of the electron line density during the passage of three successive LHC bunch trains or "batches" (each batch consists of 72 bunches), considering different batch-to-batch spacings. The electron cloud develops faster for the second and third batch. Thus, gaps larger than 2 μs are required to completely 'reset' the cloud between batches.

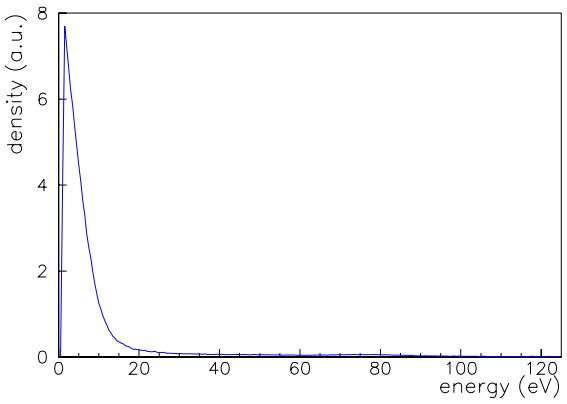

Figure 4: Energy distribution of electrons incident on LHC chamber wall for chamber half dimensions of $h_{x,y} = 22, 18$ mm.

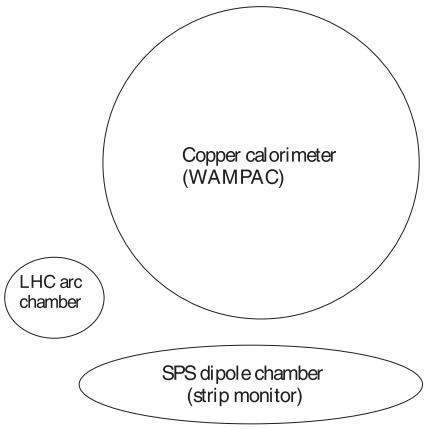

Figure 5: Transverse aperture in the LHC arcs compared with SPS vacuum chambers. Vertical dimension of SPS dipole is similar to LHC arcs.

3 ARC HEAT LOAD

Figure 7 shows the simulated heat load per unit length as a function of bunch population for a quadrupole, a dipole, and a field-free region. The heat load is highest in the field-free region. It is also higher in a quadrupole than in a dipole. This last difference is attributed to the $\cos^2\phi$ distribution of the reflected photons, which is different from earlier simulations where the reflected photons were distributed uniformly around the chamber (according to measurements, the photons are preferentially reflected in the horizontal plane across the chamber, and only few hit the top and bottom; the $\cos^2\phi$ distribution is consistent with data taken in Russia [7]. Different photon distributions were compared in Ref. [8].)

Inclusion of the elastically reflected electrons increases the simulated heat load for the LHC by a factor 2–3 compared with the case where only true secondaries are taken

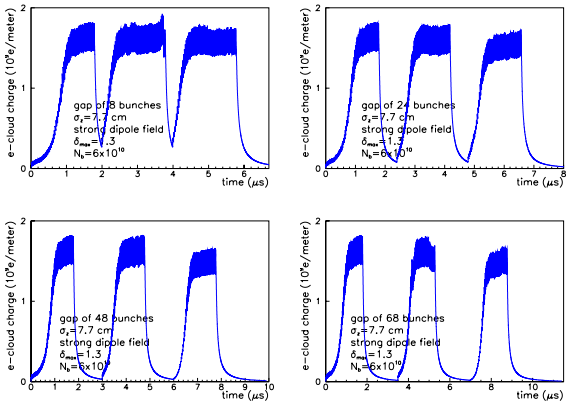

Figure 6: Evolution of electron line density in units of m^{-1} vs. time during the passage of three 72-bunch LHC batches through an LHC dipole chamber, separated by gaps of 8, 24, 48, and 68 missing bunches, for $\delta_{\max} = 1.3$.

into account. The reason why the elastically reflected electrons are so important is that the probability of elastic reflection is highest for low incident energies (for which the true secondary emission yield is small). In the simulation, most of the electrons hitting the beam pipe are yet unperturbed secondaries and have a low energy. The elastic reflection allows them to survive inside the vacuum chamber until the arrival of the next bunch, where they gain additional energy that is deposited on the chamber wall. In other words, the elastic reflection lengthens the survival time of the electrons, and this raises the heat load.

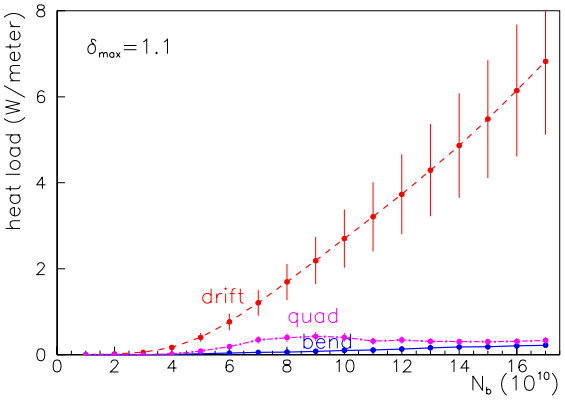

Figure 7: Simulated heat load per unit length in the LHC as a function of bunch population N_b, for various magnetic fields. Other parameters: $\delta_{\max} = 1.1$, $\epsilon_{\max} = 262$ eV, $R = 5\%$, $Y = 5\%$, and elastic electron reflection is included. The dipole field results in the smallest heat load.

Taking into account that each arc half cell comprises $l_{\mathrm{dip}} = 3 \times 14.3$ m $= 42.9$ m of dipole field, $l_{\mathrm{drift}} =$

$(3 \times 1.36 + 2.425)$ m $= 6.505$ m of field-free region, and $l_{\rm quad} = 4.045$ m of quadrupoles, from simulations such as those in Fig. 7 the average heat load per meter in the LHC arcs can be computed. This is shown in Fig. 8 as a function of bunch intensity, together with the available cooling capacity. The cooling capacity decreases for higher currents, since the cooling needs for synchrotron radiation and impedance heating increase linearly and quadratically with current, respectively. For the ultimate intensity of $N_b = 1.67 \times 10^{10}$ the average arc heat load from the chamber impedance is estimated to be about 0.41 W/m and that from synchrotron radiation 0.25 W/m [9].

The different heat-load curves in Fig. 8 refer to different values of $\delta_{\rm max}$. In most cases a steep increase in the heat load around $N_b \approx 6 \times 10^{10}$ can be noted. This steep increase will limit the maximum bunch population during the LHC commissioning, for the nominal bunch spacing of 25 ns. According to these simulations, the design bunch population of $N_b = 1.1 \times 10^{11}$ can be reached for $\delta_{\rm max} \approx 1.1$.

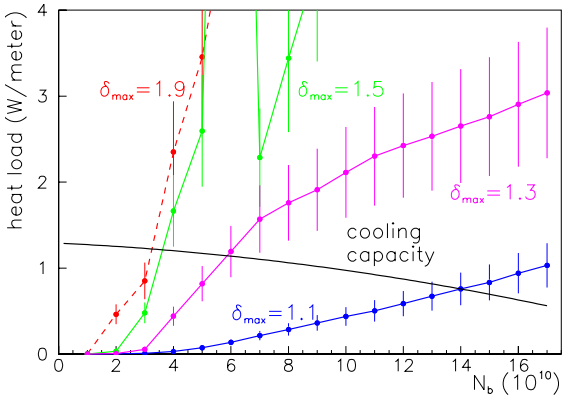

Figure 8: Simulated average LHC arc heat load and cooling capacity as a function of bunch population N_b, for various $\delta_{\rm max}$. Other parameters are $\epsilon_{\rm max} = 262$ eV, $R = 5\%$, $Y = 5\%$, and elastic electron reflection is included.

4 HEAT LOAD ON THE COLD BORE

Figure 9 displays a schematic of the Cu-coated LHC beam screen, which is installed inside the cold bore superconducting magnets and held at a temperature of 5–20 K. The beam screen accommodates several rows of pumping slots, which have a width of 1.5 mm millimeter and a length of 8 mm [10]. The thickness of the beam-screen wall is 1 mm.

Electrons passing through the pumping slots can impinge on the 1.9-K cold bore. The cooling capacity for the cold bore is much smaller than that for the screen, and, hence, an important question is the persistence of multipacting in the presence of the slots and the power deposited through these slots.

In this context, we recall the spatial distibution of electrons multipacting in an LHC dipole field. A typical example is illustrated in Fig. 10. Above about half the nominal bunch population ($N_b \geq 5 \times 10^{10}$), the electron cloud takes the form of two vertical strips with an increased density of electrons. These stripes are attributed to the maximum in the curve of the secondary emission yield as a function of primary electron energy.

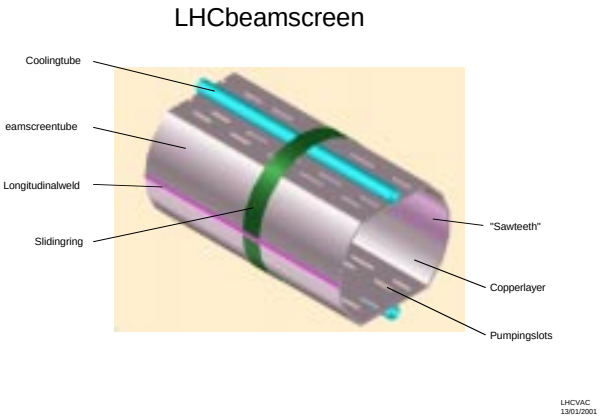

Figure 9: Schematic of the LHC beam screen operating at $T \approx$5–20 K. [Courtesy I. Collins, 2001].

For a reduced bunch population ($N_b < 5 \times 10^{10}$), the cloud concentrates as a single strip around the center of the chamber, since the electrons acquire less energy from a passing bunch.

The horizontal extent of the strips is comparable to the width of the pumping slots. If the strip location coincides with such a slot, a significant portion of the electron cloud could pass through these slots and hit the cold bore.

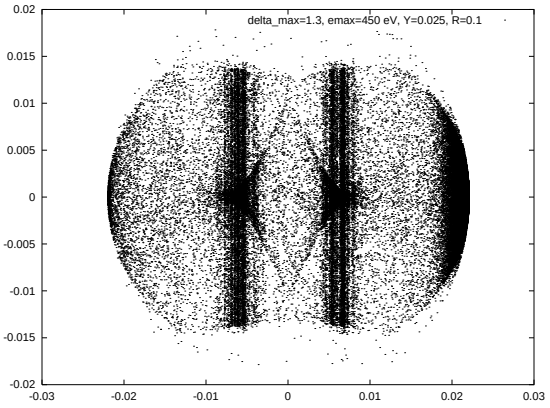

Figure 10: Snapshot of transverse e^- distribution in an LHC dipole chamber, from the first simulation for LHC [11]. Parameters: $\delta_{\rm max} = 1.3$, $\epsilon_{\rm max} = 450$ eV, $R = 0.1$, and $Y^* = 0.025$

The possible suppression of multipacting by the slots is addressed in Figure 11. This figure shows a simulation, performed for a relatively weak dipole field (0.1 T), which explores the effect of many parallel slots, spaced by 5 mm and of varying width (between 0.5 mm and 2 mm), on the

electron-cloud build up. The figure demonstrates that for a transparency as large as 40% (or width 2 mm) the electron impact rate at the position of the slots (treated as perfect absorbers) is not much different from the case without the slots.

This particular simulation was performed for the SPS, in order to predict the performance of the dedicated strip monitor that was subsequently installed, prior to the 2001 SPS run. Given the similarity of the vertical chamber height and the beam parameters, we expect that the situation for the LHC will be about the same.

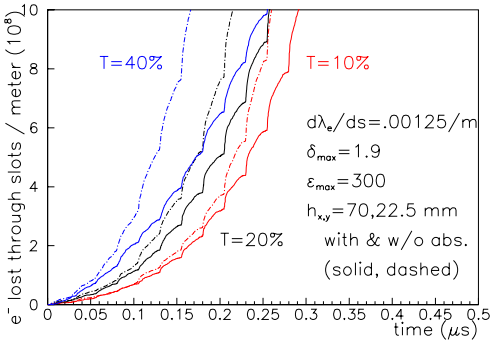

Figure 11: Simulated effect of detector or pumping slot transparency T on electron flow through the slots (solid) compared with the flow in the absence of the slots (dashed). The simulation was performed using a library Runge-Kutta integration, for a field of 0.1 T.

5 INSTABILITIES

The electron cloud can drive both multibunch and single-bunch instabilities. The multi-bunch instability is not believed to be a problem in the LHC [12], due to the high beam energy and the natural betatron frequency spread.

To estimate the strength of the single-bunch instability, we assume that the density of the electron cloud always reaches the neutralization value

$$\rho_{e,\mathrm{sat}} = \frac{N_b}{\pi L_{\mathrm{sep}} h_x h_y} \,, \qquad (2)$$

where N_b is the bunch population, L_{sep} the bunch spacing, $h_{x,y}$ the chamber half dimensions.

Employing a 2-particle model [13] we can estimate the electron density at the TMCI threshold as

$$\rho_{e,\mathrm{thresh}} \approx \frac{2\gamma Q_s}{\pi \beta_y r_p C} \,, \qquad (3)$$

where Q_s denotes the synchrotron tune, β_y the average beta function, r_p the classical proton radius, and C the ring cirumference.

The neutralization and threshold densities for various accelerators at CERN are listed in Table 2. While the PS appears marginally safe, for both the SPS and the LHC the estimated saturation density exceeds the TMCI threshold. In the case of the LHC, the heat load may set a tighter tolerance on the electron density. Nevertheless, Table 2 indicates that the single bunch instability driven by the electron cloud could become a problem at injection into the LHC.

We note that for various machines (KEKB and SPS), the threshold predicted by the 2-particle model was found to be consistent with that obtained from a detailed TMCI calculation using the simulated wake field of the electron cloud [14] and also with the threshold inferred from macroparticle tracking simulations [15, 16].

Table 2 further lists the electron oscillation frequency inside the bunch, $\omega_{e;x,y} \approx c(2N_b r_e/(\sqrt{2\pi}\sigma_z\sigma_{x,y}(\sigma_x + \sigma_y)))^{1/2}$, and the electron density enhancement near the beam axis at the end of the bunch passage H_e ('electron pinch' [17]), which is roughly given by $H_e \approx (1 + 4\sigma_z\omega_{e,x}/(\pi c)) \times (1 + 4\sigma_z\omega_{e,y}/(\pi c))$.

Table 2: Estimated TMCI thresholds for the LHC beam in the PS, SPS, and LHC.

accelerator	PS (26 GeV)	SPS (26 GeV)	LHC (450 GeV)	LHC (7 TeV)
e^- osc./bunch $n_{\mathrm{osc}} \equiv \omega_e\sigma_z/(\pi c)$	1	0.75	0.5	3
density enh. H_e	26	14	8	190
saturation density $\rho_{e,\mathrm{sat}}$ [10^{12} m^{-3}]	1.7	2.7	11.3	11.3
TMCI threshold $\rho_{e,\mathrm{thresh}}$ [10^{12} m^{-3}]	5	0.25	0.56	3
density ratio $\rho_{e,\mathrm{sat}}/\rho_{e,\mathrm{thresh}}$	0.35	11	20	4

6 LHC RECIPE

The present LHC design foresees four measures to suppress the electron cloud:

- In the arc dipoles a sawtooth chamber will be employed in order to reduce the photon reflectivity. Typical longitudinal distance between two sawtooths is 500 μm and their height about 30 μm. Measurement of photon reflectivity and photoemission yields on chamber prototypes were promising [18]. The sawtooth reduces the forward scattered photon reflectivity R to 1.3% (for comparison co-laminated Cu can have $R \approx 80\%$). A prototype sawtooth chamber is shown in Fig. 12.

  Note that although the forward scattered photon reflectivity of the sawtooth is small, the sawtooth may give rise to a 'diffuse' reflection of about 20%. The angular distribution of the diffusely reflected photons is non-uniform; only 10% of these, *i.e.*, 2% of the initial number of photons, will impinge on the bottom

and top of the chamber [19]. In most of the LHC heat-load simulations performed so far, we have assumed a uniform reflectivity R varying between 10% (initial) and 5% (final, *i.e.*, after scrubbing). This resulted in roughly the correct number of photons incident at the top and bottom. Recent simulations consider a $\cos^2\phi$ distribution for the reflected photons, and an associated total reflectivity R of 20%.

- All warm sections in the LHC straights will be coated with the newly developed getter material TiZrV [20], which after activation both provides pumping and lowers the secondary emission yield.

- Surface scrubbing during the commissioning is expected to reduce the maximum secondary emission yield to a low value. Figure 13 shows the decrease of the maximum secondary emission as a function of electron dose, as measured for a copper sample at CERN and SLAC. The CERN data indicate that a value of $\delta_{\max} = 1.1$ is not out of reach. The origin of the discrepancy between the two measurements is unclear.

- As back up solutions, the bunch spacing can be increased or satellite bunches generated to reduce the heat load.

  Figure 14 illustrates that for a 50-ns bunch spacing and a secondary emission yield $\delta_{\max} = 1.3$ (believed to be readily achieved), the bunch population can be raised to the ultimate value of $N_b \approx 1.67 \times 10^{11}$ without exceeding the cooling capacity.

  Figure 15 illustrates the effect of satellite bunches. In this example, we assume that the satellite bunches are created by an incomplete bunch compression in the PS, prior to beam extraction. This results in two satellites spaced by 5 ns, in front and behind the main bunches, respectively. The top picture shows the electron cloud build up for satellites of various intensity, where we keep the total intensity in one main bunch and two satellites constant, equal to 11×10^{10} protons. The bottom picture presents a simulation result for the same values of the main bunch intensity, but without the satellites. We observe that the satellite bunches slow down the blow up, despite of the fact that the total beam current is higher than in the second case.

  The original idea of the satellites was to quickly remove the electrons from the chamber without imparting them enough energy to produce a lot of secondaries [21]. After a significant amount of elastic electron reflection was recently taken into account and included in the simulation, their role was less clear. However, Fig. 15 illustrates that satellite bunches still help, although to a lesser extent than originally anticipated, even if a large part of low-energy electrons are elastically reflected.

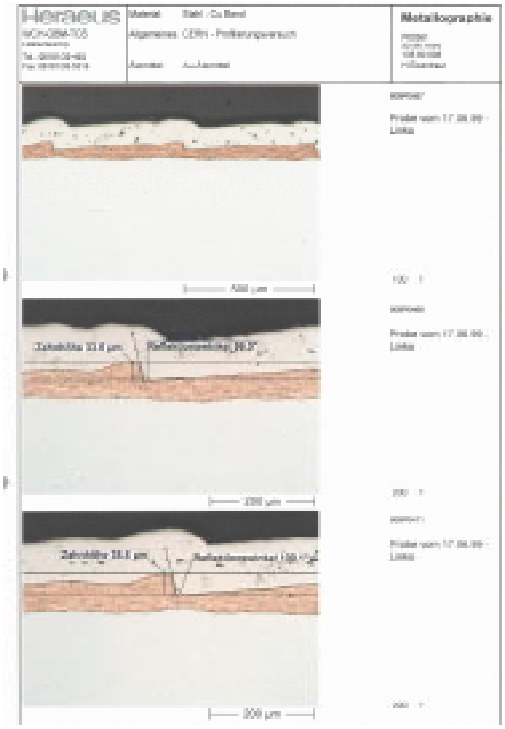

Figure 12: Sawtooth chamber protoype. [Courtesy I. Collins]

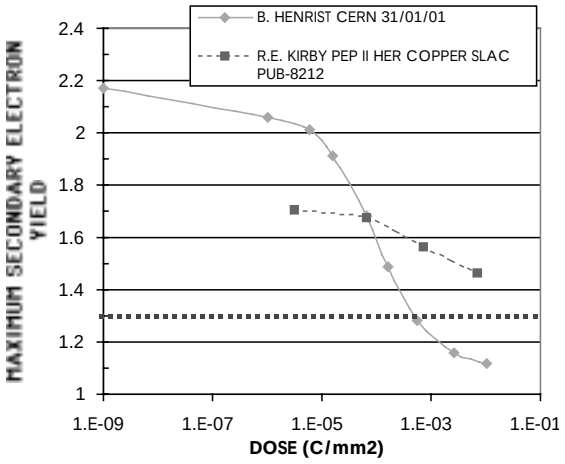

Figure 13: Comparison of dose dependence of the secondary emission yield as measured at CERN and SLAC [5].

7 LHC LUMINOSITY UPGRADE

In the framework of the LHC upgrade study [22], the effect of further shortening the bunch spacing on the arc heat load was also explored by simulation. In Figs. 16 and 17, results are shown for the rather small maximum secondary emission yield of $\delta_{\max} = 1.1$. Even for a value as low as this, the heat load reaches unacceptably high values for the nominal bunch population of $N_b = 1.1 \times 10^{11}$ if the bunch

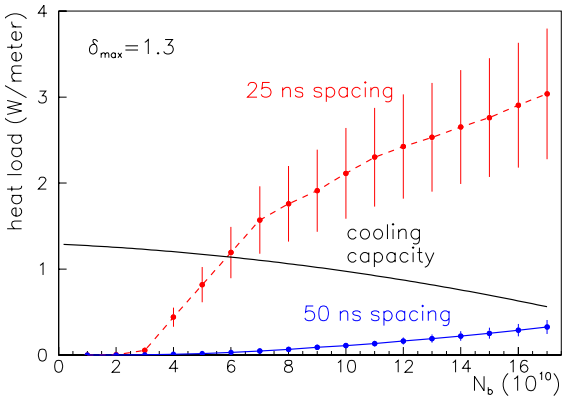

Figure 14: Simulated average LHC arc heat load & cooling capacity as a function of bunch population N_b, for 25 and 50 ns bunch spacing, and $\delta_{\max} = 1.3$. Other parameters are $\epsilon_{\max} = 240$ eV, $R = 5\%$, $Y = 5\%$; elastic electron reflection is included.

spacing is reduced below the canonical value of 25 ns. It is interesting that for higher bunch charges the head load appears to saturate. In Fig. 17 even a small improvement is visible for the shortest spacing of 2.5 ns. We take this as an indication that in the limit of a continuous beam the heat load can be much reduced.

This is further supported by a simulation of the electron-cloud heat load with a long 'superbunch', shown in Fig. 18. For a constant line density, the heat load per passing proton decreases with bunch length. The value of the heat load depends on the longitudinal bunch profile. In this example we considered a flat top with a 10% linearly rising and falling edge.

This result adds a further motivation to the idea of superbunch collisions for a future LHC upgrade. Informations related to the LHC upgrade plans can be found in Refs. [22, 23, 24].

8 CONCLUSIONS

For LHC the most worriesome effects of the electron cloud are the heat load deposited on the beam screen and the electrons passing through the pumping slots. At injection, the single-bunch instability driven by the electrons may also become a problem.

The electron-cloud simulation results are sensitive to certain model parameters, such as $\delta_{\max}$ and the fraction of reflected low-energy electrons.

The simulations predict that the electron cloud is likely to prevent LHC bunch spacings shorter than 25 ns. Superbunch collisions appear to be a promising alternative for future upgrades. They allow further increases in the luminosity while at the same time reducing the electron-cloud heat load.

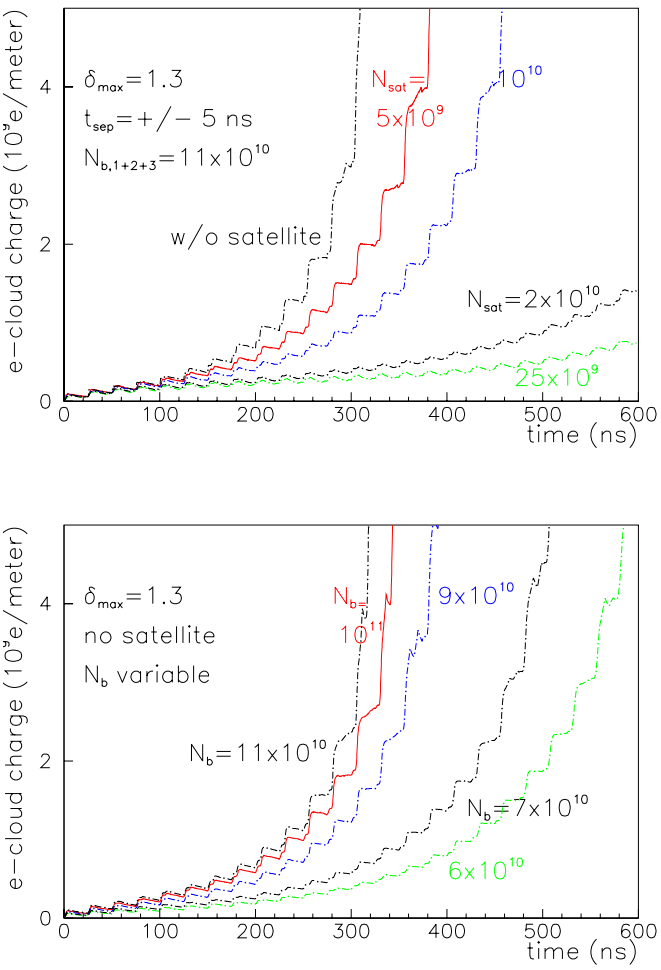

Figure 15: Simulated electron cloud build up in the LHC with (top) and without (bottom) two satellite bunches of various intensity placed one SPS bucket (5 ns) before and after the main bunches. $\sigma_z = 0.3$ m. Elastic e^- reflection included.

9 ACKNOWLEDGEMENTS

I thank G. Rumolo, G. Arduini, V. Baglin, O. Bruning, F. Caspers, A. Chao, R. Cimino, I. Collins, K. Cornelis, H. Fukuma, M. Furman, O. Grobner, S. Heifets, N. Hilleret, M. Jimenez, K. Ohmi, E. Perevedentsev, M. Pivi, A. Rossi, F. Ruggiero, L. Wang, and many others, for helpful discussions, fruitful collaboration, and many useful informations. I am grateful to F. Ruggiero for a careful reading of the manuscript.

10 REFERENCES

[1] A. Rossi, "A Simulation Study of Electron Cloud in the Experimental Regions of the LHC", these proceedings.

[2] O. Gröbner, HEACC'77, Protvino (1977).

[3] N. Hilleret, private communication, February 14, 2002.

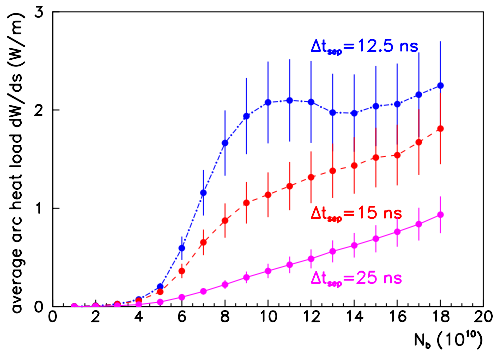

Figure 16: Simulated average arc heat load as a function of bunch population for bunch spacings of 12.5 ns, 15 ns, and 25 ns, and a maximum secondary emission yield $\delta_{\max} = 1.1$. Elastically reflected electrons are included.

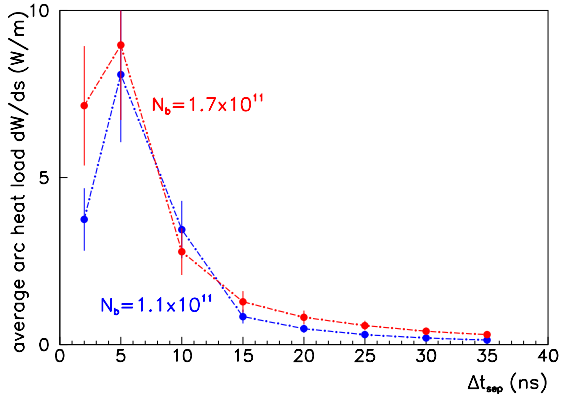

Figure 17: Simulated average arc heat load as a function of bunch spacing, for $\delta_{\max} = 1.1$ and various bunch populations.

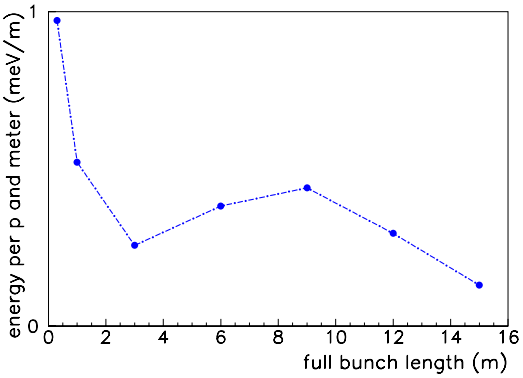

Figure 18: Simulated average energy deposition per proton vs. full bunch length for LHC dipole; line density $\lambda = 10^{12}$ m^{-1} with 10% rising and falling edge.

[4] "Tables and Graphs of Electron-Interaction Cross Sections from 10 eV to 100 GeV Derived from the LLNL Evaluated Electron Data Library (EEDL), Z=1–100", LLNL DE92–007986 (1991).

[5] V. Baglin, I. Collins, B. Henrist, N. Hilleret, G. Vorlaufer, "A Summary of Main Experimental Results Concerning the Secondary Electron Emission of Copper," LHC-Project-Report-472 (2001).

[6] F. Zimmermann, G. Rumolo, "Electron-Cloud Simulations: Build Up and Related Effects," these proceedings (2002).

[7] I. Collins, private communication (2000).

[8] G. Rumolo et al., "Simulation of the Electron-Cloud Build Up and Its Consequences on Heat Load, Beam Stability and Diagnostics," PRST-AB 012801 (2001).

[9] LHC Heat Load Working Group and private communications by L. Evans, L. Tavian and T. Durand (2001).

[10] A. Mostacci, "Beam-Wall Interaction in the LHC Liner," Ph.D. thesis, Universita di Roma 'La Sapienza' (2001).

[11] F. Zimmermann, "A simulation study of electron-cloud instability and beam-induced multipacting in the LHC", LHC Project-Report 95, and SLAC-PUB-7425 (1997).

[12] F. Zimmermann, "Electron-Cloud Simulations for SPS and LHC," Proc. Chamonix X (2000).

[13] K. Ohmi and F. Zimmermann, "Head-Tail Instability Caused by Electron Cloud in Positron Storage Rings", Phys. Rev. Letters 85, p. 3821 (2000).

[14] K. Ohmi, F. Zimmermann, E. Perevedentsev, "Wake Field and Fast Head-Tail Instability caused by an Electron Cloud," Physical Review E 65, 016502 (2002).

[15] G. Rumolo, F. Zimmermann, "Simulation of Single Bunch Instabilities Driven by Electron Cloud in the SPS," Proc. PAC'2001 Chicago, USA, and CERN-SL-2001-041 (AP) (2001).

[16] G. Rumolo, F. Zimmermann, H. Fukuma, K. Ohmi, "Electron Cloud Studies for KEKB," Proc. PAC'2001 Chicago, USA, and CERN-SL-2001-040 (AP) (2001).

[17] M. Furman and A. Zholents, "Incoherent Effects Driven by the Electron Cloud," PAC99, New York (1999).

[18] V. Baglin, I.R. Collins, and O. Grobner, "Photoelectron Yield and Photon Reflectivity from Candidate LHC Vacuum Chamber Materials with Implications to the Vacuum Chamber Design," CERN LHC Project Report 206 (1998), presented at the Sixth European Particle Accelerator Conference (EPAC98), Stockholm (1998).

[19] I. Collins, private communication (2000).

[20] C. Benvenuti, A. Escudeiro Santana and V. Ruzinov, "Ultimate pressures achieved in TiZrV sputter-coated vacuum chambers," Vacuum, Volume 60, Issue 1-2, pp. 279-284 (2001).

[21] F. Ruggiero and X. Zhang, "Collective Instabilities in the LHC: Electron Cloud and Satellite Bunches," in Proc. Workshop on Instabilities of High Intensity Hadron Beams in Rings, BNL, 28 June-1st July 1999, AIP Conf. Proceedings 496, pp. 40-48 (1999).

[22] F. Ruggiero (ed.) et al., "LHC Luminosity and Energy Upgrades: A Feasibility Study," report in preparation.

[23] F. Ruggiero an F. Zimmermann, “Luminosity Optimization Near the Beam-Beam Limit by Increasing Bunch Length or Crossing Angle,” submitted to PRST-AB, CERN-SL-2002-005 (AP) (2002).

[24] K. Takayama, J. Kichiro, M. Sakuda, M. Wake, “Super-bunch Hadron Colliders,” submitted to Physical Review Letters (2001).

ELECTRON CLOUD BUILD-UP AND RELATED INSTABILITY IN THE CERN PS

R. Cappi, M. Giovannozzi, E. Métral, G. Métral, G. Rumolo,
and
F. Zimmermann, CERN, Geneva, Switzerland

Abstract

The beam-induced electron cloud build-up is one of the major concerns for the SPS and the design of the future LHC. During the 2000 run, this effect has also been observed in the PS with the nominal LHC-type beam. The electron cloud induces a baseline distortion in electrostatic pick-up signals, both during the last turns in the PS, when the full bunch length is reduced to less than 4 ns, and in the transfer line between the PS and the SPS rings. In the year 2001, modifications in the rf-hardware allowed us to study the properties of the beam instability related with the electron cloud phenomenon for a bunch length of about 10 ns. The complete set of experimental observations carried out in the PS machine is presented and discussed in detail.

1 INTRODUCTION

Since the first studies concerning the potential harmful effect of the electron cloud build-up in the CERN LHC machine (see [1] and references therein), the research shifted from purely theoretical to more experimental activities. After the PS complex started to produce and deliver an LHC-like proton beam [2, 3], the SPS machine observed strong electron cloud build-up associated with a vertical instability [4, 5]. Intense efforts were devoted to improve the understanding of the complex phenomena by using the SPS as a LHC test-bed.

When the nominal LHC beam was generated by the PS machine [6], it was somewhat natural to investigate whether such a machine was also affected by electron cloud phenomena. It turned out that this was the case [7] and the standard signature, baseline drift in electrostatic devices, was observed. Thanks to the clean experimental conditions available in the PS machine, with stable beam circulating on the high-energy flat-top, further studies were devoted to the analysis of a possible electron cloud instability affecting the LHC beam. Interestingly, it turned out that, due to the very principle used to generate such a beam, the instability could not develop.

The nominal LHC beam at the exit of the PS consists of a train of 72 bunches, each of 1.1×10^{11} protons, spaced by 25 ns and with a momentum of 26 GeV/*c*. The longitudinal emittance at 2σ is 0.35 eVs (obtained by means of successive longitudinal bunch splitting [8, 9]), and the normalised rms transverse ones are 2.5 μm. Just before extraction, the bunches are compressed from ≈ 16 to ≈ 4 ns total length, within about 100 turns (i.e. about 200 μs). This is achieved by bunch rotation after a non-adiabatic increase of the rf-voltage. The rotating bunches in the mis-matched bucket are ejected after one quarter of the synchrotron period, when the minimum length is reached. However, by using adiabatic rf-gymnastics it was possible to obtain 72 bunches, 10 ns long, circulating for about 100 ms. Under these conditions, the beam instability was observed.

In the present paper, the observations made with the LHC-type beam in the PS ring and in the transfer line joining the PS to the SPS are described in Section 2. In Section 3 the influence on the electron cloud build-up of the longitudinal bunch train structure and solenoidal field is presented. The outcome of the investigations concerning the beam instability is reported in Section 4, where also some possible remedies are outlined. Finally, conclusions are drawn in Section 5.

2 ELECTRON CLOUD BUILD-UP

2.1 PS Ring

An electron cloud build-up was observed during the last turns in the PS, when the bunch compression takes place. The electron cloud induces baseline distortions in electrostatic pick-up signals. The effect is essentially visible in the vertical plane, as illustrated in Fig. 1. The pick-up has the bandwidth $0.2 - 30$ MHz, and is located near a combined function bending magnet.

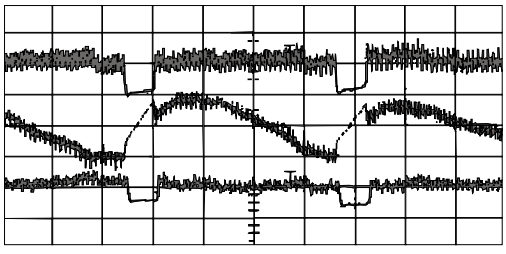

Figure 1: Measured baseline drift in a PS electrostatic pick-up during bunch compression prior to extraction. From top to bottom: Σ, Δy, and Δx. The 30 MHz bandwidth of the pick-up does not allow discriminating the 4 ns long bunches. The bunch train lasts 1.8 μs and the gap is 320 ns. The time scale is 500 ns/div.

2.2 *TT2 Transfer line between PS and SPS*

The electron cloud build-up was also observed in the TT2 (single-pass) transfer line between PS and SPS (see Fig. 2).

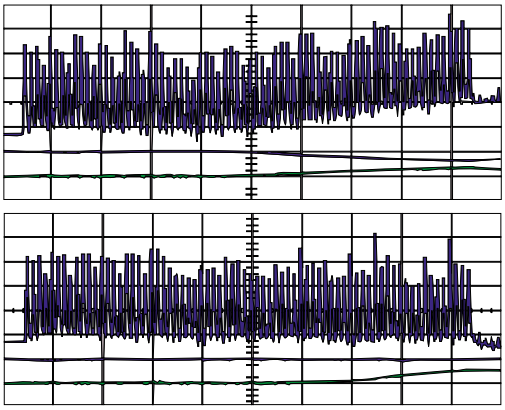

Figure 2: Measured baseline drift in a TT2 electrostatic pick-up: $I_{solenoid} = 0$ (upper) and $I_{solenoid} = 10$ A (lower). From top to bottom: Σ , Δx, and Δy (Δx, Δy signals almost coincide with the grid-lines). This pick-up has a bandwidth wide enough to allow discriminating the short bunches. Such a structure is not observable on Δx and Δy signals as the beam is centred in the pick-up. The time scale is 200 ns/div.

Here the pick-up is located in a field-free region, and its bandwidth is $0.006 - 400$ MHz. The capacitance of the device is $C = 500$ pF and the voltage corresponding to the drift of the baseline is estimated to be $V \approx 300$ mV. Hence the number of electrons pulled out of the electrostatic pick-up electrodes is given by

$$n_e = \frac{C\,V}{e} \approx 10^9. \qquad (1)$$

However, in this case electron cloud effects seem to lead only to instrumentation problems: observations indicate that the beam quality, i.e. the beam position and the transverse beam emittance, are not affected. This is due to the fact that the time of electron cloud-beam interaction is short compared to the rise-time of the related instability.

Finally, it is worthwhile mentioning that electron cloud build-up also perturbs the emittance measurement devices installed in the TT2 transfer line. The standard approach to determine the beam emittance, provided the dispersion function is known all along a transfer line, consists in measuring transverse beam profiles at three different locations [10]. The devices installed in TT2 are secondary emission monitors made of thin wires. In Fig. 3 (left) typical beam profiles for the LHC-type beam without the final bunch rotation are shown. All of them have a nice Gaussian-like shape. However, when the bunch rotation is turned on, beam profiles are strongly perturbed (see the right part of Fig. 3).

It is interesting to mention that a clear non-zero signal

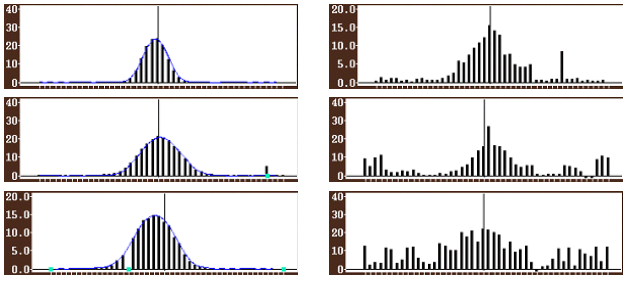

Figure 3: Transverse beam profiles measured with secondary emission monitors at three different locations in the TT2 transfer line. The measurements performed without bunch rotation are shown on the left, while the profiles on the right are obtained with the final bunch rotation active.

is present even when the monitors are retracted from the beam when the bunch rotation is active. Of course, no signal is present in the absence of bunch rotation (no electron cloud build-up) and with the monitors out of beam.

3 CONTROL OF ELECTRON CLOUD BUILD-UP

The build-up of an electron cloud can be either suppressed or strongly reduced by acting on a number of physical parameters. Observations were made of the dependence on the bunch spacing and on the presence of gaps in the bunch train. Furthermore, the effect of a solenoidal field on the dynamics of the electron cloud was also studied.

3.1 *Bunch Spacing*

A variant of the nominal LHC beam with a larger bunch spacing, 50 ns instead of 25 ns, was tested during the years 2000 and 2001. Originally, the presence of strong longitudinal coupled bunch instabilities made it impossible to achieve the nominal intensity per bunch. After a series of improvements on the HOM of the rf-cavities [11], it was possible to obtain the nominal beam intensity, namely $N_b \approx 1.1 \times 10^{11}$, during the 2001 run.

The signals detected on a pick-up in the PS machine (upper) and in the TT2 transfer line (lower) are shown in Fig. 4. Under these conditions the electron cloud build-up is substantially reduced: not only is the baseline drift in the Σ signal smaller than for the 25 ns case, but also starts later along the bunch train.

3.2 *Gaps in the Bunch Train*

The evolution of the baseline drift in a TT2 electrostatic pick-up is depicted in Fig. 5, where gaps of 12 bunches (corresponding to 320 ns) are introduced. The gap is obtained by removing one PS Booster bunch at PS injection. Electron cloud build-up always shows up at the end of the bunch train, independently of the gap position. These measurements show that a gap of 320 ns is not sufficient to reset

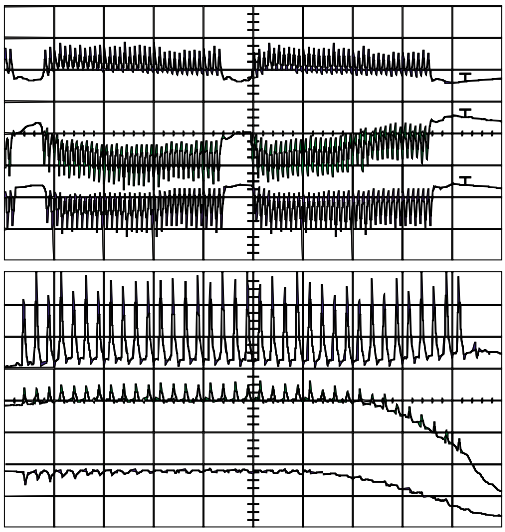

Figure 4: Measured baseline drift in a PS electrostatic pick-up (upper) and in TT2 (lower) for the 50 ns spacing LHC-type beam. From top to bottom: Σ, Δy, and Δx. The electron cloud build-up is delayed with respect to the 25 ns case and the drift is also reduced. The time scale is 500 ns/div (upper) and 200 ns (lower).

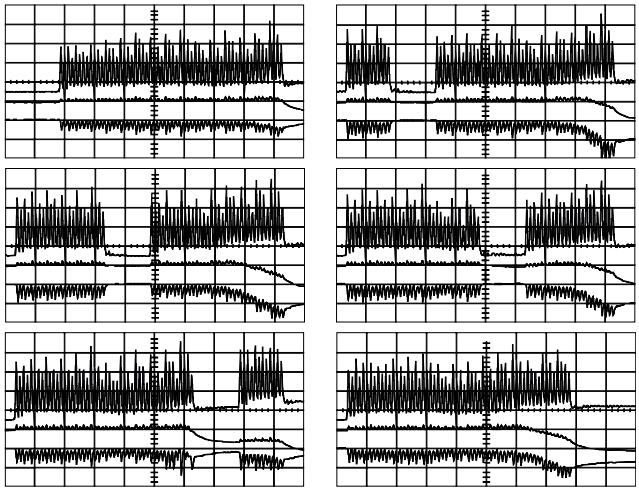

Figure 5: Measured baseline drift in a TT2 electrostatic pick-up, with the six possible cases of 12 missing bunches. From top to bottom: Σ, Δx, and Δy. The time scale is 200 ns/div.

the memory of the electron cloud: the electron cloud density is rapidly re-established behind the gap.

Observations performed in the presence of 6 gaps of 120 ns are shown in Fig. 6. Even in this case a drift of the baseline is visible at the end of the bunch train.

Finally, the case of 84 bunches filling 84 buckets, was also studied. The signals are shown in Fig. 7, where the measurements made with a pick-up in the last turns in the PS machine (upper) and in the TT2 transfer line (lower) are shown.

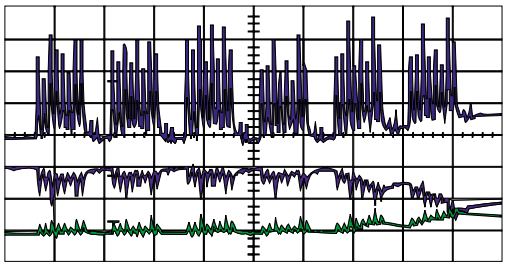

Figure 6: Measured baseline drift in a TT2 electrostatic pick-up with 6 gaps of 120 ns. From top to bottom: Σ, Δx, and Δy. The time scale is 200 ns/div.

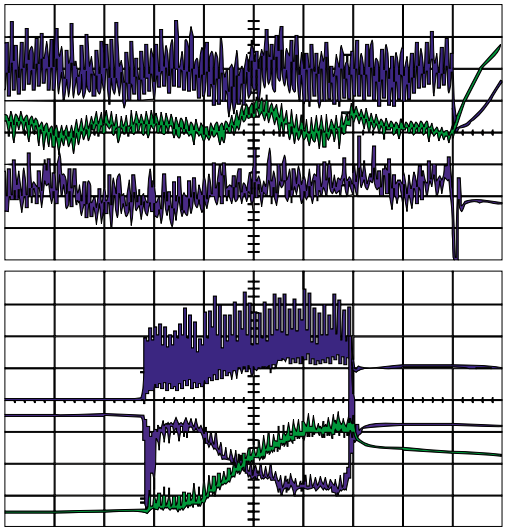

Figure 7: Measured baseline drift in a PS electrostatic pick-up in the last turns before extraction (upper) and in TT2 (lower) for the 25 ns spacing with 84 bunches (i.e. no gap). The time scale is 1 μs/div (upper) and 500 ns (lower). A strong electron cloud build-up is clearly visible. The spike on the Δx signal for the TT2 pick-up is generated by the bunches badly ejected due to the finite rise-time of the extraction kicker. From top to bottom: Σ, Δx, and Δy.

The build-up of the electron cloud is the strongest among the different cases considered here. Yet, even under these extreme conditions, which were obtained for only a fraction of milliseconds, the beam was stable.

3.3 Solenoidal Field

The investigations related to the electron cloud build-up in the B-factories and lepton rings, like KEKB, PEP-II, and BEPC, clearly showed the beneficial effect of solenoidal field on the machine performance (see Refs. [12, 13, 14]). In fact, the longitudinal solenoid field, although quite small, keeps the electrons close to the chamber wall and thus suppresses the beam-induced multipacting.

Hence, the same technique was applied in the TT2 transfer line to confirm the hypothesis that the source of the perturbations of the beam diagnostics was really the electron cloud build-up. To this end, coils were installed at both ends of the wide-band electrostatic pick-up. Each of the coils is made of 80 windings over a length of about 0.08 m. The coils have an inner diameter of about 0.13 m and an outer one of a bout 0.25 m. The distance between the two extreme ends of the coils is 0.4 m, while the longitudinal size of the pick-up is about 0.16 m. The maximum current is 10 A. The pick-up, together with the additional coils used to generate the solenoidal field can be seen in Fig. 8.

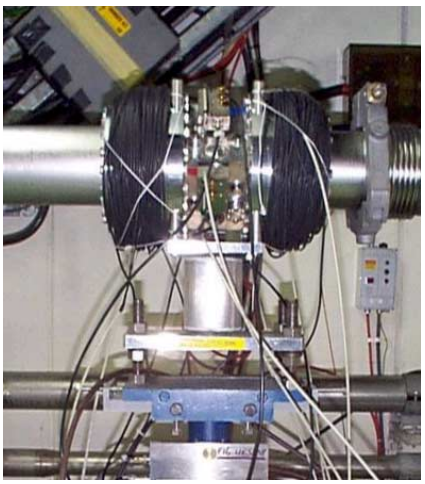

Figure 8: View of the electrostatic pick-up installed in the TT2 transfer line. The two coils are clearly seen on both sides of the device.

The value of the longitudinal component of the magnetic field along the axis of the pick-up is shown in Fig. 9.

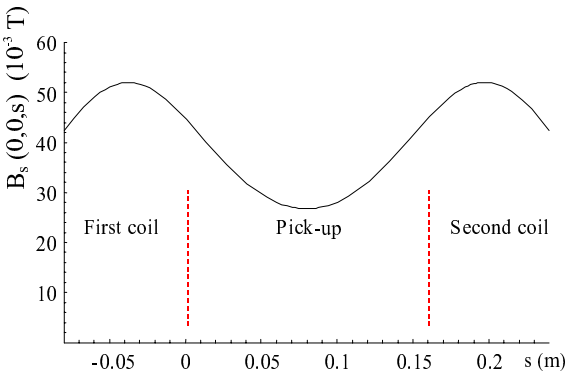

Figure 9: Absolute value of $B_s(0,0,s)$ generated by the two coils installed at both ends of the wide-band electrostatic pick-up for the maximum current.

By applying a weak solenoidal field in the TT2 electrostatic pick-up, the baseline distortion could be eliminated (see Fig. 2). A residual effect is visible, however, on the vertical signal, which may be due to the non-ideal solenoidal field created.

4 INSTABILITIES

After having detected the electron cloud build-up, the next step consisted in studying the related instability in more detail.

It was already clear that for the nominal LHC beam the electron cloud only perturbed the beam diagnostics, the beam quality being unaffected. Hence, a different approach was used where the method of producing the beam was modified. Instead of applying a non-adiabatic bunch rotation by using 80 MHz cavities on top of the 40 MHz, an adiabatic rf-gymnastics was used.

The signal of a horizontal pick-up in the PS ring was frequency-analysed to keep track of the evolution of the first unstable betatron line (about 357 kHz). It was possible to observe a horizontal single-bunch instability with a threshold at $N_b^{th} \approx 4.6 \times 10^{10}$ p/b and a rise-time of $3-4$ ms above the threshold. In Fig. 10 such a signal is shown for six different values of N_b. All the plots cover a time interval of 200 ms before beam extraction. The first case refers to an intensity just below the threshold, while the second one is just above N_b^{th}. The rise time is higher than in the other cases, but this is due to the fact that the measurement is taken near the threshold. The linear amplitude increase in logarithmic scale is clearly visible in all five cases plotted in Fig. 10.

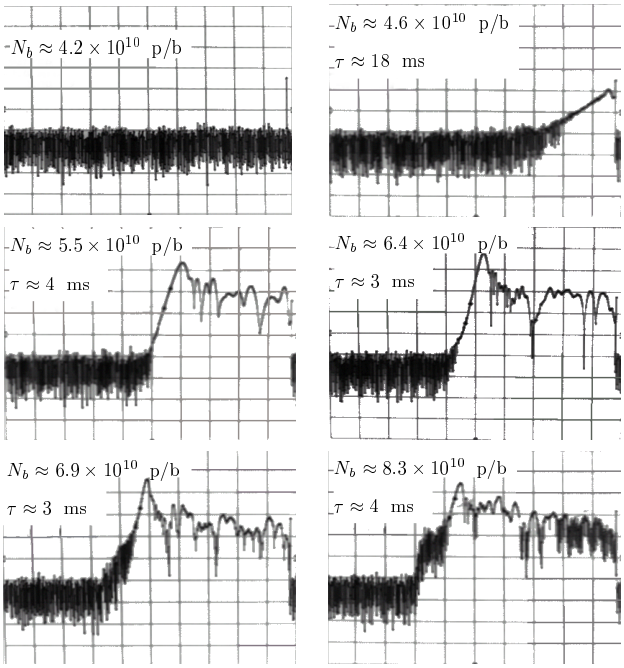

Figure 10: Rise-time of the horizontal instability as a function of the bunch intensity. The signal is obtained with a spectrum analyser with zero frequency span and central frequency 357 kHz. The beam is extracted at the end of the horizontal scale. The time scale is 20 ms/div, while the vertical scale is 10 dB/div.

Some additional information for the case $N_b \approx 5.5 \times 10^{10}$ p/b is shown in Fig. 11. Together with the evolution of the first unstable betatron line (upper left part), the Fourier analysis of the same signal is shown in the upper right picture. In the lower part, the signals from pick-ups in the PS ring (left) and TT2 transfer line (right) are shown.

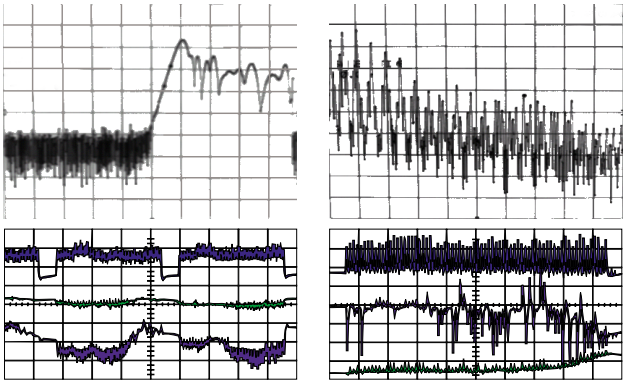

Figure 11: Instability footprint for $N_b \approx 5.5 \times 10^{10}$ p/b. The signal obtained via a spectrum analyser with zero frequency span and central frequency of 357 kHz is shown in the upper left part. The time scale is 20 ms/div, while the vertical scale is 10 dB/div. A Fourier analysis (from $0 - 10$ MHz) is shown in the upper right part. The time scale is 2 ms/div, while the vertical scale is 10 dB/div. In the lower part, the signals from a pick-up in the PS ring some tens of ms before extraction (left) and the TT2 transfer line (right) are shown. The time scale is 500 ns/div (left) and 200 ns/div (right). From top to bottom: Σ, Δy, and Δx.

It is clear that: i) the strong instability is visible only in the horizontal plane and ii) no regular pattern can be detected in the horizontal position along the bunch train. This seems to rule out a multi-bunch instability.

Two points should be stressed: firstly, the PS lattice is made of combined function magnets (dipole field with quadrupole component); secondly the fraction of machine circumference occupied by the combined function elements is about 90 %. Therefore, it is clear that the characteristics of the beam instability will be dictated by the properties of the electron cloud in the main magnets. In addition, due to the peculiar field configuration of a combined function magnet, the property that the wake field in the horizontal plane is close to zero, as for a vertical dipole field, no longer holds true [15], which may explain why a horizontal instability can develop.

4.1 Remedies

A number of measurements were devoted to finding physical quantities to be used to damp the instability. The first attempt consisted in changing the horizontal chromaticity ξ_x, normally set to about 0.1 on the high-energy flat-top. Similarly to what was done in the SPS [4], ξ_x was increased up to $\xi_x \approx 0.5$, but no variation in the instability rise-time was detected.

This fact is in good agreement with theoretical estimates [16] obtained by approximating the electron cloud with a broadband impedance [17] and using the horizontal wake field computed for the PS main magnet [15]. The resulting instability rise-time τ as a function of ξ_x is shown in Fig. 12: the weak dependence of τ on ξ_x in the range $0.15 \leq \xi_x \leq 0.5$ is clearly seen.

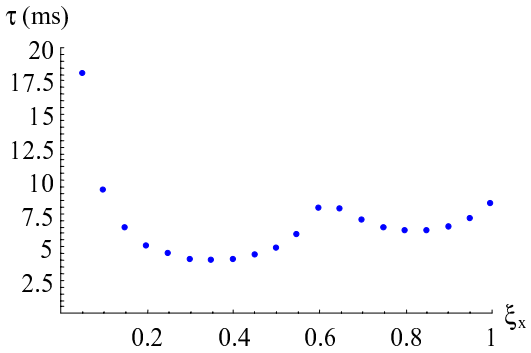

Figure 12: Dependence of the horizontal head-tail instability rise-time τ on ξ_x for the theoretical model of the PS.

Finally, octupoles were powered in an attempt to stabilise the beam. Under these new conditions, only a marginal effect was observed, despite the rather large current used (almost near to the maximum sustainable by the power converter). The corresponding octupole-induced tune-spread at half-width half-height [18, 19] can be estimated to be $\Delta Q_{x,HWHH} \approx 4 \times 10^{-5}$ and $\Delta Q_{y,HWHH} \approx 5 \times 10^{-5}$.

5 CONCLUSIONS AND OUTLOOK

Since generating the required LHC beam in the PS, intense experimental efforts were devoted to measuring electron cloud build-up and related instabilities. As far as the nominal beam is concerned, the conditions to generate an electron cloud build-up are met only when no time is left for the related instability to develop. This is due to the specific rf-manipulation, a non-adiabatic bunch rotation performed a few turns before beam extraction.

However, it was possible to study the build-up both at extraction in the PS ring and in the transfer line between the PS and SPS, as a function of some bunch parameters like bunch spacing, gaps in the bunch train, and presence of a solenoidal field around an electrostatic pick-up.

These observations lead to the conclusion that, for the nominal LHC beam, the electron cloud build-up does not alter the beam characteristics. Such a cloud only constitutes a perturbing effect for the different type of beam diagnostics, like electrostatic pick-ups and secondary emission monitors.

By introducing a modified rf-gymnastic, (an adiabatic bunch rotation reducing the bunch length from 16 ns to 10 ns), it was possible to keep the shortened beam circulating for about 100 ms. Under these conditions, it was possible to observe a horizontal single-bunch instability with threshold $N_b^{th} \approx 4.6 \times 10^{10}$ p/b, and rise-time τ of about $3 - 4$ ms above threshold. No sign of instability was observed in the vertical plane. This seems to be linked to the peculiarity of the PS lattice whose main magnets are combined function magnets. According to preliminary numerical simulations, the main wake field is produced in the horizontal plane. The observations could be explained by the head-tail formalism.

The influence of chromaticity was measured, revealing only a marginal effect on the beam dynamics, in agreement with theoretical predictions. Finally, the effect of octupoles was also tried out, showing only a small stabilising effect. It is worth mentioning that a variant of the nominal LHC beam with a 50 ns bunch spacing completely removed the instability.

Additional measurements are foreseen for the year 2002 run, to get more quantitative results on the properties of the beam instability related to the electron cloud build-up.

6 ACKNOWLEDGEMENTS

We would like to thank the PS operation crew and the experts of the rf and beam diagnostics groups for constant support during the measurement campaign.

7 REFERENCES

[1] F. Zimmermann, "A Simulation Study of the Electron Cloud Instability and Beam-Induced Multi-Pacting in the LHC", *CERN LHC Project Report* **95** (1997).

[2] R. Cappi, R. Garoby, M. Martini, J.-P. Riunaud, K. Schindl, "The PS as LHC Proton Source: Results of the Two-Week Beam Test in December 1993", *CERN PS (DI)* **94-11** (1994).

[3] K. Schindl for the PS Staff, in *Fourth European Particle Accelerator Conference*, edited by V. Suller et al. (Edition Frontièrs, Gif sur Yvette, 1994) p. 500.

[4] G. Arduini et al., in *EPAC2000*, edited by J. Poole, Ch. Petit-Jean-Genaz (European Phys. Soc., Geneva, 2000) p. 939.

[5] G. Arduini et al., in *EPAC2000*, edited by J. Poole, Ch. Petit-Jean-Genaz (European Phys. Soc., Geneva, 2000) p. 259.

[6] M. Benedikt, R. Cappi, M. Chanel, R. Garoby, M. Giovannozzi, S. Hancock, M. Martini, E. Métral, G. Métral, K. Schindl, J.-L. Vallet, "Performance of the LHC Pre-Injectors", *CERN PS (DR)* **2001-011** (2001).

[7] R. Cappi, M. Giovannozzi, E. Métral, G. Métral, F. Zimmermann, in *2001 Particle Accelerator Conference*, edited by P.W. Lucas and S. Webber (IEEE Computer Society Press, Piscataway, 2001) p. 685.

[8] R. Garoby, in *HEACC'98*, edited by I. N. Meshkov (Joint Inst. Nucl. Res., Dubna, 1998) p. 172.

[9] R. Garoby, S. Hancock, J.-L. Vallet, in *EPAC2000*, edited by J. Poole, Ch. Petit-Jean-Genaz (European Phys. Soc., Geneva, 2000) p. 304.

[10] P. J. Bryant, K. Johnsen, "Circular Accelerators and Storage Rings", (Cambridge University Press, NY, 1993).

[11] R. Garoby, in *LHC Workshop - Chamonix XI*, edited by J. Poole (CERN SL 2001-003 (DI), Geneva, 2001) p. 32.

[12] Y. Funakoshi et al., in *EPAC2000*, edited by J. Poole, Ch. Petit-Jean-Genaz (European Phys. Soc., Geneva, 2000) p. 28.

[13] J. T. Seeman et al., in *EPAC2000*, edited by J. Poole, Ch. Petit-Jean-Genaz (European Phys. Soc., Geneva, 2000) p. 38.

[14] Z. Y. Guo et al., in *2001 Particle Accelerator Conference*, edited by P.W. Lucas and S. Webber (IEEE Computer Society Press, Piscataway, 2001) p. 676.

[15] R. Cappi, M. Giovannozzi, E. Métral, G. Métral, G. Rumolo, F. Zimmermann, "Electron Cloud Build Up and Instability: Comparison Between Observations and Numerical Simulations for the CERN PS", these proceedings.

[16] E. Métral, "Effect of bunch length, chromaticity, and linear coupling on the transverse mode-coupling instability due to electron cloud", these proceedings.

[17] K. Ohmi, E. Perevedentsev, F. Zimmermann, "Study of the Fast Head-Tail Instability Caused by Electron Cloud", *CERN SL (AP)* **2001-011** (2001).

[18] D. Möhl, "On Landau Damping of Dipole Modes by Nonlinear Space Charge and Octupoles", *CERN PS (DI)* **95-08** (1995).

[19] R. Cappi, R. Garoby, E. Métral, in *Workshop on Instabilities of High Intensity Hadron Beams in Rings*, edited by T. Roser and S. Y. Zhang (American Institute of Physics, Melville, New York, 1999) p. 116.

ELECTRON CLOUD MEASUREMENTS AND SIMULATIONS FOR RHIC*

W. Fischer†, J.M. Brennan, M. Blaskiewicz, and T. Satogata
Brookhaven National Laboratory, Upton, NY 11973, USA

Abstract

Intense ion beams in RHIC lead to a rise in the vacuum pressure. Electron clouds can contribute to such a process. To measure electron cloud densities the coherent tune shift along the bunch train was observed with different bunch spacings and intensities. From the measured coherent tune shift electron cloud densities are computed and compared with densities obtained in electron cloud simulations.

1 INTRODUCTION

During the RHIC 2001 gold run the number of ions per bunch was continually increased up to the design value of 10^9 at the end of the run. Furthermore, it was attempted to double the number of bunches per ring from 55 to 110. Operation with 110 bunches led to pressure bumps with pressures high enough to prevent operation. In some instances the pressure in the warm sections increased from 10^{-9} Torr to 10^{-4} Torr [2]. With the design intensity of 10^9 ions per bunch and 55 bunches in each beam stored at injection, the vacuum system also aborted the beams. Basic machine parameters are listed in Tab. 1, a complete overview can be found in Ref. [1].

Measurements were initiated to characterize the electron cloud built-up and to investigate the possible role of electron clouds in the pressure rise. Since no dedicated electron detectors are currently available in RHIC these measurements were beam-based. To obtain an estimate of the electron cloud density, the coherent tune shift along the bunch train was determined. The estimated electron cloud densities can be compared with simulation results. Such comparisons were also done for the low energy ring of KEKB [3] and the SPS [4, 5].

The last RHIC run also allowed the measurement of proton beams. Gold and proton beams have the same number of bunches and approximately the same charge per bunch (see Tab. 1), but their interaction with the rest gas and the wall is different [6]. All tune shift measurements were performed at injection, where gold and proton beams have the same rigidity. The RHIC beam pipe is round almost everywhere. The average beta functions are the same for both planes, so are the beam emittances.

2 COHERENT TUNE SHIFT MEASUREMENTS

Coherent tunes shifts along bunch trains at injection were measured with two methods. First, a single beam position monitor (BPM) in each plane recorded the injection oscillations of the last incoming bunch. These BPMs are part of the tune meter system [7]. Typically 1024 turns were recorded and the tunes are obtained from a Fast Fourier Transform (FFT) of the coherent beam oscillations. An example is shown in Fig. 1. In this case 110 bunches were injected with an average intensity of $0.3 \cdot 10^{11}$ protons per bunch. The total tune shift after 110 bunches amounts to $2.5 \cdot 10^{-3}$. For gold beams and proton beams with large bunch spacing the resolution of these tune measurements was comparable to the tune shifts observed. The tune measurements were improved with a second method.

Table 1: Machine and beam parameters for gold and protons during RHIC Run 2001/2002, at injection.

parameter	unit	Au^{79+}	p^+
atomic number Z	...	79	1
mass number A	...	197	1
relativistic γ	...	10.5	25.9
harmonic no. h	...	360	360
no. of bunches	...	55/110	55/110
bunch spacing	ns	216/108	216/108
ions per bunch N_b	...	10^9	10^{11}
emitt. $\epsilon_{N\,x,y\,95\%}$	μm	10	25
bunch area $S_{95\%}$	eV·s/u	0.4	1.0
full bunch length	ns	18	14

The orbit system was set to record the injection oscillations of the last incoming bunch in 12 BPMs. In this measurement, all BPM data were filtered and the peak in the spectrum interpolated. In addition, the tune of each bunch

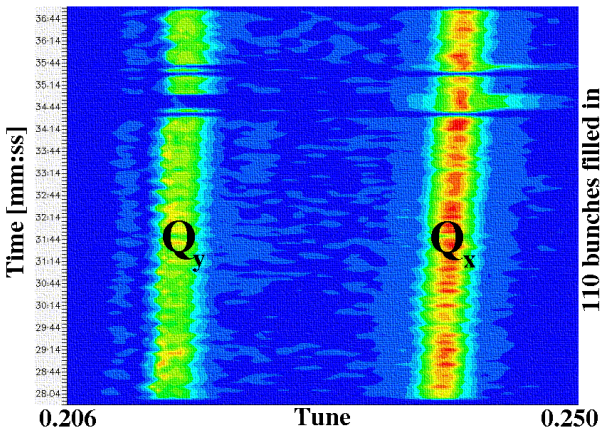

Figure 1: Coherent tunes measured along a Yellow train of 110 proton bunches with 105 ns spacing. Due to coupling both transverse tunes are visible.

* Work supported by US DOE under contract DE-AC02-98CH10886.
† Email: Wolfram.Fischer@bnl.gov

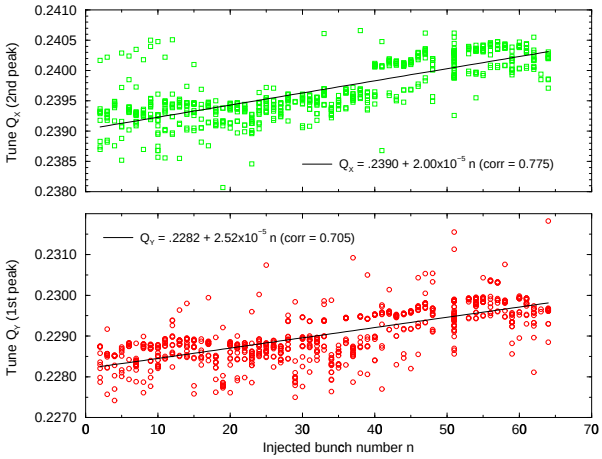

Figure 2: Coherent tunes measured along a Blue train of 63 gold bunches with 105 ns spacing. Individual dots correspond to the tunes from different BPMs. The solid lines are linear fits to the data.

could be obtained as an average of the 12 BPM measurements. This procedure is outside the current operational capabilities of the BPM system. A measurement is shown in Fig. 2. In this case a train of 63 bunches was injected with an average intensity $0.65 \cdot 10^9$ gold ions. The vacuum system aborted the fill. Furthermore, a transfer function measurement was tested from which the tunes along the bunch trains can be obtained.

In the measurements, an increase in both transverse tunes was observed, consistent with the existence of an electron cloud. The tune shift is about the same for the horizontal and vertical plane.

In Tab. 2 the results of all measurements are summarized. Measured tune shifts are of order 10^{-3} and are sometimes comparable to the measurement resolution. The data are consistent with the expectation that higher beam intensities and shorter bunch spacing lead to larger tune shifts.

3 ELECTRON CLOUD DENSITIES

A bunch passing each turn through a static electron cloud with uniform spatial density ρ_e experiences a coherent tune shift [8–10]

$$\Delta Q_{x,y} = \rho_e \left(\frac{r_p Z}{\gamma A} \right) \frac{h_{y,x} \beta_{x,y} L}{(h_x + h_y)}, \qquad (1)$$

where $h_{x,y}$ are the semi axes of an elliptical chamber, $\beta_{x,y}$ the average beta functions, L the length of the sections with electron clouds, and $r_p = 1.5347 \cdot 10^{-18}$ m the classical proton radius. In the case of a round beam chamber ($h_x = h_y = h$) and round beams ($\beta_x = \beta_y = \beta$) the tune shifts in both planes are the same ($\Delta Q_x = \Delta Q_y = \Delta Q$) and Eq. (1) can be simplified to

$$\Delta Q = \rho_e \left(\frac{r_p Z}{\gamma A} \right) \frac{\beta L}{2}. \qquad (2)$$

Table 2: Measured coherent tune shifts ΔQ along bunch trains. The values given are the difference in tune between bunch 55 and bunch 1, and are averaged over the horizontal and vertical tune shift. The number of measurements is shown in brackets.

bunch spacing	charge per bunch	tune shift ΔQ	
		Au^{79+}	p^+
[ns]	$[10^{10}e]$	$[10^{-3}]$	$[10^{-3}]$
216	7.6	1.1 (2)	–
216	8.7	–	0.3 (12)
108	3.0	–	1.3 (2)
108	5.4	1.1 (4)	–

Assuming that the electron cloud fills the whole beam pipe, the electron line density is $\lambda_e = \pi r^2 \rho_e$ where r denotes the average beam pipe inner radius. The charge line density is given by $\lambda_{ce} = \lambda_e e$ where e is the electron charge.

We consider the cases of electron clouds in the whole ring and clouds in the warm regions only. The latter is motivated by the fact that significant pressure rises were only observed in warm region.

For relativistic ion beams with the same rigidity the factor $(r_p Z/\gamma A)$ in Eq. (2) is approximately constant. However, gold and proton beams were injected into different lattices, resulting in different values for β in both cases.

The relevant machine parameters for all cases and the computed electron cloud densities are shown in Tab. 3. With the assumptions made, one expects charge line densities of 0.2 to 2 nC/m to account for the measured tune shifts.

Eq. (2) gives only a rough estimate for the electron cloud density for two reasons. First, with long bunches the cloud may not be static while the bunch is passing through. In RHIC electrons can perform a few oscillations during a bunch passage. Second, the cloud density may not be distributed uniformly in space. In Ref. [10] the effect of

Table 3: Machine parameters and computed electron cloud densities for different cloud lengths and species.

parameter	unit	Au^{79+}	p^+
tune shift ΔQ	10^{-3}	1.1	1.3
r whole ring	m	0.04	
r warm regions only	m	0.06	
β whole ring	m	30	36
β warm regions only	m	42	76
L whole ring	m	3834	
L warm regions only	m	700	
ρ_e whole ring	10^{11} m^{-3}	3.3	2.9
ρ_e warm regions only	10^{11} m^{-3}	12.8	7.6
λ_e whole ring	10^9 m^{-1}	1.6	1.4
λ_e warm regions only	10^9 m^{-1}	14.5	8.6
λ_{ce} whole ring	nC·m^{-1}	0.26	0.22
λ_{ce} warm regions only	nC·m^{-1}	2.32	1.38

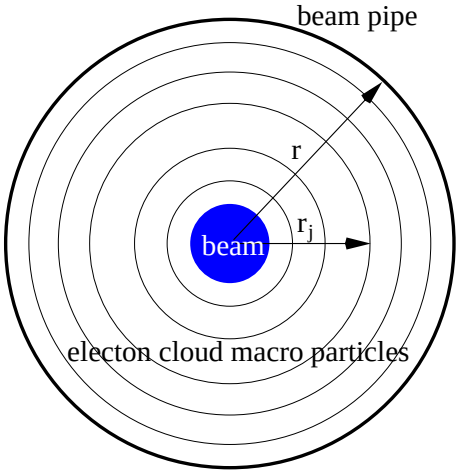

Figure 3: Geometry used in the electron cloud simulations.

the bunch length on the observed tune shift is investigated analytically and numerically. Significant deviations from Eq. (2) are found for electron clouds of size comparable to the beam size while the equation holds for electron clouds large compared to the beam size. In the simulations reported in Sec. 5 it is found that the electron cloud is much larger than the beam size. This was also found in a RHIC simulation with another code [11]. A transversely large electron cloud, filling most of the beam pipe, is also a good approximation for a cloud with uniform spatial density. Thus Eq. (2) should give a useful estimate for the electron cloud densities.

4 ELECTRON CLOUD SIMULATIONS

The computer code used here was written by one of the authors (M.B.) to study both the effects of electron gap survival and the electric fields generated by the electrons [12]. It was used previously for the PSR [13] and the SNS [14].

The code assumes that the positively charged ion beam and the electron cloud are both cylindrically symmetric within a round, straight vacuum chamber, without an external magnetic field. Longitudinal electric fields are ignored, since they produce velocities small compared to the beam velocity. The spatial distribution of the electron cloud is modeled as a sum of N_{macro} cylindrical shells which serve as macro particles. This is shown in Fig. 3. The macro particle shells can have an angular momentum.

The evolution of the cloud is computed by accelerating the shells, and creating secondary electrons when the macro particles hit the wall. In addition, electrons are created either at the wall or in the beam pipe with a generation rate proportional to the instantaneous beam line density. The generation rate must be estimated outside the program from processes such as rest gas ionization or beam loss driven electron generation.

The acceleration of shell j, with radius r_j, due to shell k, with radius r_k is taken to be nonzero only if $r_j > r_k$. In this case the acceleration is

$$\ddot{r}_j = 2r_e c^2 \lambda_k \frac{r_j}{d^2 + r_j^2}, \tag{3}$$

where r_e is the classical electron radius, c the speed of light and λ_k is the electron line density of shell k. The smoothing length d is typically an order of magnitude smaller than the beam size. The electric field due to the ion beam has the same form as that due to electrons at $r = 0$, λ_e being replaced by the instantaneous beam line density multiplied by the ion charge state, $Z\lambda_b$.

The time dependence of the instantaneous beam line density is given by

$$\lambda_b(t) = \lambda_{b,peak}\left(1 - \frac{t^2}{\tau^2}\right)^n, \tag{4}$$

where n can be chosen to fit the measured longitudinal beam profile. For large n formula (4) approximates a Gaussian beam profile. τ is a measure for the beam length.

The beam is typically divided into several thousand longitudinal slices N_{slice}, and the electron cloud is updated with every longitudinal slice. Electron macro particles can carry different charges with a minimum and maximum charge defined. Macro particle numbers range from hundreds to hundreds of thousands.

The generation of secondary electrons follows largely a model that is presented in Ref. [15]. When an electron macro particle with energy E hits the wall, it is first determined whether the electron is reflected or generates secondary electrons. In the following, x_r denotes a random number out of a uniform distribution between zero and one. The electron is reflected if

$$x_{r1} < P_\infty + (P_0 - P_\infty)e^{-E/E_{\text{reflect}}}, \tag{5}$$

where P_0, P_∞, and E_{reflect} are input parameters that should be determined in measurements. P_0 and P_∞ are the probabilities of reflection at zero and large energy respectively.

If the electron macro particle is reflected, it can be reflected elastically or it can be rediffused. It is rediffused if

$$x_{r2} < P_{\text{rediffuse}}, \tag{6}$$

where $P_{\text{rediffuse}}$ is an input parameter. Otherwise it is elastically reflected. In the former case the energy of the outgoing electron macro particle is $x_{r3}E$; in the latter case it is E.

If the electron macro particle is not reflected, it generates secondary electron macro particles with the emission yield δ given by

$$\delta(E) = \delta_{max} \times 1.1\left(\frac{1 - \exp\left[-2.3(E/E_{max})^{1.35}\right]}{(E/E_{max})^{0.35}}\right). \tag{7}$$

δ_{max} and E_{max} are input parameters. The line density of the generated macro particle is

$$\lambda_{k,out} = \lambda_k \delta(E) e^{\alpha_\delta(1-\cos\theta)}, \tag{8}$$

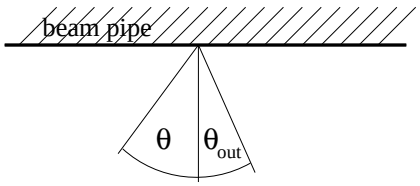

Figure 4: Definition of angle θ.

where α_δ is an input parameter and θ is the incident angle relative to the surface normal (see Fig. 4). If the line density is below the set limit, the macro particle is dropped. If the line density is above the set limit, more than one macro particle is generated. The energy of the generated macro particles is

$$E_{out} = E_{\mathrm{secondary}} \tan\left(\frac{\pi}{2} x_{r4}\right). \qquad (9)$$

$E_{\mathrm{secondary}}$ is an input parameter.

The distribution of the output angle θ_{out} is the same for reflected and secondary electrons, and independent of the incident angle θ, thus assuming a rough surface. The distribution of θ_{out} is given by

$$P(\theta)\, d\theta \propto (\cos\theta)^{\alpha_\theta} \sin\theta\, d\theta, \qquad (10)$$

where the parameter α_θ is an input parameter between zero (equivalent to black body radiation) and infinity ($\theta_{out} = \mathrm{const} = \pi/2$). The list of input parameters is shown in Tab. 4.

5 SIMULATION RESULTS

Since the simulations have many input parameters and the result is very sensitive to changes in a number of those we first define reference cases for gold and proton beams. The reference cases should be close to worst case scenarios with respect to the beam parameters. We will then vary input parameter in one of the reference cases to find the sensitivity of the result with respect to these parameters.

The two reference cases are based on design intensities and short bunch spacing. The cases differ slightly in the charge per bunch and significantly in the bunch length. Furthermore, rest gas ionization is assumed for the proton case and loss-driven electron generation in the gold case. Beam and beam pipe sizes correspond to an assumed electron cloud in the whole machine. The two cases are listed in Tab. 4.

In Figs. 5-10 the simulation output is shown for the proton reference case. Fig. 5 shows the ion beam and electron cloud charge line densities. After 25 bunches the electron cloud is saturated at approximately 0.3 nC/m. The saturation is also visible in Fig. 8 which only shows the last three bunches. The saturation charge line density is comparable to expectations from the tune shift measurements (cf. Tab. 3). However, the tune shift measurements were done at lower bunch charges.

Table 4: List of input parameters for electron cloud simulations. For gold and proton beams reference cases are presented with design intensity and twice the design bunch number.

parameter	unit	Au^{79+}	p^+
bunch spacing	ns	108	
bunches	...	55	
rms beam radius	mm	2.2	2.4
pipe radius	mm	40	
electrons generated/bunch	...	40000	100
electron generation radius	mm	40	2.4
full bunch length	ns	18	14
bunch shape parameter n	...	3	3
bunch charge	nC	13	16
longitudinal slices	...	5000	
macro particles, initially	...	2500	250
smoothing length d	mm	0.1	
λ_{ce}, initial	$\mathrm{pC{\cdot}m^{-1}}$	1.6	
P_0	...	0.8	
P_∞	...	0.2	
E_{reflect}	eV	60	
$P_{\mathrm{rediffuse}}$	...	0.5	
δ_{max}	...	2.5	
E_{max}	eV	300	
$E_{\mathrm{secondary}}$	eV	20	
α_δ	...	0.5	
α_θ	...	1.0	

Figs. 6 and 9 show the transverse rms size of the ion beam and electron cloud for the whole bunch train and the last three bunches respectively. The electron cloud size drops while the second half of the bunch is passing, as accelerated electrons hit the wall. On average the electron cloud is much larger than the ion beam and its rms size is consistent with a approximately uniform density. For a transverse uniformly distributed electron cloud, the rms size would be $r/\sqrt{2}$.

In Figs. 7 and 10 the average kinetic energy of the electrons and the electron current into the wall are shown. From this, an estimate of the heat load into the wall can be obtained. From Fig. 10 one finds an average kinetic energy of approximately 0.03 keV and average electron current of about 20 mA/m. This corresponds to a heat load of 0.6 W/m or 1.8 kW for the cold part of the ring, assuming that all kinetic energy is transformed into heat. No increased heat load was observed during the tests in 2001. The minimum detectable heat load is 150W [16].

The simulation of the gold beam reference case shows no significant increase in the initial electron line density. The final density after 55 bunches is two orders of magnitude smaller than in the proton reference case. This is largely due to the longer bunches and the reduced charge per bunch.

The sensitivity of the computed electron cloud density with respect to the input parameters was estimated by varying single input parameters only. This is shown in Tab. 5.

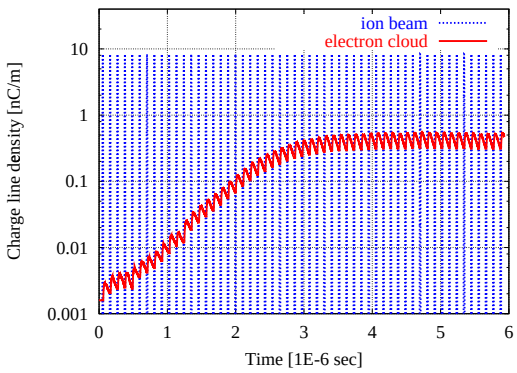

Figure 5: Ion beam and electron cloud line density for the proton reference case.

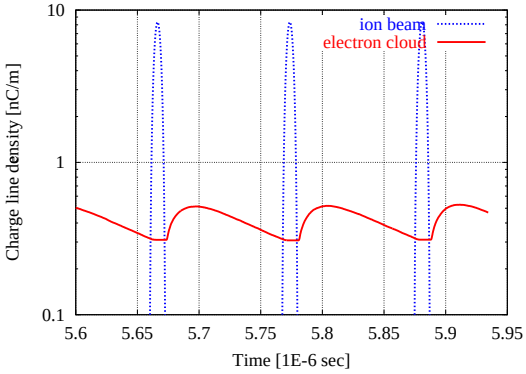

Figure 8: Ion beam and electron cloud line density for the last three bunches of the proton reference case.

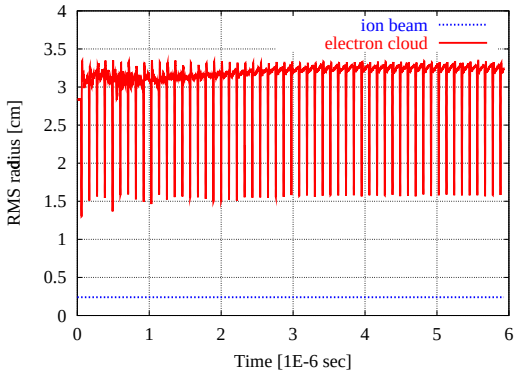

Figure 6: Ion beam and electron cloud transverse rms sizes for the proton reference case.

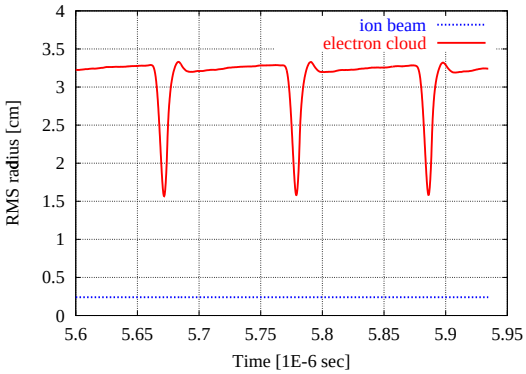

Figure 9: Ion beam and electron cloud transverse rms sizes for the last three bunches of the proton reference case.

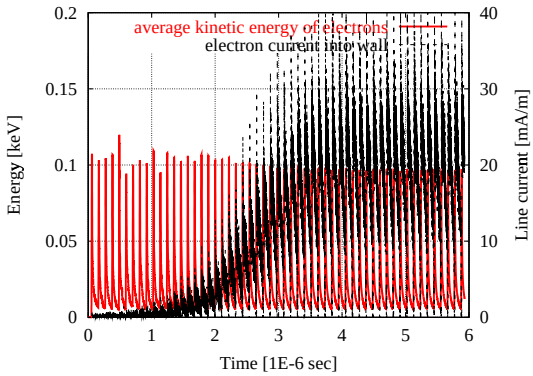

Figure 7: Average kinetic energy of electrons and electron current into the beam pipe wall for the proton reference case.

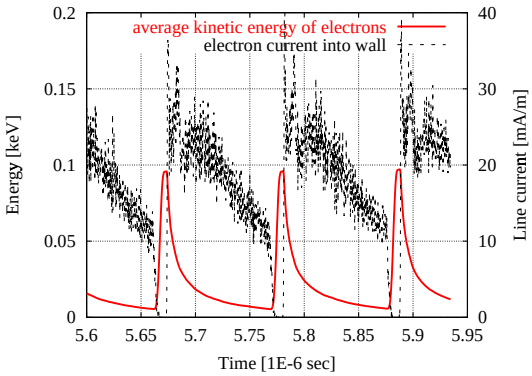

Figure 10: Average kinetic of electrons and current into the beam pipe wall for the last three bunches of the proton reference case.

Table 5: Maximum charge line density after 55 bunches in simulations under variation of input parameters. In each case only one parameter of the proton reference case is changed and the resulting line density is shown together with its relative change.

parameter	unit	value	change [%]	λ_{ce} [nC/m]
(ref. case p)	...	...	...	**0.5**
bunch spacing	ns	216	$+100$	0.00
beam radius	mm	4.8	$+100$	0.4
pipe radius	mm	60	$+50$	0.02
e-gen./bunch	...	50	-50	0.5
e-gen./bunch	...	1000	$+1000$	0.5
e-gen. radius	mm	40	$+1660$	0.5
bunch length	ns	18	$+28$	0.4
bunch length	ns	10	-28	0.6
bunch shape n	...	1	...	0.3
bunch shape n	...	6	...	0.6
bunch charge	nC	12	-25	0.00
bunch charge	nC	14	-12	0.2
bunch charge	nC	18	$+12$	0.8
N_{slices}	...	10000	$+200$	0.5
N_{macro}, initial	...	2500	$+1000$	0.5
smoothing d	mm	0.01	-90	0.5
λ_{ce}, initial	pC/m	0.016	-99	0.5
P_0	...	0.7	-12	0.2
P_∞	...	0.1	-50	0.5
E_{reflect}	eV	80	$+33$	0.6
$P_{\mathrm{rediffuse}}$	...	0.4	-20	0.6
δ_{max}	...	2.0	-20	0.00
δ_{max}	...	2.2	-12	0.01
E_{max}	eV	350	$+17$	0.1
$E_{\mathrm{secondary}}$	eV	30	$+50$	0.9
α_δ	...	0.4	-20	0.4
α_θ	...	0.0	-100	0.3
α_θ	...	5.0	$+500$	0.9

The simulation result is not sensitive to the number or location of electrons generated during a bunch passage, the number of longitudinal slices, the number of initial macro particles or the smoothing length d. It is also not sensitive to the initial line electron line density so that the final line density is determined through the parameters of the multiplication process. However, the result is, to a varying degree, sensitive to almost all other parameters.

6 SUMMARY

The signs of the measured coherent horizontal and vertical tune shifts along bunch trains in RHIC are consistent with the existence of electron clouds. From the measured tune shifts electron cloud densities were estimated. Electron cloud densities of the same order of magnitude could also be obtained in simulations with beam intensities somewhat higher than in the measurements. The cloud densities estimated from the tune shift measurements could not be reproduced with the bunch intensities in the measurement. Thus, physical effects may be missing in the simulation or there is an insufficient knowledge of the surface parameters.

7 ACKNOWLEDGMENTS

The authors would like to thank for support and discussions: M. Bai, P. Cameron, M.A. Furman, M. Harrison, H.C. Hseuh, T. Kerner, W. MacKay, T. Nicoletti, F. Pilat, M. Pivi, T. Roser, W.C. Turner, S. Tepikian, D. Trbojevic, S.Y. Zhang, and F. Zimmermann.

8 REFERENCES

[1] H. Hahn (editor), "RHIC design manual", revision of October 2000, http://www.rhichome.bnl.gov/NT-share/rhicdm/00_toc1i.htm.

[2] S.Y. Zhang, "RHIC vacuum pressure bump", BNL C-A/AP/67 (2002).

[3] G. Rumolo, F. Zimmermann, H. Fukuma, and K. Ohmi, "Electron cloud studies for KEKB", proceedings of the 2001 Particle Accelerator Conference, Chicago (2001).

[4] G. Arduini, K. Cornelis, G. Ferioli, L. Jensen, and F. Zimmermann, "Transverse instabilities of the LHC proton beam in the SPS", proceedings of the 2000 European Particle Accelerator Conference, Vienna (2001).

[5] G. Arduini, K. Cornelis, W. Höfle, G. Rumolo, and F. Zimmermann, "Transverse behavior of the LHC proton beam in the SPS: an update", proceedings of the 2001 Particle Accelerator Conference, Chicago (2001).

[6] W. Fischer et al., "Vacuum pressure rise with intense ion beams in RHIC", to be published in the proceedings of the 2002 European Particle Accelerator Conference, Paris (2002).

[7] P. Cameron, R. Connolly, A. Drees, T. Ryan, H. Schmickler, T. Shea, and D. Trbojevic, " ARTUS: A Rhic TUne monitor System", BNL RHIC/AP/155 (1998).

[8] M.A. Furman and A.A. Zholents, "Incoherent effects driven by the electron cloud", proceedings of the 1999 Particle Accelerator Conference, New York (1999).

[9] F. Zimmermann, "The electron cloud instability: summary of measurements and understanding", proceedings of the 2001 Particle Accelerator Conference, Chicago (2001).

[10] K. Ohmi, S. Heifets, and F. Zimmermann, "Study of coherent tune shift caused by electron cloud in positron storage rings", proceedings of the 2001 Asian Particle Accelerator Conference, Beijing; CERN SL-2001-062 (AP) (2001).

[11] M.A. Furman, private communication (2001).

[12] M. Blaskiewicz, computer program csec (2001).

[13] M. Blaskiewicz et al, these proceedings (2002).

[14] V. Danilov, A. Aleksandrov, M. Blaskiewicz, and J. Wei, "Calculations of electron accumulation in the SNS storage ring", proceedings of the 2001 Particle Accelerator Conference, Chicago (2001).

[15] M.A. Furman and M. Pivi, "Microscopic probabilistic model for the simulation of secondary electron emission", LBNL-49711, CBP Note-415 (2002).

[16] T. Nicoletti, private communication (2001).

SIMULATIONS OF ELECTRON CLOUD BUILD-UP AND SATURATION IN THE APS*

K. C. Harkay and R. A. Rosenberg, ANL, Argonne, IL 60439, USA†
M. A. Furman and M. Pivi, LBNL, Berkeley, CA 94720, USA‡

Abstract

In studies with positron beams in the Advanced Photon Source, a dramatic amplification was observed in the electron cloud for certain bunch current and bunch spacings. In modeling presented previously, we found qualitative agreement with the observed beam-induced multipacting condition, provided reasonable values were chosen for the secondary electron yield parameters, including the energy distribution. In this paper, we model and discuss the build-up and saturation process observed over long bunch trains at the resonance condition. Understanding this saturation mechanism in more detail may have implications for predicting electron cloud amplification, multipacting, and instabilities in future rings.

1 INTRODUCTION

In recent years, numerous observations of electron cloud effects (ECEs) have been reported in high-energy particle accelerators or storage rings, in some cases after operating them in new configurations [1]. These effects range in severity from vacuum degradation to emittance blowup, and generally become noticed when they degrade the accelerator performance. One of the many challenges in predicting beam-cloud interactions is understanding the electron cloud generation. A code developed at LBNL, POSINST, models the various processes giving rise to the cloud [2]. Uncertainties in characterizing the surface properties of the vacuum chamber, especially relating to secondary electron emission, can lead to uncertainties in the predicted cloud density. The goal of this modeling effort is to benchmark the code POSINST against measurements of the electron cloud (EC) properties undertaken at the Advanced Photon Source (APS), thereby providing realistic limits on the critical input parameters.

Dedicated electron diagnostics known as retarding-field analyzers (RFAs), first designed and implemented at the APS [3,4], were used in a series of experiments designed to study electron cloud effects induced by both positron and electron beams. As previously reported, a dramatic amplification was observed in the EC for certain bunch current and bunch spacings for positron beams [5]. This gain is attributed to beam-induced multipacting (BIM) and was accompanied by an anomalous vacuum pressure rise. A more modest amplification was observed for electron beams. In addition, before converting the APS to electron beam operation, a horizontal coupled-bunch instability was observed for positron beams at BIM conditions. This has not been observed for electron beams at identical operating conditions. In fact, ECEs do not limit the APS performance when operated with electrons, as is presently the case.

In previous modeling of positron beams [6], we found qualitative agreement with the observations for the BIM condition. Reasonable values were chosen for the secondary electron (SE) yield coefficient, the SE energy distribution, and the rediffused electron component. These assumptions are consistent with bench measurements [7,8]. Using these same input parameters, we then modeled the EC build-up and saturation process observed over long bunch trains at the resonance condition. It is hoped that this effort will lend insights into EC production in the APS, that can then be applied to other machines.

Three preliminary observations can be made: (1) the electron cloud is sensitive to details of the secondary electron energy spectrum, (2) the correct choice of these parameters should reproduce all the experimental data in a given machine, and (3) the measured longitudinal variation of the electron cloud density, which could be important, is not modeled.

2 REVIEW OF PRIOR RESULTS

A special vacuum chamber, equipped with ten RFA electron energy analyzers, was built and installed in a field-free region in the APS storage ring [5]. The locations of some of the components are shown in Fig. 1. EA6 is a copper end absorber designed to intercept high-energy photons to protect downstream structures. The schematic in Fig. 2 shows two RFAs mounted on a standard-aperture chamber. The approximate limits of the radiation fan at the location of detector 6 are shown for synchrotron photon energies above the photoelectron work function,

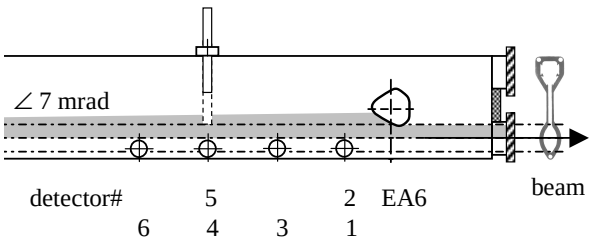

Figure 1: RFA detectors (1-6) mounted on APS chamber, top view, also showing the synchrotron radiation fan from the downstream bending magnet and the absorber, EA6.

*Work supported by U.S. Department of Energy, Office of Basic Energy Sciences under Contract Nos. W-31-109-ENG-38 and DE-AC03-76SF00098, and by the SNS project.
† harkay@aps.anl.gov and rar@aps.anl.gov
‡ mafurman@lbl.gov and mpivi@lbl.gov

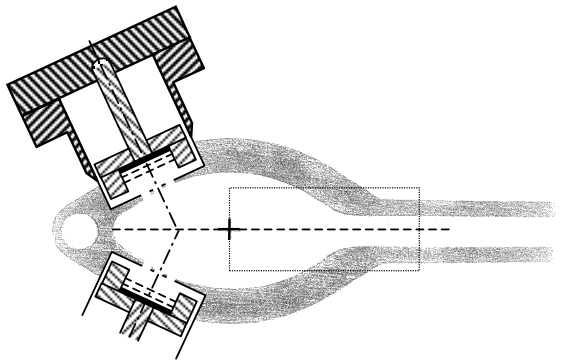

Figure 2: Mounting of two RFAs on a standard aluminum (Al) APS chamber, cross-sectional view. The RFA consists of two grids and a graphite-coated collector biased at +45V. The first grid is grounded and the second can be biased for electron energy selection [3,4].

~ 4 eV. Most of the high-energy photons exit through the antechamber slot.

The relevant APS parameters used in the previous [6] and present simulations are shown in Table 1. The parameter δ_{max} gives the maximum value of the secondary electron yield coefficient, which occurs at an incident energy E_{max}. Because the APS data were acquired over a long period of operation, we are interested in modeling the effects of surface conditioning by beam scrubbing, which lowers δ_{max}. Values of δ_{max} ranging from 2.2 to 3.3 are consistent with conditioned and unconditioned, oxidized Al, respectively.

Table 1: Simulation Parameters for APS

		BIM, Ref. [6]	EC build-up
Circumference	m	1104	
Beam energy	GeV	7	
Harmonic no.		1296	
Rf frequency	MHz	351.93	
Bunch population	(2 mA)	4.6×10^{10}	
rms bunch length	mm	5	
Transverse rms sizes	μm	300, 50	
Chamber semiaxes	cm	4.25, 2.1	
Antechamber slot height	cm	1	
Eff. photoelect. yield		0.1	
No. photons per e+		0.07	
δ_{max}		3.3	3.0 & 2.2
E_{max}	eV	280	300
No. kicks over bunch		5	11

The simulations in Ref. [6] were repeated with a slight modification (δ_{max} = 3.1). Also, the code output was scaled to account for the transmission attenuation in the experiment: The measured RFA grid transmission is 0.8, while the calculated transmission through the vacuum penetration is 0.6, giving a total detection efficiency of 0.5. Figure 3 shows a comparison between the modeled and measured electron wall current for ten positron bunches as a function of bunch spacing. The retarding voltage is positive to maximize the collector current. The model reproduces the broad peak centered around a 20-ns spacing (7 λ_{rf}); however, the sharp, resonant peak at 7 λ_{rf} is not reproduced. The position of the peak in the modeled result was very sensitive to the shape of the secondary electron energy spectrum, the mean energy in particular. The width of the broad peak was sensitive to assumptions about the rediffused electron component. It is interesting to note that BIM was never observed until the dedicated EC study: standard user operation with positron beams typically used 1 λ_{rf} or 54 λ_{rf} bunch spacing, well outside the position of the resonant peak.

The data in the main plot in Fig. 3 were acquired shortly after the new chamber was installed (< 1 Amp-hours (Ah) of operation). The inset shows the normalized signal after > 60 Ah. The peak signal is reduced by a factor of two due to a surface conditioning effect. The accumulated electron dose (in C/mm^2) was calculated using the measured wall current for the standard user configuration, assuming this was used the majority of the time. In the next section, we describe studies of the EC build-up over long bunch trains. The bunch train data were acquired after ~100 Ah, so we expect that δ_{max} may be further reduced relative to the initial state.

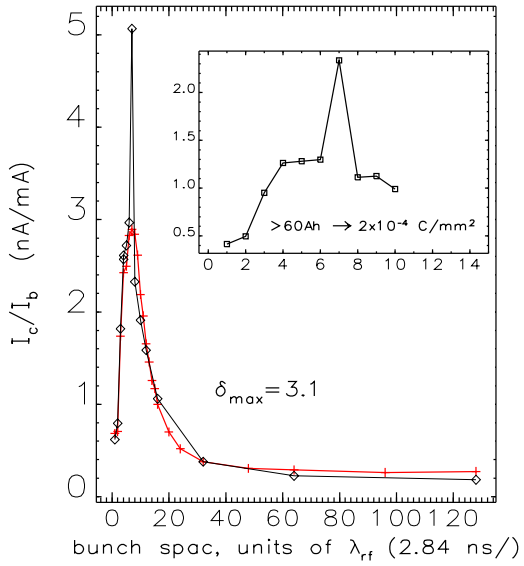

Figure 3: Measured (diamonds) and simulated (crosses) electron wall current (I_c) for BIM in APS, normalized to the total beam current (I_b) (ten e+ bunches; 2 mA/bunch).

3 MEASURED ELECTRON CLOUD BUILD-UP

Before discussing the electron cloud build-up and saturation, it should be noted that significant variation was seen from one detector to another, especially for BIM conditions [5]. The gain in the detector signals as a function of bunch spacing or number of bunches varied according to location. Detectors near the absorber EA6 typically exhibited the smallest gains (factors of 2-3),

while detectors 6, 7, and 8 exhibited gains of over a factor of 100. The effect of EA6 as a local source of electrons dominates in the detectors nearby. Farther from EA6, the situation is dramatically different, and the effect of multipacting is more easily observed.

Measurements of the electron cloud build-up and saturation are shown in Fig. 4. The variation in detector location can be seen. In the main plot, the normalized wall current is plotted as a function of bunches in the train: the bunch spacing is fixed at the BIM condition (7 λ_{rf}), and the bunch current is fixed at 2 mA. The vacuum pressure, P, measured near detector 9 is also plotted (located 3 m upstream from EA6). The exponential rise, the number of bunches after which the cloud saturates, and saturation level at 100 mA (total current) all vary; the level varies by up to a factor of three. The inset in the figure shows the cloud build-up at detector 6 when the bunch current is varied.

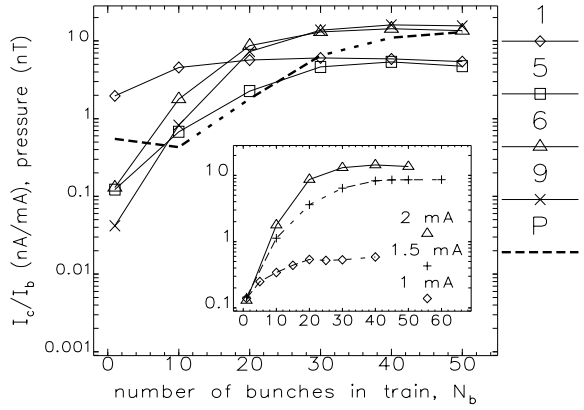

Figure 4: Measured EC build-up and saturation over positron bunch train (main plot: detectors 1, 5, 6, and 9 with 2 mA/bunch; inset: det. 6 only).

From Fig. 4, the cloud density can be very roughly estimated given the measured wall flux and the average electron velocity. It is interesting to compare this to the average beam density. For example, taking 100 mA total current, 2 mA/bunch, and the average energy from the differentiated dI_c/dV, 100 eV (where V is the bias voltage):

$$n_{EC} = I_c / (A_{RFA}\, e\, \langle v_e \rangle) = 10^4 \text{ cm}^{-3}$$
$$n_{beam} = n_b / A_{vc} / t_{sep} * \text{fill fraction} = 10^6 \text{ cm}^{-3}.$$

Here A_{RFA} is the detector aperture area, ~1 cm^2; A_{vc} is the vacuum chamber cross-section area; t_{sep} is the bunch separation in units of time, $\langle v_e \rangle$ is the velocity of the average-energy electron, 6×10^8 cm/s; and e is the electron charge. Saturation is observed at about 1% of the average beam density for 1.5 and 2 mA/bunch; and at only ~0.1% for 1 mA/bunch.

A preliminary analysis of turn-by-turn beam position monitor (BPM) data acquired during the final run with positrons shows that a horizontal coupled-bunch instability occurs for a bunch spacing 7 λ_{rf} (20 ns) and ~2 mA/bunch; i.e., the BIM conditions. Figure 5 shows the horizontal bunch centroid offset for each of 50 bunches, 90 mA total. Five consecutive turns are shown (ν_x = 0.2). This instability is not observed with electron beams for otherwise identical conditions. Analyses of these data are ongoing.

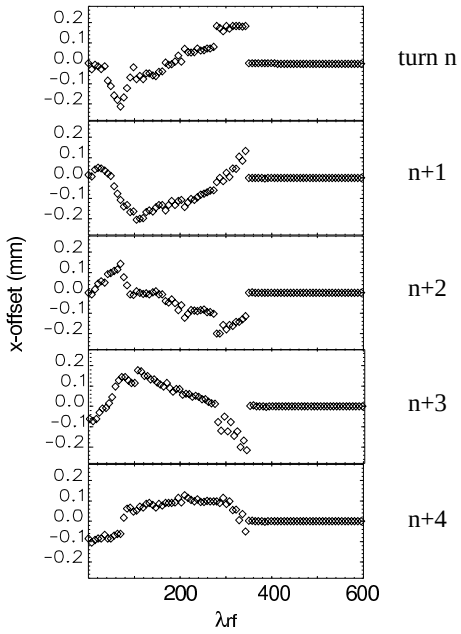

Figure 5: Bunch-by-bunch horizontal centroid oscillations using turn-by-turn BPM data acquisition for positron beam (50 bunches, 90 mA total, BIM spacing). The head of the train is on the left.

4 SIMULATIONS OF EC BUILD-UP

Using the input parameters determined to give the best fit of the measured electron wall current with bunch spacing (Fig. 3), the electron cloud was modeled as a function of bunch train length. The beam model corresponds to the beam conditions in Fig. 4 (fixed bunch current). To study the effects of conditioning of the aluminum chamber surface, two values of δ_{max} were com-

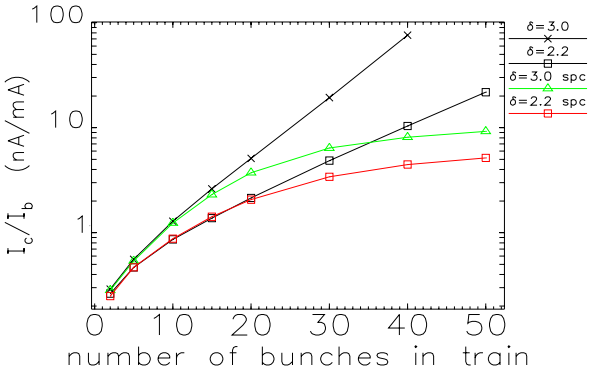

Figure 6: Simulation comparison of δ_{max} and effect of space charge for positron bunch trains in the APS.

pared (recall explanation above Table 1). Finally, the space charge of the cloud was optionally included. The results are shown in Fig. 6. As expected, saturation of the cloud results only when space charge is included, and occurs after about 20 or 30 bunches. The saturation level at 100 mA differs by only a factor of ~2 for the two values of δ_{max}. This would imply that the saturation level is a relatively weak function of this parameter.

The simulated electron cloud build-up can now be compared to the measured data; this is shown in Fig. 7. The fit is reasonably good in the best case (det. 5), shown in (a); however, the fit at the other detectors is marginal, shown in (b). The variation in the electron cloud saturation level as a function of detector location is about as large (3×) as it is for the two chosen values of δ_{max} (2×).

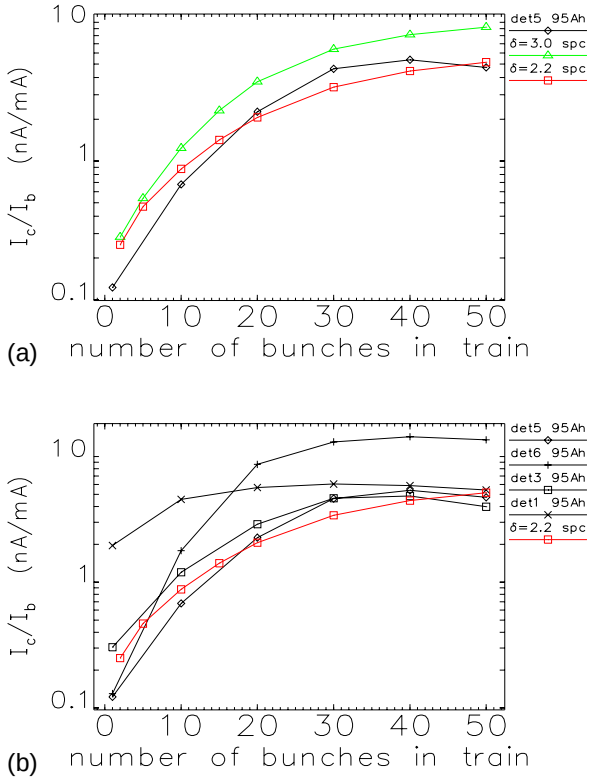

Figure 7: Measured and simulated EC detector current for positron bunch trains: (a) det. 5 and (b) several detectors.

Another test of the model is how well the electron energy spectra are reproduced. A representative set of RFA data showing the integrated electron energy (a) and differentiated signals (dI_c/dV, converted to wall flux) (b) is shown in Fig. 8. The low-energy part of the distributions are fit well with a Lorentzian function. The high-energy part results from electrons accelerated by the beam, and falls off exponentially. For the longest spacing (128 λ_{rf}), there is virtually no exponential tail; we can assume that most of the cloud electrons have been lost before the next bunch passage. For bunch spacings at the BIM resonance, the exponential tail is the longest. Additional features on the tail suggest a resonance condition that "selects" electrons at a certain distance from the beam at each bunch passage, resulting in an energy "peak." A preliminary analysis of the modeled energy spectra shows qualitative similarities to these data. We expect to analyze the measured electron energy distribution in more detail in the future.

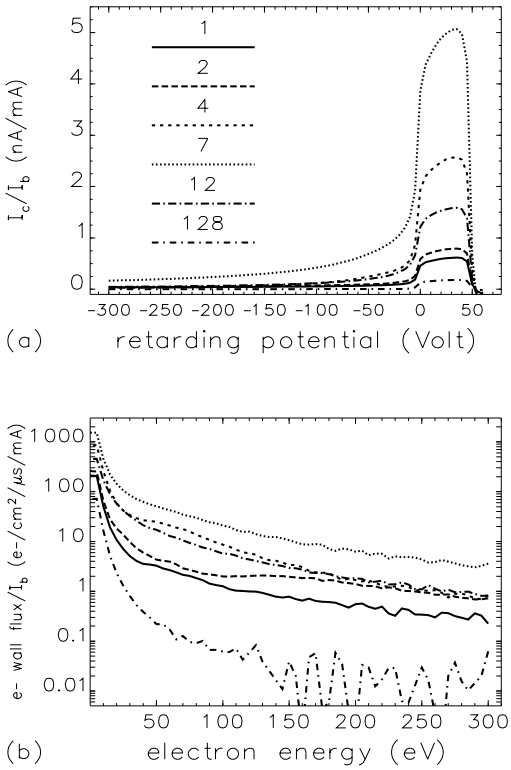

Figure 8: Energy distribution dependence on positron beam operating conditions (ten bunches, constant 2 mA/bunch vs. bunch spacing in units of λ_{rf}); (a) Normalized I_c and (b) dI_c/dV.

5 SUMMARY AND DISCUSSION

A number of observations at the APS have been made for positron and electron beams using dedicated electron diagnostics known as RFAs. These data are being used to help benchmark the code POSINST, developed at LBNL. In summary, electron cloud amplification was observed with positron *and* electron beams (more modest for the latter). A horizontal coupled-bunch instability (CBI) was observed with positron beams at the BIM condition: ~ 2 mA/bunch at a 20-ns bunch spacing (7 λ_{rf}). The instability was not observed for electron beams at these same operating conditions. The EC was observed to saturate after a train of 20–30 bunches at levels varying by up to a factor of three measured at different locations in a field-free region. This variation is primarily due to the influence of a photon absorber. A surface conditioning

effect was observed after a period of beam operation: the electron cloud signal was reduced by a factor of two after an estimated surface electron dose of 2×10^{-4} C/mm^2.

Comparison of simulations with EC measurements have given the following results. Reasonable agreement was found modeling a beam of ten positron bunches whose spacing was varied. The simulation reproduced the shape and position of a broad peak in the collected electron wall current as a function of bunch spacing. It did not, however, reproduce the sharp peak observed at the optimal BIM conditions noted above. The comparison was very sensitive to secondary electron parameters, especially the secondary energy spectrum and the rediffused component.

Using the same secondary electron parameters used to model the BIM resonance described above, the build-up and saturation of the electron cloud over positron bunch trains at the BIM conditions was modeled. To account for surface conditioning effects, different values of δ_{max} were compared, corresponding to conditioned and unconditioned, oxidized Al surfaces. Reasonable qualitative agreement was found compared with the data from one detector. However, the variations observed as a function of detector location were not modeled. This lack of agreement is almost certainly due to geometrical details of the vacuum chamber and photon illumination that are not included in the model. On the other hand, the modeled saturation level varies by a factor of two for a range of values of δ_{max}. The sensitivity of the saturation level to δ_{max} is of the order of the local density variation. The uncertainty in predicting the EC density is thus estimated to be about a factor of two to three.

Given the progress in understanding EC-induced effects at existing accelerators, we may be able to predict EC-induced instability thresholds in future accelerators within an error given by the secondary electron energy spectrum uncertainties, which at present limit a proper parametrization. Including 3D details of the vacuum chamber geometry to model the local EC density variation is also likely to be important. Furthermore, we need to include the important reflected component of the low-energy electrons, which may give an enhancement of the saturation level. This component has not been considered in the simulations shown, but has been included in more recent versions of the POSINST code [9]. Finally, at the APS, a CBI was observed for 2 mA/bunch but not 1.5 mA/bunch, although the estimated average neutralization was the same for both. Other figures-of-merit are clearly important in defining the EC-induced instability threshold.

EC diagnostics have largely been implemented only in field-free regions, with the exception of the CERN Super Proton Synchrotron (SPS) [10]. The EC in the dipoles is considered to be one of the most important contributions to the observed horizontal CBI in that ring; how important is this contribution for positron rings? Electrons trapped in the quadrupole magnet fields may also contribute.

Low-energy (< 5 eV) electrons may never collide with the chamber walls and are thus difficult to measure with a standard RFA. An electron sweeper developed at the PSR was designed to address this issue [11], and experimental results indicate that the properties of this low-energy contribution are very different from those of the multipacting electrons. This question is likely to be a challenge for positron and electron rings as well.

Finally, there is a question as to whether EC instabilities are likely to occur in electron rings. There is an indication that electron cloud build-up does occur for electron beams (e.g., in the APS); the instability threshold may simply be higher in electron rings compared to positron rings.

6 REFERENCES

[1] See other papers presented at this workshop. Additional information can be found in the following workshop proceedings:
Int'l. Workshop on Two-Stream Instabilities in Particle Accelerators and Storage Rings, KEK Tsukuba, Japan, Sept. 2001; http://conference.kek.jp/two-stream/
8th ICFA Mini Workshop on Two-Stream Instabilities in Particle Accelerators and Storage Rings, Santa Fe, NM Feb 2000; http://www.aps.anl.gov/conferences/icfa/two-stream.html

[2] M. A. Furman and G. R. Lambertson, Proc. of Int'l. Workshop on Multibunch Instabilities in Future Electron and Positron Accelerators (MBI-97), KEK, Tsukuba, Japan (Jul. 1997) (KEK Proceedings 97-17, Dec. 1997, 170 and 234); http://www.lbl.gov/~miguel/MBI-97-ECI-PEPII.pdf.
M. A. Furman, Report No. LBNL-41482/CBP Note-247/LHC Project Report 180 (May 1998); http://www.lbl.gov/~miguel/LHCpr180.pdf.

[3] R. A. Rosenberg and K. C. Harkay, Nucl. Instrum. Methods **A453**, 507 (2000).

[4] R. A. Rosenberg and K. C. Harkay, Proc. of 2001 Part. Accel. Conf., 2069 (2001).

[5] K. C. Harkay and R. A. Rosenberg, Proc. of 1999 Part. Accel. Conf., 1641 (1999).

[6] M. Furman, M. Pivi, K. Harkay, R. Rosenberg, Proc. of 2001 Part. Accel. Conf., 679 (2001).

[7] R. Kirby and F. King, Nucl. Instrum. Methods **A469** (1), 1 (2001); also Report No. SLAC-PUB-8212 (Oct. 2000).

[8] V. Baglin, I. Collins, B. Henrist, N. Hilleret, and G. Vorlaufer, Report No. CERN-LHC-Project-Report-472 (Aug. 2001).

[9] M. A. Furman and M. T. F. Pivi, Report No. LBNL-49711/CBP Note-415 (May 2002).

[10] M. Jiminez et al., "Electron Cloud Diagnostics in the SPS Machine," Proc. of Int'l. Workshop on Two-Stream Instabilities in Particle Accelerators and Storage Rings, KEK Tsukuba, Japan, Sept. 2001; http://conference.kek.jp/two-stream/ and "Electron Cloud Observations in the SPS," these proceedings.

[11] R. Macek et al., Proc. of 2001 Part. Accel. Conf., 688 (2001).

SECONDARY ELECTRON EMISSION DATA FOR THE SIMULATION OF ELECTRON CLOUD

B. Henrist, N. Hilleret, M. Jimenez, C. Scheuerlein, M. Taborelli, G. Vorlaufer

CERN, Geneva, Switzerland

Abstract

The secondary electron yield is one of the determinant parameters entering in the simulation of the electron cloud phenomenon. As secondary electron emission is a surface process, it is strongly influenced by slight modifications of the materials outer layers. This presentation will try to summarize various numerical formulae describing the main input data needed for the simulation of the electron multiplication in the electron cloud process

1 INTRODUCTION

The electron cloud effect [1-3] is a possible limitation for the operation of LHC and of its injector, the SPS. Apart from dissipating an excessive power on the LHC beam screen, it can induce detrimental oscillations of the proton beams which degrade their emittance and hence the achievable luminosity in the interaction points. Accurate simulation programs are necessary to predict the behaviour of future machines and adapt possible cures, e.g. surface treatments, to meet the expected performance. The electron cloud mechanism depends partly on the generation of secondary electrons by electron impact on the vacuum chamber hence it is important to provide, for the simulation programs good fits to analytical formulae able to represent the main characteristics of the secondary electron emission. This paper presents various equations from the existing literature and their comparison to data collected for the copper surface of the future LHC.

2 EMPIRICAL FORMULAE AND NUMERICAL VALUES FOR SIMULATIONS

For the simulation of the electron cloud phenomenon, it is necessary to use various analytical formulae reproducing the variation of different characteristics of the secondary electron emission. These formulae are also very important in the field of surface physics e.g. for the prediction of contrast in scanning electron microscopy[4], or for the study of electronic devices using electron mutiplication [5]. For this reason the mechanisms leading to the secondary electron emission have been studied in details and appropriate analytical formulae either based on physical models or purely empirical have been published. They describe the main features of the secondary electron emission, namely : the variation of the secondary electron yield (S.E.Y.) as a function of the primary electron energy (E_p) or the secondary electron energy distribution. In such formulae, fitting parameters must be determined by measurements of samples corresponding to the material investigated. This is especially true in the case of accelerators as the surfaces involved are far from being ideal but are technical surfaces processed according to procedures applicable to many square meters as this is the case for the copper cladded LHC beam-screen. The following paragraphs will give the fitting parameters that can be used to describe analytically the secondary electron emission of this surface. The copper samples were cleaned by immersion in an alkaline detergent (NGL Cleaning Technology 17.40) followed by rinsing in demineralised water and ethanol.

2.1 Variation of the S.E.Y. with the primary electron energy

The secondary electron emission can be described using a simplified two steps model [6, 7]:

- The deposition of energy by the primary electron at a constant rate along its trajectory [8, 9]
- The escape of the created excited electrons with a probability decreasing exponentially with the distance to the surface [10]

The use of reduced S.E.Y. (ratio of the S.E.Y. to the maximum S.E.Y., δ_m) and of reduced energy (ratio of the energy to the energy of the maximum S.E.Y., E_m) allows to replace difficult to obtain constants by two more accessible quantities δ_m and E_m. This useful

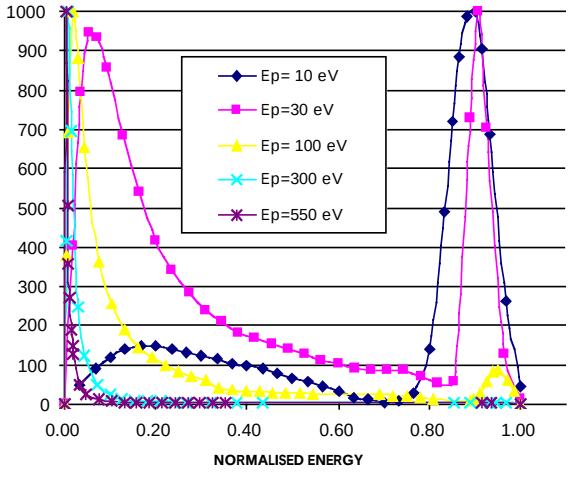

Figure 1: Normalised secondary electron energy distribution for conditioned copper

normalisation [11] was used to give an analytical expression for the variation of the S.E.Y.[4, 7, 12] which was simplified by M. Furman [2, 12] to be incorporated in simulation codes of the electron cloud effect. However this formula (1)

:

$$\delta_s = \delta_{MAX} \frac{s \times \left(\frac{E_p}{E_{MAX}}\right)}{s - 1 + \left(\frac{E_p}{E_{MAX}}\right)^s} \quad (1)$$

underestimates the S.E.Y. of primary electrons with very low energy [12]. This is due to the basic assumptions quoted before which do not consider the possibility of reflection. This event has a high probability for low

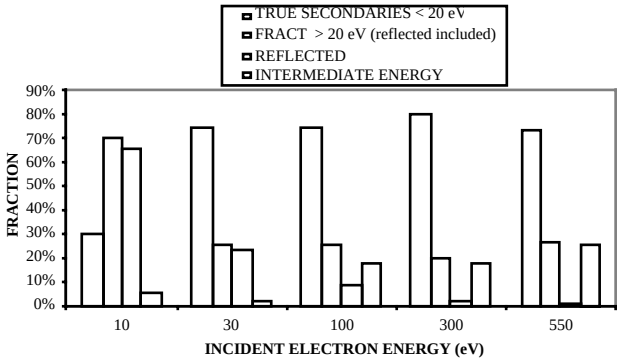

Figure 2: Variation of the energy repartition of reemitted electrons as a function of the primary electron energy (E_p)

energy incident electrons (E< 30 eV) as can be seen in figure 1 which shows the normalised intensity (1 for the highest peak) as a function of the normalised energy (1 for the incident energy). More generally, figure 2 gives

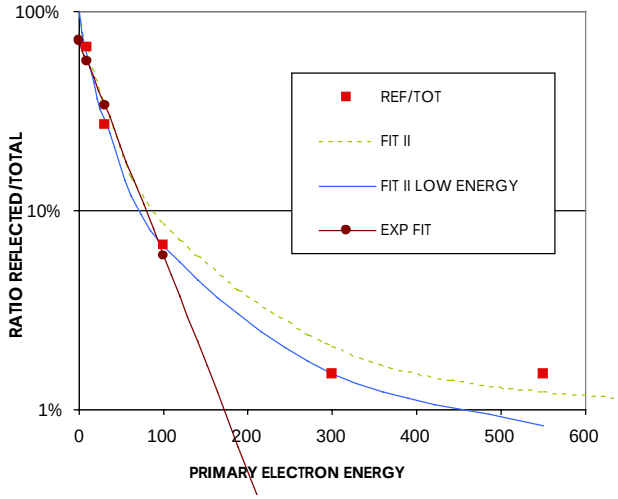

Figure 3: The ratio (f) between the reflected and the total number of re-emitted electrons for copper (squares) and the fitting laws

the ratio between the various categories of reemitted electrons for copper. These categories have been arbitrarily defined according to their energies (E) as "true secondaries": (E < 20 eV), "reflected": electrons: in the reflected peak and "intermediate": electrons with an energy between 20 eV and the reflected peak energy .

Table 1: Fitting parameters for the expression of the reflected fraction f in the case of copper

Fitting coefficient	Low energy (<300 eV)	Higher energy (<2000 eV)
A0	20.699890	0.300207076
A1	-7.07605	0.044915014
A2	0.483547	-0.155498672
A3	0	9.50318×10^{-4}
E0	56.914686	0
Curve label	FIT II low energy	FIT II

To improve the accuracy of formula (1) for electrons of low energy (< 100 eV), measurements of the secondary electron energy distribution have been used to evaluate the fraction (f) of reflected electrons in the total energy distribution. Figure 3 shows this fraction in the case of copper. To fit the experimental points (squares) the expression described by Scholtz et al [13] has been used :

$$\ln(f) = A_0 + A_1 \times (\ln(E_p + E_0)) + A_2 \times (\ln(E_p + E_0))^2 + A_3 \times (\ln(E_p + E_0))^3$$

where E_p is the primary electron energy and the other terms are fitting parameters given in table 1.

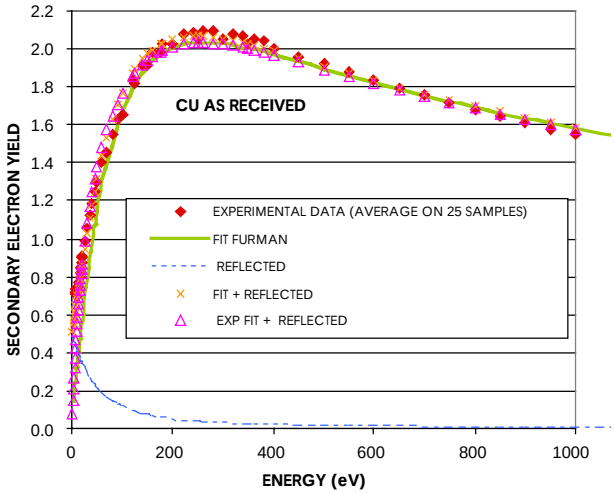

Figure 4: Comparison between fitting formulae and experimental data for as received copper.

The formula used to account for the reflected electron contribution f at low energy combined with formula (1) has been checked against the measured value of the total secondary electron yield (δ_t) in the case of as received copper. To calculate δ_t, the following formula was considered, where δ_S is the true secondary yield given by formula 1 and δ_R is the yield of reflected electron:

$$\delta_t = \delta_S + \delta_R ,$$

$$\delta_R = f \times \delta_t \Rightarrow \delta_t = \delta_S + f \times \delta_t$$

Hence: $$\delta_t = \delta_s \times \frac{1}{(1-f)}$$

A comparison of the fitting formula to experimental data is given in figures 4 and 5 for the case of as received copper. Figure 5 is an enlargement of figure 4 for low incident energies. These fits were obtained using for the

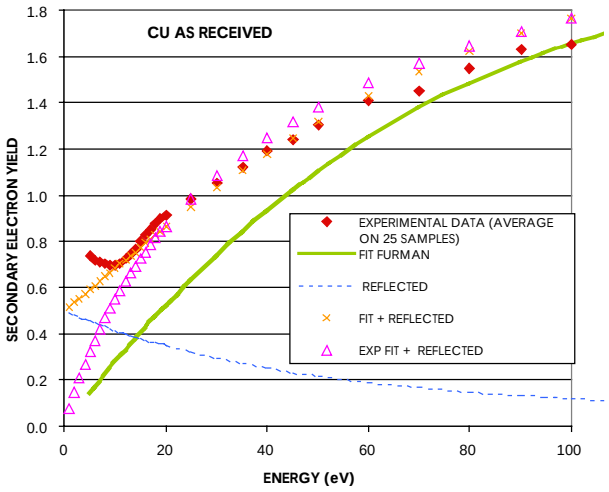

Figure 5: Comparison between fitting formulae and experimental data for as received copper at low incident energy

formula 1 the parameters listed in table 2. The curves in figure 5 show the importance of the reflected electron contribution to fit the low energy data with a good accuracy. The increase of the secondary electron yield at very low impact energy (below 5 eV) has been also measured for pure copper by Myers [14].

Table 2: Fit parameter for the true secondary electron yield (formula 1)

SAMPLE STATE	AS RECEIVED
δ_{MAX}	2.03
E_{MAX}	262
s	1.39

2.2 Fitting formula for the true secondary electron energy distribution

In reference [13] the following formula is proposed to fit the true secondary electron energy distribution i.e. the low energy electrons.

$$(2) \qquad D(E_s) = C \times \exp\left\{-\frac{\left[\ln\frac{E_s}{E_0}\right]^2}{2\tau^2}\right\}$$

where E_s is the secondary electron energy, E_0, τ and C are fitting parameters. To obtain a fit to our experimental data in the case of as received copper, the value of these constants are listed in the table 3. As already mentioned, this formula is only valid for true secondary electrons and an upper limit is given in table 3 for the validity of this expression. This limit is usually around 20 eV but at very low primary energy it can be as low as 5 eV because of the importance of the reflected peak at this low incident energy and of the corresponding electron depletion at energies immediately lower.

Table 3: Fitting parameters for various primary electron energies (formula 2)

PRIMARY ENERGY (eV)	C	E_0	τ	UPPER ENERGY BOUND (eV)
10	0.277	1.57	0.985	5
30	0.136	1.9	0.99	22
100	.126	1.58	1.16	22
300	.155	2.1	0.85	21
550	0.2	1.48	0.909	26

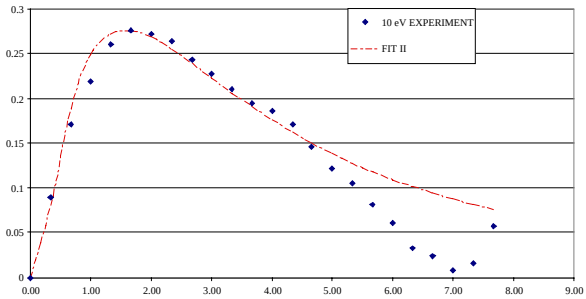

Figure 6: Comparison between the fitted curve and the experimental data for as received copper and 10 eV primary electron energy

This is illustrated in figure 6 where the result of the fit is compared to the experimental points for 10 eV primary electron energy. Figure 7 shows the good agreement obtained at higher primary electron energy (100 eV)

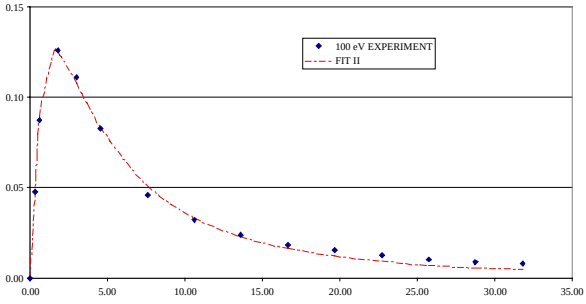

Figure 7: Fitted secondary electron energy distribution for 100 eV electrons impinging on as received copper

2.3 Fitting formula for the true secondary electron energy distribution

The effect of the angle of incidence of the primary electrons is also of great importance for the electron cloud generation as in accelerators arcs, the electrons spiral along the magnetic field lines. As the primary electrons dissipate their energy closer to the surface, an enhancement of the secondary electron yield can be expected when the angle of incidence decreases (90 degree corresponding to normal incidence). This effect is shown in figure 8 where the S.E.Y normalised to 1 at normal incidence is plotted for various primary energy as a function of the angle of incidence for a baked

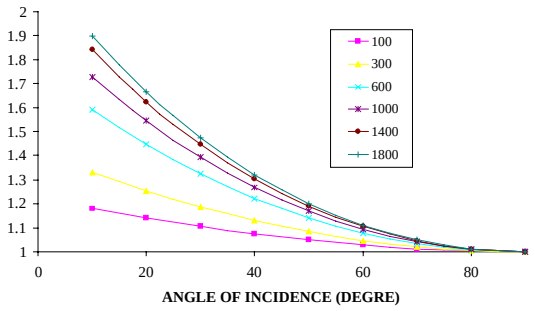

niobium surface.

Figure 8: The variation of niobium secondary electron yield as a function of the angle of incidence

This dependence has been expressed analytically by several authors[7, 12, 15] following the simplified model depicted in 2.1. K is the fitting parameter:

$$\delta = \delta_{90} \times e^{K(1-\cos(\pi/2-\theta))} \quad (3)$$

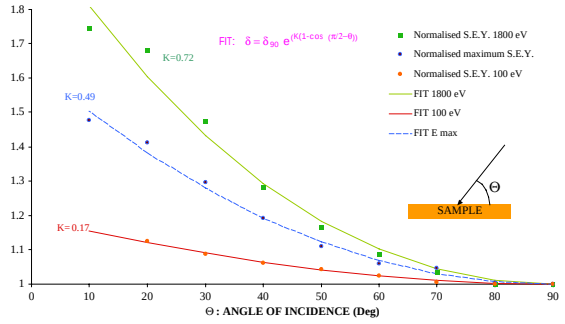

Figure 9: Fit of the secondary electron yield angular dependence for a niobium surface using (3)

The application of (3) in the case of a baked niobium sample is shown in figure 9 where the variation of the S.E.Y. is shown at 2 incident energies : 100 eV, 1800 eV and for the maximum yield. This graph demonstrate again the larger enhancement of the yield for small angles at higher energy and the validity of the approximations leading to equation (3). It must be stressed that at energies higher than some keV (3) is no more valid and a law as $\cos(\theta)^{-\bullet}$ becomes more appropriate [4].

3 CONCLUSIONS

Various equations have been fitted to experimental data in the case of copper and niobium. It was demonstrated that they represent with a good accuracy the main characteristics of the secondary electron emission. A combination of formulae representing the variation of the true secondary electron yield corrected for the reflected electron fraction gives a good approximation to the variation of the secondary electron yield with the incident electron energy at low energy. The angular dependence of the yield has been studied in the case of niobium and the proposed fitting expression was also found adapted.

4 REFERENCES

1. Ruggiero, F. *A review of new manifestations of collective effects*. in *Sixth European Particle Accelerator Conference, EPAC98,*. 1998. Stockholm,.
2. Furman, M.A., *The Electron-Cloud Effect in the Arcs of the LHC.* CERN-LHC-Project-Report-180, 1998: p. 20 May 1998.
3. Bruning, O., et al., *Electron cloud and beam scrubbing in the LHC.* Proceedings of the IEEE Particle Accelerator Conference, 1999. **4**: p. 2629-2631.
4. Seiler, H., *Secondary electron emission in the scanning electron microscope.* Journal of Applied Physics, 1983. **54**(11): p. r1-r18.
5. Shih, A., et al., *Secondary electron emission studies.* Vacuum Electron Sources; Applied Surface Science, 1997. **111**: p. 251-258.
6. Salow, H., *Sekundäre elektronen emission.* Physik. Z., 1940. **41**: p. 434-442.
7. Bruining , H., *Physics an Application of Secondary Electron Emission.* 1954, London: Pergamon.
8. Young, J.R., *Dissipation of energy by 2.5-10 keV electrons in Al_2O_3.* J. Appl. Phys, 1957. **28**: p. 524-530.
9. Young, J.R., *Penetration of electrons in Al_2O_3-films.* Phys. Rev, 1956. **103**: p. 292-293.
10. Wittry, D.B., Kyser,D.F., *Cathodoluminescence at p-n junctions in GaAs.* J. Appl. Phys, 1965. **36**: p. 1387.
11. Baroody, E.M., Phys. Rev, 1950. **78**: p. 780.
12. Dekker, A.J., *Secondary electron emission*, in *Solid State Phys.* 1958, Academic Press: New York. p. 251-315.
13. Scholtz, J.J., D. Dijkkamp, and R.W.A. Schmitz, *Secondary electron emission properties.* Philips Journal of Research, 1996. **50**(3-4): p. 375-389.
14. Myers, H.P., *The secondary emission from copper and silver films obtained with primary electron energies below 10 eV.* Proc. Roy.Soc., 1952. **A 215**: p. 329-345.
15. Kollath, R., *Sekundärelektronen-Emisssion fester Körper bei Bestrahlung mit Elektronen*, in *Handbuch der Physik.* 1956, Springer: Berlin. p. 232-303.

SPS ELECTRON CLOUD HEAT LOAD MEASUREMENTS WITH WAMPAC AND SIMULATIONS

V. Baglin and B. Jenninger, CERN, 1211 Geneva 23, Switzerland.

Abstract

A calorimeter, WAMPAC, operating at room temperature has been designed and installed into the SPS to measure directly the electron cloud induced heat load due to the LHC type proton beam. Theoretical behaviour, calibrations, measurement protocols, preliminary results and simulation benchmarking are presented. Scaling of the results to the LHC indicated a linear heating power in a LHC dipole of about 500 mW.m^{-1} for 5 10^{10} protons.bunch^{-1} for a copper surface which is not fully conditioned (maximum of secondary electron yield ~ 1.9).

1 INTRODUCTION

In the cryogenic elements of the Large Hadron Collider (LHC), the proton beams will be contained inside a perforated 'beam screen' (BS), cooled at a temperature between ~ 5 K and 20 K. Apart to provide pumping, the BS is necessary to intercept the beam induced heat loads such as synchrotron radiation (SR), photoelectrons and resistive wall losses, in order to avoid their dissipation in the 1.9 K cold bore (CB) of the superconducting magnets. Electrons liberated into the beam vacuum chamber are accelerated towards the beam screen due to the electric field of a passing proton bunch. The impact energy of the electrons on the wall produces secondary electrons that may lead to a build up of an electron cloud due to the successive bunches [1]. Preliminary estimations of the heat load deposited by the electron cloud onto the beam screen indicated a non negligible contribution to the total heat load budget [1, 2, 3]. Last estimations, including elastic reflection of electrons, give linear heat input in the LHC arc dipole of 3.5 W.m^{-1} for an unscrubbed copper surface and 0.22 W.m^{-1} for a fully scrubbed surface [4]. In the dipole assembly at ~ 5 to 20 K temperature level, the installed cooling power is 1.13 W.m^{-1} per aperture [5]. At nominal beam current, the total heat load budget is 0.72 W.m^{-1} per aperture. The allocation to electron cloud is 28 % *i.e.* ~ 0.22 W.m^{-1} for the dipole field region and 22 % *i.e.* ~ 1.9 W.m^{-1} for the field free region [6].

An electron cloud activity has been observed in the SPS with LHC type beams [7]. It is therefore of great importance to measure the heat load deposited by this multipacting effect, in order to benchmark the simulations. For this purpose the WArm MultiPActing Calorimeter (WAMPAC), which measures directly the beam induced heat, was installed at the beginning of 2001 in section 417, long straight section 4, of the SPS.

2 PRINCIPLES

The calorimeter consists of a thermally floating copper screen, which is installed inside the SPS LSS type vacuum chamber. This screen is equipped with temperature sensors (thermocouple type E) and a heater for calibration of the calorimeter. The heat load into the calorimeter is measured as a function of the temperature evolution of the screen.

2.1 Heat equations

Physically, the heat input to the screen is balanced by the thermal resistance through radiative and contact heat losses and by the warming up of the screen. The dynamic behaviour is described with the differential equation below :

$$\dot{Q} - R \cdot \Delta T - C\,\Delta\dot{T} = 0 \qquad (1)$$

$\dot{Q}$ is the heat load on the screen, ΔT is the temperature difference between copper screen T and vacuum chamber T_v, R is the thermal resistance between screen and vacuum chamber and C is the thermal capacitance of the screen

Since initially there is no temperature difference between the copper screen and the vacuum chamber *i.e.* $\Delta T(t=0) = 0$ and since at equilibrium $\Delta\dot{T} = 0$, the solution of the differential equation is:

$$\Delta T(t) = \dot{Q} \cdot R \cdot \left(1 - e^{-\frac{t}{RC}}\right) \qquad (2)$$

With the time constant:

$$\tau = RC \qquad (3)$$

The slope is :

$$\frac{d\Delta T(t)}{dt} = \frac{\dot{Q}}{C} \cdot e^{-\frac{t}{RC}} \qquad (4)$$

The thermal resistance R is defined by the two resistances in parallel of the thermal radiation, R_{Rad} and the thermal contact, R_{cond} :

$$\boxed{R = \frac{R_{Rad}\,R_{cond}}{R_{Rad} + R_{cond}}} \qquad (5)$$

For small temperature differences ΔT between the copper screen and the vacuum chamber, the radiative heat flow $\dot{Q}_R$ versus the vacuum envelope is :

$$\dot{Q}_R = \sigma\,\varepsilon\,S\,F\left(T^4 - T_v^4\right) \approx \sigma\,\varepsilon\,S\,F\,4T^3\,\Delta T \quad (6)$$

where σ = 5.67 10^{-8} W.m^{-2}.K^{-4} is the Stefan-Boltzmann-Constant, ε is the effective emissivity, *F* is the view factor between screen and vacuum chamber, *S* is the surface area of the copper screen 'seen' by the vacuum chamber.

Thus, by definition, the radiative thermal resistance is:

$$R_{Rad} = \frac{\Delta T}{\dot{Q}_R} \approx \frac{1}{\sigma\,\varepsilon\,S\,F\,4T^3} \quad (7)$$

The copper screen is centred inside the vacuum chamber with small stainless steel screws at each end. The conductive resistance between screen and vacuum chamber is dominated by the contacts, which makes it difficult to estimate beforehand the conductive thermal resistance by a purely analytical approach. The approach taken was to measure the electrical resistance. The similarity of the mechanisms of thermal and electrical conduction in metals therefore relates the conductive thermal resistance R_{cond} and electrical resistance R_{el} [8]. For stainless steel and at room temperature: λ ~ 15 W.m^{-1}K^{-1} (thermal conductivity) and ρ ~ 7 10^{-7} Ω.m (electrical resistivity).

$$R_{cond} \approx \frac{R_{el}}{\lambda\rho} \quad (8)$$

The thermal capacitance, C, is defined by specific heat of copper c times the mass of the copper screen M :

$$\boxed{C = c\,\mathrm{M}} \quad (9)$$

2.2 Measurements

The only expected measurable beam induced heat load is due to the electron cloud activity because heat input from image currents are negligible and estimated to be about 5 mW.m^{-1} for the nominal LHC beam in SPS (4 batches of 72 bunches at 10^{11} protons.bunch^{-1}). Figure 1 shows an ideal measurement cycle for this set-up where the relative temperature is plotted versus time. For the analysis of the measurements only temperature changes are taken into account, and not the absolute values. When heat is deposited onto the copper screen, the relative temperature increases, following the thermal capacity, up to an equilibrium defined by the thermal resistance. When the heat load is suppressed, the system cools down back to the initial value.

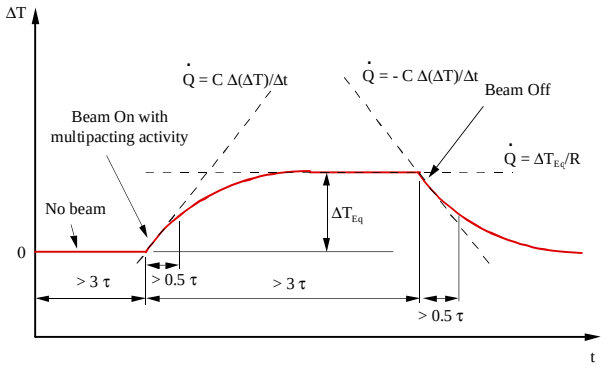

Figure 1 : Ideal measurement cycle.

Two independent methods are used to determine the heat load from an ideal measurement cycle:

1. Using (4) at t = 0, the measure of the initial warm-up slope, which is determined by the thermal capacitance of the copper screen, allows to compute the heat load. To avoid uncertainty in the measurement due to temperature instability, the slope is measured during the first hour of warming up which gives an accuracy of 30 % (if the temperature were stable, a slope measured during 5 minutes will give an accuracy better than 5 %). The start of the cool-down slope from equilibrium is identical to the warm-up slope, but with negative sign (equation (1) with the following boundary conditions : $\Delta T(t=0) = \dot{Q}\cdot R$ and $\Delta T(t=\infty) = 0$).

$$\dot{Q} = C\,\frac{\Delta(\Delta T)}{\Delta t} \quad (10)$$

2. Using (2) at t = ∞, the measure of the equilibrium temperature ΔT_{Eq}, which is determined by the thermal conductance to the vacuum envelope, allows to compute the heat load. In this case, the equilibrium temperature is measured after 3 hours of constant beam condition which gives about 70 % of the correct value.

$$\dot{Q} = \frac{\Delta T_{Eq}}{R} \quad (11)$$

3 EXPERIMENTAL SETUP

3.1 Description

Figure 2 shows a schematic of the experimental set-up. A circular OFHC copper screen is installed inside an SPS vacuum chamber. This screen is 1.3 m long, 0.14 m diameter and 0.5 mm thick. The screen has been cleaned according to CERN standard procedure. It is equipped with 5, type E, thermocouples (TC1, TC2, TC3, TC4 and TC5), which are equally distributed over the length. A calibration heater was brazed over the full length of the screen. Additional thermocouples are installed on the vacuum chamber (TC6) and suspended in the air (TC7) around the experiment. A calibrated Bayard-

Alpert vacuum gauge, type 305, and a pick-up electrode are installed close to the copper screen to detect the electron cloud activity identified by the pressure rise of the system due to electron stimulated desorption. A solenoid coil, wrapped around the vacuum chamber can be powered to attenuate the multipacting activity. Since the multipacting threshold is lower in a dipole field [9], permanent dipole magnets (~ 0.05 T) have been installed over a length of 0.7 m to trigger multipacting at a lower beam current than in field free region. Indeed, part of the current limitation in the SPS is due to strong ESD observed in the dipole regions. The data acquisition was performed with a dedicated LabVIEW software. About 100 measurements are averaged and logged every 5 minutes.

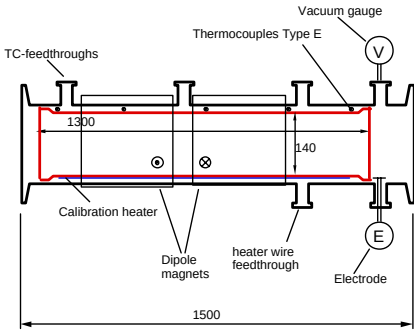

Figure 2**:** Schematic of the WAMPAC calorimeter

Figure 3 shows photographs of the WAMPAC copper screen and the WAMPAC experiment installed into the SPS.

Figure 3: Photographs of the WAMPAC copper screen and of WAMPAC installed in the SPS section 417 with and without dipole magnets.

3.2 Theoretical thermal properties

The time constant, thermal resistance and thermal capacitance could be computed and compared with calibration data using (3), (5), (9) and standard data from copper (emissivity, $\varepsilon = 0.05$, specific heat of copper, c = 400 J.kg^{-1}.K^{-1}). The view factor, F, of the copper screen inserted into the SPS chamber is assumed to be unity. The copper screen mass, M, is 3 kg, has a surface area, S, of 0.6 m^2 and operates at T = 293 K (Stefan-Boltzmann constant σ = 5.67 10^{8} W.m^{-2}.K^{-4}). The measured electrical resistance between screen and vacuum chamber was 0.5 mΩ, corresponding to conductive thermal resistance of R_{cond} ~ 48 K.W^{-1}. The radiative thermal resistance is R_{rad} ~ 6 K.W^{-1}. The total thermal resistance R is therefore dominated by radiation. The corresponding theoretical thermal capacitance, C, resistance, R and time constant, τ are shown in Table 1.

Table 1 : Theoretical thermal capacitance, C, thermal resistance, R and time constant τ.

C (J.K^{-1})	R (K.W^{-1})	τ (hours)
1200	6	2

3.3 Effect of dipole field on temperature homogenity

With the additional dipole field, the heat deposition into the copper screen is not homogeneous. The heat is only deposited along the magnetic fields *i.e.* maxiumun heat deposition at the poles. Longitudinally the heat is mainly deposited in the region with magnetic field, because of the lower multipacting threshold in the magnetic field region. Therefore, both the thermal diffusion time constants (azimutal and longitudinal) have to be considered, and have to be smaller than the warmup time constant of the system.

The one dimensional diffusion time constant is related to the thermal diffusivity by (12). The thermal diffusivity being the ratio of the thermal conductivity, λ, to the product of the material density, φ by the specific heat, c. For copper (λ = 400 W.m^{-1}.K^{-1} and φ = 8900 kg.m^{-3}), the thermal diffusivity equals 1.1 10^{-4} m^2.s^{-1}.

$$\tau_D = \frac{L^2}{D} = \frac{L^2}{\lambda / \varphi c} \qquad (12)$$

This diffusion time constant is a measure of the time delay to a change in temperature of a point at the distance L from the heat source. Azimuthally, the distance L is about the quarter of the tube circumference (*i.e.* L_A ~ 0.11 m) and longitudinally it is the length between the end of the magnetic field region and the end of the tube (*i.e.* L_L ~ 0.3 m), therefore :

- the azimutal diffusion time constant is: τ_{DA} = 110 s
- the longitudinal time constant is: τ_{DL} = 820 s

Thus, both diffusion time constants are small compared to the system time constant, τ, of 2 hours.

Similarly, to get a homogenous temperature on the copper screen under steady state conditions, the longitudinal and azimuthal thermal resistance of the screen has to be small compared with the the local thermal resistance versus the vacuum envelope.

For a copper screen diameter of 0.14 m and a thickness of 0.5 mm and using for the azimutal and longitudinal resistance the same lengths as for the diffusion time constants, we get the following thermal resistances:

- azimutal thermal resistance: $R_A = 0.9$ K.W^{-1}
- longitudinal thermal resistance : $R_L = 3.4$ K.W^{-1}

The thermal resistances are still small compared with the resistance versus the vacuum envelope for the same area and does therefore not yet significantly modify the temperature homogenity. A further reduction of the wall thickness, however, might have a non-negligible influence on the steady state temperature distribution.

3.4 Calibration and sensitivity

The precise values of the thermal capacitance and resistance can be determined during an *in-situ* calibration using the linear heater by applying a known heat load. From equation (10), the thermal capacitance is obtained by the initial warm-up slope after switching on the heater. After reaching equilibrium *i.e.* a few time constant, the thermal resistance is obtained by equation (11). Finally, The time constant, τ, is deduced from equation (3). Table 2 shows the measured thermodynamic properties and demonstrate that the predicted values from Table 1 are in good agreement with the measured data.

Table 2 : Measured thermal capacitance, *C*, thermal resistance, *R* and time constant τ.

C (J.K^{-1})	R (K.W^{-1})	τ (hours)
1330	7	2.6

.

Figure 4 shows a typical *in-situ* calibration cycle. The increase in the relative temperature, Δ(TCi – TC6) with i = 1 to 5, is plotted has a function of time when the heater is set to 0.1 W.m^{-1} and then to 0.02 W.m^{-1}. About 6 calibration measurements were performed, the average of the measured slopes is 2.7 K.W^{-1}.h^{-1} which corresponds to a thermal capicitance of 1330 J.K^{-1}. In stable conditions, as demonstrated by the second increase in relative temperature, the apparatus sensitivity is, at least, 0.02 W.m^{-1}.

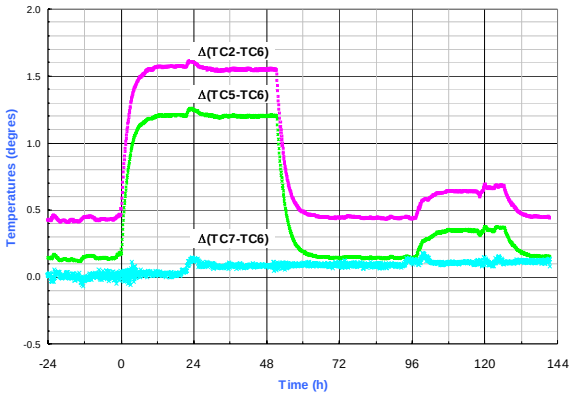

Figure 4 : Typical *in-situ* calibration cycle. The relative temperature increase correspond to 0.1 W/m and 0.02 W/m respectively. The average of the measured slopes is 2.7 K.W^{-1}.h^{-1}.

4 RESULTS

After commissioning of the experimental set-up several periods dedicated to electron cloud studies were performed with the SPS. We present here the very first observation of a temperature increase inside the calorimeter. Figure 5 shows the relative temperature and pressure increases, observed when LHC type beam was circulating in the calorimeter. The time-axis indicates the number of hours passed since recording. At time < 115 h, the SPS was running with standard fixed target beams. During this period the pressure in the system was about 2 10^{-9} Torr and only minor temperature variations were observed (TC2, TC3 and TC5), which were mainly due to temperature fluctuations in the SPS tunnel. The machine development (MD) period with LHC type beam started at time =115 h and lasted until time = 135 h. During this period, several pressure increases up to 10^{-7} Torr are observed. These pressure increases are due to electron stimulated desorption from electron multipacting. It should be noted that during this period the other SPS instrumentation devices such as pressure gauges, pick-ups, strip detectors, *etc*. also indicated electron cloud activity [10]. In general, the beam conditions were not stable all along this MD-period. However, a dedicated period with constant beam parameters over several hours (hour 133-135) could be obtained, enough time to determine the beam induced heat load. This beam was made of 3 consecutive batches separated by 225 ns of 72 bunches each, separated by 25 ns with ~ 5 10^{10} protons.bunch^{-1} [10]. During this period a relative temperature increase, close to sensitivity limit, of about 0.2 degrees and significant pressure

increase is observed. From the measurement of the initial slope during the first hour of the electron cloud activity, a slope of ~ 0.075 degres.h^{-1} could be measured. This slope corresponds to a total deposited power onto the calorimeter of ~ 30 mW. At time > 135 h, the MD was completed and SPS was back to normal operation. The relative temperatures and pressure recover to their previous value before MD.

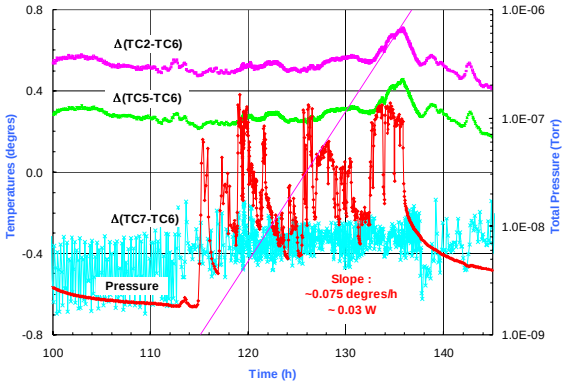

Figure 5 : Relative temperature and pressure observations when a LHC type beam of 3 consecutive batches of 72 bunches with 5 10^{10} proton.bunch^{-1} was circulating in the SPS.

Figure 6 shows the detail of the relative temperature increase observed during the electron cloud activity depicted in Figure 5. As mentioned in section 3.5, if the heat input is constant during a time larger than a few time constants, here about 1.5 time constants, the warm-up slope is almost equal to the final cool-down slope. The value of the two slopes are in relatively good agreement. The measure of the equilibrium temperature after 3 hours of operation gives a similar heat load as in the slope measurement case *i.e.* 40 to 60 mW/m .

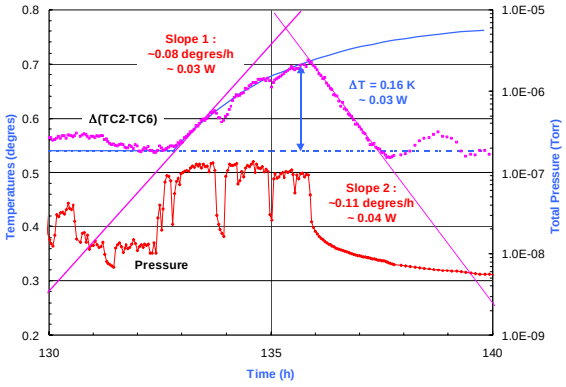

Figure 6 : Detail of the relative temperature increase observed during electron cloud activity of Figure 5.

5 BENCHMARKING SIMULATIONS

The measurements presented in 4 are used to benchmark two types of simulation code.

The "analytical" approach [1] computes the average kinetic energy of the electrons, moving along vertical field lines, kicked by a gaussian beam. This results in an average secondary electron yield <SEY> curve and an average electron energy as a function of radial position (Figure 7). Assuming that only the surface having a <SEY> above one *i.e.* from 0 to 5 mm in the present case, participates in the multipacting process and thus contribute to the heat load, their average energy is about 44 eV. If the electron cloud density is defined by its saturation limit, about 10^{9} electron/m [11], the computed power is 68 mW/m in fairly good agreement with the measurements.

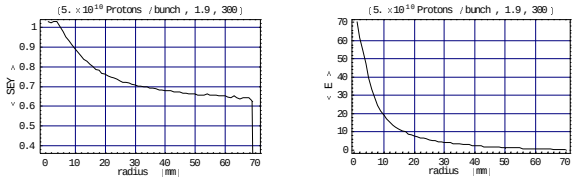

Figure 7 : Average secondary electron yield and average electron energy versus the radial position.

The "macroparticle" approach [12] follows the evolution of macroparticles through the 3 batches of proton bunches. All fundamental ingredients such as pressure, SEY curve, elastic reflection, space charge are included. Figure 8 shows the computed electron density in the Wampac during the passage of the LHC type beam. From the average energy of the electron cloud, the electron flux at saturation, the saturation time and the duty cycle, a power of 31 mW/m could be computed.

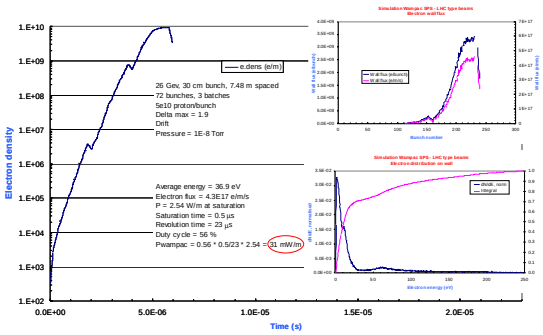

Figure 8 : Electron density, electron wall flux and electron energy in Wampac computed for a maximum secondary electron yield of 1.9.

Table 3 shows a compilation of several simulations performed with the beam parameters of paragraph 4 but without magnetic field for reasons of simplicity. It is shown that the measurements can be reasonably well obtained. A strong sensitivity is noted with the variation of the maximum of the SEY, δ_{max}.

Table 3 : Simulated power in Wampac as a function of the maximum of the SEY.

Pressure [Torr]	δ_{max}	<E> [eV]	Flux [e/m/s]	Sat. Power [W/m]	Wampac Power [mW/m]
10^{-8}	1.90	36.9	$4\ 10^{17}$	2.54	31
10^{-8}	1.95	32.9	$5\ 10^{17}$	2.64	66
10^{-8}	2.00	29.2	$6\ 10^{17}$	2.80	78

6 ESTIMATING LHC HEAT LOADS

The heat load measured with the calorimeter inside the SPS can be scaled to estimate the linear heat load into the LHC. If we assume that the electron cloud activity is nearly independent of the chamber diameter in the range 50 to 140 mm and of the dipole field in the range 0.5 to 8.5 T, only three corrections should be applied. 1) Since multipacting occurs only in the dipole a correction due to the dipole length, L, should be added, 2) the filling factor, f, and 3) the duty cycle, d, of the SPS should be taken into account. Under these assumptions, the LHC linear heat load, P_{LHC}, could be computed from the WAMPAC measurement, P_{Wampac}, by :

$$P_{LHC} = \frac{1}{L \times f \times d} P_{Wampac} \qquad (13)$$

With the parameters from Figure 5, L = 0.7 m, f = 2/11 (three batch are circulating in the SPS but about one batch is required to trigger the electron cloud [9]), d = 56 % and P_{Wampac} = 30 to 40 mW, the estimated LHC heat load with $5\ 10^{10}$ protons.bunch^{-1} in a dipole region and a maximum secondary electron yield (SEY) of about 1.9 is [13] :

$$P_{LHC} \approx 0.4 \text{ to } 0.5 \text{ W.m}^{-1} \qquad (14)$$

7 CONCLUSIONS

Preliminary measurements with the SPS calorimeter, WAMPAC, are presented. The calorimeter performance agrees with predictions. It has been demonstrated that a linear heat load of ~ 20 mW.m^{-1} can be measured.

Under a dipole configuration, to reduce the electron cloud activity threshold, a power of 40 to 60 mW/m was measured when LHC type beams were circulating in the SPS. The measurements performed in the SPS are in good agreement with the code predictions.

The equivalent LHC linear heat load into the dipole was estimated to be ~ 0.5 W.m^{-1} for a current of $5\ 10^{10}$ protons.bunch^{-1} and a Cu surface having a maximum secondary electron yield of ~ 1.9.

To reduce the vertical aperture to 40 mm and simulate closer the LHC arc beam screen conditions, a new calorimeter has been installed during this shut down in a SPS dipole chamber. Since predicted vertical electron stripes have been shown to exist [9], this new calorimeter might be equipped, in the future, with a perforated copper screen and allow a direct measurement of the heat load which could be dissipated onto the LHC cold bore.

Finally, the COLDEX, an instrument to simulate as close as possible the arc beam vacuum system, was installed during this shutdown. Comparison of beam induced gas desorption, heat load deposited by a LHC type beam in a room temperature and in a cryogenic environment shall be performed.

8 ACKNOWLEDGEMENTS

The work performed, during the installation of WAMPAC in the SPS tunnel, by the LHC-VAC SL section and especially the team of G. Mathis is gratefully acknowledged. We would like to thank G. Arduini, the SL operation group and M. Jimenez for providing and coordinating the LHC type beams in the SPS. O. Gröbner, G. Rumolo and F. Zimmermann are acknowledged to allow the benchmarking of their code.

REFERENCES

[1] Beam induced multipacting, O. Gröbner. LHC Project Report 127, July 1997.

[2] Simulations for the beam induced electron cloud in the LHC beam screen with magnetic field and image charges, O. Brüning. LHC Project Report 158, November 1997.

[3] The electron cloud effect in the arcs of the LHC, M. Furman. LHC Project Report 180, November 1998.

[4] Electron cloud simulation an update, F. Zimmermann. Proceeding of XI Chamonix workshop, January 2001.

[5] Advances in cryogenics at the Large Hadron Collider, P. Lebrun. LHC Project Report 211, July 1998.

[6] Heat load working group home page, Main dipole nominal dynamic heat load last updated 26/3/01 by Th. Durand. http://lhc-mgt-hlwg.web.cern.ch/lhc-mgt-hlwg/

[7] Electron cloud : SPS observations with LHC type beams, G. Arduini, K. Cornelis, J. M. Jimenez, G. Moulard, M. Pivi and K. Weiss. Proceeding of X Chamonix workshop, January 2000.

[8] Estimation of thermal resistance from room temperature electrical resistance measurements for different LHC beam screen support systems, B. Jenninger. LHC Project Note 189, May 1999.

[9] M. Jimenez, LHC Machine Advising Committee 12/11/01.

[10] M. Jimenez, private communication 27/11/01.

[11] Electron cloud : an analytic view, L. Vos. LHC project note 150, 1998.

[12] G. Rumolo and F. Zimmermann, these proceedings.
[13] B. Henrist, private communication 27/11/01. The secondary electron yield measurement device is installed in SPS sector 520 where most of the time a dipole field of 70 gauss is applied. The measurement was performed just before (24/10/01, 0h22) and after (25/10/0, 8h511) the MD period and the SEY did not change appreciably during this period.

Impact of Microwaves on the Electron Cloud and Incoherent Effects

F.-J. Decker, SLAC, Stanford, USA; F. Caspers, F. Zimmermann, CERN, Geneva, Switzerland

Abstract

We consider the use of microwaves for manipulating the electron cloud, describing an exploratory experiment at PEP-II as well as computer simulations of the electron cloud build up in the presence of a microwave for an LHC dipole. We then show that the incoherent effects of the electron cloud — energy loss and transverse emittance growth due to scattering off the electrons — are negligible. This suggests that the disturbance of the coherent electron motion may be another possible application of microwaves, which could prevent beam emittance growth and beam loss.

1 INTRODUCTION

More than 20 years ago the electron cloud was suppressed in the CERN ISR by installing clearing electrodes over 95% of the circumference. An rf field might have a similar effect. Indeed the use of ac clearing fields (at that time in the MHz range, well below the pipe cutoff frequency) was already proposed for electron-clearing in the ISR by W. Schnell. This idea (but now using microwaves above cutoff) was revived more recently [1].

An rf field could either suppress the electron cloud build up or enhance the surface conditioning. The attenuation of an rf signal could also be used for measuring the density of the cloud [2]. In addition, rf fields or microwaves could perturb the electron coherence, thereby weakening the effect of the electron cloud on the beam. Such schemes would work equally for proton or positron storage rings which are afflicted by the electron cloud.

The absorption of microwaves by the vacuum chamber will generate additional heat load (a concern for the LHC). A trade off must then be made between this added heat and the reduction of the energy deposited by the electron cloud, also taking into account the consequences for beam instabilities.

Compared with conventional clearing electrodes a clear advantage of the approach using microwaves is that the latter can be fed into the beam pipe using existing BPM buttons, or a few special input couplers, spaced at distances of about 100 m. This allows for retrofitting an existing accelerator, and does not at all, or only marginally, affect the impedance budget. On the other hand, dc clearing electrodes, requiring a much narrower spacing on the cm length scale, require extensive additional installations and may represent a significant source of impedance.

A possible choice of rf field mode is a "waveguide" mode, which should not disturb the beam, but might perturb the electrons forming the cloud. In principle, the injection of an rf wave requires an input coupler (maybe BPM button), an rf power source of 10-100 W (possibly more), variable in frequency, phase, maybe chirp, etc.

The waveguide mode chosen could be an H-wave (TE mode) or a E-wave (TM mode). These modes couple either not at all, or only weakly, with the particle beam moving at the speed of light, but strongly with the 'static' electron cloud.

2 EXPERIMENT AT PEP-II

A non-invasive exploratory test was performed at PEP-II. The underlying idea of the experiment was that waveguide modes in the vacuum chamber can be excited by mode converters like the movable collimators. So, the two collimator pairs in PR02 might already be doing this, *i.e.*, they may give rise to trapped rf modes at a certain power level (in this respect it would be interesting to check the bellows temperature in that region). Both H and E-type trapped modes are characterized by a small R/Q and a high Q value. The H mode does not couple to the beam. Also E-modes which resonate over a long distance show virtually no interaction with the beam; indeed their coupling to the beam is zero in the limit of an infinitely long distance.

An electron cloud detector, like the vacuum pump reading, should be able to detect any change in the electron flow. (In the worst case if there is no detectable electron cloud and therefore no reading in the nominal condition, one might have to switch off the electron-cloud suppressing solenoid in the region of interest, which would make the experiment more invasive.)

The experimental procedure was as follows: We moved the collimator jaws inwards or outwards (preferentially those jaws which do not contribute much to background reduction) and watched for *any* change in the pump current in that region. Since the pumps are shielded, they should not be sensitive to changes in the rf fields. The rf signal can only influence the amount of electrons penetrating through the shielding.

Following this procedure, on May 16, 2002, during normal colliding-beam operation the collimators in the PEP-II LER in PR02 (in front of the detector) were moved inwards by about 3 mm, to see if the generated wakefield has an effect on the electron cloud detected by the pump currents in this area. The horizontal collimators are located at positions 3077/3076 and 3044/3043. The pump current readings were observed at VP3044 (single), VP3054 (duplett with 3065) and VP3075 (duplett with 3081); see the diagram of the LER interaction region (IR) in Fig. 1. The base pressure without beam is about 1 ntorr or below. With beam the pressure readings increased to 42, 140, and 4 ntorr for the different pumps. So, the first two pumps recorded a

strong electron current from the cloud while the last one might only have detected the real vacuum pressure.

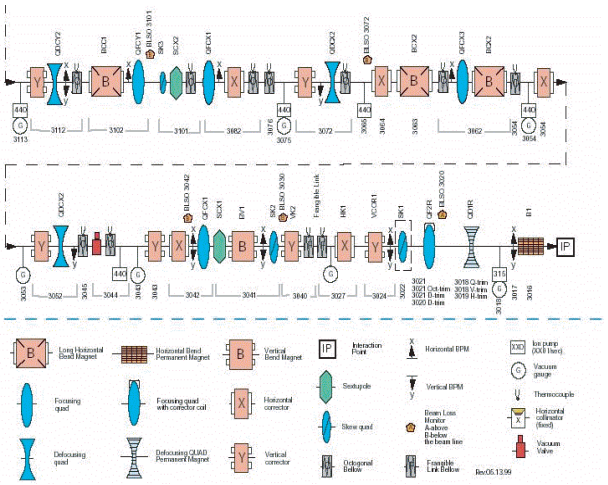

Figure 1: Schematic of PEP-II LER IR.

The observation was only about a 0.5 ntorr effect. The pressure-reading change was especially pronounced in VP3075 (see Fig. 2). At a time of about 1200–1400 s the first collimator jaw was moved inwards (observing backgrounds, lifetime, loss rate), then the second between 1500–1700 s, the third between 1900–2000 s, the last between 2150 and 2300 s. All collimator jaws got restored at once to their original settings at 2500 s. VP3044 sees a little of that restore (Fig. 3), while at 3054 there is no signal (Fig. 4).

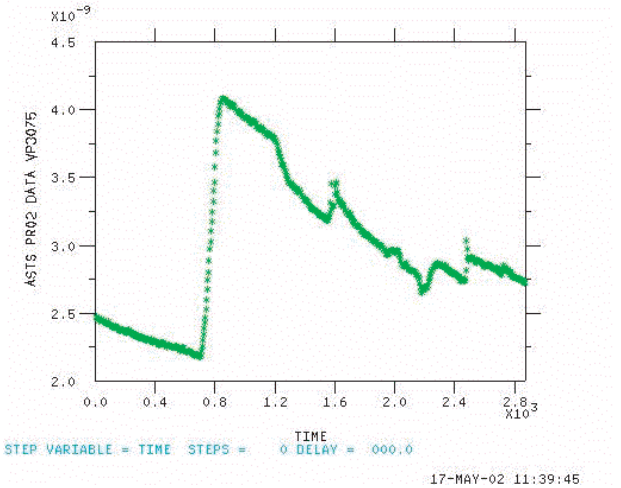

Figure 2: Pump reading VP3075 as a function of time.

The observed effect is small, presumably since the PEP-II collimators are designed with a taper such that they exhibit a smooth slope up and down between the regular beam pipe and the smallest gap, which effectively suppresses the

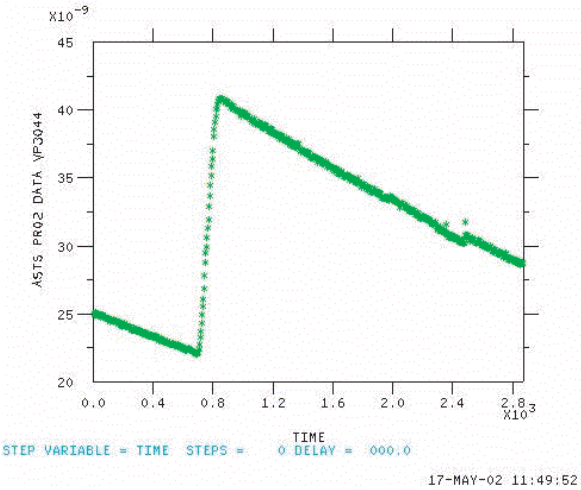

Figure 3: Pump reading VP3044 as a function of time.

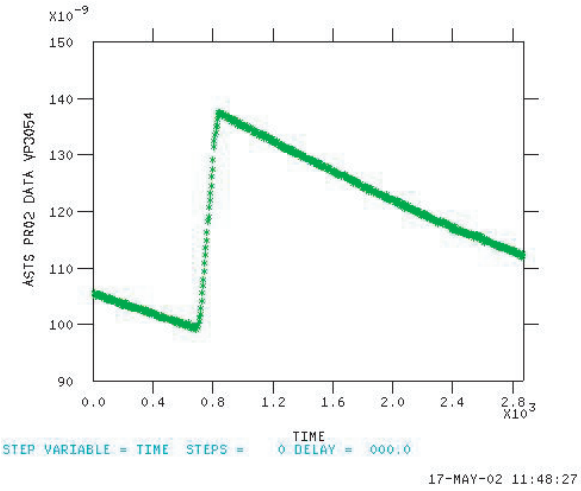

Figure 4: Pump reading VP3054 as a function of time.

wakefield generation. Nevertheless, we observe about a 0.5-1% change and the vacuum reading is actually reduced, which is the opposite of what is expected due to additional outgassing. We may need to optimize the frequency of the wake field to obtain a clearer effect.

Regardless, this measurement constitutes a first proof of principle that wake fields (microwaves) can influence the electron cloud.

3 SIMULATION FOR THE LHC

At first glance, it appears that the electron motion can only slightly be perturbed by microwaves [1], *e.g.*, for a field amplitude of 100 kV/m at 5 GHz, the electrons are accelerated to 4×10^5 m/s, which corresponds to a kinetic energy of only 0.44 eV, and to an excursion of ± 18 μm.

As an example, we have simulated the effect of an H_{11}-wave for LHC proton-beam parameters at injection: $N_b = 1.1 \times 10^{11}$ protons per bunch, $\sigma_x = 1.2$ mm, $\sigma_y = 1.2$ mm, $\sigma_z = 13$ cm, $\delta_{\max} = 1.6$, $\epsilon_{\max} = 300$, and $d\lambda_e/ds = 2.5 \times 10^{-7}$ m^{-1}s^{-1}, the creation rate of primary electrons per passing proton; elastic electron reflection on the chamber wall was included. According to the simulation, the rf field strongly increases the multipacting, as is illustrated in Fig. 5. This could be exploited for in-situ surface conditioning (with or without beam, possibly in combination with a gas discharge).

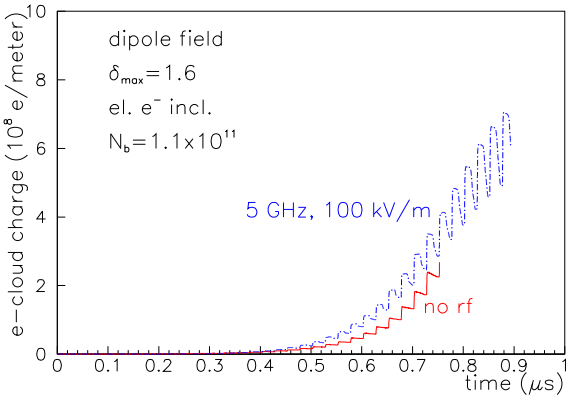

Figure 5: Simulation of electron-cloud build up in an LHC dipole chamber with 2-cm radius with and without an additional 5-GHz H-mode microwave of amplitude 100 kV/m.

In the simulation, the fields for the H_{11}-wave inside a dipole magnet were parametrized as

$$E_x = A_0(J_1(u) - uJ_1'(u))xy/r^3 \quad (1)$$
$$E_y = A_0(J_1(u)y^2 + uJ_1'(u)x^2)/r^3 \quad (2)$$
$$E_z = 0 \quad (3)$$
$$B_x = (A_0/Z_f)\,\mu_0(uJ_1'(u)x^2 + J_1(u)y^2)/r^3 \quad (4)$$
$$B_y = B + (A_0/Z_f)\,\mu_0(uJ_1'(u) - J_1(u))xy/r^3 \quad (5)$$
$$B_z = (A_z/Z_f)\mu_0 u^2\lambda_h/(2\pi)J_1(u)y/r^3\,, \quad (6)$$

where $A = E_y 4b/3.7$, $\omega_w = 2\pi f_0$, $\lambda_0 = 2\pi c/\omega_w$, $\lambda_{11} = 1.71 \times 2b$, $\mu_0 = 4\,pi10^{-7}$ N sA^{-2}, $Z_0 = 377\ \Omega$, $Z_f = Z_0/\sqrt{1-(\lambda_0/\lambda_{11})^2}$, $\lambda_h = \lambda_0/\sqrt{1-(\lambda_0/\lambda_{11})^2}$ $\beta_0 = 2\pi/\lambda_h$, $r = \sqrt{x^2+y^2}$, $u = r3.7/(2b)$, $A_0 = A\cos(\beta_0 z - \omega_w t)$, and $A_z = A\sin(\beta_0 z - \omega_w t)$, $b = 2$ cm the chamber radius, and $B = 0.5$ T the static dipole field. Note that for $b = 2$ cm, the cutoff frequency of the beam pipe is $f_c = c/\lambda_c = c/(3.412b) \approx 4.4$ GHz.

4 INCOHERENT EFFECTS OF THE ELECTRON CLOUD

In this section, we digress from the microwaves, and study whether incoherent effects of the electron cloud may be important. We consider the example of the proton beam in the LHC. However, the formulae equally apply to a positron beam.

Specifically, we compute the average energy loss and the increase in the transverse proton-beam emittance due to scattering off the electron cloud. For the cross sections and integration limits, we mainly use expressions found in Chapter 13 of Ref. [3] or slight modifications thereof.

4.1 Energy Loss

The cross section per unit energy interval for energy loss T follows from the Rutherford formula. It is

$$\frac{d\sigma}{dT} = \frac{2\pi Z^2 mc^2 r_e^2}{\beta^2 T^2}\,. \quad (7)$$

To compute the total cross section, we integrate this expression from $T_{\min}$ to $T_{\max}$.

Maximum momentum transfer occurs if the electron reverses its direction. This corresponds to the classical limit

$$T_{\max,\mathrm{class}} = \frac{2\gamma^2\beta^2 mc^2}{1 + 2mE/(M^2c^2) + m^2/M^2} \approx 2\gamma^2\beta^2 mc^2 \quad (8)$$

where m is the electron mass, M the mass of the beam particle, Ze the charge of the beam particle ($Z = 1$ for protons, but the equations also remain valid for heavy ions), and E the beam energy. The above approximation is usually justified except possibly for the LHC at top energy.

There is also a quantum-mechanical limit, given by

$$T_{\max,\mathrm{quant}} = \eta^2 T_{\max,\mathrm{class}} \quad (9)$$

where

$$\eta = \frac{Zr_e mc^2}{\hbar\beta c}\,. \quad (10)$$

The smaller of the two values (8) and (9) applies. For $\beta \approx 1$, and $Z = 1$ one has $\eta \approx 0.007$ and we should use the quantum limit.

Concerning the minimum energy transfer, we note that the maximum impact parameter is equal to the radius of the vacuum chamber, a, and from this we obtain the classical and quantum limits

$$T_{\min,\mathrm{class}} = \frac{2Z^2 r_e^2 mc^2}{\beta^2}\frac{1}{a^2} \quad (11)$$

and

$$T_{\min,\mathrm{quant}} = \frac{2Z^2 r_e^2 mc^2}{\beta^2}\frac{1}{a^2}\frac{1}{\eta^2}\,. \quad (12)$$

In this case, the larger of the two limits (11) and (12) should be taken, which again is the quantum expression.

The total energy loss per revolution is $\Delta E = C\rho_e \int (d\sigma/dT)T\,dT$, or

$$\Delta E = \rho_e C\frac{2\pi Z^2 r_e^2 mc^2}{\beta^2}\ln\frac{T_{\max}}{T_{\min}}\,. \quad (13)$$

Assuming a typical electron cloud density $\rho_e = 10^{12}$ m^{-3}, $C \approx 27$ km, $E = 7$ TeV, and $a \approx 2$ cm, we find

$\Delta E \approx 86$ μeV per proton and turn. This appears negligible.

For completeness we note that the total scattering cross section $\sigma_{\rm tot} = \int (d\sigma/dT) dT$ is

$$\sigma_{\rm tot} = \frac{2\pi Z^2 r_e^2 mc^2}{\beta^2} \left(\frac{1}{T_{\rm min}} - \frac{1}{T_{\rm max}} \right) . \qquad (14)$$

Thus the total number of scattering events per proton and per turn is

$$n_{\rm scatt} = \sigma_{\rm tot} \rho_e C , \qquad (15)$$

which in our example amounts to about 2×10^9.

4.2 Emittance Growth

For a single scattering event, the mean square scattering angle of an electron in the rest frame of the proton is

$$< \theta^2 > = \theta_{\rm min}^2 \ln \frac{T_{\rm max}}{T_{\rm min}} , \qquad (16)$$

where $\theta_{\rm min}$ equals

$$\theta_{\rm min,class} = \frac{Z r_e}{\gamma a} \qquad (17)$$

or

$$\theta_{\rm min,quant} = \frac{Z r_e}{\gamma a \eta} , \qquad (18)$$

whichever is larger. The scattering angle of the proton is smaller by a factor m/M (the ratio of electron and proton mass). The emittance growth per turn is

$$\frac{\Delta \epsilon}{\Delta t} = c \beta \rho_e \sigma_{\rm tot} \frac{m^2}{M^2} \theta_{\rm min}^2 \ln \frac{T_{\rm max}}{T_{\rm min}} . \qquad (19)$$

Here, β denotes the average beta function.

This amounts to a minuscule growth rate for the normalized transverse emittance ($\epsilon_N = \gamma \epsilon$) of $d\epsilon_N/dt \approx 3 \times 10^{-30}$ m/s.

5 CONCLUSIONS

We have discussed the possibility to use rf microwaves for suppressing the build up of the electron cloud and for reducing its detrimental effects on the beam. The microwave approach offers a number of significant advantages compared with dc clearing electrodes, in particular the retrofitting potential and an insignificant change of the accelerator impedance.

A first experimental test at PEP-II indicates that the elecron cloud can indeed be affected by collimator wake fields or, more generally, microwaves. Earlier peculiar observations with a horizontal collimator and adjacent BPM in LEP have pointed to a similar interference of wake fields and photo-electron motion [4].

In the PEP-II experiment the excited frequency lines were related to the beam harmonics. In future dedicated applications of microwaves this does not need to be the case. In fact, with external excitation it will be safer to choose rf frequencies which do not coincide with harmonic frequencies of the beam, in order to preclude any harmful interaction via E-waves. It might also be interesting to modulate the rf amplitude, frequency, and phase, as well as a simultaneously excitate waves at multiple frequencies.

In electron-cloud simulations for the LHC the inclusion of an rf H-wave above the chamber cutoff frequency enhances the electron cloud build up for all frequencies and field strengths explored. This indicates that microwaves might enhance the surface conditioning.

Another aspect considered is the interaction of the electron cloud with the particle beam. Incoherent scattering off the cloud electrons is estimated to be a negligible effect. This suggests that disturbing the coherent motion of the electrons may prove an efficient means of preventing beam quality degradation. Microwaves sent through the vacuum chamber could as well serve this purpose.

6 REFERENCES

[1] A. Chao, private communication, KEK MBI workshop (1997); F. Caspers, proposal at ECLOUD'02 (2002).

[2] S. Heifets, private communication at ECLOUD'02 (2002).

[3] J.D. Jackson, "Classical Electrodynamics," Third Edition, John Wiley (1999).

[4] G. Vismara, "The QD20 Phenomenon," CERN BI Day 1998.

ADIABATIC THEORY OF ELECTRON OSCILLATIONS AND ITS APPLICATION TO SIS100/SIS200

P. Zenkevich and N. Mustafin
Institute for Theoretical and Experimental Physics, B. Cheremushkinskaya, 25, 127259, Moscow, Russia
O. Boine-Frankenheim
Gesellschaft fur Swerionenforschung, Planckstr., 1, D-64291, Darmstadt, Germany

Abstract

We consider an accumulation of the long-lived ionization electrons in the electron cloud, which appears in the storage ring around the bunched ion beam in presence of ion leakage in the gap. In the frame of a one-dimensional model, transverse electron motion is defined by the second order non-linear differential equation with periodic coefficients depending on the ion longitudinal density. For 'smooth' density distributions an approximate solution of the equation can be written in adiabatic form. Adiabaticity perturbations results in half-integer resonances with strengths defined by leakage factor and neutralization degree. The action of these resonances in presence of nonlinearity limits the 'survival' region where electrons can be accumulated. Electron concentration in this region is defined by the balance between electron creation due to ionization and electron losses due to electron scattering on primary ions. An estimation of neutralization degrees for SIS100/SIS200 (the rings now under design in GSI) has shown that for reasonable leakage factors and nominal gas pressure the electron concentration is small.

1 INTRODUCTION

An interaction of the electron cloud with the circular ion beam can result in development of electron-ion dipole instability, which was forecast many years ago [1]–[3]. Recently this instability attracted significant attention due to its experimental observation in high-current proton beams (see, for example, Ref. [4]). The instability is especially dangerous for ions with high charge number due to large ionization cross-sections and large yield of electrons from ions hitting the wall of the vacuum chamber.

A new accelerator complex is currently under construction at GSI (Germany) [5]. This complex includes two synchrotrons/storage rings: SIS100 and SIS200. Four ion bunches (for example, ions $^{+28}\mathrm{U}^{238}$) should be injected in SIS100 from synchrotron SIS18 with a time interval of 1/3 s. Then the ions are accelerated and injected in SIS200, which is used as a 'stretcher' for physics experiments. Parameters of both machines are given in Table 1.

The goal of this paper is to investigate the electron cloud accumulation in these accelerators. For chosen beam parameters the number of electrons born due to secondary emission (SEM) from the wall seems to be comparatively small. Thus we limit ourselves to investigation of long-lived electrons born inside the beam due to the ionization of the residual gas. Accumulation of such electrons is possible only if part of the ions escape from the bunch in the gap [6]. If the electron space charge density is less than the minimal ion density in the gap such ions provide the focusing and give to electrons a possibility to survive after a passage of many bunches.

Table 1: Parameters of SIS100 and SIS200

Circumference (m)	1080	1080
Energy (MeV/u)	100	1000
Process time (s)	1	1
Number of bunches	4	None (1)
Kind of ions	$^{238}\mathrm{U}^{+28}$	$^{238}\mathrm{U}^{+28}$
Number of ions in each bunch N_b	2.5×10^{11}	10^{12}
Bunch length L_b (m)	216	(864)
rms vertical bunch size a_v (m)	0.015	0.01
rms horizontal bunch size a_h (m)	0.015	0.01
Vacuum chamber radius (m)	0.05	0.05
Pressure (10^{-10} mbar, without beam)	0.05	0.1

One-dimensional (vertical) electron oscillations are described by a non-linear equation of the second order whose solution depends on longitudinal and transverse distributions of the ions in the ring (Section 2). In this Section it is shown that for 'smooth' longitudinal distributions (continuous with its derivative) the amplitude of the electron oscillations is defined by the adiabatic law.

In a frame of linear theory non-adiabaticity of oscillations results in a set of half-integer resonances whose strengths are expressed through the trace of a transfer matrix (TrM_T) (Section 3). Examination of these resonances for SIS100 has shown that their effect depends on the number of bunches in the ring (filling scheme) and longitudinal distribution of the ions in the bunch as well as on the values of the leakage factor and neutralization degree. The most dangerous case corresponds to a completely filled ring (four bunches) and a smooth (continuous with its derivative) distribution. If the resonances are crossed due to modulation of the electron bounce frequency (such modulation can appear due to longitudinal electron motion) then these resonances result in electron heating.

The action of non-linearity results in the appearance of a 'physical chamber aperture' where the electrons can survive for a very long time (Section 4). The value of this aperture depends on the values of the leakage factor and neutralization degree, as well as on the longitudinal distribution of the ions.

These results are applied to the calculation of the equilibrium neutralization degree (Section 5). The scheme is the following:

1) The main source of electrons is ionization of residual gas.

2) The rate of heating is defined by electron scattering on the ions of the primary beam.

3) An electron is lost when its adiabatic invariant corresponds to the 'physical aperture'.

The analysis results in the expression for an equilibrium neutralization degree similar to the expression derived earlier for coasting beams [7]. However, in a bunched beam the neutralization degree is decreased as the third power of the dimensionless (divided by the r.m.s. ion beam size) physical aperture of the electron oscillations.

Application of this theory to SIS100 and SIS200 (Section 6) has shown that for both machine and nominal (very low) pressure the expected values of neutralization degree are small. However, the pressure increase (for example due to desorption of the gas from the walls) can change the situation.

2 TRANSVERSE ELECTRON OSCILLATIONS AND ADIABATIC INVARIANT

A dimensionless equation of one-dimensional (vertical) electron oscillations can be written as follows:

$$y'' + (2\pi Q_0)^2 F(\tau) y \Phi(x,y) = 0 \ , \qquad (1)$$

where $y = Y/a_e, x = X/a_e$ (Y, X = vertical and horizontal electron deviations, a_e = r.m.s. transverse beam size), independent variable $\tau = t/T$ (t = time, T = period of the ion line density variation); Q_0 = 'average electron betatron tune', equal to the number of betatron oscillations on the bunch length for uniform ion density.

$$Q_0 = \sqrt{\frac{N_b r_e Z_i R}{\pi \beta^2 a^2 h}} \ ,$$

where r_e is the classical electron radius, N_b is the number of ions inside the bunch, β is the ion relativistic parameter, Z_i is the charge ion number, R is the ring radius, h the number of bunches; the function $\Phi(x,y)$ defines the transverse distribution of the gradient. For a round Gaussian beam $\Phi(x,y) = (1 - \exp[-(x^2+y^2)])/(x^2+y^2)$. In Eq. (1), the 'instantaneous tune' $\Omega(\tau) = 2\pi Q_0 \sqrt{F(\tau)\Phi(x,y)}$.

Longitudinal distribution of the charge density in the bunch $F(\tau) = [Z_i\lambda_i(\tau) - \lambda_e]/\langle[Z_i\lambda_i(\tau) - \lambda_e]\rangle$, where $\lambda_i(\tau)$ is an ion longitudinal density inside the bunch, λ_e is an electron longitudinal density (uniform), the sign $\langle\rangle$ means averaging on the bunch length.

We have considered four models (in all cases the density in the gap is uniform):

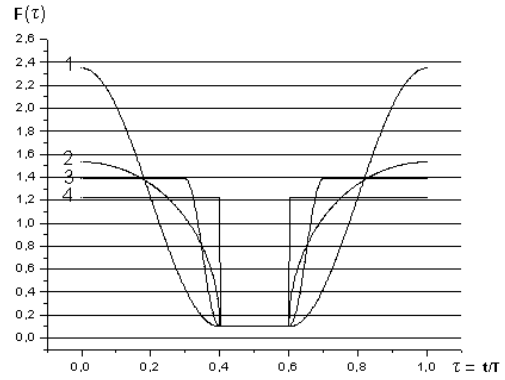

Figure 1: Different longitudinal distributions used in calculations (1 – smcos, 2 – elliptic, 3 – cosine, 4 – square).

1) The 'square' model with uniform density in the bunch.

2) The 'elliptical model' with elliptical density in the bunch.

3) The 'cosine model' with flat top of the bunch and cosine law in the bunch edge.

4) The smooth 'cosine model' with cosine density in the bunch.

These distributions are plotted in Fig. 1. Let us remark that the first model has breaks in the function and its derivative, the second one – only in derivative, the third and fourth functions are continuous with derivatives.

As is well known [8] for 'good' functions (positive and continuous with their derivatives) the 'adiabatic invariant' is approximately conserved. In our case the adiabatic invariant is

$$I(y_{\max},\tau) = 4\int_0^{y_{\max}} y' dy = 8\pi Q_0 \sqrt{F(\tau)} \int_0^{y_{\max}} \sqrt{H(y_{\max}) - H(y)} dy, H(y) = \int_0^y u\Phi(x,u)du \ . \qquad (2)$$

The maximal value of action corresponds to the gap centre ($\tau = 0.5$) and $y_{\max} = b$ (b is the ratio of the vacuum chamber aperture to the beam size a). In another point of the bunch $y_{\max}$ is defined by the equation $I(y_{\max},\tau) = I(b, 0.5)$. Using this expression, we can find the dependence of $y_{\max}$ on τ for different values of the parameters χ, η (the 'gap density parameter' χ is equal to the ratio of ion density in the gap to ion density in the centre of the bunch, the 'neutralization degree' $\eta = N_e/Z_i N_i$ is the relation of the number of electrons in the ring N_e to the number of ions in the ring N_i). A typical dependence of the electron beam size on τ for different values of $\chi(\eta = 0)$ is given in Fig. 2.

Adiabaticity criterion:

$$K_{ad} = \frac{d\Omega(\tau)}{d\tau} T/\Omega(\tau) = \frac{dF(\tau)}{d\tau} T/F(\tau) \ll 1 \ . \qquad (3)$$

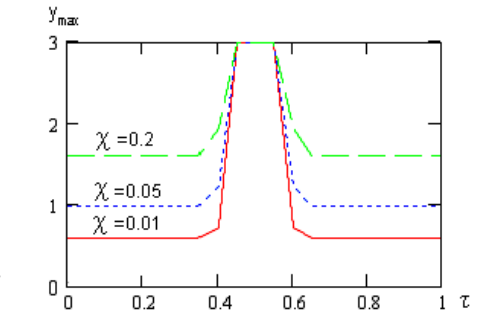

Figure 2: Dependence of normalized electron beam size $u = y_{\max}(s,\chi)$ on τ for different values of parameter $\chi(\eta = 0)$.

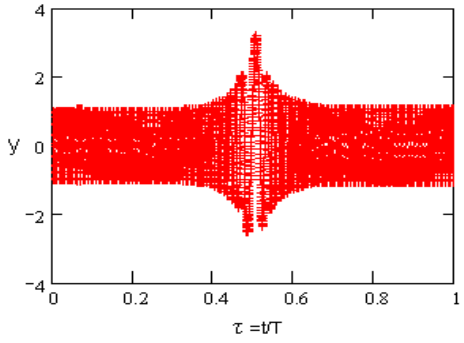

Figure 3: Trajectory for $\chi = 0.01$. Maximal deviation is equal to 3.19 (in accordance with adiabatic theory 3.16).

The adiabaticity criterion depends on the form of longitudinal distribution, as well as on the variables χ, η, τ; it reaches maximal value near the bunch edge. Let us remark that the adiabaticity confines even for large values of the adiabaticity criterion. For illustration let us see the example of trajectory shown in Fig. 3.

3 LINEAR OSCILLATIONS

An adiabatic solution in the linear case is:

$$y = a\varphi(\tau) + CC, \varphi(\tau) = \exp[i2\pi Q_0 \int_0^\tau \sqrt{F(\tau_1)}d\tau_1]/\sqrt{2\pi Q_0\sqrt{F(\tau)}}\,. \quad (4)$$

Here a is the complex amplitude, CC means complex conjugate number, $\varphi(\tau)$ is the 'adiabatic Floquet function'; the adiabatic invariant $I = 4|a|^2$. The adiabaticity perturbations result in amplitude perturbations. Using the method for the complex amplitude variation we obtain:

$$a' = -\frac{i}{2}\left\{a\varphi(\tau)\left[-\frac{\Omega''}{2\Omega} + \frac{3(\Omega')^2}{4\Omega^2}\right] + CC\right\}\varphi^*(\tau)\,. \quad (5)$$

Analysis of the equation shows that the adiabaticity perturbations produce a set of half-integer resonances with strength depending on $\Omega'(\tau), \Omega''(\tau)$. The resonance strengths can be calculated using standard matrix procedure. Eigenvalues of the transfer matrix $M_T\lambda_{1,2} = Tr(M_T)/2 \pm \sqrt{[Tr(M_T)/2]^2 - 1}$. If $|Tr(M_T)| < 2$, eigenvalues are imaginary and the motion is stable. In the opposite case a motion is unstable, and resonance strength

$$g = \ln\left[|Tr(M_T)|/2 + \sqrt{[Tr(M_T)/2]^2 - 1}\right]\,. \quad (6)$$

Owing to longitudinal motion the electrons cross these resonances. Using the theory of fast resonance crossing [9], we obtain the average rate of the invariant growth because of half-integer resonances

$$\langle\frac{dI}{d\tau}\rangle \approx \frac{\langle I\rangle}{8}\langle[(0.5TrM_T)^2 - 1]\rangle\,. \quad (7)$$

We see that in the frame of a linear model all electrons should be lost after some time interval. The rate of resonance heating strongly depends on the longitudinal density distribution.

As an example we have examined linear electron dynamics during the injection in SIS100 when five different schemes of bunch location are possible: 1) only one bunch in the ring; 2) two bunches in opposite separatrices; 3) two bunches in neighbouring separatrices; 4) one bunch is absent; 5) all four bunches are present.

The results of calculations have shown that stability strongly depends on the filling schemes and longitudinal distributions. The most unstable, of course, is the simple 'square bucket' model, which has breaks in function. In Fig. 4 we see the 'classical' picture: dependence of the 'focusing factor' $K^1_{foc} = Tr(M_T)/2$ on the leakage factor μ, which is equal to the ratio of the ion number in the gap to the ion number in the bunch. We see that for the 'smooth' model the focusing is much better, and oscillations become stable (i.e. adiabatical) for very small leakage factors.

At Fig. 5 is plotted a dependence of the focusing factor $K^2_{foc} = 0.5|TrM_T| - 1$ on the beam radius for $\mu = 0.1$, $\eta = 0$ (elliptical model). These pictures have a typical resonance character. The resonance strength is much higher for one bunch, then for four bunches.

Owing to random variations of tune the electrons cross the resonances. The heating rate is defined by

$$\langle\frac{dI}{dt}\rangle \approx \frac{\langle I\rangle}{8T}K^3_{foc},\ K^3_{foc} = \langle\frac{Tr(M_T)^2}{2}\rangle - 1\,. \quad (8)$$

At Fig. 6 is plotted a dependence of this factor on μ for $\eta = 0$ and the elliptical model. We see that the filling scheme with four bunches is much more dangerous than the last ones.

Equation (8) shows that in the linear approximation the adiabaticity perturbations result in diffusion which for a long enough time results in the loss of all particles. The situation is changed with field non-linearity.

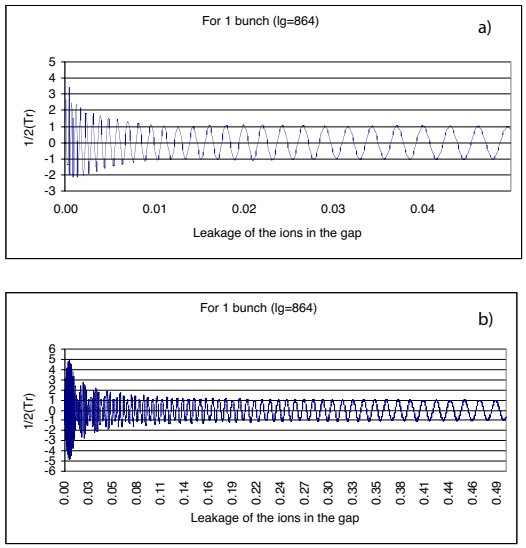

Figure 4: Dependence of K^1_{foc} on μ for single-bunch mode; (a) smooth cosine model, (b) elliptical model.

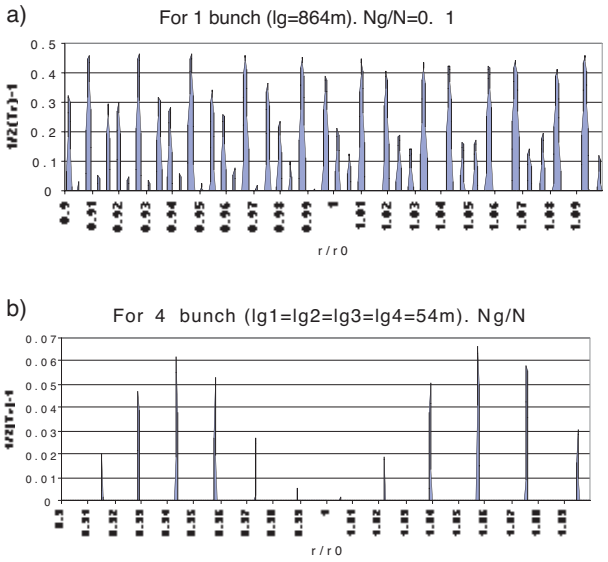

Figure 5: Dependence of K^2_{foc} on the beam size for the elliptical model and $\mu = 0.1$; (a) one bunch, (b) four bunches.

4 NON-LINEAR OSCILLATIONS

As is well known non-linearity stabilizes the oscillations. For illustration let us consider a half-integer resonance in presence of non-linearity. Then the normalized (divided on resonance strength) Hamiltonian $H = kI^2 + I\cos(2\theta)$. The corresponding phase diagram in the I, χ plane is plotted in Fig. 7.

The character of stability depends on the chamber aperture $I_{\max}$. From the diagram we see that if the chamber aperture $I_{\max} > 0.2$ (this value corresponds to the separatrix), for each initial phase there are particles which live infinitely long.

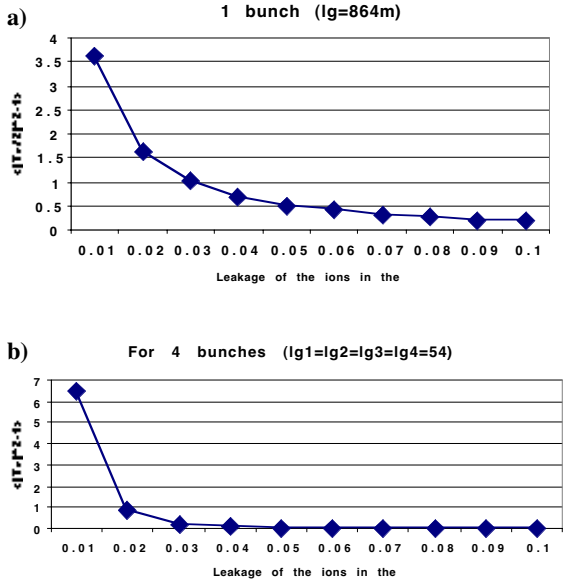

Figure 6: Dependence of K^3_{foc} on μ for the elliptical model; (a) one bunch, (b) four bunches.

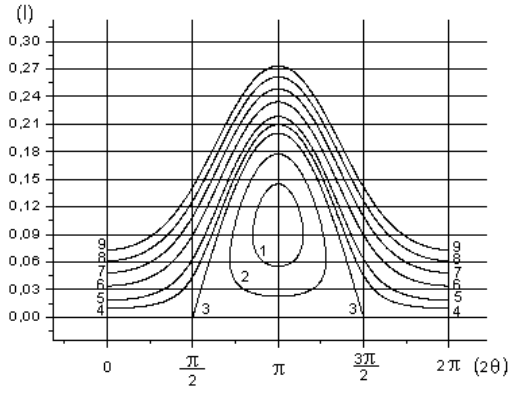

Figure 7: Phase diagram in action-phase plane for half-integer resonance in presence of cubic non-linearity ($k = 5$); curves: $1 - \mathrm{H} = -0.04$; $2 - \mathrm{H} = -0.02$; $3 - \mathrm{H} = 0.0$; $4 - \mathrm{H} = 0.01$; $5 - \mathrm{H} = 0.02$; $6 - \mathrm{H} = 0.04$; $7 - \mathrm{H} = 0.06$; $8 - \mathrm{H} = 0.08$; $9 - \mathrm{H} = 0.1$).

We have calculated the dependence of the electron maximal amplitude at the bunch centre on the time for different numbers of the ions in the beam, different values of 'gap factor' and neutralization $\eta = 0$ (SIS100, 4 bunches, 'cosine model').

We see from Fig. 8 that for high time intervals the amplitude of the surviving particles goes to some limit depending on the gap density factor $\chi(Y(\chi))$. Similar results are obtained for SIS200 (Fig. 9).

In the following text we use the term 'sharp border model': we assume that particles survive only if $Y < Y(\chi)$, (the parameter $Y(\chi)$ will be named 'physical chamber aperture' for the electrons).

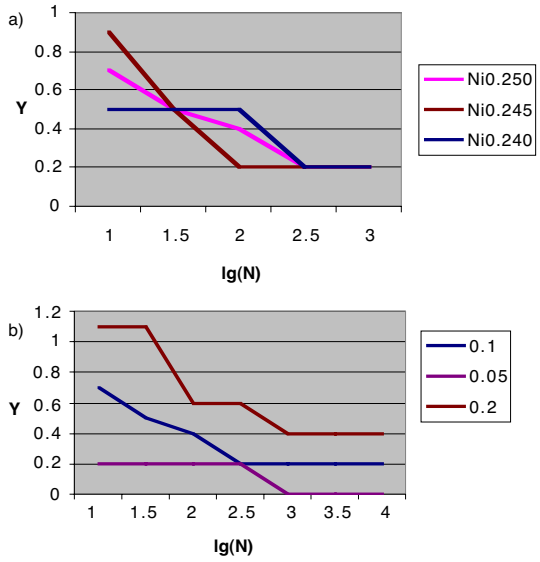

Figure 8: a) SIS100, four bunches, dependence of Y on $N = t/T$, for different values of the number of ions in the bunch in $10^{12} N_i$ (curves: $1 - N_i = 0.245$; $2 - N_i = 0.25$; $3 - N_i = 0.24$); $\chi = 0.1$; $\eta = 0$. b) SIS100, dependence of Y on $N = t/T$, for different values of χ (curves: $1 - \chi = 0.2$; $2 - \chi = 0.1$; $3 - \chi = 0.05$), $(N_i 0 = 0.25 \times 10^{12}), \eta = 0$.

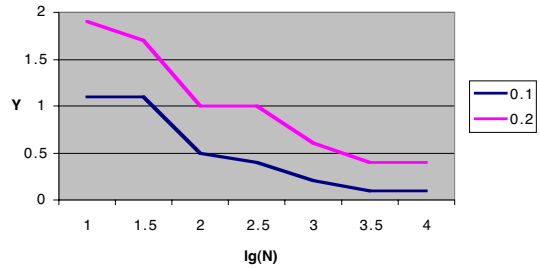

Figure 9: SIS200, dependence of $Y = Y_{AP}(\chi, \eta, N)$ on $N = t/T$, for different values of χ (curves: $1 - \chi = 0.2$; $2 - \chi = 0.1$), $(N_i 0 = 1 \times 10^{12}), \eta = 0$.

5 NEUTRALIZATION DEGREE

The ionization rate per ion may be written as follows

$$\frac{1}{T_{ion}} = \frac{1}{N_i}\frac{dN_e}{dt} = \beta c N_{Losch} P \langle \sigma_{ion} \rangle \ , \qquad (9)$$

where P is the residual gas pressure (in bar), $N_{Losch} = 2.7 \times 10^{19}$ cm^{-3} (Loschmidt number), $\langle \sigma_{ion} \rangle$ = ionization cross-section averaged on beam components; partial ionization cross-section is defined by [10]:

$$\begin{aligned} \sigma_{ion}^m &= Z_i^2 K \tfrac{\Omega_m(\beta)}{\beta^2}, \\ \Omega_m(\beta) &= C_m + M_m^2 \left(\ln \tfrac{\beta^2}{1-\beta^2} - \beta^2 \right) \end{aligned} \ . \qquad (10)$$

Here $K = 1.87 \times 10^{20}$ cm^2, the parameters C_m and K_m depend on the kind of gas.

Let us limit ourselves to a case of small neutralization degree. Then the rate of birth for ionization electrons in the 'survival layer' is

$$\left(\frac{dN_e}{dt}\right)_{surv} \approx \frac{N_i}{T_{ion}} Y(\chi) \ . \qquad (11)$$

The lifetime of these electrons is defined by Coulomb scattering of electrons on circulating ions. The heating rate is [7]:

$$\frac{dW_e}{dt} = E_0 \frac{4\pi c \rho_i r_e^2 Z_i^2}{\beta} L_{Coul} \ . \qquad (12)$$

The energy, corresponding to the 'physical aperture', for paraxial electrons is $W_e^{\lim} \approx E_0 2\pi Z_i \rho_i a^2 r_e Y(\chi)^2$, and the mean energy of born electrons $\langle W_e \rangle \approx W_e^{\lim}/2$; then we find the electron lifetime:

$$T_{life} \approx \frac{W_e^{lim}}{2} \Big/ \left(\frac{1}{2}\frac{dW_e}{dt}\right) = \frac{\beta a^2 Y(\chi)^2}{2 c r_e Z_i L_{Coul}} \ . \qquad (13)$$

Using Eqs. (9–13) we obtain the following equation for neutralization degree

$$\frac{d\eta}{dt} = \frac{Y(\chi)^2}{T^0_{neutr}} - \frac{\eta}{T^0_{life} Y(\chi)} \ . \qquad (14)$$

Here $T^0_{neutr} = T_{ion} Z_i$, $T^0_{life} = T_{life}/Y(\chi)^2$. If $\eta_0 \ll \chi$ and $\tau \gg \tau_{life}$, an approximate solution for neutralization degree can be written analytically in the following form:

$$\eta^{eq} = \eta_0^{eq} Y(\chi_-)^3, \eta_0^{eq} = K_0 a^2 P \langle \Omega_m(\beta) \rangle \qquad (15)$$

where a is in centimetres, P is in 10^{-10} mbar, and the constant

$$K_0 = \frac{10^{-13} N_{Losch} K}{2 r_e L_{Coul}} = \frac{0.0992}{L_{Coul}} \ .$$

An interesting feature of this expression is the weak dependence of the equilibrium neutralization degree on β and the independence from the ion charge Z_i.

Let us underline that in a frame of this simple model the equilibrium neutralization for coasting beam is defined by η_0^{eq}; the reduction of the electron population due to bunching is described by the multiplier $Y(\chi)^3$.

6 APPLICATION TO SIS100/SIS200

Estimations for SIS200 (coasting beam) have shown that for nominal vacuum pressure the neutralization degree is an

Table 2: Neutralization parameters for SIS100-SIS200: kind of ions $^{+28}U^{238}$, in SIS100 $P = 5 \times 10^{-12}$ mbar, in SIS200 $P = 10 \times 10^{-12}$ mbar, gas composition coincides with measured gas composition in SIS-18 ($H_2 = 65\%,\ O/H_2O = 17\%,\ CO/N_2 = 8\%,\ Ar = 4\%,\ Cl = 4\%,\ CO_2 = 1\%$).

Machine	SIS100 $\chi = 0.1$	SIS100 $\chi = 0.2$	SIS200 $\chi = 0.1$	SIS200 $\chi = 0.2$
$\langle\sigma_{ion}\rangle(10^{-16}$ cm$^2)$	10.3	10.3	7.25	0.05
τ^0_{neutr} (s)	15.6	15.6	13.1	13.1
τ^0_{life} (s)	0.102	0.102	0.092	0.092
$\eta_0^{eq} = \tau^0_{life}/\tau^0_{neutr}$	6.5×10^{-3}	6.5×10^{-3}	7.0×10^{-3}	7.0×10^{-3}
$Y(\chi)$	0.2	0.4	0.1	0.4
$\tau_{life}(\chi)$	0.0204	0.0408	0.0092	0.368
$\eta_0(\chi) = \eta_0^{eq} Y(\chi)^3$	5.2×10^{-5}	4.2×10^{-4}	7.0×10^{-6}	4.5×10^{-4}

order of 0.6–0.8%. However, the situation can become dangerous if the pressure increases sharply due to gas desorption. In this case the electron concentration can be diminished by beam bunching in one bunch (bunch length = 80% from the circumference).

The calculated values of equilibrium neutralization degree are given in Table 2. We see that these values are comparatively small (let us remark that the real neutralization degree will be less to an order of magnitude since typical system time is less than neutralization time to an order of magnitude).

7 RESULTS AND DISCUSSION

1) In the presence of non-linearity periodic variations of the electrical field result in the appearance of 'physical aperture', i.e. maximal amplitude of oscillations for 'surviving' electrons.

2) The degree of neutralization is determined by the balance between electron creation due to ionization and electron loss due to Coulomb collisions with circulating ions; bunching of the beam results in the reduction of the equilibrium neutralization degree as the third power of normalized (divided on r.m.s. beam size a) physical aperture.

3) The application of the model to SIS100/SIS200 has shown that for nominal vacuum pressure typical values of neutralization degree are small.

Further plans:

1) To check the model by comparison with more detailed numerical calculations.

2) To estimate the influence of other electron sources (SEM electrons and electrons born in walls due to ion–electron emission).

8 REFERENCES

[1] B. Chirikov, Sov. Atomic Energy, vol. **19**, p. 1149, 1965.

[2] D. Koshkarev and P. Zenkevich, ITEP Preprint, 1970; Part. Accel. vol. **3**, p. 1, 1972.

[3] E. Keil and B. Zotter, CERN, CERN/ISR-TH/71-58, 1971.

[4] Workshop on Two-Stream Instabilities in Accelerators and Storage Rings, Los Alamos, 16–18 February 2000.

[5] GSI project.

[6] D. Neuffer, E. Colton et al., Nucl. Instrum. Methods, vol. **A321**, p. 1, 1992.

[7] P.R. Zenkevich, AIP Conference Proceedings **480**, p. 74, 1998.

[8] L. Landau and Ye. Livshits, 'Mechanics', (1961).

[9] P.A. Sturrock, Ann. Phys., vol. **3**, p. 113, 1958.

[10] F. Baconnier, A. Poncet and R.F. Tavarez, CAS Proceedings, CERN 94–01, Genève, p. 525, 1994.

Electron-Cloud Simulations: Build Up and Related Effects*

G. Rumolo and F. Zimmermann, CERN, Geneva, Switzerland

Abstract

ECLOUD is a simulation programme developed at CERN which models the process of build up of an electron cloud inside the vacuum chamber for proton or positron beams, which is due to a primary source (photoemission or residual gas ionization) and secondary emission. The main ingredients of the code are described here with special emphasis on the physical modeling of processes like secondary emission and elastic reflection of the electrons at the pipe walls. Electron energy spectra, heat load on the LHC beam screen, spatial patterns of the electron cloud, electron flux at pick-up buttons, multi-bunch instability growth rates, electron trapping by magnetic fields, and electron-cloud build up for electron beams can also be studied using these simulations.

1 INTRODUCTION

This paper consists of two parts. In the first, we describe the simulation model, including the treatment of photoemission, secondary emission, magnetic fields, beam fields, image charges, and electron space charge. In the second part, we present example simulation results, such as a comparison of multipacting thresholds in a dipole field and in a field-free region (for the SPS), the electron-cloud build up for the SPS fixed-target beam, the electron signal detected by LHC button pick ups, growth rates for the multibunch instability in the LHC, the spatial structure of the electron cloud in dipole and quadrupole magnets, the probability of electron trapping in a quadrupole field (for the KEKB LER), and the electron-cloud build up for an electron beam (KEKB HER).

2 SIMULATION CODE

2.1 General Remarks

The programme ECLOUD models the build up of the electron cloud during the passage of a bunch train. Its first version was written at CERN in 1997 [1]. Since then continually extended, updated, and improved [2, 3, 4, 5, 6]. A preliminary user guide is available [7]. The code can be downloaded from the CERN electron-cloud web site [8].

The basic layout of the ECLOUD programme is similar to the code PEI, developped by K. Ohmi at KEK in 1995, and to POSINST, written by M. Furman and G. Lambertson at LBNL since 1995 [9, 10]. Other codes modelling electron cloud build up are due to T.-S. Wang (LANL), L. Wang (KEK), Z. Guo (IHEP), and M. Blaskiewicz (BNL).

We will illustrate the main features of ECLOUD and typical simulation results presenting various applications to the LHC, SPS, and KEKB. A table with pertinent beam parameters for these machines can be found in Ref. [11]. A companion paper reports further results for the LHC [12].

2.2 Simulation Recipe

The simulation recipe of ECLOUD is illustrated by the schematic in Fig. 1. The main ingredients have been described in Refs. [4, 5, 6].

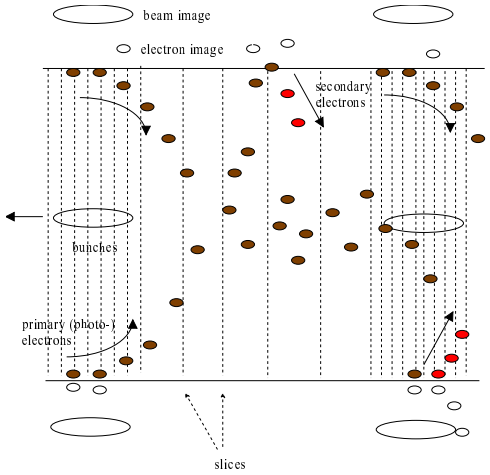

Figure 1: Schematic of simulation recipe.

A certain section of the vacuum chamber, typically 1 m long, is simulated. The magnetic field in this region is specified as an input.

The primary electrons, which are created by photoemission or beam loss on the wall, or due to ionization inside the beam volume, are represented by macro-electrons, whose charge is (much) larger than the charge of a real electron.

Both the bunches and the gap between bunches are sliced into segments, of the order of 50–200 each. The slices inside the bunch are usually choosen shorter than those in the gap, in order to accurately model the motion of the electron under the strong accelerating field of the beam. For each bunch slice a certain number of macro-electrons are generated, and existing macro-electrons are propagated in the field of the bunch (and external magnetic fields, etc.). Typically, per passing bunch a total of 1000–2000 macro-electrons are launched on the wall, or inside the beam.

* Simulation models and code flexibility have continually improved thanks to intense and fruitful collaboration with: G. Arduini, V. Baglin, S. Berg, O. Brüning, F. Caspers, A. Chao, R. Cimino, I. Collins, K. Cornelis, H. Fukuma, M. Furman, O. Gröbner, S. Heifets, N. Hilleret, M. Jimenez, K. Ohmi, E. Perevedentsev, M. Pivi, A. Rossi, F. Ruggiero, G. Stupakov, L. Wang, and many others.

The electron motion is computed in 3 dimensions. The boundary conditions are effectively periodic in z. In addition to the beam field and the magnetic fields, also the electron space-charge field, beam-image charges and electron image fields are taken into account. The electron space-charge field is important, as without it the electron cloud build up would continue indefinitely. The space charge of the electrons causes a saturation of the build up at an electron cloud density close to the average neutralization density, for which the average electric field on the wall is zero. Image charges are important if the chamber is not round, if the beam orbit is offset from the center of the beam pipe, or if the electron cloud is not uniform (*e.g.*, in a dipole magnet).

Whenever a macro-electron hits the wall, it is remitted at the same location as (either true or elastically reflected) secondary electron and its charge is changed according to the value of the secondary emission yield computed as a function of its energy and its angle of incidence. This is a difference to the code POSINST where all macro-electrons have identical charge.

Between bunches the macro-electrons only experience the magnetic field, and the direct and image fields of the electron cloud itself. The latter two are approximated either by discrete kicks, applied after each slice, or by a contunuous constant acceleration over the length of the slice.

The LHC chamber cross section is a circle that is vertically cut off, as shown in Fig. 2. When computing particle loss or launching new particles we use the actual boundary (the solid line in the figure). For the image-charge calculation we approximate the geometry by the inscribed ellipse, making use of an analytical expression for the image charge with elliptical boundary (see below).

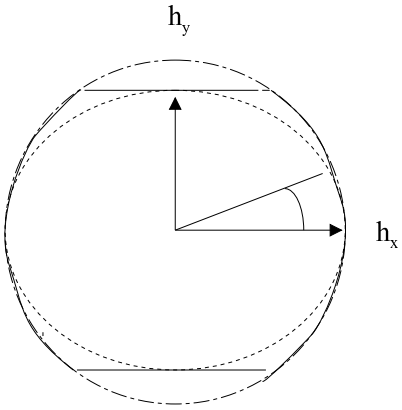

Figure 2: Transverse aperture in the LHC arcs. The solid line describes the actual cross section of the LHC beam screen.

2.3 *Photoemission*

The photoemission is characterized by 3 input variables: (1) the number of photons emitted per meter and per beam particle, (2) the photon reflectivity R, and (3) the azimuthal distribution of the reflected photons.

If $R = 0$, all photoelectrons are emitted from the horizontally outward side of the chamber, constrained to a cone with rms angle ϕ of order $1/\gamma$. If $R > 0$, a fraction R of the photoelectrons is launched at other azimuthal angles ϕ around the wall of the chamber. Figure 3 shows two initial distributions of the photo-electron starting positions as a functon of the transverse azimuthal angle ϕ. The two distributions depicted correspond to $R = 10\%$ and $R = 100\%$, respectively, and to an approximately uniform reflection. This example refers to the LHC chamber; a small distortion is caused by the vertical chamber cut off.

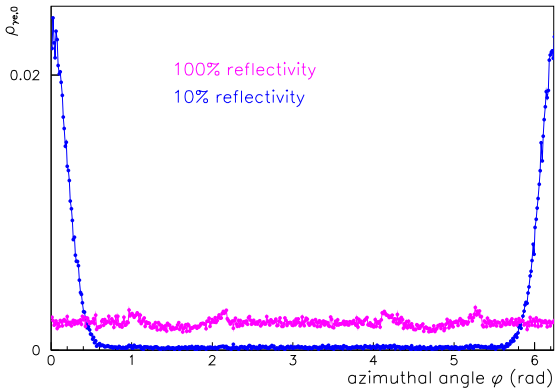

Figure 3: Initial azimuthal distribution of photoelectrons for 10% and 100% photon reflectivity.

Figure 4 defines the photon reflection angle θ. Measurements in Russia have shown that, for the LHC sawtooth chamber, the distribution of the diffusely reflected photons is not uniform, but consistent with a $\cos^2\theta$ distribution [13].

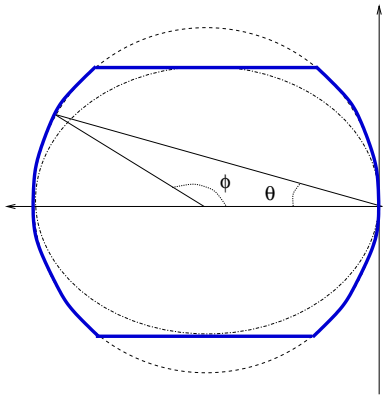

Figure 4: Definition of angles ϕ and θ.

Various distributions for the photoelectrons are compared in Fig. 5. They can be selected as input to the pro-

gramme. The dependence of the LHC heat load on the photon distribution was studied in Ref. [5].

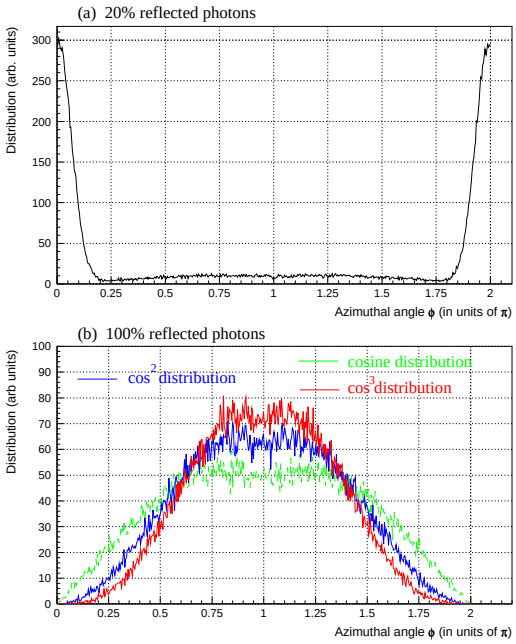

Figure 5: Initial azimuthal distribution of photoelectrons for (a) 20% and (b) 100% photon reflectivity, considering different distributions [5].

After determining the launch points of the primary photo-electrons, we now address their initial velocity. The initial angular velocity distribution of the newly generated primary electrons is assumed to be uniform in the two spherical coordinates $\tilde{\theta}$ and $\tilde{\phi}$, which are defined with respect to the local surface normal (note that these angles $\tilde{\phi}$ and $\tilde{\theta}$ refer to the azimuthal and polar angles in the local coordinate system at the point of electron emission; they are different from the angles θ and ϕ mentioned above). The energy distribution of the emitted photoelectrons is modelled as a truncated Gaussian centered at 7 eV, with a standard deviation of 5 eV.

Figure 6 displays the initial energy distribution of the photoelectrons as well as the distribution after the first bunch passage, for an LHC dipole.

2.4 *Magnetic Field*

Standard possibilities include field-free region, strong or weak dipole, quadrupole, or solenoid. All these fields may vary with longitudinal position z. More generally, an arbitrary field can be calculated, as long as it is expressed in analytical form.

As an example, in a paraxial approximation the magnetic field components for a periodic series of solenoids are

$$\begin{aligned} B_x(x,y,z) &= -\frac{1}{2}B_0 kx\cos kz \\ B_y(x,y,z) &= -\frac{1}{2}B_0 ky\cos kz \end{aligned} \quad (1)$$

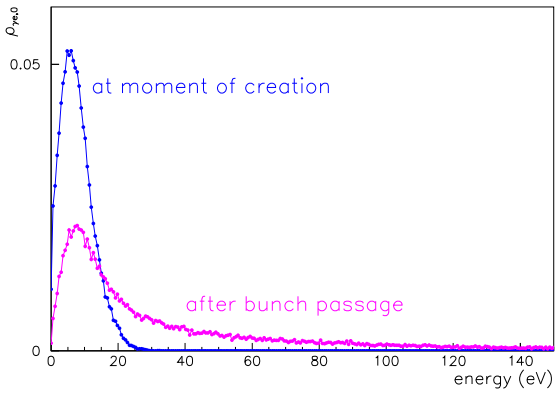

Figure 6: Initial photoelectron energy distribution at the moment of emission and after the first bunch passage, for an LHC dipole.

$$B_z(x,y,z) = B_{z0} + B_0 \sin kz\ .$$

Supposing that the field B_z is sinusoidal, on axis the exact field components follow from Maxwell's equations as [14]

$$\begin{aligned} B_z(r,z) &= B_0 I_0(kr)\cos kz \\ B_r(r,z) &= B_0 I_1(kr)\sin kz\ . \end{aligned} \quad (2)$$

Expanding the Bessel functions to first order in radius r, this reduces to the previous formulae.

Further extensions are possible and more than one Fourier component can be kept in the longitudinal field expansion to characterize the more realistic case of a periodic array of solenoids of finite length. Field expressions for this situation were derived by E. Perevedentsev. They read [14]

$$B_r = B_0 \frac{2ka}{\pi} \sum_{n=1}^{\infty} \sin nkh\ K_1(nka)\ I_1(nkr)\ \sin nkz \quad (3)$$

$$B_z = B_0 \left(\frac{2h}{L} + \frac{2ka}{\pi} \sum_{n=1}^{\infty} \sin nkh\ K_1(nka)\ I_0(nkr)\ \cos nkz \right), \quad (4)$$

where the I and K are modified Bessel functions of the first order, a is the solenoid radius, h the solenoid length, L the distance between adjacent solenoids with equal polarity, and B_0 a normalization constant, roughly equal to the field on axis inside the solenoid. in the simulation, the infinite series is truncated at some order, *e.g.*, $n = 5$–50. A similar formula, with odd harmonics doubled and even harmonics set to zero, describes the case of solenoids with alternating polarity, separated by $L/2$. All these expressions

are implemented in ECLOUD and were used for example in simulations for the KEK B factory [15].

The electron motion in field-free region is simply a drift, between kicks (step changes in momentum) representing the effect of the beam field, the electron space charge, and the image charges. For the LHC we often consider a strong dipole, for which we freeze the horizontal and longitudinal position and only consider momentum transfer and electron motion in the vertical direction. This approximation is motivated by the high cyclotron frequency (many cyclotron oscillations per bunch length), namely

$$\omega_c = \frac{eBc}{m_e c^2}\frac{2\sigma_z}{2\pi} \approx 120 \qquad (5)$$

for the LHC at 7 TeV ($B = 8.4$ T), and by the small Larmor radius r_L of 6μm for an electron energy of 200 eV. The situation is sketched in Fig. 7. The initial momentum components transverse to the vertical direction are however taken into account in the simulation, namely, when we compute the impact angle on the chamber wall. The angle of incidence modestly influences the secondary emission yield.

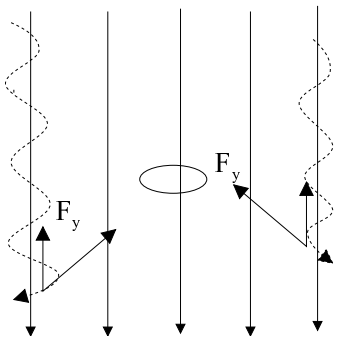

Figure 7: Schematic view of electron motion in a strong vertical dipole field.

For other fields (*e.g.*, 'weaker' dipoles, quadrupoles, solenoids) we use a Runge-Kutta integration. The user can choose between two different Runge-Kutta integrators, taken from the CERN library or the NAG library, respectively.

2.5 *Beam and Image Fields*

Beam fields are calculated using the standard expression à la Bassetti-Erskine [16] or the simpler formula for round beams. An elegant expression for the field at large distances from a line charge which includes the image charges in an elliptical conducting chamber was given by M. Furman [17]. Denoting by $\mathcal{E} = \mathcal{E}_x + i\mathcal{E}_y$ the complex electric field, Furman's expression reads [17]

$$\mathcal{E} \approx \frac{2}{\bar{z}-\bar{z}_0} + \frac{4}{g}\sum_{n=1}^{\infty} e^{-n\mu_c}\left[\frac{\cosh n\mu_0 \cos n\phi_0}{\cosh n\mu_c} + \right.$$

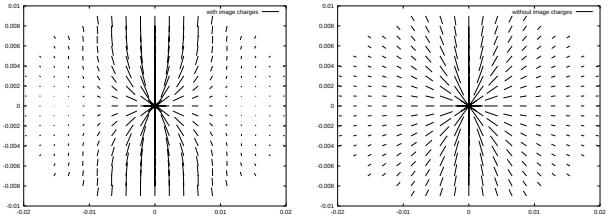

Figure 8: Electric field pattern for a beam centered in an elliptical chamber with [left] and without [right] image charges.

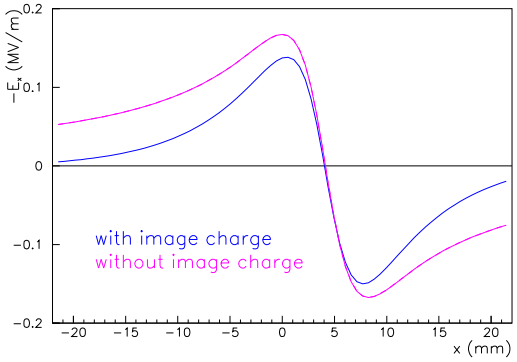

Figure 9: Horizontal electric beam field vs. horizontal position at $y = 0$ for an elliptical chamber with 22×10 mm half apertures and a beam offset of 4.3 mm in both transverse planes.

$$\left. i\,\frac{\sinh n\mu_0 \sin n\phi_0}{\sinh n\mu_c}\right] \frac{\sinh n\bar{q}}{\sinh \bar{q}} \qquad (6)$$

where $z = x + iy = g\,\cosh q = g\,\cosh(\mu + i\phi)$ denotes the test position, $z_0 = x_0 + iy_0 = g\cosh q_0 = g\cosh(\mu_0 + i\phi_0)$ the position of the source, and both $g = \sqrt{a^2 - b^2}$ and $\mu_c = \tanh^{-1}(b/a)$ characterize the vacuum chamber with semi-axes a and b. In the simulation, the infinite sum is truncated at order $n = 30$.

Figure 8 shows the beam field lines in an elliptical chamber calculated with and without the beam image charges. Figures 9 and 10 depict the horizontal and vertical electric fields for an offset beam as a function of horizontal position, again with and without including the field from the image charges. All three figures demonstrate that the image charges can significantly alter the electron motion.

Image charges of the electron cloud can also be taken into account. The electron charges are assigned to points on a grid, typically consisting of 20×20 or 25×25 points, and the image forces are evaluated for each of the grid points. An example of the electron-cloud self field with and without image charges is shown in Fig. 11.

The minimum number of slices required to accurately model a bunch passage can be determined by considering the motion of electrons with different start positions.

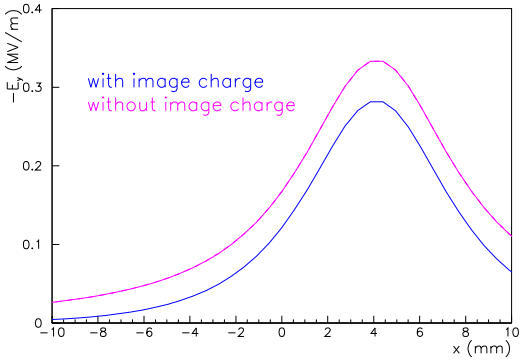

Figure 10: Vertical electric beam field vs. horizontal position at $y = 0$ for an elliptical chamber with 22×10 mm half apertures and a beam offset of 4.3 mm in both transverse planes.

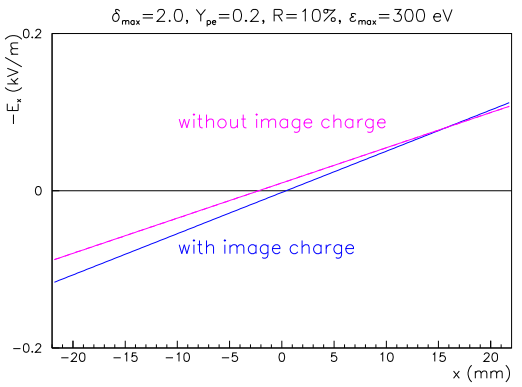

Figure 11: Horizontal electric space-charge field of electron cloud vs. horizontal position after the passage of 8 bunches in the LHC. Parameters: $\delta_{\max} = 2.0$, $Y_{pe} = 0.2$, $R = 0.1$, $\epsilon_{\max} = 300$ eV.

Electrons at large amplitudes do not move much during the bunch passage and simply receive a kick. Electrons near the bunch oscillate in the beam potential. This is shown in Fig. 12. The two amplitude regimes have been called the 'kick region' and the 'autonomous region', respectively, by S. Berg [18].

Hence, it is not surprising that the energy gain of an electron also varies with its initial amplitude. The energy gain further depends on the longitudinal bunch profile. Figure 13 shows a calculation for three different bunch distributions [18]. At the LHC, the maximum possible energy gain is about 2 keV.

2.6 *Secondary Emission*

Typical measured energy spectra of the emitted secondary electrons are shown in Fig. 14. The figure reveals that the

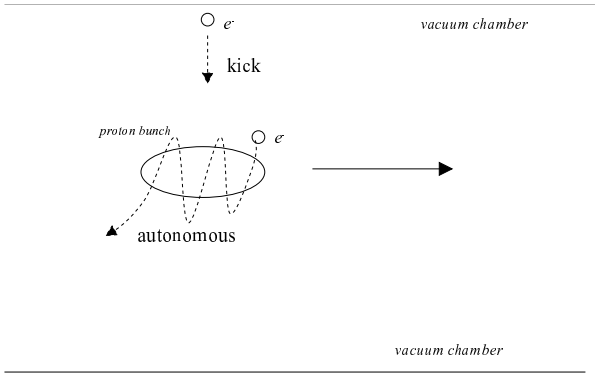

Figure 12: The electron motion during a bunch passage differs qualitatively, depending on the initial position [18].

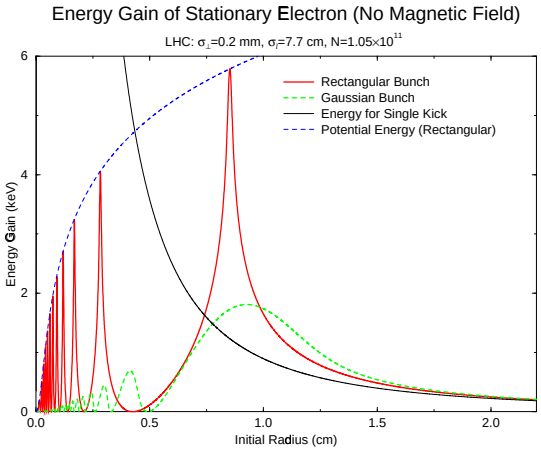

Figure 13: Maximum energy gain of an electron vs. initial particle radial position for nominal LHC parameters [18].

energy spectrum consists of three components: true secondaries with an energy of a few eV, elastically reflected whose energy equals the energy of the incident particle, and rediffused (*i.e.*, the remaining electrons, at intermediate energies).

The relative magnitude of these three components depends on the incident energy. In our simulations with ECLOUD, we presently only distinguish between elastically reflected and true secondaries. The total yield is taken to be the sum of these two components,

$$\delta_{\rm se} = \delta_{\rm tse} + \delta_{\rm el} \ , \tag{7}$$

where $\delta_{\rm tse}$ denotes the yield of true secondaries and $\delta_{\rm el}$ the yield of elastically reflected. Both are functions of the primary-electron energy E and angle of incidence with respect to the surface θ (this θ is not the same as the angle θ of Fig. 4). The elastically reflected electrons are particularly important for small incident energies. There the true yield becomes negligible, whereas for decreasing primary energy the elastic yield converges against a finite value between 30 and 60%. As a consequence, low-energy electrons hitting

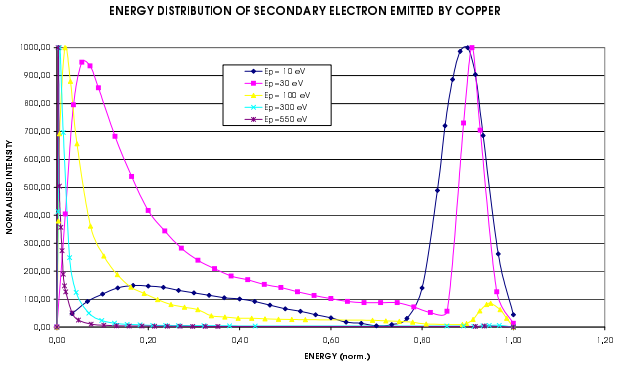

Figure 14: Normalized secondary electron energy distribution for conditioned copper, revealing three components: true secondaries ($E \ll E_p$), elastically scattered ($E \approx E_p$) and rediffused (in between) [19].

the wall (which are the majority), are not lost, but reflected with a rather high probability, and then can survive until they are accelerated by the next bunch passing by. Thereby the inclusion of elastic reflection results in an increase of the simulated LHC heat load by a factor 2–3 [20].

The actual representation of $\delta_{\rm el}$ and $\delta_{\rm tse}$ is based on a parametrization of measurements provided by the CERN LHC Vacuum group [19].

According to Furman [10], Seiler [21] and Kirby [22] the yield for the true secondaries can be written

$$\delta_{\rm tse}(E_{\rm p},\theta) = \delta_{\rm max}\, 1.11\, x^{-0.35}\, \left(1-e^{-2.3x^{1.35}}\right) \exp\left(0.5\,(1-\cos\theta)\right)\ , \qquad (8)$$

where $x = E_{\rm p}\ (1+0.7(1-\cos\theta))/\epsilon_{\rm max}$ [10].

An alternative expression for the true secondaries was proposed by M. Furman [10]:

$$\delta_{\rm tse}(E_{\rm p},\theta) = \delta_{\rm max}\, \frac{s\times x}{s-1+x^s} \exp\left(0.5\,(1-\cos\theta)\right)\ , \qquad (9)$$

and x is defined as above.

In 2002, we replaced formula (8) by (9), using $s = 1.35$ (this is the value measured for fully conditioned copper; prior to conditioning one finds $s = 1.39$ [19]).

The yield of the true secondaries is then characterized by only two free parameters: $\delta_{\rm max}$ and $\epsilon_{\rm max}$. These specify the energy $\epsilon_{\rm max}$ for which the (true) secondary emission yield is maximum and the value of the maximum yield for perpendicular incidence, $\delta_{\rm max}$.

The yield of the elastically reflected electrons is written

$$\delta_{\rm el}(E_{\rm p}) = f\delta_{\rm se}(E_{\rm p},\theta)\ , \qquad (10)$$

where f was obtained from recent measurements on copper [19], which were fitted to the expression

$$f = \exp\left(A_0 + A_1\ln(E_{\rm p}+E_0) + A_2(\ln(E_{\rm p}+E_0))^2 + A_3(\ln(E_{\rm p}+E_0))^3\right)\ . \qquad (11)$$

Fits were performed over two different energy ranges. For $E_{\rm p} \le 300$ eV, the fitted coefficients are [19] $A_0 = 20.7$, $A_1 = -7.08$, $A_2 = 0.484$, $A_3 = 0$, and $E_0 = 56.9$ eV, while, for $E_{\rm p} \le 2000$eV, $A_0 = -5.1$, $A_1 = 5.6$, $A_2 = -1.62$, $A_3 = 1.1\times10^{-5}$, and $E_0 = 29$ eV. Again, all these functions are implemented in the code ECLOUD.

The total secondary emission yield so obtained is illustrated in Fig. 15. For comparison, earlier models without any elastic reflection (in 1999) and with a larger elastic component (2000) are also shown. At the ECLOUD'02 workshop it was remarked that even the latest parametrization is not representative, especially at higher energies [23].

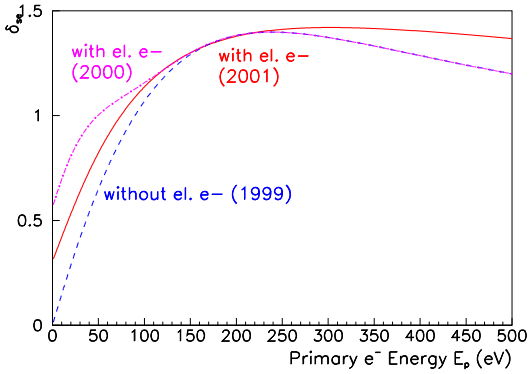

Figure 15: Secondary emission yield for perpendicular incidence vs. primary electron energy with and w/o elastically scattered electrons.

If an electron hits the wall, we determine randomly whether the re-emitted electron represents a true secondary or an elastic electron. More precisely, we choose a random number rand between 0 and 1. If rand $< f \equiv \delta_{\rm el}/\delta_{\rm se}$, we take the electron to be an elastic one; otherwise, if rand $\ge f$, we treat it as a true secondary.

A recent empirical fit by N. Hilleret [24] of the measured energy spectra for the true secondaries emitted from copper to the formula [25]

$$\rho(E) = C\exp\left[-\frac{(\ln E/E_0)^2}{2\tau^2}\right] \qquad (12)$$

yields a good representation of the measurements for $C \approx 0.2$, $E_0 \approx 1.8$ eV, and $\tau \approx 1$ [24]. Equation (12) and its illustration in Fig. 16 show the correct asymptotic behaviour at low energy; namely $\rho(E)$ approaches zero as the energy E goes to zero, a result also expected from phase-space considerations [26]. Previously, the inital energy distribution of the secondary electrons was often taken to be a half Gaussian centered at 0 with rms spread 5 eV, which is also indicated in the figure.

The initial angular distribution of the secondary electrons is taken to be of the form $dN/d\Omega \propto \cos\theta$ [21], which results in $dN/d\theta \propto \sin\theta\cos\theta$, where θ denotes the polar angle with respect to the surface normal. This is illustrated in Fig. 17.

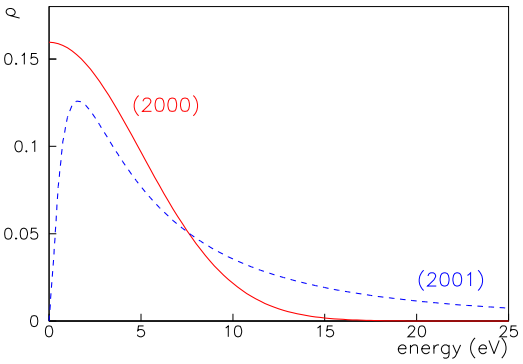

Figure 16: Initial energy spectrum of true secondaries as modelled in 1999/2000 compared with new parametrization by Noel Hilleret [24].

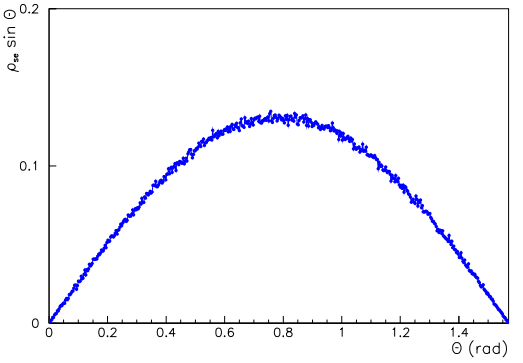

Figure 17: Initial angular distribution $dN/d\theta$ of secondary electrons vs. the polar angle θ with respect to the surface normal.

2.7 Longitudinal Electron Motion

Longitudinal motion of the electrons is included in the simulations. Several effects give rise to this motion [20].

First, the secondary electrons are emitted at an angle θ with respect to the surface normal, following a $\cos\theta$ distribution. Projecting onto the longitudinal direction, we estimate $< \theta_z^2 > \approx 0.37$ rad^2. The typical longitudinal velocity at emission is

$$v_{z,\mathrm{em}} \approx c \left(\frac{2}{m_e c^2} < \theta_z^2 > E_{\mathrm{rms}} \right)^{1/2} \qquad (13)$$

where $E_{\mathrm{rms}} \approx 5$ eV is the rms emission energy. This evaluates to $v_{z,\mathrm{em}} \approx 10^6$ ms^{-1}.

For the LHC, a second contribution comes from the magnetic field of the beam. If the electron is initially at rest, its longitudinal velocity after the bunch passage is [28]

$$v_{z,\mathrm{mag}} \approx \frac{1}{2}\frac{v_\perp^2}{c} \approx \frac{\Delta E_{\max}}{mc} \approx \frac{2cN_b r_e}{\sqrt{2\pi}\sigma_z} \log \frac{r_c}{c_0 \sigma_\perp} \qquad (14)$$

where $c_0 \approx 1.06$, and [18]

$$r_c \approx 2\sqrt{N_b r_e \sigma_z \sqrt{2/\pi}} \qquad (15)$$

Inserting the LHC parameters, we find $r_c \approx 8.5$ mm (this is the critical radius separating the kick approximation and the autonomous region [18]), and $v_{e,\mathrm{mag}} \approx 3 \times 10^6$ ms^{-1}. Simulations show that for LHC the electron energy gain $\Delta E_{\max}$ is about a factor 3 smaller than predicted by the above analytical approximation. Therefore, a more realistic estimate is $v_{e,\mathrm{mag}} \approx 10^6$ ms^{-1}, which is comparable to the longitudinal emission velocity. This order of magnitude was confirmed by simulations [27].

However, in a strong dipole field both the beam magnetic field and the emission velocity can be neglected. In this case, the electrons undergo a rapid cyclotron oscillation. Superimposed is a uniform longitudinal motion ($\vec{E} \times \vec{B}$ drift). We estimate the maximum drift velocity encountered during the bunch passage as

$$v_{e,\mathrm{drift}} \approx \frac{N_b e}{\sqrt{2\pi}\sigma_z 4\pi\epsilon_0(\sigma_x + \sigma_y)B} , \qquad (16)$$

where B is the dipole magnetic field. For the LHC parameters, we obtain $v_{e,\mathrm{drift}} \approx 1.6 \times 10^5$ ms^{-1}.

A quadrupole magnet also causes a 'gradient drift' at a velocity equal to

$$v_{e,\mathrm{gradient}} = \frac{r_L^2 \omega_c}{2} \frac{(\vec{\nabla}\vec{B}) \times \vec{B}}{B^2} , \qquad (17)$$

where $r_L = p_e/(eB)$ is the Larmor radius and $\omega_c = eB/m_e$ the (non-relativistic) cyclotron frequency. Using $\vec{B} = 200$ T/m, $B = 2$ T (*i.e.*, considering an electron at amplitude 1 cm), and a typical electron energy of 100 eV, we obtain $v_{e,\mathrm{gradient}} \approx 5 \times 10^3$ ms^{-1}.

Thus, in a field-free region we expect longitudinal electron motion at a typical speed of a few 10^6 ms^{-1}, whereas in an 8.4-T dipole field the maximum longitudinal velocity does not exceed 2×10^5 ms^{-1}. The average drift velocity in a dipole is even lower by a factor 50, because the beam is absent most of time. Finally, the gradient drift in a quadrupole of about 5×10^3 ms^{-1} may be comparable to the average drift in a dipole.

Our estimates are confirmed by simulations for field-free regions and dipoles, as is illustratred in Fig. 18.

The relatively low longitudinal speed implies that electrons are lost transversely to the wall before they can traverse a longitudinal distance comparable to the magnet dimensions. This provides a justification why we may separately simulate the electron cloud build up for regions of different magnetic fields without taking into account any electron exchange between those regions.

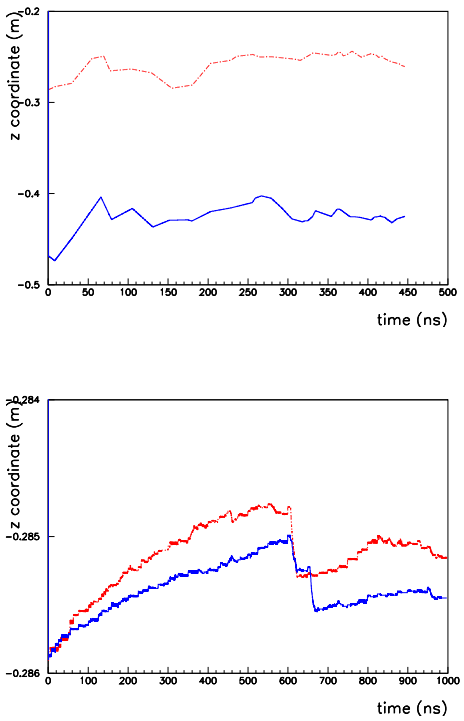

Figure 18: Longitudinal coordinate versus time for two sample electron trajectories in a field free region (top) and in a 1-T dipole field (bottom).

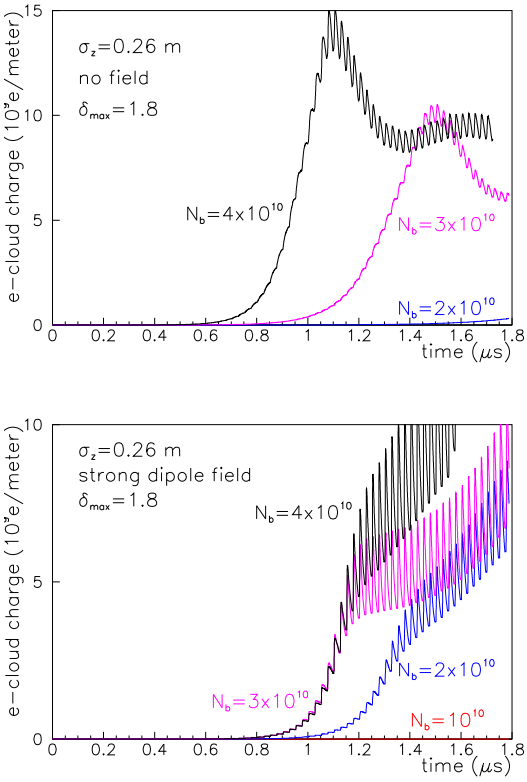

Figure 19: Simulated electron-cloud build up in the SPS for a field-free region (top) and a strong dipole (bottom), comparing various bunch populations. In field-free regions threshold is higher, but the build up above the threshold stronger.

3 EXAMPLE RESULTS

3.1 Electron Cloud Build-Up in Dipoles and Field-Free Regions, Energy Spectrum

Figure 19 shows the simulated build up of an electron cloud for a field-free region and for a dipole field in the CERN SPS. The chamber dimensions are assumed to be the same in the two cases, with $h_x = 76$ mm, and $h_y = 17.5$ mm (flat geometry). The various curves refer to different bunch intensities. The figure demonstrates that in the dipole field significant electron build up starts at a lower bunch intensity, although at higher intensities the cloud can reach larger densities in the field-free region. The lower threshold for the dipole field is attributed to the flatness of the chamber. The 'overshoot' before saturation that is visible for the field-free region appears to be related to the elastically reflected electrons.

Simulations were also performed for the SPS fixed target beam. This beam consists of 2 trains of about 2100 bunches with a bunch spacing of 5 ns, a train-to-train spacing of 1.05 μs and a single-bunch intensity N_b below 10^{10} protons per bunch. Figure 20 compares the simulated electron cloud build for $N_b = 5 \times 10^9$ and $N_b = 7 \times 10^9$, considering a maximum secondary emission yield of $\delta_{\max} = 1.8$. No build up is observed for the lower bunch intensity, but a significant build up occurs in the second case. Thus, the simulated threshold of electron amplification due to multipacting is about $N_b \approx 6 \times 10^9$, which is roughly consistent with observations [29]. In these simulations, we have assumed the measured rms transverse beam sizes of $\sigma_x = 1.2$ mm and $\sigma_y = 0.7$ mm, and an rms bunch length of $\sigma_z = 0.1875$ m. All these numbers are considerably smaller than for the LHC type beam, which explains why the multipacting here occurs for smaller bunch intensity.

In Sect. 2 we mentioned that the motion of electrons in a dipole field can be modelled in different ways. For example, in one approach, we ignore the horizontal and longitudinal motion, in the other we employ a library Runge-Kutta integration. Figure 22 compares the simulated electron build up computed by these two approaches for a 0.26-T field in the KEKB High Energy Ring. The agreement is quite reasonable, even for a field as low as this.

3.2 Multibunch Wake

The electron cloud couples the motion of subsequent bunches. A displaced bunch disturbs the symmetry of the cloud, and the following bunch receives a net deflection. This effect is illustrated in Fig. 23 for an LHC bunch train.

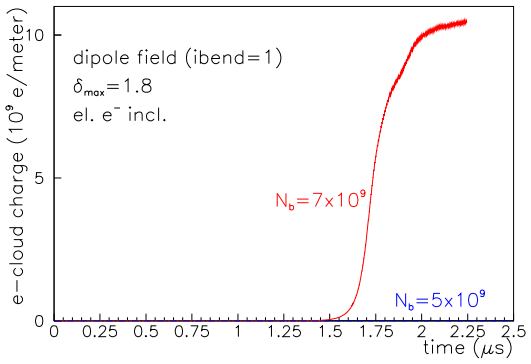

Figure 20: Electron-cloud line density vs. time in a dipole field for the SPS fixed-target beam with 5-ns spacing.

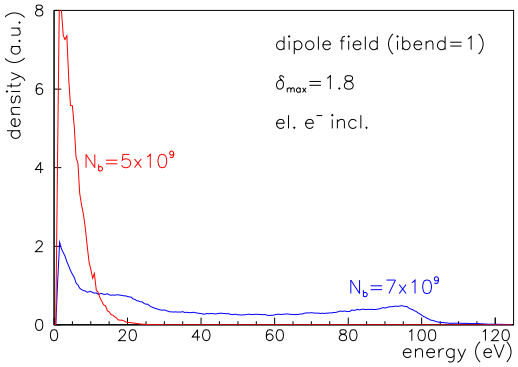

Figure 21: Energy spectrum of electrons hitting the wall in a dipole field for the SPS fixed-target beam with 5-ns spacing, comparing two different bunch intensities.

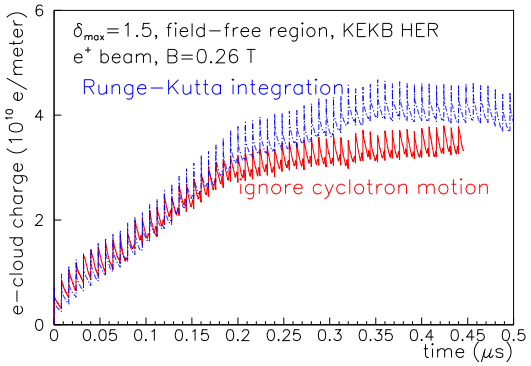

Figure 22: Electron-cloud line density vs. time in a 0.26-T dipole field for an positron beam in the KEKB HER comparing two different models of electron motion.

Thus, similar to a multibunch wake field, the electron cloud couples the motion of subsequent bunches.

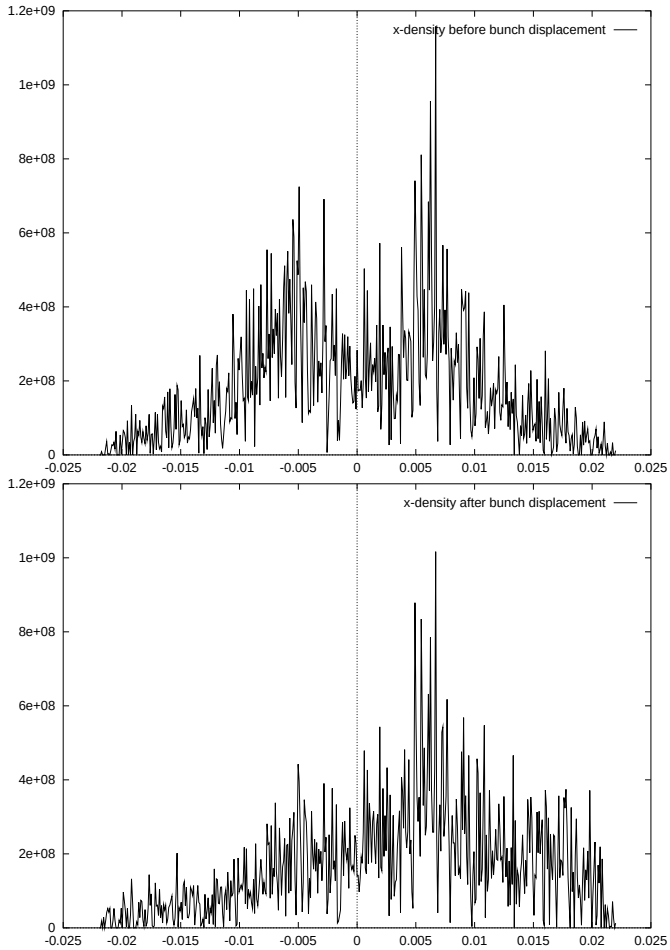

Figure 23: Projected horizontal electron charge density in an LHC bending magnet before the 41st bunch in the train is horizontally displaced by 1 cm (top) and just prior to the arrival of the 42nd buncha (bottom) [4]. The horizontal axis is in units of meters; the vertical coordinate is the charge (in units of e) per bin and per grid point. Other parameters: 500 grid points, $\delta_{\max} = 1.7$, $R = 1$, $Y^* = 1$.

The ECLOUD programme computes the effective wake field as follows. After a stationary cloud is established, one of the bunches is displaced transversely by an amount Δx or Δy. Then, we calculate the kick that the disturbed e^- cloud exerts on the next bunch. This yields an estimate of the bunch-to-bunch dipole wake field $W_1(L_{sep})$ [31, 10, 1]:

$$W_1(L_{sep}) = \sum_i \frac{2y_i Q_i}{N_b r_i^2(\Delta y)} \left(1 - \exp\left(-\frac{r_i^2}{2\sigma^2}\right)\right) \frac{C}{l_b}, \tag{18}$$

where $r_i = (x_i^2 + y_i^2)^{1/2}$ (the radial distance of the ith macro-electron from the beam axis), C is the ring circumference, l_b is the simulated length of bending magnet, and Q_i denotes the charge of the ith macro-electron.

The bunch-to–bunch wake field can give rise to a multi-bunch instability. From the wake field acting between successive bunches, we can estimate the instability growth time. To obtain this growth rate, we assume that the ring is uniformly filled with M bunches and that the wake of the electron cloud decays rapidly and only couples subsequent bunches. Then the complex frequency shift of μth mode is given by [30]

$$\Omega^{(\mu)}_{y\ (x)} - \omega_{\beta,y\ (x)} = \frac{N_b r_p c^2}{2\gamma C \omega_\beta} W_{1,y\ (x)} e^{i2\pi(\mu+Q_y\ (x))/M} \tag{19}$$

and the rise time for the fastest growing mode is

$$\tau \approx \frac{4\pi\gamma Q_y\ (x)}{N_b r_p c W_{1,y\ (x)}} \tag{20}$$

If the ring is not uniformly filled and there are clearing gaps, the growth is not exponential but

$$y_n \sim \frac{1}{n!}(t/\tau)^n\ \hat{y}_0 \tag{21}$$

for the nth bunch in a train. It was pointed out by M. Furman [31] that the parameter τ is exactly the same as the exponential growth time for the uniform fill, which was given above.

Simulated horizontal and vertical multi-bunch instability growth rates for the LHC at 7 TeV are shown in Fig. 24 as a function of the maximum secondary emission yield $\delta_{\max}$. The instability is slow, with rise times longer than 1 second. We expect that it is Landau damped by the natural intra-bunch tune spread.

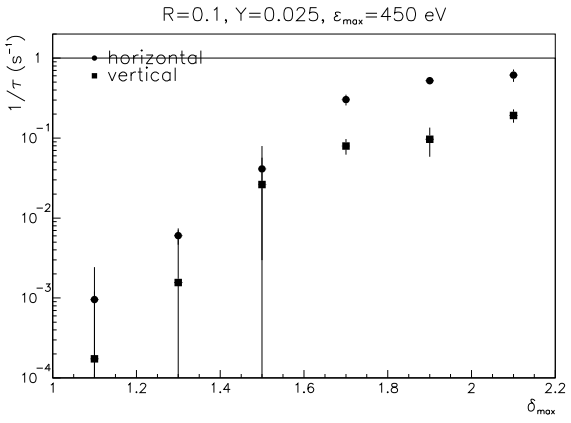

Figure 24: Multibunch instability growth rate as a function of maximum secondary emission yield $\delta_{\max}$ for the LHC at 7 TeV [4]. Other parameters: $\epsilon_{\max} = 450$ eV, $R = 10\%$, and $Y_{pe} = 0.025$.

3.3 *Effect on Beam Diagnostics*

The impact of the electron cloud on the reading of LHC beam-position monitors (BPMs) was studied in Ref. [5]. Figure 25 shows a schematic of a BPM in the LHC arc. The direct synchrotron radiation hits the horizontally outward electrode. Photoelectrons are emitted primarily from this electrode, which results in a net flow of electrons to the other 3 BPM buttons.

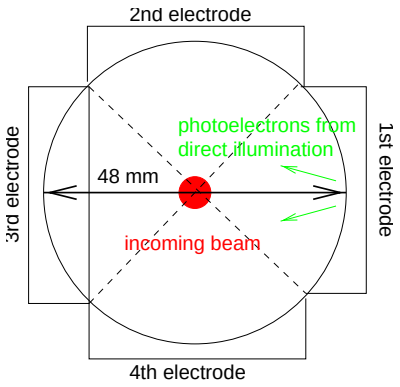

Figure 25: Schematic cross section of a BPM in the LHC arc [5]. Length of the device is 24 mm. Direct synchrotron radiation illuminates the first electrode.

Figure 26 shows a simulation result for the electron current on the four electrodes, experienced during the passage of an LHC batch [5]. It illustrates the continuous loss of electrons from the first to the other three electrodes. At larger values of $\delta_{\max}$ (bottom picture), a random component due to multipacting is added to the average current flow determined by the synchrotron radiation.

Figure 27 illustrates the time and frequency structure of the electron current at one of the electrodes [5]. The electron signals peak during the bunch passages, and the frequency spectrum roughly images the bunch frequency contents.

The response the BPM processing electronics to the simulated input signal was studied independently by R. Jones [32]. He found that the reading error induced by the electron cloud is quite small, of the order of 2 μm [32].

3.4 *Spatial Structure of the Electron Cloud*

In a LHC or SPS dipole magnet, at sufficiently high bunch charges the cloud consists primarily of two vertical strips located on either side of the beam. These stripes are attributed to the maximum in the secondary emission yield curve. Electrons in the strip region aquire a typical energy close to this maximum. In 2001 a dedicated monitor was installed in the SPS which directly demonstrated the existence of the two strips at sufficiently high current [33].

Figure 28 shows the simulated flux of electrons on the chamber wall for SPS parameters. In this simulation the primary electrons (thought to be due to beam loss or gas ionization) were launched at the chamber wall, uniformly distributed as a function of azimuthal energy. For higher bunch charges, two strips exist, located symmetrically about the position of the beam (only the right-hand

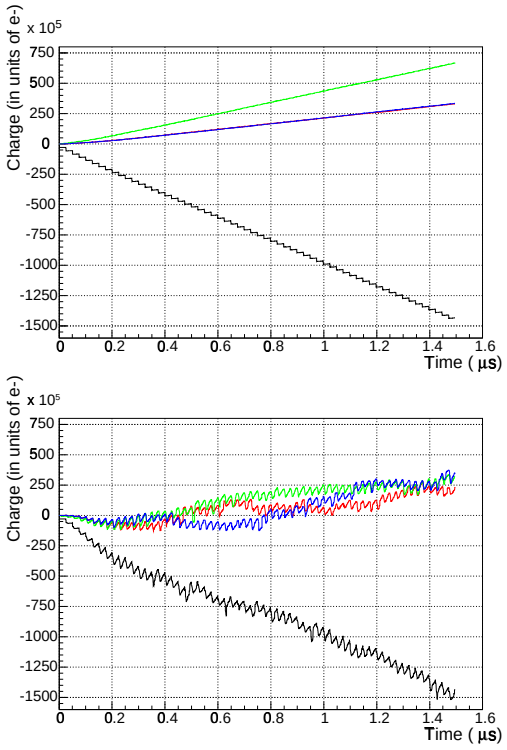

Figure 26: Net charge deposited or emitted at each BPM electrode for $\delta_{\max} = 1.1$ (top) and $\delta_{\max} = 1.9$ (bottom) [5]. Negative values indicate that a net flow of electrons away from the plate.

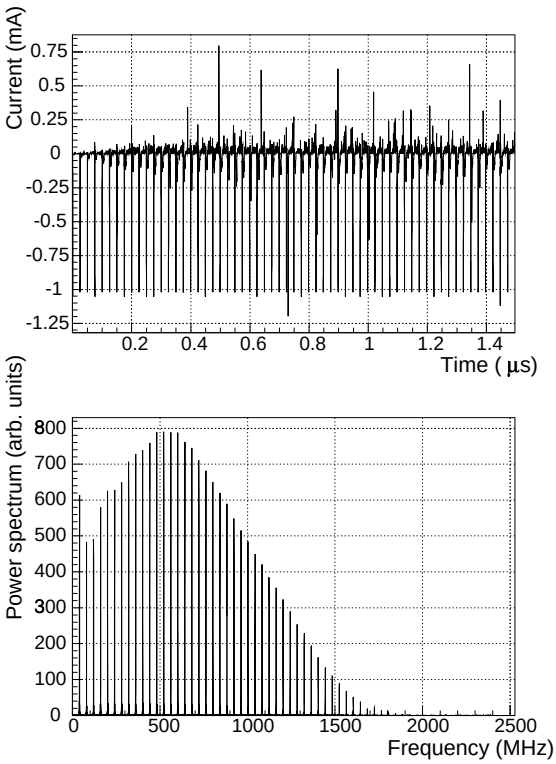

Figure 27: Instantaneous electron current at the first electrode vs. time (top) and its power density spectrum vs. frequency (bottom) for a maximum secondary emission yield $\delta_{\max} = 1.5$ [5]. In the top picture, the large negative spikes which coincide with bunch passages represent the primary photoemission. In the bottom picture, the fall-off of the signal power spectrum occurs near the bunch frequency $f_{\rm bunch} = c/(2\pi\sigma_z) \approx 700$ MHz.

side is shown). At $N_b = 8 \times 10^{10}$ in the simulation there is even evidence for a third strip emerging again at the center of the chamber.

Figure 29 compares simulation results where in the first case the electrons are launched at the wall, and in the second inside the beam volume in order to more accurately model the gas ionization by the beam. The spatial structure is clearly different in the two cases. In particular, the vertical strips cannot build up in the second case, because no primary electrons are present at their horizontal location. This figure also demonstrates the effect of changing the value of $\epsilon_{\max}$, *i.e.*, the incident energy where the secondary emission yield assumes a maximum value. Each curve corresponds to a different $\epsilon_{\max}$. For lower values of $\epsilon_{\max}$ the strips move outwards, and, in addition, the electron flux increases strongly.

Despite of the difference in the spatial structure, the total number of electrons and their build-up time are quite similar for these two cases, as is illustrated in Fig. 30.

Finally, Fig. 31 shows the simulated electron cloud distribution in an LHC quadrupole magnet. The cloud exhibits a fourfold symmetry corresponding to the symmetry of the magnetic field. Strong multipacting and heat load deposition primarily occur along the diagonals at 45°, which pass through the center of the chamber [36]. In the other regions, electrons might become trapped in the magnetic field [37]. This aspect will be addressed in the next section.

3.5 *Electron Trapping in Quadrupoles*

It was first discovered in simulations by L. Wang [37], that after acceleration by the beam electrons can become trapped inside a quadrupole field, like in a magnetic bottle.

Figures 32 and 33 show the simulated build up of electrons during the passage of a 50-bunch train as well as the subsequent decay of the cloud. In the first picture all electric fields are taken into account during the decay; the second picture shows the decay if electrons experience only the magnetic field.

In neither case does the number of electrons shrink to zero, over the time scale considered, raising the possibility that a certain fraction of the electron might remain trapped forever.

In the case without image and space-charge forces, if only the magnetic field is present, the trapping condition

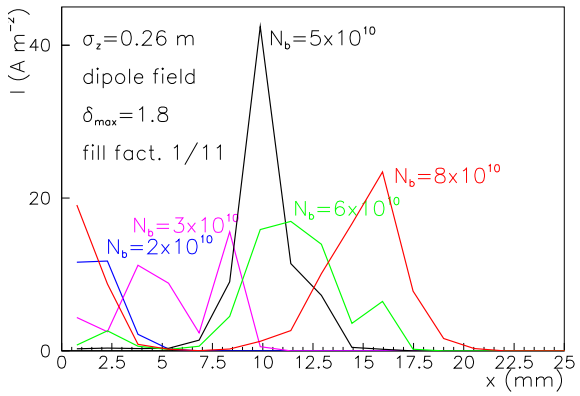

Figure 28: Simulated electron flux on chamber wall in A/m^2 vs. the horizontal position in an SPS dipole, for different values of the bunch population. Simulation parameters: $\sigma_x = 3.5$ mm, $\sigma_y = 1.6$ mm, $\sigma_z = 0.26$ m, $\delta_{\max} = 1.8$, $\epsilon_{\max} = 300$ eV, $d\lambda_e/ds = 2.5 \times 10^{-7}$ m^{-1} per proton, $h_x = 76$ mm, $h_y = 17.5$ mm, $L_{\rm sep} = 7.48$ m, $B = 0.2$ T; elastic electron reflection included.

is given by [34]

$$T \equiv \frac{v_{\rm tot}^2 B_{\rm local}}{v_\perp^2 B_{\rm pipe}} < 1 \ , \qquad (22)$$

where $v_{\rm tot}$ denotes the total velocity of the electron, $f_\perp$ the velocity components transverse to the local magnetic field, $B_{\rm local}$ the local field strength, and $B_{\rm pipe}$ the field at the chamber wall following the magnetic field lines.

Figure 34 displays a histogram of the quantity $\ln(T)$, evaluated for all electrons after the passage of 50 bunches through a KEKB-LER quadrupole. Trapping corresponds to $\log(T) < 0$.

Finally, Fig. 35 depicts the fraction of electrons for which the trapping condition $\log(T) < 0$ is fulfilled as a function of time, for the two cases corresponding to Figs. 32 and 33.

3.6 *Electron Cloud Build Up for Electron Beams*

For an electron beam and for a positron beam the number of photo-electrons is the same. In the case of the electron beam, the primary photoelectrons, if emitted at the time of the bunch passage, are immediately repelled by the beam field. Therefore, the electron cloud build up should be reduced compared with that for a positron beam.

However, even if the photo-electrons are repelled they might be reflected back from the chamber wall with a high probability. In addition, in the case of one or several photon reflections, the photo-electrons may be emitted after the bunch has completely passed by [39]. Then they do not experience the repelling field of the bunch which generated

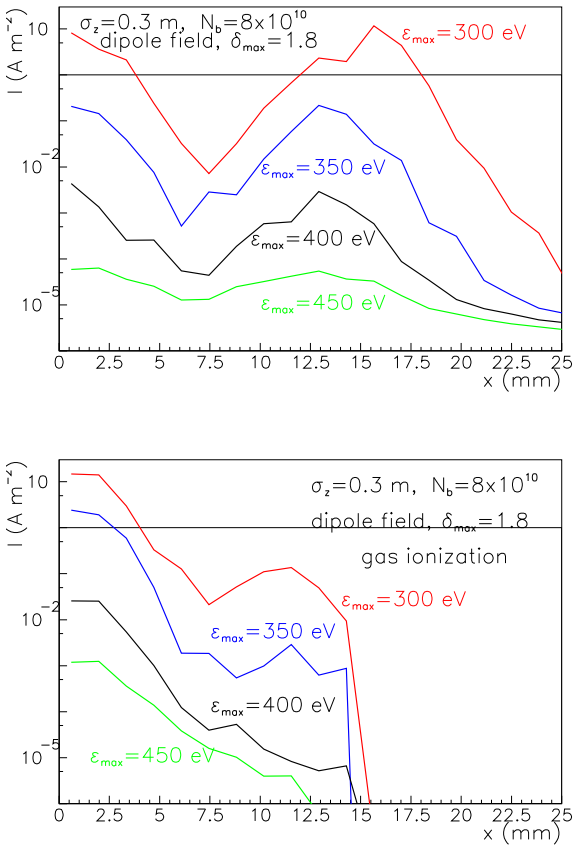

Figure 29: Electron flux on chamber wall in A/m^2 vs. the horizontal position in an SPS dipole for various values of $\epsilon_{\max}$; top: launching primary e$^-$ at the wall; bottom: launching primary e$^-$ inside beam (ionization). Simulation parameters: $\sigma_x = 3.5$ mm, $\sigma_y = 1.6$ mm, $\delta_{\max} = 1.8$, $d\lambda_e/ds = 2.5 \times 10^{-7}$ m^{-1} per proton, $N_b = 8 \times 10^{10}$, $h_x = 76$ mm, $h_y = 17.5$ mm, $L_{\rm sep} = 7.48$ m, $B = 0.2$ T; elastic electron reflection included.

them. This will happen more easily for electron beams than, *e.g.*,for anti-proton beams, since the electron bunch lengths are typically much shorter.

In a recent study for the KEKB HER [35] we simulated a worst-case situation where, for the electron beam, all primary photo-electrons were launched just after the passage of the emitting bunch. Figure 36 compares the simulated build up of the electron cloud for the KEKB HER when operated with positron or electron beams of the same current. The total number of electrons differs by a factor of 4 or 5. Therefore, at high beam current we expect to observe electron-cloud effects also for the electron beams. This might be a possible explanation for a fast horizontal coupled-bunch instability which has been observed in the KEKB HER [38, 35].

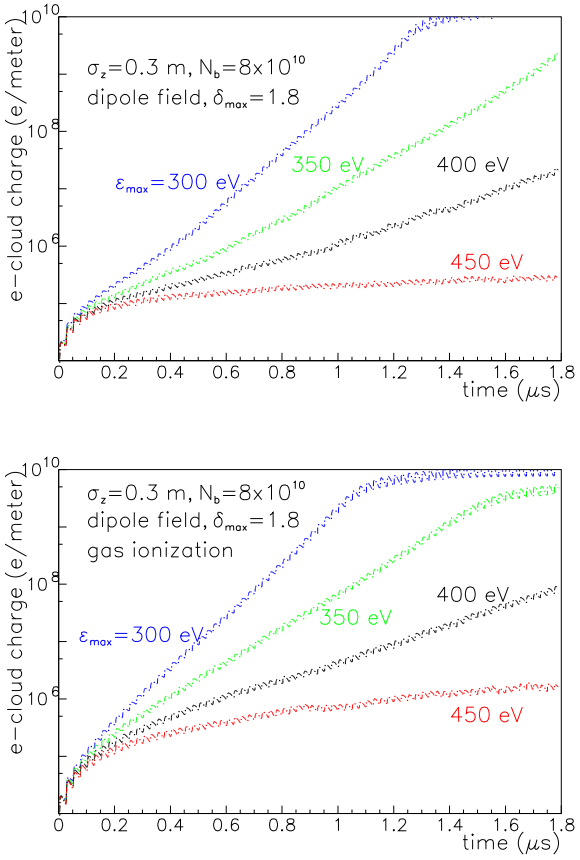

Figure 30: SPS electron line density vs. time for various values of $\epsilon_{\max}$; top: launching primary e^- at the wall; bottom: launching primary e^- inside beam (ionization). Simulation parameters: $\sigma_x = 3.5$ mm, $\sigma_y = 1.6$ mm, $\delta_{\max} = 1.8$, $d\lambda_e/ds = 2.5 \times 10^{-7}$ m^{-1} per proton, $N_b = 8 \times 10^{10}$, $h_x = 76$ mm, $h_y = 17.5$ mm, $L_{\rm sep} = 7.48$ m, $B = 0.2$ T; elastic electron reflection included.

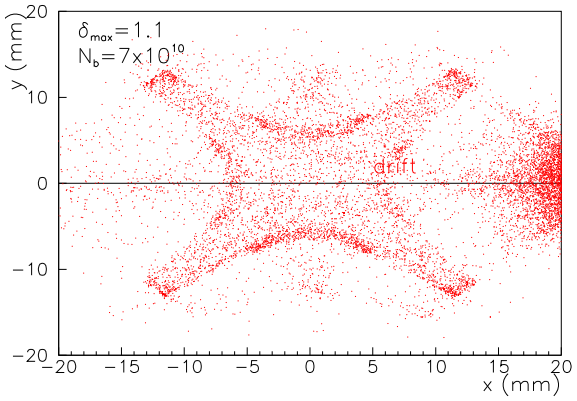

Figure 31: Snapshot of transverse electron distribution in an LHC quadrupole chamber. Parameters: $\delta_{\max} = 1.1$, $N_b = 7 \times 10^{10}$.

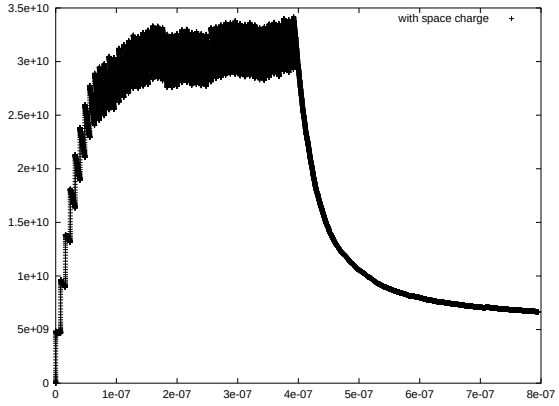

Figure 32: Simulated electron line density vs. time for a quadrupole field in the KEKB LER [35]; this simulation includes electron space-charge and image fields.

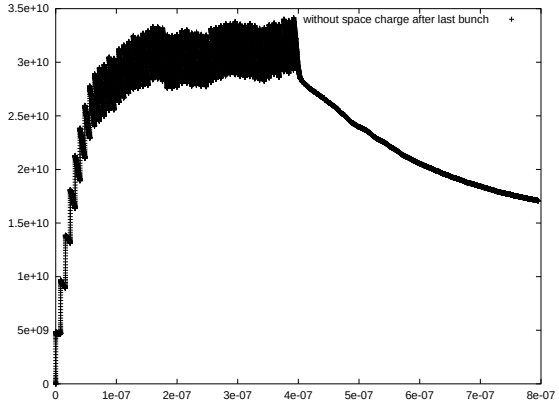

Figure 33: Simulated electron line density vs. time for a quadrupole field in the KEKB LER [35]; in this simulation electron space-charge and image fields are switched off after the passage of the last bunch, from which time onwards the electrons only experience magnetic forces.

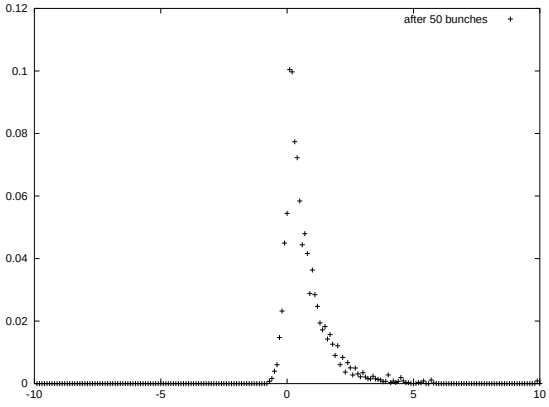

Figure 34: Histogram of simulated electron trapping parameter $\log(T)$ after the passage of 50 bunches for a quadrupole field in the KEKB LER [35].

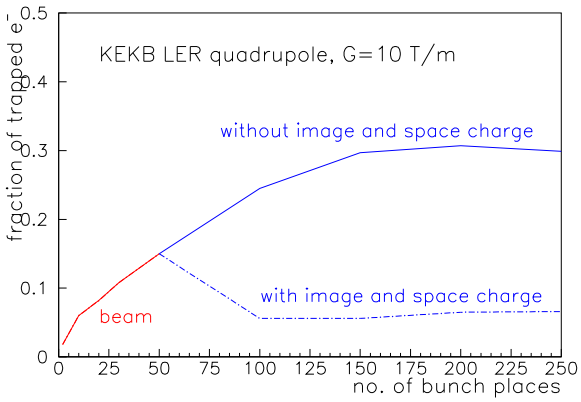

Figure 35: Fraction of electrons for which $\log(T) < 0$ (*i.e.*, for which the trapping condition is fulfilled) as a function of bunch-space number [35]. The beam stops after 50 bunches.

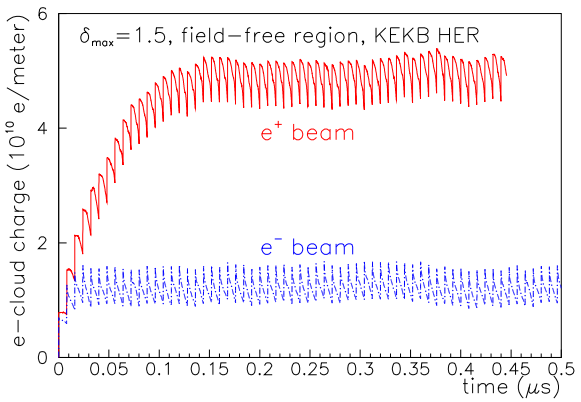

Figure 36: Electron-cloud line density vs. time in a 0.26-T dipole field for the KEKB HER comparing electron beam and positron beams [35].

4 CONCLUSIONS

Simulations of electron-cloud build up and heat load (for LHC) are sensitive to the parametrization of secondary emission and photoemission. Important are also the beam and electron image charges, the electron space charge, and magnetic fields, even if they are only a few Gauss.

The simulated electron-cloud build up is in good agreement with observations for the CERN SPS, the CERN PS [40], and the KEKB LER.

The largest remaining discrepancy between SPS measurements and simulations pertains to the exact position of the vertical stripes in an SPS dipole. The present difference is about a factor of two for a bunch population of $N_b \approx 8 \times 10^{10}$, the simulation predicting a larger distance between the strips and the beam axis. It is conceivable that this discrepancy can be resolved by a different parametrization of the secondary emission yield [41].

Simulations with the code ECLOUD confirm that a certain fraction of electrons, between 5% and 30%, may be trapped inside a quadrupole field. This corroborates previous simulation results by L. Wang [37], though the exact fraction of trapped electrons might still be different.

Finally, our simulations suggest that a significant electron cloud can also build up for an electron beam. This was illustrated with an example for the KEKB HER.

5 ACKNOWLEDGEMENTS

We would like to thank G. Arduini, V. Baglin, O. Brüning, R. Cappi, F. Caspers, A. Chao, I. Collins, K. Cornelis, H. Fukuma, M. Furman, M. Giovannozzi, O. Gröbner, K. Harkay, S. Heifets, N. Hilleret, M. Jimenez, T. Katsouleas, E. Metral, K. Ohmi, K. Oide, E. Perevedentsev, M. Pivi, A. Rossi, F. Ruggiero, L. Wang, and many others, for helpful informations and discussions.

6 REFERENCES

[1] F. Zimmermann, “A simulation study of electron-cloud instability and beam-induced multipacting in the LHC”, LHC Project-Report 95, and SLAC-PUB-7425 (1997).

[2] O. S. Brüning, “Simulations for the beam-induced electron cloud in the LHC beam screen with magnetic field and image charges,” CERN LHC PR 158 and EPAC98 (1997).

[3] F. Ruggiero and X. Zhang, “Collective Instabilities in the LHC: Electron Cloud and Satellite Bunches,” in Proc. Workshop on Instabilities of High Intensity Hadron Beams in Rings, BNL, 28 June-1st July 1999, AIP Conf. Proceedings 496, pp. 40-48 (1999).

[4] F. Zimmermann, “Electron-Cloud Simulations for SPS and LHC”, Chamonix X, CERN-SL-2000-007 (2000).

[5] G. Rumolo et al., “Simulation of the Electron-Cloud Build Up and Its Consequences on Heat Load, Beam Stability and Diagnostics,” PRST-AB 012801 (2001).

[6] G. Rumolo, F. Zimmermann, “Electron-Cloud Simulations,” Proc. Int. Workshop on Two-Stream Instabilities, KEK, Tsukuba, September 2001 (2001); in CERN SL-2001-067 (AP).

[7] G. Rumolo and F. Zimmermann, “Practical User Guide for ECloud,” CERN SL-Note-2002-016 (AP) (2002).

[8] G. Rumolo, F. Zimmermann, programme documentation at *http://wwwslap.cern.ch/collective/electron-cloud/electron-cloud.html*

[9] M.A. Furman, G.R. Lambertson, “The Electron Cloud Instability in PEP-II: An Update,” IEEE PAC 97, Vancouver (1997).

[10] M.A. Furman and G.R. Lambertson, “The Electron Cloud Effect in the arcs of the PEP-II Positron Ring,” KEK Proceedings 97-17, p. 170, December 1997 (Proc. MBI97 workshop, KEK, Y.H. Chin, ed.) (1997).

[11] F. Zimmermann, “The Electron Cloud Instability: Summary of Measurements and Understanding,” Proc. PAC’2001 Chicago, USA, CERN-SL-2001-035 (AP) (2001).

[12] F. Zimmermann, “Electron-Cloud Effects in the LHC,” presented at ECLOUD’02, Geneva April 2002 (2002).

[13] I. Collins, private communcation (2000).

[14] E. Perevedentsev, “Periodic Solenoid Field”, unpublished note, KEK, November 2000.

[15] F. Zimmermann, H. Fukuma, and K. Ohmi, “More Electron Cloud Studies for KEKB: Long-Term Evolution, Solenoid Patterns, and Fast Blow Up,” CERN-SL-Note-2000-061 AP (2000).

[16] M. Bassetti and G. A. Erskine, “Closed Expression For The Electrical Field Of A Two-Dimensional Gaussian Charge,” CERN-ISR-TH/80-06 (1980).

[17] M. Furman, “Comments on the Electron-Cloud Effect in the LHC Dipole Bending Magnets”, KEK Proceedings 97-17, p. 234, December 1997 (Proc. MBI97 workshop, KEK, Y.H. Chin, ed.) (1997).

[18] J.S. Berg, “Energy Gain in an Electron Cloud during the Passage of a Bunch”, LHC Project Note 97 (1997).

[19] V. Baglin, I. Collins, B. Henrist, N. Hilleret, G. Vorlaufer, “A Summary of the Main Experimental Results Concerning the Secondary Electron Emission of Copper,” LHC-Project-Report-472 (2001).

[20] F. Zimmermann, “Electron-Cloud Simulations: An Update”, Chamonix XI, CERN-SL-2001-003-DI (2001).

[21] H. Seiler, “Secondary electron emission in the scanning electron microscope”, J. Appl. Phys. 54 (11) (1983).

[22] R. Kirby, et al., “Secondary Electron Emission from Accelerator Materials,” Proc. 8th ICFA Beam Dynamics Mini-Workshop on Two-Stream Instabilities, Santa Fe (2000); R. Kirby and F. King, “Secondary Electron Emission Yields from PEP-II Accelerator Materials”, SLAC-PUB-8212 (2000).

[23] O. Grobner amd N. Hilleret, private communcations at ECLOUD’02 (2002).

[24] N. Hilleret, “An empirical fit to the true secondary electron energy distribution,” unpublished draft, dated 23.10.01 (2001).

[25] J.J. Scholtz, D. Dijkkamp, R.W.A. Schmitz, Philips J. Res. 50, 375–389 (1996).

[26] A. Chao, K. Oide, comments at the International Workshop on Two-Stream Instabilities, KEK, September 2001 (2001).

[27] A. Arauzo and F. Zimmermann, “Electron-Cloud Energy and Angular Distributions,” CERN-SL-Note-2000-057 AP (2000).

[28] J. Buon, F. Couchot, J. Jeanjean, F. Le Diberder, V. Lepeltier, H. Nguyen Ngoc, J. Perez-y-Jorba, P. Chen, “A Beam Size Monitor for the Final Focus Test Beam,” NIM A 306, p. 93 (1991).

[29] G. Arduini, private communication (2001).

[30] A.W. Chao, “Physics of Collective Beam Instabilities in High Energy Accelerators”, Wiley (1993).

[31] M. Furman and G. Lambertson, “The Electron-Cloud Effect in the LER: A Status Report,” and subsequent discussion during the PEP-II MAC meeting, SLAC, 7 January 1997 (1997).

[32] R. Jones, private communication (2000).

[33] M. Jimenez et al., these proceedings.

[34] private discussion with K. Ohmi, L.Wang, and K. Oide (2002).

[35] F. Zimmermann, “Accelerator Physics Studies for KEKB: Electron Trapping, Electron Cloud in the HER, Closed-Orbit Drift, Horizontal Instability and Tune Shift,” CERN SL-Note-2002-017 (AP) (2002).

[36] F. Zimmermann, H. Fukuma, and K. Ohmi, “More Electron-Cloud Studies for KEKB: Long-Term Evolution, Solenoid Patterns, and Fast Blow Up,” CERN SL-Note-2000-061 AP (2000).

[37] L. Wang, Proc. Int. Workshop on Two-Stream Instabilities, KEK, Tsukuba, September 2001 (2001).

[38] S.S. Win, H. Fukuma, E. Kikutani, M. Tobiyama, “Observation of Transverse Coupled Bunch Instability at KEKB,” APAC01 (2001).

[39] J. Galayda, private communcation, visit at APS, February 1997 (1997).

[40] R. Cappi et al., these proceedings.

[41] O. Grobner commented during the workshop that the parametrization employed may not be representative.

3D SIMULATION OF PHOTOELECTRON CLOUD IN KEKB LER

L. F. Wang*, H. Fukuma, K. Ohmi, S. Kurokawa, K. Oide and F. Zimmermann+
High Energy Accelerator Research Organization (KEK), Tsukuba, Ibaraki 305-0801, Japan
+CERN, Geneva, Switzerland

Abstract

A 3-dimension particle in cell simulation code is developed to study the photoelectron cloud instabilities in KEK LER. The program has been decribed in detail. Numerical examples are shown for the photoelectron motion in various kinds of magnetic fields. Simulation shows solenoid is very effective to confine the photoelectron to the vicinity of the vacuum chamber wall and make a photoelectron free region at the vacuum pipe center. The more uniform the solenoid field, the more effective the field. Multipacting can occur in drift region and dipole magnet. Special trapping occurs in quadrupole and sextupole magnets.

1 INTRODUCTION

A blow-up of the vertical beam size is observed in the KEKB positron ring (LER)[1] and it is one of the serious problems limiting the luminosity of KEKB. F. Zimmerman and K. Ohmi [2-3] explained the blow-up as a single-bunch instability of a positron bunch due to electron cloud generated by photoemission and secondary emission. The blow-up depends on the electron cloud density near the beam. Solenoid has been installed in the LER ring in order to clear the photoelectron near the beam. It was effective on reducing vertical blow-up [4]. A 3D PIC simulation code is developed to study the effects of these various magnetic field on the photoelectron formation, distribution, space charge effect, and so on. The program and some numerical examples are described in detail.

2 COMPUTER PROGRAM

The positron bunch is longitudinally divided into a number of slices according to Gaussian distribution. Such slices interact with photoelectrons transversely and oscillate according to the transfer matrix of the linear optics. Acceleration of RF cavity and synchrotron radiation are also included in longitudinal phase space.

Photoelectrons are emitted when positron slices pass through a beam pipe with length L, which is usually chosen as 1 or 2 m. A photoelectron yield of 0.1 is assumed in simulation and 30% of the photoelectrons are produced by the reflective photons. The center of photoelectron energy distribution is 5 eV with rms (root mean square) energy spread of 5 eV. In our simulation, the photoelectrons are represented by macro-particles, which move in 3-dimensional space under the force:

$$\mathbf{F}_e = \mathbf{F}_p + \mathbf{F}_{space} + \mathbf{F}_B \qquad (1)$$

where $\mathbf{F_p}$ is the force by positron beam which is given by the Bassetti Formula and $\mathbf{F_{space}}$ is the space charge force of the photoelectron. $\mathbf{F_B}$ is the force by magnetic field on the photoelectron. The result for without space charge force case has been shown in Ref. [5]. A 3D PIC space charge solver has been developed to study the space-charge force. The secondary emission is also included in the program. The simulation model is shown in figure 1.

The parameters used in the simulation are shown in table 1.

Variable	Symbol	Value
Ring circumference	C	3016.26 m
RF bucket length	s_{rf}	0.589 m
Bunch spacing	s_b	4 RF buckets
Bunch population	N	3.3×10^{10}
Average vertical betatron function	β_y	10 m
Average horizontal betatron function	β_x	10 m
Horizontal emittance	ε_x	1.8×10^{-8} m
Vertical emittance	ε_y	3.6×10^{-10} m
Betatron tune	ν_x/ν_y	45.52/44.09
Rms bunch length	σ_l	4 mm
Chamber diameter	$2R$	100 mm

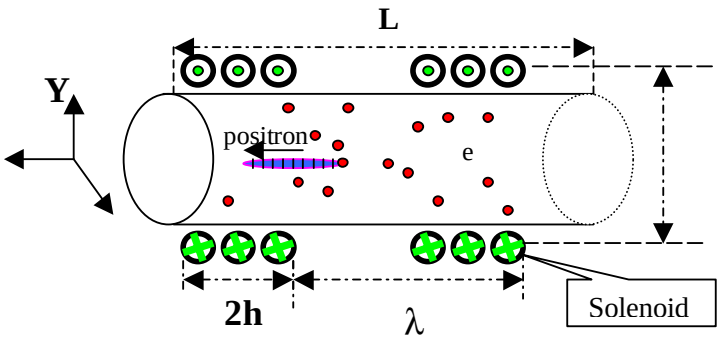

Figure 1. The scheme of the simulation model

2.1 3D PIC Space Charge Solver

The direct particle-particle method is easy for developing the program and has high accuracy.

*On leave from IHEP, Beijing

However, it has a very low efficiency. The mesh method seems to be applied by all particle simulation programs.

The vacuum chamber of LER is round shape with a radius of 50 mm. Photoelectrons are distributed within the chamber as shown in Figure 2 for solenoid case. The regular mesh as applied in the study of bunch beam case can't satisfy here because the complex shape of the vacuum chamber. Therefore, an irregular mesh is applied for the photoelectron cloud as shown in Figure 3. Similar mesh can be applied for the ante-chamber as in PEP-II.

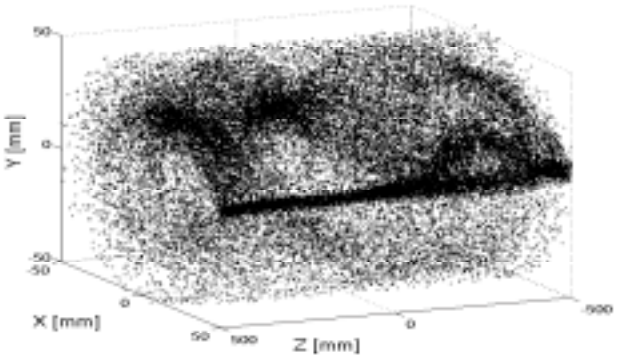

Figure 2: Example of photoelectron cloud distribution in the vacuum chamber

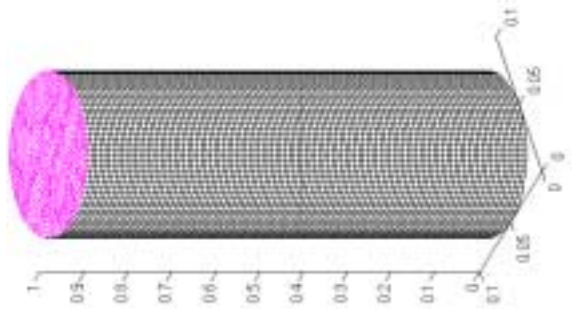

Figure 3: Mesh example of the vacuum chamber for photoelectron cloud

There are many charge assignment methods. The mesh in our method is an irregular mesh with brick elements. The charge Q_0 of a photoelectron is assigned to each node *i* of the element in which the photoelectron stays according to the shape function N_i

$$Q_i = N_i Q_0 . \tag{2}$$

Figure 4 shows the distribution of the macro-particle and charge at mesh node in one transverse section. The number of elements in this transverse section is 276, which is a small number. It already shows good representing of the real electron cloud distribution.

For the isoparametric element, the charge assignment scheme in Eq.(2) has all characters of charge assignment function such as

$$\sum_i N_i = 1 \tag{3}$$

$$\sum_i N_i \mathbf{r}_i = \mathbf{r} \tag{4}$$

The property of the shape function in Eq.(3) keeps the charge conservation. It can be called Cloud-in-a-Cell (CIC) scheme. But it is different from the so-called CIC scheme applied in general particle simulation:

(1) The general CIC method applies a regular mesh. However, our scheme uses an irregular mesh, which makes this method can be successfully applied to the complex boundary problem such as the very flat beam case and ante-chamber.

(2) General CIC is for 2D, the charge assignment function has a clear meaning such as the cloud area. There is exact the same assignment function in finite element field for the simple element, such as square element. However, Our scheme is for 3D and the assignment has not a clear physical meaning for a high order element. And, there are many kinds of elements in the finite element methods. Among them, the high order element can be applied to improve the accuracy of the method, which is much better than the nearest-grid-point assignment.

Therefore, our scheme has very serious advantages: general boundary and high accuracy. Adaptive mesh can be applied in the case of the electron concentrating at some small region, such as the long-range beam-beam simulation. However, our method is complicated to be applied comparing with the regular mesh CIC method.

The electron cloud (both the density and distribution) changes with time. We assume a quasi-static condition. The scalar potential satisfies (at each moment)

$$\Delta\phi = -\rho / \varepsilon_0 , \tag{5}$$

Eq.(5) can be solved by using the finite element method. We can get the finite element equation

$$\mathbf{A}\phi = \mathbf{B} . \tag{6}$$

Here the stiffness matrix **A** depends only on the mesh and **B** is the source term. The matrix **A** is extremely sparse and there are well-known methods for handing such linear problems, such as conjugate gradient method, profile or frontal technique. Fortunately, the vacuum chamber of LER is round shape. We can also find the Green function to get the potential. The potential ϕ at **R** is available with the Green function $G(\mathbf{R}, \mathbf{R'})$

$$\phi(\mathbf{R}) = \int_0^L dz' \int_0^{2\pi} d\theta' \int_0^a r' dr' f(\mathbf{R}') G(\mathbf{R}, \mathbf{R}') \tag{7}$$

$$G(\mathbf{R}, \mathbf{R}') = \frac{e}{L} \ln \frac{\rho^2 + r^2 r'^2 / \rho^2 - 2rr' \cos(\theta - \theta')}{r^2 + r'^2 - 2rr' \cos(\theta - \theta')}$$
$$+ \frac{4e}{L} \sum_{n=1}^{\infty} \cos nk(z - z') \left\{ K_0(nk\sqrt{r^2 + r'^2 - 2rr' \cos(\theta - \theta')}) \right.$$
$$\left. - \sum_{m=0}^{\infty} (2 - \delta_{m0}) \frac{K_m(nk\rho)}{I_m(nk\rho)} I_m(nkr) I_m(nkr') \cos m(\theta - \theta') \right\} \tag{8}$$

where L is the period length of the vacuum chamber, ρ is the pipe radius, **R'** is the source position, and **R** is the potential position, $k=2\pi/L$. The cylindrical coordinates with z-axis along the axis of the pipe, **R**=(r,θ, z), **R'**=(r',θ', z') are used.

After finding the potential, the force on each particle is interpolated by using the same shape function in order to keep the momentum conservation. Unlike the general PIC method, we calculate the force on particle directly using the potential at mesh node instead of the mesh-defined force field

$$\mathbf{E} = \sum_i \nabla N_i \cdot \phi_i \qquad (9)$$

The potential and field of the space charge at one transverse section are shown in Figure 5 for the case as Figure 4.

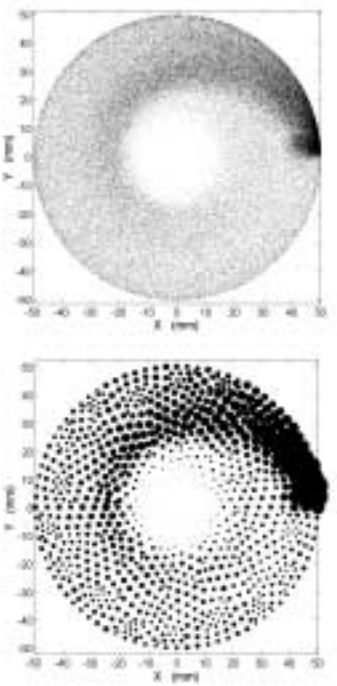

Figure 4 Charge assignment of the PIC method, Above: Transverse distribution of the macro particles in solenoid. Bottom: Transverse distribution of the mesh-defined charge by charge assignment.

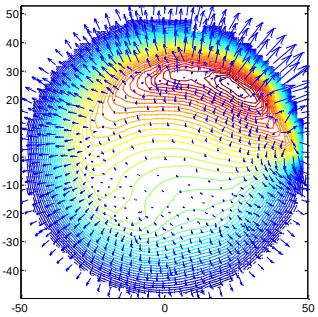

FIGURE 5 Potential and field of space charge at one transverse section

2.2 Magnetic field and beam force

Various magnetic fields can be applied and included in the program. For example, C-Yoke magnet field, solenoid, dipole magnet, quadrupole magnet and sextupole magnet. The general 3-dimensional magnetic field can be input as either formulae or tables. The following paragraphs show a few of types of the magnetic fields in KEKB.

The C-Yoke magnet can be arranged in a dipole or quadrupole configuration with equal polarity (EP) or alternating polarity (AP). For the C-yoke dipole, the field can be approximately expressed as

$$B_x = 0 \qquad (10)$$

$$B_y = a + b\cos(kz) \qquad (11)$$

$$B_z = -bk\sin(kz) \qquad (12)$$

where a=141G, b=94G, λ=0.1m and a=0, b=235G, λ= 0.2 m for the case of adjacent dipoles with equal polarity and alternating polarity, respectively. The magnet field in a C-yoke quadrupole is

$$B_x = (a + b\cos kz)y \qquad (13)$$

$$B_y = (a + b\cos kz)x \qquad (14)$$

$$B_z = -bk\sin(kz)xy \qquad (15)$$

where a=0.3T/m, b=0.2T/m, λ=0.1m and a=0, b=0.5T/m, λ=0.2m for the equal polarity and alternating polarity, respectively.

When the periodic solenoids are arranged with the same current direction in the coil, we call this kind of arrangement equal polarity configuration. In this case, the magnetic field can be approximately expressed as

$$B_z(x,y,z) = B_{z0} + B_0\sin kz, \qquad (16)$$

$$B_x(x,y,z) = -0.5B_0 kx\cos kz, \qquad (17)$$

$$B_y(x,y,z) = -0.5B_0 ky\cos kz. \qquad (18)$$

When the solenoids current takes alternating direction, which is called alternating polarity configuration, the longitudinal filed is expressed as

$$B_z(x,y,z) = B_0\sin kz \qquad (19)$$

The transverse field components are the same as equal polarity case.

Most of bending magnets in LER are normal bending magnets with B=0.848T. Typical quadrupole and sextupole field gradient are 10.3 T/m and 350 T/m^2 KEKB LER, respectively.

The positron bunch is assumed rigid gaussian distribution. The kick on photoelectrons is given by the Bassetti formula

$$\Delta\upsilon_y + i\Delta\upsilon_x = Nr_e c\cdot\sqrt{\frac{2\pi}{\sigma_{x,y}(\sigma_x+\sigma_y)}}\,f(x,y),$$

$$f(x,y) = w\left(\frac{x+iy}{\sqrt{2(\sigma_x^2-\sigma_y^2)}}\right) -$$

$$\exp(-\frac{x^2}{2\sigma_x^2}-\frac{y^2}{2\sigma_y^2})w\left(\frac{x\sigma_y/\sigma_x+iy\sigma_x/\sigma_y}{\sqrt{2(\sigma_x^2-\sigma_y^2)}}\right) \quad (20).$$

where σ_x and σ_y are the positron bunch transverse size.

The image current effect is also included in the program. The shape of the vacuum chamber in KEKB LER is round. Therefore, the image current is easily found. In case of the arbitrary chamber shape, PIC method can be applied for the space charge force of the positron bunch.

3 SIMULATION EXAMPLES

The build up and the distribution of electron cloud (e-cloud) in a few of typical magnetic fields are discussed in this section.

3.1 Effect of C-Yoke magnet and solenoid field on the confinement of the photoelectrons

Permanent C-yoke magnets were attached to vacuum ducts to sweep out the electrons from November 1999 to July 2000. The photoelectron cloud density near the beam is non-zero for all C-yoke magnet configuration as shown in figure 6 for equal polarity quadrupole configuration. However, it is zero for equal polarity solenoid with B_{z0}=30 Gauss, B_0=20 Gauss and $\lambda=2\pi/k$=1 m as shown in figure 4. Simulation studies show that uniform longitudinal solenoid field is better. Details about the solenoid effect on the photoelectron cloud can be found from reference [6]. The conclusion is that solenoid is better than C-yoke magnet. The solenoid effect also has been studied in reference [7]. The photoelectron cloud density near the beam is non-zero in reference [7], which is different from our result.

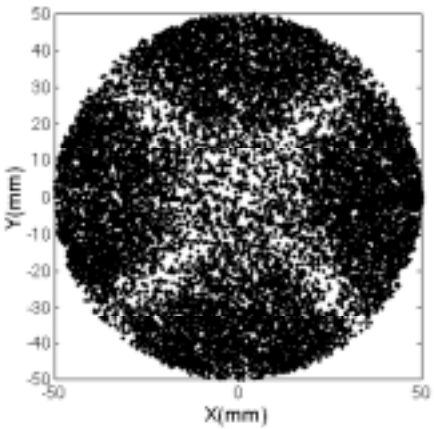

Figure 6 Electron cloud distribution in C-Yoke quadrupole with equal polarity configuration

Figure 7 shows the photoelectron distribution on the chamber wall in the solenoid field case. The photoelectrons hit the chamber wall and lost or produce secondary electrons. The solenoid field is non-uniform in longitudinal direction, which causes the lost cloud distribution also longitudinal position dependent. The azimuth angle distribution of the lost photoelectron depends on the current direction in the solenoid coil because different longitudinal magnetic field direction will cause different deflexion direction of the photoelectron motion. As a result, the current of photoelectron monitor depends on both the longitudinal position of the monitor and the current direction in solenoid coil.

The photoelectrons in solenoid field couldn't receive more energy from the positron bunch because they are confined far from the chamber center by solenoid magnetic field. Therefore, there is no multi-pacting in solenoid case. The heat-load on the chamber wall due to the hitting of the photoelectrons is also smaller for the same reason. It can be concluded that solenoid works very well with zero photoelectron density at chamber center and lower heat-load on the chamber wall because there is no multi-pacting in this case.

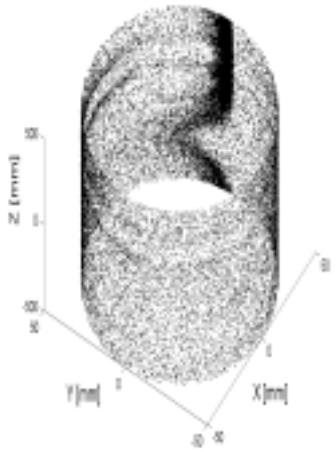

Figure 7 Lost Cloud Distribution around the chamber wall in solenoid case.

3.2 Multi-pacting in drift region and dipole magnet

In drift region, the photoelectrons are focused by the force of the positron bunches and then there is a very larger photoelectron density at chamber center. The photoelectrons near the chamber center cloud receive more energy from the positron bunches. Such higher energy photoelectrons then cause multi-pacing when they hit the chamber wall. The photoelectron density at the chamber center is $10^{13}m^{-3}$, which is 10 times larger than the saturation level. The transverse distribution of the photoelectron cloud in drift region is shown in figure 8. Heat-load is also a serious problem in drift region because photoelectron can receive more energy from positron bunches and the amount of lost photoelectrons on the wall is large. Drift region is the most dangerous case on both beam dynamics and heat-load.

Figure 9 shows the photoelectron cloud distribution inside dipole magnet. Two multi-pacting regions are clear shown in the figure. The central region is non-

multipacting region because the photoelectrons moves along the vertical field lines with the horizontal coordinate around zero cloud receive more energy. The energy of the photoelectrons decreases from horizontal center to both sides. On the other word, the energy of the photoelectrons decreases with the horizontal coordinate |x| as the shown in figure 10. As we known, the true secondary emission yield is smaller than one for photoelectrons with both very large and small energy. As a result, multi-pacting happens in the two regions near the chamber center. The position of the multi-pacting region depends on the energy of the photoelectrons, which is decided by the interaction of photoelectrons and positron bunches. Therefore, the filling patter of the beam, such as bunch current and bunch spacing, can change the multi-pacting area. In general, when the bunch current increase, the multi-pacting region will move to the area with larger |x| and the width of multi-pacting region also will increase at the same time. The exact results depend on the interaction between the photoelectron cloud and positron bunches. The mechanism of the multi-pacting in dipole magnet is clearly shown in figure 10.

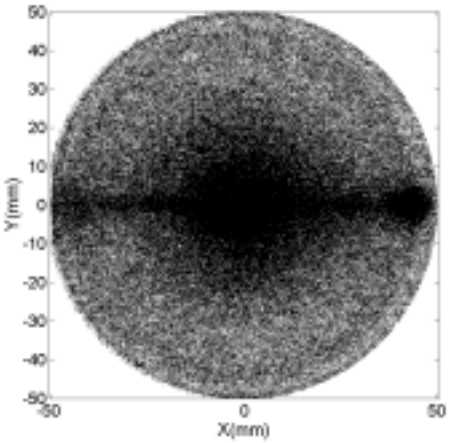

Figure 8 Electron cloud distribution in drift region

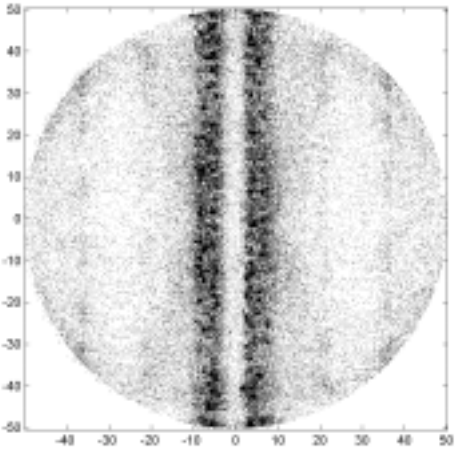

Figure 9 Electron cloud distribution in dipole magnet

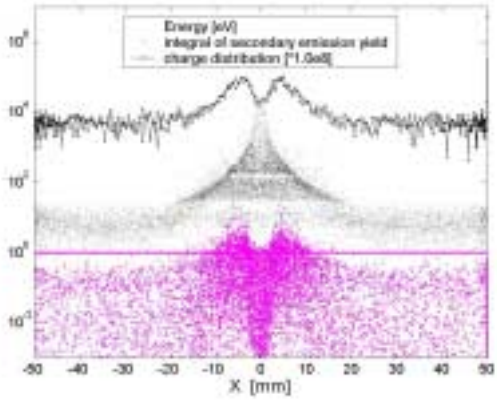

Figure 10 Mechanism of the multi-pacting in dipole magnet. Black dot is the energy of photoelectrons which hit the chamber wall. Pink dot shows the multiply of secondary emission yield of the photoelectrons which hit the wall. The black solid shows the lost photoelectron charge distribution.

3.3 Photoelectron Trapping in quadrupole and sextupole magnets

It is very interesting that more than 90% of the photoelectrons can be seriously trapped by quadrupole and sextupole magnetic field during the bunch train separation as shown in figure 11. The photoelectron density is almost constant during the train gap in these two fields. However, the density decays quickly in dipole magnet. Figure 12 shows one typical trapped electron orbit in normal quadrupole field during the train gap. The drift time is about 960ns. The trapped electron spirals in an ever-tighter orbit along the magnetic field line when the field becomes stronger, converting more and more translational energy into energy of rotation until its velocity along the field line vanish. Then the electron turns around, still spiraling in the same sense, and move back along the field line. Figure 13 shows the electron-trapping phenomena in normal sextupole. The electron-trapping phenomena are very similar with the plasma trapping in the mirror magnetic field.

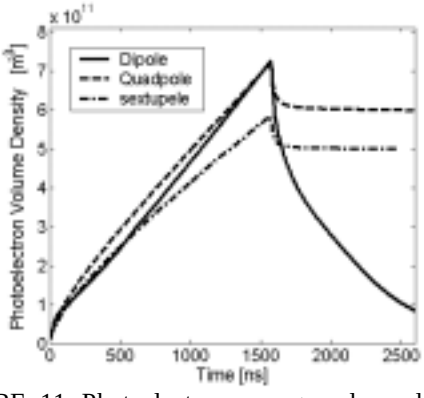

FIGURE. 11 Photoelectron average volume density in different magnet fields as a function of time for a train

with 200 bunches spaced by 7.86 ns and followed by a long gap.

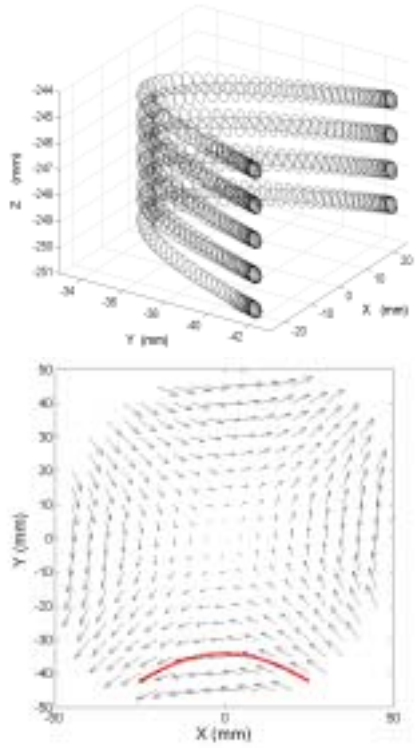

Figure 12 Photoelectron Trapping in Quadrupole Magnetic Field During the Train Gap. Above: 3D orbit; Bottom: 2D orbit (red line) and quadrupole field (black arrow)

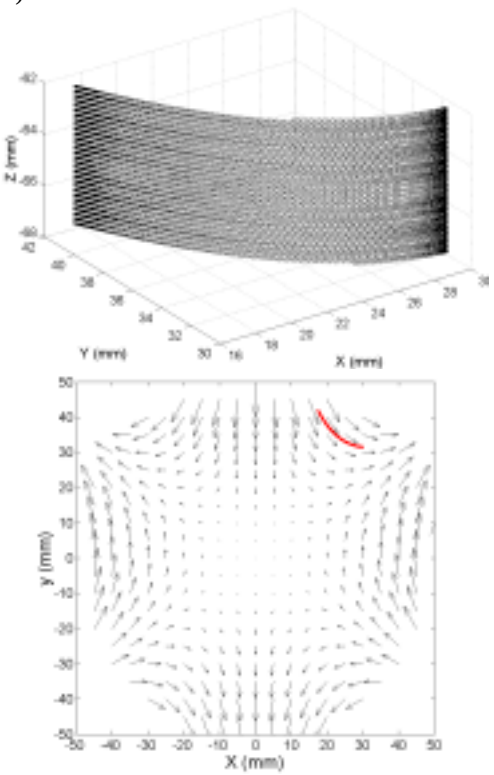

Figure 13 Photoelectron Trapping in Normal Sextupole Magnetic Field During the Train Gap. Above: 3D orbit; Bottom: 2D orbit (red line) and sextupole field (black arrow).

We first describe the motion of photoelectron in pure magnetic field and then focus on the effects of positron beam.

First we consider the case of no electric field, which is almost true for electron cloud during the bunch train-separation where the space charge potential of the electron cloud is neglectable comparing with the magnetic potential in normal magnets. Since the direction of magnetic force acting on the electron is perpendicular to the electron velocity, the electron kinetic energy is therefore conserved,

$$W = \frac{m\upsilon^2}{2} = cons\tan t \tag{21}$$

The motion of the electron in magnetic field can be regarded as the superposition of the gyration motion around the guiding center and the motion of the guiding center. The gyration motion of electron is a rapid rotation around the magnetic field line. The motion of the guiding center is the average motion over the gyration.

Consider the case in which the magnetic field slowly varies in space. The variation is assumed to be sufficiently slow that the magnetic field at the electron position hardly changes during the cyclotron motion. This is true for our case where the magnetic filed is strong except for the central region of the chamber and the electron energy is low, which means small Larmor radius and short period. While the period of a spiraling electron changes as it moves into regions where the magnetic field is weaker or stronger, the product $T \times E$, the period T times the energy E, is almost a constant. It is not an exact constant, but if the rate of change is slow enough, e.g. if the field changes rather slowly, it comes very close. A certain quality, an "adiabatic invariant", is almost kept at a constant value. In more general way, the action of a system with canonical variables *q* and *p*, defined by

$$J = \oint pdq \tag{22}$$

is a constant under a slow change in an external parameter. Here " represents an integral over one period of the motion. Therefore, for such a quasi-periodic motion, there exists two adiabatic invariation given by [8]

$$J_\perp = \oint m\upsilon_\perp \rho_s d\varphi = \frac{4\pi m}{e}\mu_m, \tag{23}$$

$$J_\parallel = \oint m\upsilon_\parallel dl, \tag{24}$$

where

$$\mu_m = \frac{m\upsilon_\perp^2}{2B} \tag{25}$$

is the magnetic moment, $\upsilon_\perp$ is the gyration velocity, $\rho_s = \frac{m\upsilon_\perp}{|e|B}$ is the Larmor radius and υ is the parallel or longitudinal velocity which is parallel to the magnetic field. $J_\perp$ and J are called the transverse and parallel adiabatic invariation, respectively.

As the guiding center of the electron moves along the field line, which will be explained below, the magnetic field strength at the electron changes. Because the magnetic moment and kinetic energy of the electron are conserved, the kinetic energy of the parallel motion varies according to the relation

$$\frac{1}{2}m\upsilon_\parallel^2 + \mu_m B = const. \qquad (26)$$

Recalling the motion of a pendulum in the earth weight potential, Eq.(26) implies that the guiding center motion along the field line behaves like a particle motion in a magnetic potential energy $\mu_m B$. The magnetic field is mirror field in quadrupole and sextupole magnets, in which magnetic filed is weaker at the center and is stronger at both ends of the mirror field line. When the guiding center of electron moves along the field line from weaker field region to stronger field region, the parallel velocity decreases and the gyration velocity increases and the electron is heated. This kind of heating is called adiabatic heating in the plasma field. Therefore, the electron spirals in an ever-tighter orbit because the period of gyration motion and parallel velocity become smaller and smaller. When the electron comes to the point where the parallel velocity vanishes, the electron direction of motion is reversed. The parallel velocity of the reflected electron is increased when it moves along the field line and gets maximum value at the weakest field point (mirror point). Then it continues a similar motion along the other side of the mirror point. Such kind of trap is called magnetic mirror trap. The motion of electron in mirror field is shown in figure 14. The trap condition is

$$m\upsilon_\parallel^2 / 2 < \mu_m (B_{\max} - B), \qquad (27)$$

where υ is the parallel velocity at position with magnetic field B, B_{max} is the maximum magnetic field along this field line, which is located near the vacuum chamber wall in our case. Note the trap strongly depends on the electron velocity υ_0 and $\upsilon_{\perp 0}$. According to Eqs. (21), (23) and (25), the trap happens if

$$\frac{\upsilon_{\perp 0}^2}{\upsilon_{\perp 0}^2 + \upsilon_{\parallel 0}^2} > \frac{B_0}{B_{\max}}, \qquad (28)$$

where B_0 is the field at one position with velocity υ_0 and $\upsilon_{\perp 0}$. The trap condition Eq.(28) can be more conveniently described as

$$\Gamma_{trap} > 1 \qquad (29)$$

with the trap factor

$$\Gamma_{trap} = \frac{F_\upsilon}{F_B} = \frac{\upsilon_{\perp 0}^2}{\upsilon_{\perp 0}^2 + \upsilon_{\parallel 0}^2} \frac{B_{\max}}{B_0}. \qquad (30)$$

Where F_υ and F_B is left and right part of Eq. (28), respectively. When the trap factor Γ_{trap} is bigger than 1, the electron is trapped.

According Eqs. (29-30), a photoelectron could be trapped if its kinetic energy of gyration motion increases. The electron can receive transverse energy around the mirror point where the electric field direction of positron bunch is in the gyration motion plane. However, a short bunch is required for the electron to efficiently receive transverse energy because the effect of a long positron bunch on the transverse energy can cancel over many periods of gyration motion. Therefore, a short positron bunch, when compared with the cyclotron period at the mirror point, is very effective to increase the photoelectron energy distribution F_υ by increasing the kinetic energy of the gyration motion and then can cause the trapping of the photoelectrons. In the case of short positron bunch, electrons can get more kinetic energy of the gyration motion around the mirror points due to the high beam potential at that point and the short interaction time. A long positron bunch has less average effect on transverse energy of the photoelectron for all the field lines. Therefore, there the effect is weak on the trap of the photoelectron. The trapping requirement for positron bunch length can be described as

$$\sigma_l < \frac{2\pi cm}{e}\frac{1}{B} \qquad (31)$$

where B is the field at the mirror point. Eq.(31) can be written in a more convenient way as $\sigma_l(mm) < 10.7/B(T)$, which means the positron bunch length should be shorter than 10.7 mm for a field line with 1 T magnetic field at the mirror point.

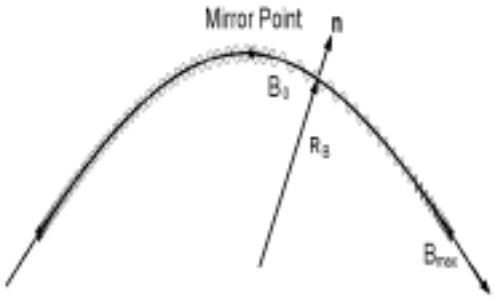

Figure 14 Motion of electron in a mirror magnetic field

3.4 Heat-load of photoelectron cloud

The lost photoelectrons, which hit the chamber wall, can cause the temperature increment of the vacuum chamber. The heat-load depends on the quantity and energy of the photoelectrons which hit the vacuum chamber wall. In drift region, the photoelectrons have

higher energy and larger quantity due to the multi-pacting. Therefore, there are larger loss rate of photoelectrons on the wall and higher heat-load. Multi-pacting occurs in two small regions in dipole magnet. The heat-load distribution is also two peaks at these two multi-pacting regions. On the other hand, there is lower heat-load in solenoid and quadrupole and sextupole cases where multi-pacting couldn't occur. Figures 15-16 show the lost photoelectron charge and heat-load azimuth angle distribution for the different fields.

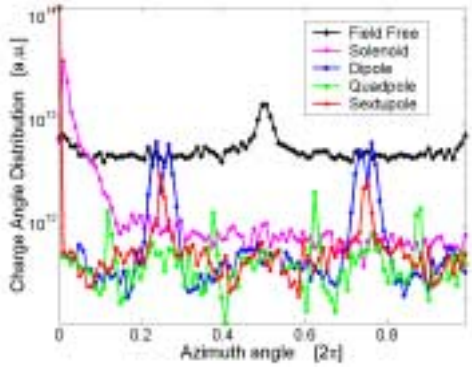

Figure 15 Charge azimuth angle distributions of the lost photoelectrons in different fields, which hit the vacuum chamber wall.

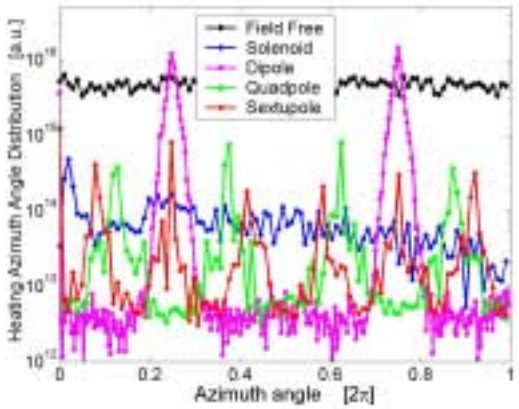

Figure 16 Heat-load azimuth angle distributions due to the lost photoelectrons in different fields, which hit the vacuum chamber wall.

3.5 Build up of electron cloud

Figures 17-18 show the average and center volume density in different magnetic fields as a function of time for a train with 200 bunches spaced by 7.86 ns and followed by a long bunch train gap. The saturation time decay time during the bunch train gap in field free case is the shortest because there is no magnetic field to confine the photoelectrons. One the other hand, the decay time is very large in quadrupole and sextupole magnet due to the deep trapping. The preliminary photoelectrons don't contribute to the make-up of the photoelectron cloud in dipole, quadrupole and sextupole magnets. At the same time there is a trapping phenomenon in quadrupole and sextupole magnets and there is muti-pacting phenomenon in dipole magnet. All these characters cause the average cloud density in these three fields is almost a linear function of the time during the build-up process.

The photoelectron density near the beam is zero in solenoid case and is small in quadrupole and sextupole cases. Therefore, the deeply trapped photoelectrons in quadrupole and sextupole magnets mainly contribute to the coupled bunch instabilities. The photoelectron densities near the beam in drift region and dipole is bigger. Photoelectron in these two cases is important for the blow-up of the positron bunch.

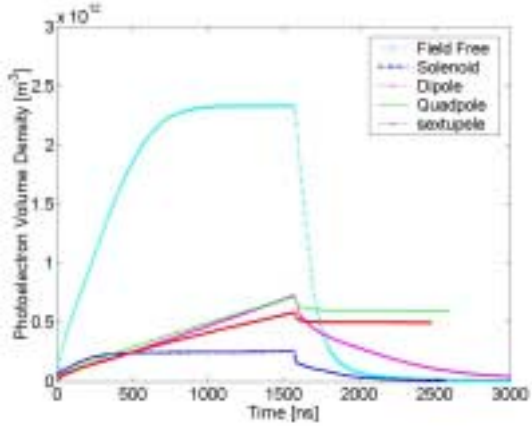

Figure 17 Photoelectron average volume densities in different magnet field as a function of time for a train with 200 bunches spaced by 7.86 ns and followed by a long bunch train gap.

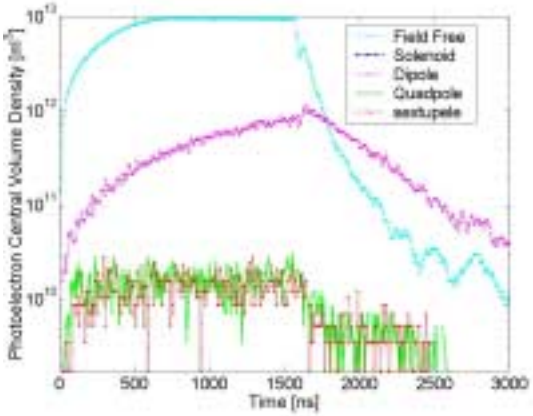

Figure 18 Photoelectron volume densities at pipe center for different magnet field cases as a function of time for a train with 100 bunches spaced by 7.86 ns and followed by a long bunch train gap.

4 SUMMARY AND CONCLUSIONS

A complete 3D PIC program has been developed. The Particle-In-Cell (PIC) method is applied to the 3D space charge of the photoelectron cloud. The simulation shows that the magnetic field can reduce the electron density at the pipe center. Uniform solenoid field is the most effective field to confine the

photoelectron to the vicinity of the vacuum chamber wall and solenoid is better than other kind of magnets. Solenoid works well with zero photoelectron central density and lower heat-load. Multi-pacting occurs in drift region and dipole magnet. A serious electron-trapping phenomenon during the train gap has been found in normal quadrupole and sextupole, whose mechanism is the mirror magnetic field trap.

5 ACKNOWLEDGEMENT

We thank Prof. A. Chao, K. Nakajima and E. Perevedentsev for helpful discussion. Thank KEKB commissioning group for all their help, information and discussion.

6 REFERENCE

[1] H. Fukuma, et al., “Observation of vertical beam blow-up in KEKB low energy ring”, EPAC2000, 2000.

[2] F.Zimmermann, "Electron-Cloud Studies for the Low-Energy Ring of KEKB", CERN-SL-Note-004, 2000.

[3] K. Ohmi and F. Zimmermann, “Head-tail instability caused by electron cloud in positron storage rings”, Physics Review Letter (85): 3821, 2000.

[4] H. Fukuma et al., "Study of vertical beam blowup in KEKB low energy ring", HEACC2001.

[5] L. Wang, et al., "3D simulation of photoelectron cloud ", 2001 Particle Accelerator Conference (PAC2001) CHICAGO, ILLINOIS USA, JUNE 18-22, 2001.

[6] L.F. Wang, H. Fukuma, K. Ohmi, "Simulation Study of Photoelectron Motion in Solenoid Field", KEK-2001-2, 2001.

[7] F.Zimmermann,“Electron Cloud at the KEKB Low Energy Ring:Simulations of Central Cloud Density, Bunch Filling Patterns,Magnetic Fields,and Lost Electrons ”,CERN-SL-2000-017 (AP)(May,2000).

[8] Kenro Miyamoto, Plasma Physics for Nuclear Fusion. (MIT Press, Cambridge, Massachusetts, and London, England, 1980).

A SIMULATION STUDY OF THE ELECTRON CLOUD IN THE EXPERIMENTAL REGIONS OF LHC

A. Rossi, G. Rumolo and F. Zimmermann, CERN, Geneva, Switzerland

Abstract

The LHC experimental regions (ATLAS, ALICE, CMS and LHCb) are characterised by having a variable geometry, non-uniform magnetic field, and the presence of two beams that may collide at the Interaction Point (IP). A detailed study of electron multipacting in the experimental chambers is needed to establish the pressure increase due to electron stimulated desorption, especially critical in the experimental regions. Furthermore, knowledge of the predicted electron cloud density all along the experimental regions will allow for an estimation of its possible effects on the beam stability.

1 INTRODUCTION

Photoemission and/or ionisation of the residual gas inside the beam pipe causes production of electrons (as well as of positive ions), which then move under the action of the beam field forces and their own space charge. These primary electrons can initiate a multipacting process, which eventually leads to the build up of a quasi-stationary electron cloud. Positive ions, on the other hand, are not expected to cause major inconveniences, since they have short survival times, low impact energies and a very low equilibrium density compared with that of the electrons [1]. It is supposed that the beam current is lower than the critical current, at which ion-induced pressure instability occurs [2].

In the interaction regions of the LHC (namely at ATLAS, ALICE, and CMS detectors), the maximum acceptable residual gas density is limited by the background noise induced to the detectors by nuclear gas scattering [3, 4, 5]. Electrons accelerated by the beam space charge and impinging on the walls with energies larger than about 10 eV [6] can desorb molecules and contribute to the residual gas density. Moreover, the electron cloud may affect the beam stability and luminosity in collision.

The aim of this study is to evaluate electron cloud build up in the LHC experimental areas and its effects on the residual gas pressure.

The features of the electron cloud build-up are presented and discussed in Sec. 2: electron density saturation value, electron flux to the walls, and energy spectrum of the electrons that hit the wall. Based on these results, for the relevant cases the pressure rise induced by electron desorption is calculated in Sec. 3. In Sec. 4, preliminary results of the code benchmarking are presented, with conclusions in Sec. 5.

2 ELECTRON CLOUD BUILD-UP

2.1 LHC experimental regions layout

An example of layout of experimental beam vacuum chambers is given in Fig. 1. The experimental chambers differ from the standard arc chambers mainly because of their variable geometry, the non-uniform magnetic fields, and the two beams travelling in opposite directions. Practically all the experimental chambers are at room temperature and they are coated with low activation sputtered TiZrV Non-Evaporable Getters (NEG's) [7]. The TiZrV NEG has been chosen, among other reasons, because it can limit electron multipacting due to its low Secondary Emission Yield (SEY). It was found that, after only 200°C activation, the maximum SEY, δ_{max}, becomes about 1.1 for incident electron energies between 300 and 400 eV [8]. The SEY remains below 1.2 even after saturation of the NEG surface with CO or water vapour [9]. However, after a few air venting/activation cycles, the maximum SEY can increase up to $\delta_{max} \sim 1.4$ [10].

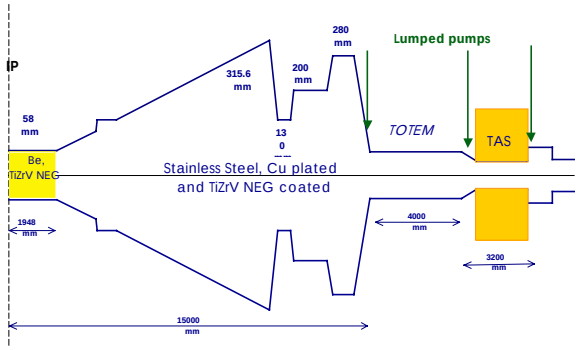

Figure 1: CMS-TOTEM beam pipe layout

2.2 Electron cloud simulation parameters

As the experiments are supposed to run independently of one another, we cannot rely on the experimental solenoid field (in the central sections of ATLAS and CMS) to prevent multipacting. Therefore, the simulations have been carried out assuming field free regions, which is the worst case.

The study of multipacting in the experimental regions has been conducted using ECLOUD [11] and considering the following set of parameters and/or assumptions:

1. The maximum SEY is 1.1 or 1.4.
2. We have assumed the elastic reflection to occur as on the copper samples recently measured [12]. Elastic reflection is anyway strongly dependent on the surface roughness more than on the material on which the electrons impinge.
3. The photon flux to the wall for the LHC geometry has been evaluated using the code developed by F. Zimmermann [13]. We expect the photon flux in the straight experimental areas to be sensibly smaller than the one in the arcs.
4. Bunch transverse sizes have been taken at injection and at top energy, both at the interaction points and up to 20m downstream. The study shows, that there is no strong dependence of the electron multipacting on this parameter. This was predictable since for the cases considered, the beam was much smaller than the pipe cross section.
5. The two cases of two beams reaching a selected location simultaneously (25ns bunch spacing and double bunch intensity) and two beams at half distance (12.5ns bunch spacing and single bunch nominal intensity) have been simulated.
6. Geometry variable in steps from the smallest to the largest diameter for each experimental region.
7. The effects of RF traps in enlarged sections of the chambers have not been taken into account.

Table 1. LHC parameters assumed in the electron cloud simulations

	symbol	value
bunch proton population	N_b	1.05×10^{11}
bunch spacing		7.48 m
r.m.s. bunch length		7.5 cm
proton energy		7 TeV
primary ph-e rate per photon		2.98×10^{-7}
Reflectivity		10%
max secondary emission yield	SEY	1.1 and 1.4
energy of max SEY		300 eV
energy distr. for sec. Electrons		Gaussian
r.m.s. horizontal beam size		15.86 - 444 μm
r.m.s. vertical beam size		"
radial half aperture		22 to 200 mm

2.3. Simulation results: electron density and flux to the wall

The electron line density (e^-/m) and flux to the wall (e^-/s/m) are displayed in Fig. 2, 3 and 4 for different chamber radii, and for SEY = 1.4. It can be observed that, despite the low value of SEY, there is an electron cloud build up. Both the rise time and saturation values depend on the chamber radius. No obvious correlation was found.

In Fig. 5, the saturation values of the electron flux to the wall per unit wall area (e^-/s/cm^2), with SEY = 1.1 and SEY = 1.4 are compared. The saturation levels appear to be more sensitive to a variation of SEY for radii > 70 mm. For the calculations of the residual gas density it was assumed that the electron flux to the wall is a step function, given the shape of the curves and that the two cases considered (simultaneous arrival and half bunch spacing) should correspond to the extreme cases. The values used are shown in Fig. 5, with blue dotted lines.

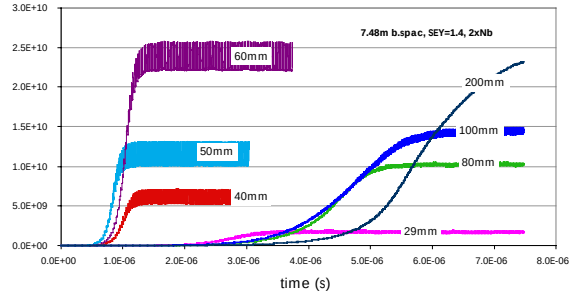

Figure 2: Time evolution of the electron line density (e^-/ m) for different chamber radii, for two beams arriving simultaneously (nominal bunch spacing and double bunch current).

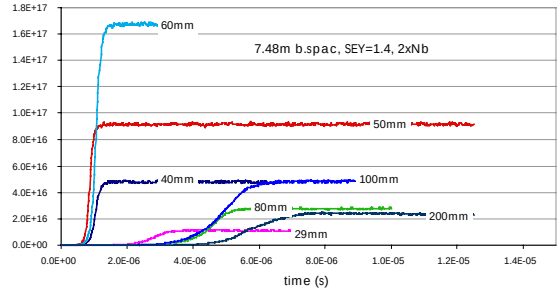

Figure 3: Time evolution of the electron flux to the wall (e^-/s/m) for different chamber radii, for two beams arriving simultaneously (nominal bunch spacing and double bunch current).

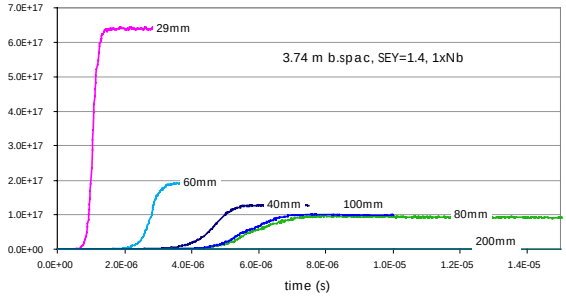

Figure 4: Time evolution of the electron flux to the wall (e^-/s/m) for different chamber radii, for two beams at half nominal bunch spacing and bunch current.

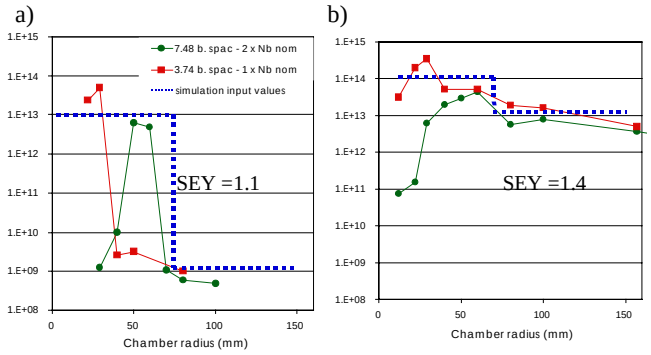

Figure 5: Saturation value of the electron flux to the wall ($e^-/s/cm^2$) as a fuction of the chamber radius, and the values used for the calculations of the gas density in the experimental regions. a) SEY = 1.1; b) SEY = 1.4.

2.4. Simulation results: electron impact energy distribution at the wall

The electron impact energy distribution at the wall is displayed in Fig. 6 for the two cases of beams arriving simultaneously and with half nominal bunch spacing. The maximum impact energy varies between 2.5 keV for the latter case and 4.5 keV for simultaneous beams (which corresponds to twice the bunch current). Both figures display an energy range from 0 to 160 eV to show that a non negligible fraction of the electrons impinge on the walls with an energy larger than 10 eV, that is larger than the threshold energy for stimulated gas desorption [6].

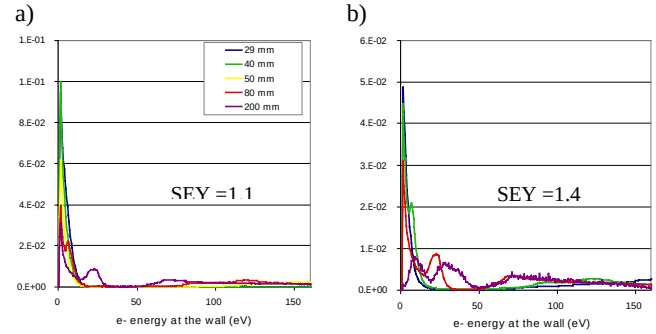

Figure 6: Electron energy distribution at the wall (eV). a) beams arriving simultaneously, with double current. b) beam at half of the nominal bunch spacing and nominal current.

3 MOLECULAR DENSITY ESTIMATION IN THE EXPERIMENTAL REGIONS

3.1. Molecular density estimation parameters

As mentioned in the previous section, a large fraction of the electrons impinging on the wall will cause gas desorption. The Electron Stimulated Desorption yield (ESD) depends on the impact energy [6]. The values for ESD used for the estimates of the residual gas density are listed in Table 2 for TiZrV coating [14]. Since the ESD varies by a factor of ~ 2 between 100 and 300 eV, and given the spread of measured data in the literature, a constant value for all energies was assumed.

Table 2 also contains other parameters relevant for the molecular density estimations, such as the Photon Stimulated gas Desorption (PSD) from TiZrV NEG coating and its sticking coefficients. It should be noted that the desorption yields from NEG coating are reached with other materials after a long conditioning (about 1 year LHC beam time).

Table 2. LHC parameters assumed in the residual gas density estimations for the TiZrV NEG coating

Desorption Yield	H_2	CH_4	CO	CO_2
PSD[i]	2.5×10^{-7}	2.5×10^{-9}	1.25×10^{-8}	1.25×10^{-8}
ESD[ii] [14]	2.0×10^{-4}	5.0×10^{-6}	1.0×10^{-4}	1.0×10^{-4}
Sticking Coefficient				
Freshly activated NEG[iii] [7]	5.0×10^{-3}	0	1.0×10^{-1}	1.0×10^{-1}
Cycled NEG[iv] [7]	5.0×10^{-4}	0	1.0×10^{-2}	1.0×10^{-2}

[i] Corrected for grazing incidence (factor of 5 larger at grazing incidence [15] than perpendicular incidence [16]) and considering the expected 12eV critical energy at the LHC interaction regions [17].

[ii] ~500eV incident energy.

[iii] Corresponding to SEY = 1.1.

[iv] Cycled = exposed to air at atmospheric pressure and reactivated several (~ 10) times. SEY = 1.4.

3.2 Results

The density profiles for the ATLAS and CMS (with TOTEM) experimental beam pipe are presented in Fig. 7 and 8. The 'static' density (Fig. 7.1 a) and 8.1, a)) is estimated for a freshly activated NEG coating and is compared to the expected values during proton beam operations (SEY = 1.1, Fig. 7.1 b) and 8.1, b)). It should be noted that the major contribution to the gas density is given by electron induced desorption, since photon induced desorption is at least 2 orders of magnitude smaller. In both cases, the main gas species is methane. The ATLAS beam pipe has a smaller cross section, which accounts for the higher density of CH_4, whose pumping is conductance limited.

After the NEG coating has been exposed to air at atmospheric pressure (due for example to maintenance works) and reactivated for about 10 times, the δ_{max} increases to ~ 1.4 with a consequent increase of the electron cloud activity, as detailed in section 2. At the same time, the sticking coefficients, and therefore the distributed pumping, is reduced to about one tenth of the initial value. Both phenomena lead to a further increase in the molecular density as shown in Fig. 7.2 and 8.2. The hydrogen density is now comparable to that of methane,

since the distributed pumping speed for hydrogen is low, while the pumping of methane is not affected by the NEG deterioration.

Note that, beyond 22 m from the IP, the surface is supposed to be at cryogenic temperature. Here, the distributed pumping is effective for methane, but lower than the NEG pumping for the other gas species.

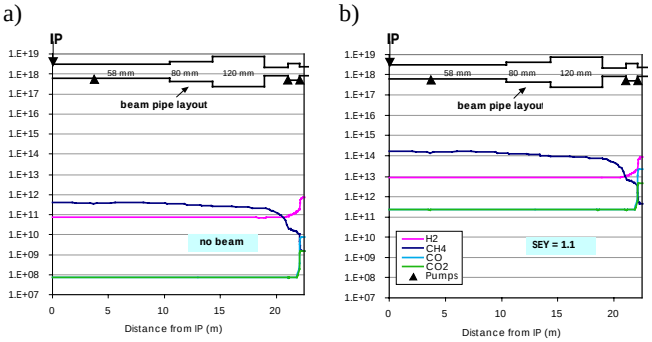

Figure 7.1 : ATLAS experiment. Molecular density distribution (molecules/m^3) as a function of the distance from the experiment interaction point (IP) for a freshly activated TiZrV NEG coating. a) : no running beam (static). b) : density rise due to electron desorption (main contribution) with SEY = 1.1.

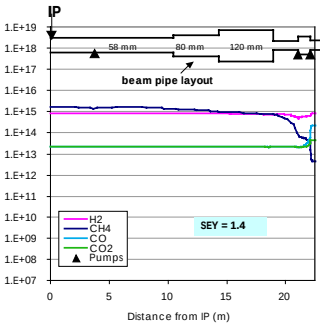

Figure 7.2 : ATLAS experiment. Molecular density distribution (molecules/m^3) as a function of the distance from IP. The pressure increase due to electron desorrption (main contribution) with SEY = 1.4 and 1/10 of NEG pumping.

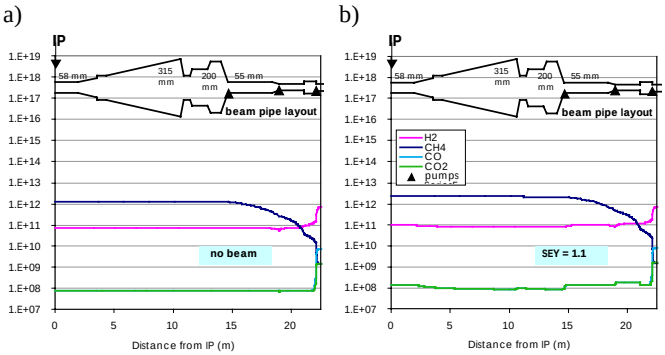

Figure 8.1 : CMS experiment. . Molecular density distribution (molecules/m^3) as a function of the distance from the IP for a freshly activated TiZrV NEG coating. a) : no running beam (static). b) : density rise due to electron desorption (main contribution) with a SEY = 1.1.

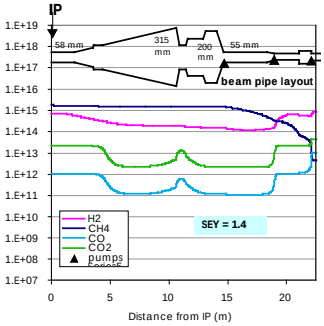

Figure 8.2 : CMS experiment. Molecular density distribution (molecules/m^3) as a function of the distance from the experiment interaction points (IP). The density increase due to electron desorrption (main contribution) is shown for a SEY = 1.4 and 1/10 of the initial NEG pumping.

The profile of the CO and CO_2 gas density in the CMS geometry results from a larger electron flux to the wall in the smaller cross sections (as detailed in Sect. 2.3) and a reduced NEG pumping (which is proportional to the pipe surface area).

4. BENCHMARKING

If the quantitative results of the electron cloud simulations are correct, the main contribution to the residual gas density comes from electron induced gas desorption, as it was explained in the previous section. Since these values are used to assess the validity of the experimental beam chambers design, benchmarking of the simulation results against experimental data is urgently needed. For example, for the CMS experiment, the background noise corresponding to the density levels estimated for SEY = 1.4 is very close to the maximum value the detector can tolerate [18].

In this section, preliminary results of the electron cloud code benchmarking are presented. The time evolution curves of the electron build-up signal [19] (negative voltage) during experiments in the CERN SPS with LHC type proton beam (25 ns bunch spacing) are compared with the simulation results. The data cannot be converted into number of electrons collected by the pick-up per second, because the instrument was not calibrated prior to the run. In Fig. 9.a) the electron build-up was measured with a train of 72 bunches, 8.3×10^{10} protons/bunch. The pressure measured was about 2×10^{-7} Torr.

The input data for the simulations that best reproduce the experimental data are listed in Table 3. It was assumed that the primary electrons are created by ionisation of the residual gas by the proton beam, as it should be in the SPS. The beam structure and the values assumed for the gas pressure were the same as recorded during the experiments.

Table 3. LHC parameters assumed in the electron cloud simulations for the benchmarking

	value
bunch proton population	8.3×10^{10}
bunch spacing	7.48 m
r.m.s. bunch length	30 cm
proton energy	26 GeV
residual gas pressure	2×10^{-7} and 4×10^{-8} Torr
gas ionisation cross section	2 MBarn
max secondary emission yield	1.6
energy of max SEY	300 eV
energy distr. for sec. electrons	Gaussian
r.m.s. horizontal beam size	444 μm
r.m.s. vertical beam size	"
radial half horizontal aperture	76 mm
radial half vertical aperture	17.5 mm

The time evolution of the experimental data are well reproduced by the simulations. In Fig. 9.a) the flux of electrons incident on the pick up is plotted as a function of time. In Fig. 9.b), the electron line density resulting from the simulations is displayed.

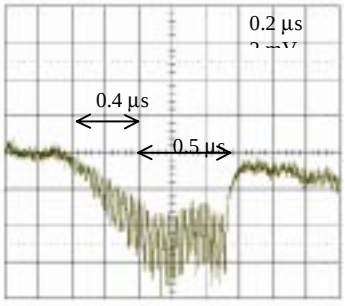

a)

Courtesy of M. Jimenez [19]

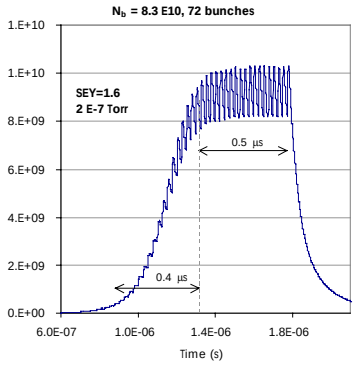

b)

Figure 9: Time evolution with a train of 72 bunches. The the experimental data (electron flux to the wall, a) are compared to simulation results (electron line density, b).

5 CONCLUSIONS AND FUTURE WORK

The variation of the electron cloud activity with radius (as for the LHC experimental beam pipe geometry) and SEY characteristic of TiZrV NEG coating have been simulated using ECLOUD. The results of the simulations have been used as input to estimate the residual gas density in the interaction regions during proton beam running. It was found that, despite the low SEY of the TiZrV NEG coating after activation, the levels of electron flux to the wall at saturation can induce a gas desorption which will dominate the residual gas density.

Benchmarking of the simulation results are promising. Further effort should be put into this to validate quantitatively the code results so as to use it as a design tool.

The effects of the electron cloud on the beam dynamics are to be analysed.

6 REFERENCES

[1] G. Rumolo and F. Zimmermann, CERN-SL-2001-014-AP.
[2] A. Mathewson, Maui, Hawai, November 3-9, 1994.
[3] ALICE Technical Proposal, CERN/LHCC/95-71.
[4] ATLAS TDR 13, CERN/LHCC/99-01.
[5] CMS Technical Proposal, CERN/LHCC/94-38.
[6] G. Vorlaufer, N. Hilleret, F. Billard, CERN Vac. Tech. Note 00-32.
[7] C. Benvenuti et al., Vacuum 60 (2001) 57-65.
[8] C. Scheuerlein et al., CERN EST/2000-07 (SM).
[9] B. Henrist et al., CERN Vac. Tech. Note 98-08.
[10] B. Henrist and C. Scheuerlein, CERN Vac. Tech. Note 98-20.
[11] G. Rumolo and F. Zimmermann, same proceedings.
[12] V. Baglin, I. Collins, B. Henrist, N. Hilleret, G. Vorlaufer, CERN, LHC-Project-Report-472.
[13] F. Zimmermann, CERN, LHC Project Report 237 (2000).
[14] C. Benvenuti, P. Chiggiato, F. Cicoira, V. Rouzinov, Vacuum 50 N. 1-2 (1998) 57-63.
[15] O. Gröbner, A.G. Mathewson, H. Störi, P. Strubin, R. Souchet, Vacuum 33, N. 7 (1983) 397-406
[16] V. Baglin, C. Benvenuti, P. Costa Pinto, P. Chiggiato, N. Hilleret, A. Rossi, presented at IVC 15, San Francisco, Nov 2001.
[17] J. Gómez-Goñi et al., J. Vac. Sci. Technol. A 12(4) Jul/Aug 1994.
[18] M. Huhtinen, CMS-TOTEM beam pipe EDR, CERN, April 2002.
[19] M. Jimenez et al., proceedings of 11th Chamonix workshop, 2001.

Qualitative Analysis of Electron cloud effects in the NLC damping ring*

S. Heifets, Stanford Linear Accelerator Center, Stanford University, Stanford, CA 94309, USA

Abstract

The qualitative analysis of the electron cloud formation is presented. Results are compared with simulations for the NLC damping ring [1].

1 INTRODUCTION

Since the discovery of instability at KEK photon factory [2], it was realized that the electron cloud can drive the fast multi-bunch [3] and, later, the single bunch instabilities [4] in the positron storage rings. The instabilities affect performance of the B-factories and design of the future linear colliders.

Effects of the e-cloud on the beam dynamics is conveniently described by the effective wake field [5] which can be calculated [6] given the density of the e-cloud. The estimate of the density is the main difficulty of the problem. The e-cloud is neither static in time nor uniform in space and depends on the bunch population N_b, bunch spacing s_b, geometry of the beam pipe, the flux of the synchrotron radiation (SR) photons, and the yield of secondary electrons. Due to these difficulties, the density is usually determined either by elaborate simulations or considered as a fitting parameter. Nevertheless, it is highly desirable to have some analytic estimate of the density to interpret the results of simulations and for scaling of these results with machine parameters. The goal of the paper is to provide such an estimate. Results of the analysis are applied to the NLC main damping ring and compared with the simulations for the NLC [1]. The relevant parameters of the ring are listed in Table.

The electron cloud where electrons moves randomly and can be characterized by some quasi-steady equilibrium distribution can exist only in the case of small currents. That is true for both practically important cases where electrons are generated by synchrotron radiation or are result of the beam induced multipactoring.

The paper is organized as following. We start with a simple case of the coasting beam where electrons oscillate in the self-consistent potential well and can be described by the Boltzmann distribution. Then, to define the temperature of the distribution, we need to consider bunched beam. The temperature is defined by the equilibrium of the energy losses. The next step is to take into account the multipactoring. It is shown that the space-charge potential of the secondary electrons generates a potential bump at the wall which defined by the equilibrium of the average number of electrons in the cloud. Effect of the finite bunch length in Section 6. Wherever it is possible, our results are compared with simulations [1].

* Work supported by Department of Energy contract DE–AC03–76SF00515.

2 STEADY-STATE: COASTING BEAM, NO SR

Let us start with a coasting beam with the average linear density N_b/s_b in a round beam pipe. Electrons of the cloud oscillate in the steady-state potential $U = U_{beam} + USC$ of the relativistic beam (in units of mc^2)

$$U_{beam} = -\frac{N_b r_e}{s_b}\ln[\frac{b^2}{r^2+\sigma_y(\sigma_x+\sigma_y)}], \qquad (1)$$

plus the space-charge potential of the cloud

$$U_{SC} = 4\pi r_e[\int_0^b r'dr'n(r')\ln\frac{b}{r'} - \int_0^r r'dr'n(r')\ln\frac{r}{r'}]. \qquad (2)$$

The steady-state density corresponds to the condition that the total radial field $\propto (dU/dr)_{r=b}$ at the wall is zero. This condition defines the average density in the steady-state

$$n_0 = \frac{2\pi}{\pi b^2}\int rdrn(r) = \frac{N_b}{\pi s_b b^2}. \qquad (3)$$

This is the well known condition of neutrality which is, actually, independent of the form of the distribution $n(r)$.

For the NLC parameters, $n_0 = 2.2\,10^7\ cm^3$. This agrees quite well with the results of simulations [1] which give the average in time density at saturation $3.0\,10^7\ cm^{-3}$ at low level SR.

The average over time distribution function of electrons trapped in this potential well can be taken as Boltzmann distribution

$$\rho(r,v) = |N|e^{-\frac{1}{T}[(1/2)(v/c)^2+U(r)]}, \qquad (4)$$

where T is temperature in units of mc^2, $|N|$ is the normalization factor related to the average density n_0 is $\int 2\pi r dr dv\rho(r,v) = \pi b^2 n_0$. The density of the cloud

$$n_{cl}(r) = \int dv\rho = |N|c\sqrt{2\pi T}e^{-U/T} = n_0\frac{b^2}{2}\frac{e^{-U/T}}{\int rdre^{-U(r)/T}}. \qquad (5)$$

The potential U in Eq. (5) is the total potential $U = U_b + U_{cl}$ of the beam and the cloud. The later is defined by the Poisson equation with the right-hand-side (RHS) proportional to $n_{cl}(r)$.

Let us define dimensionless $x = r/b$ and measure all potentials in units of T, introducing $V(x) = (U(r)/T)_{r=bx}$. Then, for a cylindrically symmetric beam pipe, $V(x) = V_{cl} - g\ln(1/x)$ where

$$g = \frac{2N_b r_e}{Ts_b}, \quad \hat{g} = \frac{2\pi r_e b^2}{T}n_0. \qquad (6)$$

The Poisson equation for V_{cl} takes the form

$$\frac{1}{x}\frac{\partial}{\partial x}x\frac{\partial V_{cl}}{\partial x} = -\hat{g}\frac{e^{-V(x)}}{\int xdxe^{-V(x)}}. \quad (7)$$

In the stationary case, the total potential $U(r)$ and the force $dU(r)/dr$ are zero at $r = b$. That gives the boundary conditions $V(1) = 0$, $(dV/dx)_{x=1} = 0$ or, for the space-charge potential, or

$$V_{cl}(1) = 0, \quad (\frac{dV_{cl}}{dx})_{x=1} = -g. \quad (8)$$

The space-charge potential is finite at $x = 0$. Integration of Eq. (7) with the weight x gives $(dV_{cl}/dx)_{x=1} = -\hat{g}$. Comparison of this result with Eq. (8) gives $\hat{g} = g$ and defines the average density

$$n_0 = \frac{N_b}{\pi s_b b^2}, \quad (9)$$

reproducing the density given by the condition of neutrality. Note, that the average density n_0 is independent of the shape of the density $n_{cl}(r)$ and temperature T.

Potentials $V(x)$, $V_{cl}(x)$, and

$$n_{cl} = \frac{n_0}{2}\frac{e^{-V(x)}}{\int_0^1 xdxe^{-V(x)}} \quad (10)$$

depend only on one parameter g. It is defined in the next section.

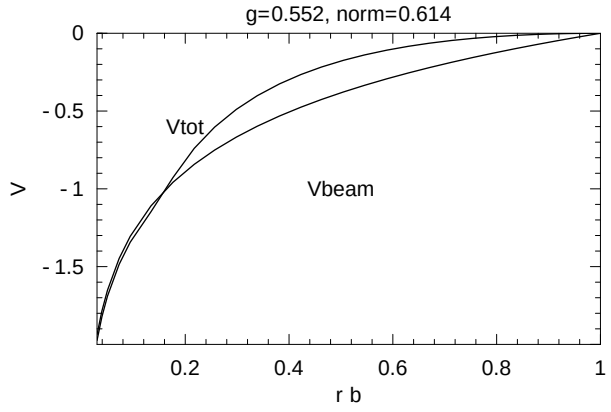

Figure 1: *Total self-consistent potential $V(x)$ and the beam potential $V_b = -g\ln(1/x)$ vs $x = r/b$. Parameter g is found from Eq. (16).*

3 STATIONARY DISTRIBUTION, BUNCHED BEAM

In the approximation of the averaged beam potential, electrons have regular motion oscillating in the self-consistent potential well. The averaging of the beam potential is a standard trick used for the similar problem of the ion instability. For the e-cloud this approximation require justification due to high frequency of the electron oscillations. For example, for the NLC DR, the linear frequency of oscillations

$$\Omega_{0y} = c0\sqrt{\frac{2N_b r_e}{s_b(\sigma_x + \sigma_y)\sigma_y}} \quad (11)$$

is equal to $\bar{\Omega}_{0,y}/2\pi = 31.7$ GHz and the number of oscillations between bunches $\bar{\Omega}_{0,y}s_b/(2\pi c) >> 1$. Obviously, the beam potential cannot be approximated by a potential of the coasting beam.

Nevertheless, an electron moves between bunches only by the distance small compared to beam pipe radius. Hence, before an electron can reach the wall, it is kicked by $v/c = 2N_b r_e/r$ several times. Electrons move changing direction and the motion is similar to a random walk. We can estimate the number of kicks n_{pass} an electron gets before it can reach the wall from

$$n_{pass} < (\frac{2N_b r_e s_b}{r})^2 >= b^2, \quad (12)$$

what defines n_{pass}. It is clear again that it makes sense to speak about e-cloud only for $\kappa \equiv 2N_b r_e s_b/b^2 << 1$. For the NLC parameters, $n_{pass} \simeq 3 - 4$ in agreement with simulations.

In the previous section, the temperature T remains undefined. Now we take into account the beam bunching considering bunches as point-like macro particles. The goal is to define the temperature T and the average over time density of the cloud.

The bunching of the beam has several implications. First, an electron in the beam pipe experiences periodic kicks. Neglecting the space-charge potential, we can write a simplectic map $M(x, v)$ giving transformation of the electron coordinates per bunch spacing $[x, v] - > [\bar{x}, \bar{v}] = M(x, v)[x, v]$. The eigen values of the Jacobian $D[M[x, v], \{x, v\}]$ are real only for $x < \sigma_\perp/b$, i.e. in the region of the linear motion.

Elsewhere the motion is chaotic and the average in time distribution function can be taken in the form of Eq. (4) although the approximation of the coasting beam is not valid. That is possible due to the other effects of the bunched beam: heating of the cloud caused by the kicks balanced by the cooling of the cloud due to the loss of electrons.

A kick from a bunch increases the average energy of the e-cloud by

$$\Delta E_{gain} = 2\pi \int rdrdv\rho(r, v)(\frac{2N_b r_e}{r})^2, \quad (13)$$

where integration is over the phase space of the cloud.

The electrons in the vicinity of the beam are kicked to the wall and are replaced with the low energy secondary electrons. The later process produces cooling. To be lost, an electron has to reach the wall before the next bunch arrives. The trajectory of an electron between bunches can be estimated as following. Consider an electron with the

initial conditions $r, v/c$ just before a bunch arrives. A bunch changes $\beta = v/c$ to $\beta_0 = v/c - 2N_b r_e/r$. After that, an electron moves in the field of the space charge. Let us assume, for a moment, a uniform density of the cloud, $n_{cl}(r) = n_0$. Then, the space-charge force is $2\pi r_e n_0 r$ and the electron is at $\bar{r} = r\cosh(\Omega_{pl} s_b/c) + (c\beta_0/\Omega_{pl})\sinh(\Omega_{pl} s_b/c)$ at the time of arrival of the next bunch. Here $(\Omega_{pl}/c)^2 = 2\pi n_0 r_e$. A quasi-stationary cloud can exist only if $(\Omega_{pl} s_b/c)^2 << 1$. For the NLC parameters, $n_0 = 2.2\,10^7\ cm^{-3}$, and $(\Omega_{pl} s_b/c)^2 = 0.277$. In the case of small (Ω_{pl}/c), $\bar{r} = r + (v/c - 2N_b r_e/r)s_b$ and is independent on n_0. The electron hits the wall if $|\bar{r}| > b$, or

$$\frac{v}{c} > \frac{b-r}{s_b} + \frac{2N_b r_e}{r}, \quad \text{or} \quad \frac{v}{c} < -\frac{b+r}{s_b} + \frac{2N_b r_e}{r}. \quad (14)$$

All electrons within this part of the phase space get lost and are replaced by the electrons from the cloud. The energy loss is equal to the energy of the lost particles before they were kicked to the wall:

$$\Delta E_{loss} = 2\pi \int r dr dv \rho(r,v)[\frac{1}{2}\frac{v^2}{c^2} + U(r)], \quad (15)$$

where integration is restricted by the condition Eq. (14) and $0 < r < b$. Here we neglected the energy brought to the cloud by the low energy secondary electrons coming in from the wall.

The balance of energies Eq. (13) and Eq. (15) gives the following equation:

$$g\kappa \int_0^1 \frac{dx}{x} e^{-V(x)} F(x) = \int_0^1 x dx e^{-V(x)}[(\frac{1}{2} + V(x))(1 - F(x)) + \frac{1}{2\sqrt{\pi}}(z_+ e^{-z_+^2} + z_- e^{-z_-^2})], \quad (16)$$

where

$$F(x) = (1/2)(Erf[z_+] + Erf[z_-]), \quad \kappa = 2N_b r_e s_b/b^2, \quad (17)$$

and

$$z_+ = \sqrt{\frac{g}{2p}}(1 - x + \frac{p}{x}), \quad z_- = \sqrt{\frac{g}{2p}}(1 + x - \frac{p}{x}). \quad (18)$$

Let us remind that, given κ, $V(x)$ depends only on g. Eq. (16) defines g, i.e. the temperature T. It is plausible to expect that $g \simeq 1/\ln(1/\kappa)$. The solution of Eq. (7) and Eq. (16) can be obtained numerically. Calculations for the NLC parameter $\kappa = 0.277$ define $g = 0.552$, what is close to the estimate above, $1/\ln(1/\kappa) = 0.780$. The temperature in units of mc^2 is $T = g(2N_b r_e/s_b)$, or $T = 92.4$ eV. The potential $V(x)$ is shown in Fig. 5. At small distances it goes as beam potential but at large distances is flatter due to the space charge contribution. The density profile $n(x)/n_0$, Eq. (10), for the same parameters is shown in Fig. 2. The

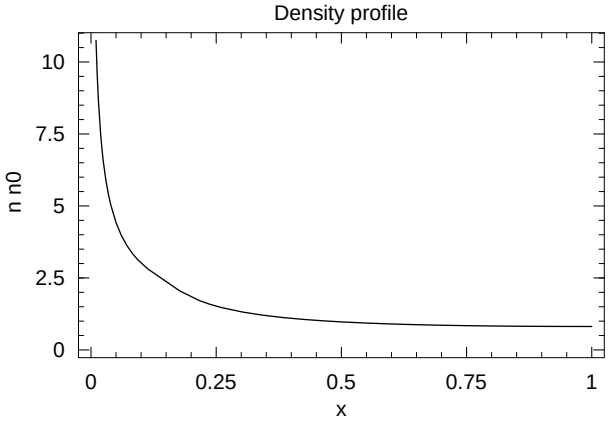

Figure 2: *The density* $n(r)/n_0$, $n_0 = 2.2\,10^7\ cm^{-3}$ *vs* $x = r/b$ *for the NLC parameter* $2N_b r_e s_b/b^2 = 0.277$.

density at the beam line (at the moment of a bunch arrival) is substantially larger that the average density n_0.

The number of electrons with the energy E hitting the wall of the drift chamber with the length L_d is

$$\frac{dN(E)}{dE} = 2\pi L_d \int r dr dv \rho(r,v)\delta[\frac{1}{2}(\frac{v}{c} - \frac{2N_b r_e}{r})^2 + U(r) - E], \quad (19)$$

where integration is taken over the region $v/c > \sqrt{2T} z_+$ and $v/c < -\sqrt{2T} z_-$, and ρ is the distribution function at the moment of bunch arrival.

The result of calculations is shown in Fig. 3. Parameters are the same as in Fig. 2.

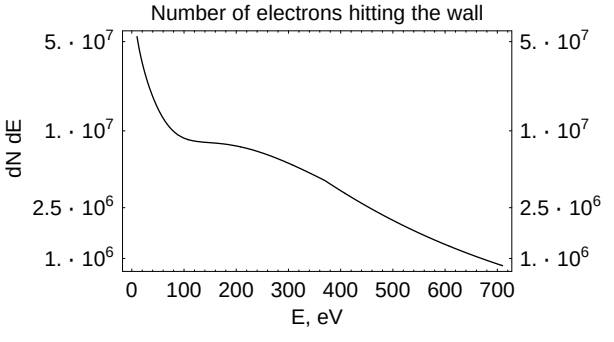

Figure 3: *Number of electrons per bunch* $dN/dE\ 1/eV$ *accelerated from the e-cloud and hitting the wall with energy* E.

Finally, the number of electrons hitting the wall per pass-

ing bunch is given by the integral

$$N_{loss} = 2\pi L_d \int r dr dv \rho(r,v) \qquad (20)$$

where the integration is over the region $v/c > \sqrt{2T} z_+$ and $v/c < -\sqrt{2T} z_-$. Calculation gives $N_{loss} = 5.53\,10^9$, 31% of the total $N_{tot} = \pi b^2 L_d n_0 = 1.74\,10^{10}$ electrons in the cloud in the drift with length L_d. This result may be compared with the simple estimate which assumes that all particles within radius r, where $(2N_b r_e/r)s_b > b$ are lost. If the density would be constant $n_0 = 2.2\,10^7\ 1/cm^3$, then $N_{loss} = 1.37\,10^9$. The actual number is higher because the density at the beam line is higher than the average density n_0.

The total energy loss is given by the integral

$$\frac{E_{loss}}{T} = \frac{\pi b^2 n_0}{\int_0^1 x dx Exp[-V(x)]} \int x dx e^{-V(x)} \int du e^{-u^2} [(u - \frac{1}{x}\sqrt{\frac{\kappa g}{2}})^2 + V(x)]. \qquad (21)$$

Here the variable $u = (v/c)/\sqrt{2T}$, and the integral is taken over $|x + u\sqrt{2\kappa/g} - \kappa/x| > 1$. Numeric integration gives power loss $(c/s_b)E_{loss} = 101\,W/m$.

4 JETS

Another effect of the bunched beam is production of jets of electrons.

Simulations show that, at the high level of the SR, the average electron density is higher than at the low level of the SR by a factor of two. (It is worth noting that a round beam pipe without the ante-chamber was used in simulations). For large SR, the primary photo-electrons move as a compact jet toward the beam line getting a kick

$$\Delta(\frac{v}{c}) = -\frac{2N_b r_e}{r} \qquad (22)$$

from the parent bunch.

The density of a jet may be higher than that given by the condition of neutrality and depends on the yield η of the secondary electron emission, number of jets k_{jets} within the beam pipe, and the volume of a jet. The density averaged over the length L_d of the drift section where SR is absorbed and over the beam pipe cross-section,

$$< n_{e\gamma} >= Y \frac{N_\gamma N_b}{\pi b^2 L_d} k_{jets}, \qquad (23)$$

is proportional to the number of photons

$$N_\gamma = \frac{5\alpha_0 \gamma}{2\sqrt{3}} \frac{L_b}{R} \qquad (24)$$

radiated by a positron in the bend with radius R and length L_b per pass.

For the NLC parameters and $Y = 0.2$, $k_{jets} = 2$ and the average density $< n_{e\gamma} >= 5.5\,10^7\ 1/cm^3$ is very close to the result of simulations $6.\,10^7\ cm^{-3}$ with the large yield Y of the primary photo-electrons.

The jets may also explain why the electron density at the beam pipe line in simulations is much higher than the average electron density.

Initial energy spread of the primary photo-electrons leads to the difference in the distances of electrons in the jet from the beam line. Interaction with the bunch translates this difference in the energy spread of the electrons hitting the beam pipe wall. If the shortest distance of the jet centroid from the beam line is *d*, then

$$\frac{dN}{dE} = \frac{Y N_b N_\gamma}{l_{jet}} (\frac{2N_b r_e}{mc^2}) (\frac{mc^2}{2E})^{3/2}. \qquad (25)$$

The distribution is shown in Fig. 4 for $Y = 0.2$.

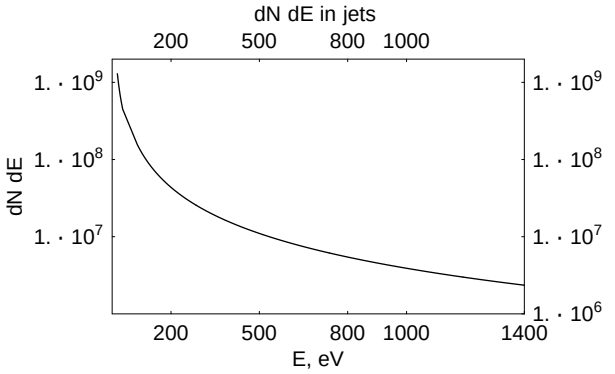

Figure 4: *Number of electrons dN/dE hitting the wall per bunch. Electrons are accelerated by the beam while a jet crosses the beam line. $Y = 0.2$*

5 SATURATION

High energy electrons hitting the wall produce secondary electrons which, after thermalization, may increase the density of the cloud in the avalanche-like way. Let us estimate the number of bunches m needed to reach saturation of the cloud density $n_0 = 2.2\,10^7\ 1/cm^3$. At the low level of the photo-electric yield $Y = 0.002$ taken in simulations [1], the SR adds to the average density $n_{SR} = 5.5\,10^5\ 1/cm^3$ per bunch (see Eq. (23)). Most of these electrons go wall-to-wall and only $(\eta - 1)n_{SR}$ of the secondary electrons remain in the cloud. Due to the multipactoring the density increases exponentially:

$$\frac{dn}{dm} = -\xi n + \eta\xi n + (\eta - 1)n_{SR}, \quad n = \frac{n_{SR}}{\xi}[e^{\xi(\eta-1)m} - 1]. \qquad (26)$$

Here we introduced parameter $\xi = N_{loss}/N_{tot}$ defining the fraction of the cloud participating in multipactoring. The

estimate of the previous section gives $\xi = 0.3$ and the density reaches saturation after

$$m = \frac{1}{\xi(\eta-1)} \ln[\frac{n_0}{n_{SR}}\xi + 1] \qquad (27)$$

passes. For the NLC DR, $m = 19$ for $\eta = 1.45$. At the high SR photon flux, where $n_{SR} \simeq n_0$, the number of passes to reach saturation os of the order of $[\xi(\eta-1)]^{-1} \simeq 7$. These estimates are in reasonable agreement with the simulations.

6 EFFECT OF THE MULTIPACTORING

It was mentioned above, that, for $\kappa > 1$, there are two region of distances from the beam line: in the vicinity of the beam, where electrons are wiped out by each passing bunch, and another one close to the wall.

The multipactoring adds the third region. Generally, there is a bump of the potential well in the vicinity of the wall which defines how many of the secondary electrons can go to the central regions. Such a sheath works as a virtual cathode. The density in the sheath near the wall depends on the balance of the number of electrons kicked to the wall from the central region and the number of electrons produced at the wall by the SR and multipactoring.

In the equilibrium, the number of lost particles is equal to the particles coming to the cloud from the wall. If the yield of secondary electrons is high, to sustain the equilibrium, the total potential changes to stop the back flow of the secondary electrons.

The distribution function $\rho(r,v)$ satisfies the Liouville equation with the source S,

$$\frac{\partial\rho}{\partial t} + v\frac{\partial\rho}{\partial r} - c^2\frac{\partial U(r)}{\partial r}\frac{\partial\rho}{\partial v} = S\frac{\delta(r-b)}{2\pi r}f(v). \qquad (28)$$

Here $f(v)$ is normalized distribution of the secondary electrons over velocity,

$$f(v) = \frac{v}{c^2T_w}e^{-\frac{v^2}{2c^2T_w}}, \quad \int_{-\infty}^{0} dv f(v) = 1. \qquad (29)$$

The temperature T_w is equal to the average energy of secondary electrons E_0 in units of mc^2, $T_w = \int dv(v^2/2c^2)f(v)$. In the estimate we assume $E_0 = 2$ eV, $T_w = 4.0\,10^{-6}$. The source S_{cl}, the number of secondary electrons ejected from the wall per unit time and unit length of the beam pipe, is given by the number of lost electrons dN_{loss}/ds and the yield of the secondary electrons η, $S_{cl} = (\eta-1)(c/s_b)dN_{loss}/ds$. (More exactly, S_{cl} is given only by the lost particles with the sufficiently high energy, $E > 50$ eV). If there is the SR flux, it adds S_{SR}, $S = S_{cl} + S_{SR}$,

$$S_{SR} = YN_\gamma N_b \frac{c}{s_b L_d}. \qquad (30)$$

We imply here that electrons generated at the wall are thermalized and are added to the e-cloud. This process works as a sink for the generated electrons and allows us to consider the average in time electron density $\rho(r,v) = \rho_{cl}(H) + \rho_s(r,v)$, where $H = v^2/2c^2 + U(r)$. Here the first term is the distribution function of the cloud and the second term describes secondary electrons,

$$\rho_s(r,v) = \frac{S}{2\pi b}\frac{f(c\sqrt{2H})}{c\sqrt{2H}}\Theta(b-r). \qquad (31)$$

The density of the secondary electrons $n_s = \int dv\rho_s$ at the wall is

$$n_s(r) = \frac{S}{2bc\sqrt{2\pi T_w}}. \qquad (32)$$

The total potential at the wall $V(1) = 0$, and in the vicinity of the wall can be expanded in series $V(x) = (1-x)V_1 + (1-x)^2(V_2/2) + ...$ To have maximum at $x_{max} < 1$, V_2 has to be negative. The potential is maximum $V_{max} = -V_1^2/(2V_2)$ at the distance $\Delta = (1-x_{max}) = -V_1/V_2$ from the wall. Hence, $V_1 > 0$. The Poisson equation at $x \to 1$ relates the coefficients V_1, and V_2, $V_2 - V_1 = -G$, where

$$G = S\frac{r_e b}{cT}\sqrt{\frac{2\pi}{T_w}} + \frac{2\pi r_e b^2 n_0}{T\int_0^1 xdxexp[-V(x)]}. \qquad (33)$$

The second term in the right-hand-side is due to the density of the cloud.

To stop secondary electrons to go into the beam pipe, the maximum of the potential V_{max} has to be of the order of T_w/T. V_{max} can be estimated equating the number of particles returning to the cloud to dN_{loss}/ds. Electrons that go back into the beam pipe have to have energy $v^2/(2c^2) > TV_{max}$,

$$(\frac{dN}{ds})_{back} = \frac{s_b}{c}\int_{v/c<-\sqrt{2TV_{max}}} 2\pi r dr dv S f(v)\frac{\delta(r-b)}{2\pi r}$$
$$= \frac{s_b}{c}Se^{-V_{max}T/T_w}. \qquad (34)$$

Substituting S and equating that to $(dN/ds)_{loss} = N_{loss}/L_d$ defined by Eq. (**??**), we get

$$V_{max} = \frac{T_w}{T}\ln[\eta + \frac{YN_\gamma N_b}{N_{loss}}]. \qquad (35)$$

This defines $V_1 = V_2 + G$ and $\Delta = -V_1/V_2$,

$$\Delta = \frac{-V_{max} + \sqrt{V_{max}^2 + 2GV_{max}}}{V_{max} + G - \sqrt{V_{max}^2 + 2GV_{max}}}. \qquad (36)$$

This result has meaning only if $\Delta << 1$, i.e. for the large enough density of the cloud. Otherwise, the height of the potential barrier can not reach T_w and the density keeps building up.

If $G << V_{max}$,

$$\Delta = \frac{2V_{max}}{G}. \qquad (37)$$

For the NLC parameters and $\eta = 1.45$, $\Delta = 0.082$ and $V_{max} = 0.032$ or 2.95 eV.

Although the height of the potential bump at the $r_{max} = b(1-\Delta)$ is small, of the order of T_w, it changes the equilibrium density of the cloud. To see the effect on the average density, let us again integrate the Poisson equation

$$\frac{1}{r}\frac{d}{dr}r\frac{dU_{cl}}{dr} = -4\pi r_e n_{cl}(r) \tag{38}$$

over r with the weight r in the interval $0 < r < r_{max}$. Because U_{cl} is finite at $r = 0$, we get for the average density

$$< n_{cl} > \equiv \frac{2}{r_{max}^2}\int_0^{r_{max}} n_{cl}(r) r dr$$
$$= -\frac{1}{2\pi r_{max}}(\frac{dU_{cl}}{dr})_{r=r_{max}}. \tag{39}$$

The total potential $U(r) = U_{cl} - gT\ln(b/r)$ is maximum at $r = r_{max}$. Therefore, $(\frac{dU_{cl}}{dr})_{r=r_{max}} = -gT/r_{max}$, and

$$< n_{cl} >= \frac{gT}{2\pi}(\frac{1}{r_{max}})^2. \tag{40}$$

Substitution of g from Eq. (6) and $r_{max} = b(1-\Delta)$ gives

$$< n_{cl} >= n_0(\frac{1}{(1-\Delta)})^2. \tag{41}$$

The average density is higher than that given by the condition of neutrality but the difference is small provided $\Delta << 1$.

It is worth noting that, without the potential barrier, primary photo-electrons with positive energy go above the potential well. They add to the average density of electrons but their space charge reduces the density of the cloud in such a way that the total average density is still given by the condition of neutrality.

Electrons reflected by the potential barrier hit the wall again increasing the power deposited to the wall. The power deposited by this mechanism depends on the yields,

$$\frac{dP}{ds} = \frac{c}{s_b}T_w[(\eta-1)\pi b^2 n_0\frac{N_{loss}}{N_{tot}}$$
$$+ \quad YN_\gamma\frac{N_b}{L_d}][1-(1+V_{max}\frac{T}{T_w})e^{-V_{max}T/T_w}] \tag{42}$$

For the NLC DR this contribution is negligible, less than W/m.

Another effect of the secondary electrons trapped at the wall is the introduction of a small azimuthal asymmetry of the potential well for the beam particles. The dipole component of such perturbation may cause an orbit distortion and the quadrupole component leads to the asymmetric dependence of the tune on the beam current. The estimate shows, however, that these effects are small.

7 EFFECT OF THE FINITE BUNCH LENGTH

We assumed everywhere above that a bunch can be described as a point-like macro particle. The finite bunch length may substantially change the number of lost particles from the region near the beam. As it was mentioned in Section 2, the number of oscillations within the bunch length for such electrons is large. (It may be not true for the electrons far away from the beam because the frequency of oscillations decreases with amplitude). The field of a bunch at a given location around the ring varies slowly compared to the period of oscillations and can be considered as an adiabatic perturbation. As it is well known, the amplitude of oscillations in this case returns to the initial value when the perturbation is turned off. It means, that an electron may decrease the amplitude of oscillations while bunch is passing by, but retains the initial velocity and position after the bunch goes away. These arguments mean that the number of the high energy electrons hitting the wall and power deposition are smaller for the larger bunch length. On the other hand, low energy electrons in vicinity of the beam can live there for a long time what would mean larger density at the beam line. From this point of view, it is preferable to have short bunches but with a large bunch current to be in the regime where electrons go wall-to-wall in one pass.

One of implications of the finite bunch length is the betatron tune variation along the bunch. The kick from the head of a bunch causes motion of the e-cloud electrons toward the beam line and increases density of e-cloud in the tail of the bunch. The tune spread is of the order of the tune shift:

$$\Delta Q = \frac{2\pi r_e n_0 < R >^2}{\gamma Q}, \tag{43}$$

where $< R >$ is the average machine radius. The tune spread for the NLC is large, $\Delta Q = 0.0207$ at $n_0 = 2.22\,10^7\ 1/cm^{-3}$. The interaction with the dense jets can change tune of the bunches in the head of the bunch train differently than for the rest of the bunches causing tune variation along the bunch train.

8 EFFECT ON THE WAKE FIELD

The wake field of the cloud with the average density n_0 can be estimated analytically [5, 6]. For a long bunch, the short-range wake per unit length has the form of a single mode

$$W_{bunch}(z) = W_m\frac{2n(\kappa)l_b}{N_b}(\frac{\Omega_B}{c})\sin(\mu\xi)e^{-\frac{\mu\xi}{2Q}}, \tag{44}$$

where the e-cloud density is taken at $r_{min} = b\kappa$ to take into account that the density at the beam line is different than the average density, $\Omega_B/2\pi$ is the linear bunch frequency of oscillations,

$$(\frac{\Omega_B}{c})^2 = \frac{2N_b r_e}{\sigma_y(\sigma_x+\sigma_y)\sigma_z\sqrt{2\pi}}, \tag{45}$$

$\xi = \Omega_B z/c$, $l_b = \sigma_z\sqrt{2\pi}$, and W_m, μ and Q are characteristics of the wake with weak dependence on the aspect ratio σ_y/σ_x and the beam pipe aperture. They were calculated in the reference [6]: $W_m = 1.2$, $\mu = 0.9$, and $Q = 5$.

The bunch shunt impedance R_s per turn

$$\frac{R_s^{bunch}}{Q} = 2\pi R \frac{Z_0}{4\pi} \frac{2n(\kappa)l_b}{N_b} W_m \qquad (46)$$

is $R_s \simeq 2.3$ MOhm/m.

8.1 Transverse coupled bunch instability

For a single bunch stability, $\Omega_B/c = 53\ 1/cm$ and $W_{max} = 4\,10^3\ cm^{-2}$.

To consider the CB instability, the long-range (LR) wake has to be scaled from the short-range wake Eq. (44) replacing the bunch length by s_b and, secondly, using the average density n_0. The maximum value of the LR wake is:

$$W_{LR}(z) = W_m \frac{n_0 s_b}{N_b} (\frac{\Omega_{beam}}{c}), \qquad (47)$$

where

$$(\frac{\Omega_{beam}}{c})^2 = \frac{2N_b r_e}{s_b r_{min}^2}. \qquad (48)$$

Here $r_{min} \simeq N_b r_e s_b/b$ estimates the range of distances $r_{min} < r < b$ where electrons survive after a bunch pass.

The LR shunt impedance R_s^{beam} per turn

$$\frac{R_s^{beam}}{Q} = 2\pi R \frac{Z_0}{4\pi} \frac{n_0 s_b}{N_b} W_m \qquad (49)$$

is $R_s^{beam} \simeq 134$ MOhm/m for the NLC DR nominal parameters, by a factor of two larger than in the simulations [1].

The maximum growth rate of the transverse CB

$$\frac{1}{\tau} = \frac{I_{beam} R_s^{beam}}{(E/e)} \frac{c_0 \beta_y}{4\pi R} e^{-(\Omega/c)_{beam}\sigma_z)^2} \qquad (50)$$

is $\tau = 0.01$ ms.

9 SUMMARY

At high currents, electrons may go wall-to-wall between bunches and electron cloud, in the usual sense, does not exist.

Thermalization of electrons, takes place at a moderate current within some distances from the beam. Even if the number of the linear oscillations per bunch is large, such electrons can be described by the Boltzmann distribution due to randomness of the electron motion.

The jets of primary and secondary electrons may have high density and explain the high energy tail in the distribution of electrons hitting the wall.

A simple model of the e-cloud formations allows us to reproduce main results obtained in simulations explaining the level of the density at saturation and it dependence on the $\gamma - e$ yield. The temperature of the distribution is defined by the condition of the energy equilibrium. The multipactoring does not change the temperature much but rather affects the distribution of electrons in the vicinity of the wall. That explains why the average density of the cloud is close to that given by the condition of neutrality. The final bunch length may change the power deposited to the wall and the density of electrons at the beam line. Interaction with the cloud can cause the tune variation along the bunch train. Transverse CB instability requires strong feedback.

Acknowledgments

I thank M. Pivi for providing us with the results of his simulations and T. Raubenheimer for initiating this study.

10 REFERENCES

[1] Mauro Pivi and M. Furman, Electron cloud in the NLC damping ring, LBNL, September 17, 2001 (unpublished)

[2] Izawa, Y. Sato, and T. Toyomasu, "The Vertical Instability in a Positron Bunched Beam," Phys. Rev. Lett. **74** 5044 (1995).

[3] K. Ohmi, "Beam-Photoelectron Interactions in Positron Storage Rings," Phys. Rev. Lett. **75** 1526 (1995).

[4] H. Fukuma *et al.*, "Observation of Vertical Beam Blow-up in KEKB Low Energy Ring." Proc. EPAC, Vienna, Austria , 2000, p. 1124.

[5] K. Ohmi and F. Zimmermann, "Head-Tail Instability Caused by Electron Clouds in Positron Rings," Phys. Rev. Lett. **85** 3821 (2000).

[6] S. Heifets, Wake field of the e-cloud, SLAC-PUB-9025, 11/2001

[7] K. Satoh and Y.H. Chin, "Transverse Mode Coupling in a Bunched Beam," Nucl. Instr. Meth. **207**, 309 (1983).

11 APPENDIX: RESULTS FOR THE NLC MAIN DR

Parameter	Description	Value
E, (GeV)	beam energy	1.98
C, m	circumference	299.792
β_x, m	horizontal	3.64
β_y, m	vertical	7.06
ν_x, m	horizontal tune	27.261
ν_y, m	vertical tune	11.136
ν_s	synch.tune	0.0035
b, cm	beam pipe radius	1.6
B, T	dipole field	1.2
L_b, m	bend length	0.96
L_d, m	drift length	0.975
E_0, eV	peak of secondary electrons	5.0
E_T, eV	energy spread of secondary electrons	2.0
Y,	photo-electric yield (low/high SR)	0.002/0.2
η,	secondary emission yield,	1.45
s_b, m	bunch spacing	0.84
$N_b\ 10^{10}$	bunch population,	1.5
$e_{x,N}$, mm mrad	norm. x-emitt.	3.86
$e_{Y,N}$, mm mrad	norm y-emitt.	0.018
σ_z, mm	rms bunch length	3.6
$\delta\,10^{-3}$	relat. energy spread	0.909

Table 1: Global parameters for the NLC main damping ring

Parameter	Description	Simul.	Analytic	
I_{beam}, Amp	aver.beam current	0.86	0.86	
n_0, $10^{13}\,m^{-3}$	average density	3.0	2.2	
n_{eff}, $10^{13}\,m^{-3}$,	effective density		3.11	
f_{beam}, MHz	LR wake frequency		152	
f_{beam}/f_{rev}		100-200	152	
W_{LR} period in s_b		4	4.7	
$W^y_{bunch}\,m^{-2}$	short range W_{max}		$4.E7$	
$W^y_{beam}\,10^6\,m^{-2}$	LR W_{max}	0.60	1.4	
R^y_s MOhm/m	SR shunt		2.3	
R^y_s MOhm/m	LR shunt		134	
τ_x ms	LR growth time		0.018	
τ_y ms	LR growth time	0.1	0.01	
$\Delta\nu_y$,	incoher. tune spread		0.021	
T	temperature, eV		92.2	
N_{loss}/N_{tot}	lost per bunch		0.32	
Number of passes to saturat.	(high/low) SR	8/25	7/18	
P_{wall} W/m	power to the wall	80.	87.	
κ	parameter		0.277	0.0694
g	parameter		0.5529	0.743
norm	parameter $\int xdxe^{-V}$		0.614	
V_{max}	potent. bump, eV		0.8	
Δ	parameter		0.067	

Table 2: Comparison of the calculations with simulations [1].

ELECTRON-CLOUD UPDATED SIMULATION RESULTS FOR THE PSR, AND RECENT RESULTS FOR THE SNS. *

M. Pivi and M. A. Furman,† LBNL, Berkeley, CA94720, USA

Abstract

We present recent simulation results for the main features of the electron cloud in the storage ring of the Spallation Neutron Source (SNS) at Oak Ridge, and updated results for the Proton Storage Ring (PSR) at Los Alamos. In particular, a complete refined model for the secondary emission process including the so called true secondary, rediffused and backscattered electrons has been included in the simulation code.

1 INTRODUCTION

The Spallation Neutron Source (SNS) under construction at the Oak Ridge National Laboratory (ORNL), has initiated studies on the possible electron-cloud effect, which may limit the performances of the proton storage ring. A similar high-intensity instability which has been observed in the PSR at the Los Alamos National Laboratory (LANL) for more than 13 years, is now recognized to be, although not conclusively proven, an electron-cloud effect. Since 1987 the PSR has reported a fast instability that is responsible for proton losses and collective beam motion above a certain current threshold, and is accompanied by a large number of electrons. This instability is now believed to be due to the collective coupling between an electron cloud and the proton beam [1, 2]. Such instability is a particular manifestation of the electron-cloud effect (ECE) that has been observed or is expected at various other machines. In this article we present simulation results for the SNS and for PSR ring obtained with the ECE code that has been developed at LBNL over the past 6 years, suitably augmented to deal with very long and intense bunches such as in the case of long proton beams. At the present stage, we have restricted our studies to look in detail at the dynamics of the electron cloud rather than the instability *per se*. Thus in all results presented here, the proton beam is assumed to be a static distribution of given charge and shape moving on its nominal closed orbit, while the electrons are treated fully dynamically. This approximation is valid for stable beam operation, and it is probably reasonable for mild instability. We defer issues like the current instability threshold, growth rate and frequency spectrum to future studies. We compared in [3] our results for the electron current and energy spectrum of the electrons hitting the walls of the chamber against measurements obtained in the PSR by means of dedicated electron probes. From such comparisons we can assess the effects of several important parameters such as the secondary electron yield (SEY) at the walls of the chamber, the proton loss rate and electron yield, etc. Furthermore, we can infer details of the electron cloud in the vicinity of the proton beam, such as the neutralization factor, which is important for a self-consistent treatment of the coupled e-p problem [4].

* Work supported by the SNS project and by the US DOE under contract DE-AC03-76SF00098.

† mpivi@lbl.gov and mafurman@lbl.gov

Table 1: Simulation parameters for the PSR and SNS.

Parameter	Symbol	PSR	SNS
proton beam energy	E, GeV	1.735	1.9
dipole field	B, T	1.2	0.78
bunch population	N_p, $\times 10^{13}$	5	20.5
ring circumference	C, m	90	248
revolution period	T, ns	350	945
bunch length	b_l, ns	254	760
gauss. tr. bunch size	σ_x, σ_y, mm	10, 10	
flat tr. bunch size	r_x, r_y, mm		28, 28
beam pipe semi-axes	a, b, cm	5,5	10,10
proton loss rate	p_{loss}, $\times 10^{-6}$	4	0.11
proton-electron yield	Y,	100	100
No. kicks/bunch	N_k	1001	5001
No. steps during gap	N_g	100	250
SEY params:			
max sec. yield	δ_{max}	2.0	2.0
energy at yield max	E_{max}, eV	300	300
yield low energy el.	$\delta(0)$	0.5	0.5

2 PHYSICAL MODEL

2.1 Sources of electrons

In this article we consider what we expect to be the main two sources of electrons for proton storage rings as the SNS and the PSR, namely: lost protons hitting the vacuum chamber walls, and secondary emission from electrons hitting the walls (we are not interested here in simulating the electron cloud in the vicinity of the stripper foil). Although our code accommodates other sources of electrons, such as residual gas ionization, we have turned them off for the purposes of this article.

2.2 Secondary emission process

We represent the SEY $\delta(E_0)$ and the corresponding emitted-electron energy spectrum $d\delta/dE$ (E_0 =incident electron energy, E = emitted secondary energy) by a detailed model described elsewhere [5]. Its parameters were obtained from detailed fits to the measured SEY of stainless steel (St. St.) [6]. The main SEY parameters are

the energy E_{max} at which $\delta(E_0)$ is maximum, and the peak value itself, $\delta_{max} = \delta(E_{max})$ (see Table 1). Furthermore, for the results shown below, we do take into account the elastic backscattered and rediffused components of the secondary emitted-electron energy spectrum $d\delta/dE$. The backscattered component typically becomes more important at low incident electron energies. To account for this behavior we have used a fit extrapolated data for copper measured at CERN [7].

The value of $\delta(E_0)$ at incident electron energies $E_0 < 10eV$ is an important parameter since it determines the electron accumulation rate, and also the electron survival rate at the end of the gap. This quantity is difficult to measure experimentally, and remains an uncertainty for the model. In our simulations we have made the assumption that $\delta(0) \simeq 0.5$. In this case, the simulated electron density increases by a factor ~ 3 and the peak detector current by almost a factor ~ 2.5, relative to the $\delta(0) \simeq 0.1$ case (refer to previous results for PSR with no rediffused nor backscattered electrons, see [3]). These are examples of strong parameter sensitivity that calls for further experimental investigations.

2.3 Simulation Model

The SNS and the PSR rings store a single proton bunch of length τ_b followed by a gap of length τ_g with a typical current intensity profile shown in Figs. 2 and 4. In our simulation we assume a Gaussian transverse PSR beam with rms sizes $\sigma_x = \sigma_y = 10mm$, , and we use the actually measured longitudinal intensity profile. A flat transverse beam with $r_x = r_y = 28mm$ is assumed for the SNS. We simulate the passage of the proton bunch in a field-free region with a vacuum chamber which we take to be a cylindrical perfectly-conducting pipe. The number of electrons generated by lost protons hitting the vacuum chamber wall is $N_p \times Y \times p_{loss}$ per turn for the whole ring, where Y is the effective electron yield per lost proton, and p_{loss} is the proton loss rate per turn for the whole ring per beam proton. We assume the lost- proton time distribution to be proportional to the instantaneous bunch intensity. The electrons are then simulated by macroparticles. The secondary electron mechanism adds to these a variable number of macroparticles, generated according to the SEY model mentioned above. The bunch is divided up into slices, so that the macroparticles experience N_k kicks during the bunch passage. We divide the interbunch gap into N_g intermediate steps. The space charge force is computed and applied at each slice in the bunch and each step in the gap. The image forces from both protons and electrons are taken into account, assuming a perfectly conducting wall. Typical parameter values are shown in Table 1.

3 RESULTS AND DISCUSSION

The possible amplification mechanism which may take place in long-beam machines is explained in Fig. 1. An electron present in the vacuum chamber before the bunch passage oscillates in the beam well potential, and it is released at the end of the beam passage. Instead, electrons generated at the wall by proton losses at the maximum of the beam pulse are accelerated and decelerated by the beam potential and hit the opposite wall with a net energy gain, producing secondary electrons.

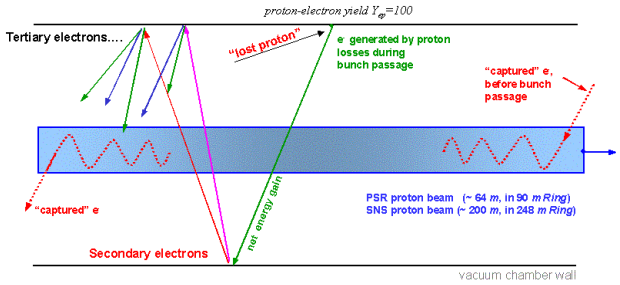

Figure 1: Electron multiplication mechanism in long proton bunches.

Electrons which survive the gap between two bunch passages will increase in number. The electrons gradually increase in number during successive bunch passages until, owing to the space-charge forces, a balance is reached between emitted and absorbed electrons. The build-up of the electron cloud in a PSR field-free region and a dipole section during the passage of the beam is shown in Fig. 2. The saturation level in the PSR is reached after few bunch passages, when assuming $\delta_{max} = 2$. The estimated average number of electrons in a field free region is $\sim 4 \times 10^7 e^-/cm^3$ or $50nC/m$. The neutralization factor or fractional charge neutralization, ratio e^-/p^+, during a bunch passage is shown in Fig. 3.

The SNS beam pipe chamber will be coated with TiN, and recent measurements of an *as-received* SNS sample of the TiN coated vacuum chamber, has shown $\delta_{max} = 2$ [8]. Consistent results where obtained at KEK [9]. The build-up of the electron cloud in the SNS field-free region and a dipole section during the passage of the beam is shown in Fig. 4 for $\delta_{max} = 2$. Due to a large electron multiplication, we have used a very low initial number of macroparticles per bunch passage. The simulations present a signif icant fluctuation in the turn-by-turn electron density, and we are going to refine the code to accomplish for the SNS case. Simulation results for the SNS [10] show a qualitative agreement, but a lower estimated electron density. The neutralization factor during a bunch passage is shown in Fig. 5. The tune shift due to electron neutralization of a factor ~ 1 may be estimated, for example, at 25% beam intensity, by

$$dQ_{ec} = -0.25\, f\, \gamma^2\, dQ_{sc} \sim -2\, dQ_{sc} = -0.4 \qquad (1)$$

where dQ_{sc}=0.2 is the space charge tune shift, $\gamma = 2.066$ is the usual relativistic factor of the beam, and *f* is the neutralization factor. Once the secondary electron yield has decreased to 1.3 and 1.1, we were able to increase signif

icantly the number of macroparticles to account for better statistics. The build-up of the electron cloud during the first few bunch passages is shown in Fig.6.

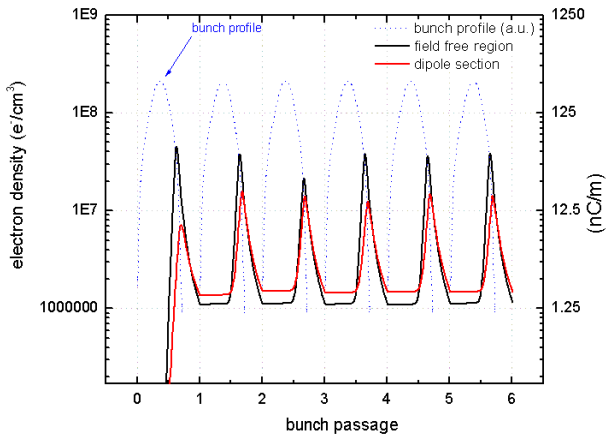

Figure 2: Simulated electron density during the first bunch passages, in a PSR field-free region and a dipole section. The saturation level is reached after few bunch passages.

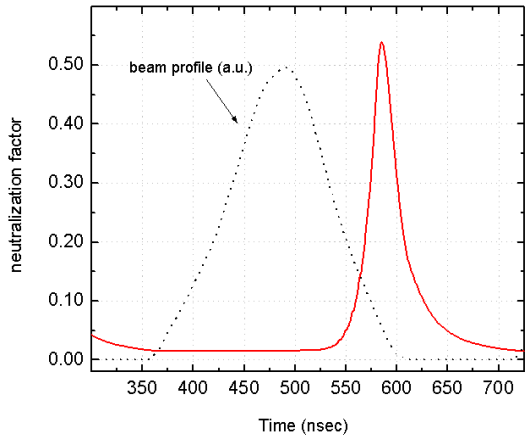

Figure 3: Simulated electron neutralization factor in a PSR field-free region, the fractional charge neutralization reaches 50% at the tail of the bunch.

4 CONCLUSION

A complete refined model for the secondary emission including the so-called true secondary, rediffused and backscattered electrons has been recently included in the code. We present an update of computer simulation results for the main features of the electron cloud at the Proton Storage Ring (PSR) and recent simulation results for the Spallation Neutron Source (SNS). Preliminary simulations for the SNS, show that a density of $\geq 150nC/m$ may be reached in a field-free region, leading to a significant tune shift given by electron neutralization. Due to a large unexpected electron multiplication in the case of the SNS, we have used a low number of macroparticles per bunch passage. The code is going to be implemented to accomplish for the SNS case.

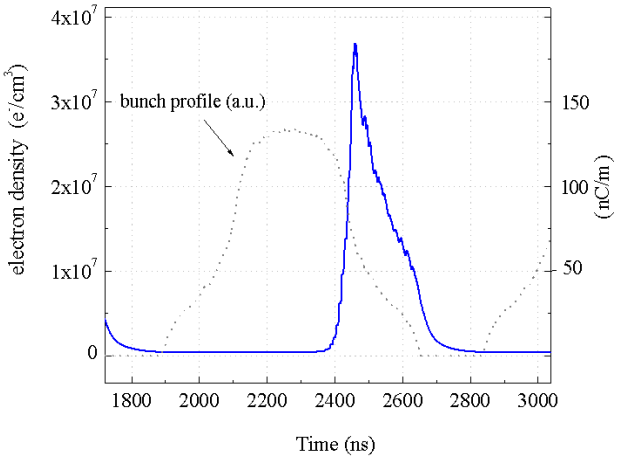

Figure 4: Simulated electron density during the first bunch passages, in a SNS field-free region.

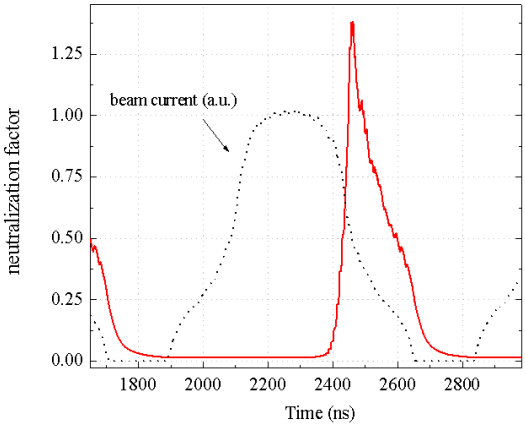

Figure 5: Simulated electron neutralization factor in a SNS field-free region, the fractional charge neutralization exceeds 1 at the tail of the bunch.

5 ACKNOWLEDGEMENTS

We are particularly grateful to our colleagues of the PSR Instability Studies Program for many stimulating discussions, M. Blaskiewicz, K. Harkay, R. Davidson, H. Qin, P. Channell, T. S. Wang. We are especially grateful to R. Macek for discussions and for providing us the experimental data. Thanks to Y.H. Cai, F. Zimmermann, N. Hilleret, J.Wei, A. Wolski, S. Heifets, T. Raubenheimer, R. Kirby, A. Alexandrov, V. Danilov. We are grateful to NERSC for supercomputer support.

6 REFERENCES

[1] For a summary, see: Proc. *ICFA Workshop on Two-Stream Instabilities*, Santa Fe, NM, US, Feb. 16-18, 2000, http://www.aps.anl.gov/conferences/icfa/two-

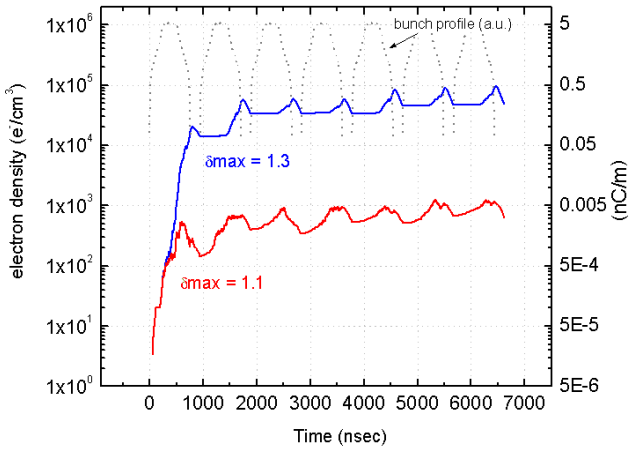

Figure 6: Build-up of the electron cloud in the SNS field-free region assuming a $\delta_{max} = 1.3$ and 1.1. The electrons gradually increase in number during successive bunch passages until, owing to the space-charge forces, a balance is reached between emitted and absorbed electrons.

stream.html, or also *International Workshop on Two-Stream Instabilities in Particle Accelerators and Storage Rings*, at KEK Tsukuba, Japan, September 11-14, 2001, http://conference.kek.jp/two-stream/.

[2] R. Macek, these proceedings.

[3] M. Furman and M. Pivi, Proc. PAC01, Chicago, IL, p. 708.

[4] For an updated on the self consistent treatment of the instability see, for example, Physical Review Special Topic, *Special Collection Edition on Electron Cloud and Two-Stream Interactions in Long-Bunch Proton Beams*, future publication.

[5] M. A. Furman and M. Pivi *Microscopic Probabilistic Model for the Simulation of the Secondary Electron Emission*, LBNL-49711, CBP Note-415, to be submitted to Physics Review ST, May 2002.

[6] R. Kirby, private communication.

[7] V. Baglin, I. Collins, B. Henrist, N. Hilleret, G. Vorlaufer, *A Summary of Main Experimental Results Concerning the Secondary Electron Emission of Copper*, LHC-Project-Report-472.

[8] M. Blaskiewicz, private communication, May 2002.

[9] T. Toyama, K. Ohmi, *Study for ep Instability in High Intensity Proton Ring*, these proceedings.

[10] M. Blaskiewicz *Electron Cloud in the PSR and SNS* these proceedings.

SIMULATION OF HEAD-TAIL INSTABILITY CAUSED BY ELECTRON CLOUD IN THE POSITRON RING AT PEP-II*

Yunhai Cai, SLAC, Stanford, CA 94309, USA

Abstract

The head-tail instability caused by an electron cloud in positron storage rings is studied numerically using a simple model. In the model, the positron beam is longitudinally divided into many slices that have a fixed transverse size. The centroid of each slice evolves dynamically according to the interaction with a two-dimensional electron cloud at a given azimuthal location in the ring and a six-dimensional lattice map. A sudden and huge increase of the projected beam size and the mode coupling in the dipole spectrum are observed in the simulation at the threshold of the instability. Even below the threshold, the vertical beam size increases along a bunch train that has 8.5 ns bunch spacing. Above the threshold, a positive chromaticity can damp down the centroid motion but has very little effect on the blowup of the beam size. The results of the simulation are consistent with many observations at PEP-II.

1 INTRODUCTION

The transverse couple-bunch instability caused by an electron cloud in a positron storage ring was first observed in the spectrum of coherent dipole oscillation in the KEK Photon Factory [1]. The photoelectron produced by the synchrotron radiation is proposed as the primary cause of the instability by Ohmi [2]. He has simulated the production of the photoelectron and showed that the effective wake field due to the electron cloud couples the dipole motion between bunches and hence causes the coupled bunch instability for the positron beam. This instability can be controlled by a strong bunch-by-bunch feedback as demonstrated in the Low Energy Ring (LER) of KEK-B and PEP-II.

However, even with suppressed dipole oscillations, the electron cloud still causes significant emittance growth as observed recently in KEK and PEP-II B-factories [3, 4]. The growth has been explained numerically as a result of head-tail instability caused by the electron cloud by Ohmi and Zimmermann [5]. Since there is no direct experimental confirmation of the proposed theory, it is important to continue the study to establish the link between theory and experiment.

In this paper, we first briefly describe the physics and approximation in the simulation in the section 2 and 3. Then we make a simulation in section 5 and 6 to identify the threshold of the instability both in terms of the emittance growth and mode coupling. In section 7 and 8, we simulate the emittance growth below and above the threshold. Finally, we make a summary of the whole investigation. The focus of the simulation is on the observable in the ring. Where possible, we will make a comparison between experimental observations and the simulation.

There are two main sources of electrons: photoelectrons generated from the synchrotron radiation and secondary electrons from the multipacting on the vacuum chamber. The detail of how the electron cloud is generated can be found in the work by Furman and Lambertson [6]. In this paper, the density and distribution of the electron cloud are treated as an initial input to the simulation. We will concentrate on how the positron beam interacts with the electron cloud once the electrons are generated and reach the saturation density.

2 BEAM AND ELECTRON CLOUD

For the beam and electron cloud, we use a simple simulation model introduced by Ohmi and Zimmermann [5]. In the model, the transverse distribution of the electron cloud is represented by N_m macro particles at a given azimuthal location s in the positron ring,

$$\rho_{\perp}^{e}(\vec{x}_e, \vec{v}_e; s) = \frac{1}{N_m}\sum_{n=1}^{N_m}\delta(\vec{x}_e - \vec{x_e}_n(s))\delta(\vec{v}_e - \vec{v_e}_n(s)),$$

where $\vec{x}_e$ and $\vec{v}_e$ are the transverse coordinate and velocity for the electrons. The distribution of the positron bunch is represented by N_s longitudinal macro slices as illustrated in Fig. 1. All slices are assumed to have a rigid Gaussian distribution of transverse rms sizes (σ_x, σ_y). The centroid of each slice is treated as a dynamical variable in 6D phase space.

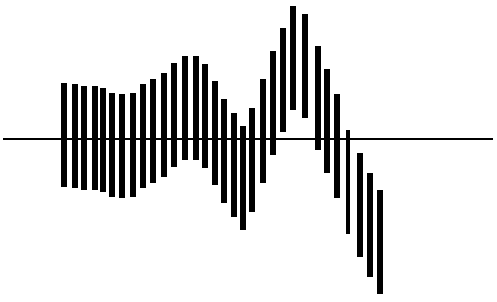

Figure 1: A positron bunch modeled as many longitudinal slices with a rigid transverse Gaussian distribution.

Transversely, we use the 2D vector $\vec{x}_c$ and $\vec{p}_c$ to describe the centroid coordinate and the canonical momentum of the slices. At the beginning of the simulation, all the transverse coordinates and momenta of the slice centroid are set to zero. Longitudinally, the centroid coordinate z and mo-

* Work supported by the Department of Energy under Contract No. DE-AC03-76SF00515

mentum p_z of the slices are initialized to a Gaussian distribution with rms bunch length σ_z and energy spread σ_p respectively.

To speed up the simulation, all electrons are lumped into one single slice at a given azimuthal location s with average β function. This approximation is justified because we know that the head-tail instability is rather insensitive to the location of the impedance. Before the arrival of the positron bunch, the distribution of the electron cloud is re-initialized to a Gaussian distribution with sizes σ_x^e and σ_y^e and the velocities of the electrons are reset to zero. The slices of the bunch are sorted according to their longitudinal positions. Staring with the head, the slices collide with the electron cloud sequentially in time. Under the assumption of a Gaussian distribution, the kick experienced by the i^{th} electron from the electric field of the n^{th} slice is

$$\delta\vec{v_{ei}} = -\frac{2N_b r_e c}{N_s}\vec{F_G}(\vec{x_{ei}} - \vec{x_{cn}}; \vec{\sigma}), \tag{1}$$

where N_b is the number of positron in a single bunch, r_e is the classical electron radius, c is the speed of light, and $\vec{F_G}$ is given by the Erskine-Bassetti formula [7]. The kick by the electron cloud to the centroid of the slice is expressed as

$$\delta\vec{p_{cn}} = -\frac{2r_e N_e}{N_m\gamma}\sum_{i=1}^{N_m}\vec{F_G}(\vec{x_{cn}} - \vec{x_{ei}}; \vec{\sigma}), \tag{2}$$

where N_e is the number of electrons and $N_e = 2\pi\sigma_x^e\sigma_y^e C n_e$ for the electron cloud with an initial transverse Gaussian distribution, C is the circumference of the ring, and n_e is the density of the electron cloud. Note that the distribution of the electron cloud is not directly used in the calculation and the expression is based on the conservation of the momentum. The approximation is valid only when the size of the electron cloud is much larger than the size of the beam. Between the collisions of two adjacent slices the electrons drift, $\delta\vec{x_e} = \vec{v_e} * dz/c$, where dz is the longitudinal distance between two slices.

3 LATTICE MAP

To see the dynamical effects of the positron beam, we track the centroid of the slices with its betatron and synchrotron motions. We first transfer the phase-space coordinates to the normalized coordinates with a matrix,

$$A_x^{-1} = \begin{pmatrix} \frac{1}{\sqrt{\beta_x}} & 0 \\ \frac{\alpha_x}{\sqrt{\beta_x}} & \sqrt{\beta_x} \end{pmatrix}, \tag{3}$$

where β_x and α_x are the Courant-Snyder parameters. Then we perform a rotation and radiation damping on the normalized coordinates by another matrix,

$$R_x = e^{-\frac{1}{\tau_x}}\begin{pmatrix} \cos(2\pi\nu_x) & \sin(2\pi\nu_x) \\ -\sin(2\pi\nu_x) & \cos(2\pi\nu_x) \end{pmatrix}, \tag{4}$$

where ν_x is the betatron tune and τ_x is damping time in unit of turn. Here we apply the radiation damping on the centroid of slice because the centroid of the beam always damps to a closed orbit while the positions of individual positron will be balanced between the noise of quantum excitation and radiation damping to reach a finite beam size. To apply lattice chromaticity, we simply use $\nu_x = \nu_x^0 + \xi_x p_z$. Finally, we transfer the coordinate back to physical phase space with the inverse of the matrix A_x^{-1},

$$A_x = \begin{pmatrix} \sqrt{\beta_x} & 0 \\ -\frac{\alpha_x}{\sqrt{\beta_x}} & \frac{1}{\sqrt{\beta_x}} \end{pmatrix}. \tag{5}$$

In the vertical and longitudinal planes, similar formulas are applied. In the longitudinal plane, we have $\beta_z = \sigma_z/\sigma_p$, $\alpha_z = 0$, and $\tau_z = 0$.

4 PARAMETERS

The LER at PEP-II is a positron storage ring. The current operating parameters are tabulated in Table 1. Wiggler magnets in the machine are turned off for higher luminosity. The bunch charge N_b is chosen to correspond to the peak value in regular operation. The vertical emittance is estimated from the luminosity scan. The other parameters are at their design values which are very close to the measured values.

Table 1: Parameters for the LER at PEP-II

Parameter	**Description**	**Value**
E (Gev)	Beam energy	3.1
C (m)	Circumference	2200
N_b	Number of positrons	1.0×10^{11}
β_x (m)	Average horizontal beta	16.52
β_y (m)	Average vertical beta	17.83
τ_t (turn)	Transverse damping time	9740
ϵ_x (nm-rad)	Horizontal emittance	24.0
ϵ_y (nm-rad)	Vertical emittance	1.50
σ_z (cm)	Bunch length	1.30
σ_p	Energy spread	7.7×10^{-4}
ν_x	Horizontal tune	0.649
ν_y	Vertical tune	0.564
ν_s	Synchrotron tune	0.025

The parameters related to the electron cloud are not yet well established. Based on the recent simulation [8] for the generation of an electron cloud, the saturation density is $n_e^s \simeq 2 \times 10^5 \mathrm{cm}^{-3}$. Since we are interested in only the dynamics of the single bunch in this study, the density is an input parameter in the simulation. The transverse rms sizes of the initial electron distribution when the positron bunch arrives are $\sigma_x^e = 6\mathrm{mm}$ and $\sigma_y^e = 3\mathrm{mm}$. These sizes are much larger than the beam sizes and consistent with the shape of the electron cloud when the density is saturated in the cloud generating simulation.

5 THRESHOLD OF THE INSTABILITY

The algorithm outlined in previous sections has been implemented in an object-oriented C++ class library. In the library, the electron cloud and positron bunch are independent objects that can be constructed by the users. There is no limitation on how many objects of cloud or bunch are allowed in the simulation, and clouds can have different parameters as instances of the cloud class. These features provide us with great flexibility to study various phenomena of the electron cloud instability.

In the simulation, we use a thousand slices for the position bunch and ten thousands macro particles for the electron cloud to ensure a reasonable numerical convergence. The chromaticity is set at zero unless we mention the value explicitly.

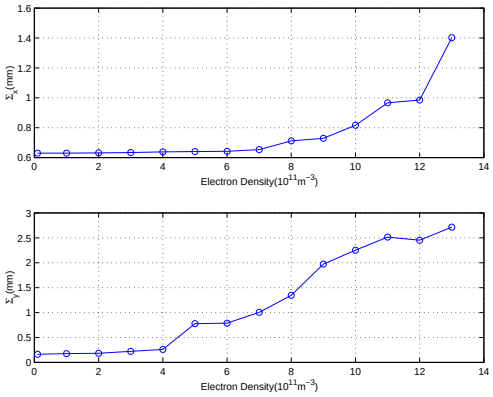

Figure 2: Threshold of head-tail instability caused by electron cloud.

To study the dynamical effects on the positron beam, we vary the density of the electron cloud n_e from 1×10^5 to 1×10^6 cm^{-3}. At each density, we tracked the bunch for 1500 turns. To quantify the emittance growth of the single bunch, we define a projected beam size as $\Sigma_y = \sqrt{\sigma_y^2 + \sigma_y^{c\,2}}$, where σ_y^c is the rms spread of slice centroid. This projected beam size can be measured with a synchrotron light monitor.

The projected beam size at end of the tracking are plotted as a function of the cloud density in Fig. 2. It is clear from the figure that the relative growth of the beam size is much larger in the vertical plane than in the horizontal plane. There is a sudden and huge increase of the beam size in the vertical plane near the density $n_e^{th} = 5 \times 10^5$ cm^{-3}, which we call the threshold of the emittance growth caused by the electron cloud. It will become clear in the next section that it is the also the threshold of the head-tail instability.

Beyond the threshold, the projected beam size becomes much larger than the initial beam size. The increase of emittance significantly reduces the luminosity in the collider and therefore B-factories are limited by this effect in general. Once the instability occurs, the growth time is on the order of the synchrotron period, that is about 40 turns in the simulation. The growth time becomes shorter as the density increases. Below the threshold, there is still sizable growth of the emittance. That will be the subject of a latter section.

6 DIPOLE SPECTRUM AND MODE COUPLING

The head-tail instability can be driven by conventional impedance from the radio-frequency cavities. The effects have been simulated by Myers [9]. For impedance induced by the electron cloud, similar effects should apply. Here we analyze the Fourier spectrum of the beam centroid that is calculated as an average of the slice centroid. The vertical dipole spectra at five different densities below the threshold density n_e^{th} are shown in Fig. 3. We can see from the figure that all modes are shifting upward as the density increases because of the coherent tune shift generated by the electron cloud. Due to the focusing effect of the electron cloud, the modes shift in the opposite direction of its conventional counterpart, in which the zero mode is shifting downward as the impedance increases.

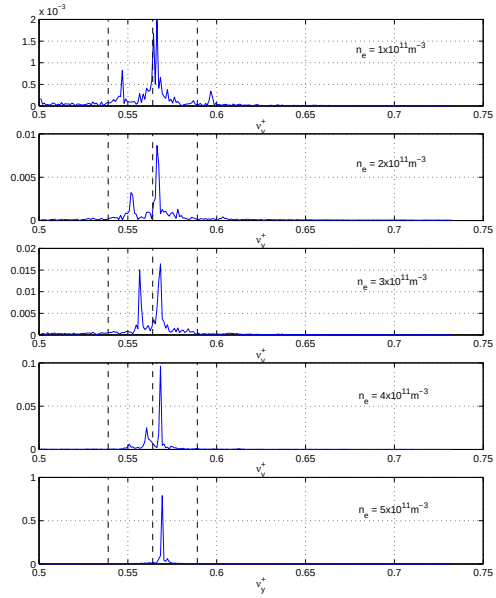

Figure 3: Fourier spectrum of the beam centroid as the density of the electron cloud increases to the threshold. The dashed lines present the betatron tune and synchrotron sidebands.

Since the "$l = -1$" mode, which starts at the lower synchrotron sideband, moves faster than the "$l = 0$" mode starting at the betatron tune, two modes finally merge with each other at the threshold density n_e^{th} as shown in Fig. 3. This behavior is called mode coupling in the literature [10]. The density at which two modes merge is the threshold of the strong head-tail instability. Note that this threshold coincides with the one at which a sudden and huge growth of emittance occurs as we discussed in the last section.

These beam spectra can be measured with a standard spectrum analyzer. The observation of twin peaks that approach each other as the beam current increases is very important experimental evidence to confirm that the head-tail instability is indeed the cause of the single-bunch emittance growth. Since the electron cloud can be generated only when the total beam current is very high and there are many bunches in the ring, the measurement needs to be carried out under the setting of multi-bunch operation although the head-tail instability itself is a single-bunch effect.

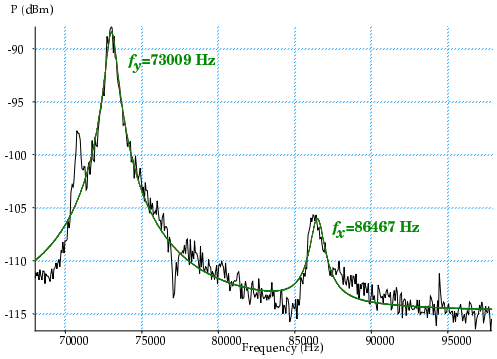

Figure 4: A measurment of the vertical spectrum in the LER with a single beam, 762 bunches with mini gaps and 5% abort gap. The green line is a fit of a double-Lorentzian squared to the data. Squared because this are power spectrum. (Courtesy of Uli Wienands, 2002.)

A measurement of the vertical dipole spectrum at 939mA beam current with bunch spacing $s_b = 8.5\text{ns}$ has been carried out for the LER at PEP-II and shown in Fig. 4. The measured spectrum matches well to the simulated spectrum shown in the first plot in Fig. 3 in terms of the direction and value of the mode shift. The agreement indicates that the electron cloud density is about $n_e \simeq 1 \times 10^5\text{cm}^{-3}$ when the beam current is near 1A in the ring. This density is half of the saturated density in the recent simulation for generating the cloud as we mentioned earlier. The density is also below the threshold density n_e^{th}. The density is about 1% of the average neutralization density $N_b/(\pi h_x h_y L_b)$, where h_x and h_y are the half aperture of the horizontal and vertical chamber respectively, and L_b is the bunch spacing. This ultra low density of the electron cloud near the beam may be attributed to the solenoid winding on the beam pipe.

7 BEAM BLOWUP ALONG A BUNCH TRAIN

In general, when a bunch train is used in the ring, the electron cloud density along the train fits well to the equation

$$n_e(t) = n_e^s[1 - \exp(-t/\tau)], \qquad (6)$$

where τ is the time constant to reach the saturation density n_e^s. For the current operation of the PEP-II, we use a single long train with bunch spacing $s_b = 8.5\text{ns}$ and 5% abort gap. In this bunch pattern, $n_e^s = 2 \times 10^5\text{cm}^{-3}$ and $\tau = 50\text{ns}$ based on the recent simulation [8] for the cloud generation. Clearly, the density in the ring is below the head-tail threshold $n_e^{th} = 5 \times 10^5\text{cm}^{-3}$. However, there is still sizable emittance growth below n_e^{th} as we have noticed in the previous simulation.

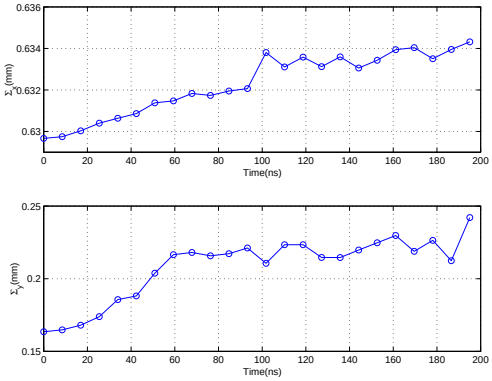

Figure 5: Beam size increase along a bunch train with 8.5ns bunch spacing.

To study in detail the emittance growth below the threshold density, we track the first 20 bunches in the train up to 5000 turns. Each bunch interacts with an electron cloud with the density according to Eqn. 6. The projected beam size at the end of the tracking is shown in Fig. 5. We can see a 30% increase of the vertical beam size along the train. The increase is consistent with the observation seen at KEK-B [3] although the parameters of the rings may differ. It is also consistent with the bunch-by-bunch luminosity measurement [11] at PEP-II. That indicates again, independently, that the density in the ring is quite low compared to the neutralization density.

8 EFFECT OF CHROMATICITY

As we have shown in the simulation, the strong head-tail instability occurs at a threshold density when chromaticity is set at zero. Beyond the threshold, the beam size increases dramatically. The chromaticity is known for stabilizing the conventional head-tail instability. In this section, we will study the effects when the instability is driven by the electron cloud.

We track a bunch through 1500 turns at different vertical chromaticity ranging from -10 to 10 with a fixed density $n_e = 8 \times 10^5\text{cm}^{-3}$ which is above the threshold density n_e^{th}. The turn-by-turn dipole motion of the bunch is plotted in Fig. 6 at three settings of chromaticity: namely +2, 0, and -2. As clearly shown in the figure, the positive chromaticity damps down the unstable motion, the negative chromaticity actually magnifies the motion, and at zero chromaticity, the modulation of synchrotron oscillation stabilizes the motion to a finite amplitude.

The most machines are likely operated with the positive chromaticity that significantly suppresses the dipole motion

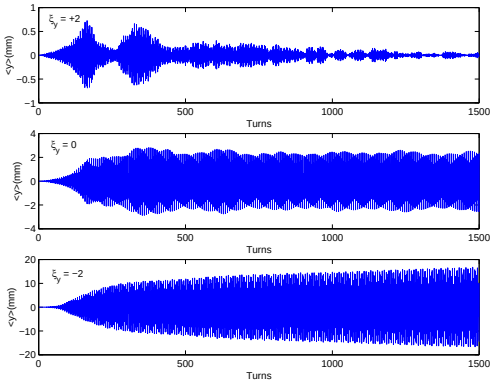

Figure 6: Evolution of beam centroid with three different chromaticities: +2, 0, and -2.

as shown in the simulation. That explains why the mode coupling in the dipole spectrum is so hard to be observed. To make a measurement, one has to set the chromaticity near zero.

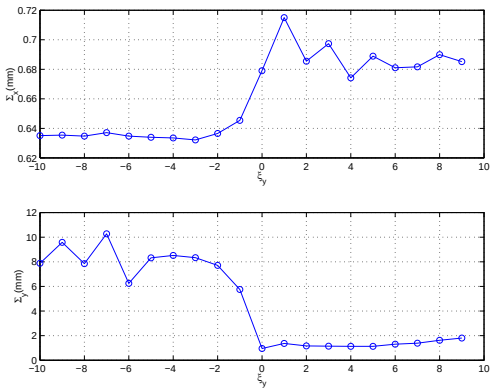

Figure 7: Projected vertical beam size as a function of vertical chromaticity.

The effect of chromaticity on the beam size is shown in Fig. 7. One can see that the positive chromaticity up to 10 units does not change the beam size and the negative one makes a very large blowup in beam size. This behavior is consistent with the experimental observation at PEP-II.

9 SUMMARY

Dynamical interaction between the positron bunch and electron cloud has been simulated in a simple model. We find that the density threshold of the strong head-tail instability is $n_e^{th} \simeq 5\times10^5\mathrm{cm}^{-3}$, which is approximately 5% of the neutralization density. At the threshold, we see the two modes merging into a single mode and a sudden and huge increase of the beam size. Even below the threshold, the beam size still blows up significantly. Based on comparison to experimental observation, we can conclude that the LER at PEP-II is operated (or limited) below the threshold density. The cloud density near the beam is a small percentage of the neutralization density when the ring is operated the regular bunch pattern and beam current.

It is surprising that such a simple model can explain so many experimental observations. In the model, the main mechanism of the beam blowup is explained with the spread of the transverse centroid of the longitudinal slides.

Many additional simulations have been done for the investigation. Here, we will summarize the main results. Although they are many parameters related to the dynamics, the important ones are the beam energy and intensity, bunch length, average beta function, chromaticity, and synchrotron tune. In general, a higher energy, lower beta function, and shorter synchrotron period alleviate the head-tail instability. The positive chromaticity suppresses the unstable dipole motion but has litter effect on the beam size when the density is above the threshold. The Landau damping from the tune spread generated by the second order perturbation of the very strong sextupoles in the ring is not large enough to damp down the instability.

Once the instability starts, we can do little about the vertical blowup of the beam size. The huge emittance growth reduces the single bunch luminosity, limits the total currents in the storage ring, and hence limits the total luminosity.

We have ignored analytical approach to the instability in this paper. The analytical treatment has been covered by Heifets in this proceeding. The wake field for a coasting beam extracted from this code has been compared to his analytical result. The agreement is very good. So we expect similar results can be obtained with analytical estimate.

There is still one of puzzle remained to be resolved: The beam size blowup is also observed in the horizontal plane in PEP-II while the blowup always occurs in the vertical plane in the simulation. One possible explanation for this discrepancy is due to the large coupling that is not yet included in the simulation.

10 ACKNOWLEDGMENTS

I would like to thank M. Furman, S. Heifets, M. Pivi, and J. Seeman for their collaboration. I would also like to thank F.-J. Decker, R. Holtzapple, A. Kulikov, K. Ohmi, and especially U. Wienands for many helpful discussions and sharing the experimental data and NERSC for supercomputer support.

11 REFERENCES

[1] M. Izawa, Y. Sato, and T. Toyomasu, "The Vertical Instability in a Positron Bunched Beam," Phys. Rev. Lett. **74** 5044 (1995).

[2] K. Ohmi, "Beam-Photoelectron Interactions in Positron Storage Rings," Phys. Rev. Lett. **75** 1526 (1995).

[3] H. Fukuma *et al*, "Observation of Vertical Beam Blow-up in KEKB Low Energy Ring," Proc. EPAC, Vienna, Austria, 2000, p. 1124.

[4] A. Kulikov, *et al*, "The Electron Cloud Instability at PEP-II," Proc. PAC, Chicago, 2001, p. 1903.

[5] K. Ohmi and F. Zimmermann, “Head-Tail Instability Caused by Electron Clouds in Positron Rings,” Phys. Rev. Lett. **85** 3821 (2000).

[6] M. A. Furman and G. R. Lambertson, Proc. Intl. Workshop on Multibunch Instabilities in Future Electron and Positron Acceletors(BMI-97), KEK, Tsukuba, Japan, 15-18 July 1997.

[7] M. Bassetti and G. Erskine, CERN ISR TH/80-06 (1980).

[8] M. Pivi, Private communication.

[9] S. Myers, Proc. IEEE Part. Conf., Washingtaon, 1987, p. 503.

[10] A. W. Chao, *Physics of Collective Beam Instabilities in High Energy Accelerators* (Wiley-Interscience Publication, New York, (1993).

[11] F.-J. Decker, *et al*, “Complicated Bunch Pattern in PEP-II,” Proc. PAC, Chicago, 2001, p. 1963.

Electron Cloud Simulations: Beam Instabilities and Wake Fields

G. Rumolo and F. Zimmermann
SL/AP, CERN, Geneva, Switzerland

Abstract

HEADTAIL is a simulation programme developed at CERN which is aimed at studying the single-bunch instability arising from the interaction on successive turns of a single bunch with the cloud generated by the previous bunches. The code includes chromaticity, space charge tune spread, broad-band impedance and detuning with amplitude for more realistic simulation. Examples of application are shown. Transverse and longitudinal wake functions are also outputs of the HEADTAIL code.

1 INTRODUCTION

Two different aspects of the electron-cloud phenomenon are modelled and simulated by means of the two programmes ECLOUD [1] and HEADTAIL, developed at CERN.

The first program ECLOUD simulates the build up of the electron cloud during the passage of a bunch train. It provides information on the transverse electron distribution inside the vacuum chamber, the time evolution of the total number of electrons, the energy spectrum of electrons impinging on the wall, and the corresponding heat load [2]. These outputs have already proven extremely interesting both for comparison with existing data on the electron cloud in the SPS [3, 4, 5] and for extrapolation to the LHC, like the estimation of heat load [6] or of the pressure rise in the experimental areas [4]. Furthermore, the electron density value at saturation can be used as an input to study the possible destabilizing effect of the cloud on a bunch that goes through it.

The second program HEADTAIL models the interaction of a single bunch with an electron cloud on successive turns. The cloud is assumed to be generated by the preceding bunches, and is generally assumed to be initially uniform, although other initial distributions can be considered. As observed above, its density is inferred from parallel simulations with the ECLOUD code. The electrons give rise to a head-tail wake field, which amplifies any initial small deformation in the bunch shape, *e.g.*, due to the finite number of macroparticles in the simulation. Without synchrotron motion, the resulting instability resembles the beam break up in a linac [7, 8]. If synchrotron motion is included, the instability becomes similar to a regular Transverse Mode Coupling Instability (TMCI) [9]. It induces a transverse centroid motion of the longitudinal bunch slices and also a substantial emittance growth. In our simulation, the interaction between beam and cloud is calculated by computing the electric fields of either species on a two-dimensional grid, from which we then deduce the force exerted on the macroparticles of the opposite species. The code optionally includes nonzero chromaticity in both transverse planes, the additional effect of a broad-band resonator, space charge or beam-beam, and amplitude detuning. Electrons can evolve in a field-free region or in different magnetic field configurations (strong dipole, solenoid or combined function magnet).

HEADTAIL can be used to compute the single bunch transverse wake field, the single bunch instability threshold, and the instability growth rate above the threshold. It also contains all the necessary information to extract the longitudinal wake field and the resulting potential-well distortion. Moreover, the structure of the program easily allows us to isolate single effects or to study the synergy between them. Detailed description of the code structure and applications are presented in the following sections.

2 DESCRIPTION OF THE SIMULATION CODE HEADTAIL

The electron cloud can act as a short-range wake field, and drive a single bunch instability [10, 11]. Such kind of instability is held to be responsible for the vertical emittance blow-up that is observed at the KEK B factory [12], and also for that in SPS. Next we describe the model that we have employed to simulate single bunch effects due to the electron cloud.

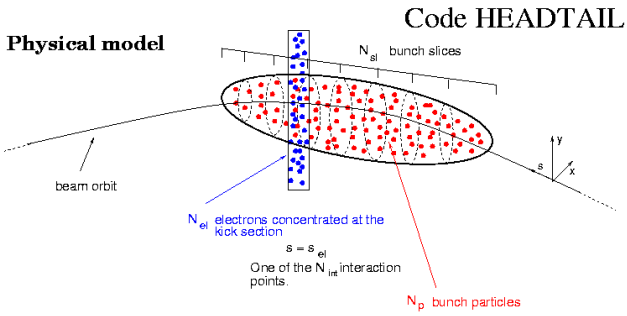

Figure 1: Schematic of the simulation recipe.

A proton or positron bunch interacts with the electron cloud during its passage. When we study the single-bunch effects of the electron cloud, only perturbations of the cloud induced by the passing bunch are considered. All the relevant bunch and lattice parameters, as well as the average equilibrium density of the electron cloud along the ring, are basic input parameters for the simulation of the coupled motion between bunch and cloud electrons. For sim-

plicity, the kick approximation is used for the action of the electron cloud on the bunch: the cloud is assumed to be localised at one or more definite positions along the ring, $s = n \times s_{\rm el}$ with $n = 0, 1, .., (N_{\rm int} - 1)$. Both the cloud and the bunch are modelled as ensembles of macro-particles (with $N_{\rm p}$ bunch macro-particles and $N_{\rm e}$ macro-electrons in the cloud). The bunch is also divided into $N_{\rm sl}$ slices, which interact with the electron cloud after one another and cause the distortion of the initially uniform cloud distribution that can significantly affect the tail of the bunch. The principle of the simulation is illustrated in Fig. 1. The interaction between bunch particles and cloud electrons is expressed by the equations of motion:

$$\frac{\mathrm{d}^2 \underline{x}_{\rm p,i}(s)}{\mathrm{d}s^2} + \underline{\underline{K}}(s)\underline{x}_{\rm p,i}(s) = \left(\frac{\mathrm{e}}{\gamma \mathrm{m_p c^2}}\right) \cdot \cdot \sum_{n=0}^{N_{\rm int}-1} \underline{E}_e(\underline{x}_{\rm p,i}(s); f_{\rm e}(x,y,t))\delta(s - n s_{\rm el}) \quad , \quad (1)$$

$$\frac{\mathrm{d}^2 \underline{x}_{\rm e,j}}{\mathrm{d}t^2} = -\left(\frac{\mathrm{e}}{\mathrm{m_e}}\right)\left(\underline{E}_p(\underline{x}_{\rm e,j}; f_{\rm p,SL}(x,y)) + + \frac{\mathrm{d}\underline{x}_{\rm e,j}}{\mathrm{d}t} \times \underline{B}_{\rm ext}\right) \quad , \quad (2)$$

where the positions of electrons and bunch particles are represented by the vectors $\underline{x}_{\rm e} \equiv (x_{\rm e}, y_{\rm e})$ and $\underline{x}_{\rm p}(s) \equiv (x_{\rm p}, y_{\rm p}, z_{\rm p})$, $z = s - ct$ being a co-moving longitudinal coordinate; $\underline{\underline{K}}(s)$ is the transfer matrix with the focusing strengths between two interaction points; $f_{\rm e}(x,y)$ and $f_{\rm p,SL}(x,y)$ represent the distribution functions of the electron cloud and of the bunch particles contained in one slice, respectively; $\underline{E}_{e,p}$ is the electric field of the electrons and of the beam, respectively, calculated by means of a Particle-In-Cell (PIC) algorithm adapted to our code from D. Schulte's Guinea-Pig code for beam-beam studies; $\underline{B}_{\rm ext}$ is an external magnetic field that can significantly influence the electron dynamics in the region where the cloud is expected to be the strongest. The field of the electron cloud acting on itself can optionally be included [13], though the effect during the bunch passage is small in most cases, and hence it is normally neglected.

The momentum changes of electrons and beam macro-particles due to their mutual attraction are computed in time steps that correspond to the different longitudinal slices into which the bunch is subdivided. Between two interactions, the bunch is propagated around the arcs of the storage ring, where the betatron motion in both planes is modelled by a rotation matrix. Synchrotron motion is also included. Hence, the beam macro-particles slowly interchange their longitudinal positions, and in particular can move across slices between turns. The effect of chromaticity is modelled by an additional rotation matrix which depends on the energy of each particle. With a further rotation, the tune shift due to space charge or beam-beam can be introduced in the bunch motion. Depending on whether this last rotation is applied around the center of the chamber or around the center of each individual bunch slice $\bar{x}(z)$, it models either a beam-beam interaction or a space charge force. Amplitude detuning is optionally introduced as a tune dependence on the single particle actions, $I_{x,y}$. Finally, a regular transverse impedance, represented by the broad-band resonator

$$Z_{1\perp} = \frac{\omega_R}{\omega} \frac{Z_t}{1 + \mathrm{i}Q\left(\frac{\omega_R}{\omega} - \frac{\omega}{\omega_R}\right)} \quad ,$$

can optionally be included. Putting it all together, the transverse phase space coordinates of the generic bunch macro-particle are transformed over one turn according to:

$$\begin{pmatrix} x_{n+1} \\ x'_{n+1} \end{pmatrix} = \mathbf{M}_1(\delta p) \cdot \mathbf{M}_2(I_x, I_y) \cdot \cdot \left[\mathbf{M}_{\rm sc}(z) \begin{pmatrix} x_n - \bar{x}(z) \\ x'_n + \Delta x'_{\rm EC,Z} - \bar{x'}(z) \end{pmatrix} + \begin{pmatrix} \bar{x}(z) \\ \bar{x'}(z) \end{pmatrix}\right] \cdot$$

Table 1: SPS parameters used in the simulations.

variable	symbol	value
Circumference	C	6900 m
Beam momentum	p	26 GeV/c
Chamber half width	h_x	70 mm
Chamber half height	h_y	22.5 mm
Bunch population	N_b	10^{11}
Rms bunch length	σ_z	30 cm
Rms energy spread	$\delta p/p_0$	0.0011
Slip factor	η	5.78×10^{-4}
Synchrotron tune	Q_s	0.0022
Betatron tune	$Q_{x,y}$	26.6
Average beta function	β	15 m
Rms hor. beam size	σ_x	3 mm
Rms vert. beam size	σ_y	2.3 mm
Chromaticities	$\xi_{x,y}$	up to 0.4
Electron-cloud density	ρ_e	10^{12} m^{-3}
Vertical shunt impedance	Z_t	20 MΩ/m
Quality factor	Q	1
Resonant frequency	ω_R	$2\pi\times$ 1.3 GHz

3 SIMULATION OF THE ELECTRON CLOUD INDUCED INSTABILITY AT THE CERN SPS

As explained above, our code tracks electrons transversely along each bunch passage, and bunch particles over many turns.

The simulated electron motion reveals how electrons are progressively focused towards the bunch region as the bunch goes by. In Fig. 2 the electron phase spaces and distributions are shown, as they appear at the end of the interaction with one bunch (having started from transverse uniform distributions). The simulation has been performed

here with the PIC code; the agreement with the evolution predicted by a soft-Gaussian approximation is excellent, as may be deduced from the pictures in Ref. [14].

As far as SPS simulations are concerned (for parameters,

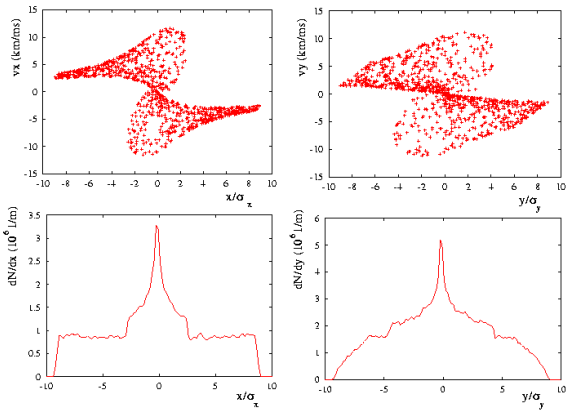

Figure 2: Horizontal and vertical phase space of the electrons after a bunch has gone through (top pictures), and relative distributions (bottom pictures).

see Table 1), It is interesting to observe in Fig. 3 how an SPS bunch containing $N_b = 8 \times 10^{10}$ protons would suffer a strong dipole mode instability under the effect of the broad-band impedance alone, but now this effect gets actually damped by space charge and enhanced by the electron cloud. The instability manifests itself only in the vertical plane. There are at least two good reasons to account for that: firstly, in the vertical plane the impedance is larger [15], and secondly, there is evidence that in the SPS the electron cloud is mostly localised in the arcs, where there is a strong vertical magnetic field and therefore the electrons are mostly pinched vertically by the passing bunch. A positive chromaticity can strongly damp the instability, as shown in Fig.4 where the emittance growth over 12 ms is plotted for three different values of chromaticity.

In the SPS at 26 GeV/c space charge seems to play a

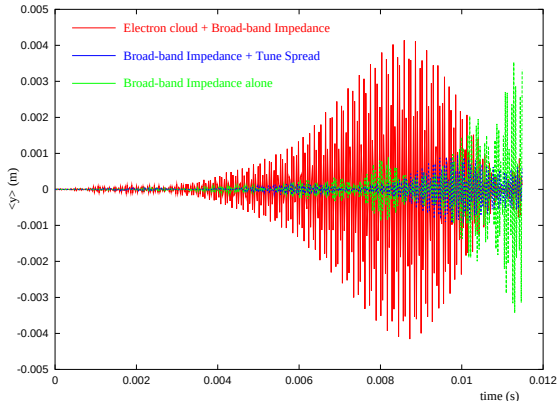

Figure 3: Evolution of the centroid vertical position of an SPS bunch over 500 turns for the three labelled cases.

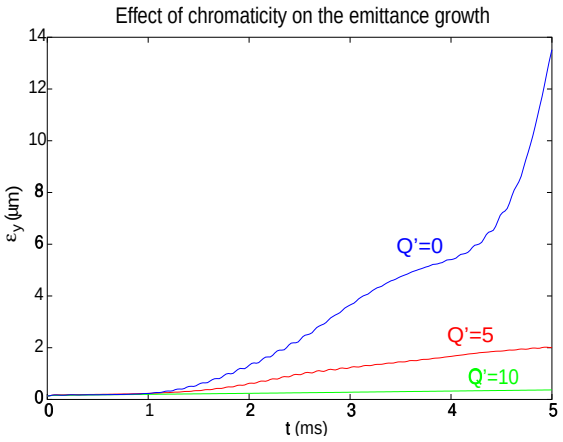

Figure 4: Vertical emittance versus time for three different values of chromaticity. Broad band impedance [15] and space charge are included.

key role, since it actually causes a coherent centroid motion even where electron cloud alone would cause only incoherent emittance growth. Comparison of Figs. 5 and 6 reveals that space charge renders the beam motion more unstable and violent. In particular, it leads to slice centroid oscillations along the bunch. On the other hand, the simulation without space charge shows only a persistent emittance growth, occurring more or less uniformly along the bunch. The different signatures of the simulated instability for these two cases resemble the difference between the actual beam observations at SPS and KEKB. At the SPS injection momentum of 26 GeV/c, the beam is still affected by space charge forces, which according to our simulations might be a reason for the observed difference.

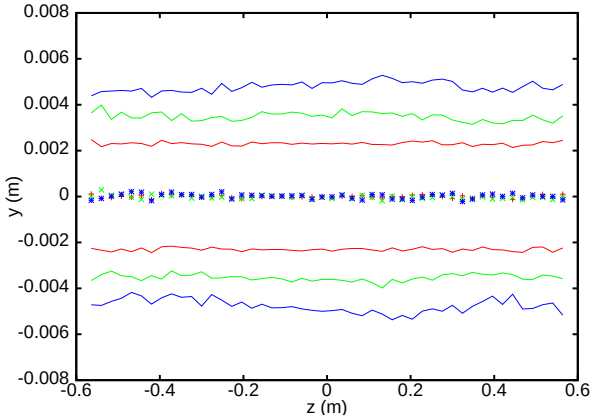

Figure 5: Simulated vertical bunch shape (centroid and rms beam size) ater 0, 250, and 500 turns in the CERN SPS without proton space charge.

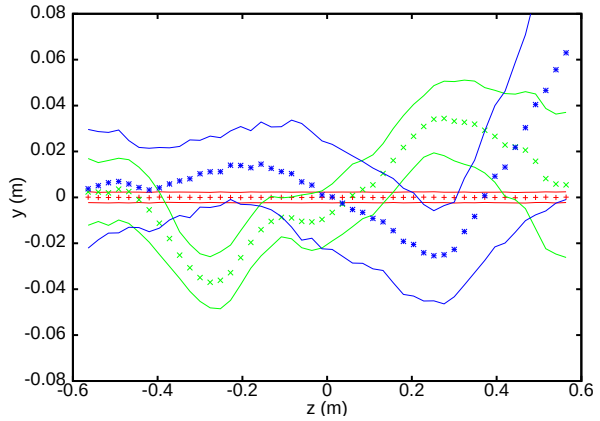

Figure 6: Simulated vertical bunch shape (centroid and rms beam size) ater 0, 250, and 500 turns in the CERN SPS with proton space charge at 26 GeV/c.

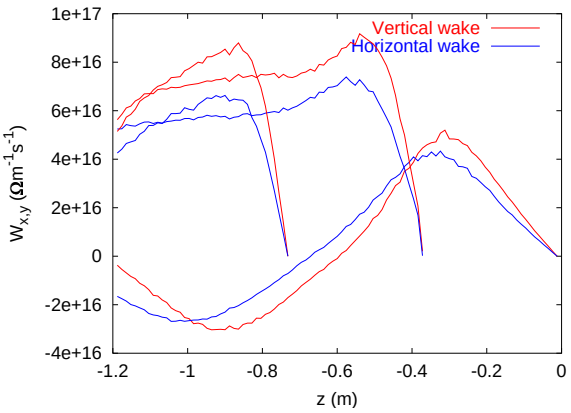

Figure 7: Horizontal and vertical averaged dipole wake functions for a uniform SPS bunch, evaluated displacing three different bunch slices at $t = 0, 3/10\Delta t_b, 3/5\Delta t_b$. The simulation has been carried out in field-free region.

4 TRANSVERSE AND LONGITUDINAL WAKE FIELDS IN THE CERN SPS

Also wake fields can be calculated by using the HEADTAIL code. In the simulation, we displace one bunch slice (for instance, vertically by an amount $\Delta y \propto \sigma_y$), and then we evaluate the electron cloud response in terms of electric field on axis ($x = y = 0$). Normalizing this field by the amount of displacement and the number of particles contained in the displaced slice, we obtain the dipole wake function on axis (in $\Omega s^{-1}m^{-1}$, after multiplication by the factor $m\gamma c^2/e^2$). As the field on axis is not directly related to the force exerted by the cloud on the slices that follow the displaced one, we can also evaluate an averaged dipole wake function from the net force caused by a displaced slice on later portions of the beam. In this case, instead of looking only at the field on axis, we calculate the overall force exerted by the distorted cloud on all the particles contained in one slice, and then divide by the total charge in that slice to obtain an effective electric field. Shapes in the two cases appear quite different, as shown in Figs. 7 and 8. Note that the two definitions of the wake would yield the same result for a conventional dipole wake field. Wake functions on axis reach much larger values and exhibit a spiky structure that is smoothed out to a more regular profile when the integration over the bunch slice is carried out. These plots correspond to an almost round beam in an SPS field-free region and are calculated for a longitudinally uniform bunch distribution. In a dipole region, the horizontal wake tends to disappear, and the vertical one becomes also weaker (see Fig. 9). Fig. 10 shows the averaged dipole wake function for offset first slice and a Gaussian bunch distribution in a dipole field region.

Even though the kick approximation allows us to use a two-dimensional model to study transverse effects, the electron cloud is in reality distributed more or less uniformly around the ring, and thus generates a longitudinal wake field which may give rise to potential well distortion and eventually micro-wave instability. The longitudinal field arises primarily from the accumulation of electrons near the center of the bunch during its passage. The code HEADTAIL does not directly compute the longitudinal electric field. However, we can obtain the latter from the time evolution of the transverse electron distribution. The idea consists in reconstructing the 3-dimensional electron distribution by identifying the time during the bunch passage with the longitudinal position along the bunch. This distribution can then be post-processed in order to compute the longitudinal electric field on a 3-dimensional grid. We assume that the initial electron distribution is unperturbed and uniform, and assign a homogeneous charge distribution to the region of the grid which lies in front of the bunch. The electric field is calculated on the 3-D grid points using a cloud-in-cell algorithm, and is then multiplied by the factor $\Delta z/C$ to account for the fact that the real electrons are distributed all around the circumference C. Figure 11 displays the longitudinal electric field $E_z(z)$ due to the electron cloud simulated for a Gaussian bunch

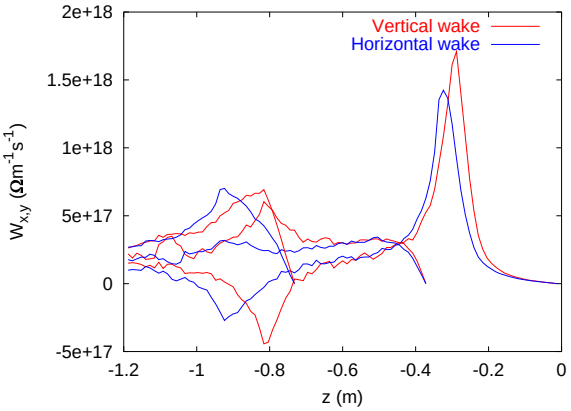

Figure 8: Horizontal and vertical wake functions on axis for a uniform SPS bunch, evaluated displacing three different bunch slices at $t = 0, 3/10\Delta t_b, 3/5\Delta t_b$. The simulation has been carried out in field-free region.

in the SPS. The bunch profile is also indicated. The field is negligibly small (in agreement with the estimation from a full 3-D plasma physics code [16]), less than 10 V/m. To estimate the possible bunch distortion due to this field, we assume a Gaussian energy distribution and compute the longitudinal bunch profile expected for the electron-cloud potential well using

$$\rho(z) = \rho(0)\exp\left[-\frac{1}{2}\left(\frac{\omega_s z}{\eta c\sigma_\delta}\right)^2 - \frac{r_0}{\eta\sigma_\delta^2\gamma C}\int_0^z \mathrm{d}z'\int_{-\infty}^{z'}\mathrm{d}z''\rho(z'')W_0(z'-z'')\right] = \\ = \rho(0)\exp\left[-\frac{1}{2}\left(\frac{\omega_s z}{\eta c\sigma_\delta}\right)^2 - \frac{r_0}{\eta\sigma_\delta^2\gamma C}\int_0^z \mathrm{d}z' W(z')\right], \quad (3)$$

where the longitudinal wake $W(z)$, wake function from a Gaussian bunch, is related to the longitudinal electric field estimated from the HEADTAIL code by

$$W(z) \approx \frac{E_z(z)}{\mathrm{e}}\left(\frac{4\pi}{Z_0 c}\right) C\,.$$

We like to call Eq. (3) the *quasi-Haissinski solution*. Unlike the real Haissinski equation [18] for an ordinary wake fiel, Eq. (3) is not self-consistent, since the field $E_z(z)$ on the RHS varies with the beam distribution in an unknown way. As reported in the first equality of Eq. (3), valid for a regular wake, the wake field can be expressed as a convolution between the distribution function and the Green function wake W_0: the equation can then be solved numerically for $\rho(z)$. For the electron cloud case, such Green function W_0 is not known, and it may not even exist owing to violations of linearity and time invariance.

Nevertheless, we can use Eq. (3) to compute the bunch profile which would be formed under the influence of the additional electric field $E_z(z)$ (neglecting its dependence on the bunch profile itself), and compare this with the initial distribution. A discrepancy would indicate a significant potential-well distortion, and therefore would require a few more iterations to determine the self-consistent bunch profile.

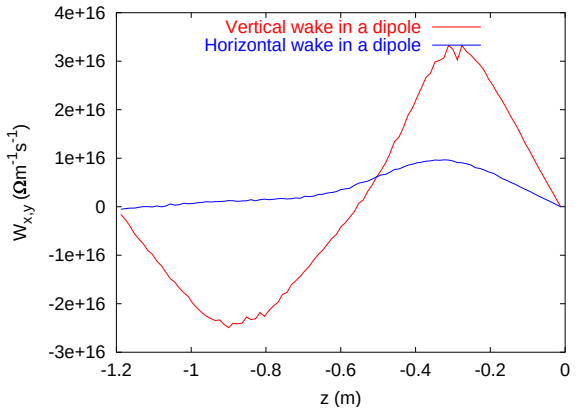

Figure 9: Horizontal and vertical averaged dipole wake functions for a uniform SPS bunch, evaluated displacing the first bunch slice, in a dipole field region.

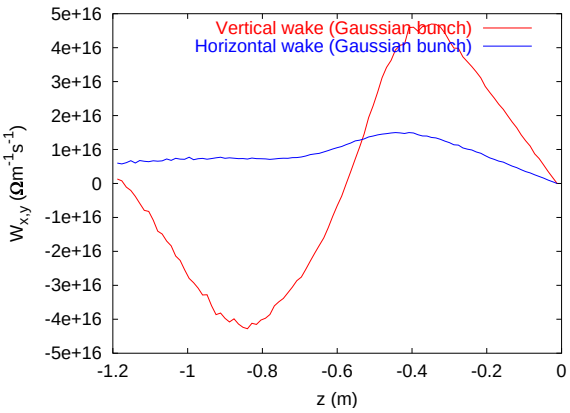

Figure 10: Horizontal and vertical averaged dipole wake functions for a Gaussian SPS bunch, evaluated displacing the first bunch slice, in a dipole field region.

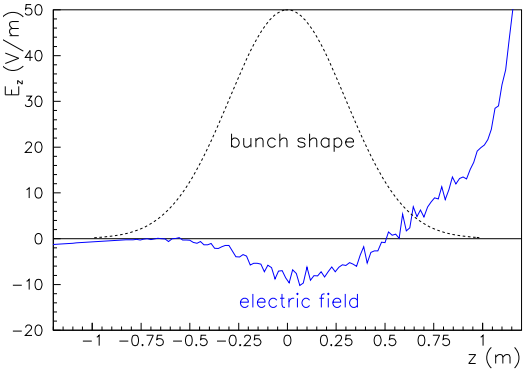

Figure 11: Longitudinal electric field due to the electron cloud for a Gaussian bunch in the SPS. Bunch head is on the left.

However, Fig. 12 shows that the initial and predicted distributions are very similar, and hence we do not expect a large effect of the electron cloud on the longitudinal bunch shape in the SPS. We note that the modified distribution is shifted slightly forward, which compensates for the additional energy loss due to the cloud.

5 APPLICATION TO THE KEKB

So far we have shown results for the CERN SPS ring. It is interesting to show, as further applications of the HEADTAIL code, a few results from simulations of the KEKB Factory Low Energy Ring. Parameters that we have used in our simulations are summarized in Table 2.

Figures 13 and 14 show horizontal and vertical centroid

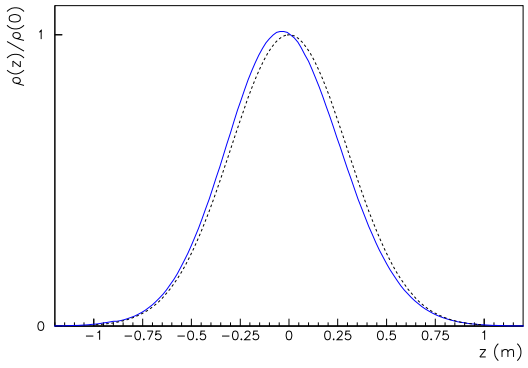

Figure 12: Equilibrium bunch density computed from the wake for a Gaussian bunch in the SPS. The Gaussian is slightly shifted.

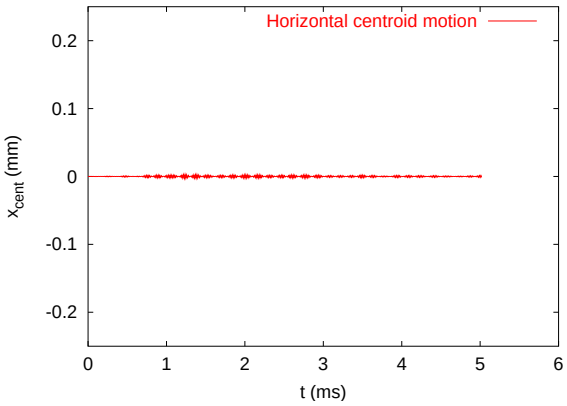

Figure 13: Horizontal centroid motion of a KEK bunch interacting with an electron cloud. Chromaticity ξ_x was set to zero. No unstable motion is visible.

Table 2: Simulation parameters for KEKB LER.

variable	symbol	value
Circumference	C	3016 m
Relativistic factor	γ	6850
Chamber radius	b	47 mm
Bunch population	N_b	$3.3 \times 10^{10} e^+$
Bunch spacing	$T_{\rm sep}$	8 ns
Rms bunch length	σ_z	4 mm
Rms hor. beam size	σ_x	420 μm
Rms vert. beam size	σ_y	60 μm
Tranverse tunes	$Q_{x,y}$	45.53/44.08
Synchrotron tune	Q_s	0.015
Slippage factor	η	1.8×10^{-4}
Average beta function	β_y	10 m
Chromaticities	$\xi_{x,y}$	up to 0.35
Solenoid field	B_z	30 G
Electron cloud density	ρ_e	10^{12} m^{-3}

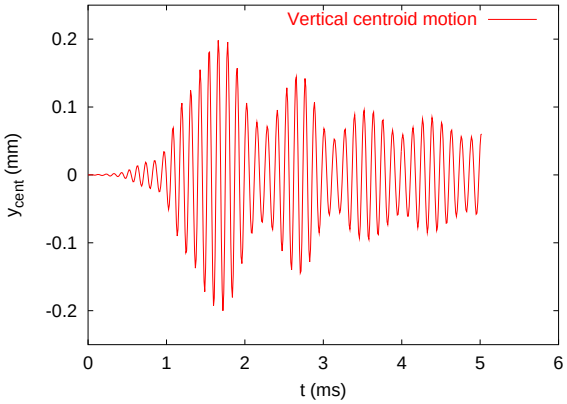

Figure 14: Vertical centroid motion of a KEK bunch interacting with an electron cloud. Chromaticity ξ_y was set to zero. The coherent dipole oscillation reveals an instability.

motion for a nominal bunch under the action of an electron cloud with density 10^{12} m^{-3} and supposed uniformly distributed all along the ring. Chromaticity was set to zero in this case. A dipole motion is observable only in the vertical direction, probably because of the flatness of the KEK bunch. To illustrate the beneficial effect of chromaticity on the instability, we show first in Fig. 15 how the vertical centroid motion is damped for high vertical chromaticity. Then, in Fig. 16 the emittance growths relative to different chromaticity values are plotted on the same graph. It is clear that higher positive chromaticities can damp the coherent emittance growth otherwise predicted for zero or very low chromaticity. For the purpose of code benchmarking and validation, we show in Fig. 17 the same chromaticity scan for KEK done by K. Ohmi [17] with his PEI code. The agreement with our results is excellent.

The influence of a solenoid field on the electron cloud driven single bunch instability can also be of interest, and it has been studied in connection with the the KEK too, since there are solenoids along 90% of the ring. In Figs. 18 and 19 the horizontal and vertical wake functions are plotted for a KEK nominal bunch and the nominal value of the solenoid field ($B_{\rm sol} = 3$ mT). The difference between the two figures is that the horizontal and vertical displacements were separately applied to the first bunch slice: nevertheless, the expected effect of exciting a wake in the orthogonal plane is in neither case quite visible in both planes in spite of the coupling in the electron motion due to the solenoid. This is because the KEK bunch is very short and the solenoid field not strong enough to efficiently couple planes over one bunch pass (electron cyclotron period for $B_{\rm sol} = 3$ mT is $T_c = 12$ ns, and the KEK bunch length is $\Delta t_b = 0.053$ ns). In Ref. [13] it was shown how for a long SPS bunch in a solenoid a strong effect was visible in both planes even after displacing a bunch slice only in one plane. When the coupling is effective, the wake field becomes much weaker and the instability is likely to be cured [13], as appears from the loss of pinching shown in Fig. 20 for an SPS bunch propagated through an electron cloud in a solenoid field region ($B_z = 0, 2.5, 10$ mT).

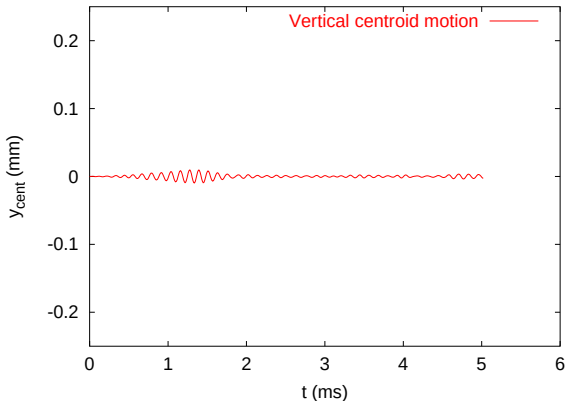

Figure 15: Vertical centroid motion of a KEK bunch interacting with an electron cloud. Chromaticity ξ_y was set to 0.35. The coherent dipole oscillation is damped with respect to the case with zero chromaticity.

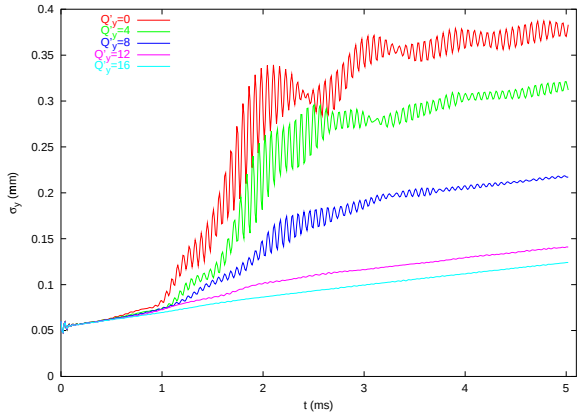

Figure 16: Vertical rms-size growth of a KEK bunch over 500 turns for different values of chromaticity (labelled in $Q'_y = \xi_y \cdot Q_y$. Chromaticity helps against the e-cloud instability. All plots have been obtained using the HEADTAIL code.

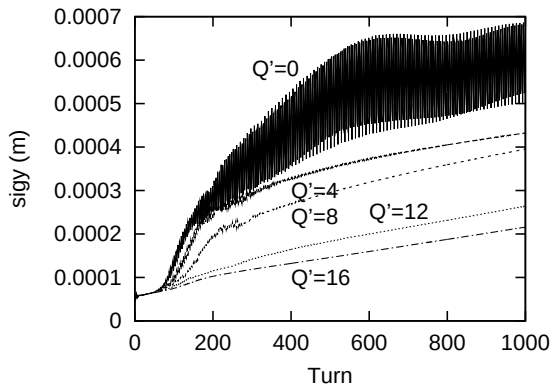

Figure 17: Vertical rms-size growth of a KEK bunch for different values of the chromaticity (labelled in $Q' = \xi_y \cdot Q_y$. Chromaticity helps against the e-cloud instability. All plots have been obtained using the PEI code by K. Ohmi (Courtesy K. Ohmi).

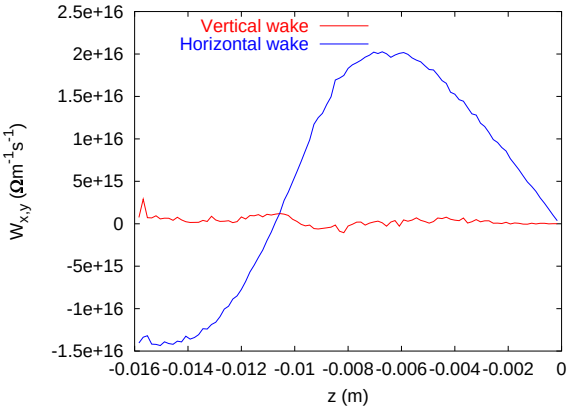

Figure 18: Horizontal and vertical wake functions along a KEK bunch that goes through an electron cloud inside a 30 G solenoid field region. The bunch head was displaced only horizontally by an amount $\Delta x = \sigma_x/10$.

6 CONCLUSIONS AND OUTLOOK

In conclusion, in this paper we have described the code HEADTAIL that was developed at CERN in order to study the degrading effect of an electron cloud on the single bunch. Examples of application have been shown, with special emphasis to the CERN SPS. Growth rate of the instability and beneficial effect of chromaticity, as experimentally observed [19], have been reproduced by simulations including electron cloud, space charge and broad band impedance. It has also been highlighted that space charge plays a key role in destabilizing the centroid beam motion: when its effect is neglected only an incoherent emittance growth is predicted to occur.

Transverse and longitudinal wake functions have been calculated by means of the HEADTAIL code. Transverse wakes can be of great interest to predict the instability threshold from the TMCI theory, although this theory can only be applied in first approximation, and needs to be adapted to this particular case. The electron cloud wake fields are not conventional, because they strongly depend on the position along the bunch from where they get excited. Work is being carried out to take into account this feature in the theory [20]. Assuming the electron distributions at subsequent times to be those at subsequent longitudinal positions (with the appropriate scaling factor), the longitudinal wake field has also been evaluated from the output of the HEADTAIL code, and found to be small. It can only slightly affect the bunch shape and is not likely to be responsible for any microwave instability.

The results of the HEADTAIL code have been benchmarked against the predictions of Ohmi's PEI code: the beneficial effect of chromaticity on the electron cloud single bunch instability for a KEK bunch has been reproduced by both codes in excellent agreement.

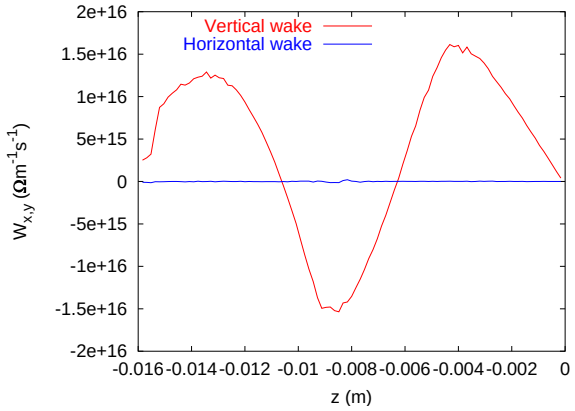

Figure 19: Horizontal and vertical wake functions along a KEK bunch that goes through an electron cloud inside a 30 G solenoid field region. The bunch head was displaced only vertically by an amount $\Delta y = \sigma_y/10$.

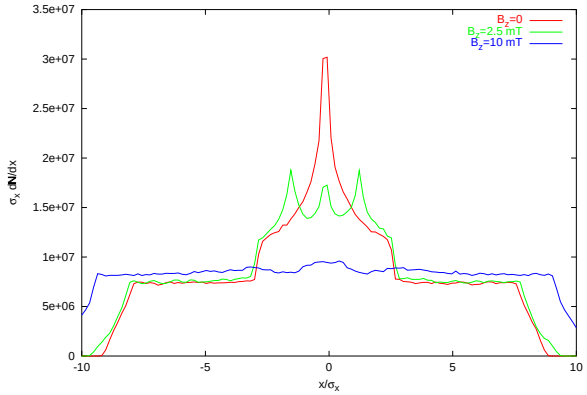

Figure 20: Electron densities along the x-axis after 4/5 of the SPS bunch has passed through the cloud and for $B_z = 0, 2.5, 10$ mT. This simulation result shows how the pinching effect disappears when the solenoid field is strong enough as to significantly couple the electron motion over one bunch pass.

7 ACKNOWLEDGEMENTS

The authors would like to thank F. Ruggiero, D. Schulte, G. Arduini, K. Cornelis, E. Métral, M. Giovannozzi, A. Rossi, K. Ohmi, E. Perevedentsev, and T. Katsouleas for helpful discussion and information.

8 REFERENCES

[1] F. Zimmermann and G. Rumolo, “Electron Cloud Simulation: Build Up and Related Effects”, these proceedings

[2] G. Rumolo and F. Zimmermann, “Practical User Guide for ECLOUD” CERN-SL-Note-2002-016 (AP)

[3] V. Baglin and B. Jenninger, “SPS electron cloud heat load measurement with WAMPAC and simulation”, these proceedings

[4] A. Rossi, G. Rumolo and F. Zimmermann, “Simulation Study of Electron Cloud in the Experimental Regions of the LHC”, these proceedings

[5] M. Jimenez *et al.*, “Electron-Cloud Observations in the SPS”, these proceedings

[6] F. Zimmermann, “Electron Cloud in the LHC”, these proceedings

[7] K. Ohmi and F. Zimmermann, Phys. Rev. Lett. **85**, 3821 (2000).

[8] G. Rumolo, F. Ruggiero and F. Zimmermann, Phys. Rev. ST Accel. Beams, **4**, 012801 (2001).

[9] K. Ohmi,, F. Zimmermann and E. Perevedentsev, Phys. Rev. E **65** (2002) 016502

[10] F. Zimmermann, “Electron-Cloud Studies for the Low-Energy Ring of KEKB,” CERN SL-Note-2000-004 AP (2000).

[11] K. Ohmi and F. Zimmermann, “Head-Tail Instability caused by Electron Cloud in Positron Storage Rings”, CERN-SL-Note-2000-015 AP (2000).

[12] H. Fukuma, *et al.*, “Observation of Vertical Beam Blow-Up in KEK Low Energy Ring”, in Proc. of EPAC 2000, Vienna (2000).

[13] G. Rumolo and F. Zimmermann, “Contributions of the SL-AP Group to the Two-stream Instabilities Workshop”, CERN SL-2001-067 (2001).

[14] G. Rumolo and F. Zimmermann, “Theory and Simulation of the Electron Cloud Instability” Chamonix XI, CERN SL-2001-003 (DI)

[15] H. Burkhardt, G. Rumolo and F. Zimmermann, “Measurements of SPS Single Bunch Coherent Tune Shifts and Head-Tail Growth Rates in the Year 2001” CERN, SL-Note-2001-043 (MD)

[16] T. Katsouleas *et al.*, “Plasma Modelling of Collective Wakefields in Electron Clouds”, these proceedings.

[17] K. Ohmi, “Particle-In-Cell Simulation of Beam-Electron Cloud Interactions” Proc. PAC 2001, Chicago, USA (2001).

[18] J. Haissiniski, Nuovo Cimento **18B**, 72 (1973)

[19] K. Cornelis *et al.*, “Electron Cloud Instability in the SPS”, these proceedings.

[20] E. Perevedentsev *et al.*, “Head-Tail Instability Caused by Electron-Cloud”, these proceedings.

STUDY FOR AN EP INSTABILITY

IN THE JOINT PROJECT OF KEK AND JAERI

T. Toyama, Y. Irie, S. Kato, K. Ohmi, C. Ohmori, K. Satoh and M. Uota

KEK, Oho, Tsukuba, Ibaraki 305-0801, Japan

N. Hayashi

JAERI, Tokai, Naka, Ibaraki 319-1195, Japan

Abstract

An e-p instability has been observed in some proton rings. This instability, which causes beam loss, limits the performance of the ring. The instability may be serious for 3 GeV and 50 GeV proton rings in JKJ. We have studied the e-p instability in several high-intensity proton rings: JKJ, PSR, ISIS and AGS. This work informs JKJ whether we have to take measures to cure the instability. A TiN coating on the chamber surface is one of remedies. Results of SEY measurements performed at KEK are discussed. The observation of electron cloud candidates at the KEK 12 GeV PS Main Ring is also presented.

1 INTRODUCTION

A high-intensity proton accelerator facility has been proposed in Japan as a joint project of KEK and JAERI (JKJ). The facility would be equipped with two proton rings: a 3 GeV rapid cycling synchrotron and a 50 GeV proton synchrotron [1]. The bunch population, which would be $4x10^{13}$, compares with that of PSR at Los Alamos National Laboratory [2]. The e-p instability is potentially a serious problem for these two rings of JKJ.

Not all high-intensity proton rings suffer from an electron cloud instability. For example, the instability has not been observed at a rapid cycling synchrotron, ISIS in Rutherford Appleton Laboratory [3], although it has an intensity comparable with PSR. AGS in Brookhaven National Laboratory has intensity with only a few factor difference of the JKJ 50 GeV ring. However, the instability has not been observed yet [4]. It is worth comparing these proton rings from the viewpoint of the electron cloud instability. The parameters of these proton rings are summarized in Table 1 [5].

The electron cloud could cause both coupled and single bunch instabilities. A perturbation of the cloud induced by a bunch, which affects other bunches, causes a coupled bunch instability. A perturbation induced by a part of a bunch, which affects other part of the bunch, causes a single bunch instability. In these rings, both the bunch length and the bunch spacing are several tens meters. At first sight, a bunch spacing of several tens meters seems to be long enough to decay the perturbation (wake field) of a bunch. We focus on the single bunch instability in this paper. The coupled bunch effect will be discussed at some other opportunity.

The 50 GeV ring in JKJ should supply not only a fast-extracted beam, but also a slow-extracted beam. An electron cloud build-up and an instability of a coasting proton beam would occur in somewhat different ways, which is not covered here, although it is very crucial.

It is important to know the secondary electron yield efficiency (SEY) not only as a candidate of remedies, but also as an input of a computer simulation. The results of ongoing measurements of SEY at KEK are discussed for several materials. The observation of electron cloud candidates at the KEK 12 GeV PS Main Ring is also discussed as a benchmark of the computer simulation, although not yet confirmed.

2 FORMATION OF AN ELECTRON CLOUD

In this section, the electron cloud density of each ring is evaluated based on a computer simulation considering the primary and secondary electrons.

Three possibilities of primary electron production are considered: i.e. the ionization of residual gas due to the proton beam, electron emission due to protons impinging on the vacuum chamber wall, and stripping at the foil for H-minus charge exchange injection.

The ionization cross-sections for CO and H_2 are estimated to be $\sigma(CO) < 1.3x10^{-22}$ m^2 and $\sigma(H_2) < 0.3x10^{-22}$ m^2 using Bethe formula. The molecular density (d_m) is related to the partial pressure in nPa by the relation at 20 ºC, $d_m(m^{-3}) = 2.4x10^{11}\ P_m$ (nPa). The electron production rate is $Y_{1,i} = 7.7\times10^{-9}$ e$^-$/(m·p) at $2x10^{-7}$ Pa, where e$^-$/(m·p) means the number of emitted electrons per one proton incident per meter.

On the other hand the electron production rate due to proton loss is assumed to be $Y_{1,\ell} = 4.4\times10^{-6}$ e$^-$/(m·p) at the chamber surface, assuming a proton loss rate of $4x10^{-6}$ per revolution and one hundred electron emissions per one proton loss. Here, the assumption of M. Furman et al. [6] is adopted. The electron production rate due to proton loss is a third order of magnitude larger than that due to ionization.

Electrons stripped at the foil have a kinetic energy of 217 keV during H-minus charge-exchange injection. The leakage magnetic fields of bump magnets is estimated to be larger than 20 G around the foil. Almost all of the

Table 1. Basic parameters of the proton rings.

Variable	symbol	Joint project				PSR	ISIS	AGS
		3GeV RCS		50GeV MR				
		inj.	ext.	inj.	ext.		inj.	inj.
circumference	L(m)	348.3	348.3	1567.5	1567.5	90	163	800
Lorentz factor	γ	1.4	4.2	4.2	54	1.85	1.07	3.0
Bunch population	$N_p(x10^{13})$	4.15	4.15	4.15	4.15	3	1.25	1.2
Number of bunches	n_b	2	2	8	8	1	2	6
Harmonic number	h	2	2	9	9	1	2	6
Rms beam size	σ_r(cm)	1.9	1.2	1.1	0.35	1.0	3.8	0.7
Bunch length	ℓ_p(m)	110	82	82	16	65	60	68
Rms energy spread	$\sigma_E/E(\%)$	0.6	0.7	0.7	0.25	0.25	0.025	0.28
Slippage factor	η	-0.48	-0.047	-0.058	-0.0013	-0.187		-0.146
Synchrotron tune	Q_s	0.0058	0.0005	0.0026	0.0001	0.0003		0.0017
Beam pipe radius	R(cm)	12.5	12.5	6.5	6.5	5	8	5

stripped electrons will be bent by these fields. The electron production rate is $2\times N_p/T_{rev} \sim 5.4\ 10^{11}$ e^-/turn. Converting into the electron yield per one proton incident per meter reads $Y_{1,foil} = 1.9\times10^{-5}$ $e^-/(m\cdot p)$. This value is four times larger than $Y_{1,\ell}$. These electrons, however, may not cause big trouble, because (1) primary electrons of 217 keV are swept from the beam orbit, and (2) secondary electrons of a few tens eV are easily localized by the leakage fields.

In the simulation, therefore, electron production due to proton loss dominates the electron cloud build-up.

The secondary electron yield, which is the number of electrons created by an electron incidence with some energy, is approximated by true secondary electron yield, as follows [7, 8]:

$$Y_2 = Y_S \times \frac{E}{E_{\max}} \frac{1.44}{0.44 + (E/E_{\max})^{1.44}}.$$

Y_S=2.1 and E_{max}=200 eV are used. Rediffused and elastic reflected electrons are not included in this simulation. SEY is varying in a practical situation, depending on materials, surface conditions and so on. Simple aspect is as follows. If an electron hits the wall n times on average, multiplication will amount to Y_2^n. Taking into account n =10 - 100 per one bunch passage, it is easily seen that a small change in Y_2 causes a large multiplication. This shows the importance of reducing SEY.

Electron cloud formation is estimated by tracking the transverse 2D motion of electrons produced by the primary and secondary electron emission. Primary electrons are produced at the chamber wall with energies of 10±5 eV. At position s along the ring, electrons move under an electric potential generated by a rigid proton beam of sinusoidal shape ($\lambda_p(s\text{-}vt) = (\pi N_p / 2\ell_p)$ sin $(\pi (s\text{-}vt) / \ell_p)$). Space charge force between electrons is neglected because the average neutralization factor is less than 0.1 in the rings discussed here. The magnetic fields are also neglected in the whole ring for simplicity.

The amplification factor (A_e), the number of multiplied electrons divided by the number of primary electrons per one bunch passage, is calculated for several stages of the relevant rings using the parameters in Table 1. The results are shown in Figure 1. This characterizes the amplification factor due to secondary electron emission. At every bunch passage a peak is formed by trailing-edge multipacting. Although it decays after the bunch passage, a considerable rate of electrons remains in the vacuum chamber upon the arrival of the next bunch. The base line increases as remaining electrons accumulate. Finally equilibrium is reached in 5 – 10 bunches passage. The peak and bottom values of the amplification factor and the neutralization factor are summarized in Table 2. The neutralization factor strongly depends on several parameters: the beam size, chamber size, bunch length and bunch spacing.

3 INSTABILITY CAUSED BY AN ELECTRON CLOUD

In this section the beam stability is evaluated based on a wake field approach and a coasting beam approximation because $\omega_e\ \sigma_z/c >> 1$ and the instability may be fast enough regardless of the synchrotron oscillation. Both the proton beam and the electron cloud are assumed to have a rigid Gaussian distribution. By linearizing the coupled motion, the proton motion can be considered to be a forced oscillation with the wake field that is generated by the proton beam passing through the electron cloud. Including the damping effect due to electron oscillation frequency spread, the wake is expressed as [9,10]

$$W(z) = c\,\frac{R_s}{Q}\,\frac{\omega_e}{\overline{\omega}}\,\exp(\frac{\alpha}{c}z)\ sin(\frac{\overline{\omega}}{c}z),$$

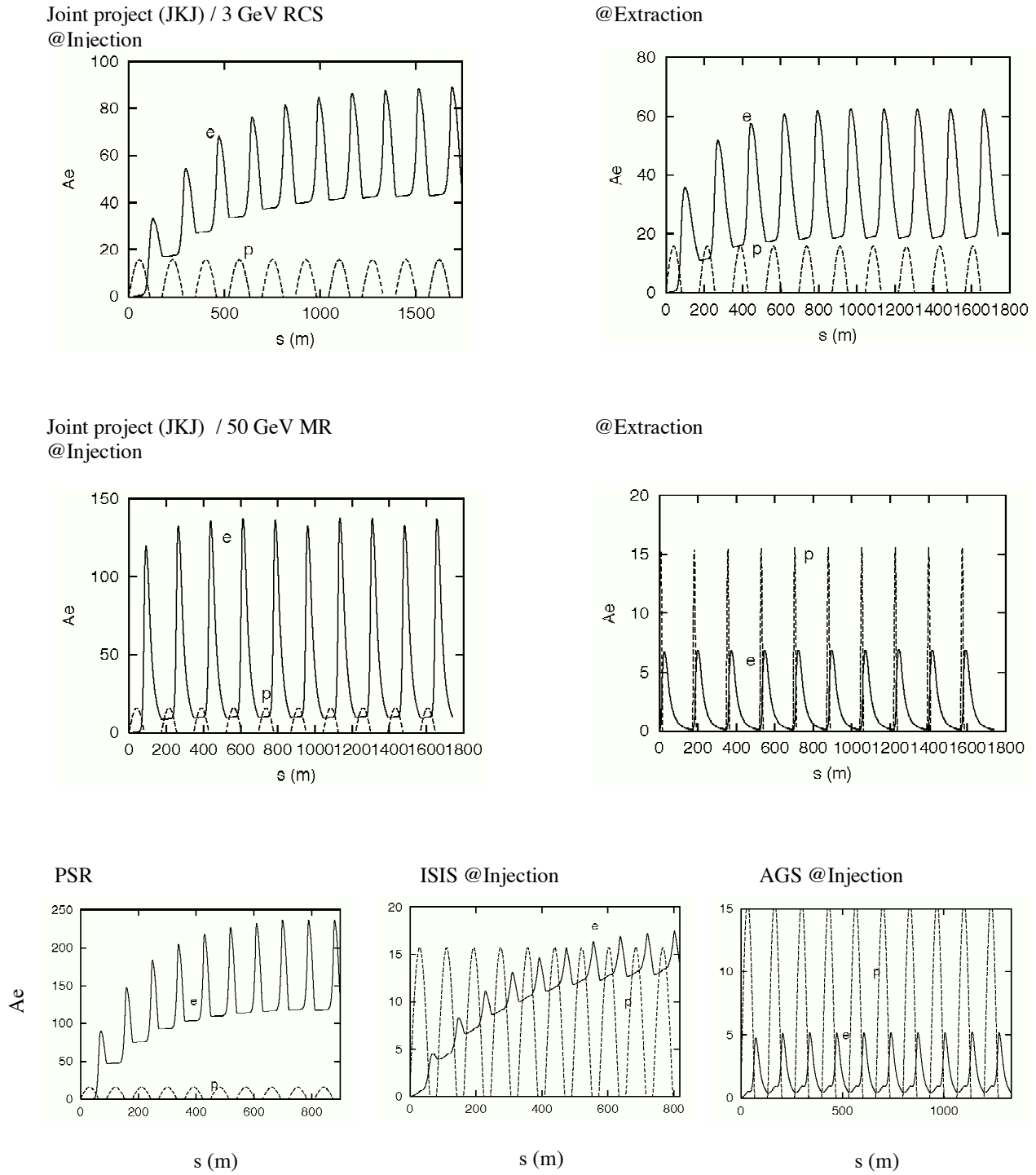

Figure 1. Electron amplification factor and proton beam density for the JKJ 3 GeV RCS, 50 GeV MR, PSR, ISIS and AGS. The dashed curves are the proton beam densities of a "half-sin" bunch (arbitrary unit). The parameters listed in Table 1 were used for the simulation.

Table 2. Electron cloud build-up of the proton rings.

Variable	Joint project				PSR	ISIS	AGS
	3 GeV RCS		50 GeV MR				
	inj.	ext.	inj.	ext.		inj.	inj.
Ae(bottom)	42.0	18.0	9.4	0.13	118	12.9	0.42
Ae(peak)	87.6	62	136	6.9	236	17.5	5.18
η(bottom)	0.020	0.0067	0.0035	0.00001	0.034	0.003	0.0001
η(peak)	0.042	0.023	0.05	0.0005	0.067	0.005	0.0015

Table 3. Wake field and stability for the electron cloud instability.

Variable	Joint project				PSR	ISIS	AGS
	3 GeV RCS		50 GeV MR				
	inj.	ext.	inj.	ext.		inj.	inj.
$Z(\omega_e)_L/Q$ (MΩ/m)	0.29	0.24	0.68	0.019	0.46	0.0051	0.024
$Z(\omega_e)_H/Q$ (MΩ/m)	0.61	0.83	9.7	0.96	0.90	0.0085	0.37
$\omega_e \ell_p / c$	133	182	199	276	166	27	153
U_L	0.07	0.23	0.11	0.02	1.6	0.09	0.004
U_H	0.23	0.78	1.6	1.2	3.2	0.14	0.06

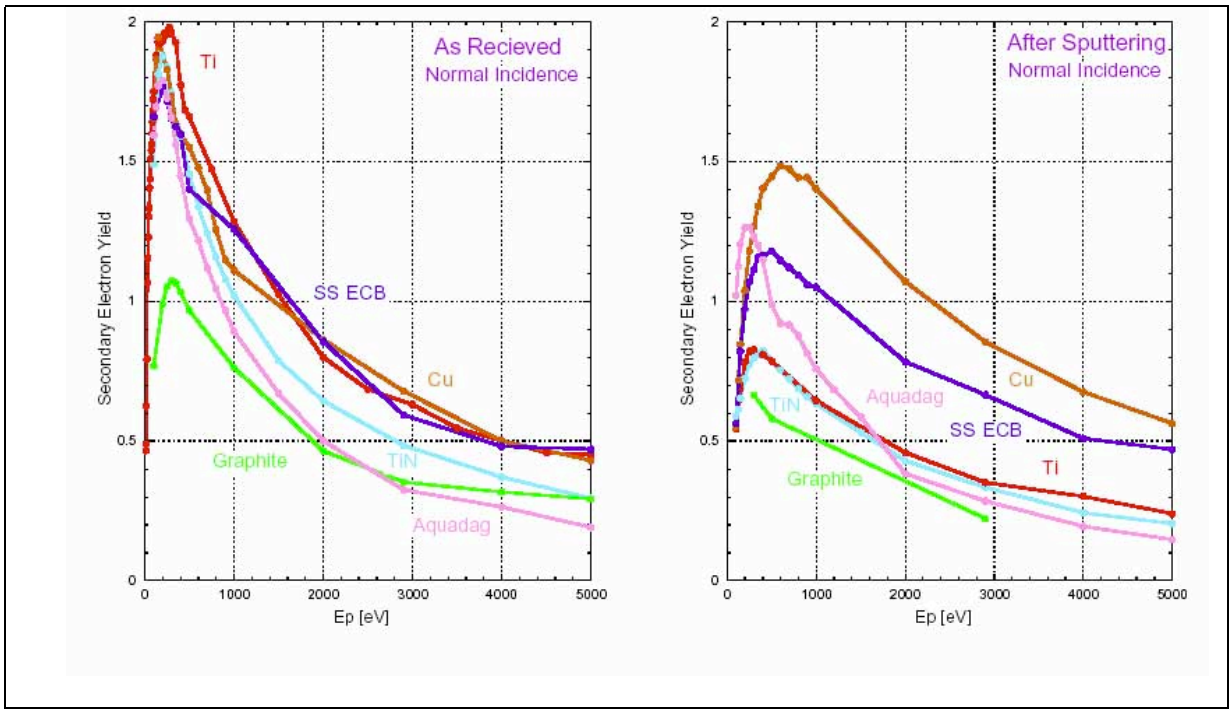

Figure 2. Dependence of the secondary electron yields on the primary electron energies at the surface as-received and after sputtering.

c : *light speed*,

R_s : *shunt impedance*,

Q : *quality factor*,

ω_e : *resonance angular frequency*,

$\alpha = \omega_e / 2Q$,

$\overline{\omega} = \sqrt{\omega_e^2 - \alpha^2}$.

Corresponding transverse impedance is given by Fourier transformation of the wake field:

$$Z_\perp(\omega) = \frac{Z_0}{4\pi}\frac{\lambda_e}{\lambda_p}\frac{L}{2\sigma_r^2}\frac{\omega_e}{\omega}\frac{Q}{1+iQ(\frac{\omega_e}{\omega}-\frac{\omega}{\omega_e})},$$

Z_0 : *vacuum impedance*,

λ_e = *line density of the electron cloud*,

λ_p = *line density of the proton beam*,

L : *circumference*

σ_r : *rms bunch radius.*

Making use of this coupling impedance, the dispersion relation is obtained [11, 12]:

$$U \equiv \frac{\sqrt{3}\lambda_p r_0 \beta_r \omega_0}{\gamma \omega_e \eta \sigma_\delta}\frac{|Z_\perp(\omega_e)|}{Z_0} = 1$$

or

$$\frac{\sqrt{3}\lambda_p r_0 \beta_r}{\gamma \nu_s \omega_e \sigma_z / c}\frac{|Z_\perp(\omega_e)|}{Z_0} = 1$$

r_0 : *classical radius of protons*,

β_r : *betatron function*

γ : *relativistic factor*,

η : *phase slip factor*,

σ_δ : *relative energy rms spread*,

σ_z : *bunch length*.

For U>1, the beam is unstable. In Table 3, two values of U_H and U_L are listed. They are unstable criteria for the peak and bottom values of the neutralization factor, respectively. For ISIS, the slippage factor and the synchrotron tune are assumed to be the same as PSR. PSR is unstable. On the other hand, ISIS and AGS are stable. These results qualitatively agree with the observations. The rings of the joint project are in-between.

4 SEY MEASUREMENTS

In this section, the results of ongoing measurements of SEY at KEK are discussed for several materials. A series of measurements of the secondary electron yields were made using an electron beam of 0.5 mm in diameter with an energy range of 100 to 5000 eV and a current of some tens nA, or using an argon ion beam with a raster-scanned size of a few mm^2, an energy of 5000 eV and a current of some tens nA. Surfaces of sample materials were analysed with x-ray photoelectron spectroscopy (XPS) or Auger electron spectroscopy (AES). The base pressure of the main chamber where all of the measurements were performed was close to 10^{-8} Pa. A detailed description of the experiment is reported in [13].

Figure 2 shows the dependence of the secondary electron yields on the primary electron energy with normal incidence at the as-received surfaces and after sputtering with argon ions. Although a titanium as-received sample showed the highest yield, the yields of the others, except an isotropic graphite, were close to the peak of titanium, as seen on the left. At a high energy region, the yields of the metals as-received appeared to be similar. However, the yields of the carbon materials and the TiN film showed lower. The yields of the all materials were reduced after the argon ion sputtering. The isotropic graphite showed the lowest value of 0.66 as well, even after slight sputtering, reaching almost its clean surface. Since the carbon and oxygen impurities in the TiN film reached their saturation and remained even after sputtering of a thickness of 65nm, those impurities may have been included in the film, itself, during its preparation. Their reduction may reduce the yields of TiN further.

The simulation here doesn't reflect the above results yet. Further investigation on electron cloud build-up will be performed by using these results.

5 ELECTRON CLOUD IN THE KEK-PS

There had been no evidence of electron cloud effects in the KEK-12 GeV-PS Main Ring. This January electrostatic pick-ups were installed in the MR to measure the transverse monopole, dipole and quadrupole component of the beam [14]. Four electrodes for monopole (by Σ) and quadrupole measurement were directly connected to the center control room on trial. Although a 50 ohm termination is normal, the measurement with a high impedance termination was intentionally performed to observe an electron cloud. Baseline drifts were observed around the transition energy and around the beginning of the flat top even at a relatively low intensity operation of 2.5×10^{12} protons per pulse (9 bunches), as shown in Fig. 3. The rf frequency sweeps from 6 MHz to 8 MHz. The full bunch length varies from ~ 90 ns at injection to ~ 30 ns at transition energy. The top trace is the number of particles, the middle trace a pick-up signal and the bottom trace the bunch signal from a wideband wall current monitor (WCM) in each figure. The envelope of the WCM signal peaks at the transition energy. With a 50 ohm termination the pick-up signal has a similar shape as the WCM signal. This implies a charge-up of the pick-ups with a negative current of a few microamperes.

Although there seems to be no instability and no problem for operation, the following experiments were performed to clarify the source of the baseline drift: baseline drift vs. bias voltage with various bunch numbers and with or without a magnetic solenoid field. The first idea was that it came from some resonance of the system because a preferred frequency seems to exist.

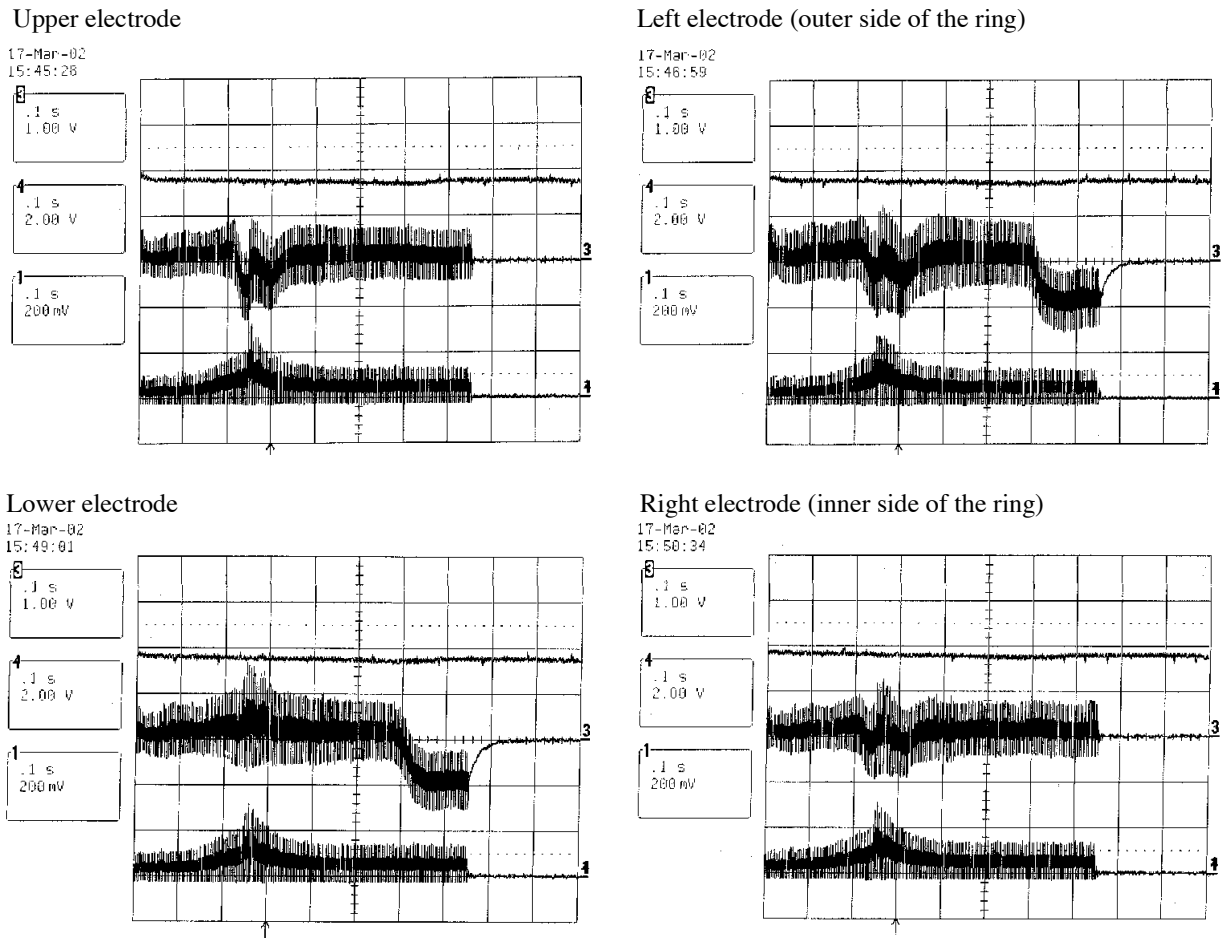

Figure 3. Baseline drifts around the transition energy and around the beginning of the flat top at a relatively low intensity operation of 2.5×10^{12} protons per pulse (9 bunches). Trigger: 400 ms after the beginning of acceleration indicated by the arrow. The transition energy is ~350 ms after the beginning of acceleration.

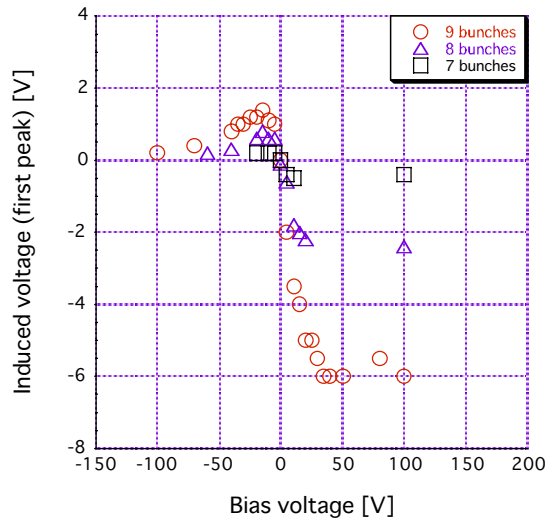

Figure 4. Peak voltage of the baseline drift at the transition energy with the number of bunches (7, 8 and 9).

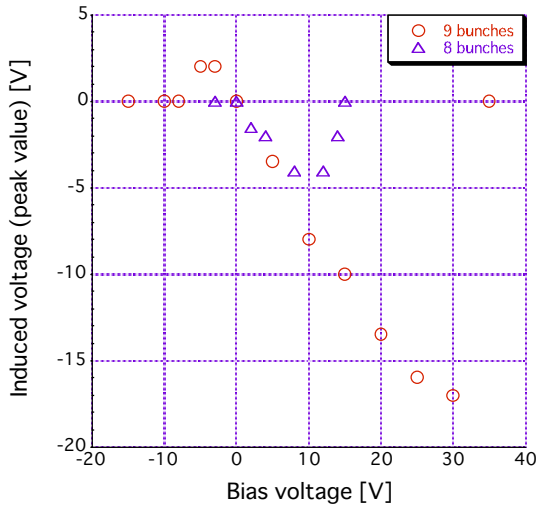

Figure 5. At a fixed bunch number 9, the peak voltage of the baseline drift measured with the solenoid current of 0, 10, 20 and 30 A.

If it comes from some geometrical reason, there may be no saturation. On the other hand, if it comes from electrons, there may be saturation.

Figure 4 shows the peak voltage of the baseline drift at the transition energy with seven, eight or nine successive bunches. The baseline drift was saturated by applying more than ~40 V of positive bias. With increasing the negative bias, the baseline once increases and then decreases, and gradually approaches to zero. This saturation level decreased with increasing bunch gap. In this measurement the bunch population was kept at 2.8×10^{11} protons. The baseline drift was not detectable if the bunch number was less than 6.

At a fixed bunch number of 9, the peak voltage of the baseline drift was measured with solenoid currents of 0, 10, 20 and 30 A, as shown in Fig. 5. The field distribution at 25 A is plotted in Fig. 6, more than 25 G at the vacuum chamber surface. The Lamor radius at 300 eV electron is ~23 mm at 25 G, which can force electrons away from the beam.

Although the above experiments do not contradict the statement that the baseline drift comes from the electron cloud, further study is necessary to confirm it.

To get an impression, the electron build-up was calculated with the beam parameters of the experiments. The simulation was basically the same as that described in the previous section. The only difference is that the effect of reflected electrons was checked. The results were quite different whether elastic reflected electrons were included or not, as shown in Fig. 7. Without elastic reflected electrons, Ae is ~7, while including them causes a large Ae of more than 260, not saturated yet, as shown in Fig. 7. Elastic reflection may lengthen the electron lifetime and make Ae larger. Introducing an electron space charge may work in the opposite way, i.e. to suppress electrons generation.

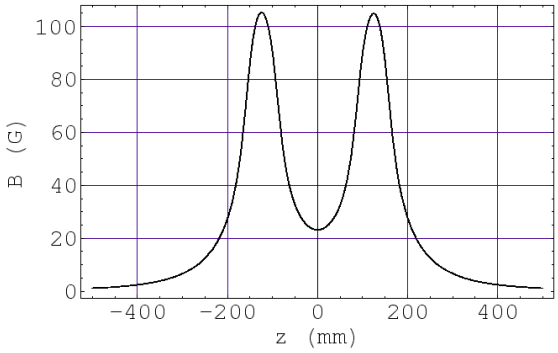

Figure 6. Magnetic fields at the vacuum chamber surface at a current of 25 A. The pick-up of 300 mm in length is located at |z| < 150 mm.

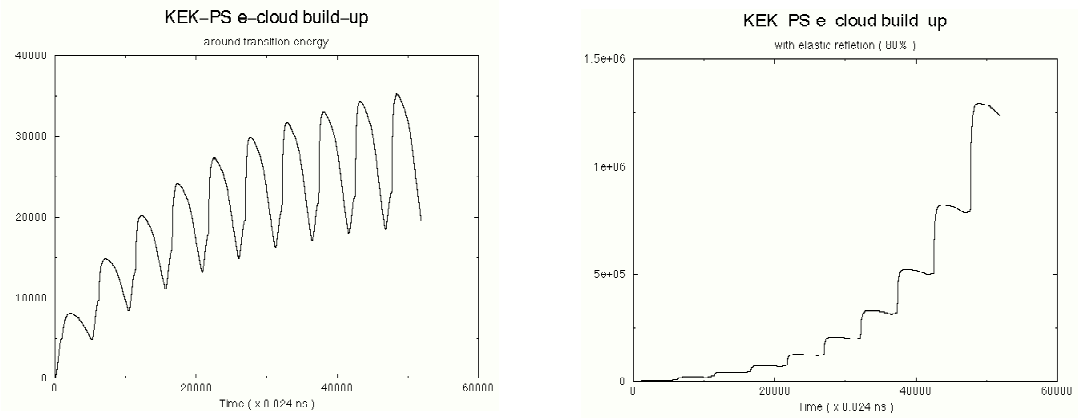

Figure 7. Simulation of electron build-up around the transition energy. Primary electrons of 5000 are generated at every bunch passage. The left plot is only with true secondary electrons. In addition, the right plot includes elastically reflected electrons.

6 SUMMARY

Electron cloud build-up and beam stability were evaluated for high intensity proton rings: JKJ 3 GeV RCS, 50 GeV MR, LANL PSR, RAL ISIS and BNL AGS. The assumptions in the simulation were as follows: estimated in field free region, included only true secondary electrons, without space charge effect. The number of primary electrons is amplified by

trailing-edge multipacting. The rate strongly depends on the secondary electron yield, beam shape, and chamber geometry. Then, using the neutralization factor obtained by the simulation, the beam stability was evaluated using a coasting beam model. The obtained stabilities agree qualitatively with observations in the existing machines. The neutralization factor due to the electron cloud was less than 0.1, neglecting elastic reflection in the secondary electron emission and electron space charge. This low neutralization degree justifies the neglecting electron space charge. However, including the elastic reflection in the secondary electron emission raises the neutralization factor by more than one order of magnitude. Including both the elastic reflection and the electron space charge may tend to cancel each other. This is a subject for future study.

A low SEY material, such as TiN, may improve the stability, if surface processing is carefully performed. Further experiments, including *in situ* measurement with several materials are foreseen, if the described baseline drift phenomena at the pickups in KEK-PS are confirmed to be the result of an electron cloud effect.

7 REFERENCES

[1] JAERI/KEK Joint Project Team, Accelerator Technical Design Report for High-Intensity Proton Accelerator Facility Project, .

[2] R. J. Macek et al., Proc. of Part. Acel. Conf. 2001, p. 688.

[3] G. H. Rees, AIP Proceedings 496 (1999) p. 17.

[4] T. Roser, AIP Proceedings 496 (1999) p. 22.

[5] C. Ohmori, http://hadron.kek.jp/member/chihiro/ep.html, (in Japanese).

[6] M. A. Furman and M. Pivi, Proc. of Part. Acel. Conf. 2001, 707.

[7] M. A. Furman and G. R. Lanbertson, Proc. Intern. Workshop on Multibunch Instabilities in Future Electron and Positron Accelerators (MBI-97), KEKProceedings 97-17 (1997) p.170.

[8] M. A. Furman, LBL-41482/CBP Note 247/LHC Project Report 180, May 20, 1998.

[9] K. Ohmi and F. Zimmermann, Phys. Rev. Lett. 85, 3821 (2000).

[10] K. Ohmi, F. Zimmermann and E. Perevedentsev, Phys. Rev. E 65, 16502 (2002).

[11] A. W. Chao, Physics of Colelctive Beam Instabilities in High Energy Accelerators, Wiley-Interscience Publication.

[12] E. Keil and B. Zotter, CERN-ISR-TH/71-58.

[13] S. Kato and M. Nishiwaki, section 2.3.8.2 in Accelerator Technical Design Report for High-Intensity Proton Accelerator Facility Project.

[14] T. Toyama, KEK Internal Report, ASN-452 (in Japanese) 2001.

Study of electron cloud build-up and instability in high intensity proton rings

K. Ohmi, T. Toyama, C. Ohmori
KEK, Oho, Tsukuba, 305-0801, Japan

Abstract

An e^-p instability has been observed in some proton rings. The instability, which causes beam loss, limits performance of the ring. The instability may be serious for 3 GeV and 50 GeV proton storage rings in Japan Hadron Facility (JHF). We study the e^-p instability in several high intensity proton storage rings operated in the world. This work informs JHF whether we have to take measures to cure the instability, for example apply a TiN coating on the chamber surface.

1 INTRODUCTION

The electron-proton (e^-p) instability has been discussed for a long time. The first work was done at CERN-ISR [1, 2]. An instability was observed at the operation of coasting beam and it was cured using clearing electrodes. After that, an instability has been observed for bunched proton beam in a proton synchrotron ring at Los Alamos National Laboratory (LANL-PSR) [3]. They reported that the instability was caused by an electron cloud. In their scenario, primary electrons were produced by proton losses at the chamber surface, and an electron cloud was formed by the trailing edge multi-pacting [3, 4]. Electrons, which are produced by the head part of the beam, are accelerated by the body part of beam, and released at the trailing edge. The accelerated electrons create secondary electrons at the chamber surface. The secondary electrons are amplified at every hitting of the chamber wall.

A high intensity proton accelerator facility has been proposed in Japan as a joint project of KEK and JAERI. The facility, which is named Japan Hadron Facility (JHF), is equipped by two proton rings: a 3GeV rapid cycle synchrotron and a 50GeV proton synchrotron. The bunch population, which is 4.15×10^{13}, compares with that of PSR. The electron cloud instability may be serious for these two rings of JHF.

The electron cloud instability has not been observed in all high intensity proton rings. For example, the instability has not been observed at the rapid cycle synchrotron ISIS in Rutherford Laboratory at the bunch intensity comparable with PSR. AGS has an intensity which is only a small factor different from that of JHF-50GeV, but the instability has not been observed. It is worthwhile to compare these proton rings from the point of view of the electron cloud instability. The parameters of these rings are summarized in Table 1.

The electron cloud causes both the coupled and the single bunch instabilities. A perturbation of the cloud induced by a bunch affects other bunches, and causes the coupled bunch instability. A perturbation induced by a part of a bunch affects other part of the own bunch, and causes the single bunch instability. In these rings, bunch length and free space between bunches are several 10 m both. At a first sight, the free space of several 10m seems to be enough long to smear out perturbation of the bunch. Hence, we focus on the single bunch instability in this paper.

We discuss formation of the electron cloud in Sec.2. Electrons created by ionization and proton loss are taken into account as the primary ones. Secondary electrons are created by hitting of the originary electrons on the chamber wall. The electron cloud density of each ring is estimated by a computer simulation considering the primary and the secondary electrons. We study the instability of proton beam interacting with the electron cloud in Sec.3. We analyze the instability with a tracking simulation [5] and a wake field approach [6].

2 FORMATION OF ELECTRON CLOUD

We discuss electron production and formation of the cloud. Many possibilities for primary electron production are considered. Ionization of residual gas due to proton beam creates electrons and ions. The ions create electrons when they are absorbed at the chamber surface [7, 8]. Electrons are also created by proton absorption at the beam chamber surface. H^- injection is a direct electron source. We classify the electron sources roughly into two categories for initial condition of electrons: that is, the electrons produced at the chamber surface and at the beam position.

The yield of ionization electrons is determined by the ionization cross-section and vacuum pressure in the beam chamber. Electrons are produced along the beam trajectory. Electron production at the chamber surface is rather complex. It is not well-known how many electrons are produced by proton beam, though there are many candidates. R. Macek et. al. measured number of electrons hitting the chamber wall using button electrodes at PSR [3]. They observed a peak current of $400\mu A/cm^2$ with the width of 50ns at the revolution period of 350ns with the proton current of 20A. In the positron machine, KEKB-LER, we observed electron current of $1 - 10\mu A/cm^2$ in DC at the positron current of 600mA. These measurements show that the number of electrons produced in high intensity proton rings is comparable with that of positron storage rings. It is surprising that proton rings have such a highly efficient electron production mechanism.

In KEKB, the electron current is understood to be due to photoelectron emission caused by synchrotron radiation. A probability for a positron to emit a synchrotron radiation photon at the travel distance of 1 m is 0.15, and 10% of the

Table 1: Basic parameters of the proton rings

variable	symbol	JHF				PSR	ISIS	AGS
		3GeV		50GeV				
		inj.	ext.	inj.	ext.			
circumference	L(m)	348.3	348.3	1567.5	1567.5	90	163	800
relativistic factor	γ	1.4	4.2	4.2	54.	1.85	1.07	3.0
bunch population	$N_p(\times 10^{13})$	4.15	4.15	4.15	4.15	3	1.25	1.2
number of bunches	n_b	2	2	8	8	1	2	6
harmonic number	H	2	2	9	9	1	2	6
rms beam sizes	σ_r(cm)	1.9	1.2	1.1	0.5	1.0	3.8	0.7
bunch length	ℓ_p(m)	110	82	82	16	65	60	68
rms energy spread	$\sigma_E/E(\%)$	0.6	0.7	0.7	0.25	0.25		0.28
slippage factor	η	-0.48	-0.047	-0.058	-0.0013	-0.187		-0.146
synchrotron tune	Q_s	0.0058	0.0005	0.0026	0.0001	0.0003	0.0003	0.0017
beam pipe radius	$R(cm)$	12.5	12.5	6.5	6.5	5	8	5

photons create photoelectrons: i.e., the electron production rate is $Y_1 = 1.5 \times 10^{-2} e^-/(m \cdot e^+)$. The observed current value well coincides with simulations taking into account the electron yield, their motion and geometry of the button electrodes.

To explain the observed current at the proton machine, R. Macek et. al. proposed electron production due to proton loss at the chamber surface [3]. M. Furman et.al. [4] use electron production rate $Y_1 = 4.4 \times 10^{-6} e^-/(m \cdot p)$ at the chamber surface. They have observed proton loss of 4×10^{-6} per turn at PSR (L=90m). They assume that a proton creates 100 electrons at its loss. Though this rate is still smaller than that of KEKB, multipacting due to secondary electrons makes up the difference. The number of amplified electrons was consistent with the electron current measurement.

Since we do not have clear information about the rate for JHF, we use this primary electron yield in our calculation, although this value may depend on energy, chamber geometry, surface condition, etc.

We also investigate ionization electrons. These electrons are produced by the ionization of residual gas in the chamber. Ionization cross-section for CO and H_2 is estimated as $\sigma(CO) = 1.3 \times 10^{-22} m^{-2}$ and $\sigma(H_2) = 0.3 \times 10^{-22} m^{-2}$ using the Bethe formula [9]. The molecular density d_m is related to the partial pressure in nPa by the relation at $20°C$, $d_m(m^{-3}) = 2.4 \times 10^{11} P_m(nPa)$. The electron production rate is $7.7 \times 10^{-9} e^-/(m \cdot p)$ at 2×10^{-7}Pa. The production rate is 7 orders at magnitude smaller than that of the photoelectron in KEKB, and is 3 orders smaller than that of the proton loss.

Secondary electron production plays an important role for electron cloud build-up in proton rings, because primary electrons are much less than that of positron ring. Secondary yield [10], which is the number of electrons created by an electron incidence with an energy, is approximated by the formula,

$$Y_2 = Y_s \times \frac{E}{E_{max}} \frac{1.44}{0.44 + (E/E_{max})^{1.44}}. \qquad (1)$$

Fig.1 shows the secondary yield for $Y_s = 2.1$ and $E_{max} = 200eV$. These values are obtained for aluminum by measurements [11].

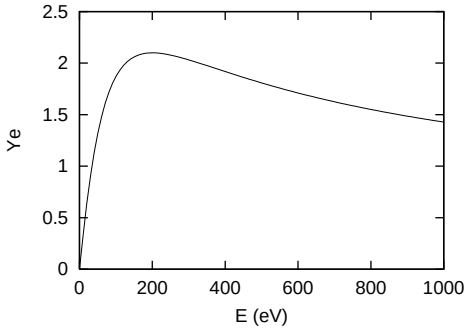

Figure 1: Secondary electron yield depending on incident electron energy for $Y_s = 2.1$ and $E_{max} = 200eV$

.

2.1 *Simulation of electron cloud formation*

Electron cloud formation is estimated by tracking the motion of electrons produced by the primary and the secondary electron emission [10, 12]. The motion of electrons is calculated in the transverse two dimensional plane. We consider electron cloud distribution at the position s_e. The distribution and line density $\lambda_e(z)$ is assumed to be dependent only on $z = s_e - vt$, but to be independent on s_e for the choice of independent variables (z, s). We neglect space charge force between electrons in present simulation, because the average neutralization factor $\lambda_e/\bar{\lambda}_p$ is of the order of 0.1 in our case as it is seen later, where λ_e and $\bar{\lambda}_p$ are

the electron line density and the proton average line density, respectively. Therefore the results shown below are scaled by the yield of primary electrons. However electron motion during the beam passage absence is important for the survivor of electrons, which are the seeds of multipacting due to the next bunch. We will include the space charge force in the near future.

The proton beam is sliced along longitudinal direction with an equal step. Each slice has a local proton density $\lambda(z_i)_p$. Electrons are tracked step by step along the passage of the proton beam. Equation of motion for electrons is expressed by

$$\frac{d^2\boldsymbol{x}(t)}{dt^2} = -\frac{2\lambda_p(s_e - vt)r_e c^2}{(\sigma_x + \sigma_y)\sigma_y}\boldsymbol{F}_G(\boldsymbol{x}(t)), \qquad (2)$$

where the force $\boldsymbol{F}_G(\boldsymbol{x})$ is expressed by the Bassetti-Erskine formula normalized so that $\boldsymbol{F}_G \rightarrow \boldsymbol{x}/|\boldsymbol{x}|^2$ as $\boldsymbol{x} \rightarrow \infty$. t is time when the beam slice at $z = s_e - vt$ arrived at electron position s_e. The equation is integrated with the time step of the slice width.

The electrons are produced at the chamber surface or at the beam position, when proton beam passes through the longitudinal positions. The number of production is proportional to the local proton density. We produce primary macro-electrons of $1.0-1.5\times10^4 e/N_p$ for a proton bunch passage in this simulation. The longitudinal charge distribution of the proton bunch is assumed to be expressed by a sinusoidal function as

$$\rho_p = \frac{\pi N_p}{2\ell_p}\sin\frac{\pi z}{\ell_p}. \qquad (3)$$

The number of electrons in the chamber is calculated during passage of 10 proton bunches. Fig.2 shows the number of electrons as a function of s. The vertical axis is the number of electrons which is normalized by the number of primary electrons produced by a bunch, $A_e(z) = \lambda_e(z)/(Y_1 N_p)$. A_e characterizes the amplification factor due to secondary emission.

The electron cloud density gradually increases at the beginning of the interaction, and suddenly increases at the bunch tail. This is due to the trailing edge multipacting [4]. The number of electrons decreases after finishing of the multipacting, but considerable quantity of electrons remains in the chamber at arrival of next bunch. The quantity depends on the ring and beam parameters. Electrons accumulate gradually again with a sudden leap at the tail of the 2nd bunch. These processes, in which the number of electrons increases and decreases, are repeated every passage of bunches. The numbers of electrons at top and bottom arrive at certain values after 5-10 bunches passage. The arrived values and the number of bunches to pass depend on the ring and beam parameters.

Fig.3 shows the transverse distribution of electrons during the passage of the last (10-th) bunch. The figure shows that electrons distribute widely at the start of the interaction with the bunch and are gathered at the beam position

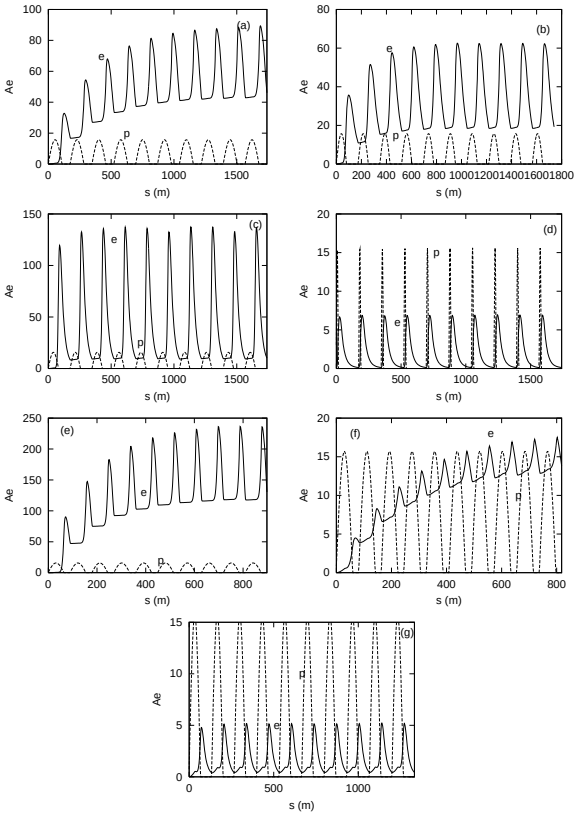

Figure 2: Electron amplification factor and proton beam density (arbit. unit). Electrons are produced at the chamber surface. (a) 3GeV inj (b) 3GeV ext (c) 50GeV inj (d) 50GeV ext. (e) PSR (f) ISIS (g) AGS

immediately, and splash after the interaction. The last picture shows the vertical distribution of electrons after 50m passage. The cloud size is comparable or a little larger than the beam size.

We also investigated electron cloud build-up due to ionization. Electrons are produced at the beam position. The initial energy of ionization electron is neglected. If the energy of electron is high enough to escape the beam potential, the production yield contributes to Y_1 at the chamber surface. Fig.4 shows the number of electrons A_e for zero initial energy. The number is far less than that produced at chamber. Electrons can not get sufficient energy to produce secondary electrons.

We now estimate neutralization factor of the electron cloud for proton beam. The proton and electron line densities are functions of z. The neutralization factor is defined as electron cloud line density divided by the average proton line density, $f(z) = \lambda_e(z)/\bar{\lambda}_p$, which is function of z. The neutralization factor is expressed by

$$f(z) = \frac{A_e(z)Y_1 N_p}{N_p/\ell_p} = A_e(z)Y_1\ell_p. \qquad (4)$$

Table 2 shows peak and bottom values of the neutralization factor for each ring. The neutralization factor strongly

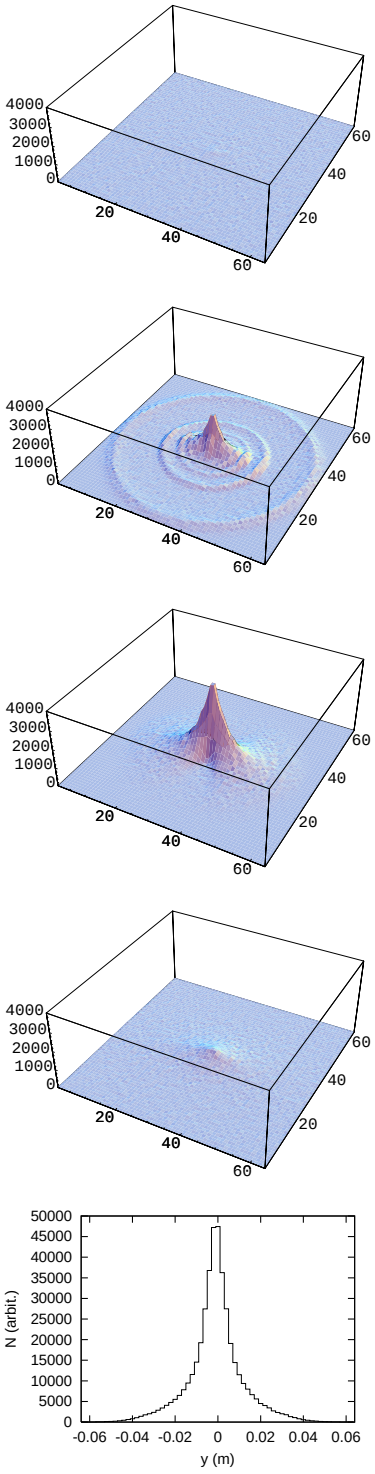

Figure 3: Transverse electron distribution during the passage of the last (10-th) bunch (1-st) 0m, (2-nd) 10m, (3-rd) 50m, and (4-th) 100m, and (5-th) vertical distribution after 50m passage.

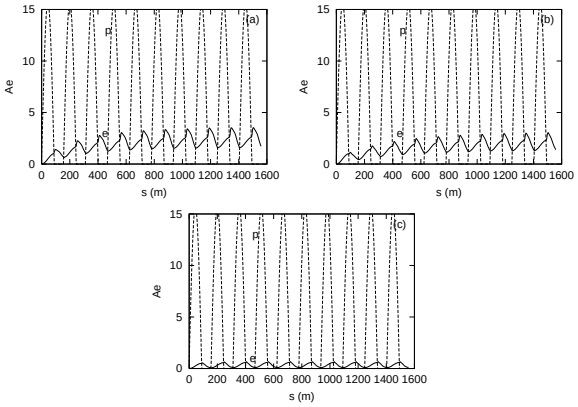

Figure 4: Electron amplification factor and proton beam density (arbit. unit). Electrons are produced at the beam position. (a) 3GeV injection (b) 3GeV extraction (c) 50GeV injection

depends on the parameters: beam size, chamber size, bunch length, and bunch spacing.

We got some characteristics concerning electron cloud in this simulation. The characteristics are used to estimate instability in the next section. They are summarized as follows,

- Electron cloud arrives at an equilibrium density after around 10 bunches passage.
- Leading-edge of the proton beam passes through the electron cloud which is formed by previous bunches. The electron cloud distributes all over the chamber.
- Electrons are gathered at the beam position immediately at the passage of the leading-edge.
- Number of electrons suddenly increases by $2 \sim 10$ times depending on the beam and ring parameters at the trailing-edge of the proton beam.

3 INSTABILITY CAUSED BY ELECTRON CLOUD

We discuss the instability caused by the electron cloud. The instability is studied by simulation using beam tracking and the wake field approach. We study the transverse dipole mode instability, in which the beam can have dipole moment $\bar{\boldsymbol{x}}(z,s)$, where $\bar{\boldsymbol{x}}(z,s)$ is a function of z.

3.1 Simulation using beam tracking

The electron cloud is created and accumulated by passage of bunch by bunch as is shown in the previous section. We study motion of proton bunches interacting with the electron cloud using a tracking simulation. For simplicity, we use the characteristics of the electron cloud summarized in the previous section. Electrons are assumed to be always uniformly distributed with a certain density in

Table 2: Electron cloud build-up of the proton rings

variable	JHF				PSR	ISIS	AGS
	3GeV		50GeV				
	inj.	ext.	inj.	ext.			
A_e(bottom)	42.0	18.0	9.4	0.13	118.	12.9	0.42
A_e(peak)	87.6	62.	136.	6.9	236.	17.5	5.18
η(bottom)	0.020	0.0067	0.0035	0.00001	0.034	0.003	0.0001
η(peak)	0.042	0.023	0.05	0.0005	0.067	0.005	0.0015

the vacuum chamber at the beginning of interaction with a proton bunch: that is, they do not have memory due to interactions with previous bunches.

A proton bunch is represented by macro-particles which are located along z with equal spacing. Each macro-particle has a charge and a mass corresponding to the proton line density. The macro-particle is free for dipole motion with dipole moment characterized by $\bar{\boldsymbol{x}}_p(z_i, s) = (\bar{x}_p, \bar{y}_p)$, but the emittance (size) is kept to be constant. Electron cloud is set at one or some positions of the ring, and is represented by a large number of point-like macro-particles. The electrons are initialized by uniform distribution in every interaction with the beam.

The equation of motion is expressed by

$$\frac{d^2\bar{\boldsymbol{x}}_{p,i}}{ds^2} + K(s)\bar{\boldsymbol{x}}_{p,i} = -\frac{2r_p}{\gamma}\sum_{a=1}^{N_e}\boldsymbol{F}_G(\bar{\boldsymbol{x}}_{p,i} - \boldsymbol{x}_{e,a}; \boldsymbol{\sigma}) \quad (5)$$

$$\frac{d^2\boldsymbol{x}_{e,a}}{dt^2} = -2\lambda_p(z) r_e c \boldsymbol{F}_G(\boldsymbol{x}_{e,a} - \bar{\boldsymbol{x}}_{p,i}; \boldsymbol{\sigma}). \quad (6)$$

Motion of the macro-electrons and macro-protons is tracked during the beam passage. After that, macro-protons are transferred by the lattice magnets, and then interact with randomly initialized electrons again. These procedures are repeated in every interaction of the bunch and cloud.

We performed the simulation for JHF 3GeV and 50GeV rings at injection. The neutralization factor was 2% and 4% for 3GeV and 50GeV rings, respectively. These value are bottom values in the Table 2. Fig.5 shows the vertical dipole moment of a proton bunch $y_p(z_i, s)$ along the longitudinal position z at $s = 20 \times L$. Excitation of dipole mode with the frequency ω_e is seen. We got similar signal for the horizontal moment.

Fig.6 shows the variation of dipole moment, J_y, where $J_y = (\gamma y^2 + 2\alpha y y' + \beta y'^2)/2$ is maximum value along z.

To discuss the beam stability, we compare the growth rate with the Landau damping rate. We take into account the Landau damping caused by longitudinal motion of bunch, which disturbs the coherence of the dipole motion. Landau damping rate is given by $\omega_e \eta \sigma_\delta = \omega_s \omega_e \sigma_z / c$ for a long bunched beam [13]. The beam stability is estimated by these ratios,

$$U \equiv \frac{\sqrt{3}}{\Delta\omega\tau_g} = \frac{\sqrt{3}T_0/\tau_g}{2\pi\nu_s\omega_e\sigma_z/c}. \quad (7)$$

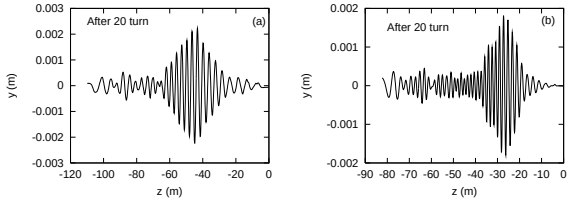

Figure 5: Vertical dipole moments for JHF 3GeV and 50 GeV rings at injection. The right-left correspond to the head-tail of a bunch, respectively. Pictures (a) and (b) are obtained for 3 GeV and 50 GeV, respectively.

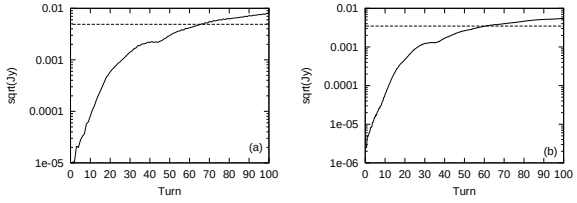

Figure 6: Growth of the vertical dipole instability for JHF 3GeV and 50 GeV rings at injection. The right-left correspond to the head-tail of a bunch, respectively. Pictures (a) and (b) are obtained for 3 GeV and 50 GeV, respectively.

where $\sqrt{3}$ is used as a normal stability condition.

For JHF 3GeV and 50 GeV at injection, the growth rate T_0/τ_g for small amplitude is $0.2(< 0.1\sigma_r) \sim 0.1(\approx 0.1\sigma_r)$ in the both cases. U is obtained as

$$U = 0.15 \sim 0.07 \quad \text{3GeV} \quad (8)$$

$$U = 0.23 \sim 0.12 \quad \text{50GeV}. \quad (9)$$

Although the growths in Figure 6 are very fast, Landau damping suppresses the instability because of large $\omega_e \sigma_z / c$.

3.2 Wake field induced by electron cloud and beam stability

Here we treat the instability with analytic approach using the wake field induced by electron cloud. We know that the electron cloud was gathered near to the beam immediately at beginning of the interaction with the beam, and the beam

interacted with the pinched electron distribution during the passage through the cloud. The size of electron cloud is about the same as the beam size. We regard the system as an interaction between the coasting beam and the electron cloud with Gaussian distribution. We take linear term of the interaction. The motions of the beam and electron cloud are characterized by $y_p(s,z)$ and $y_e(s,t)$, respectively. The equations of motion for the beam and cloud are expressed as follows,

$$\frac{d^2y_p(s,z)}{ds^2} + \left(\frac{\omega_{\beta,y}}{c}\right)^2 y_p(s,z) = -\left(\frac{\omega_{p,y}}{c}\right)^2 (y_p(s,z) - y_e(s,(s+z)/c)) \quad (10)$$

$$\frac{d^2y_e(s,t)}{dt^2} = -\omega_{e,y}^2(y_e(s,t) - y_p(s,ct-s)), \quad (11)$$

where $\omega_{\beta,y}$ denotes the angular betatron frequency without electron interaction. The two coefficients $\omega_{p,y}$ and $\omega_{e,y}$ characterize the linearized force between the beam and cloud, and are given by

$$\omega_{p,y}^2 = \frac{\lambda_e r_e c^2}{\gamma(\sigma_x+\sigma_y)\sigma_y}, \qquad \omega_{e,y}^2 = \frac{\lambda_p r_e c^2}{(\sigma_x+\sigma_y)\sigma_y}, \quad (12)$$

where λ_e and λ_p are the line densities of the cloud and beam, and σ_x and σ_y are the horizontal and vertical beam sizes, respectively.

From Eq.(10) and (11), an equation for the beam motion is obtained as follows,

$$\frac{d^2y_p(s,z)}{ds^2} + \left(\frac{\tilde{\omega}_\beta}{c}\right)^2 y_p(s,z) = \frac{\omega_p^2\omega_e}{c^3}\int_z^\infty y_p(s,z')\sin\frac{\omega_e}{c}(z-z')dz'. \quad (13)$$

Here $\tilde{\omega}_\beta^2 = \omega_\beta^2 + \omega_p^2$ is the angular betatron frequency including the frequency shift due to the electron cloud. The right-hand side of Eq.(13) can be represented by a wake function, which depends only on the longitudinal distance. Integrated over the ring circumference L, the wake function can be written as

$$W_1(z)[\mathrm{m}^{-2}] = cR_S/Q\,\sin\left(\frac{\omega_e}{c}z\right), \quad (14)$$

where

$$cR_S/Q = \frac{\lambda_e}{\lambda_p}\frac{L}{(\sigma_x+\sigma_y)\sigma_y}\frac{\omega_e}{c}. \quad (15)$$

This wake field does not damp for z in this model: i.e., in the word of impedance, the Q factor is infinite. Actually the frequency spread of ω_e should be taken into account. We add a damping term $2\alpha y_e$ in the left hand side of Eq.(11). The damping factor α corresponds to the frequency spread of ω_e. The wake field is now expressed by

$$W(z) = c\frac{R_S}{Q}\frac{\omega_e}{\tilde{\omega}}\exp\left(\frac{\alpha}{c}z\right)\sin\left(\frac{\tilde{\omega}}{c}z\right), \quad (16)$$

where $\alpha = \omega_e/2Q$ and $\tilde{\omega} = \sqrt{\omega_e^2 - \alpha^2}$. Note that $z < 0$ for backward direction.

In this framework the frequency spread (α or Q) is not determined. The spread is caused by nonlinear interaction with beam, proton distribution along z and beam size modulation due to β function variation. An estimation of Q caused by nonlinear interaction is given in Ref.[6]. The wake field is calculated by the same simulation method. Fig.5 shows the wake field for JHF-50GeV at injection. The resonator parameters are obtained by fitting the figure

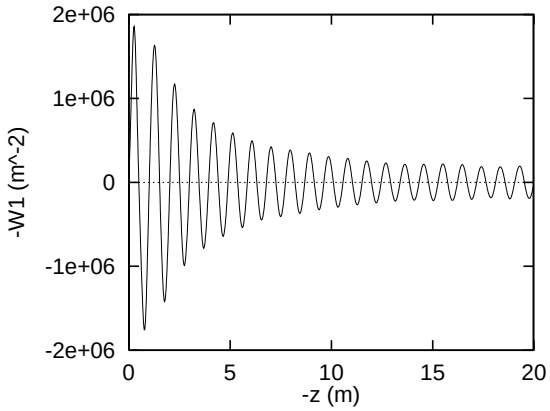

Figure 7: Wake field caused by electron cloud for JHF 50 GeV at injection.

as follows,

$$\begin{aligned} \frac{cR_s}{Q} &= 1.9\times10^6 m^{-2} \qquad (1.1\times10^6 m^{-2}) \\ \omega_e &= 1.9\times10^9 s^{-1} \qquad (1.2\times10^9 s^{-1}) \\ Q &= 13. \end{aligned} \quad (17)$$

The number enclosed in brackets is analytical value given by Eqs.(12) and (15). cR_S/Q and ω_e are somewhat larger values than the analytical ones. Q=13 was obtained by the simulation with the account of the nonlinearity of the beam-cloud interaction. The Q value is conjectured to be further reduced for considering the longitudinal proton distribution and modulation of the beta function.

Corresponding effective transverse impedance is given by Fourier transformation of the wake field.

$$Z_1(\omega) = \frac{c}{\omega}\frac{R_S}{1+iQ\left(\frac{\omega_e}{\omega}-\frac{\omega}{\omega_e}\right)} = \frac{\lambda_e}{\lambda_p}\frac{L}{\sigma_y(\sigma_x+\sigma_y)}\frac{\omega_e}{\omega}\frac{Z_0}{4\pi}\frac{i}{\left(\frac{\omega}{\omega_e}-\frac{\omega_e}{\omega}\right)+i\frac{1}{Q}}, \quad (18)$$

where Z_0 is the vacuum impedance 377Ω.

We discuss the stability of beam which experiences the effective impedance. Since the bunch length is very long, $\omega_e\ell/c \gg 1$, the coasting beam approximation is used. The

stability criterion is given by the dispersion relation as follows [13],

$$U \equiv \frac{\sqrt{3}\lambda_p r_0 \beta \omega_0}{\gamma \omega_e \eta \sigma_\delta} \frac{|Z_\perp(\omega_e)|}{Z_0} = \frac{\sqrt{3}\lambda_p r_0 \beta}{\gamma \nu_s \omega_e \sigma_z / c} \frac{|Z_\perp(\omega_e)|}{Z_0} = 1. \quad (19)$$

For $U > 1$, the beam is unstable. U for various rings are calculated using Eq.(15) and parameters in Table 1 and 2. The Q value is 5. The results on the stability are shown in Table 3.

The table includes two values of U_H and U_L, which are the criteria for the peak and bottom values of neutralization factor, respectively. It is the same meaning for $Z_{H(L)}$.

This result, which shows that the $e^- p$ instability is serious for PSR but is not for ISIS, is consistent with experimental results. In JHF, some of U_H exceed 1.

4 CONCLUSION

We discussed the electron cloud build-up and instability in some high intensity proton rings shown in Table 1. We studied the electron cloud build-up using a computer simulation. Primary electrons were produced at the chamber surface or at the beam position. We considered the yields of $Y_{1,\ell} = 4.4 \times 10^{-6}/(m \cdot p)$ at the chamber surface. The electrons appear due to proton loss, ion hitting or other mechanisms. The ionization yield was $Y_{1,i} = 7.7 \times 10^{-9}/(m \cdot p)$ (2×10^{-7}Pa). The ionization electron can be neglected for the vacuum pressure less than 10^{-5}Pa, if we use the yield $Y_{1,\ell}$ from the chamber surface.

The primary electrons are amplified by the secondary electron emission at the chamber surface. The electrons experience the energy gain due to the beam force, create secondary electrons, and cause multipacting. The amplification rate was estimated to be an order of 100 in the present model. The neutralization factors for some proton rings are summarized in Table 2. We have to note that the rate depends on the secondary yield, beam shape and chamber geometry. It has to be kept in mind that Y_1 is difficult to estimate in individual machines.

In this calculation, the space charge force between electrons and the elastic scattering (reflection) of electrons [14] are not considered. These may be important, because elastic scattering continues to supply electrons up to the space charge limit. We should not discard the ionization as the electron source [15].

The beam stability is estimated by a tracking simulation and coasting beam model using the wake field due to the electron cloud. The results are summarized in Table 3. The tracking simulation showed consistent results as the coasting beam model. In the results, PSR was the most severe for the instability, while ISIS was safe. JHF-3GeV is medium between PSR and ISIS. For large scale rings, AGS is safe. JHF-50GeV is more severe than AGS. Since the stability criterion U exceeds 1 at the peak cloud density for 50GeV ring, and is closed to 1 for 3GeV ring, we have to take care of the instability. We should estimate the cloud density more carefully, including the space charge between electrons, elastic scattering of electrons, effects of lattice magnet, etc.

The secondary electrons play important roles for the electron cloud instability in proton rings. Application of the TiN coating to reduce the secondary yield is a very powerful cure for this instability.

The authors thank A. Valishev for reading this manuscript.

5 REFERENCES

[1] H.G. Hereward, CERN 71-15 (1971).

[2] E. Keil and B. Zotter, CERN-ISR-TH/71-58 (1971).

[3] R. J.Macek, et. al., Proceedings of Part. Accel. Conf. 2001, 688 (2001)

[4] M. A.Furman, M. Pivi, Proceedings of Part. Accel. Conf. 2001, 707 (2001)

[5] K. Ohmi and F. Zimmermann, Phys. Rev. Lett., **85**, 3821 (2000).

[6] K. Ohmi, F. Zimmermann, E.Perevedentsev, Phys. Rev. E **65**, 16502 (2002).

[7] R. J.Macek, private communications.

[8] Y. Mori, private communications.

[9] Y. Baconnier, CERN report 85-19, pp.267 (1985).

[10] M. A.Furman and G. R.Lambertson, Proceedings of MBI97, KEK Proceedings 97-17, 170 (1997).

[11] T. Toyama et.al., in this proceeding,

[12] K. Ohmi, Phys. Rev. Lett., **75**, 1526 (1995).

[13] A.W. Chao, *Physics of Collective Beam Instabilities in High Energy Accelerators*, Wiley-Interscience Publication.

[14] V. Baglin et. al.,LHC-Project-Report-472.

[15] F. Zimmermann, Proceedings of Chamonix XI, CERN-SL-2001-003 DI.

Table 3: Wake field and stability for electron cloud instability

variable	JHF				PSR	ISIS	AGS
	3GeV		50GeV				
	inj.	ext.	inj.	ext.			
$Z(\omega_e)_L/Q(M\Omega/m)$	0.29	0.24	0.68	0.019	0.46	0.0051	0.024
$Z(\omega_e)_H/Q(M\Omega/m)$	0.61	0.83	9.7	0.96	0.90	0.0085	0.37
$\omega_e \ell_p/c$	133	182	199	276	166	27	153
U_L	0.07	0.23	0.11	0.02	1.6	0.09	0.004
U_H	0.15	0.78	1.6	1.2	3.2	0.14	0.06

HEAD-TAIL INSTABILITY CAUSED BY ELECTRON CLOUD

E. Perevedentsev*, Budker Institute of Nuclear Physics, Novosibirsk, Russia

Abstract

The strong head-tail instability of a positron or proton bunch may be caused by wakefields arising in the electron cloud present in the beam pipe. These wakefields are known to produce both deflection and tuneshift varying along the bunch. We discuss a model involving this tuneshift as well as the machine chromaticity and transverse feedback.

1 INTRODUCTION

The recent years brought a lot of information concerning the influence of electron cloud on collective dynamics of positron/proton beams, see [1] and references therein. Particularly, observations of the thresholds and growth rates of the transverse beam instabilities at KEKB LER, CERN SPS, and other machines seem to be consistent with the hypothesis of the head-tail instability in a single bunch caused by the cloud wakefields [2], degradation of the effective transverse emittance being a manifestation of this instability.

Our objective in this paper is a detailed characterization of the strong head-tail instability, provided the cloud response is already known. We first consider the properties and parametrization of the electron cloud wake in Sections 2,3. In Section 4.1 we summarize essentials of the standard technique for analysis of single-turn instabilities in a bunched beam, see e. g. [3]. The stability analysis is based on finding the complex tunes of transverse (synchrobetatron) modes from linearized Vlasov equation. We emphasize the role of the machine chromaticity in control of the mode growth rates. The transverse electron cloud wake known from simulations is then used for characterizing the chromaticity-dependent mode tunes in KEKB LER and CERN SPS.

The standard wake and impedance approach can be modified so as to include some specific features of the cloud response. In Section 4.2 we include in our consideration the betatron tune variation along the bunch due to difference in incoherent tuneshifts caused by growth of the cloud density during the bunch passage (pinching of the cloud).

Simulation of the cloud response shows that the cloud pinching results in non-trivial behavior of the transverse dipole wakefield [4, 5], and in Sections 4.3, 4.4 we present the modification of the standard Vlasov eigenvalue problem for the wake function $W_1(z, z')$ which is not reducible to the difference argument $z - z'$.

In Appendices we discuss why the modes with very high order can be disregarded in practical situations. The standard approach can include a simplified model of the transverse bunch-to-bunch feedback, its influence on the beam instability due to electron cloud is discussed in Section 5.

Using the presented techniques, we discuss the typical behavior of the head-tail modes in Section 6, using the parameters of the electron cloud wake for KEKB LER and CERN SPS.

Section 7 is devoted to the estimate of stability based on the coasting-beam limit. And finally, we summarize the results in Conclusion.

2 EQUATIONS OF MOTION

Following the theory of beam-ion or beam-electron interaction [6] we derive one-dimensional equations of motion for our case where the photoelectron cloud is already present prior to arrival of the bunch whose motion is studied.

We write the linear equations for the beam centroid offset $y_b(s,t)$, and electron cloud centroid $y_c(s,t)$ at the machine azimuth s at the time t. Uniform longitudinal density is assumed in both the electron cloud and positron bunch, as well as equal transverse sizes.

$$\begin{aligned}\left(\frac{1}{c}\frac{\partial}{\partial t}+\frac{\partial}{\partial s}\right)^2 y_b(s,t) &+ k_0^2\, y_b(s,t) \\ &= g\,\left(y_c(s,t)-y_b(s,t)\right), \\ \frac{\partial^2}{\partial t^2} y_c(s,t) &= \omega_c^2\,\left(y_b(s,t)-y_c(s,t)\right).\end{aligned}$$

Betatron oscillations of the beam are taken in the smooth form with $k_0 = 1/\beta$, β being the vertical amplitude function.

The beam-cloud interaction parameter g can be expressed as

$$g = \frac{4n_c(\pi\sigma_x\sigma_y)\,e^2}{\gamma mc^2\,\sigma_y(\sigma_x+\sigma_y)} = \frac{4\pi n_c r_e \sigma_x}{\gamma(\sigma_x+\sigma_y)},$$

n_c is the time-averaged electron cloud density,
σ_y and σ_x are the vertical and horizontal beam sizes,
e is the electron charge,
m is its rest mass,
γ is the beam Lorentz-factor,
c is the speed of light,
r_e is the classical electron radius.

Electrons of the cloud oscillate in the bunch space charge field with the frequency ω_c,

$$\omega_c^2 = \frac{4N_b\, r_e c^2}{\sqrt{2\pi}\sigma_z\sigma_y(\sigma_x+\sigma_y)},$$

* perevedent@inp.nsk.su

here N_b is the bunch population and σ_z is its Gaussian length.

We can obtain the equation for the beam centroid alone,

$$\frac{\partial^2}{\partial s^2}y(s,z)+k^2\,y(s,z)=g\frac{\omega_c}{c}\int_0^z dz'\sin\frac{\omega_c}{c}(z-z')y(s,z').$$

With a slowly-varying complex amplitude $A(s,z)$ of the betatron oscillation,

$$y(s,z)=\mathrm{Re}A(s,z)e^{-iks},$$

after averaging out the A^* term on the right-hand side, we have

$$\frac{\partial}{\partial s}A(s,z)=i\frac{g}{2k}\frac{\omega_c}{c}\int_0^z dz'\sin\frac{\omega_c}{c}(z-z')A(s,z')\,.$$

Thus the problem is reduced to the beam breakup with an oscillating transverse dipole wake function $W(z-z')$,

$$W(z-z')\propto g\frac{\omega_c\sigma_z}{cN_b}\sin\frac{\omega_c}{c}(z-z').$$

3 DECOHERENCE AND PARAMETRIZATION OF THE WAKE FUNCTION

Non-uniformity of the positron bunch density leads to the frequency spread of the photoelectron oscillation and results in decoherence of the cloud response. A simple estimate can be done by averaging the wake with a weight function $f(x)$ which implies e. g. horizontal non-uniformity of the bunch distribution affecting the vertical wake function:

$$W(\omega_c,z)\to\int W(\omega_c(x),z)f(x)dx\,.$$

If we take a Gaussian distribution of the beam density,

$$f(x)=\sqrt{\frac{2}{\pi}}e^{-x^2/2},$$

then

$$\omega_c(x)=\omega_0 e^{-x^2/4}.$$

Hence we obtain the wake with the account of decoherence,

$$\tilde{W}(z)=g\frac{\omega_0 l}{c}\int_0^\infty\sin\left(\frac{\omega_0 z}{c}e^{-x^2/4}\right)\sqrt{\frac{2}{\pi}}e^{-3x^2/4}dx\,.$$

The result can be expressed in terms of the Struve function and can be fitted either by the Bessel function $J_1(\omega_0 z/c)$ for large z, or by the broad-band resonator wake,

$$\begin{aligned}W_1(z) &= \frac{cR_S\omega_R}{Q\bar{\omega}}e^{-\alpha z/c}\sin\frac{\bar{\omega}z}{c},\ (z>0),\\ \alpha &= \frac{\omega_R}{2Q},\qquad \bar{\omega}=\sqrt{\omega_R^2-\alpha^2}.\end{aligned}$$

Figure 1 shows the comparison of these fits with actual $\tilde{W}(z)$.

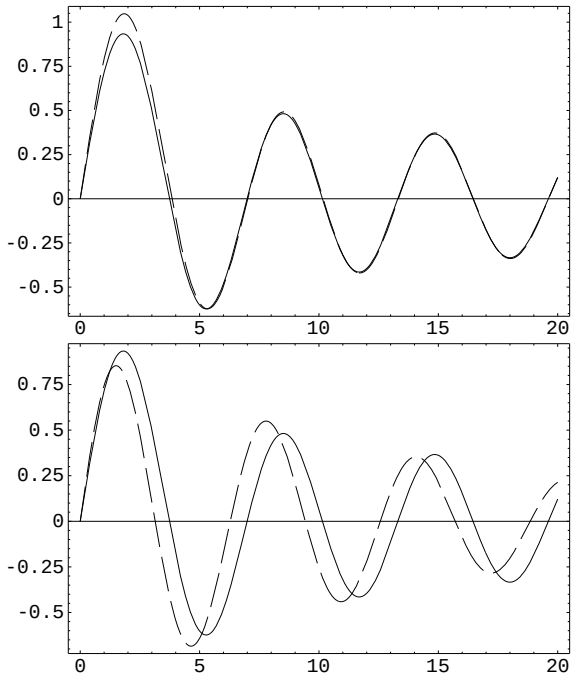

Figure 1: The decoherence wake $\tilde{W}(z)$ (solid line) and the fitting function (dashed line). Top: fit by the Bessel function $J_1(\omega_0 z/c)$; bottom: fit by the broad-band resonator with $\overline{\omega}=\omega_0$.

The corresponding transverse impedance is sampled by the long bunch spectrum in the low-frequency range ($\omega_R\sigma_z/c\sim 3$ at KEKB LER),

$$Z_1=\frac{cR_S/Q}{\frac{\omega}{Q}+i\left(\omega_R-\frac{\omega^2}{\omega_R}\right)}\approx\frac{cR_S}{Q\omega_R}\left(\frac{\omega}{Q\omega_R}-i\right).$$

The broad-band resonator parameters relevant to the KEKB LER and the SPS (see Table 1 for the parameter lists) are determined from the simulations of the wake function [4, 5], and listed in Tables 2,3.

4 STRONG HEAD-TAIL INSTABILITY

In contrast to the beam break-up problem in a linac, the dynamics in a circular machine is strongly affected by the synchrotron oscillations. The electron cloud effect on coherent motion of the single bunch can be modelled by the strong head-tail instability [2]. This will be the framework of the stability analysis in the following section.

4.1 Standard Case, the Transverse Wake Function in the Form $W(z-z')$[1]

Notation:

N_b is the number of positrons in a bunch,

[1] In this subsection we closely follow the derivation presented in Chapter VI of A.W. Chao, *Physics of Collective Instabilities in High Energy Accelerators* (J. Wiley, New York,1993), and refer to the equations therein using the format "Eq. (6.xxx)" in the following part of the paper.

Table 1: Basic parameters of the KEKB LER and CERN SPS

variable	KEKB-LER	SPS
particle type	e^+	p
circumference	3016 m	6900 m
beam energy	3.5 GeV	26 GeV
bunch population	3.3×10^{10}	$1. \times 10^{11}$
bunch spacing	8 ns	—
rms beam sizes	0.42 mm	3 mm
	0.06 mm	2.3 mm
bunch length	5 mm	30 cm
rms energy spread	0.0007	0.002
slippage factor	1.8×10^{-4}	5.8×10^{-4}
chromaticity	$4/8$	$0/10$
synchrotron tune	0.015	0.0046
betatron tune	∼46.	26.7
average beta function	15 m	40 m

Table 2: Analytically determined parameters for wake force induced by electron cloud using the resonator approximation. R/Q in units of Ω can be obtained by $cR_S/Q \times 30$. cR_S/Q and ω_b^2, which linearly depend on ρ, are evaluated for $\rho_c = 10^{12}$ m^{-3}.

	KEKB-LER		CERN-SPS
	x	y	y
$\omega_c[\mathrm{s}^{-1}]$	6.4×10^{10}	1.70×10^{11}	1.5×10^9
$\omega_b[\mathrm{s}^{-1}]$	1.7×10^5	4.5×10^5	1.4×10^5
$cR_S/Q[\mathrm{m}^{-2}]$	1.5×10^5	2.9×10^6	8.3×10^5

Table 3: Simulated parameters for the wake field induced by an electron cloud of density $\rho_e = 10^{12}$ m^{-3}, as obtained by fitting to the resonator model.

	KEKB-LER		SPS
	x	y	y
$\omega_R[\mathrm{s}^{-1}]$	8.7×10^{10}	2.2×10^{11}	1.5×10^9
Q	2.7	6.3	4.9
$cR_S/Q[\mathrm{m}^{-2}]$	2.9×10^6	8.3×10^6	3.2×10^6

$\rho_{x(y)}(s, z')$ is the horizontal (vertical) dipole moment of particles at z',
η is the slippage factor,
δ is the relative momentum deviation,
$\omega_{\beta,x(y)} = c/\beta_{x(y)}$ is the horizontal (vertical) angular betatron frequency in the smooth approximation,
$\xi = \dfrac{E}{\omega_{\beta,x(y)}} \dfrac{\partial \omega_{\beta,x(y)}}{\partial E}$ is the chromaticity,
ω_s is the angular synchrotron frequency.

The beam distribution function can be split into the unperturbed term and a single-frequency perturbation,

$$\Psi = \Psi_0 + \Psi_1 e^{-i\Omega s/c},$$

and Ψ_0 is expressed via functions of the unperturbed invariants of motion for each degree of freedom,

$$\Psi_0 = \psi_0(q)\varphi_0(r),$$

where

$$\begin{aligned} r &= \sqrt{z^2 + \left(\frac{\eta c}{\omega_s}\delta\right)^2}, \\ z &= r\cos\phi, \quad \delta = \frac{\omega_s r}{\eta c}\sin\phi\,, \\ q &= \sqrt{y^2 + \left(\frac{c}{\omega_{\beta,y}}p_y\right)^2}, \\ y &= q\cos\theta, \quad p_y = -\frac{q\omega_{\beta,y}}{c}\sin\theta\,. \end{aligned}$$

The Vlasov equation is linearized for a small perturbation of the distribution function, $\Psi_1(q, \theta, r, \phi)$:

$$\left[i\frac{\Omega}{c}\Psi_1 - \frac{\omega_\beta}{c}(1+\xi\delta)\frac{\partial\Psi_1}{\partial\theta} - \frac{\omega_s}{c}\frac{\partial\Psi_1}{\partial\phi}\right]e^{-i\Omega s/c} + \frac{c^2}{\omega_\beta}\frac{\partial\Psi_0}{\partial q}\sin\theta F(s,z) = 0, \qquad (1)$$

where the action of transverse dipole wakefield $W_1(z - z')$ is represented by the force

$$F(s,z) = -\frac{N_b r_e}{\gamma}\int W_y(z-z')\rho_{y,1}(s,z')dz', \qquad (2)$$

and $\rho_{y,1}(s, z')$ is the vertical dipole moment of particles at z' for the perturbed distribution Ψ_1.

In the dipole approximation, the solution should be a function of q and θ in the form which follows from Eqs. (6.168–169,175),

$$\Psi_1 \propto \frac{\partial\Psi_0}{\partial q}e^{i\theta}K(r)\sum_{lk} a_{lk}f_{lk}(r)e^{il\phi}e^{i\chi(\phi)}, \qquad (3)$$

where $\chi(\phi)$ is the chromatic phase, $\chi(\phi) = \xi\omega_\beta r\cos\phi/c\eta$, and $f_{lk}(r)$ form a set of orthogonal functions which characterize radial modes and satisfy the normalization

$$\int_0^\infty K(r)f_{lk}(r)f_{lk'}(r)rdr = \delta_{kk'}, \qquad (4)$$

$K(r)$ being the weight function of radial modes. This weight function is related to the unperturbed longitudinal distribution $\varphi_0(r)$:

$$K(r) = \frac{\omega_s}{\eta c}\varphi_0(r). \qquad (5)$$

By using the expansion Eq. (3) in Eq. (1), replacing $\sin\theta \to e^{i\theta}/2i$ in the smooth approximation, rewriting the force Eq. (2) in the frequency domain via the impedance,

and substituting the Fourier transform of the dipole moment distribution from Eq. (6.75), the problem is reduced to a linear equation set, and Ω is to be found from the corresponding eigenvalue problem,

$$\left(\frac{\Omega-\omega_\beta}{\omega_s}\right) a_{lk} = (l\delta_{ll'}\delta_{kk'} + M_{lk,l'k'})\, a_{l'k'}\,. \quad (6)$$

The matrix M is expressed by

$$\begin{aligned} M_{lk,l'k'} &= -i\frac{N_b r_e c}{2\gamma T_0\omega_\beta\omega_s} i^{l-l'} \quad (7)\\ &\times\int_{-\infty}^{\infty} Z_1(\omega) g_{lk}(\omega-\omega_\xi) g_{l'k'}(\omega-\omega_\xi)\, d\omega \end{aligned}$$

where we introduced

$$g_{lk}(\omega) = \int_0^\infty r dr K(r) f_{lk}(r) J_l\left(\frac{\omega}{c} r\right), \quad (8)$$

and $\omega_\xi = \xi\omega_\beta/\eta$ is the chromatic frequency.

The wake force enters via its impedance representation,

$$Z_1(\omega) = i\int_{-\infty}^{\infty} \frac{dz}{c} e^{-i\omega z/c} W_1(z). \quad (9)$$

If we take the broad-band resonator impedance model, then for given shunt impedance R_S, quality factor Q, and resonator frequency ω_R, the impedance is expressed as

$$Z_1(\omega) = \frac{c}{\omega}\frac{R_S}{1+iQ\left(\frac{\omega_R}{\omega}-\frac{\omega}{\omega_R}\right)}. \quad (10)$$

For a Gaussian distribution in the longitudinal phase space, the unperturbed distribution function and the weight function can be written as

$$\varphi_0(r) = \frac{\eta c e^{-r^2/2\sigma^2}}{2\pi\sigma^2\omega_s}, \quad K(r) = \frac{e^{-r^2/2\sigma^2}}{2\pi\sigma^2}. \quad (11)$$

The orthonormal radial functions are the generalized Laguerre polynomials

$$f_{lk}(r) = \sqrt{\frac{2\pi k!}{(|l|+k)!}}\left(\frac{r}{\sqrt{2}\sigma}\right)^{|l|} L_k^{|l|}\left(\frac{r^2}{2\sigma^2}\right), \quad (12)$$

then from Eq. (8),

$$\begin{aligned} g_{lk}(\omega) &= \frac{\varepsilon(l)}{\sqrt{2\pi k!(|l|+k)!}}\left(\frac{\omega\sigma}{\sqrt{2}c}\right)^{|l|+2k} e^{-\omega^2\sigma^2/2c^2},\\ \varepsilon(l) &= \begin{cases} 1\,, & l\ge 0\,;\\ (-1)^l, & l<0\,. \end{cases} \quad (13) \end{aligned}$$

This corresponds to the Hermite modes of the dipole moment,

$$\rho_y(z) \propto e^{-z^2/2\sigma^2} H_{|l|+2k}\left(\frac{z}{\sqrt{2}\sigma}\right). \quad (14)$$

We consider here the azimuthal mode coupling only for three lowest radial modes ($k = 0, 1, 2$). The coupling matrix consists of 9 blocks,

$$M = \begin{pmatrix} l\delta_{ll'}+M_{l0,l'0} & M_{l0,l'1} & M_{l0,l'2}\\ M_{l1,l'0} & l\delta_{ll'}+M_{l1,l'1} & M_{l1,l'2}\\ M_{l2,l'0} & M_{l2,l'1} & l\delta_{ll'}+M_{l2,l'2}\end{pmatrix}, \quad (15)$$

$$\begin{aligned} M_{lk,l'k'} &= -i\frac{N_b r_e c}{4\pi\gamma T_0\omega_\beta\omega_s}\frac{i^{l-l'}\varepsilon(l)\varepsilon(l')}{\sqrt{k!(|l|+k)!k'!(|l'|+k')!}}\\ &\times\int_{-\infty}^{\infty} Z_1(\omega+\omega_\xi) e^{-\omega^2\sigma^2/c^2}\left(\frac{\omega\sigma}{\sqrt{2}c}\right)^{|l|+|l'|+2(k+k')} d\omega. \end{aligned}$$

Before computing, the integration variable ω should be changed to the dimensionless $w = \omega\sigma/c$, and accordingly we introduce

$$\begin{aligned} w_R = \omega_R\sigma/c, \quad \chi = \omega_\xi\sigma/c = \nu_\beta\xi\frac{\sigma_E/E}{\nu_S},\\ \frac{c}{\sigma}Z_1(\omega) = \frac{cR_S/Q}{w/Q+i(w_R-w^2/w_R)}. \quad (16) \end{aligned}$$

Here χ is the effective value of chromatic phase for a Gaussian bunch, and the impedance is substituted from the broad-band resonator model, Eq. (10). Then we rewrite the mode coupling matrix as

$$\begin{aligned} M_{lk,l'k'} &= -i\frac{N_b r_e c(cR_S/Q)}{4\pi\gamma T_0\omega_\beta\omega_s}\frac{i^{l-l'}\varepsilon(l)\varepsilon(l')}{\sqrt{k!(|l|+k)!k'!(|l'|+k')!}}\\ &\times\int_{-\infty}^{\infty}\frac{(w/\sqrt{2})^{|l|+|l'|+2(k+k')} e^{-w^2} dw}{(w+\chi)/Q+i(w_R-(w+\chi)^2/w_R)}. \quad (17) \end{aligned}$$

The tune of each mode $(\Omega-\omega_\beta)/\omega_s$ is obtained by solving the eigenvalue problem, Eq. (6), for matrix $l\delta_{ll'}\delta_{kk'} + M_{lk,l'k'}$. At $N_b \to 0$ the mode frequency $\Omega = \omega_\beta + l\omega_s$ corresponds to the lth synchrobetatron sideband. The matrix has infinite dimension because of $-\infty < l < \infty$.

For most cases considered below we can truncate the matrix at $-5 \le l \le 4$, and calculate the eigenvalues numerically. To check-up the convergency, we compared the eigenvalues with those of the truncation at $-9 \le l \le 6$.

4.2 Betatron Tune Variation Along the Bunch

The transverse fields of the positron/proton bunch cause variation of the effective transverse size of electron cloud over the bunch passage. The variable density of the cloud results in different incoherent tuneshifts along the bunch. Simulation shows that in some cases we can only consider the linear part of the tune variation along the bunch [5].

Let us modify the standard analysis of Section 4.1 to include this effect. Now, in addition to the chromaticity effect, we have to introduce the betatron frequency variation term $\zeta z/\sigma$, then

$$\omega_\beta(\delta, z) = \omega_\beta(1+\xi\delta+\zeta z/\sigma)$$

and the transverse dipole perturbation Ψ_1 in the Vlasov equation (1) should be decomposed as

$$\Psi_1 \propto \frac{\partial \Psi_0}{\partial q} e^{i\theta} K(r) \sum_{lk} a_{lk} f_{lk}(r) e^{il\phi} e^{i\chi(\phi) - i\Delta(\phi)}, \quad (18)$$

where besides the chromatic phase,

$$\chi(\phi) = \xi \omega_\beta r \cos\phi / c\eta = \omega_\xi r \cos\phi / c, \; \omega_\xi = \xi \omega_\beta / c\eta,$$

we introduced

$$\Delta(\phi) = \zeta \omega_\beta r \sin\phi / \sigma\omega_s = \omega_\zeta r \sin\phi / c, \; \omega_\zeta = \zeta \omega_\beta c / \sigma \omega_s.$$

This will modify the Bessel function argument in Eqs. (6.74,75) and henceforth,

$$\int_0^{2\pi} \frac{d\phi}{2\pi} \exp[-il\phi + i\omega \frac{z}{c} - i(\omega_\xi \cos\phi - \omega_\zeta \sin\phi)\frac{r}{c}]$$
$$= i^l e^{-il\phi_0} J_l(\frac{r}{c}\sqrt{(\omega - \omega_\xi)^2 + \omega_\zeta^2}),$$

where

$$\phi_0 = \arg(\omega - \omega_\xi + i\omega_\zeta).$$

As a consequence, we should modify the mode spectra in Eq. (7) using Eq. (8),

$$g_{lk}(\sqrt{(\omega - \omega_\xi)^2 + \omega_\zeta^2}) = e^{-il\phi_0} \int_0^\infty r dr K(r) f_{lk}(r)$$
$$\times J_l(\frac{r}{c}\sqrt{(\omega - \omega_\xi)^2 + \omega_\zeta^2}),$$

and thus the formalism for the longitudinal tune variation is ready.

For the Gaussian bunch we only have to replace the arguments of $g_{lk}(\omega)$ in Eq. (13),

$$\begin{aligned} g_{lk}(\omega - \omega_\xi, \omega_\zeta) &= \frac{\varepsilon(l) e^{-((\omega-\omega_\xi)^2 + \omega_\zeta^2)\sigma^2/2c^2}}{\sqrt{2\pi k!(|l|+k)!}} \\ &\times \left(\frac{\sigma(\omega - \omega_\xi - i\omega_\zeta)}{\sqrt{2}c}\right)^{|l|} \\ &\times \left(\frac{\sigma^2((\omega-\omega_\xi)^2 + \omega_\zeta^2)}{2c^2}\right)^k, \\ \varepsilon(l) &= \begin{cases} 1, & l \geq 0\,; \\ (-1)^l, & l < 0\,. \end{cases} \end{aligned}$$

The final form of the coupling matrix for the Gaussian bunch and broad-band resonator impedance now is

$$M_{lk,l'k'} = -i \frac{N_b r_e c (cR_S/Q)}{4\pi\gamma T_0 \omega_\beta \omega_s} \frac{i^{l-l'} \varepsilon(l)\varepsilon(l')}{\sqrt{k!(|l|+k)!k'!(|l'|+k')!}}$$
$$\times \int_{-\infty}^{\infty} \frac{A(w) dw}{(w+\chi)/Q + i(w_R - (w+\chi)^2/w_R)}, \quad (19)$$

$$A(w) = \frac{(w - i\Delta)^{|l|}(w + i\Delta)^{|l'|}(w^2 + \Delta^2)^{k+k'}}{2^{k+k'+(|l|+|l'|)/2}} e^{-w^2 - \Delta^2}.$$

The eigenvalues do not depend on the sign of Δ.

With the same SPS parameters as used in Figs. 6,7, we can see in Figs. 15,16 the stabilizing effect of the tune variation at $\Delta \geq 1$, as predicted in [7]. The positive chromaticity effect remains, see Fig. 17.

4.3 General Case, the Transverse Wake Function in the Form $W(z, z')$

For more general situations, e. g., for the electron cloud response to dipole perturbations, translation invariance in z does not hold, and the wake function cannot be reduced to the form $W(z - z')$. We now trace the differences in the linearized Vlasov formalism resulting from the general form of the wake, $W_1(z, z')$. This function must vanish for $z > z'$.

First we introduce its full Fourier transform $\hat{Z}_1(\omega, \omega')$ and call it *a generalized impedance*,

$$W_1(z, z') = \int\int \frac{d\omega}{2\pi}\frac{d\omega'}{2\pi}\frac{1}{i}\hat{Z}_1(\omega, \omega')\, e^{i(\omega z - \omega' z')/c}. \quad (20)$$

The particular case where $\hat{Z}_1(\omega, \omega') = 2\pi\delta(\omega - \omega')Z(\omega)$ corresponds to the conventional wake $W_1(z - z')$.

Substituting Eq. (20) into Eq. (2), we find the transverse force

$$F(s, z) = -\frac{N_b r_e}{\gamma} e^{-i\Omega s/c} \int W_1(z, z')\rho_1(z')dz'$$
$$= \frac{N_b r_e}{\gamma} e^{-i\Omega s/c} \int \frac{d\omega}{2\pi} e^{i\omega z} \int \frac{d\omega'}{2\pi} \tilde{\rho}_1(\omega')\hat{Z}_1(\omega, \omega'), \quad (21)$$

where

$$\tilde{\rho}_1(\omega) = \int dz\, e^{-i\omega z/c} \rho_1(z) \quad (22)$$

is the Fourier transform of the beam dipole moment distribution $\rho_1(z)$. Using a derivation shown in Eq. (6.75), we arrive at the result of Eq. (6.178),

$$\tilde{\rho}_1(\omega') = 2\pi \frac{\omega_s}{c\eta} \sum_{l,k} \int_0^\infty r dr K(r)$$
$$\times a_{lk} f_{lk} i^{-l} J_l((\omega' - \omega_\xi)r/c). \quad (23)$$

We put this expression in Eq. (1) transformed appropriately (cf. the derivation of Eq. (6.177)),

$$i\left(\frac{\Omega - \omega_\beta}{\omega_s} - l\right) K(r) \sum_{k'} a_{lk'} f_{lk'} = \frac{N_b r_e c i^l \varphi_0(r)}{4\pi\gamma\omega_\beta\omega_s T_0}$$
$$\times \int \frac{d\omega}{2\pi} J_l((\omega - \omega_\xi)r/c) \int \frac{d\omega'}{2\pi} \tilde{\rho}_1(\omega')\hat{Z}_1(\omega, \omega'), \quad (24)$$

and relating the weight function $K(r)$ to the unperturbed distribution $\varphi_0(r)$, Eq. (5), we only need to use the orthonormality condition Eq. (4) to reduce the integral equation Eq. (24) to a linear equation set in the basis of mode functions f_{lk},

$$\left(\frac{\Omega - \omega_\beta}{\omega_s} - l\right) a_{lk} = -\frac{N_b r_e c}{2\gamma\omega_\beta\omega_s T_0} \sum_{l'k'} \hat{M}_{lk,l'k'} a_{l'k'}, \quad (25)$$

where the general mode coupling matrix $\hat{M}_{lk,l'k'}$ is expressed via the generalized impedance,

$$\hat{M}_{lk,l'k'} = -i \frac{N_b r_e c i^{l-l'}}{4\pi\gamma\omega_\beta\omega_s T_0}$$

$$\times \int\int d\omega d\omega' g_{lk}(\omega-\omega_\xi) g_{l'k'}(\omega'-\omega_\xi) \hat{Z}_1(\omega,\omega'), \quad (26)$$

while the mode spectrum $g_{lk}(\omega)$ is given by Eq. (8), as for the standard case.

Going to the time domain, we introduce the dipole moment distributions corresponding to the mode spectra,

$$\tilde{g}_{lk}(z) = \int \frac{d\omega}{2\pi c}\, g_{lk}(\omega) e^{i\omega z/c}, \quad \tilde{g}_{lk}(-z) = \tilde{g}^*_{lk}(z), \quad (27)$$

and rewrite the double integral, in Eq. (26),

$$\hat{M}_{lk,l'k'} = \frac{\pi N_b r_e c i^{l-l'}}{\gamma\omega_\beta\omega_s T_0} \int_{-\infty}^{\infty} dz\, \tilde{g}^*_{lk}(z) \times \int_z^{\infty} dz' \tilde{g}_{l'k'}(z') W(z,z') e^{-i\omega_\xi (z-z')} \quad (28)$$

It is easy see that at vanishing chromaticity, $\omega_\xi = 0$, all the matrix elements are real numbers.

This time-domain form may give an advantage in computation of the mode coupling matrix.

4.4 Gaussian Bunch

For the radial head-tail modes of the Gaussian bunch, we use Eqs. (11-13) to write the final form of the mode coupling matrix,

$$\hat{M}_{lk,l'k'} = -i \frac{N_b r_e c}{8\pi^2\gamma T_0 \omega_\beta\omega_s} \frac{i^{l-l'}\varepsilon(l)\varepsilon(l')}{\sqrt{k!(|l|+k)!k'!(|l'|+k')!}} \times \int_{-\infty}^{\infty}\int_{-\infty}^{\infty} d\omega d\omega' \hat{Z}_1(\omega+\omega_\xi, \omega'+\omega_\xi) \times \left(\frac{\omega\sigma}{\sqrt{2}c}\right)^{|l|+2k} \left(\frac{\omega'\sigma}{\sqrt{2}c}\right)^{|l'|+2k'} e^{-(\omega^2+\omega'^2)\sigma^2/2c^2}. \quad (29)$$

To obtain the time-domain form, we transform the mode spectra, Eq. (13), and get

$$\tilde{g}_{lk}(z) = \frac{\Gamma(k+\frac{1+|l|}{2})}{2\pi\sigma\sqrt{\pi k!(|l|+k)!}}\, {}_1F_1(k+\frac{1+|l|}{2}, \frac{1}{2}; -\frac{z^2}{2\sigma^2}), \quad (30)$$

for even l, and

$$\tilde{g}_{lk}(z) = i\mathrm{sign}l \frac{\Gamma(k+1+\frac{|l|}{2})}{2\pi\sigma\sqrt{\pi k!(|l|+k)!}} \left(\frac{z}{\sqrt{2}\sigma}\right) \times {}_1F_1(k+1+\frac{|l|}{2}, \frac{3}{2}; -\frac{z^2}{2\sigma^2}), \quad (31)$$

for odd l. Of course, the hypergeometric function can be reduced to the "oscillator wave functions" expressed via the Hermite polynomials, see Eq. (14). However, for higher-order modes the above form is more efficient in computation. For $z \geq \sigma\sqrt{|l|+2k}$ these functions have a Gaussian cut-off, and thus the infinite integration range in Eq. (28) is not a serious problem. Finally we have to substitute Eqs. (30,31) into Eq. (28) in order to evaluate the general mode coupling matrix for the Gaussian bunch.

5 A SIMPLE MODEL OF TRANSVERSE FEEDBACK

A bunch-to-bunch feedback integrates the dipole moment over the total bunch length ($\sigma_z = 5$mm at KEKB!) and applies its proportional kick after one turn, with a tunable gain and phase shift. The feedback kicker pulse is practically constant over this bunch length. At KEKB $2\pi\nu_s \ll 1$, thus the one-turn delay may not cause a problem like in LEP machine.

Assuming a perfectly linear (no gain saturation) and noiseless feedback hardware, we can describe its action by an equivalent transverse impedance,

$$Z_{FB} = -ig_{FB} e^{i\phi_{FB}} \delta(\omega)$$

where g_{FB} and ϕ_{FB} are the feedback gain and phase.

The feedback phase parameter can be tuned to purely resistive, $\phi_{FB} = \pi/2$, or purely reactive, $\phi_{FB} = 0, \pi$, or mixed mode.

At zero chromaticity, the feedback only acts upon the $l = 0$ mode; at positive chromaticity, higher-order synchrobetatron modes are also influenced.

6 TYPICAL BEHAVIOR OF THE MODE TUNES

The eigenvalues of truncated M, Eq. (17) (i. e., tunes of each mode) are computed as functions of cR_S/Q at fixed bunch intensity, using ω_R and Q from the wake simulation for KEKB LER and CERN SPS [4, 5].

The following figures show the computed mode tunes vs R_S/Q or the cloud density ρ_c, since R_S/Q is linearly related with it.

The positive slope of all the mode tunes resulting from incoherent effect of the electron cloud (single-particle focusing by the cloud) is equal in all the modes; it is ignored in the following figures.

The parameters of the transverse dipole wake from the electron cloud correspond to large values of the wake oscillation parameter $p = \omega_R\sigma_z/c$. For KEKB LER $p = 3$, for CERN SPS $p = 1.5$. So, we are working with the case of "long" bunch, the beam spectrum samples the low-frequency part of the cloud impedance. An important consequence is that the positive chromaticity results in damping of all the lower-order head-tail modes up to orders $|l| + 2k \sim p^2$, at least for small bunch intensities, $\Delta\nu_{\mathrm{coh}} \ll \nu_s$.

The above statement does not contradict with the vanishing sum of all decrements, see Appendix A. The damping of a dozen lower-order modes is balanced by the weak anti-damping of a great many of higher-order modes. However, their weak instability is not important because of stabilization by the incoherent tune spread of any nature, or by quantum fluctuations in electron/positron machines, see Appendix B.

At high intensity the mode coupling becomes important, although for the long-bunch case the diagonal elements in

the mode coupling matrix tend to dominate. With sufficiently high chromaticities, $\chi \sim 2$, all the lower-order modes included in truncation become stable, i. e. the high positive chromaticity can significantly enhance the TMCI threshold for "long" bunches.

Figures 2,3 show the effect of positive chromaticity for the parameters of KEKB LER. With higher values of Q, see Figs. 4,5, the chromaticity effect becomes more pronounced. The instability thresholds with $Q = 1$, Figs. 2,3, are in reasonable agreement with observations of the positron beam blowup at KEKB LER [8].

The same effect is shown in Figs. 6,7 with the parameters relevant to the CERN SPS. The chromaticity dependence shown is consistent with the electron cloud instability simulation for this machine [9].

Now return to the KEKB LER. The transverse feedback is not very efficient against rather high increments of the TMCI at zero chromaticity, Fig. 8. However, the feedback tuned resistive, and in combination with the moderate positive chromaticity, can seriously raise the threshold, Fig. 9. The same enhancement from the reactive feedback alone, Figs. 10,11, leads to a conclusion that the parameters of the bunch-to-bunch feedback, including its phase, can be optimized with respect not only to the residual dipole oscillation, but also to the beam blowup believed to be caused by the electron cloud. And in combination with the chromaticity, Fig. 12, the effect of the feedback phase is stronger.

Dependence of the instability threshold on the bunch current with different filling patterns at KEKB LER is shown in Figs. 13,14. Here variation of the bunch current means proportional variation of the cloud density plus the square-root scaling of the wake oscillation frequency ω_R.

For the parameters of CERN SPS, Figs. 15,16 show the mode coupling dependence at 6 different gradients of the linear tune variation along the bunch, the tune variation of 1 means that the incoherent tune shift varies from Q_s to $-Q_s$ over $\pm\sigma_z$. The graphs demonstrate the stabilizing effect from the longitudinal variation of incoherent betatron tune, cf. [7]. Fig. 17 presents the effect of the positive chromaticity at fixed tune variation parameter.

7 MODE STABILITY IN THE COASTING BEAM LIMIT

Using the coasting-beam limit, $\omega_R\sigma_z/c \gg 1$,for estimation of the bunched-beam stability, one usually takes the maximum of $\mathrm{Re}Z_1$ to be sure that *all the modes* are stable. For the BBR $\omega_{max} \approx \omega_R$, this means $\mathrm{Re}Z_1(\omega_R)$.

However, for our case with low mode numbers, $l \sim 1$, and $lc/\sigma_z \ll \omega_R$, this will yield too strong a condition (sufficient, but not necessary).

Let us take the coasting-beam limit condition for stability in its *full form*, see Eq. (6.263) in [3]:

$$-\frac{N}{cT_0}\frac{r_e c^2}{2\gamma T_0\omega_\beta}\mathrm{Re}Z_1(n\bar\omega_0+\omega_\beta) < \Delta\delta|-n\bar\omega_0\eta+\xi\omega_\beta|,$$

with the linear density corresponding to that in the bunch,

$$\frac{N_b}{\sqrt{2\pi}\sigma_z} \leftarrow \frac{N}{cT_0},$$

and $\Delta\delta$ corresponding to σ_E/E for Gaussian bunches.

Relating this coasting beam situation to the bunched beam parameters, we should also replace

$$\begin{aligned} n\bar\omega_0 &\rightarrow \omega \text{ of the mode} \\ \xi\omega_\beta/\eta &\rightarrow \omega_\xi, \text{ the chromatic frequency} \\ c\eta\Delta\delta/\omega_s &\rightarrow \sigma_z, \text{ the bunch length} \end{aligned}$$

For the higher-order modes the accurate treatment by the TMC theory shows stability.

For the lower-order modes, $l \sim 1-2$, we take

$$\omega \simeq -\frac{c}{\sigma_z}l \ (\ll \omega_R)$$

and approximate the impedance

$$\mathrm{Re}Z_1 \approx \frac{cR_S}{Q}\frac{\omega}{Q\omega_R^2}.$$

Then, neglecting $\omega_\beta \ll \omega$, we obtain the stability condition for the lth mode

$$\frac{Nr_e c^2}{2\gamma T_0^2\omega_\beta\omega_s\sigma_z}\frac{cR_S}{Q}\frac{1}{Q\omega_R^2} < \left|1+\frac{\omega_\xi\sigma_z}{c\,l}\right| = |1+\chi/l|\,,$$

where χ is the chromatic phase. Note that $\omega_R^2 \propto N_b/\sigma_z \propto N$, $cR_S/Q \propto \rho_c$, and $\omega_s\sigma_z \propto \eta$.

Hence, we come to the scaling of the threshold level of the electron cloud density

$$\rho_{c,\mathrm{th}} \propto \eta\, Q\,|1+\chi/l|, \ \text{ for } l \sim 1-2.$$

For the case $\omega \approx -\omega_R$, we approximate

$$\mathrm{Re}Z_1 \approx \frac{cR_S}{Q}\frac{Q}{\omega_R},$$

and arrive at somewhat different stability condition,

$$\frac{Nr_e c^2}{2\gamma T_0^2\omega_\beta\omega_s\sigma_z}\frac{cR_S}{Q}\frac{Q}{\omega_R^2} < |1+\omega_\xi/\omega_R|\,,$$

whence the threshold scaling is

$$\rho_{c,\mathrm{th}} \propto \frac{\eta}{Q}|1+\chi\frac{c}{\omega_R\sigma_z}|, \ \text{ for } l \sim \omega_R\sigma_z/c,$$

i. e. the mode number is replaced with the wake oscillation parameter. In the saturation condition, $\rho_{c,\mathrm{th}} \propto N_{b,\mathrm{th}}/L_{\mathrm{sep}}$.

For the opposite situation, $\omega_R\sigma_z/c \ll 1$, from the single-bunch interaction parameter Z_1N_b/σ_z, with $Z_1 \propto \rho_c$, we find a different scaling of the instability threshold,

$$Z_1N_b/\sigma_z \propto N_b^2/\sigma_z L_{\mathrm{sep}}.$$

8 CONCLUSION

The paper presents analytical tools for studies of strong head-tail instability caused by electron cloud, including the machine chromaticity. The standard multi-mode eigenvalue analysis of the transverse mode coupling is extended by including into consideration the specific properties of the cloud response caused by its pinching, Section 4.

On the basis of this study we come to a conclusion on very important role of the high positive chromaticity, the most appropriate measure of its stabilizing effect being the respective chromatic phase χ. In different parameter sets considered in Section 6 we always obtained stabilization at $\chi \sim 2$ radian. Smaller values of the chromaticity were nevertheless efficient in combination with the transverse bunch-to-bunch feedback system.

Although it is difficult to take into full account analytically such a complex phenomenon as the electron cloud, the analytical effort applied to simplified dynamical models may provide some insight and help in better understanding the results of simulation studies of the beam dynamics under the influence of the electron cloud.

9 ACKNOWLEDGEMENTS

Important part of this work has been done during the author's visits to KEKB and CERN SL/AP, I am grateful to S.-i. Kurokawa, S. Myers and F. Ruggiero for giving me this possibility, I highly appreciate both the hospitality and ideal working environment in these laboratories. Useful discussions and collaboration with H. Burkhardt, J. Flanagan, H. Fukuma, Y. Funakoshi, T. Ieiri, S.-i. Kurokawa, K. Ohmi, K. Oide, F. Ruggiero, G. Rumolo, A.A. Valishev, L. Wang, S. Su Win, K. Yokoya, F. Zimmermann, and many other colleagues helped me a lot in this work.

10 REFERENCES

[1] F. Zimmermann, "The Electron CLoud Instability: Summary of Measurements and Understanding", presented at PAC'2001, Chicago, 2001, CERN-SL-2001-035(AP), (2001).

[2] K. Ohmi and F. Zimmermann, Phys. Rev. Lett. **85**, 3821 (2000).

[3] A.W. Chao, *Physics of Collective Instabilities in High Energy Accelerators* (J. Wiley, New York,1993).

[4] K. Ohmi et al., Phys. Rev. E **65** 016502 (2001).

[5] F. Zimmermann, G. Rumolo, elswhere these proceedings.

[6] T. Raubenheimer et al., Phys. Rev. E **52**, 5487 (1995).

[7] V.V. Danilov, Phys. Rev. ST-Accel. Beams, **1**, 041301, (1998).

[8] H. Fukuma, elswhere these proceedings.

[9] G. Rumolo, F. Zimmermann, elswhere these proceedings.

Appendix A: The Sum of Decrements for a Gaussian Bunch

The sum of eigenvalues is equal to the trace of the mode coupling matrix. Hence, from Eq. (7), the sum of the synchrobetatron mode decrements

$$\begin{aligned}\sum_{k,l}\mathrm{Im}\Omega &= -\frac{Nr_e c}{2\gamma T_0\omega_\beta} \\ &\quad\times\int_{-\infty}^{\infty} d\omega' \mathrm{Re}[Z_1(\omega'+\omega_\xi)]\sum_{k,l} g_{lk}^2(\omega')\,.\end{aligned}$$

For a Gaussian bunch, from Eq. (13),

$$\begin{aligned}2\pi\sum_{k,l} g_{lk}^2(\omega') &= e^{-\omega^2\sigma^2/c^2}\sum_{l=-\infty}^{\infty}\sum_{k=0}^{\infty}\frac{(\omega^2\sigma^2/2c^2)^{|l|+2k}}{k!(|l|+k)!} \\ &= e^{-\omega^2\sigma^2/c^2}\sum_{l=-\infty}^{\infty} I_{|l|}\left(\frac{\omega^2\sigma^2}{c^2}\right) \\ &= e^{-x}(I_0(x)+2I_1(x)+2I_2(x)+\ldots) \\ &= e^{-x}e^{x} = 1\,.\end{aligned}$$

Since wakefields are real functions of s, $\mathrm{Re}Z_1(\omega)$ is an odd function of ω with a vanishing average. Thus, the sum of the mode decrements, $\sum_{k,l}\mathrm{Im}\Omega$, also vanishes.

Appendix B: Effect of Diffusion on Higher-Order Head-Tail Modes

With the fast-oscillating wake (or for a "long" bunch), the positive chromaticity can stabilize all the lower-order head-tail modes up to mode numbers $|l|+2k \le (\omega_R\sigma_z/c)^2$. However their decrements will be compensated by (small) increments of a large number of higher-order modes to give a vanishing sum. But there is a reason why the higher-order modes are of no special concern.

In e^+e^- machines quantum fluctuations of the synchrotron radiation cause diffusion in particle oscillations. Consider $|l|, k \gg 1$, then the dipole moment is given by the Hermite mode, Eq. (14),

$$\rho_y(z) \propto e^{-z^2/2\sigma^2} H_{|l|+2k}\left(\frac{z}{\sqrt{2}\sigma}\right) \longrightarrow \cos\frac{\tilde{l}z}{\sigma},\ |z|\le\sigma.$$

In the above, $\tilde{l} = |l| + 2k$. The Green function of diffusion is

$$G(z,z') = \frac{1}{2\sqrt{\pi Dt}}\exp\left[-\frac{(z-z')^2}{4Dt}\right],$$

where the diffusion constant $D \sim \sigma^2/\tau$, and τ is the radiation damping time.

After a short time, $t \ll \omega_s^{-1}$,

$$\begin{aligned}\tilde{\rho}_y(z) &\sim \int_{-\infty}^{\infty}\rho_y(z')G(z,z')dz' \\ &\approx \cos\frac{\tilde{l}z}{\sigma}\exp\left[-\frac{\tilde{l}^2Dt}{\sigma^2}\right] \sim e^{-\tilde{l}^2t/\tau}\rho_y(z).\end{aligned}$$

Thus, while the incoherent damping gives $\tau/\tilde{l}$, the diffusion smear time is even much shorter, $\sim \tau/\tilde{l}^2$.

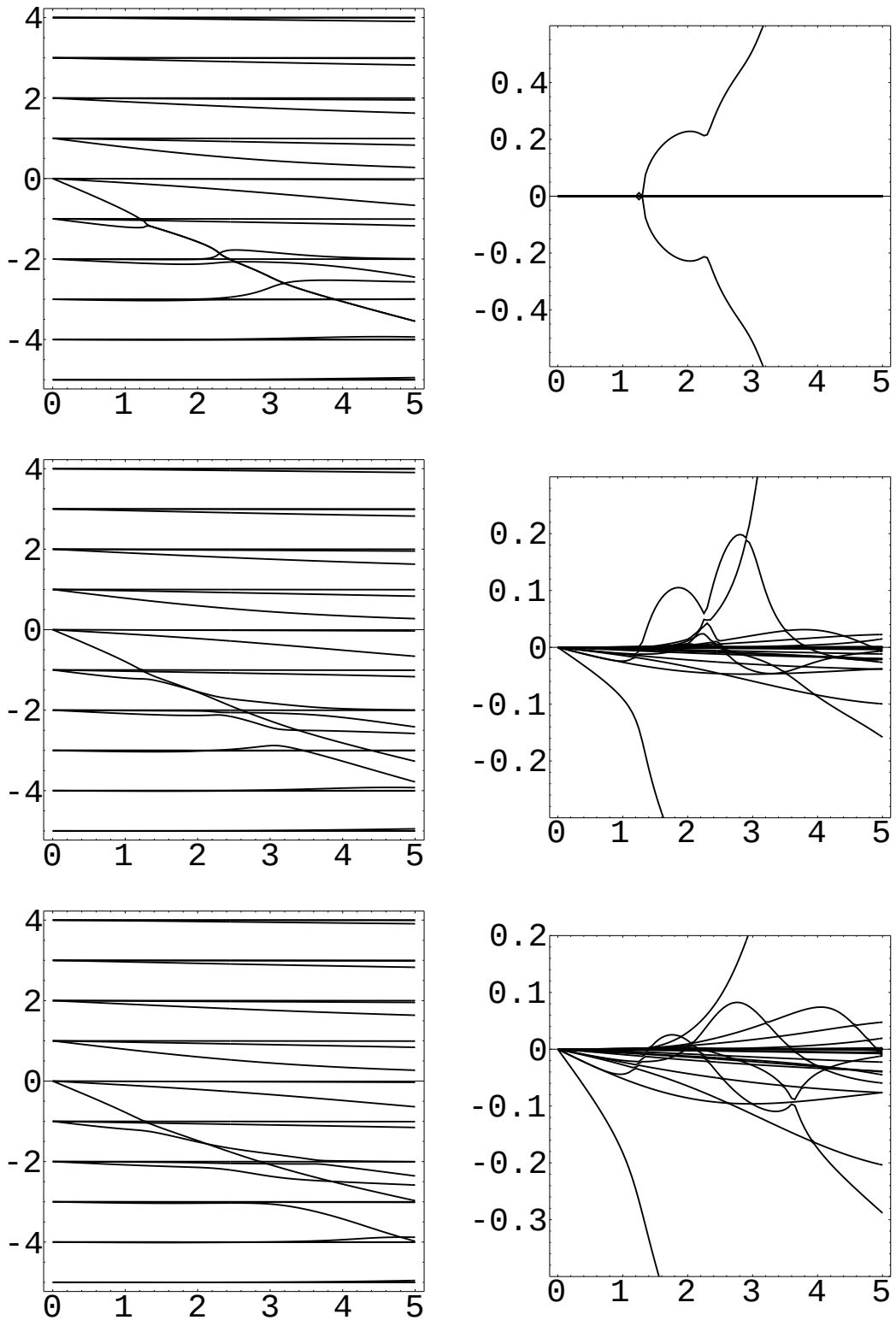

Figure 2: KEKB LER, head-tail mode tunes in units of the synchrotron tune vs the cloud density $\rho_c \times 10^{-12}\mathrm{m}^{-3}$ at $I_b = 0.52$mA, $Q = 1$. Left: real part, right: imaginary part. From top to bottom: the chromatic phase is 0.0, 0.25, 0.5.

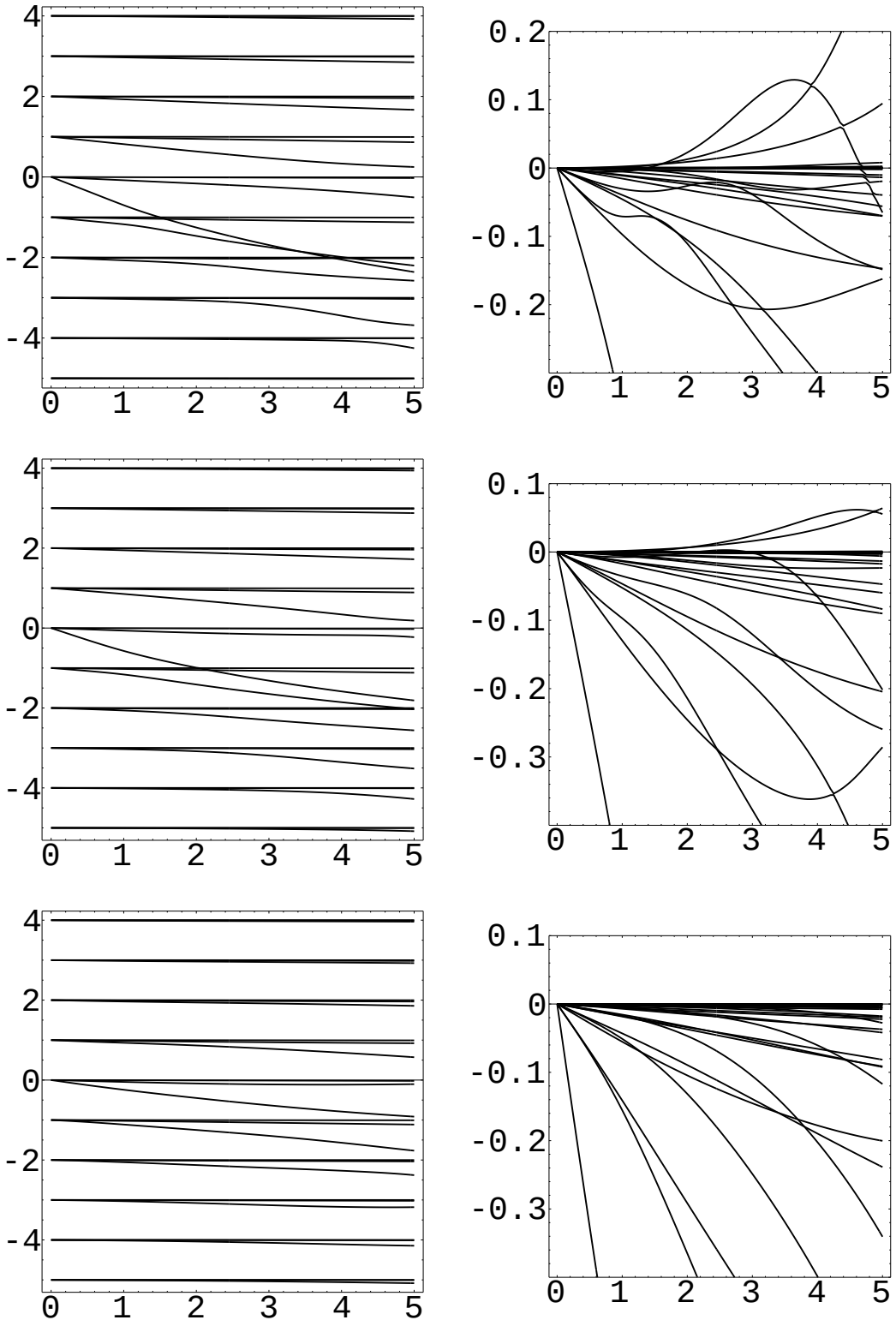

Figure 3: Continued from previous figure: KEKB LER, head-tail mode tunes in units of the synchrotron tune vs the cloud density $\rho_c \times 10^{-12}\mathrm{m}^{-3}$ at $I_b = 0.52\mathrm{mA}$, $Q = 1$. Left: real part, right: imaginary part. From top to bottom: the chromatic phase is 1.0, 1.5, 2.5.

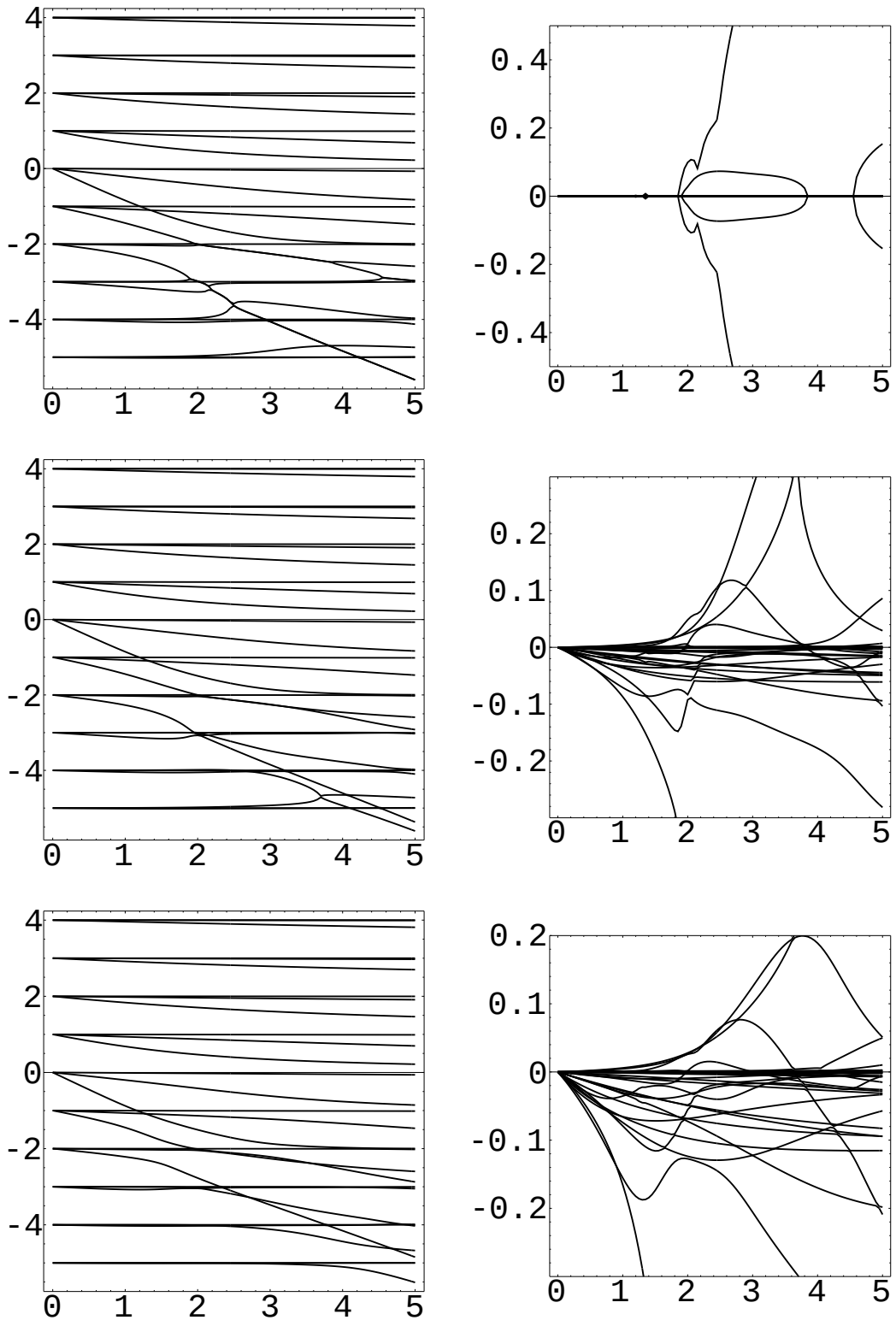

Figure 4: KEKB LER, h ead-tail mode tunes in units of the synchrotron tune vs the cloud density $\rho_c \times 10^{-12}\mathrm{m}^{-3}$ at $I_b = 0.52$mA, $Q = 6.3$. Left: real part, right: imaginary part. From top to bottom: the chromatic phase is 0.0, 0.25, 0.5.

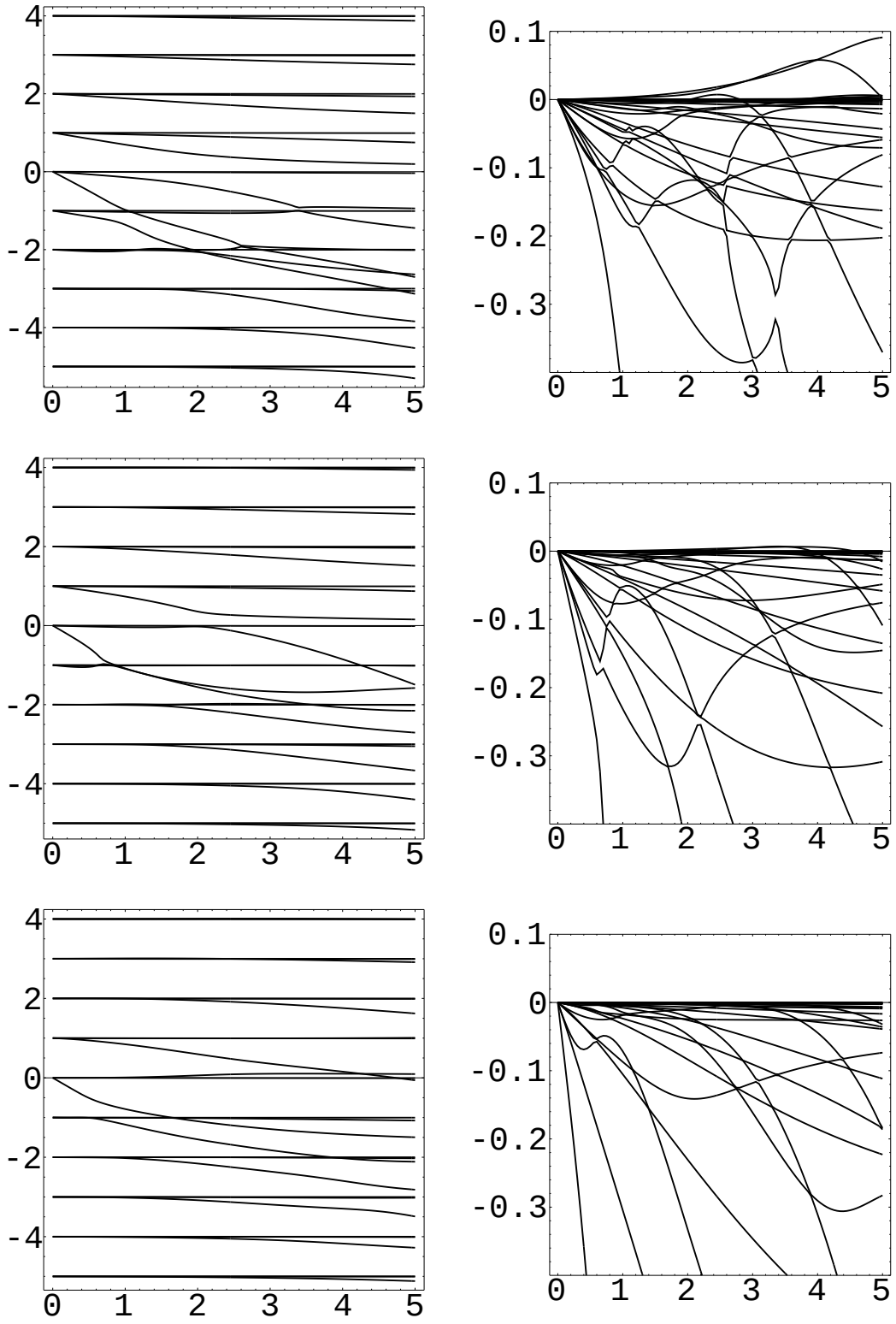

Figure 5: Continued from previous figure: KEKB LER, head-tail mode tunes in units of the synchrotron tune vs the cloud density $\rho_c \times 10^{-12}\mathrm{m}^{-3}$ at $I_b = 0.52$mA, $Q = 6.3$. Left: real part, right: imaginary part. From top to bottom: the chromatic phase is 1.0, 1.5, 2.0.

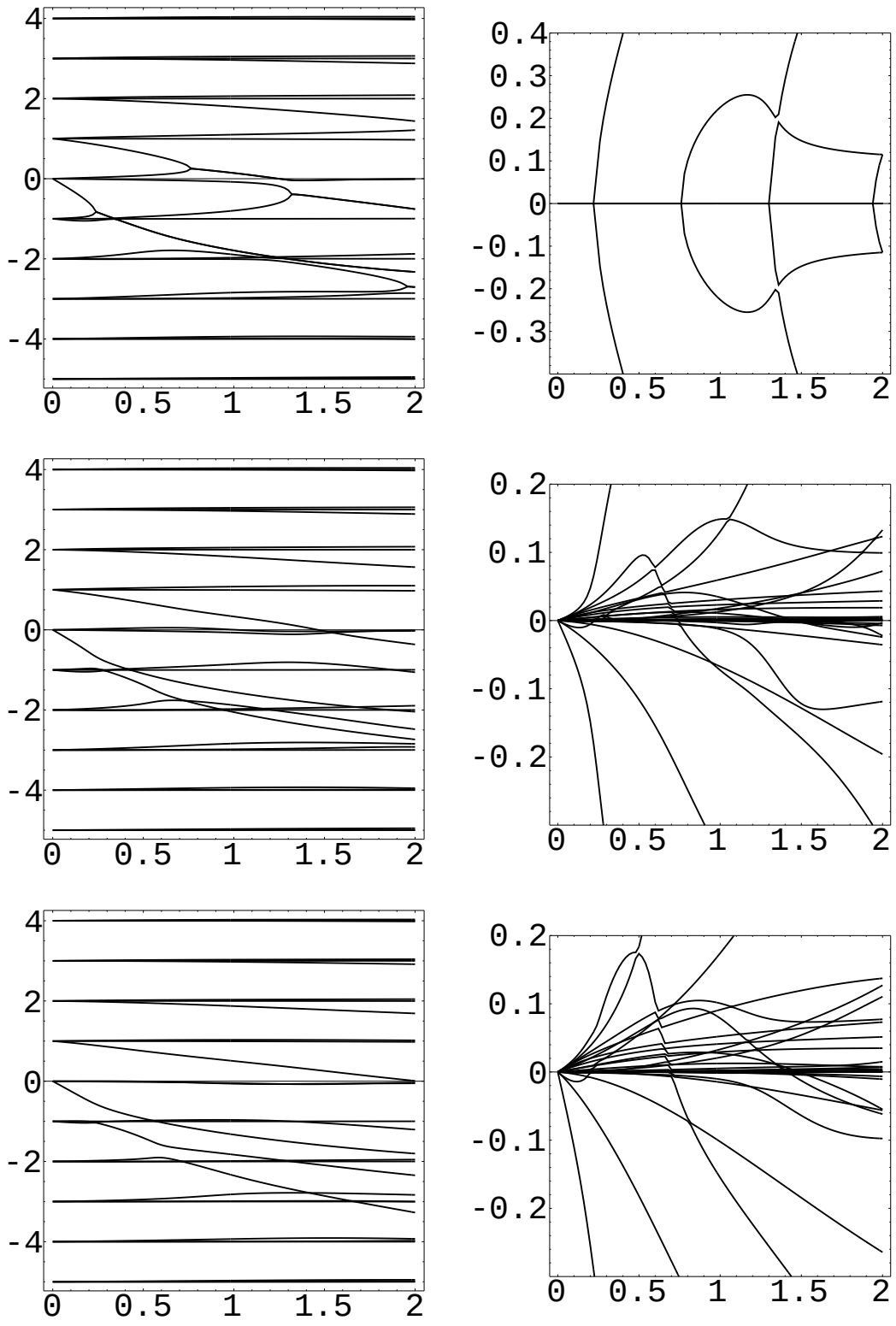

Figure 6: CERN SPS, head-tail mode tunes in units of the synchrotron tune vs the cloud density $\rho_c \times 10^{-12}\mathrm{m}^{-3}$ at $N_b = 10^{11}$, $Q = 2$. Left: real part, right: imaginary part. From top to bottom: the chromatic phase is 0.0, 0.25, 0.5.

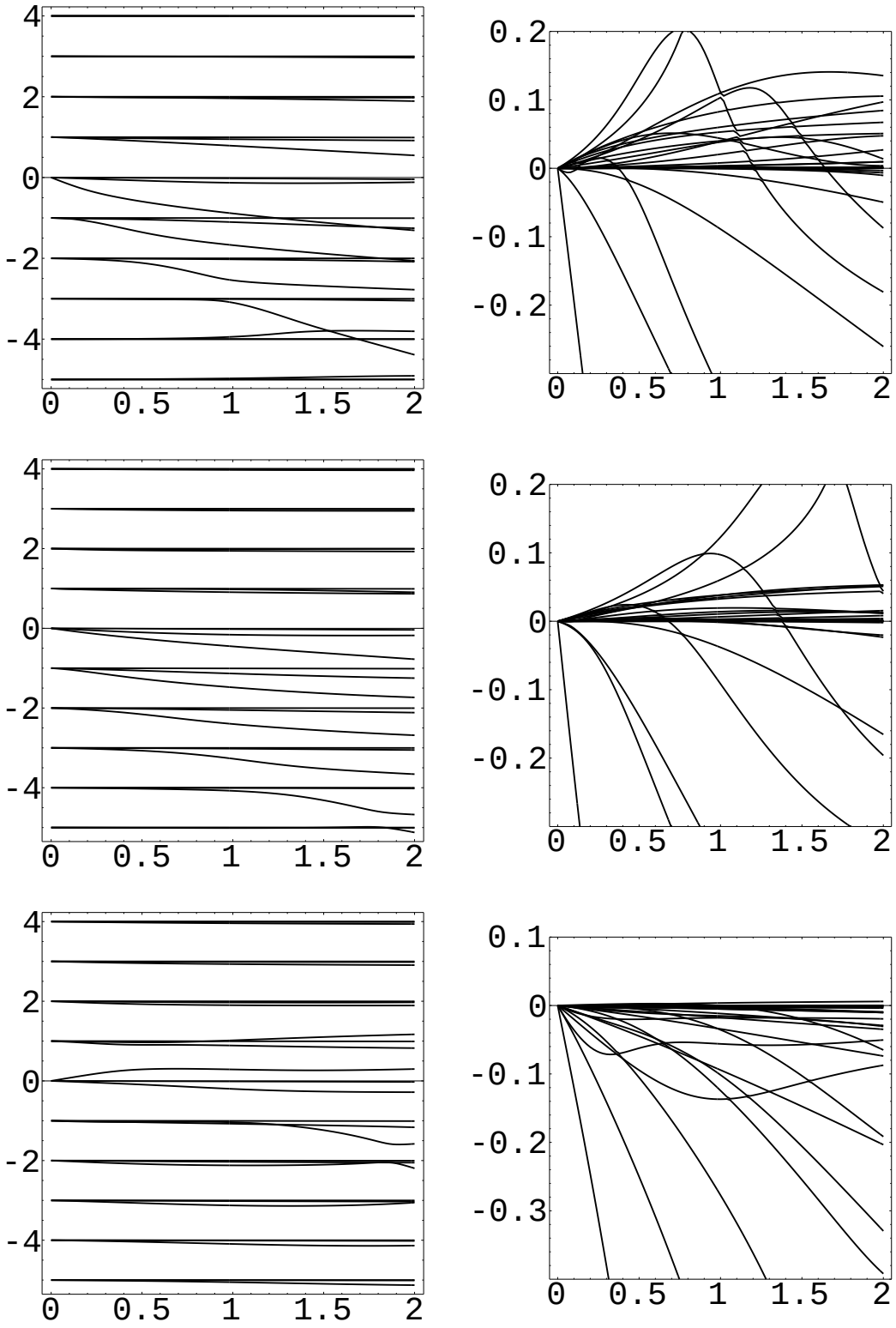

Figure 7: Continued from previous figure: CERN SPS, head-tail mode tunes in units of the synchrotron tune vs the cloud density $\rho_c \times 10^{-12}\mathrm{m}^{-3}$ at $N_b = 10^{11}$, $Q = 2$. Left: real part, right: imaginary part. From top to bottom: the chromatic phase is 1.0, 1.5, 2.5.

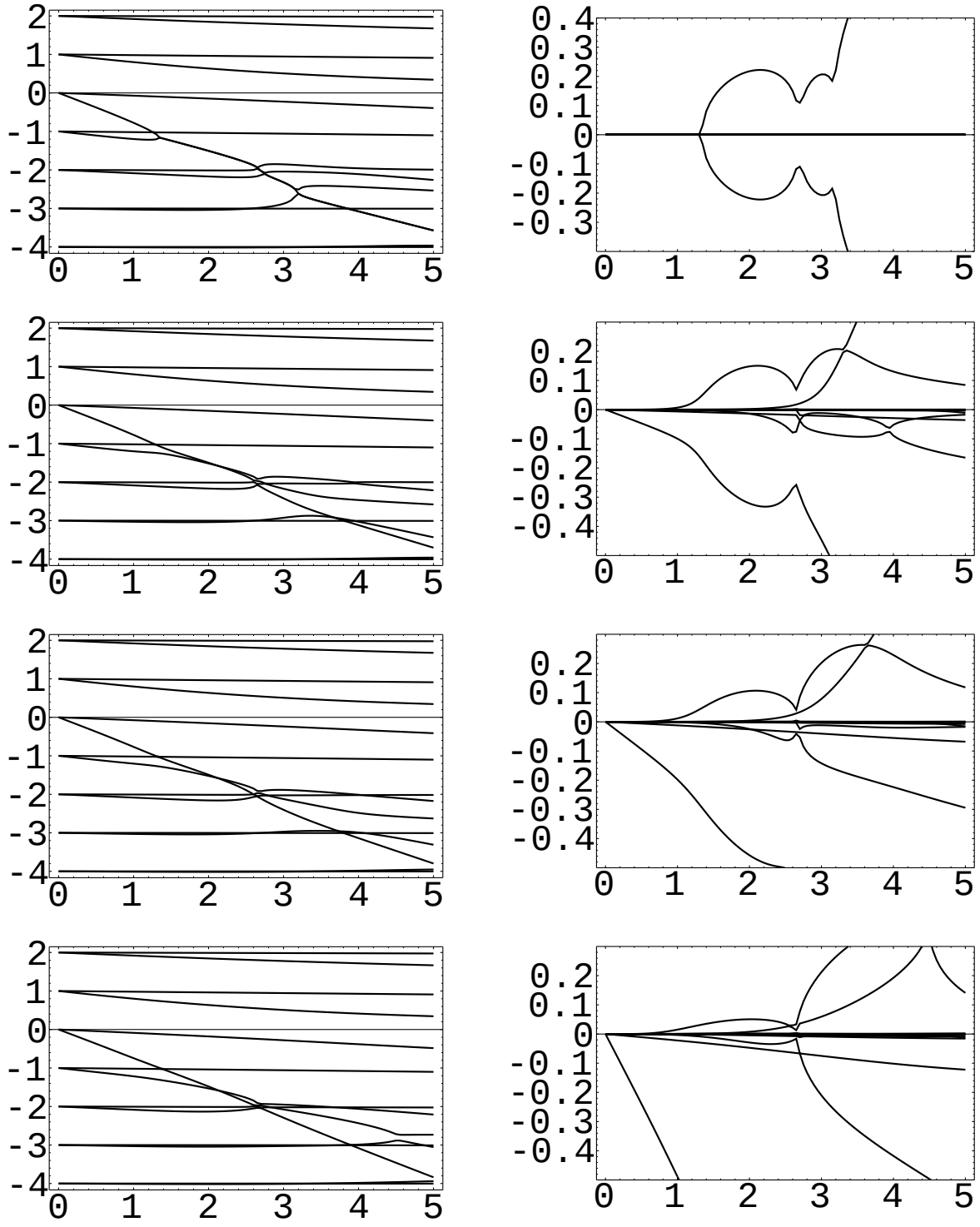

Figure 8: KEKB LER, head-tail mode tunes in units of the synchrotron tune vs the cloud density $\rho_c \times 10^{-12}\mathrm{m}^{-3}$. Left: real part, right: imaginary part. From top to bottom: the feedback damping is 0.0, 0.1, 0.2, 0.5; $Q = 1$, $I_b = 0.52$mA and zero chromaticity.

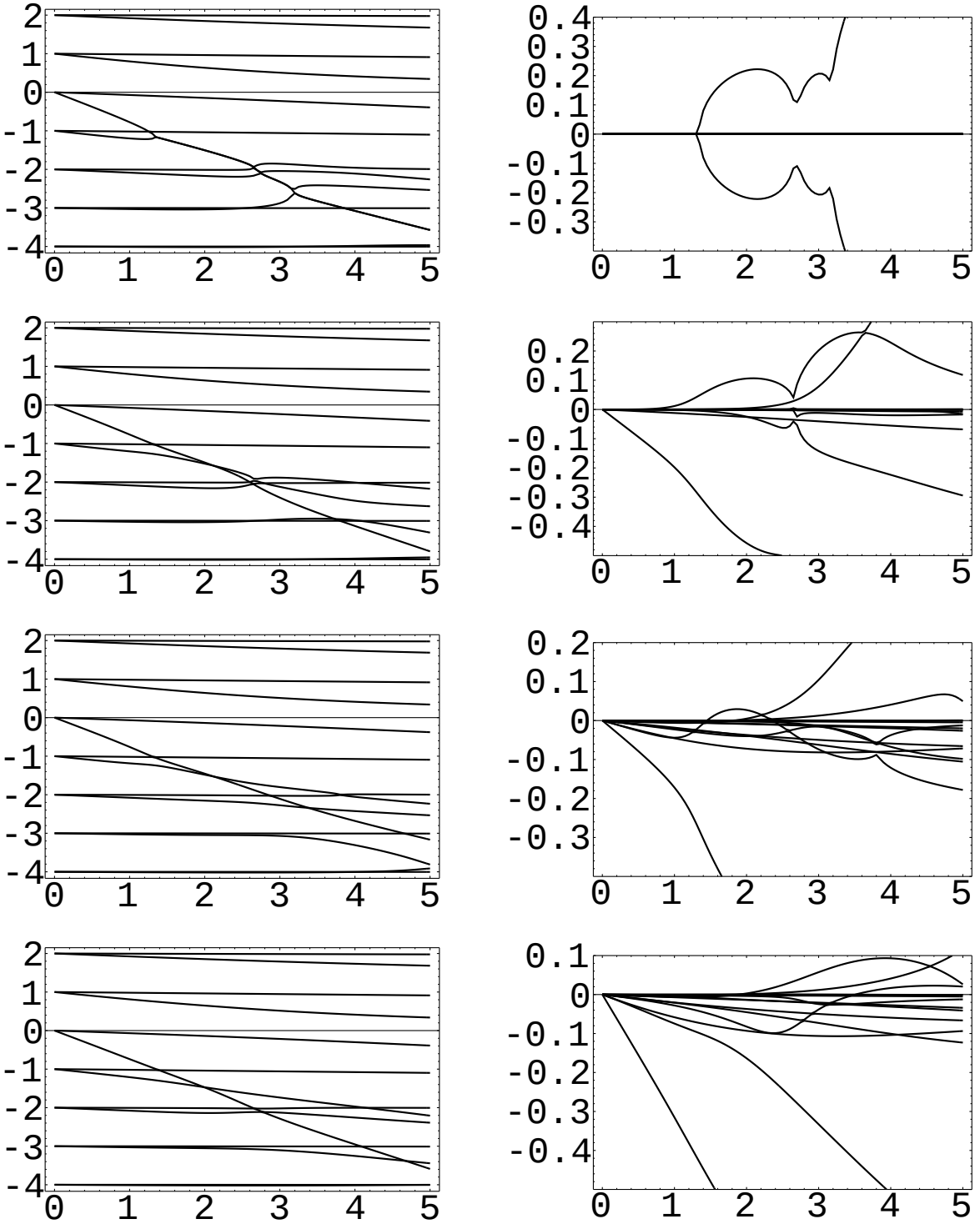

Figure 9: KEKB LER, head-tail mode tunes in units of the synchrotron tune vs the cloud density $\rho_c \times 10^{-12}\mathrm{m}^{-3}$. Left: real part, right: imaginary part. Combined action of the chromaticity and feedback, from top to bottom: a) no feedback, no chromaticity; b) the feedback damping is 0.2; c) no feedback and the chromatic phase is 0.5; d) the feedback damping is 0.2, and the chromatic phase is 0.5. $Q = 1$, $I_b = 0.52\mathrm{mA}$.

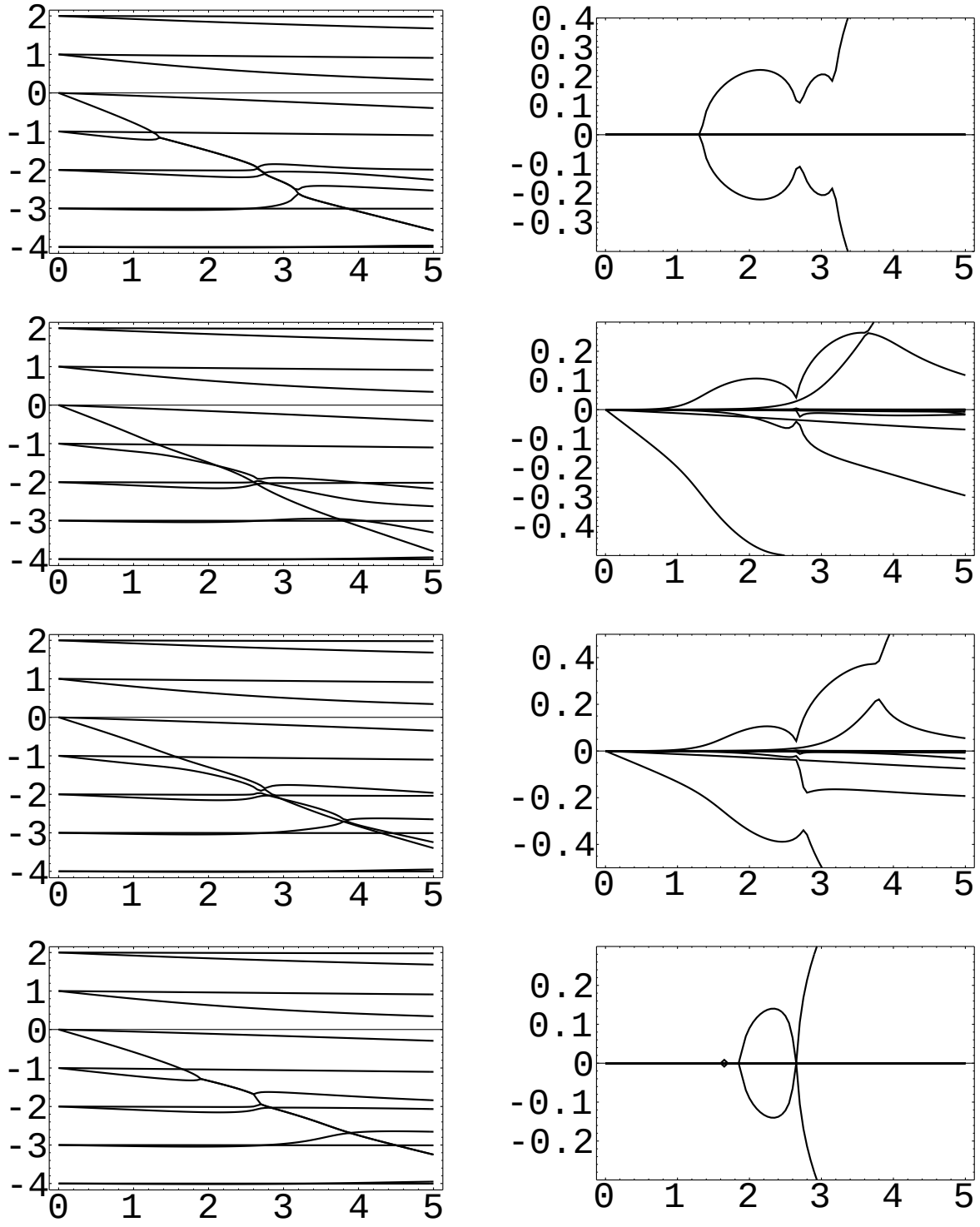

Figure 10: KEKB LER, head-tail mode tunes in units of the synchrotron tune vs the cloud density $\rho_c \times 10^{-12}\mathrm{m}^{-3}$. Left: real part, right: imaginary part. Effect of the feedback phase, from top to bottom: a) no feedback; b-d) the feedback damping is 0.2, and its phase is varied 90^o, 135^o, 180^o. $Q = 1$, $I_b = 0.52$mA.

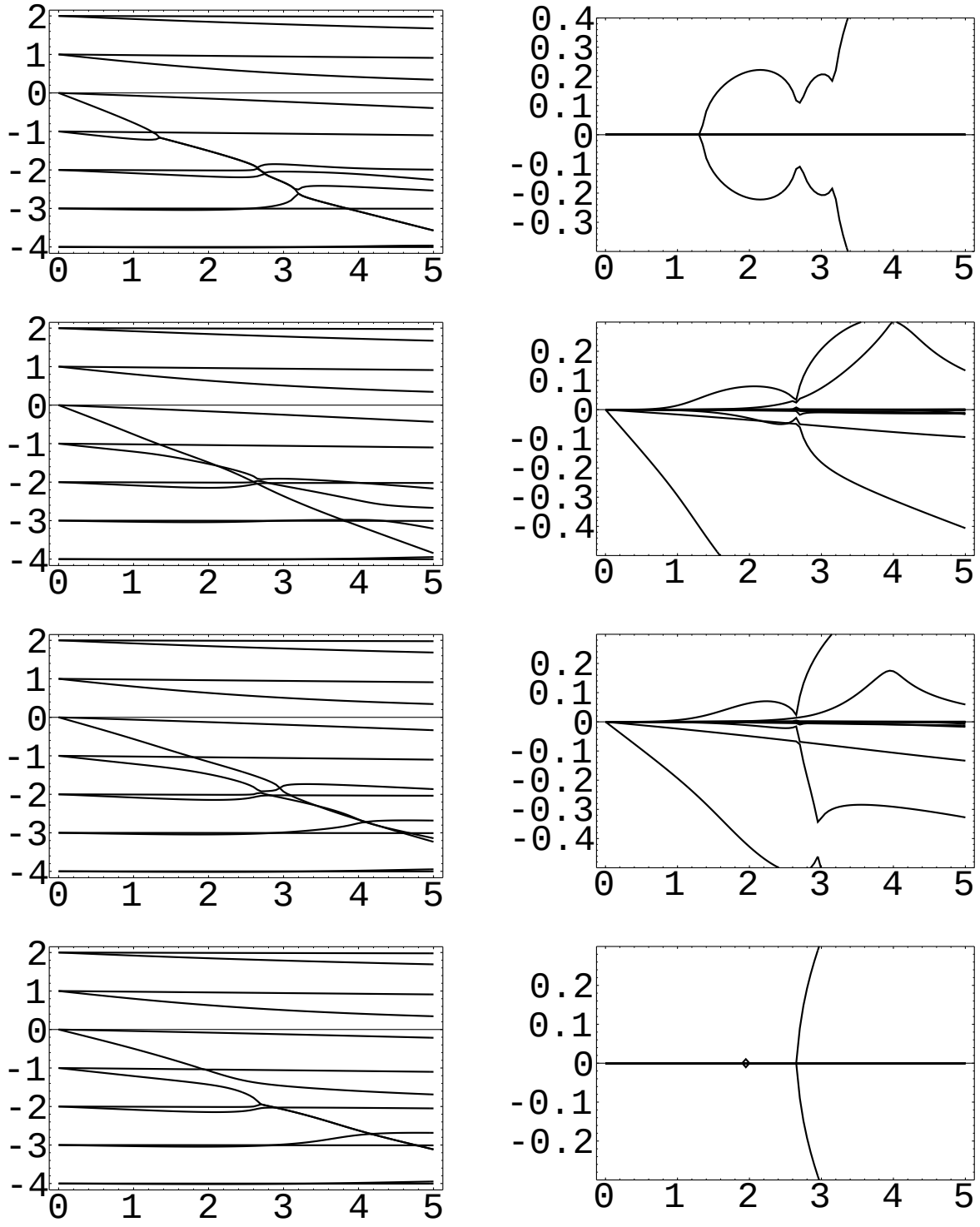

Figure 11: KEKB LER, head-tail mode tunes in units of the synchrotron tune vs the cloud density $\rho_c \times 10^{-12}\mathrm{m}^{-3}$. Left: real part, right: imaginary part. Effect of the feedback phase, from top to bottom: a) no feedback; b-d) the feedback damping is 0.3, and its phase is varied 90^o, 135^o, 180^o. $Q = 1$, $I_b = 0.52$mA.

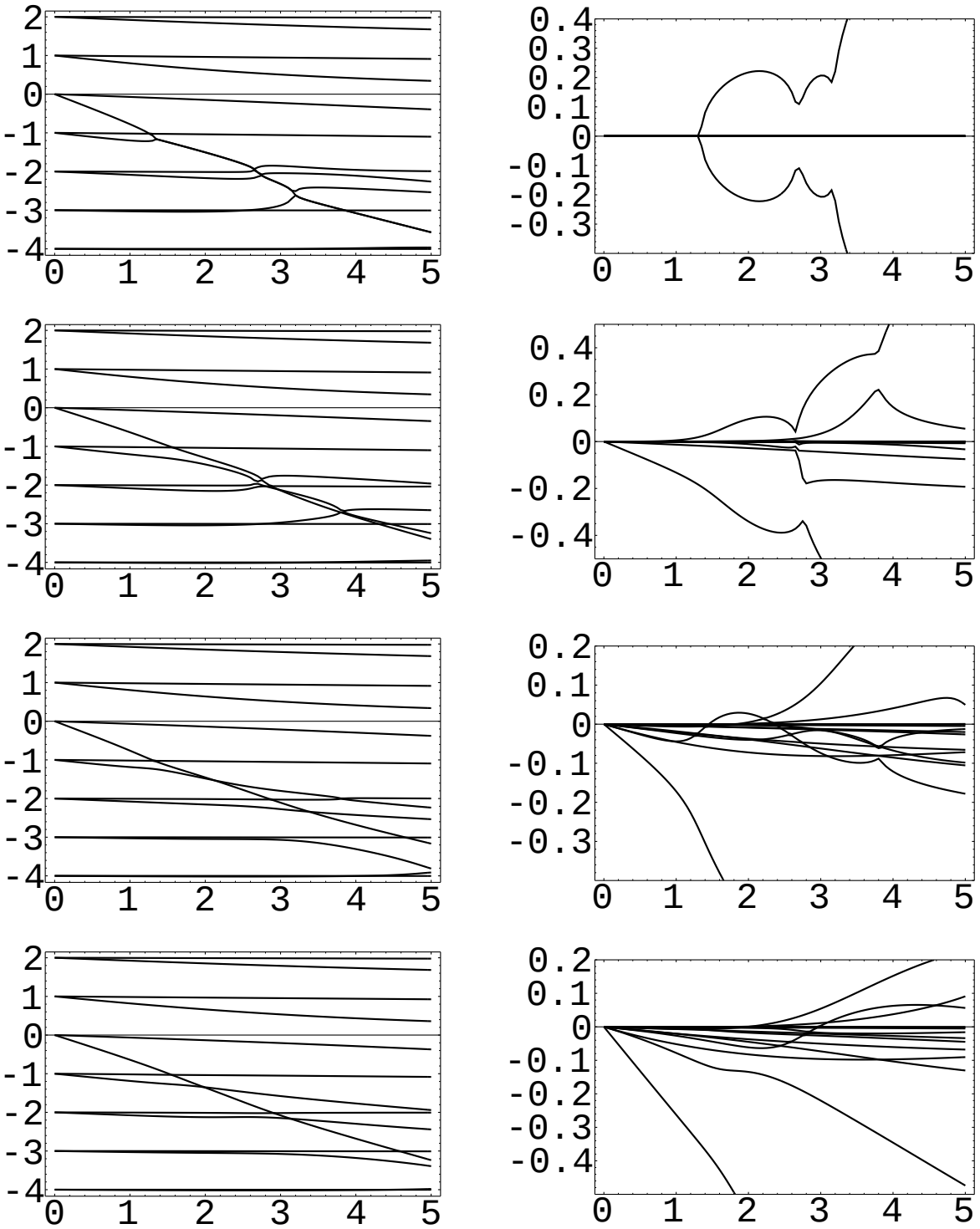

Figure 12: KEKB LER, head-tail mode tunes in units of the synchrotron tune vs the cloud density $\rho_c \times 10^{-12}\mathrm{m}^{-3}$. Left: real part, right: imaginary part. Combined action of the chromaticity and feedback, from top to bottom: a) no feedback, no chromaticity; b) the feedback damping is 0.2, its phase is 135^o; c) no feedback, the chromatic phase is 0.5; d) the feedback damping is 0.2, its phase is 135^o and the chromatic phase is 0.5. $Q = 1$, $I_b = 0.52$mA.

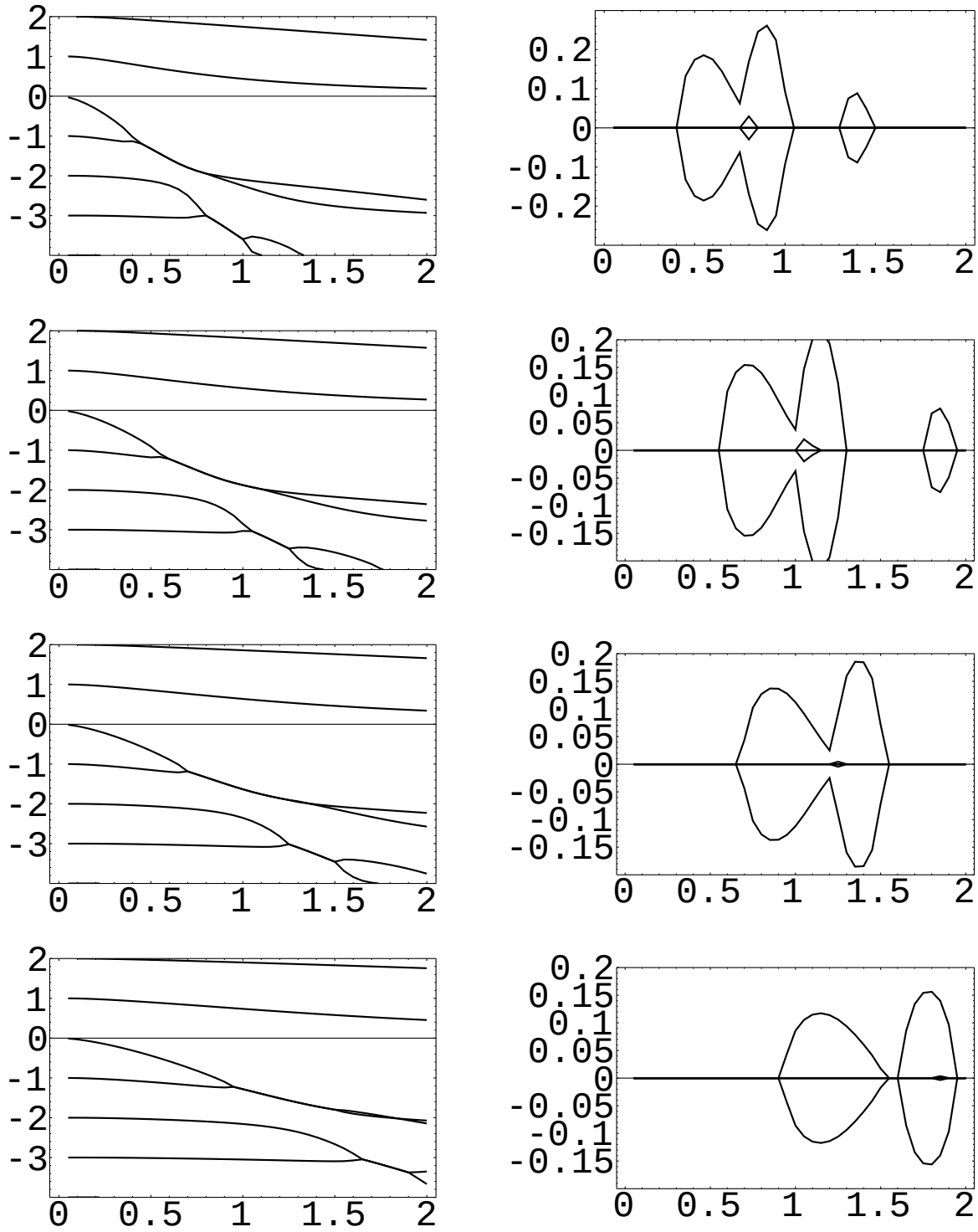

Figure 13: KEKB LER, head-tail mode tunes in units of the synchrotron tune vs the bunch current, mA. Left: real part, right: imaginary part. From top to bottom: the bunch spacing is 2, 3, 4, 6; $Q = 1$.

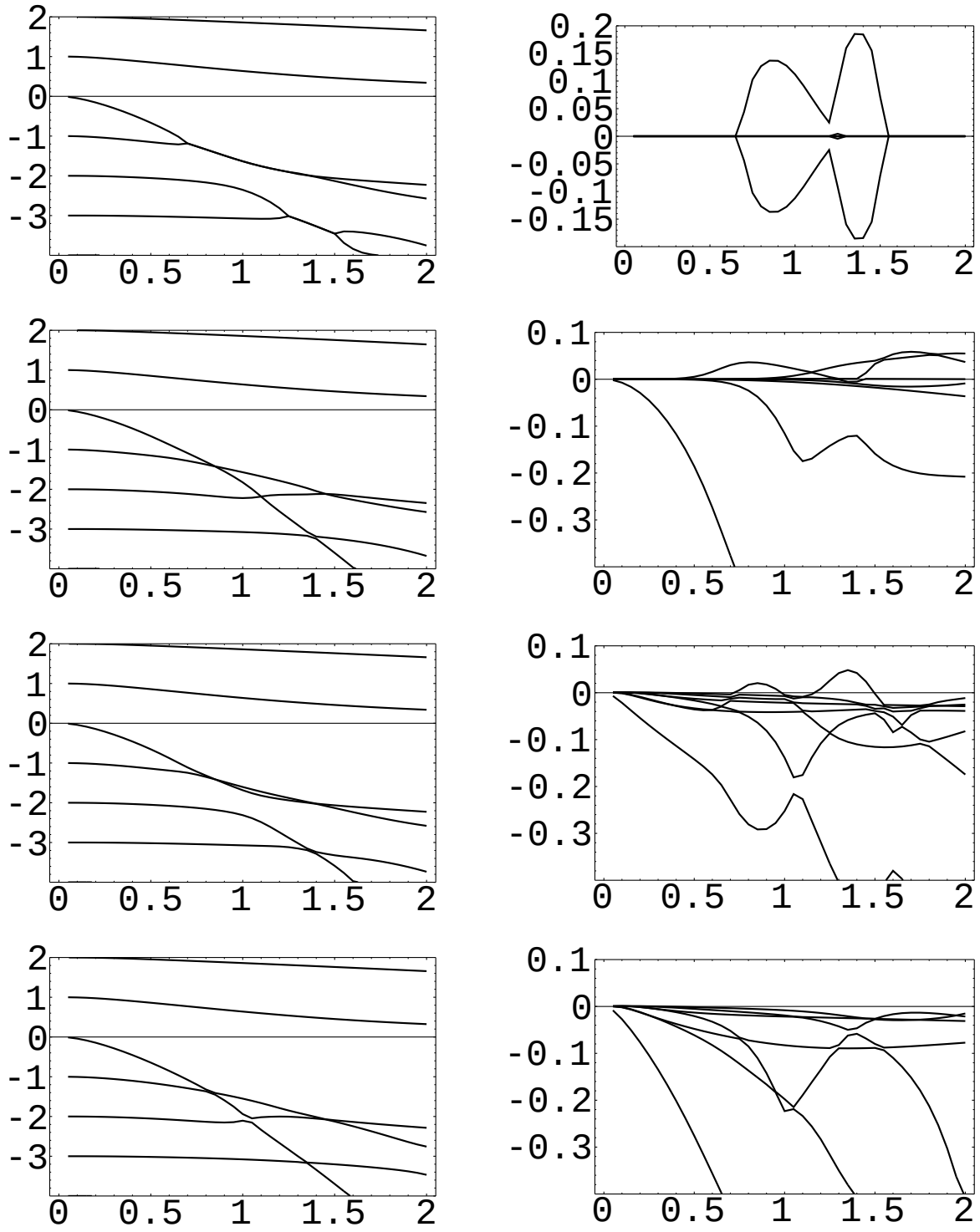

Figure 14: KEKB LER, head-tail mode tunes in units of the synchrotron tune vs the bunch current, mA. Left: real part, right: imaginary part. Combined action of the chromaticity and feedback, from top to bottom: a) no feedback, no chromaticity; b) the feedback damping is 0.2; c) no feedback and the chromatic phase is 0.5; d) the feedback damping is 0.2, and the chromatic phase is 0.5. $Q = 1$.

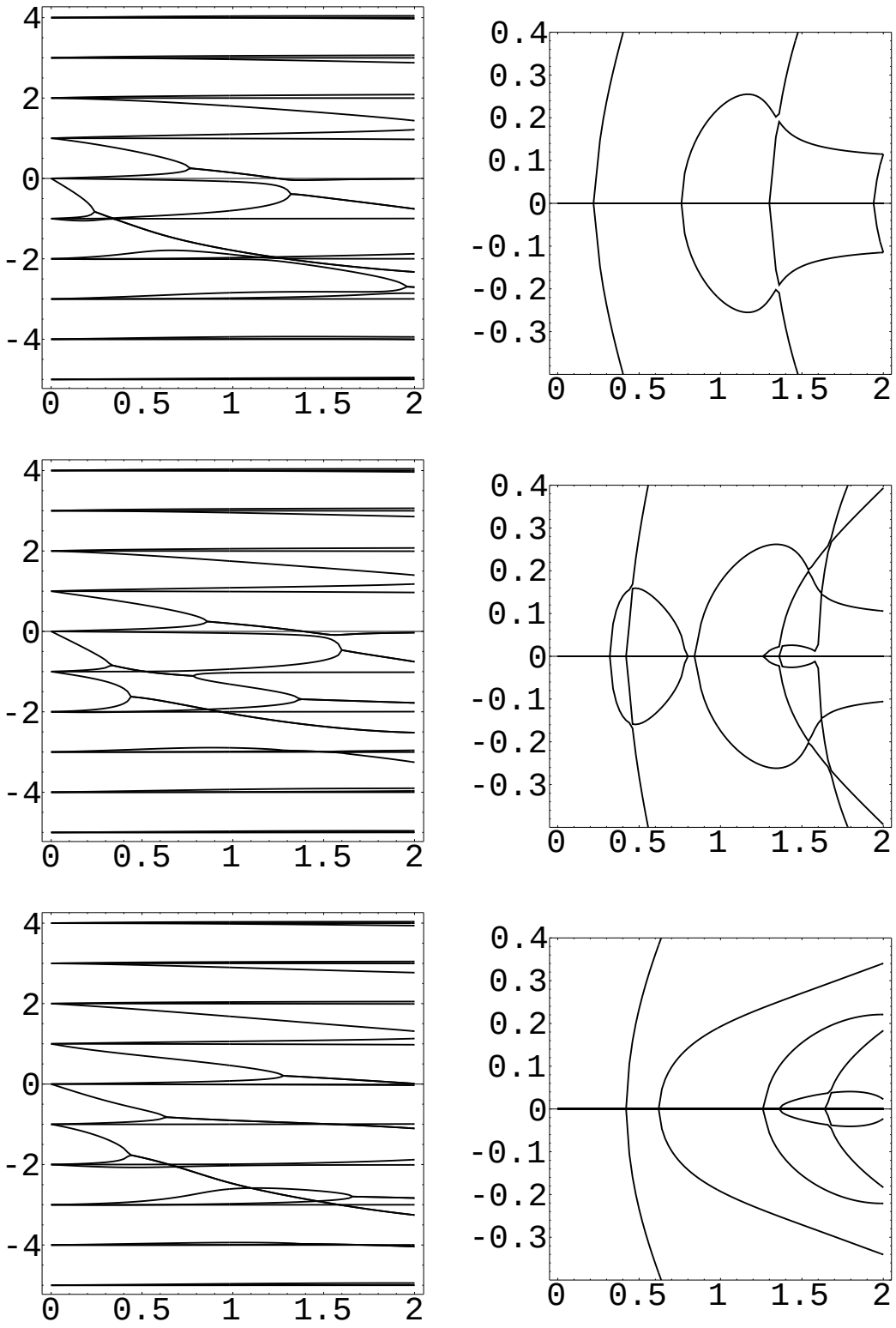

Figure 15: CERN SPS, head-tail mode tunes in units of the synchrotron tune vs the cloud density $\rho_c \times 10^{-12}\mathrm{m}^{-3}$ at $N_b = 10^{11}$, $Q = 2$, zero chromaticity, at different tune variation. Left: real part, right: imaginary part. From top to bottom: the tune variation is 0.0, 0.5, 1.0.

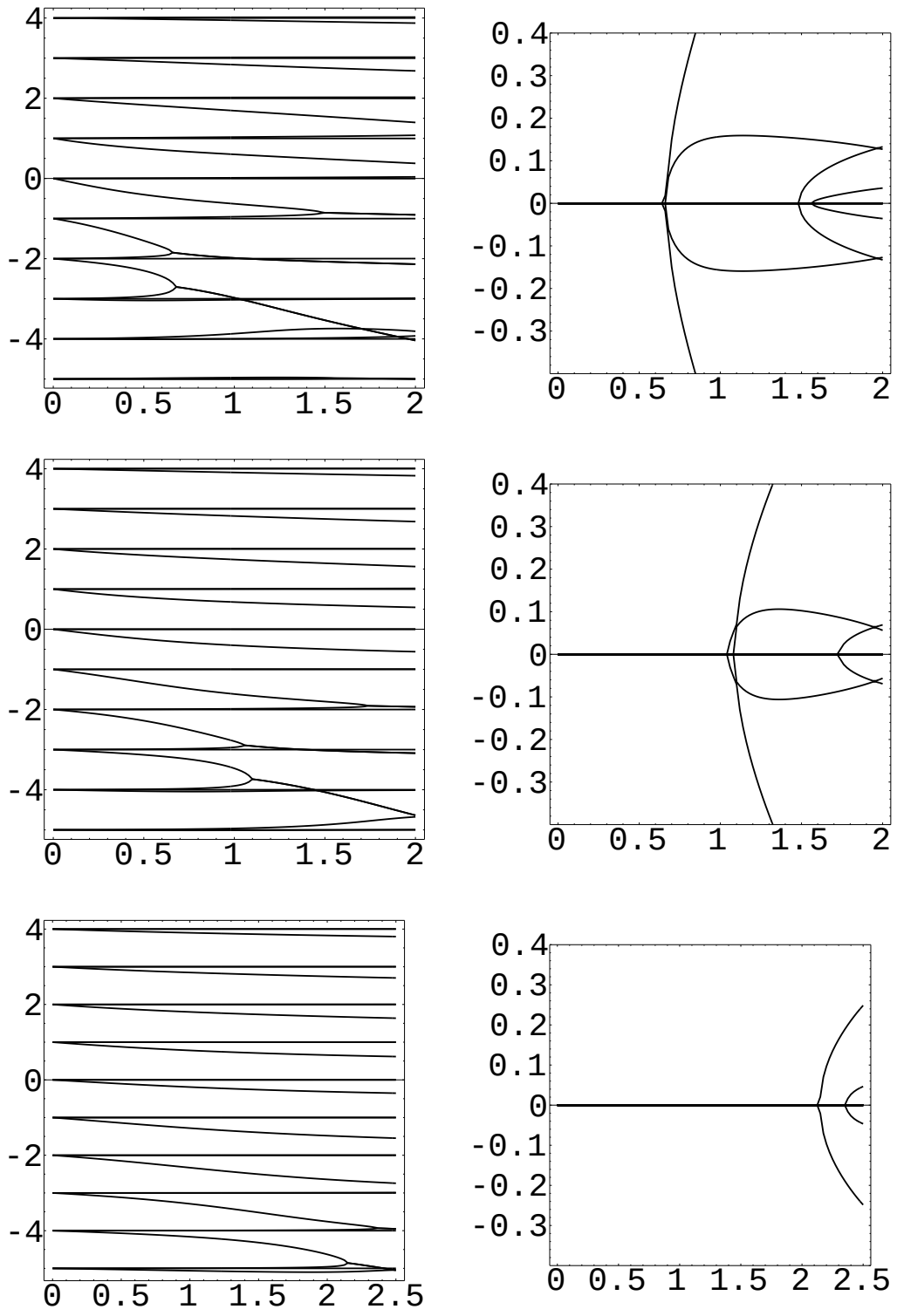

Figure 16: Continued from previous figure: CERN SPS, head-tail mode tunes in units of the synchrotron tune vs the cloud density $\rho_c \times 10^{-12}\mathrm{m}^{-3}$ at $N_b = 10^{11}$, $Q = 2$, zero chromaticity, at different tune variation. Left: real part, right: imaginary part. From top to bottom: the tune variation is 1.5, 2.0, 2.5.

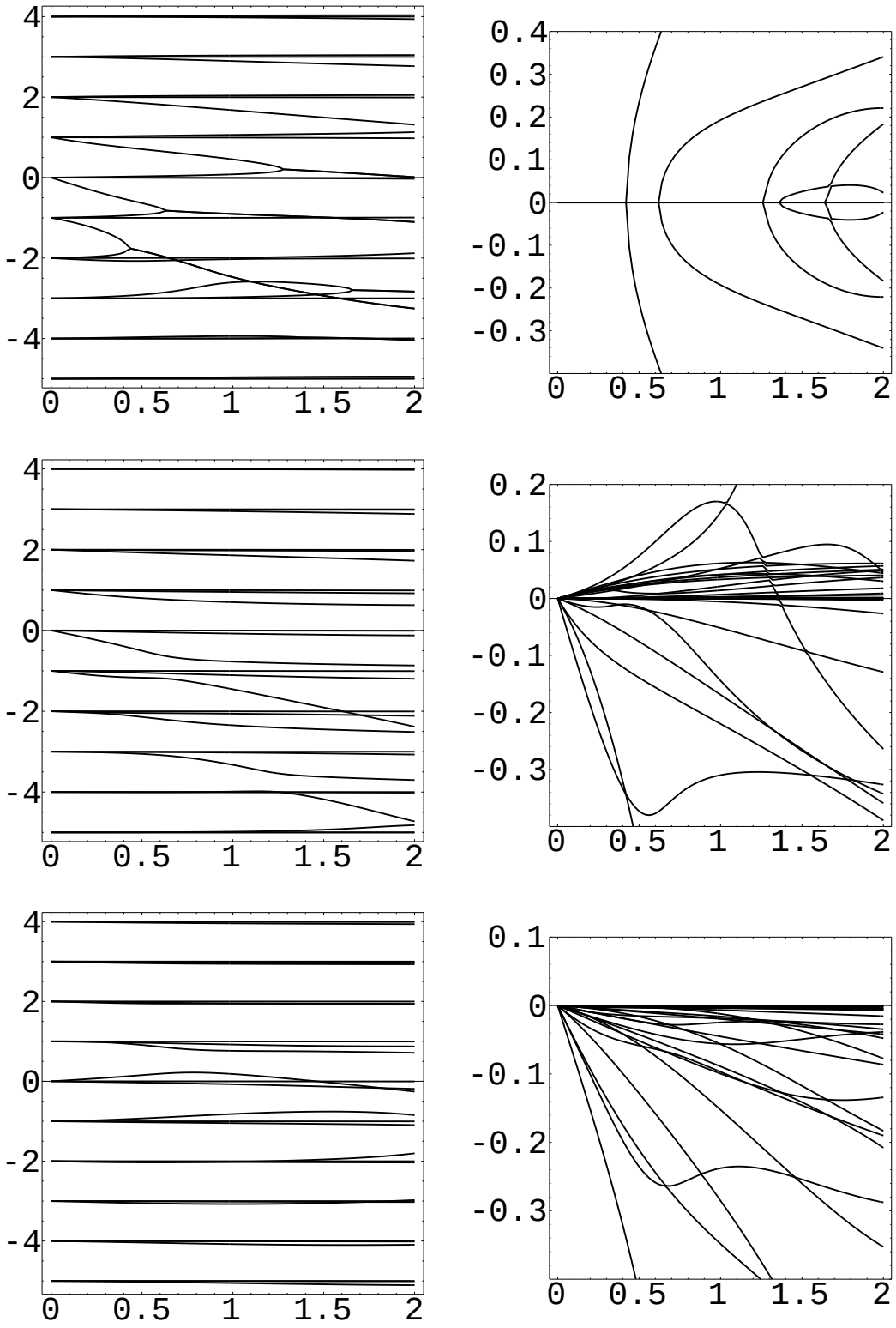

Figure 17: CERN SPS, head-tail mode tunes in units of the synchrotron tune vs the cloud density $\rho_c \times 10^{-12}\mathrm{m}^{-3}$ at $N_b = 10^{11}$, $Q = 2$, the tune variation is 1.0. Left: real part, right: imaginary part. From top to bottom: the chromatic phase is 0.0, 1.0, 2.5.

Electron cloud at high beam currents*

S. Heifets, Stanford Linear Accelerator Center, Stanford University, Stanford, CA 94309, USA

Abstract

The density and the wake fields of the e-cloud are quite different at low and high beam currents. The wake fields are derived and applied to the upgraded PEP-II B-factory.

1 INTRODUCTION: EXAMPLE

There are plans for upgrading the PEP-II B-factory to higher luminosity [1]. This could be achieved, mostly, by increasing the beam currents up to 10-20 Amp. Table I presents four possible scenarios of upgrading the PEP-II B-factory. Many potential problems hinder with the plans, the most obvious of them are related to the RF and the synchrotron radiation (SR) heat loading. Here I would like to consider only adverse effects of the beam interaction with the electron cloud.

The present wisdom predicts that the density of the cloud is defined by the condition of neutrality

$$< n >= \frac{N_b}{\pi s_b b^2}. \tag{1}$$

Therefore, the interaction with the cloud and, particularly, the tune shift

$$\Delta Q_\beta = \frac{2\pi r_e R^2 n_e}{\gamma Q_\beta} \tag{2}$$

grow proportional to the beam current. The variation of the tune along the bunch is of the same order. For the nominal PEP-II parameters, Table I (1st column), $\Delta Q_\beta = 0.052$ and is unacceptably large for higher currents.

I would like to argue that such a prediction might be wrong and the path to the high currents, at least from the point of view of e-cloud effects, is not hopeless.

Table 1: Parameters for upgraded PEP-II LER

Parameter	(I)	(II)	(III)	(IV)
n_b	750	1658	3400	3492
I_{beam}, Amp	1.750	4.0/1.4	10.0	18.0
I_{bunch}/mA	2.33	2.41	2.94	5.15
σ_z	1.1 9	0.8	0.5	0.13
$\alpha, 10^{-3}$	1.23	1.23	2.41	2.41
$\delta_0, 10^{-4}$	7.7	7.7	7.7	7.7
$N_b\, 10^{-11}$	1.07	1.1	1.35	2.36

* Work supported by Department of Energy contract DE–AC03–76SF00515.

2 RELEVANT PARAMETERS

There are two groups of electrons in the cloud: primary photo-electrons generated by the SR photons and secondary electrons generated by the beam induced multipactoring. Electrons in the first group generated at the beam pipe wall with the radius b interact with the parent bunch and accelerated (by a short bunch) to the velocity $v/c = 2N_b r_e/b$, where r_e is the classical electron radius and N_b is the bunch population. Electrons in the second group, generally, miss the parent bunch and move from the beam pipe wall with the velocity $v/c = \sqrt{2E_0/mc^2}$ until the next bunch arrives. The velocity is defined by the average energy $E_0 \simeq 5$ eV of the secondary electrons and, at high N_b, is smaller than velocity of the first group.

The process of the cloud formation depends, respectively, on two parameters:

$$\kappa = \frac{2N_b r_e s_b}{b^2} \tag{3}$$

$$\zeta = \frac{s_b}{b}\sqrt{\frac{2E_0}{mc^2}} \tag{4}$$

These parameters are the distance (in units of b) passed by electrons of each group before the next bunch arrives.

At low currents, $\kappa << 1$, electron interacts with many bunches before it reaches the opposite wall. In the opposite extreme case, $\kappa > 2$, all electrons go wall-to-wall in one bunch spacing.

The transition to the second regime can be expected, therefore, for $\kappa \simeq 1$ where the cloud is quite different than it is at low currents. For $\kappa > 1$ and $\zeta < 1$, secondary electrons are confined within the layer $\zeta < (r/b) < 1$ at the wall and are wiped out of the region $0 < (r/b) < \zeta$ close to the beam by each passing bunch. This makes the range of parameters ($\kappa > 1$ and $2 - \kappa < \zeta < 1$) quite desirable to suppress the adverse effects of the e-cloud on the beam dynamics.

The initial energy of the electron and the space-charge force neglected above do not change substantially this statement. The case of high κ is considered here for the upgrades of the PEP-II B-factory.

The heat load to the wall increases with beam current but dependence on the current is different in low and high current regimes. The energy of an electron thrown to the wall by the passing bunch $E_w \simeq (mc^2/2)(2N_b r_e/b)^2$ and, therefore, the heat load of a bunch is proportional to N_b^3 at low currents, but only N_b^2 at high currents because the cloud density at saturation may be independent on the beam current.

(It may be worth noting also that at the very large currents, the energy of electrons hitting the wall is so large

that secondary electron yield (SEY) Y rolls off and multipactoring at such high currents is always suppressed. This happens at $\kappa > \zeta\sqrt{E/E_0}$, where $E \simeq 2$ keV, $\kappa \simeq 10$. We will not consider that extreme case).

3 DENSITY OF THE E-CLOUD AT HIGH-BEAM CURRENTS

The e-cloud density at low currents is given by the condition of neutrality. It means that the sum averaged in time of the fields of the beam and of the space-charge is zero at the wall.

The condition of neutrality implies that secondary electrons remain in the cloud for a time long enough to affect the secondary electrons generated by the following bunches. In other words, the condition of neutrality and the quasi-steady equilibrium distribution of the e-cloud are justified only for small κ.

It is not the case at the high currents. In this case, all primary photo-electrons disappear just in one pass. The secondary electrons are produced with low energy $E_0 \simeq 5$eV and are locked up at the wall. The density of the secondary electrons grows until the space-charge potential of the secondary electrons is lower than E_0,

$$U \simeq \pi e^2 b^2 [1-(1-\zeta)^2] n_0 \propto E_0. \qquad (5)$$

This is a very moderate density $n_0 \simeq 2.8\,10^6\ cm^{-3}$.

The radius of the Larmor circles in the arcs may be changed by the kick from a passing bunch provided the bunch is short, $\omega_L \sigma_B/c << 1$ where $\omega_L = eH/mc$. Otherwise, there is the adiabatic invariant $L = m\omega_L r^2$ and the energy $E = L\omega$ of the Larmor motion is preserved. It means that electrons in the arcs are accumulated and may define the beam stability at the high bunch currents.

4 SIMULATIONS

Simple simulations were carried out for a round beam pipe $b = 4.5$ cm assuming that particles move only radially. Space charge was included. A bunch and the distance between bunches $s_b = 275$ cm were sliced and interaction with each slice was described as a kick. There was no source of particles except initial fill and multipactoring: particle crossing the wall with a low energy was killed and one with the energy $E > 40$ eV was replaced with $\eta = 1.45$ new electrons randomly distributed over the energy range 5 ± 2 eV. The four currents considered in simulations correspond to parameters $\zeta = 0.27$ and $\kappa = 0.22$, 0.94, 1.54 and 2.63, respectively. These cases are noted below as (a), (b), (c), and (d), respectively. Results of the simulations are shown in Figs. 1,2,3.

The results of the simulations are consistent with the qualitative argument given above:

1. The density increases with the current and goes to saturation but, at the highest current, drops to zero. This can be expected when the average density exceeds the lock-up threshold.

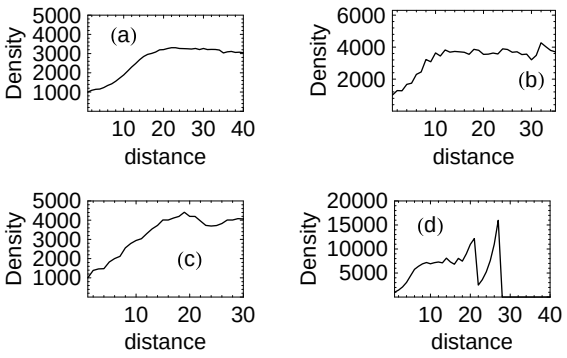

Figure 1: Total number of particles vs time (in units of bunch spacing). $\zeta = 0.27$ and $I_{beam} = 0.5\,A$, $2.15\,A$, $3.5\,A$ and $6.0\,A$ for (a),(b),(c), and (d), respectively.

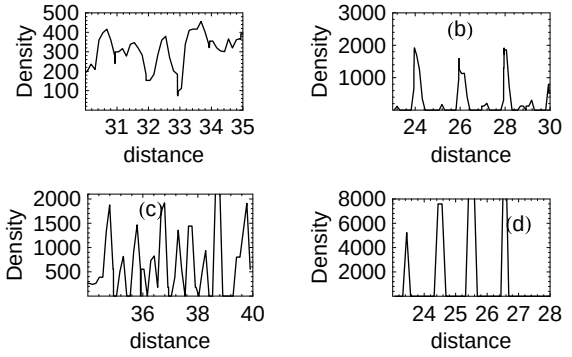

Figure 2: *Density at the beam line for the four beam currents vs time (in units of the passing bunch number). In the case (b), the density goes to zero for each other bunch. In the case (d), all bunches see minimum density.*

2. The snap-shot of the cloud distribution substantially varies in time between bunches at high currents and has only small modulation at low current.

3. Although the average density increases with current, the variation of the density at the beam line in time is substantially different for different beam currents: it is about a constant in the case (a), it is maximum at the each other bunch in the case (b), and, at the high current, the bunch sees almost zero density cloud as it can be expected for $\kappa > 2$. I think that the situation (b) can explain why luminosity of each other bunch drops in the PEP-II [2].

5 WAKES AND TUNE SHIFTS AT HIGH CURRENTS

The wake field of the electron cloud at low currents is defined by electrons oscillating in the vicinity (3-5) $\sigma_\perp$ of the beam. Such electrons pass the memory of the offset of the previous bunch to the following bunches.

The integrated single-bunch wake for a long bunch can be approximated[3], see Fig. 4, by the wake of a single

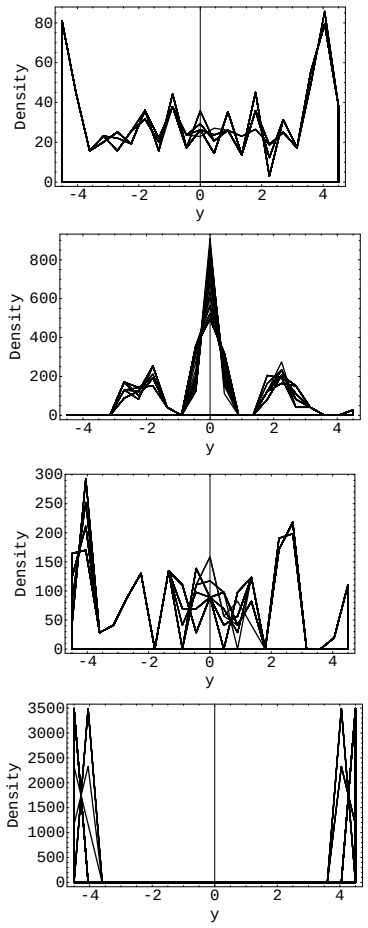

Figure 3: *Snap shots of the e-cloud distribution along the beam pipe diameter. Current increases from the top to bottom: 0.5, 2.5, 3.5 and 6 Amp, respectively.*

mode with frequency $\mu\Omega_0$,

$$W_{eff}(z) = W_{eff} 2\pi R \frac{2n_e}{(1+\sigma_y/\sigma_x)\lambda_b}(\frac{\Omega_0}{c})\sin(\mu\xi)e^{-\frac{\mu\xi}{2Q}}. \quad (6)$$

Here, n_e is the cloud density, $\lambda_b = N_b/(\sigma_z\sqrt{2\pi})$ is the bunch linear density, Ω_0 is the linear frequency of the vertical electron oscillations, $(\Omega_0/c)^2 = 2\lambda_b/(\sigma_y(\sigma_x+\sigma_y))$ and $\xi = \Omega_{bunch}z/c$. Numeric calculations [4] which take into account the frequency spread of the electrons of the e-cloud, defined parameters $W_{eff} = 1.2$, $\mu = 0.9$, $Q = 5$ which are with good accuracy independent on the rms size of the cloud.

Additional effect is given by possible asymmetry of the cloud due to primary photo-electrons or ante-chamber. For an estimate, the field of an anti-symmetric cloud with the cloud centroid at a and the linear density dN/ds can be described as a field of a thread with the linear charge density dN/ds displaced by a from the axes of the round beam pipe. The horizontal component of the m-th azimuthal harmonic of the field of the thread is

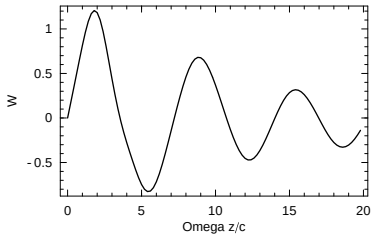

Figure 4: *Effective wake $W_{eff}(\zeta,0)$ of the cloud as function of $\zeta = \Omega_0 z/c$.*

$$E_x^{(m)} = \frac{2e}{a}\frac{dN}{ds}(\frac{r}{a})^{m-1}[1-(\frac{a}{b})^{2m}]\cos[(m-1)\phi]. \quad (7)$$

The $m = 1$ harmonic gives the steady-state horizontal force and changes the equilibrium energy of the beam by $\Delta E/E = eE_x^{(1)}\rho/E$, where ρ is the bend radius. Effect is very small. For example, let us consider the jet of the primary photo-electrons with the linear density

$$\frac{dN}{ds} = Y_{e\gamma}\frac{5\alpha_0\gamma}{2\sqrt{3}\rho}N_b\frac{L_{arcs}}{2\pi R}, \quad (8)$$

where $Y_{e\gamma} \simeq 0.1$ is number of electrons per SR photon, $\alpha_0 = 1/137$, and $L_{arcs} = 2\pi\rho$ is the total length of the bends. Let us assume that the primary photo-electrons get the kick $v/c = 2N_b r_e/b$ from the parent bunch and move to the radius $a = b - (2N_b r_e/b)s_b$ to the moment when the next bunch arrives. Taking the bunch population $N_b = 10^{11}$, the bunch spacing $s_b = 250$ cm, $\rho = 13.5$ m and $b = 4.5$ cm, we get $dN/ds = 1.8\,10^7\ 1/cm$, $a = 1.36$ cm, and $\Delta E = 3.5$ eV for 2.2 km PEP-II LER.

Effect of the asymmetry due to the ante-chamber at low beam currents depends on the parameter $\omega_{pl}s_b/c = \sqrt{2\kappa}$, where ω_{pl} is the plasma frequency $\omega_{pl}/c = \sqrt{4\pi n_0 r_e}$. Hence, at low currents $\kappa < 1$, any asymmetry of the cloud density generated by a bunch is preserved to the next bunch but hardly is larger than the effect of the asymmetry of the photo-electrons estimated above.

The mechanism of the bunch interaction through the e-cloud is different at high currents and is defined by azimuthal asymmetry of the distribution of the secondary electrons due to bunch transverse offset. The bunch with the offset x gives the asymmetric kick $(v/c)_\pm = 2N_b r_e/(b \pm x)$ to the electrons in the cloud. They reach the wall and produce secondary electrons at the different moments $t_\pm$. The secondary electrons propagating toward the following bunch are at the different distances $a_\pm = b - \zeta(1 - ct_\pm/b)$ from the beam line when the bunch arrives. The interaction with the bunch is given by the field $E_x(a_-) - E_x(a_+)$ of the $m = 1$ harmonic, see Eq. (7). Expanding the field over x, the result can be described as the transverse bunch-to-bunch wake $W_\perp$. For small $\zeta << 1$,

the integrated wake is

$$W_\perp = 2\pi R \frac{8}{b^2} \frac{1}{N_b} \frac{dN}{ds} \frac{\zeta}{\kappa}, \qquad (9)$$

where $a = b(1-\zeta)$. For $n_0 = (dN/ds)/(\pi b^2) \simeq 10^6$ cm^{-3}, $N_b = 10^{11}$, $2\pi R = 2.2$ km, and $b = 2.5$ cm, we get $\zeta = 0.4$, $\kappa = 2.25$, and $W_\perp = 11\, V/pC/cm$.

The azimuthal harmonic $m = 2$ of the e-cloud distribution gives the tune shift

$$\Delta Q_{x,y} = \mp \frac{r_e R^2}{\gamma Q_{x,y} b^2} (\frac{dN}{ds})[(\frac{b}{a})^2 - (\frac{a}{b})^2]. \qquad (10)$$

For the same parameters n_0, N_b and b as above, we get $dQ/dI_{beam} = 4.5\, 10^{-3}\ 1/Amp$.

It is worth noting that the effect of the jets of the primary photo-electrons on the beam varies along the bunch due to the changing distance from the jet to the beam line. This may cause variation of the tune shift and orbit distortion along the bunch.

6 HEAD-TAIL INSTABILITY

The wake generated by the interaction with the cloud leads to the head-tail instability [3]. A peculiar feature of the e-cloud wake that it depends on I_{bunch} due to the electron frequency dependence. The Satoh-Chin's formalism [5] can be used, in principal, to define the threshold of instability. The stability is defined by the eigen values of a matrix which has to be, as usual, replaced by a matrix of a finite rang. Simulations with a low order matrix show a certain threshold of the head-tail instability. However, the bunch again become stable at higher currents. This reduction of the growth rate may be a result of a large number of electron oscillations per bunch length $\Omega_{bunch}\sigma_l/c >> 1$ at large N_b. At the present time, it is not clear whether such an explanation is correct until the numeric results are checked with the matrices of higher rang (of the order of $(\Omega_{bunch}\sigma_l/c)2$).

7 CONCLUSION

The present theory predicts that the e-cloud becomes more dangerous at high currents. The situation might be not hopeless. The condition of neutrality predicting the growth of the e-density with current might be replaced by the lock-up condition independent of current. The distribution of electrons in the cloud changes and, at the high currents, becomes hollow. In particular, the density at the beam line which defines beam stability decreases. The head-tail instability is stabilized at high currents due to high electron frequencies.

These prediction and, in particular, the adverse effect of density fluctuations, could be verified with existing codes.

8 REFERENCES

[1] "Proposed upgrade of the B-factory", Snowmass, 2001.

[2] F.J. Decker, see this proceedings.

[3] K. Ohmi and F. Zimmermann, "Head-Tail Instability Caused by Electron Clouds in Positron Rings," Phys. Rev. Lett. **85** 3821 (2000).

[4] S. Heifets, "Wake field of the e-cloud", SLAC-PUB-9025, November, 2001.

[5] K. Satoh and Y.H. Chin, "Transverse Mode Coupling in a Bunched Beam," Nucl. Instr. Meth. **207**, 309 (1983).

EFFECT OF ELECTRON CLOUD ON THE COUPLED BUNCH INSTABILITY IN KEKB LER

Su Su Win, Hitoshi Fukuma, Kazuhito Ohmi, Shin-ichi Kurokawa
High Energy Accelerator Research Organization (KEK), Japan

Abstract

A coupled bunch instability is observed in KEKB low energy positron ring (LER). The observed mode spectrum and the growth rate of the instability change according to turning on and off the solenoid magnets which are installed to sweep out the electron cloud in LER. The simulation results are consistent with a hypothesis that the instability is caused by the electron cloud.

1 INTRODUCTION

The vertical beam blow-up caused by the electron cloud has been observed in KEKB LER [1]. To sweep out the electron cloud a large number of solenoid magnets were installed in LER. The effect of the solenoids on the blow-up was confirmed by the measurement of the beam size and the luminosity. The electron cloud can cause not only the beam blow-up but also a coupled bunch instability as K. Ohmi pointed out [2]. In fact, the coupled bunch instability which can be explained by the electron cloud was observed in KEKB PF [3] and BEPC [4].

We studied the coupled bunch instability in KEKB LER expecting that the coupled bunch instability by the electron cloud would be observed also in LER. In our experiment the mode spectrum and the growth rate were measured turning on and off the solenoids to see the effect of the electron cloud. The results were compared with computer simulation. In this paper we present the results of the measurement and the simulation on the coupled bunch instability in KEKB LER.

2 EXPERIMENT

Two kinds of solenoids were installed to sweep the electrons, one is a bobbin-type solenoid and the other a bobbinless-type solenoid [5]. The length of the bobbin-type solenoid is from 150 to 650 mm. The bobbinless-type solenoid has a length of 40 mm and mainly located on bellows and both sides of NEG pumps and ion pumps to cover the regions in which the bobbin-type solenoids can not be wound. The magnetic field at the center of a solenoid along the beam line is about 45 Gauss. The solenoids were installed several times in LER since September 2000. In January 2002 about 75% of the circumference was covered by the solenoids. Most vacuum chambers are made of copper. IR chambers and the chambers around the crossing point are made of aluminium.

The experiments were carried out in the filling pattern of the normal operation at KEKB LER. Apart from the abort gap, which was 10% of the circumference of the ring, the ring was filled with a bunch train containing 1153 positron bunches at 3.5 GeV. The bunch spacing was 8 ns and typical beam current was 600 mA. The bunch oscillation recorder [6] was used to record the bunch oscillations for 4096 turns without applying the bunch-by-bunch feedback system which is installed to suppress the transverse coupled bunch instability [7]. The bunch oscillation data were then transformed into the snapshot data as they were recorded at a fixed location [8]. The mode spectra were determined by applying fast Fourier transform (FFT) to turn by turn oscillation data. The growth rates were calculated by fitting the oscillation curve to an exponential function.

The mode spectra observed in horizontal and vertical planes without applying the solenoid field are shown in Figure 1. The mode spectra are similar showing a broad peak at the mode number around 800 both in horizontal and vertical planes. Fig. 2 shows the mode spectra with applying the solenoid field which covered about 70% of the ring. The horizontal and vertical mode spectra are similar with the same position of the peak. As can be seen in Fig. 1 and 2, the mode spectra change due to the solenoid filed, which suggests that the instability is caused by the electron cloud.

The observed growth rate is shown in Fig. 3. The horizontal and vertical growth rates were 2.0 /ms and 1.3 /ms, respectively, when solenoid-off. It decreased to 72% horizontally and 74% vertically after installing the solenoids which covered 40 % of the ring. It further decreased to 25% horizontally and 20% vertically after installing the solenoids in order to cover 70 % of the ring.

3 SIMULATION

The simulation program PEI developed by K. Ohmi [2] was used to study the coupled bunch instability due to the electron cloud. The parameters used in the simulation are listed in Table 1. At LER, the beam energy is 3.5 GeV and the critical energy is 5.84 keV. For the beam current of 600 mA, a bunch contains 3.3×10^{10} positrons. Assuming the photoelectron production yield of 0.1, total photoelectron emission is estimated to be 5×10^{8} electrons/bunch/meter. The energy distribution of initial photoelectrons was considered as Gaussian whose mean energy and the standard deviation are 10 and 5 eV, respectively. The space charge effect was taken into account in the simulation. The photoelectrons which can not traverse the vacuum chamber before the arrival of next bunch will be kicked by the interaction between positron beam and photoelectrons. The electrons close to the positron beam will experience a comparatively larger potential kick than those far from the positron beam. When the photoelectron hits the opposite wall at certain energy the secondary electrons are produced. The

secondary electron yield was assumed to have a peak at Emax = 300 eV with δmax = 1.5.

The bunch oscillations were simulated by the particle tracking in the various solenoid fields and analyzed by the same procedure as in experimental data analysis to determine the mode spectra. The growth rate was obtained from a wake function calculated by the simulation program.

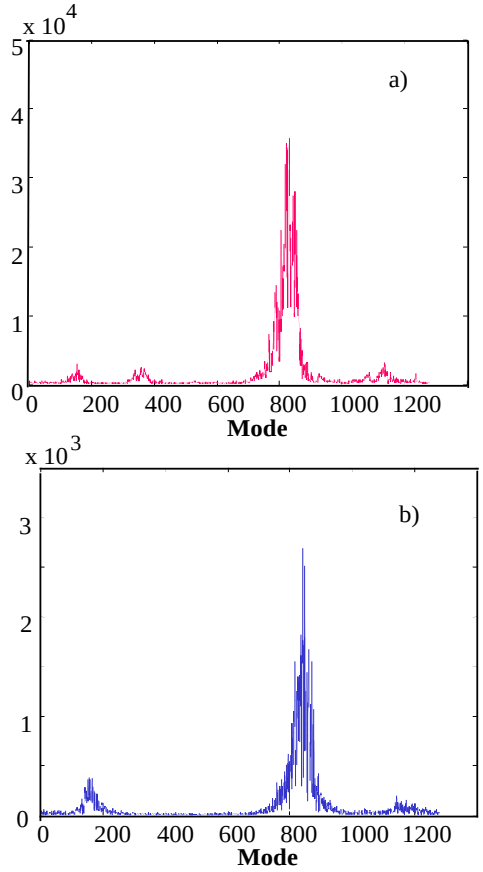

Figure 1: The mode spectra observed when solenoid-off in a) horizontal and b) vertical plane.

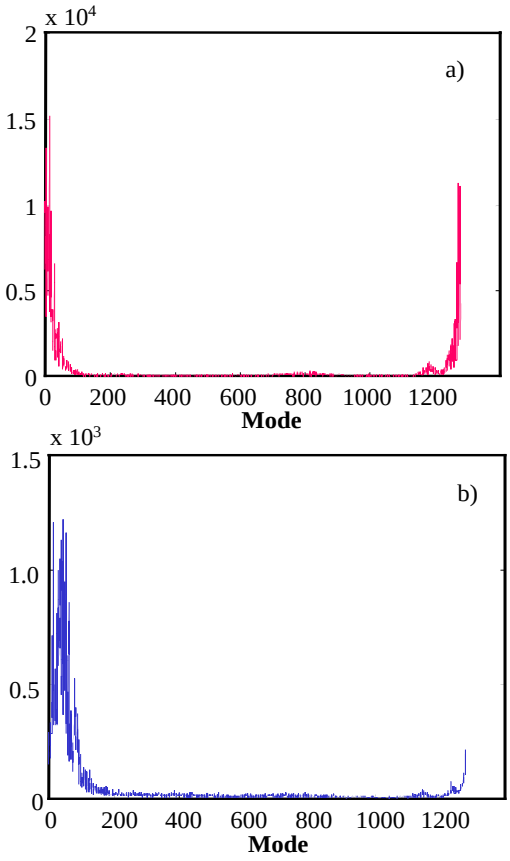

Figure 2: The mode spectra observed when solenoid-on in a) horizontal and b) vertical plane.

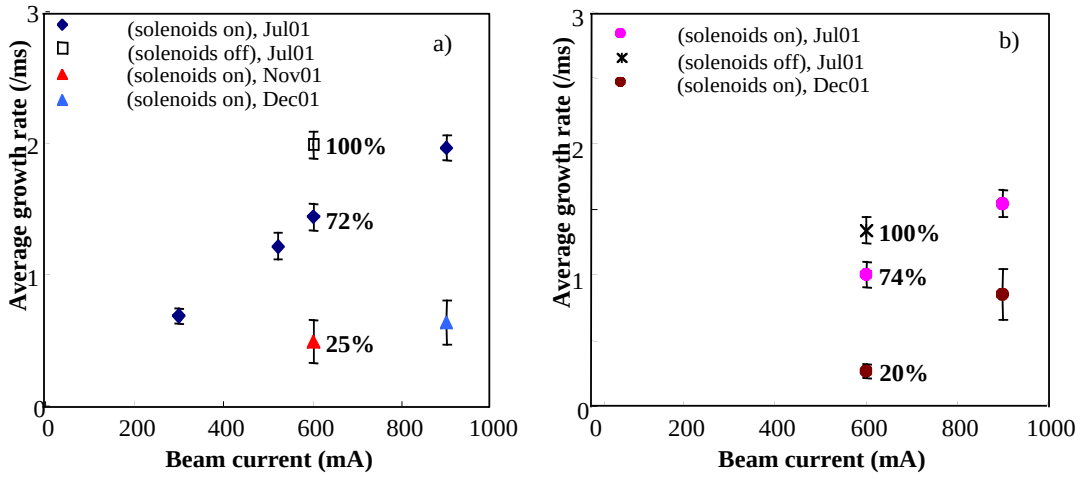

Figure 3: Growth rates of bunch oscillation at when solenoid-on and solenoid-off in a) horizontal and b) vertical plane.

Table 1: The parameters used in simulation

Circumference (m)	3016
No. of train	1
Radius of vacuum chamber (mm)	47
No. of bunches	1153
Bunch spacing (ns)	8
Bunch current (mA)	0.52
Average β_x/β_y (m)	10/10
Emittance $\varepsilon_x/\varepsilon_y$ (10^{-8} m)	1.8/0.036
Betatron tune ν_x/ν_y	45.52/43.57
Initial photoelectron energy (GeV)	10 ± 5
Photoelectron yield	0.1
Secondary electron yield δ_{max}/E_{max} (eV)	1.5/300

3.1 MODE SPECTRUM

3.1.1 Mode spectrum in case of solenoid off

Firstly, we assumed that the photoelectrons are produced at an illumination point with 30% reflection which means 30% of the photoelectrons are uniformly produced over the surface of the vacuum chamber. The electron density projected over the cross section of the vacuum chamber at the saturation of electron cloud is shown in Fig. 4. The electron density was 9.8×10^{11} electrons/m^3 at the saturation of the electron cloud. The mode spectra without applying solenoid field are shown in Fig. 5. The horizontal mode spectrum in Fig. 5a shows the peak at mode 200 which is different from the experimental observation shown in Fig. 1a. In the vertical mode spectrum shown in Fig. 5b, the peak appears at mode around 1000 and is broader than the experimentally observed one as shown in Fig. 1b.

Secondly, we assumed that the photoelectrons are produced uniformly over the surface of the vacuum chamber. The electron density at the saturation of the electron cloud was 9.8×10^{11} electrons/m^3. The electron density projected over the cross section of the vacuum chamber at the saturation of electron cloud is shown in Fig. 6. The horizontal mode spectrum is similar to the vertical mode spectrum as can be seen in Fig. 7. Each of the mode spectra has a broad peak at mode 800 and small peaks at mode 200 and 1200. Comparing with the experimental data shown in Fig. 1a and b, the mode spectra from the simulation are consistent with the experimentally observed ones in both horizontal and vertical planes.

3.1.2 Mode spectrum in case of solenoid on

Applying the solenoid field along the circumference of the ring will change the electron cloud distribution and then change the mode spectrum.

The electron density projected over the cross section of the vacuum chamber in solenoid fields of 5 ~ 20 G are shown in Fig. 8a to 8c when the photoelectrons are produced at the illumination point with 30% reflection. As the electron distribution changes due to the solenoid field, the mode spectrum also changes and is totally different from the mode spectrum which we observed in solenoid-off case, as shown in Fig. 10 and 11. The simulated mode spectrum applying 10 G solenoid filed is consistent with the experimental one both in horizontal and vertical planes.

For the uniform photoelectron production over the vacuum chamber surface, the electron distribution at the saturation of electron cloud changes as shown in Fig. 9 when solenoid fields of 5 ~ 20 G are applied. The simulated mode spectra are shown in Fig. 12 and 13 for the horizontal and vertical planes, respectively. Comparing with Fig. 2 which shows the observed mode spectra, the simulated mode spectrum applying 10 G solenoid filed is consistent with the experimental one both in horizontal and vertical planes as in the electron production at the illumination point with 30% reflection.

3.1.3 Mode spectrum by wake function

The simulation program can calculate a wake function which is produced by the electron cloud. The mode spectrum is obtained by the wake function as well as by the tracking. Some examples of the mode spectra in vertical plane by the wake function with or without applying solenoid field are shown in Fig. 14 assuming that the photoelectrons are produced at the illumination point with 30% reflection. Comparing Fig. 14a and Fig. 5b and also Fig. 14b and Fig. 11b, it can be seen that the mode spectra calculated from the particle tracking are similar with those by the wake function.

3.2 GROWTH RATES

The growth rates calculated using the wake function with and without solenoid field are shown in Table 2 for the electron production at illumination point with 30% reflection and the uniform photoelectron production.

Table 2: Growth rates when solenoid-off and solenoid-on

	Growth rate (/ms)	
	Horizontal	**Vertical**
Solenoid-off		
	2.08[a]	2.21[a]
	2.18[b]	1.96[b]
Experimental data	2.00	1.34
Solenoid field		
5 G	1.51[a]	1.03[a]
	1.23[b]	1.36[b]
10 G	0.55[a]	0.38[a]
	0.50[b]	0.31[b]
20 G	0.22[a]	0.18[a]
	0.29[b]	0.22[b]
Experimental data	0.49	0.26

a. The photoelectrons are produced at the illumination point with 30% reflection.

b. The photoelectrons are produced uniformly over the surface of vacuum chamber.

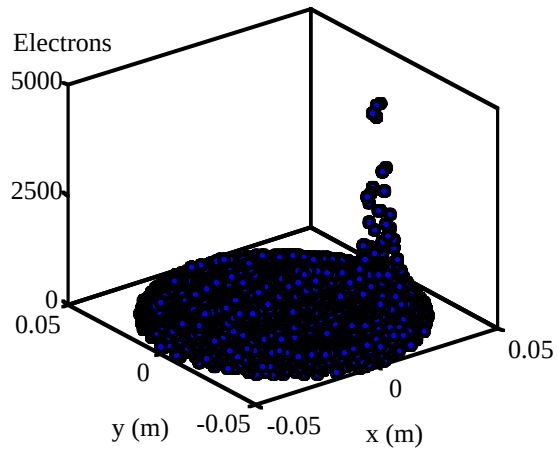

Figure 4: Electron distribution over the cross-section of the vacuum chamber assuming the photo electrons are produced at the illumination point with 30% reflection.

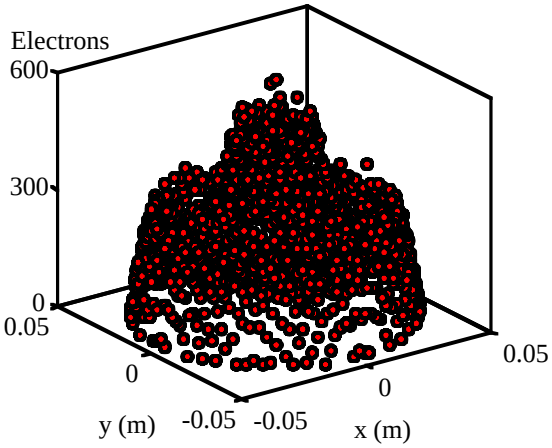

Figure 6: Electron distribution over the cross-section of the vacuum chamber assuming the photoelectrons are produced uniformly on the chamber wall.

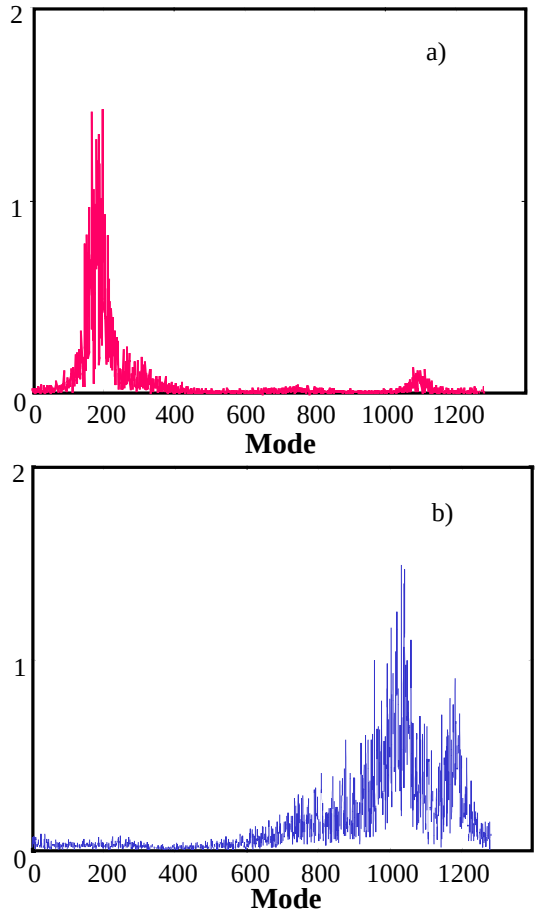

Figure 5: Mode spectra when solenoid-off assuming the photoelectrons are produced at the illumination point with 30% reflection in a) horizontal and b) vertical plane.

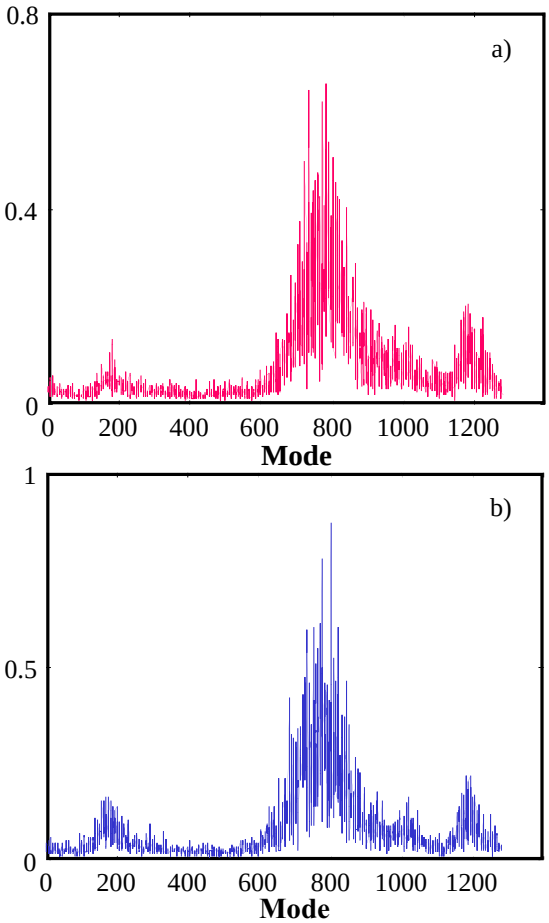

Figure 7: Mode spectra when solenoid-off assuming the photoelectrons are produced uniformly on the chamber wall in a) horizontal and b) vertical plane.

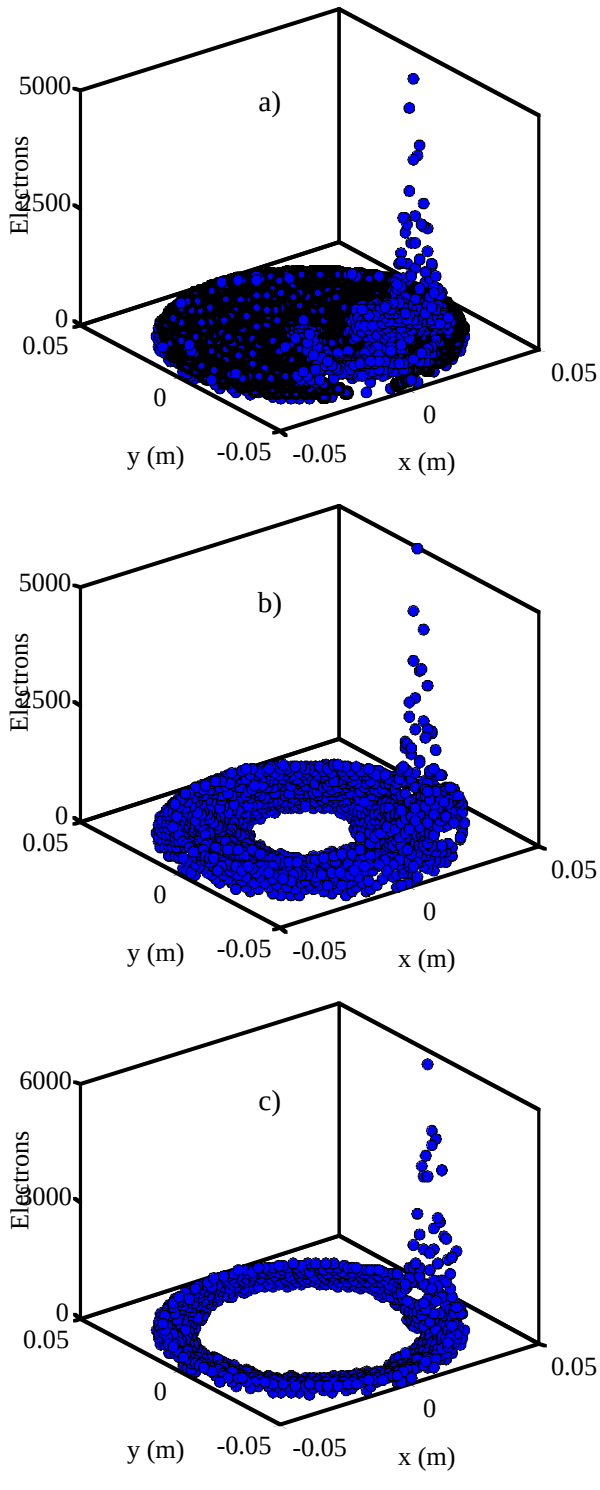

Figure 8: The projection of electrons over the cross-section of the vacuum chamber due to the solenoid fields of 5 (a), 10 (b) and 20G (c) assuming the photoelectrons are produced at illumination point with 30% reflection.

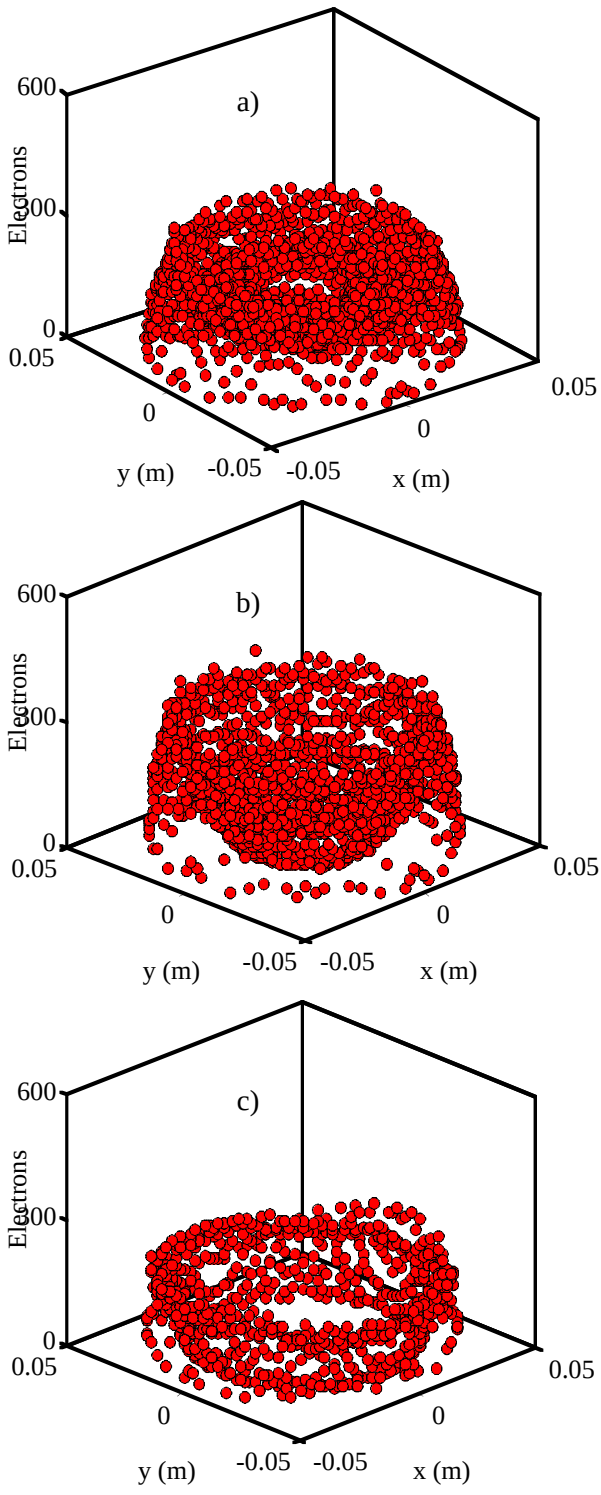

Figure 9: The projection of electrons over the cross-section of the vacuum chamber due to the solenoid fields of 5 (a), 10 (b) and 20G (c) assuming the photoelectrons are produced uniformly on the chamber wall.

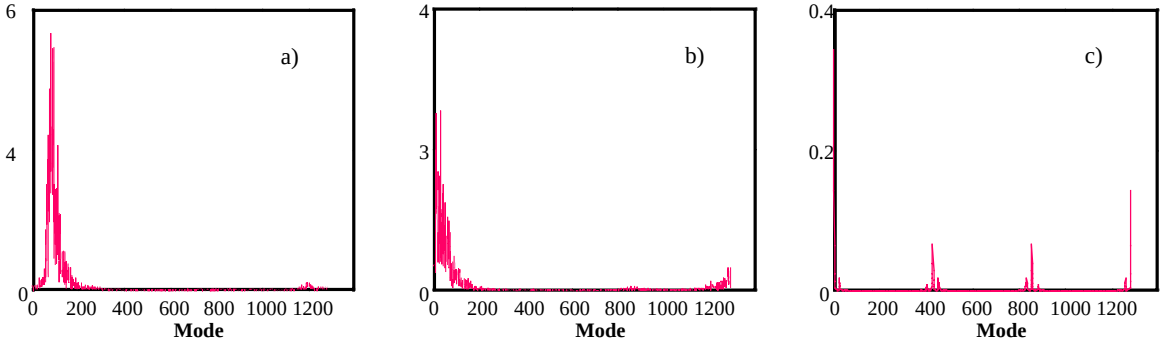

Figure 10: The mode spectra in horizontal plane due to various solenoid fields assuming the photo-electrons are produced at illumination point with 30% reflection; a) 5 G, b) 10 G and c) 20 G.

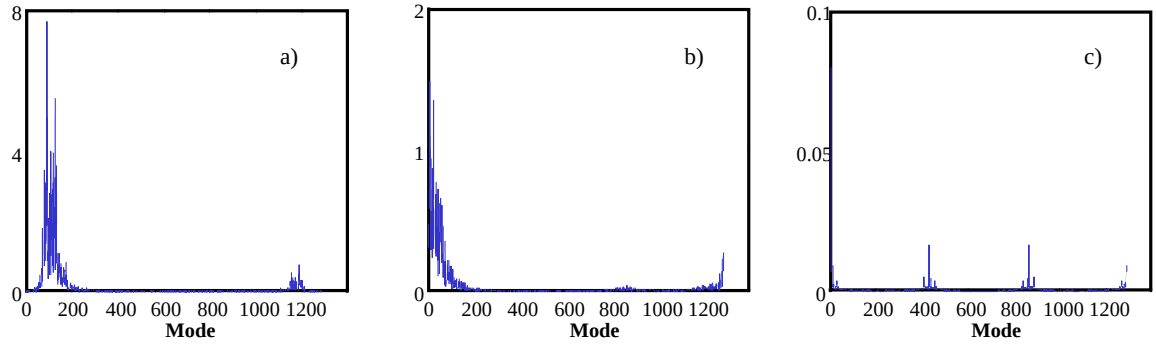

Figure 11: The mode spectra in vertical plane due to various solenoid fields assuming the photo-electrons are produced at illumination point with 30% reflection; a) 5 G, b) 10 G and c) 20 G.

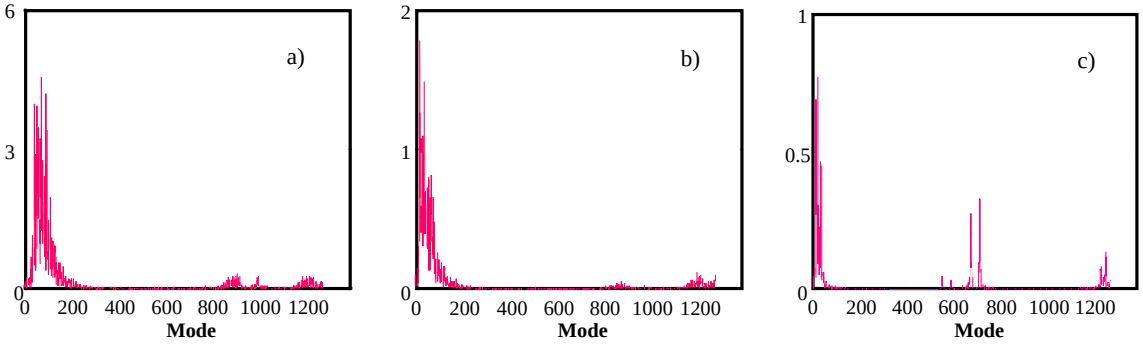

Figure 12: The mode spectra in horizontal plane due to various solenoid fields assuming the photoelectrons are produced uniformly on the chamber wall; a) 5 G, b) 10 G and c) 20 G.

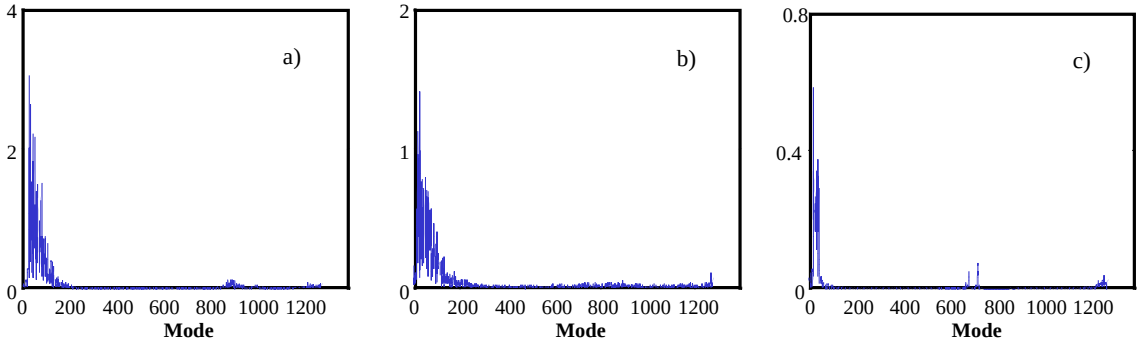

Figure 13: The mode spectra in vertical plane due to various solenoid fields assuming the photoelectrons are produced uniformly on the chamber wall; a) 5 G, b) 10 G and c) 20 G.

When solenoid-off, the simulated horizontal and vertical growth rate is 4 and 65% higher than the experimentally observed value in electron production at the illumination point and 9 and 46% higher than the observed one in uniform electron production. While the horizontal growth rate by the simulation is almost same value as that observed experimentally the vertical growth rate by the simulation is about 50% higher than the observed value.

When solenoid-on, the horizontal and vertical growth rates obtained by the simulation applying 10 G solenoid field are approximately same as the experimental values in uniform photoelectron production. The difference of simulated growth rates in two electron distributions are less than ±25% for the solenoid fields of 5, 10 and 20 G.

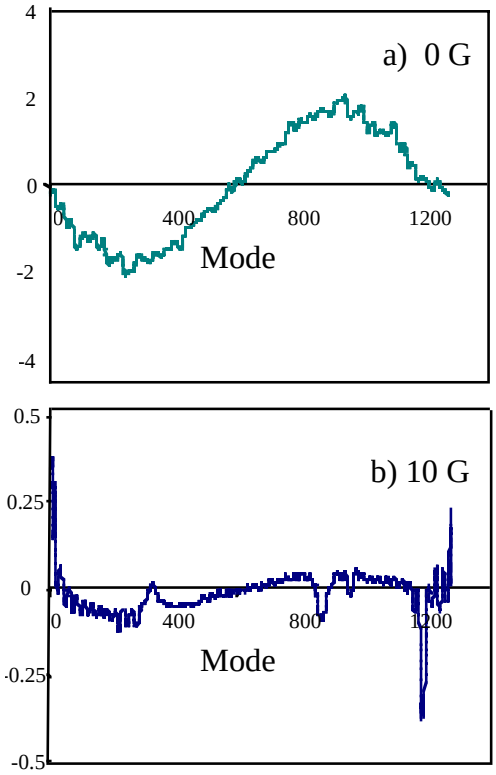

Figure 14: Mode spectra calculated the wake function.

4 SUMMARY

When the solenoids are turned off, the simulation shows inconsistent mode spectra with experimental one in horizontal plane and consistent mode spectrum in vertical plane if we assume that the photoelectrons are produced at the illumination point with 30% reflection. If we assume that the photoelectrons are produced uniformly over the surface of the vacuum chamber, the simulated mode spectra reproduce the experimental ones both in horizontal and vertical planes. While the simulated horizontal growth rate is almost same as observed value the simulated vertical growth rate is about 50% higher than observed value.

When the solenoids are turned on, the simulated mode spectra applying the 5~10 G solenoid field are consistent with those from the experiment. The simulated mode spectra seem not sensitive to the distribution of the electrons. The simulated growth rates applying 10G solenoid field are similar to the experimentally observed values.

In conclusion the simulation suggests that the electrons are produced uniformly over the surface of the vacuum chamber at least when the solenoids are turned off and that the effective magnetic field is 5~20 G to explain the observed mode spectrum and the growth rate of the coupled bunch instability.

REFERENCES

[1] H. Fukuma et al., "Observation of Vertical Beam Blow-Up in KEKB Low Energy Ring", Proceedings of EPAC2000.

[2] K. Ohmi, “Beam-photoelectron interactions in positron storage rings”, Physical Review Letters 75 (1995) 1526 .

[3] M. Izawa et al., "The Vertical Instability in a Positron Bunched Beam", Physical Review Letters 74 (1995) 5044.

[4] Z.Y. Guo et al., "Recent Studies on Beam-Photoelectron Instability in BEPC", Proceedings of PAC1999, New York, 1999, 633.

[5] H. Fukuma, "Electron Cloud Effects at KEKB", in these proceedings.

[6] J. Flannagan et al., "The KEKB bunch oscillation recorder", Proceedings of "Factories' 99", Tsukuba, KEK Proceedings 99-24, 101.

[7] M. Tobiyama and E. Kikutani, "Bunch by Bunch Feedback Systems for the KEKB Rings", KEK Proceedings 99-24, February 2000.

[8] S. S. Win et al., "Observation of transverse coupled bunch instability at KEKB", Proceedings of APAC2001.

Electron cloud effect in the damping ring of Japan Linear Collider

K. Ohmi, *
KEK, Oho, Tsukuba, Ibaraki, 305-0801, Japan

Abstract

Damping rings of Linear Collider are very low emittance ($\varepsilon < 1$nm) and high current ($I \sim 1$A) storage rings which accumulate electron and positron during several damping times. The positron damping ring seems to be serious for electron cloud instability obviously. We discuss electron cloud instability for the damping ring of Japan Linear Collider (JLC).

1 INTRODUCTION

We discuss electron cloud effects in JLC positron damping ring. The positron damping ring storages positron beam during several damping time and extracts very low emittance beam to the linear collider. The damping ring accumulates many positron bunches of the population of 0.75×10^{10} with a narrow spacing (1.4ns). The positron beam with an energy of 1.98GeV emits synchrotron radiation photons, which create a large number of photoelectrons at the chamber surface. Though ante-chambers are used to avoid the photoelectrons, considerable rate of photoelectrons and secondary electrons remain in the chamber. Study of the electron cloud effect in the damping ring is the most important subject to realise the linear collider. Some works for damping rings of linear collider projects (CLIC, NLC, TESLA and JLC) have been done in Refs.[1, 2, 3].

The parameters of JLC damping ring are shown in Table.1 [4].

Table 1: Basic parameters of the JLC damping ring

circumference	L(m)	348.3
energy	E	1.98
bunch population	N_+	0.75×10^{10}
bunch train length	n_{bunch}	192
bunch spacing	ℓ_b(ns)	1.4
gap between trains	ℓ_{gap}(ns)	60
number of bunch train	n_{tr}	4
emittance	ε_x(m)	7×10^{-10}
	ε_y(m)	5×10^{-12}
typical beta function	β (m)	10
bunch length	σ_z(mm)	5
synchrotron tune	ν_s	0.01
beam pipe radius	$R(cm)$	1.0

We discuss electron cloud build-up, coupled bunch instability and single bunch instability caused by the electron cloud in Sec.2, 3 and 4, respectively.

2 ELECTRON CLOUD BUILD-UP

We consider photo-emission and secondary emission as electron sources. The number of photon hitting the chamber wall is given by

$$n_\gamma(/m \cdot e^+) = \frac{5\pi}{\sqrt{3}} \frac{\alpha\gamma}{L}. \quad (1)$$

for a positron in a meter, where α and γ are 1/137 and the relativistic factor, respectively. The number of photoelectron produced by a positron at the chamber is given by

$$n_{e\gamma}(/m \cdot e^+) = n_\gamma Y_\gamma. \quad (2)$$

The direct photo-emission rate was estimated to be $Y_\gamma = 0.1$ for cylindrical chamber in KEKB. This value was consistent with an in situ measurement of electron current using button electrode [5]. We installed a test ante-chamber in KEKB-LER to study density and yield of the electron cloud. The value for the ante-chamber was obtained to be 1/5 for the cylindrical chamber, namely, $Y_\gamma = 0.02$. We choose the measured value $Y_\gamma = 0.02$ for the damping ring. The electron production rate is now given by

$$n_\gamma = 0.65/m \cdot e^+ \qquad n_{e\gamma} = 0.013/m \cdot e^+. \quad (3)$$

The secondary emission rate, which is the number of electron produced by an electron incident at the chamber surface, is characterized by Y_2. We assume $Y_2(E_{peak} = 200eV) = 1.0$ and its energy dependence obeys Furman's formula [6]. This number is somewhat low considering efforts of suppression of secondary yield in the future.

We calculate electron density by the simulation code PEI [7]. Space charge force of electron cloud is taken into account. The beam chamber is assumed to be cylindrical and electrons are produced uniformly along azimuthal angle in the simulation.

We calculated the electron cloud density for 1.4 ns and 2.8 ns spacing keeping the bunch population. Figure 1 shows variation of electron cloud density as a function of bunch passage. The density increases and saturates at a certain density. The density at beam position and averaged one of whole chamber are shown in the figure. The saturated density is $8 \times 10^{12} m^{-3}$ and $3 \times 10^{12} m^{-3}$ for 1.4ns and 2.8ns spacing, respectively, at center, and $6 \times 10^{12} m^{-3}$ and $2.5 \times 10^{12} m^{-3}$ for average. Since the saturation is not perfect as is shown in the figure, actual density may be somewhat higher.

3 COUPLED BUNCH INSTABILITY

The coupled bunch instability is caused by a long range ($\sim$ m) wake field induced by the electron cloud. The wake

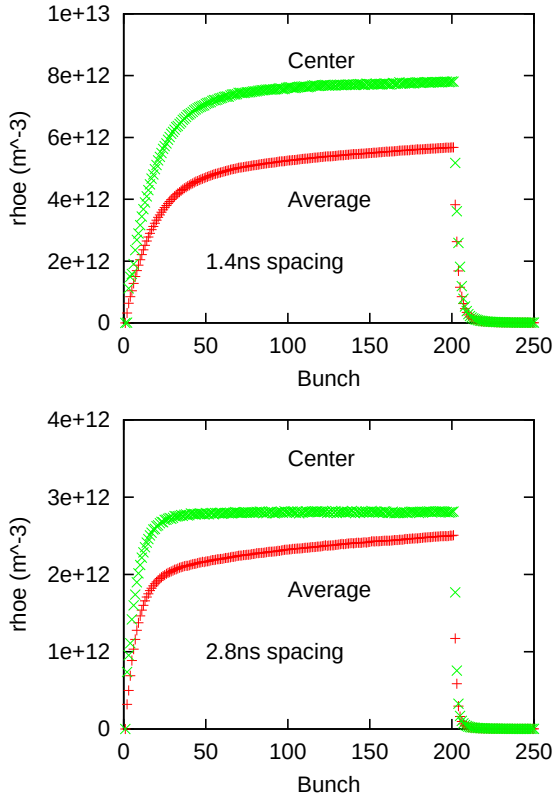

Figure 1: Electron cloud build-up in the JLC damping ring. (a) 1.4 ns spacing (b) 2.8 ns spacing.

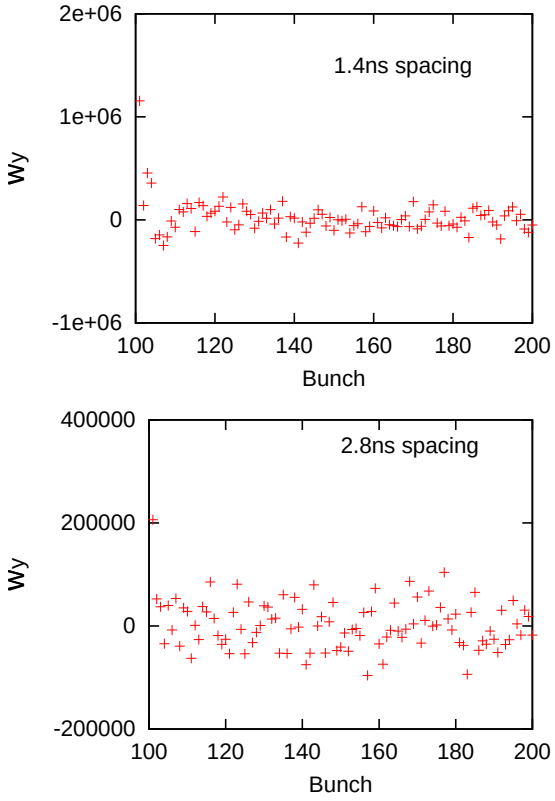

Figure 2: Long range wake field induced by the electron cloud (a) 1.4 ns spacing (b) 2.8 ns spacing. The wake field is represented by unit of velocity kick of electron cloud (m/s).

field is evaluated as follows [7],

- Primary electrons are created in every bunch passage through the chamber center with the line density $n_{e\gamma}$. Secondary electrons are created at absorption of an electron with an energy (E_{abs}) by the rate $Y_2(E_{abs})$.
- The creation process is repeated until the cloud density saturate at a certain value.
- A bunch with a slight displacement passes through the cloud, and then following bunches without displacement pass through the chamber center.
- The creation process is repeated for the displaced and following bunches.
- The following bunches experience forces from the cloud, because the cloud is perturbed by the passage of the displaced bunch. The wake field is calculated by the forces.

Figure 2 shows the wake field for 1.4ns and 2.8ns spacings.

The growth rate of the coupled bunch instability is estimated by the formula [13]

$$\Omega_m - \omega_\beta = \frac{N_e}{4\pi\gamma\nu_y N_p}\sum_{k=1}^{n}\frac{dv_{y,k}}{dy_0}e^{2\pi ik(m+\nu_y)/h}, \quad (4)$$

where N_e is the number of the photoelectron produced by a bunch through the ring circumference, N_p the number of positrons in a bunch, n the range of the wake field, and γ the Lorentz factor. $dv_{y,k}/dy_0$ is the wake field for k-th bunch due to displacement of a bunch (y_0) in unit of velocity kick of photoelectron cloud divided by the displacement. Figure 3 shows the growth of the coupled bunch mode caused by electron cloud instability.

The growth rate was obtained as 26μs (20 turn) and 130μs (100 turn) for 1.4 and 2.8ns spacings, respectively. Perhaps, it is possible to be cured for the growth 130μs, but is impossible for the growth 26μs, by using a bunch-by-bunch feedback system.

4 SINGLE BUNCH INSTABILITY

A single bunch instability is caused by a short range ($\sim cm$) wake field induced by the electron cloud. The short range wake field is analytically estimated for a simple model: that is, beam and electron cloud with the same transverse size interact with each other. We focus on the vertical instability in this paper. The wake field is represented by a resonator model. The resonator frequency (ω_e) corresponds to oscillation frequency of electrons in

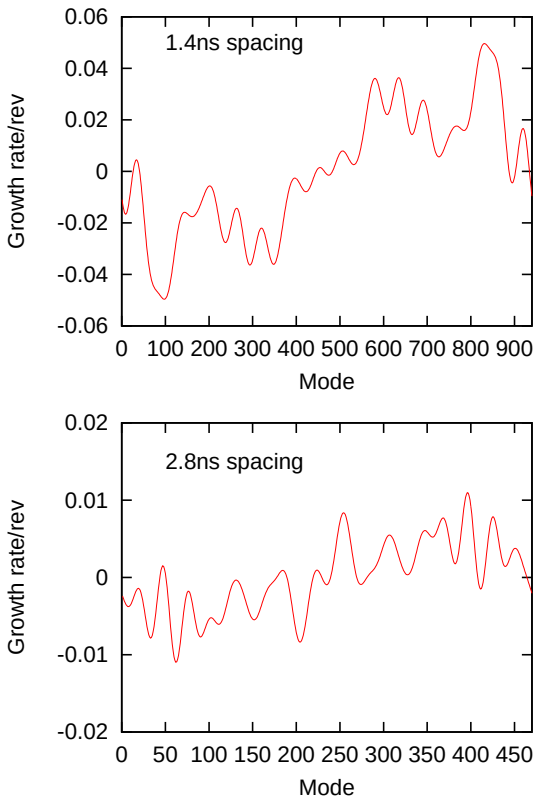

Figure 3: Growth rate for coupled bunch instability caused by the electron cloud. (a) 1.4 ns spacing (b) 2.8 ns spacing.

the beam field,

$$\omega_{e,y} = \sqrt{\frac{\lambda_+ r_e c^2}{\sigma_y(\sigma_x+\sigma_y)}}, \tag{5}$$

where λ_+ and $\sigma_{x(y)}$ are the beam line density in a bunch and transverse beam sizes, respectively. r_e and c are the electron classical radius and the speed of light, respectively. The wake field is expressed by

$$W_1(z)[\mathrm{m}^{-2}] = c\frac{R_S}{Q}\sin\left(\frac{\omega_e}{c}z\right), \tag{6}$$

where

$$c\frac{R_S}{Q} = \frac{\lambda_e}{\lambda_+}\frac{L}{\sigma_y(\sigma_x+\sigma_y)}\frac{\omega_e}{c}. \tag{7}$$

The density of electron cloud λ_e, which is local line density near the beam, is related to the electron volume density ρ_e via $\lambda_e = 2\pi\rho_e\sigma_x\sigma_y$. In our parameters,

$$cR_S/Q = 0.94\times10^7 m^{-2} \qquad \omega_e = 5.5\times10^{11}s^{-1}. \tag{8}$$

We can also estimate the wake field using numerical method. Electron cloud is much larger than beam size, nonlinear force may be important and electrons are focused (pinched) at the beam center. The numerical calculation can take into account these effects partly. The wake field is calculated in a similar way as that for the coupled bunch instability. The beam is uniformly distributed along z direction, and as the initial condition the electron cloud is set to be a uniform distribution with a large transverse size ($10\sigma_x \times 10\sigma_y$).

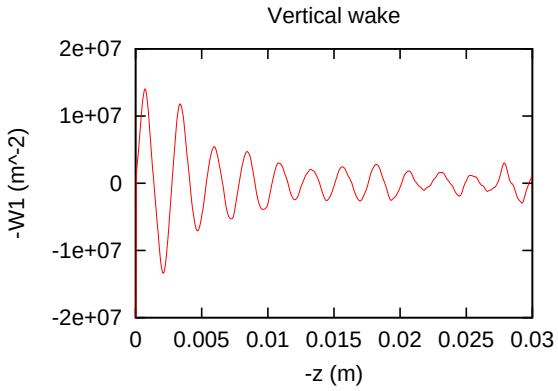

Figure 4: Short range wake field induced by the electron cloud.

Figure 4 shows the vertical wake field obtained by the simulation. The wake field in the figure damps along z due to nonlinear interaction with the electron cloud, though that in Eq.(6) does not damp, namely a finite Q factor is obtained. The figure shows a slightly larger $cR_S/Q = 1.4\times10^7 m^{-2}$ than the analytical value, and $Q \sim 3$. ω_e is close to the analytical value.

The impedance due to the electron cloud is written as

$$\begin{aligned} Z(\omega) &= \frac{cR_S}{\omega}\frac{1}{1+iQ\left(\frac{\omega_e}{\omega}-\frac{\omega}{\omega_e}\right)} \\ &= K\frac{\lambda_e}{\lambda_+}\frac{L}{\sigma_y(\sigma_x+\sigma_y)}\frac{\omega_e}{\omega}\frac{Z_0}{4\pi}\frac{i}{\left(\frac{\omega}{\omega_e}-\frac{\omega_e}{\omega}\right)+i\frac{1}{Q}}, \end{aligned} \tag{9}$$

where K is an enhancement factor due to cloud size, pinching etc. [8], and Z_0 is the impedance of vacuum (377Ω). The figure 4 shows $K = 1.5$. In the case of KEKB, the enhancement factor was $K = 2 \sim 4$ for the vertical wake field.

The single bunch instability is estimated from the wake field. We use the coasting beam model to evaluate the instability, because of $\omega_e\sigma_z/c \gg 1$. The threshold of the instability is expressed by [13]

$$U \equiv \frac{\sqrt{3}\lambda_+ r_e\beta\omega_0}{\gamma\omega_e\eta\sigma_\delta}\frac{|Z_\perp(\omega_e)|}{Z_0} = \frac{\sqrt{3}\lambda_+ r_e\beta}{\gamma\nu_s\omega_e\sigma_z/c}\frac{|Z_\perp(\omega_e)|}{Z_0} = 1. \tag{10}$$

For $U > 1$, the beam is unstable.

We estimated the threshold value of electron cloud density for various positron storage rings. The results are shown in Table 2.

The threshold density for the JLC damping ring is smaller than the predicted cloud density ($8\times10^{12}m^{-3}$ for

Table 2: Single bunch electron cloud instability in positron storage rings. The enhancement factor is chosen to be $K = 3$. The impedance is evaluated at $\rho_e = 10^{12} m^{-3}$.

variable	KEKB	PEP-II	DAFNE	JLC-DR
E(GeV)	3.5	3.1	0.51	1.98
L(m)	3016	2200	97.7	398
$N_+(10^{10})$	3.3	6	4	0.75
ν_s	0.018	0.025	0.012	0.01
$\sigma_x(\mu$m)	420	700	2000	84
$\sigma_y(\mu$m)	60	120	63	7.1
σ_z(mm)	5	12	24	5
$\omega_c \sigma_z / c$	2.5	3.2	3.2	9.1
$Z/Z_0(m^{-1})$	2877	3363	511	2184
$\rho_{e,th}(10^{12} m^{-3})$	0.54	1.2	1.9	4.4

1.4ns spacing): that is, the single bunch instability occurs in the present condition.

Though the wake field approximated by the resonator model permits us to study the instability with simple analytic methods, the estimation of the threshold includes somewhat ambiguous factors: i.e., for example, how to choose K and Q. Since K is related to pinching, one may choose $K \sim \omega_e \sigma_z / c$. A value of Q which is larger than $\omega_e \sigma_z / c$ is meanless. To remove the ambiguity, we have to do tracking simulations [9, 10, 11, 12].

5 SUMMARY

We evaluated electron cloud instabilities in the JLC damping ring. We use the electron production rate $n_e = 0.013/m \cdot e^+$ and secondary yield $Y_{2,peak} = 1$. Electron cloud is build up to the density of $8 \times 10^{12} m^{-3}$ and $3 \times 10^{12} m^{-3}$ for 1.4 and 2.8 ns spacing, respectively.

The growth times of the coupled bunch instability are 26μs (20 turns) and 130μs (100 turns) for 1.4 ns and 2.8 ns spacing, respectively. The growth time of 100 turn seems to be roughly the limit above which the instability could be cured by a bunch-by-bunch feedback system. Threshold of the single bunch instability was $\rho_e = 4.4 \times 10^{12} m^{-3}$ for $\nu_s = 0.01$. The density is a factor of two smaller than the predicted cloud density ($8 \times 10^{12} m-3$ for 1.4ns spacing). The threshold linearly depends on the synchrotron tune ν_s, which is chosen to be large value for a low emittance (low α) machine. Tracking simulations should be done to determine more accurate threshold cloud density.

We need further reduction for the electron cloud by 1/5$\sim$ 1/10, considering the growth of the coupled bunch instability and the safety margin for the single bunch instability. The vacuum chamber should be designed to reduce the electron cloud density. In situ measurements of electron cloud [14, 5] help the design of the vacuum chamber. Our target value of the electron production rate is about $n_e \sim 0.002/m \cdot e^+$.

We comment on the result for DAFNE. Photon production rate is given as $n_\gamma = 0.73/m \cdot e^+$. We study the instability briefly with parameters, the electron production rate $n_e = n_\gamma \times 0.02 = 0.015/m \cdot e^+$, the number of positron in a bunch $N_+ = 4 \times 10^{10}$, the build-up time $\tau = 10 \times \tau_b$ ($\tau_b = 6$ns) and chamber cross section $0.01 m^2$. The average electron cloud density is roughly estimated as $\rho_e = 6 \times 10^{11} m^{-3}$, that is less than the threshold value $1.9 \times 10^{12} m^{-3}$. Since DAFNE is small machine ($T_0 = 0.3\mu$s), small tune spread works to suppress the coupled bunch instability. We used the in situ value $Y = n_e / n_\gamma = 0.02$ for KEKB test ante-chamber [5]. It is interesting to measure the electron cloud in DAFNE. Since the design current of DAFNE is 5A: i.e., 5 times more, we should pay attention to the status in the future.

The author thanks F. Zimmermann for reading this manuscript.

6 REFERENCES

[1] J. Jowett, H. Owen, F. Zimmermann, Proceedings of the PAC2001, 4065 (2001).

[2] A. Wolski, in this proceeding.

[3] F. Zimmermann, private communications.

[4] K. Yokoya, private communications.

[5] K. Kanazawa, private communications.

[6] M. A.Furman and G. R.Lambertson, Proceedings of the PAC97, 1617 (1997).

[7] K. Ohmi, Phys. Rev. Lett., **75**, 1526 (1995).

[8] K. Ohmi, F. Zimmermann, E. Perevedentsev, Phys. Rev. E **65**, 16502 (2002).

[9] K. Ohmi and F. Zimmermann, Phys. Rev. Lett., **85**, 3821 (2000).

[10] G. Rumolo et. al., Proceedings of PAC2001, 1889 (2001).

[11] K.Ohmi, Proceedings of PAC2001, 1895 (2001).

[12] Y. Cai, in this proceedings.

[13] A.W. Chao, *Physics of Collective Beam Instabilities in High Energy Accelerators*, Wiley-Interscience Publication.

[14] K. Harkay, in this proceedings.

EFFECT OF BUNCH LENGTH, CHROMATICITY, AND LINEAR COUPLING ON THE TRANSVERSE MODE-COUPLING INSTABILITY DUE TO THE ELECTRON CLOUD

E. Métral, CERN, Geneva, Switzerland

Abstract

The influence of bunch length, chromaticity, and linear coupling on the transverse mode-coupling intensity threshold is discussed for the case of a bunch interacting with a broad-band resonator impedance. Two regimes are possible according to whether the total bunch length is above or below a critical value, which is about the inverse of twice the resonance frequency. If the bunch length is greater than this value, the intensity threshold in the absence of linear coupling can be approximated by the coasting-beam value multiplied by the bunching factor. Hence, it is proportional to the bunch length, and increases linearly with the ratio between the chromatic and resonance frequencies. If the bunch length is smaller than the critical value, the intensity threshold is inversely proportional to the square of the bunch length, but it still increases slowly with chromaticity. In the presence of linear coupling, the intensity threshold can be increased up to a factor two when the second transverse plane has a negligible impedance. This formalism is applied to the broad-band electron-cloud induced impedance, to evaluate the effect of bunch length, chromaticity and linear coupling on the intensity threshold of the CERN SPS beam for LHC.

1 INTRODUCTION

A vertical single-bunch instability due to the electron cloud is observed in the SPS, with rise-times faster than the synchrotron period [1,2]. The electron-cloud induced impedance has been approximated by a broad-band impedance ($Q_r \approx 1$), whose shunt impedance and resonance frequency depend on bunch length and intensity [3]. Furthermore, it has been found experimentally that increasing the chromaticity helps to increase the intensity threshold.

The purpose of this paper is to compare these observations with theoretical predictions, by evaluating the effect of bunch length and chromaticity on the intensity threshold of the CERN SPS beam for LHC. Another parameter, which could be used to increase the intensity threshold is proposed: this is linear coupling between the transverse planes.

The model used for the classical one- and two-dimensional Transverse Mode-Coupling (TMC) instability is described and discussed in Section 2. This formalism is then applied to the CERN SPS beam for LHC in Section 3.

2 THEORY

2.1 One-Dimensional

Considering the case where two adjacent head-tail modes (m and m+1) undergo a coupled motion, the stability of a high-intensity single-bunch beam can be discussed using the following determinant, e.g. for the vertical plane, [4]

$$\begin{vmatrix} \omega_c - \omega_{y,m} & -\Delta\omega^y_{m,m+1} \\ -\Delta\omega^y_{m+1,m} & \omega_c - \omega_{y,m+1} \end{vmatrix} = 0\,, \qquad (1)$$

with

$$\Delta\omega^y_{m,n} = \left(|m|+1\right)^{-1} \frac{j e \beta I_b}{2 m_0 \gamma Q_{y0} \Omega_0 L} \left(Z_y^{eff}\right)_{m,n}, \qquad (2)$$

$$\left(Z_y^{eff}\right)_{m,n} = \frac{\sum_{k=-\infty}^{k=+\infty} Z_y\left(\omega_k^y\right) h_{m,n}\left(\omega_k^y - \omega_{\xi_y}\right)}{\sum_{k=-\infty}^{k=+\infty} h_{m,m}\left(\omega_k^y - \omega_{\xi_y}\right)}, \qquad (3)$$

$$h_{m,n}(\omega) = \frac{\tau_b^2}{\pi^4}\left(|m|+1\right)\times\left(|n|+1\right)\times F_m^n \times\left\{(\omega\tau_b/\pi)^2 - \left(|m|+1\right)^2\right\}^{-1}\times\left\{(\omega\tau_b/\pi)^2 - \left(|n|+1\right)^2\right\}^{-1}, \qquad (4)$$

$$F_{m\ even}^{n\ even} = (-1)^{\left(|m|+|n|\right)/2}\times\cos^2\left[\omega\tau_b/2\right], \qquad (5)$$

$$F_{m\ even}^{n\ odd} = \frac{(-1)^{\left(|m|+|n|+3\right)/2}}{2j}\times\sin\left[\omega\tau_b\right], \qquad (6)$$

$$F_{m\ odd}^{n\ even} = \frac{(-1)^{(|m|+|n|+1)/2}}{2j} \times \sin[\omega \tau_b], \qquad (7)$$

$$F_{m\ odd}^{n\ odd} = (-1)^{(|m|+|n|+2)/2} \times \sin^2[\omega \tau_b / 2]. \qquad (8)$$

Here, ω_c is the coherent angular frequency to be determined, $\omega_{y,m} = \omega_{y0} + m\omega_s + \Delta\omega_{m,m}^y$, with $\omega_{y0} = Q_{y0}\,\Omega_0$ the unperturbed betatron angular frequency with Q_{y0} the unperturbed tune and $\Omega_0 = 2\pi f_0$ the revolution angular frequency, $m = ..., -1, 0, 1, ...$ is the head-tail mode number, $\omega_s = 2\pi f_s$ is the synchrotron angular frequency (T_s is the synchrotron period), $j = \sqrt{-1}$ is the imaginary unit, e is the elementary charge, β and γ are the relativistic velocity and mass factors, $I_b = N_b\, e\, f_0$ is the current in one bunch with N_b the number of protons in the bunch, m_0 is the proton rest mass, $L = \beta c \tau_b$ is the full (4σ) bunch length (in metres) with c the speed of light and τ_b the total bunch length (in seconds), Z_y is the coupling impedance, $\omega_k^y = (k + Q_{y0})\,\Omega_0 + m\omega_s$ with $-\infty \le k \le +\infty$, $\omega_{\xi y} = 2\pi f_{\xi y} = (\xi_y / \eta)\, Q_{y0}\, \Omega_0$ is the chromatic angular frequency, with $\xi_y = (\Delta Q_y / \Delta p)\,(p_0 / Q_{y0})$ and $\eta = \gamma_{tr}^{-2} - \gamma^{-2} = (\Delta T / T_0)/(\Delta p / p_0)$ the chromaticity and slippage factor, where p is the momentum and T the revolution period of a particle, and $h_{m,n}$ describes the cross-power densities of the mth and nth line-density modes. As can be seen from Eqs. (4-8), $h_{m,m+1}(\omega) = -h_{m+1,m}(\omega)$, which yields

$$\Delta\omega_{m+1,m}^y = -k_m^2\, \Delta\omega_{m,m+1}^y\,, \qquad (9)$$

with

$$k_m = \sqrt{\frac{|m|+1}{|m+1|+1}}\,. \qquad (10)$$

This parameter is often approximated by one [4]. Considering the case of a driving broad-band resonator, the coupling impedance is given by

$$Z_y(\omega) = \frac{\omega_r}{\omega} R_r \Big/ \left[1 - jQ_r\left(\frac{\omega_r}{\omega} - \frac{\omega}{\omega_r}\right)\right], \qquad (11)$$

where $\omega_r = 2\pi f_r$ is the resonance angular frequency, Q_r the quality factor and R_r the shunt impedance. Equation (1) leads to the following solutions for ω_c

$$\omega_c^{\pm} = \frac{1}{2} \times \left[2\omega_{y0} + (2m+1)\omega_s + \Delta\omega_{m,m}^y + \Delta\omega_{m+1,m+1}^y\right] \pm \frac{1}{2}\sqrt{\left(\omega_s + \Delta\omega_{m+1,m+1}^y - \Delta\omega_{m,m}^y\right)^2 - 4k_m^2\left(\Delta\omega_{m,m+1}^y\right)^2}\,. \qquad (12)$$

In the following, only the real parts of the complex betatron frequency shifts are considered (see Section 2.2 for a discussion on the model used). We thus write

$$\Delta\omega_{m,m}^y = a_0\, I_b\,, \qquad (13)$$

$$\Delta\omega_{m+1,m+1}^y = b_0\, I_b\,, \qquad (14)$$

$$\Delta\omega_{m,m+1}^y = c_0\, I_b\,, \qquad (15)$$

$$I_{b,th1} = \frac{\omega_s}{a_0 - b_0 + 2k_m |c_0|}\,, \qquad (16)$$

$$I_{b,th2} = \frac{\omega_s}{a_0 - b_0 - 2k_m |c_0|}\,. \qquad (17)$$

If $I_{b,th2} > 0$, then $I_{b,th2} > I_{b,th1}$. The beam is stable from zero intensity to $I_{b,th1}$. Then it is unstable between $I_{b,th1}$ and $I_{b,th2}$ (mode-coupling at $I_{b,th1}$). Finally, it is stable again above $I_{b,th2}$ (mode-decoupling at $I_{b,th2}$). This case is depicted in Fig. 1.

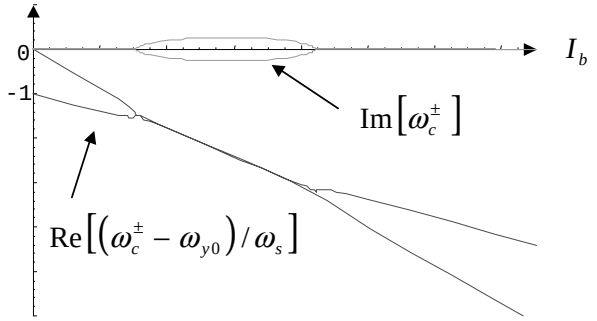

FIGURE 1. *Mode-coupling and -decoupling: the upper traces describe the imaginary parts of the coherent betatron frequencies $\omega_c^{\pm}$, and the lower traces the real parts.*

This corresponds to the case of a long bunch, whose spectra of modes 0 and –1 peak at low frequencies. Both modes couple to the inductive part of the coupling impedance, and therefore are shifted in the same direction. Moreover, their coupling to the resistive part of the coupling impedance is weak. As a consequence, when the two modes merge, they cannot develop a strong instability and are pulled apart as intensity increases. Modes of higher order can couple, but higher-order modes are more difficult to drive than lower-order ones [5].

Therefore, in our model one will always consider mode-coupling between the two most critical head-tail modes (m and m+1) overlapping the peak of the negative resistive impedance. In this case there will never be

mode-decoupling ($I_{b,th2} < 0$), and the threshold for mode-coupling is obtained at the intensity $I_{b,th1}$ (see Fig. 2).

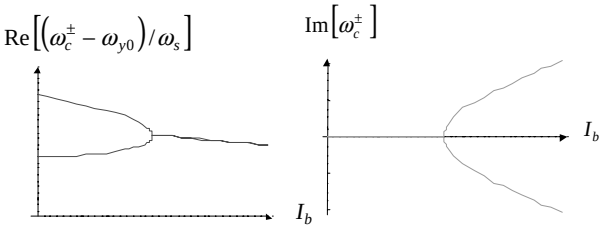

FIGURE 2. *Real (left) and imaginary (right) parts of the coherent betatron frequencies* $\omega_c^{\pm}$.

Below the intensity threshold $I_{b,th1}$, the real and imaginary parts of the coherent frequencies are given by

$$\mathrm{Re}\left(\omega_c^{\pm}\right) = \omega_{y0} + \left(m + 1/2\right)\omega_s + I_b\left(a_0 + b_0\right)/2 \pm \frac{1}{2}\sqrt{\left[\omega_s + \left(b_0 - a_0\right)I_b\right]^2 - 4k_m^2 c_0^2 I_b^2}\,, \tag{18}$$

$$\mathrm{Im}\left(\omega_c^{\pm}\right) = 0\,. \tag{19}$$

Above the intensity threshold $I_{b,th1}$, the real and imaginary parts of the coherent frequencies are given by

$$\mathrm{Re}\left(\omega_c^{\pm}\right) = \omega_{y0} + \left(m + 1/2\right)\omega_s + I_b\left(a_0 + b_0\right)/2\,, \tag{20}$$

$$\mathrm{Im}\left(\omega_c^{\pm}\right) = \pm\frac{1}{2}\sqrt{4k_m^2 c_0^2 I_b^2 - \left[\omega_s + \left(b_0 - a_0\right)I_b\right]^2}\,. \tag{21}$$

The instability rise-times are given by

$$\tau_{\pm} = \frac{-1}{\mathrm{Im}\left(\omega_c^{\pm}\right)}\,. \tag{22}$$

The rise-time of the unstable mode can be re-written

$$\tau_{-} = T_s \times \frac{1}{\pi\sqrt{\left(\alpha - 1\right)\left(\alpha q + 1\right)}}\,, \tag{23}$$

where q and α are given by

$$q = \frac{2k_m\left|c_0\right| + b_0 - a_0}{2k_m\left|c_0\right| - b_0 + a_0}\,, \qquad \alpha = \frac{I_b}{I_{b,th1}}\,. \tag{24}$$

The parameter $q \in [0,1]$: it is equal to one for long bunches and zero for short bunches. The two curves describing the two extreme cases for the rise-time given by Eq. (23) are shown in Fig. 3. It can thus be seen from Fig. 3, that the same (well-known) result is obtained in all cases: just above threshold, the instability rise-time is given by the synchrotron period.

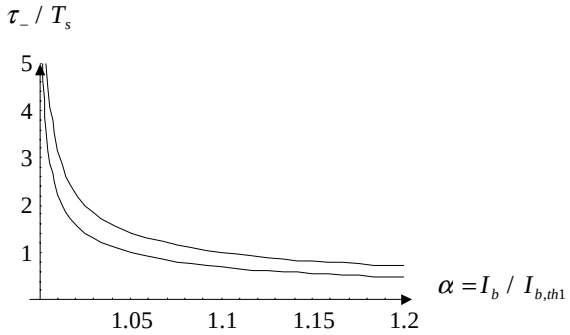

FIGURE 3. *Instability rise-time normalised to the synchrotron period vs.* $\alpha = I_b / I_{b,th1}$, *for q=0 (upper trace) and q=1 (lower trace).*

Investigate now the effect of bunch length and chromaticity on the intensity threshold. Two regimes are possible according to whether the total bunch length is above or below a critical value, which is about the inverse of twice the resonance frequency (see Fig. 4). This corresponds to the time when the wake-field becomes negative (see Fig. 5). In the frequency domain, this case corresponds to the second picture of Fig. 6.

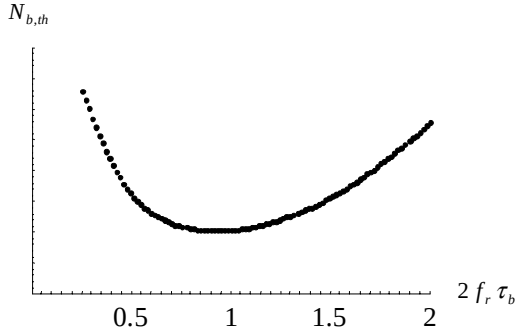

FIGURE 4. *Intensity threshold near* $2 f_r \tau_b = 1$, *by solving numerically Eq. (1) for modes 0 and -1.*

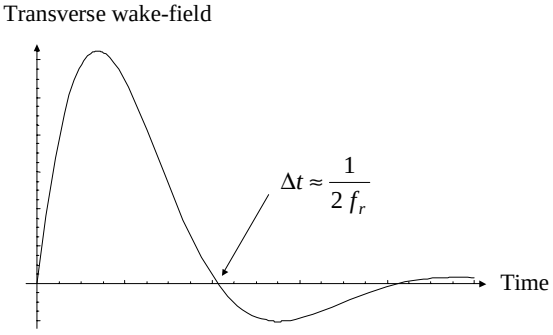

FIGURE 5. *Transverse wake-field vs. time.*

If $\tau_b \geq 0.5/f_r$, it is the "long-bunch" regime (see Fig. 6).

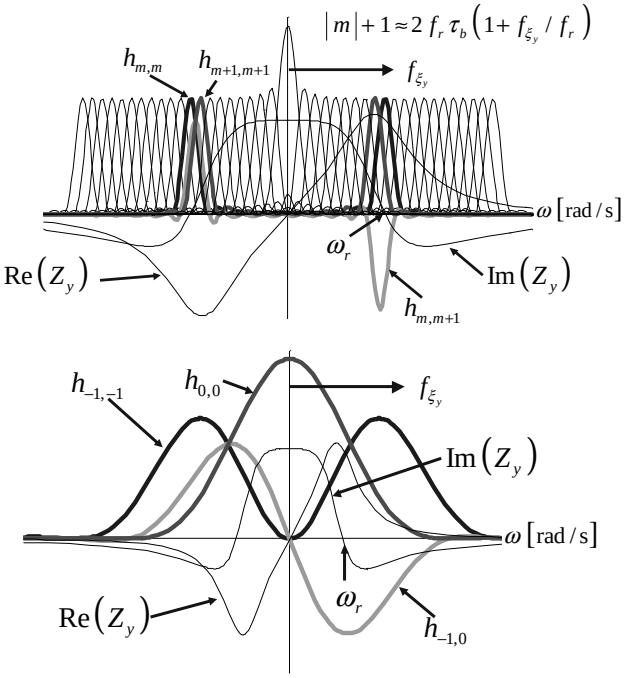

FIGURE 6. Power spectra for a long ($\tau_b >> 0.5/f_r$) and short ($\tau_b = 0.5/f_r$) bunch, in the "long-bunch" regime, and real and imaginary parts of the driving broad-band impedance.

The intensity threshold can be approximated by [4]

$$N_{b,th} = \frac{4\pi^3 f_s Q_{y0} E \tau_b^2}{e c} \times \frac{f_r}{|Z_y|} \times \left(1+\frac{f_{\xi_y}}{f_r}\right), \quad (25)$$

which can be re-written,

$$N_{b,th} = \frac{8\pi Q_{y0} |\eta| \varepsilon_l}{e \beta^2 c} \times \frac{f_r}{|Z_y|} \times \left(1+\frac{f_{\xi_y}}{f_r}\right), \quad (26)$$

using $f_s = |\eta| \times (\Delta p/p_0)_{\max}/(\pi \tau_b)$ and approximating the longitudinal emittance (at 2σ, in eV.s), by an elliptic area in the longitudinal phase space, which gives $\varepsilon_l = \beta^2 E \tau_b (\Delta p/p_0)_{\max} \pi/2$, where E is the total beam energy, and $|Z_y|$ is the peak value of the resonator. Formula (26) is the same as from (i) the coasting-beam approach using the peak values of bunch current and momentum spread [6], (ii) Ruth and Wang fast blow-up theory [7], (iii) Kernel et al. post-head-tail formalism [8], and (iv) Zotter theory for zero chromaticity [9]. In fact, if one computes the ratio between the intensity threshold obtained by simulation, solving numerically Eq. (1) for the two most critical modes given by

$$|m|+1 \approx 2 f_r \tau_b \left(1+\frac{f_{\xi_y}}{f_r}\right), \quad (27)$$

and the intensity threshold given by Eq. (26), the same kind of pictures as in Fig. 7 are obtained. The ratio is always between ~1 and ~2, as can be easily deduced from the first picture of Fig. 6 for a very long bunch. It is approximated by one [4].

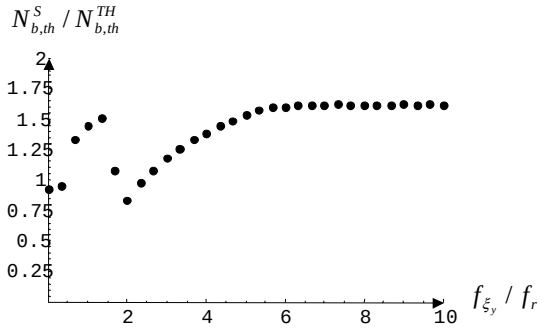

FIGURE 7. *Ratio between the intensity threshold* $N^S_{b,th}$ *computed numerically from Eq. (1) with* $2 f_r \tau_b = 10$*, and the intensity threshold* $N^{TH}_{b,th}$ *given by Eq. (26), vs.* f_{ξ_y}/f_r .

If $\tau_b < 0.5/f_r$, it is the "short-bunch" regime. The intensity threshold can be approximated by [9]

$$N^{short}_{b,th}(\xi_y = 0) = \frac{N_{b,th}(\xi_y = 0)}{(2 f_r \tau_b)^3} \times \frac{1}{2}\left[1+(2 f_r \tau_b)^2\right]. \quad (28)$$

The second term is a small term varying between ½ (when $\tau_b << 0.5/f_r$) and 1 (when $\tau_b = 0.5/f_r$). Note that the factor $(2 f_r \tau_b)^3$ is also obtained between the beam break-up "rise-times" (one *e*-folding time), which can be derived from Brandt and Gareyte formula [10] for long bunches (which is derived from Yokoya's formalism for cumulative beam break-up [11]) and from Chao et al. for short bunches [12]. The intensity threshold increases "slowly" with chromaticity, as the bunch spectrum for mode 0 extends well above the resonance frequency.

2.2 Discussion on the Model Used

The model used here for the classical TMC instability is based on the mode-coupling between the two most critical head-tail modes (*m* and *m*+1) overlapping the

peak of the negative resistive impedance. For zero chromaticity, the tune shifts are real. There is no Head-Tail (HT) instability, and above a threshold intensity, a TMC instability develops, with an instability rise-time faster than the synchrotron period. When the chromatic frequency is shifted positively (this is the stability criterion for the head-tail mode m=0), the simple model where the two regimes (HT and TMC) are treated separately is used here. Below the threshold intensity, the standing-wave patterns (head-tail modes) are treated independently. Above the threshold intensity, the wake fields couple the head-tail modes together and a travelling-wave pattern is created along the bunch. This is the TMC instability. In this paper, only the TMC intensity threshold is looked at, i.e. only the real parts of the complex coherent tune shifts are considered. Other people [13] use directly the complex tune shifts, and solve the problem numerically, thus treating both regimes at the same time. The advantage of the present formalism is that it is simple, and that it makes the link between the TMC formalism and the formula already derived when (i) the bunch length is much longer than the inverse of twice the resonance frequency, and (ii) the synchrotron frequency tends to zero (e.g. at transition), or the instability rise-time is much faster than the synchrotron period.

Note that using the same "simple" model, i.e. considering only the mode-coupling between the two most critical modes overlapping the peak of the negative resistance, the following stability criterion is obtained for the longitudinal mode-coupling instability, taking into account the potential-well distortion due to both space-charge and broad-band impedances, [14]

$$\frac{\left|Z_l^{BB}/p\right|}{1.2}\times\left[1\pm\frac{3}{4}\left(\frac{\left|Z_l^{SC}/p\right|}{\left|Z_l^{BB}/p\right|}-1\right)\right]^{1/4} \le \frac{(E/e)\beta^2\left|\eta\right|}{I_p}\times\left(\frac{\Delta p}{p_0}\right)^2_{\mathrm{FWHH}}. \tag{29}$$

Here, $I_p = 3\,e\,N_b/(2\tau_b)$ is the bunch peak current considering a parabolic line density, $\left|Z_l^{BB}(p)/p\right|$ and $\left|Z_l^{SC}(p)/p\right|$ are the peak values of the broad-band and space-charge longitudinal impedances, and the signs $\pm$ correspond to the cases below and above transition respectively. It is believed that this stability criterion is more appropriate than the one of Keil-Schnell-Boussard [15] (given by Eq. (29) with the term on the left replaced by the modulus of the coupling impedance). It is known that the Keil-Schnell stability criterion [16] for the longitudinal microwave instability of coasting beams is already a simplification, which is valid when the inductive part of the coupling impedance is smaller than the real one. When the inductive part of the coupling impedance is much greater than the real one, this stability criterion is not valid, and one has to look at the stability diagram, which is a graphical representation of the solution of the dispersion relation depicting curves of constant growth rates, and especially a threshold contour in the complex plane of the driving impedance. Equation (29) also depicts a threshold contour in the complex plane of the driving impedance.

2.3 Two-Dimensional

In the presence of linear coupling, the 2×2 determinant of Eq. (1) becomes a 4×4 determinant given by (near the coupling resonance $Q_x - Q_y = l$) [17]

$$\begin{vmatrix} \omega_c-\omega_{x,m} & -\Delta\omega^x_{m,m+1} & -\frac{\underline{\hat{K}}_0(l)R^2\Omega_0^2}{2\,\omega_{x0}} & 0 \\ -\Delta\omega^x_{m+1,m} & \omega_c-\omega_{x,m+1} & 0 & -\frac{\underline{\hat{K}}_0(l)R^2\Omega_0^2}{2\,\omega_{x0}} \\ -\frac{\underline{\hat{K}}_0(-l)R^2\Omega_0^2}{2\,\omega_{y0}} & 0 & \omega_c-\omega_{y,m} & -\Delta\omega^y_{m,m+1} \\ 0 & -\frac{\underline{\hat{K}}_0(-l)R^2\Omega_0^2}{2\,\omega_{y0}} & -\Delta\omega^y_{m+1,m} & \omega_c-\omega_{y,m+1} \end{vmatrix} = 0, \tag{30}$$

where $\omega_{x,m} = \omega_{x0} + m\,\omega_s + \Delta\omega^x_{m,m}$ and here $\omega_{y,m} = \omega_{y0} + l\,\Omega_0 + m\,\omega_s + \Delta\omega^y_{m,m}$, $\underline{\hat{K}}_0(l)$ is the lth Fourier coefficient of the skew gradient $\underline{K}_0 = (e/p_0)(\partial B_x/\partial x)$, with B_x the horizontal magnetic field, and R is the average radius of the machine. Equation (30) leads to a fourth-order equation, which can be solved on the resonance (using here the approximation $k_m \approx 1$)

$$\begin{aligned} &Q_{x0} + \frac{1}{2\Omega_0}\left(\Delta\omega^x_{m,m} + \Delta\omega^x_{m+1,m+1}\right) = \\ &Q_{y0} + l + \frac{1}{2\Omega_0}\left(\Delta\omega^y_{m,m} + \Delta\omega^y_{m+1,m+1}\right). \end{aligned} \tag{31}$$

A necessary condition for stability is given by

$$\left|\Delta\omega^x_{m,m+1} + \Delta\omega^y_{m,m+1}\right| \le \frac{1}{2}\left|2\,\omega_s + \Delta\omega^x_{m+1,m+1} + \Delta\omega^y_{m+1,m+1} - \Delta\omega^x_{m,m} - \Delta\omega^y_{m,m}\right|. \tag{32}$$

If Eq. (32) is fulfilled, then it is possible to stabilise the beam by linear coupling. Beam stability is obtained above a certain threshold for the coupling strength, whose value is given by

$$\left|\underline{\hat{K}}_0(l)\right| \geq \frac{2\sqrt{Q_{x0}\,Q_{y0}}}{R^2\,\Omega_0} \times\left[\frac{1}{2}\left(\Delta\omega^x_{m,m}-\omega_s-\Delta\omega^x_{m+1,m+1}\right)\mp\Delta\omega^x_{m,m+1}\right]^{1/2} \times\left[\frac{1}{2}\left(\Delta\omega^y_{m,m}-\omega_s-\Delta\omega^y_{m+1,m+1}\right)\pm\Delta\omega^y_{m,m+1}\right]^{1/2}. \quad (33)$$

Consider for instance the case where $\xi_x=\xi_y$, $Q_x=Q_y$, and $Z_y=\lambda Z_x$. The necessary condition for stability of Eq. (32) becomes

$$\left|\Delta\omega^y_{m,m+1}\right| \leq \frac{1}{2}\left|\omega'_s+\Delta\omega^y_{m+1,m+1}-\Delta\omega^y_{m,m}\right|, \quad (34)$$

which is the one-dimensional vertical stability criterion with the angular synchrotron frequency ω_s replaced by

$$\omega'_s=\omega_s\times\frac{2\lambda}{\lambda+1}. \quad (35)$$

A factor 2 is thus gained on the intensity threshold when $\lambda>>1$, i.e. when the second transverse plane has a negligible impedance. Note that in the case $\lambda>>1$, the same result is obtained for different chromaticities and tunes.

3 APPLICATION TO THE CERN SPS BEAM FOR LHC

The SPS electron-cloud induced impedance has been computed in Ref. 3 for $N_{b0}=7.5\times10^{10}$ p/b, considering an average density of the electron cloud of $\rho_{c0}=10^{12}$ e$^-$/m^3, longitudinal and transverse rms dimensions $\sigma_{z0}=30$ cm, $\sigma_{x0}=5$ mm and $\sigma_{y0}=3$ mm. The result is a broad-band impedance ($Q_r\approx1$), with peak value $\left|Z_{y0}\right|=20$ MΩ/m and resonance frequency $f_{r0}=220$ MHz. Furthermore, the peak impedance and resonance frequency scale as follows

$$\left|Z_y\right|=\left|Z_{y0}\right|\times\frac{\sigma_z}{\sigma_{z0}}\times\frac{\sigma_{y0}\left(\sigma_{x0}+\sigma_{y0}\right)}{\sigma_y\left(\sigma_x+\sigma_y\right)}, \quad (36)$$

$$f_r=f_{r0}\times\sqrt{\frac{\sigma_{z0}}{\sigma_z}}\times\sqrt{\frac{N_b}{N_{b0}}}\times\sqrt{\frac{\sigma_{y0}\left(\sigma_{x0}+\sigma_{y0}\right)}{\sigma_y\left(\sigma_x+\sigma_y\right)}}. \quad (37)$$

Applying Eq. (26) to find the intensity threshold with the above impedance, since $\tau_b\geq0.5/f_r$ in the cases studied, yields

$$N_{b,th}=\frac{f^2}{4\tau_b^3}\times\left(1+\sqrt{1+\frac{4g\,\xi_y\,\tau_b^2}{f}}\right)^2, \quad (38)$$

with

$$f=\frac{8\pi Q_{y0}\left|\eta\right|\varepsilon_l\,f_{r0}\,\tau_{b0}^{3/2}}{e\beta^2c\left|Z_{y0}\right|\sqrt{N_{b0}}}\times\sqrt{\frac{\sigma_y\left(\sigma_x+\sigma_y\right)}{\sigma_{y0}\left(\sigma_{x0}+\sigma_{y0}\right)}}, \quad (39)$$

$$g=\frac{Q_{y0}\,f_0\sqrt{N_{b0}}}{\eta\,f_{r0}\,\tau_{b0}^{1/2}}\times\sqrt{\frac{\sigma_y\left(\sigma_x+\sigma_y\right)}{\sigma_{y0}\left(\sigma_{x0}+\sigma_{y0}\right)}}. \quad (40)$$

The plot of Eq. (38), which describes the intensity threshold vs. both chromaticity and bunch length, is shown in Fig. 8, using the numerical values given in Table 1.

Table 1: Basic parameters of the CERN SPS.

Average machine radius	R [m]	1100
Slippage factor	η	5.5×10^{-4}
Beam energy	E [GeV]	26
Nominal bunch population	N_b [p/b]	11×10^{10}
Long. emittance (2σ)	ϵ_l [eV.s]	0.35
Nominal bunch length	σ_z [cm]	30
Nominal horiz. beam size	σ_x [mm]	2.6
Nominal vert. beam size	σ_y [mm]	1.9
Vertical tune	Q_y	~26.7

Note than the nominal bunch length is $\sigma_z=30$ cm, which corresponds to $\tau_b=4$ ns. It is found that an instability is predicted once the electron-cloud build-up is predicted and observed (3×10^{10} p/b). Keeping the same bunch length, it is predicted from Fig. 8 that the nominal beam intensity should be reached for a chromaticity of 0.88. Note that for 6×10^{10} p/b, beam stability is predicted for a chromaticity of 0.44, whereas ~0.6 has been found experimentally. The theoretical predictions seem therefore to be in good agreement with observations. It is also seen from Fig. 8, that the intensity threshold can be raised by decreasing the bunch length. Figure 9 gives the rise-time of the instability vs. bunch intensity. It is seen that for 6×10^{10} p/b, a rise-time

of ~1 ms is predicted, which is in agreement with the observations.

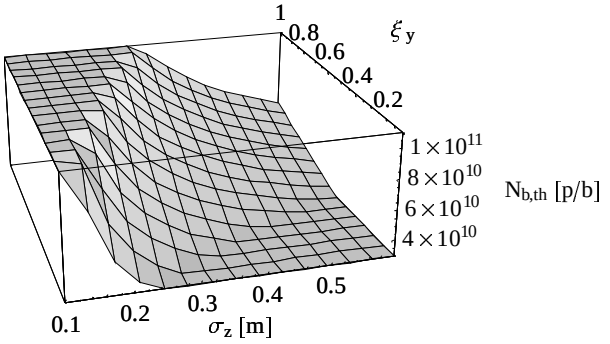

FIGURE 8. *Intensity threshold of the SPS beam for LHC vs. both chromaticity and bunch length, between* 3×10^{10} p/b *, which is the threshold for the electron-cloud build-up, and* 11×10^{10} p/b *, which is the nominal intensity.*

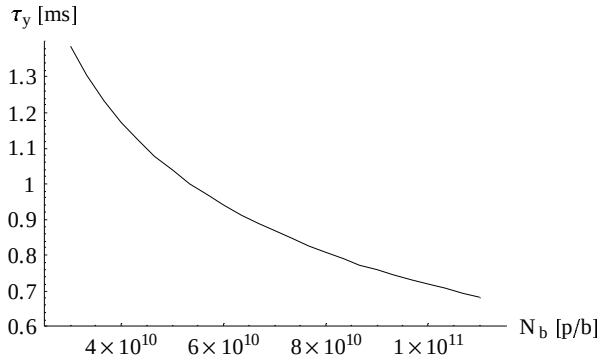

FIGURE 9. *Vertical instability rise-time for zero chromaticity vs. bunch intensity.*

Since 2/3 of the SPS circumference is composed of dipole-field regions, where the horizontal electron-cloud induced impedance is zero, linear coupling could be used to raise the intensity threshold. Figure 10 is the same as Fig. 8 but with linear coupling (see Eqs. (31) and (33)), and considering only the dipole-field regions of the SPS. It is seen that in this case the nominal intensity can be reached already for a chromaticity of 0.34 instead of 0.88 without linear coupling. Considering the same impedance in the horizontal and vertical planes of the regions without dipole fields and in the vertical plane of the dipole-field region, and zero in the horizontal plane of the dipole-field regions, yields Fig. 11. The beneficial effect of linear coupling is also observed, but slightly less than in Fig. 10, since 1/3 of the circumference has now a horizontal impedance. It is seen that in this case the nominal intensity can be reached already for a chromaticity of 0.52 instead of 0.88 without linear coupling, and 0.34 considering only the dipole-field regions.

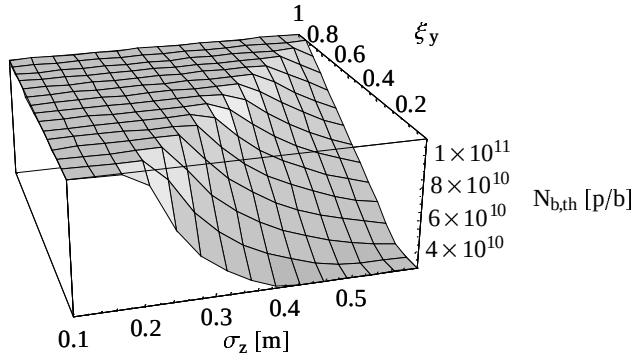

FIGURE 10. *Same as Fig. 8, but in the presence of linear coupling and considering only dipole-field regions.*

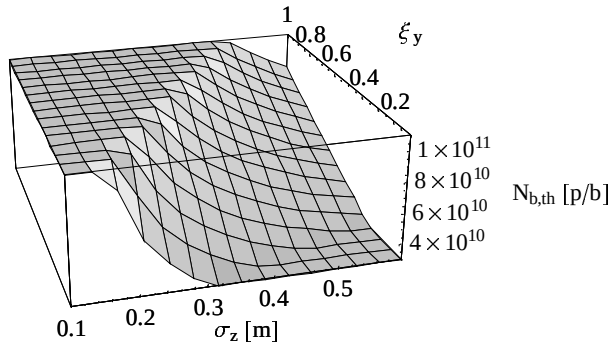

FIGURE 11. *Same as Fig. 8, but in the presence of linear coupling and considering the dipole-field regions (2/3 of the SPS circumference) and the regions without dipole field (1/3 of the SPS circumference).*

4 CONCLUSION

The equation used here for the classical transverse mode-coupling instability is the same as from (i) the coasting-beam approach using the peak values of bunch current and momentum spread, (ii) Ruth and Wang fast blow-up theory, (iii) Kernel et al. post-head-tail formalism, and (iv) Zotter theory for zero chromaticity.

This formalism has been applied to the SPS with the vertical broad-band electron-cloud induced impedance, which depends on bunch length and intensity. It is found that higher intensity thresholds can be reach by (i) increasing the chromaticity, and/or (ii) decreasing the bunch length, and/or (iii) using linear coupling.

The predicted SPS rise-time and stabilising effect of chromaticity, are in quantitative agreement with the

observations (made up to $\sim 6\times10^{10}$ p/b). It is predicted that the nominal beam should be stable for a sufficiently large chromaticity (~1). However, beam losses may appear due to other phenomena. It is proposed to use linear coupling in the SPS to reduce the value of the chromaticity needed to stabilise the nominal beam for LHC.

ACKNOWLEDGEMENTS

Many thanks to R. Cappi, G. Arduini, M. Giovannozzi, G. Rumolo, and F. Zimmermann for very helpful discussions.

REFERENCES

[1] G. Arduini, "Observations on Transverse Instabilities", Proc. of the LHC Workshop, Chamonix XI, 15-19 January 2001.

[2] Minutes of the SPS Studies Working Group, at http://sl-mgt-sps-swg.web.cern.ch/sl-mgt-sps-swg/SPS2001min10.pdf.

[3] K. Ohmi, F. Zimmermann, E. Perevedentsev, "Study of the Fast Head-Tail Instability Caused by Electron Cloud", CERN-SL-2001-011 AP, presented at HEACC2001, Tsukuba, March 2001.

[4] E. Métral, "Fast High-Intensity Single-Bunch Transverse Coherent Instability in Synchrotrons due to a Broad-Band Resonator Impedance", CERN/PS 2001-035 (AE), July 2001.

[5] J. Gareyte, "Transverse Mode Coupling Instabilities", CERN-SL-2000-075 (AP), 2000.

[6] J.L. Laclare, "Introduction to Coherent Instabilities – Coasting Beam Case", CERN Accelerator School, Gif-sur-Yvette, France, CERN 85-19, p. 377, 1985.

[7] R.D. Ruth and J.M. Wang, "Vertical Fast Blow-Up in a Single Bunch", IEEE Trans. Nucl. Sci., Vol. NS-28, No. 3, June 1981.

[8] P. Kernel, R. Nagaoka, J.-L. Revol, G. Besnier, "High Current Single Bunch Transverse Instabilities at the ESRF: a New Approach", Proc. 7th European Particle Accelerator Conference, 26th-30th June 2000, Vienna, Austria.

[9] B. Zotter, "Transverse Mode-Coupling and Head-Tail Turbulence", CERN/ISR-TH/82-10, 1982.

[10] D. Brandt, J. Gareyte, "Fast Instability of Positron Bunches in the CERN SPS", CERN SPS/88-17 (AMS), 1988.

[11] K. Yokoya, "Cumulative Beam Breakup in Large-Scale Linacs", DESY 86-084, 1986.

[12] A.W. Chao, B. Richter and C.Y. Yao, "Beam Emittance Growth Caused by Transverse Deflecting Fields in a Linear Accelerator", Nucl. Instr. Meth., 1, **178**, (1980).

[13] E. Perevedentsev, "Head-Tail Instability Caused by Electron Cloud", these proceedings.

[14] E. Métral, "Stability Criterion for the Longitudinal Mode-Coupling Instability in the Presence of Both Space-Charge and Resonator Impedances", CERN/PS 2001-063 (AE), October 2001.

[15] D. Boussard, CERN Report LabII/RF/Int./75-2, 1975.

[16] E. Keil, W. Schnell, CERN Report ISR-TH-RF/69-48, 1969.

[17] R. Cappi, E. Métral, D. Möhl, "Control of Coherent Instabilities by Linear Coupling", Proc. HEACC'2001, 26-30 March 2001, Tsukuba, Japan.

ELECTRON CLOUD BUILD-UP AND INSTABILITY: COMPARISON BETWEEN OBSERVATIONS AND NUMERICAL SIMULATIONS FOR THE CERN PS

M. Giovannozzi, E. Métral, G. Métral, G. Rumolo, F. Zimmermann, CERN, Geneva, Switzerland

Abstract

Experimental observations on the electron cloud have been collected at the CERN PS machine throughout the last two years. At the same time, an intense campaign of simulations has been carried out to understand the observed electron cloud build-up and the related instability. The results of the numerical simulations are presented in this paper and discussed in detail.

1 INTRODUCTION

Gas ionization and electron multiplication due to the secondary emission process on the inner side of the beam pipe may induce the build-up of an electron cloud, which can significantly degrade the performance of rings operating with closely spaced proton or positron bunches. The undesired electron cloud causes pressure rise and beam instability when the parameters are pushed above certain thresholds [1].

In the case of the CERN PS machine, the electron cloud has been observed since the year 2000 for LHC-type bunch trains (72 bunches of 1.1×10^{11} p/b spaced by 25 ns). The baseline drift produced by the electron signal at the pick-up electrodes has given evidence of the presence of electrons in large amount inside the beam chamber [2]. To see the degrading effects of the electron cloud on the machine performance, measurements have been carried out with the LHC beam stored in the PS at high-energy for a longer time (see Ref. [3] for more details on the beam manipulations applied). More data have been recorded concerning not only the build up process but also the induced instability [3]. The main experimental observations on the electron cloud driven instabilities in the PS can be summarised as follows. The instability manifests itself as a single-bunch phenomenon which sets in above an intensity threshold of about $4-5 \times 10^{10}$ p/b and is especially evident in the horizontal plane. Its rise-time τ is about $3-4$ ms and it causes a transverse emittance growth which can be as large as a factor 10 or 20 in the horizontal plane and 2 in the vertical plane.

The two codes developed at CERN, ECLOUD and HEADTAIL (see [4] for details), can simulate both the build-up process of the electron cloud and its expected effect on the single bunch that passes through it [1, 5, 6, 7]. This paper reports on the results of numerical simulations carried out with these two codes.

Section 2 gives a short description of the PS lattice and its main magnets. Section 3 is devoted to results of build-up simulations for both dipole and field-free regions of CERN PS, considering different bunch intensities and lengths. Using the saturation value of the cloud density as obtained in Section 3, a full instability study via computer simulations is presented in Section 4. Emphasis is put on the expected dependency of the unstable evolution on key parameters like bunch intensity, chromaticity and bunch length. Simulations for field-free regions are compared with those for a combined function magnet. Finally, conclusions are drawn in Section 5.

2 PS LATTICE AND MAIN MAGNETS

The PS lattice consists of ten super-periods each made of ten combined function magnets 4.26 m long, interlaced with eight 1.0 m and two 2.4 m drift spaces [8]. Every magnet is composed of two half-units with gradients of opposite sign, separated by a central junction. Each half-unit is made of five blocks with small gaps in between. Additional field adjustment can be made using the three currents of the pole-face winding and figure-of-eight-loop devices located on the magnet poles. These additional current loops allow controlling the machine tunes and chromaticities. The outline of the PS magnet unit in the extraction region is shown in Fig. 1.

The latest PS magnetic field measurements using Hall probes were undertaken in 1992 [9] for different operational settings of the currents in the main coil, pole-face and figure-of-eight-loop windings. The measurements have been carried out in the median plane of the laboratory test PS magnet unit U17 composed of an open half-unit followed by a closed half-unit. The resulting vertical field component data, including measurements of the central field, the end and lateral stray fields, and the field in the junction between the two half-units, produced a discrete 2D field map [9].

The measurements were carried out in a Cartesian coordinate frame. The longitudinal z-axis coincides with the magnet axis and its orientation is given by the direction of motion of the protons (see Fig. 1). The radial x-axis coincides with the mechanical symmetry axis and it points towards the exterior of the PS ring (see Fig. 1). In this reference system a regular mesh is defined and for each point in the mesh, the value of B_y has been measured in the median plane. The step size is 20 mm along the longitudinal z-axis and 10 mm along the radial x-axis. The mesh extends from -2.55 m to 2.73 m and from -70 mm to 310 mm in the

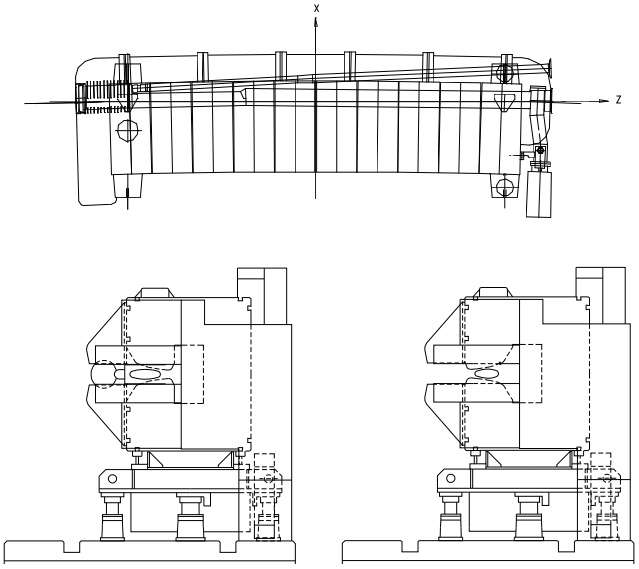

Figure 1: PS magnet unit 16. This unit is located just downstream of the extraction septum. The overall layout is shown in the upper part. The vacuum pipes for the circulating beam as well as that for the extracted one are visible. The two cross sections of the entry face (with open gap) and exit face (with closed gap) of the magnet are also shown on the left and right respectively.

longitudinal and radial directions respectively. The fitted 2D field map for the 26 GeV/c working point is shown in Fig. 2 (see Ref. [10] for more details).

This field can, in first approximation, be modelled as

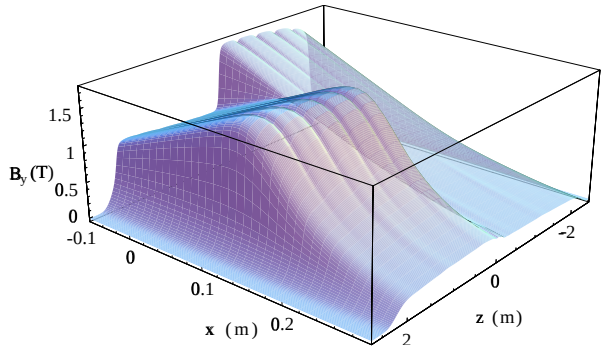

Figure 2: Polynomial field map obtained by fit of the measured field values $B_y = B_y(x, z, 0)$ for the 26 GeV/c working point. Here x stands for the transverse co-ordinate, while z is the longitudinal one.

$$\begin{aligned} B_x &= \pm G y \\ B_y &= B_{y0} \mp G x \end{aligned} \qquad (1)$$

with values for B_{y0} and G given in Table 1.

3 ELECTRON CLOUD BUILD-UP IN CERN PS

The simulation algorithm used in the ECLOUD code has already been discussed in great detail in previous papers (for instance, see [5] for the most up-to-date description). By simulating residual gas ionization and secondary emission at the chamber walls, including elastic reflection of low-energetic electrons, the code can predict whether a high density electron cloud is expected to form during the passage of a closely spaced bunch train. To simulate the PS straight sections and dipole chambers, parameters from Table 1[1] have been used. In the build-up simulations, the gradient component has been neglected as this is not expected to affect the build-up process significantly. This point has to be confirmed by additional numerical simulations.

Table 1: PS parameters used in the simulations. As far as the beam emittance is concerned, the rms physical value is quoted here.

Circumference	628 m
Relativistic γ	27.7
Number of bunches	72
Bunch spacing ($T_{\rm sep}$)	25 ns
Bunch population (N_b)	$3 - 11 \times 10^{10}$ protons
Trans. rms-sizes ($\sigma_{x,y}$)	$1.2 - 2.4/1.2$mm
Chamber half-aperture (x)	70 mm
Chamber half-aperture (y)	35 mm
Maximum SEY ($\delta_{\max}$)	1.9
$E_{\max}$	300 eV
Tunes ($Q_{x,y,s}$)	$6.25/6.25/0.0015$
Bunch rms-length (σ_z)	$0.3 - 1.2$ m
Aver. beta functions ($\beta_{x,y}$)	16 m
Rms-energy spread	$1.75 - 7 \times 10^{-4}$
Mom. compaction (α)	0.027
Chromaticities ($\xi_{x,y}$)	up to 0.5 in both planes
Dipole field (B_{y0})	1.256 T
Field gradient (G)	5.2 T/m
T_{rev}	2.2 μs

Figure 3 depicts the evolution of the electron line densities in a PS dipole chamber without (upper) and with (lower) inclusion of the elastically back-scattered electrons. Various bunch lengths are considered, representing different snap-shots during bunch compression prior to beam extraction (the bunches in the PS are compressed by a factor 4, from 16 ns to 4 ns within 100 turns). The simulation demonstrates that the electron line density grows faster the shorter the bunch, and that there is no electron cloud build-up for the initial bunch length of $4\sigma_z/\mathrm{c} = 16$ ns.

Comparing Fig. 3 (upper) and (lower), we further notice that with the elastically back-scattered electrons included,

[1] The horizontal emittance is in reality constant, but the horizontal rms-size is swept through the given range in order to account for dispersion and the different energy spreads.

the simulated equilibrium electron line densities are a factor $3-4$ higher than without. Perhaps more surprisingly, the central density is highest for intermediate bunch lengths (not shown, but see Ref. [2]), and not for the shortest. This indicates that electrons, once generated, can be more easily trapped by the potential produced by longer bunches.

Furthermore, the build-up has been simulated at different currents, to identify a possible intensity threshold. Figure 4 shows the averaged cloud density evolution corresponding to different bunch intensities from 3×10^{10} to 1.1×10^{11} (for a 4 ns long bunch). While the cloud rise-time does not appear to be much affected by this parameter (after the passage of about 40 bunches, corresponding to 1 μs, the cloud has in all cases already reached saturation), the saturation value tends to decrease with increasing current (from 10^{12} m^{-3} for $N_b = 3 \times 10^{10}$ to about 5×10^{11} m^{-3} for $N_b = 1.1 \times 10^{11}$). It is worthwhile noting that these transverse averaged values correspond to much higher values of the central density, because the electron cloud is initiated by residual gas ionization and stays therefore mostly localised around the beam due to dipole field confinement. Because of the stripe-like distribution, the central densities can reach values between 2 and 20 times larger than the transverse averaged densities. The influence of this non-uniform distribution of the electron cloud in the pipe cross-section has not been taken into account in the instability simulation of next Section.

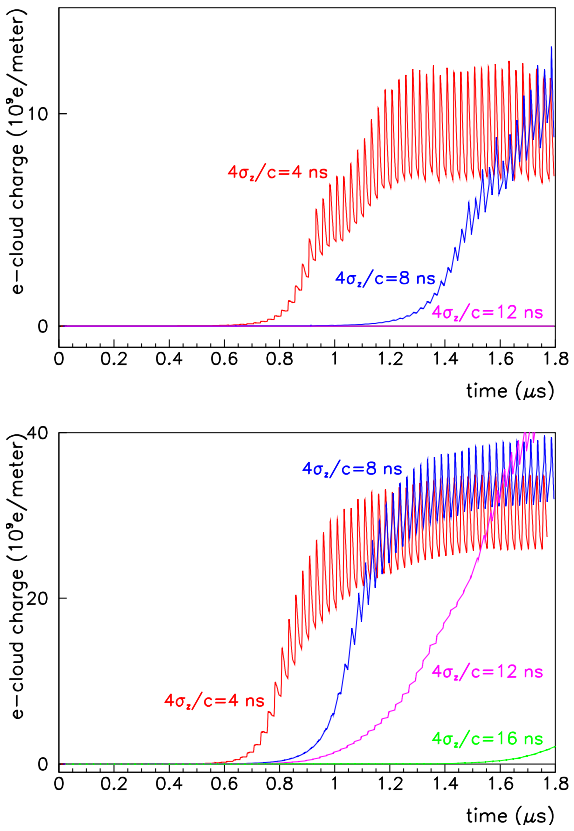

Figure 3: Electron cloud build-up in a PS dipole for different bunch lengths and without (upper) and with (lower) elastic reflection of the electrons.

The difference between the build-up in a field-free region and inside a strong dipole is shown in Fig. 5: the electron cloud builds up more rapidly in a dipole but saturates around a value which is about two thirds of that reached in a field-free region.

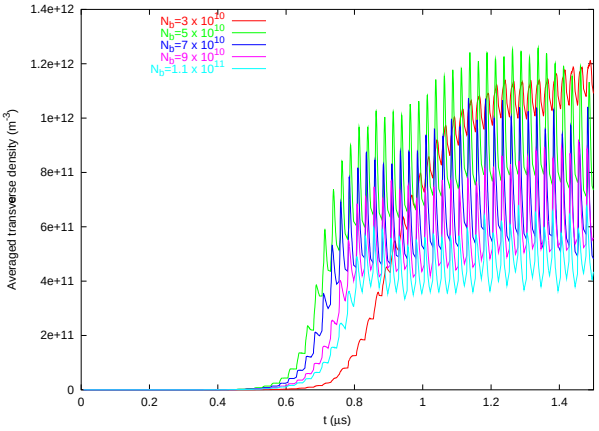

Figure 4: Electron cloud build-up in a PS dipole for different bunch intensities. The electron cloud reaches saturation after the passage of about 40 bunches.

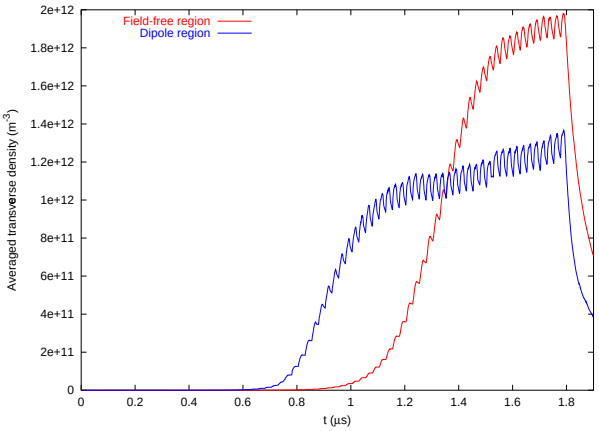

Figure 5: Electron cloud build-up inside a PS dipole and in a PS field-free region.

4 SIMULATION OF THE ELECTRON-CLOUD INDUCED SINGLE-BUNCH INSTABILITY IN CERN PS

The electron cloud driven single-bunch instability in the PS has been studied using the HEADTAIL code. As input for these simulations we have assumed an electron cloud density of about 2×10^{12} m^{-3}, consistent with the central density values given by the simulations described above. Instability simulations were originally performed in field-free regions to explore whether the parameters were in the

correct range to excite the electron cloud instability. The combined function magnetic field configuration was introduced only in a second stage.

Scans with different bunch intensities, chromaticities and bunch lengths have been made in order to isolate the dependence of the instability on each of these parameters. If not mentioned otherwise, the rms bunch length has been set to 2.5 ns (0.75 m), which is the value for which an instability at the PS was observed and monitored. The chromaticity is zero in both planes.

We first evaluate the expected oscillation frequency of

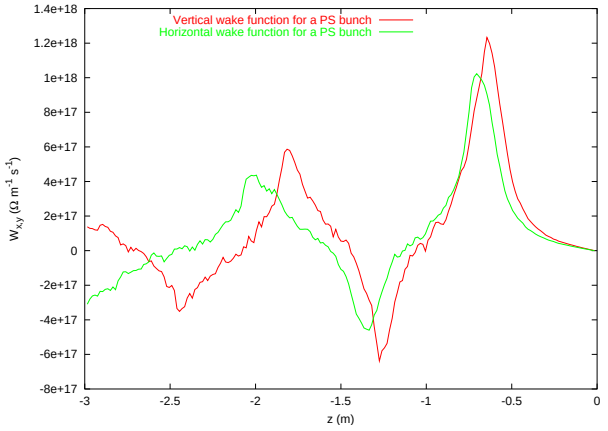

Figure 6: Horizontal and vertical wake functions due to electron cloud and bunch head displacement in a field-free region.

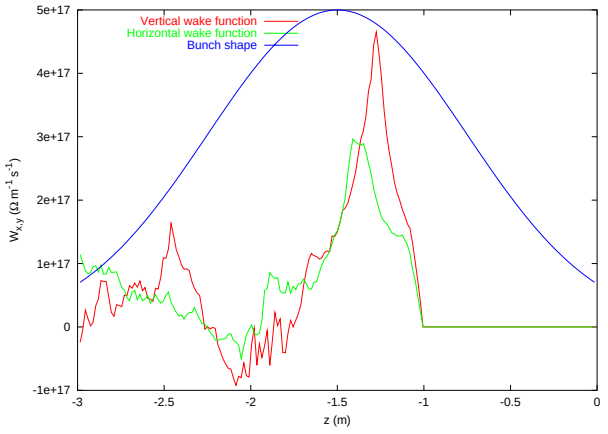

Figure 7: Horizontal and vertical wake functions due to electron cloud and a displacement located at $-4/3\ \sigma_z$ in a field-free region.

the electrons very close to the bunch transverse centre, and therefore the number of oscillations that they perform during one bunch passage. These values for a field-free region can be computed according to [11]:

$$\omega_{ex(y)} = \sqrt{\frac{N_b r_e c^2}{2\sigma_{x(y)}\sigma_z(\sigma_x+\sigma_y)}} \qquad (2)$$

$$n_{x(y)} = \frac{1}{\pi}\sqrt{\frac{2N_b\sigma_z r_e}{\sigma_{x(y)}(\sigma_x+\sigma_y)}}\ . \qquad (3)$$

Equations (2) and (3) yield $\omega_{ex} = 2\pi \times 195$ MHz and $\omega_{ey} = 2\pi \times 225$ MHz, $n_x = 1.95$ and $n_y = 2.26$ for a PS bunch of $N_b = 4 \times 10^{10}$ p/b. Figure 6 shows horizontal and vertical wake functions computed from the transverse field on the beam axis by displacing the bunch head (longitudinally located at $z = 0$; the bunch centre is at $-2\sigma_z$). The shape of the wake functions considerably changes if the displacement occurs at a different location along the bunch profile [5]: in Fig. 7 the wake functions are plotted for an offset located at $-4/3\ \sigma_z$ (i.e., after one third of the full bunch has already gone through the cloud). The period with which the wake functions oscillate corresponds to the period of oscillation of the electrons in the linear range of the beam force.

Figure 8 shows the horizontal (upper) and vertical (lower) emittance growth due to electron cloud over 3000 turns for different bunch intensities. The rise-time of the instability is always on the order of a few milliseconds, spanning between 1.5 ms for the highest intensity ($N_b = 10^{11}$ p/b) and about 5 ms for the lowest ($N_b = 3 \times 10^{10}$ p/b). It is worthwhile pointing out that in this paper the rise-time is defined in terms of emittance

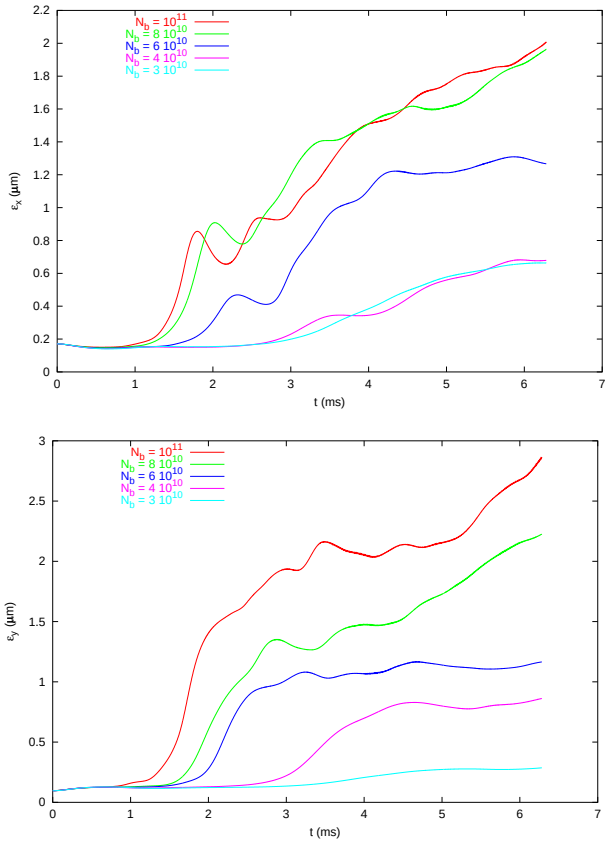

Figure 8: Horizontal (upper) and vertical (lower) emittance growth over 3000 turns for different bunch intensities.

growth and not in terms of beam-size increase. The instability appears equally in both planes. Nevertheless, a threshold for the onset at about $N_b = 3 \times 10^{10}$ p/b is more pronounced in the vertical plane.

Figure 9 shows the expected emittance growth for a

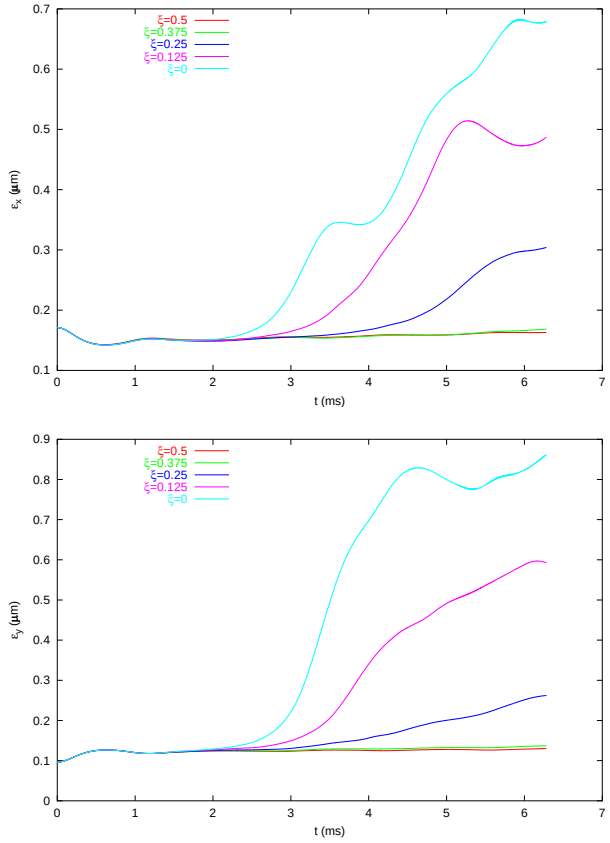

Figure 9: Horizontal (upper) and vertical (lower) emittance growth over 3000 turns for different chromaticities and $N_b = 4 \times 10^{10}$ p/b. This current value is slightly above the instability threshold.

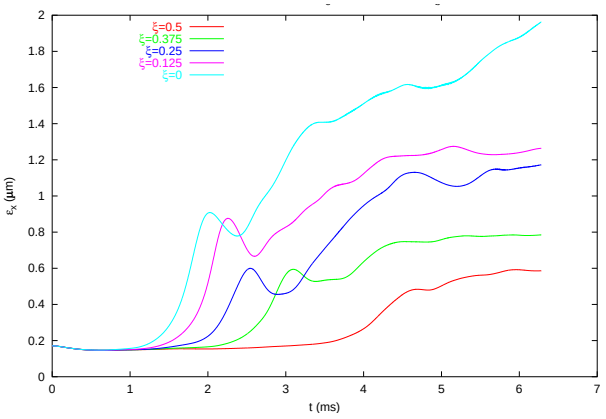

Figure 10: Vertical emittance growth over 3000 turns for different chromaticities and $N_b = 8 \times 10^{10}$ p/b. This current value is far inside the instability region.

bunch with $N_b = 4 \times 10^{10}$ p/b and for different values of (positive) chromaticity. From the pictures it appears clearly that a positive chromaticity larger than 0.3 in $\xi = Q'/Q$ can efficiently cure the degrading effect of the electron cloud. In both planes the instability growth time decreases for values of ξ up to 0.25, and finally the bunch becomes stable for higher values. At higher current ($N_b = 8 \times 10^{10}$ p/b), chromaticity can still reduce the instability, but a significant emittance growth can be observed even when ξ approaches 0.5 (see for instance Fig. 10).

The effect of bunch length has been studied by using

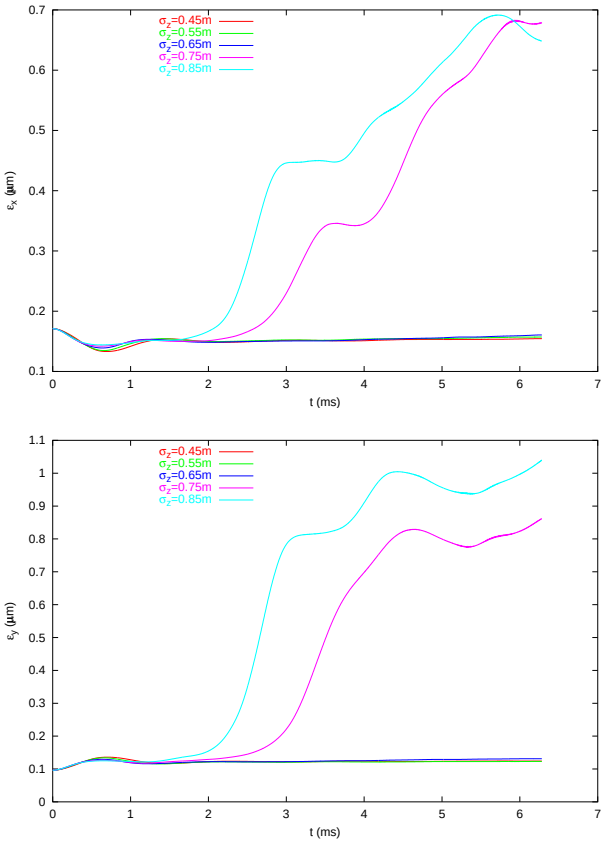

Figure 11: Horizontal (upper) and vertical (lower) emittance growth over 3000 turns for different bunch lengths and $N_b = 4 \times 10^{10}$ p/b. The bunch has been re-matched for each case by keeping the longitudinal emittance constant and changing the synchrotron tune.

two different approaches. The first one, which better reproduces what can be actually done on the machine, consists in re-matching the bunch longitudinally each time by keeping the longitudinal emittance constant, and therefore multiplying the synchrotron tune by the square of the ratio $\sigma_{z\mathrm{old}}/\sigma_{z\mathrm{new}}$. Following this re-matching procedure, we find that for low current, the bunch length $\sigma_{z\mathrm{old}} = 0.75$ m is right at the limit of the region where the instability sets in (see Fig. 11): shorter bunches are in fact stable. For higher current ($N_b = 8 \times 10^{10}$ p/b), the threshold is pushed a little lower, as shown for example in Fig. 12. As the synchrotron

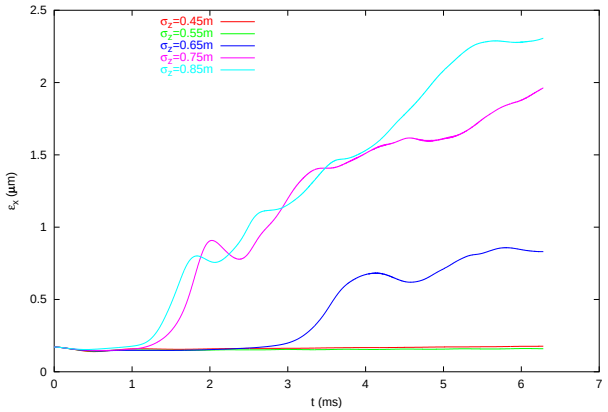

Figure 12: Vertical emittance growth over 3000 turns for different bunch lengths and $N_b = 8 \times 10^{10}$ p/b. The bunch has been re-matched for each case by keeping the longitudinal emittance constant and changing the synchrotron tune.

tune is a parameter that certainly plays a significant role in the unstable bunch dynamics, we have performed a second bunch length scan, in which in each case the re-matching was performed by scaling bunch length and momentum spread by the same factor and keeping the synchrotron tune constant. This does not correspond to what is done in the PS, but in the context of our study it is aimed at isolating the dependence of the instability on bunch length and energy spread. Again we find that shorter bunches tend to be more stable, as shown in Fig. 13, but less than in Fig. 11 and experiments done so far in PS. This indicates that a higher synchrotron tune also has a stabilising effect, as already predicted for the electron-cloud instability [12, 13] in general, and supported by a direct TMCI calculation [14]. All the above study has been done for a PS bunch going through an electron cloud in a field-free regions. Results show that this would not explain any asymmetric effect that could make the instability grow more quickly in the horizontal plane than in the vertical one [3]. As explained in Section 2, the PS ring is 90 % occupied by combined function magnets, and therefore the magnetic field should be taken into account when computing the electron motion. Looking at how the wake function shapes are changed because of this field in Fig. 14, we can observe that, contrary to the pure dipole, the combined function magnet causes a significant horizontal wake which is of lower frequency than the vertical one. The maximum amplitude of the wake strongly depends on the magnetic field gradient, as shown in Fig. 14 (upper to lower), where the wakes for three different gradient values are plotted. However, the results of numerical simulations seems to indicate that the presence of a horizontal wake alone cannot explain why a horizontal instability is observed in the PS machine [3]. Figure 15 shows the horizontal (upper) and vertical (lower) emittance growths for a single bunch interacting with an electron cloud inside a combined function magnet. The rise-time of the instability is shorter in the vertical plane, and the observed vertical emittance increase over 4000 turns is evidently much larger.

5 CONCLUSIONS

Simulations have been carried out with the ECLOUD and HEADTAIL codes to reproduce and interpret the electron cloud observations at the CERN PS. The results show that a train of bunches with the LHC nominal spacing is expected to produce an electron cloud in the PS chamber for bunch rms-lengths in the range $1 - 2$ ns. The equilibrium value reached by the cloud density at saturation is then a function of the single-bunch intensity, showing a higher value for lower currents in the range $3 - 10 \times 10^{10}$ p/b. Such an electron cloud, supposed to be uniformly distributed in the longitudinal direction all along the ring, is able to render the single bunch unstable on a time scale of few milliseconds. The simulation has shown that the instability threshold lies at around $2 - 3 \times 10^{10}$ p/b. For lower intensities no significant emittance growth is expected; for higher intensities the emittance increases by a factor as large as 20 with a rise-time that becomes shorter as the current is in-

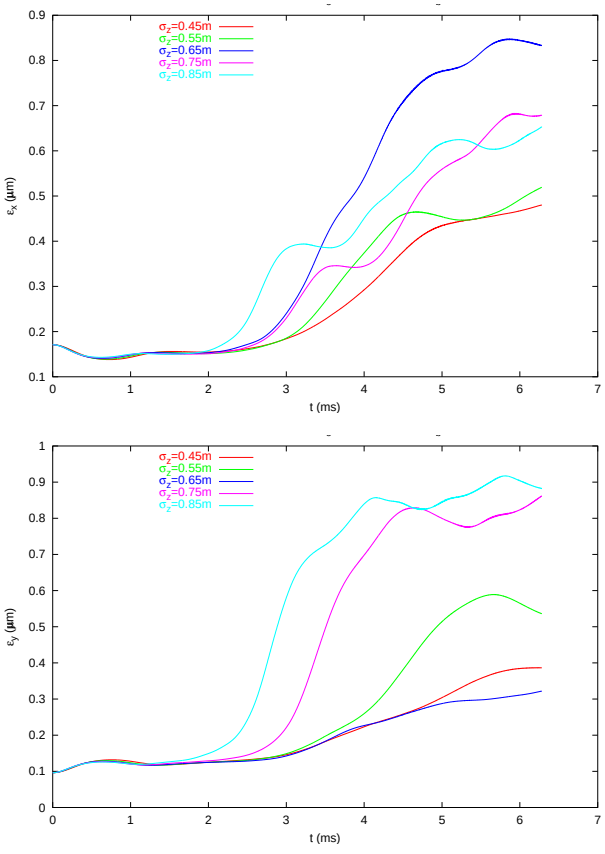

Figure 13: Horizontal (upper) and vertical (lower) emittance growth over 3000 turns for different bunch lengths and $N_b = 4 \times 10^{10}$ p/b. The bunch has been re-matched for each case by keeping the synchrotron tune constant and scaling bunch length and momentum spread by the same amount.

creased. Chromaticity seems to be an efficient cure against this kind of instability. Positive values of ξ above 0.3 can completely suppress the instability for moderate currents, whereas at higher currents even a chromaticity of $\xi = 0.5$ cannot efficiently damp it. Furthermore, it was found that shorter bunches and higher synchrotron tunes have a stabilising effect against the electron cloud. A bunch with 4 ns length is expected to remain stable even with a population of 10^{11} protons. This case cannot be studied in the PS machine, due to the non-adiabatic process used to achieve

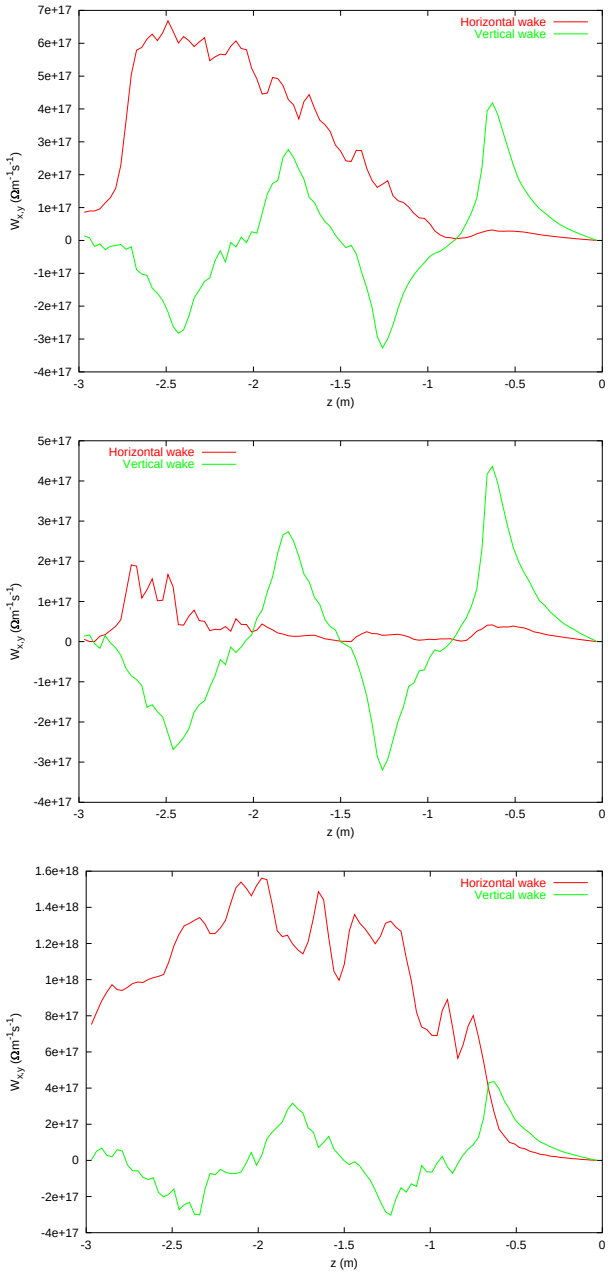

Figure 14: Horizontal and vertical wake functions due to an electron cloud inside a combined function magnet with $B_{y0} = 1.256$ T and $G = 5.2$ T/m (upper), $G = 0.52$ T/m (centre), and $G = 52$ T/m (lower).

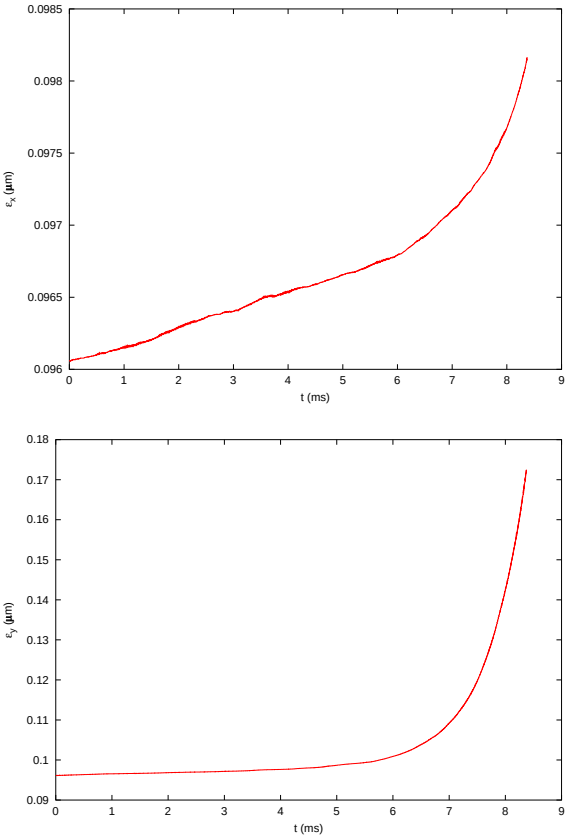

Figure 15: Horizontal (upper) and vertical (lower) emittance growth over 4000 turns for $N_b = 8 \times 10^{10}$ p/b, bunch length 0.75 m, small positive chromaticities ($\xi_{x,y} = 0.1$) and inside a combined function magnet.

the 4 ns long bunch length [3]. Instability simulations carried out in a field-free region show that the beam blow-up should occur symmetrically in the x and y planes, and in a pure dipole field it is expected only in the vertical plane [7]. A further step has been to introduce in the simulation the magnetic field from a combined function magnet acting on the electrons. Though a significant horizontal wake field is generated in this case, numerical simulations indicate that this alone still cannot explain the observation of a stronger instability in the horizontal plane. Work is presently underway and more measurements have been planned at the PS ring to achieve a better comprehension of this phenomenon.

6 ACKNOWLEDGEMENTS

The authors would like to thank R. Cappi, K. Ohmi, M. Martini, F. Ruggiero and D. Schulte for helpful discussion and information.

7 REFERENCES

[1] G. Rumolo, F. Ruggiero and F. Zimmermann, *Phys. Rev. ST Accel. Beams* **4**, (2001) 012801.

[2] R. Cappi, M. Giovannozzi, E. Métral, G. Métral, F. Zimmer-

mann, in *2001 Particle Accelerator Conference*, edited by P.W. Lucas and S. Webber (IEEE Computer Society Press, Piscataway, 2001) p. 685.

[3] R. Cappi, M. Giovannozzi, E. Metral, G. Metral, G. Rumolo and F. Zimmermann, "Electron Cloud Build-up and Related Instability in the CERN PS", these proceedings.

[4] "Electron Cloud in the LHC" web page, http://wwwslap.cern.ch/collective/electron-cloud/

[5] G. Rumolo and F. Zimmermann, "Contributions of the SL-AP Group to the Two-stream Instabilities Workshop", *CERN SL (AP)* **2001-067** (2001).

[6] F. Zimmermann and G. Rumolo, "Electron Cloud Simulations: Build-up and Related Effects", these proceedings.

[7] G. Rumolo and F. Zimmermann, "Electron Cloud Simulations: Beam Instabilities and Wake Fields", these proceedings.

[8] T. Risselada, "Beam Optics Data for the PS Ring and its Transfer Lines", *CERN PS (PA) Note* **92-04** (1992).

[9] D. Cornuet, Z. Sharifullin, "Magnetic Measurements on the PS Magnet Unit U17 with Hall Probes", *CERN AT (MA) Note* **92-23** (1992).

[10] D. Manglunki, M. Martini, "Beam Optics Modeling at CPS Extraction Throughout a non-linear Fringe field", *CERN PS (CA)* **97-018** (1997).

[11] G. Rumolo and F. Zimmermann, in *LHC Workshop - Chamonix XI*, edited by J. Poole (CERN SL 2001-003 (DI), Geneva, 2001) p. 166.

[12] K. Ohmi and F. Zimmermann, *Phys. Rev. Lett.* **85**, (2001) 3821.

[13] K. Ohmi, F. Zimmermann and E. Perevedentsev, *Phys. Rev. E* **65**, (2002) 016502.

[14] E. Metral, "Effect of Bunch Length, Chromaticity, and Linear Coupling on the Transverse Mode-Coupling Instability due to the Electron Cloud", these proceedings.

Combined phenomena of beam-beam and beam-electron cloud effects in circular e^+e^- colliders

K. Ohmi, [2]A. W. Chao
KEK, Oho, Tsukuba, 305-0801, Japan
[2] *SLAC, Stanford, CA94309, USA*

Abstract

An electron cloud causes various effects in high intensity positron storage rings. Positron beam and electron cloud can be considered a typical two stream system with a plasma frequency. Beam-beam effect is also an important issue for high luminosity circular colliders. Colliding two beams are considered as a two-stream system with another plasma frequency. We study combined phenomena of the beam-electron cloud and beam-beam effects from a viewpoint of two complex "two stream effects" with two plasma frequencies.

1 INTRODUCTION

In recent high intensity positron rings, various phenomena related to electron cloud have been observed. Coupled bunch instabilities have been observed at KEK Photon Factory and IHEP-BEPC, and beam size enlargements have been observed at B factories of SLAC (PEP-II) and KEK (KEKB). These phenomena were understood as two-stream instability of relativistic beam and slow electron cloud. The phenomena can also be understood as instabilities which is caused by wake force due to electron cloud. The coupled bunch instability is the two-stream effect characterized by average plasma frequency along bunch train, or is mediated by long range wake force of the order of bunch spacing ($\sim$1m). The beam size enlargement is the two-stream effect characterized by plasma frequency in a bunch, or mediated by short range wake force of the order of bunch length ($\sim$1cm). The positron beam, which is perturbed by the electron cloud, interacts with an electron beam in a collider. The colliding beams are regarded as a two-stream system with a plasma frequency characterized by the beam-beam force. The beam-beam interaction has a nature of a short range wake force, namely, a distortion of head part of a beam, which induces a perturbation of another beam, affects the tail part of itself. The short range wake force due to electron cloud and the beam-beam force may couple each other and cause a kind of combined phenomena.

Such combined phenomana may have been observed in KEKB. The transverse size of positron beam is enlarged beyond a threshold current due to the short range wake force at an operation with only positron beam. Luminosity is extremely low for bunch spacing narrower than 6ns even below the threshold current of the beam enlargement [1].

We study combined phenomena of the two types of "two stream system". We first discuss this instability using linearized one-two-particle model, in which e^- and e^+ beams are represented by one and two-particles, respectively. The beam-beam force is linearized in the model. The wake force due to electron cloud is approximated to be a constant along the longitudinal direction. Similar system has been studied in Refs. [2] for ordinary wake force. The combined effects based on the weak-strong beam-beam model have been discussed in Ref.[3].

We next discuss the phenomena using a tracking simulation in which each of the two beam is represented by a large number ($\sim$1,000) of macro-particles (or slices) distributed in the longitudinal phase space[4]. Each macro-particle has a transverse beam size determined by the emittance and the beta function, and nonlinearity for their interaction are taken into account. Electron cloud is represented by many ($\sim$10,000) point-like macro-particles. The beam-electron cloud interaction is evaluated by interaction between transverse Gaussian beam and each macro-electron[4].

2 TWO-STREAM FEATURES OF BEAM-ELECTRON CLOUD AND BEAM-BEAM SYSTEMS

We discuss linear theory of the combined system of beam-beam and wake field. Similar system has been already studied by E. A. Perevedentev and A. A. Valishev [2]. We study the system using an alternative point of view: *i.e.*, combined effect of beam-beam and beam-electron cloud. We start discussions of beam-electron cloud interaction. The beam-electron cloud system is a typical model of the two-stream instability. The beam slices and the cloud electrons obey the equation of motion as follows,

$$\frac{d^2\boldsymbol{x}_{e,a}}{dt^2} = -2\lambda_+(s_+)r_e c\boldsymbol{F}_G(\boldsymbol{x}_{e,a}-\bar{\boldsymbol{x}}_{+,j};\boldsymbol{\sigma})\delta(t-t_j(s_e)), \tag{1}$$

$$\frac{d^2\boldsymbol{x}_{+,j}}{ds^2}+\left(\frac{\omega_\beta}{c}\right)^2 = -\frac{2r_e}{\gamma}\sum_{a=1}^{N_e}\boldsymbol{F}_G(\bar{\boldsymbol{x}}_{+,j}-\boldsymbol{x}_{e,a};\boldsymbol{\sigma})\delta(s-s_e). \tag{2}$$

where the force $\boldsymbol{F}_G(\boldsymbol{x})$ is expressed by the Bassetti-Erskine formula normalized so that $\boldsymbol{F}_G \rightarrow \boldsymbol{x}/|\boldsymbol{x}|^2$ as $\boldsymbol{x}\rightarrow\infty$.

Electrons oscillate with an angular frequency due to the linear part of $\boldsymbol{F}_G$,

$$\omega_{e,y(x)} = \sqrt{\frac{\lambda_+ r_e}{(\sigma_{+,x}+\sigma_{+,y})\sigma_{+,y(x)}}}, \tag{3}$$

where λ_+ and $\sigma_{+,x(y)}$ are line density and horizontal (vertical) size, respectively, of the positron beam. $\omega_{e,y}$ and $\omega_{e,x}$ are about $1.9 \times 10^{11} s^{-1}$ and $7.2 \times 10^{10} s^{-1}$, respectively, with the KEKB parameters: *i.e.*, $\sigma_x = 420 \mu m$, $\sigma_y = 60 \mu m$, $\sigma_z = 5mm$ and $N_+ = 3.3 \times 10^{10} m^{-1}$. ω_e is considered as plasma frequency for the two-stream system of the beam-electron cloud. The phase advance of the electron motion during the interaction, $\phi_e = \omega_e \sigma_z / c$, characterizes the instablity. For KEKB, $\phi_{e,y} = \omega_{e,y} \sigma_z / c \approx 2.5$ and $\phi_{e,x} = \omega_{e,x} \sigma_z / c \approx 1.0$.

The beam-beam system also has a potential to cause a two-stream instability, because one beam oscillates in electro-magnetic field produced by the other beam with a certain frequency. The beam-beam force is expressed in linear regime as follows,

$$\frac{d^2 \boldsymbol{x}_{\pm,j}}{ds^2} + \left(\frac{\omega_\beta}{c}\right)^2 = -\frac{2r_e}{\gamma} \sum_{a=1}^{N_\mp} \boldsymbol{F}_G(\bar{\boldsymbol{x}}_{\pm,j} - \boldsymbol{x}_{\mp,a}; \boldsymbol{\Sigma}) \delta(s - s_\mp). \tag{4}$$

where $\Sigma_{x(y)} = \sqrt{\sigma^2_{+,x(y)} + \sigma^2_{-,x(y)}}$. Each of the beam slices is assumed to be rigid Gaussian with rms beam size $\sigma_{\pm,x(y)}$.

There is a coherent frequency during the interaction between the two beams given as follows,

$$\omega_{\pm,y(x)} = \sqrt{\frac{\lambda_\mp r_e}{\gamma_\pm (\sigma^*_{\mp,x} + \sigma^*_{\mp,y}) \sigma^*_{\mp,y(x)}}} \tag{5}$$

where $\gamma_\pm$ is the relativistic factor of positron and/or electron beam. We note that $\sigma^*_{\pm,x(y)}$, the beam size of positron and/or electron beam at an interaction point, is much smaller than $\sigma_{x(y)}$ in Eq.(3), and $\gamma \gg 1$.

The phase advance, ϕ, of the oscillation during a collision is expressed by

$$\phi_{\pm,y(x)} = \frac{\omega_{\pm,y(x)} \sigma_z}{c} = \sqrt{\frac{2\pi \xi_{y(x)} \sigma_z}{\beta_{y(x)}}} \equiv \sqrt{D_{y(x)}}, \tag{6}$$

where ξ_y is the beam-beam parameter and we have assumed that two beams have the same beam size. We call $D \equiv \phi^2_\pm$ the beam-beam disruption parameter. ϕ_y is approximately the order of unity for recent high luminosity colliders. The two-stream effect may be important under this condition. $\phi_x = \sqrt{\xi_x \beta_y / \xi_y \beta_x} \phi_y$ is smaller than ϕ_y, but the horizontal effect may be important depending on the tune as will be shown later.

3 ONE-TWO-PARTICLE MODEL

We first study the phenomena using a small number of macro-particles; i.e. one-two-particle model. The electron and positron beams are represented by one and two macro-particles, respectively, in the model. The model is reliable approximation for considering the beam-beam interaction, since the phase advance, $\phi_\pm$, is less than 1 in most cases. Furthermore the beam-electron cloud interaction is approximated to be described by a constant wake force. Although ϕ_e is larger than 1, and therefore the model is beeing stretched, we believe that the analysis remains reasonable. An analytic treatment becomes possible by the approximation.

We discuss vertical motion below. Motion of the two beams is characterized by a vector $\boldsymbol{Y}(s)$.

$$\boldsymbol{Y}(s) = (y^+_1, p^+_1, y^+_2, p^+_2, y^-, p^-)^t, \tag{7}$$

where the suffix t denotes the transpose of the matrix or vector. We consider a revolution matrix to transfer $\boldsymbol{Y}(s^* + C)$ from $\boldsymbol{Y}(s^*)$, where s^* and C are position of interaction point and circumference of a ring, respectively. The beam size (beta function) is temporarily assumed to be a constant during the collision. The synchrotron tune is assumed to be inverse of an integer ($\nu_s = 1/n_s$). We try to study for general synchrotron tune later. In particular, the tracking simulation discussed later is not limited to particular values of the synchrotron tune. The beam-beam force does not have a longitudinal component, since beta function is assumed to be constant. The two particles in the positron beam have an opposite synchrotron phase. The macro-electron always stays at the center of mass. The collision points of the two macro-positrons and the macro-electron are given by $s^* + \Delta$, where

$$\Delta = \pm \frac{\sigma_z}{2} \sin(2\pi \nu_s s / C). \tag{8}$$

The collision of i-th positron and the electron is represented by a matrix $B_i(\xi)$

$$B_1(\xi) = \begin{pmatrix} I + b(2\xi) & 0 & -b(2\xi) \\ 0 & I & 0 \\ -b(\xi) & 0 & I + b(\xi) \end{pmatrix}. \tag{9}$$

$$B_2(\xi) = \begin{pmatrix} I & 0 & 0 \\ 0 & I + b(2\xi) & -b(2\xi) \\ 0 & -b(\xi) & I + b(\xi) \end{pmatrix}. \tag{10}$$

where

$$b(\xi) = \begin{pmatrix} 0 & 0 \\ -\pi\xi & 0 \end{pmatrix}, \tag{11}$$

and I is 2×2 unit matrix.

Transfer matrix of collision at $s = \Delta$ is expressed by $B(\Delta) = D^{-1}(\Delta) B D(\Delta)$: that is, particles drift to $s = \pm\Delta$, collide and return to the interaction point. The matrix $D(\Delta)$ is expressed by

$$D(\Delta) = \begin{pmatrix} d(\Delta) & 0 & 0 \\ 0 & d(\Delta) & 0 \\ 0 & 0 & d(-\Delta) \end{pmatrix}, \tag{12}$$

where

$$d(\Delta) = \begin{pmatrix} 1 & \Delta \\ 0 & 0 \end{pmatrix}. \tag{13}$$

The transfer matrix of the collision is expressed by

$$\boldsymbol{Y}_{after}(s^*) = T_{BB}(\Delta) \boldsymbol{Y}_{before}(s^*), \tag{14}$$

where T_{BB} has two ways of representations depending on the sign of Δ: *i.e.*, which particle is at the bunch head or tail. When the first particle stays at the head of the bunch ($\Delta > 0$) in a half synchrotron period, the matrix is expressed by

$$T_{BB}(\Delta) = D^{-1}(-\Delta)B_2 D(-\Delta)D(\Delta)^{-1}B_1 D(\Delta) \tag{15}$$

In the other half synchrotron period ($\Delta < 0$), it is expressed by

$$T_{BB}(\Delta) = D^{-1}(\Delta)B_1 D(\Delta)D^{-1}(-\Delta)B_2 D(-\Delta). \tag{16}$$

The particles are transferred along arc section after the collision ($s = s^*$) to the collision point ($s = s^* + C$). The wake field affects the tail particle depending on betaton amplitude of the head particle. The transfer matrix from s^* to $s^* + C$ has two representations depending on the sign of Δ again. The matrix (T_{arc}) for $\Delta > 0$ is expressed by

$$T_{arc} = \begin{pmatrix} T_2(\mu_1) & 0 & 0 \\ A(W,\mu_1) & T_2(\mu_2) & 0 \\ 0 & 0 & T_2(\mu_e) \end{pmatrix}, \tag{17}$$

For $\Delta < 0$,

$$T_{arc} = \begin{pmatrix} T_2(\mu_1) & A(W,\mu_2) & 0 \\ 0 & T_2(\mu_2) & 0 \\ 0 & 0 & T_2(\mu_e) \end{pmatrix}, \tag{18}$$

where

$$T_2(\mu) = \begin{pmatrix} \cos\mu & \sin\mu \\ -\sin\mu & \cos\mu \end{pmatrix}. \tag{19}$$

$\mu_i = 2\pi\nu_i$ is betatron phase advance including chromatic modulation.

$$\mu_1 = \mu_p + \mu_s\chi\sin\frac{\omega_s}{c}s, \quad \mu_2 = \mu_p - \mu_s\chi\sin\frac{\omega_s}{c}s, \tag{20}$$

where

$$\chi = \frac{2\pi Q'}{\alpha L} = \frac{Q'\sigma_\delta}{\nu_s}. \tag{21}$$

$A(W,\mu)$, which describes the kick caused by the wake field is expressed by

$$A(W,\mu) = \begin{pmatrix} (W/2)\sin\mu & -(W/2)\cos\mu \\ (W/2)\cos\mu & (W/2)\sin\mu \end{pmatrix}. \tag{22}$$

The revolution matrix including the transfer of the arc section and the beam-beam interaction is expressed by

$$T_{rev}(\Delta) = T_{BB}(\Delta)T_{arc}(W,\mu), \tag{23}$$

where Δ is given by Eq.(8).

We calculate the transfer matrix for one synchrotron period ($\nu_s = 1/n_s$),

$$T_{syn} = \prod_{i=1}^{n_s} T_{rev}(\Delta_i). \tag{24}$$

The stability of the system can be discussed by eigenvalues of the 6×6 matrix (T_{syn}). The matrix is not symplectic, but its determinant is unity, because of $A(W)$. The eigenvalues are calculated numerically. When an imaginary part of the eigenvalues is nonzero, the system becomes unstable.

We first discuss vertical motion. Figure 1 shows the imaginary part of the eigenvalues as functions of betatron tune. For $W = 0$, nonzero values of imaginary part occurs only near the half integer tune as is shown in the upper picture. For $W > 0$, nonzero imaginary part occurs for all tunes: *i.e.*, the system always unstable regardless of the tune.

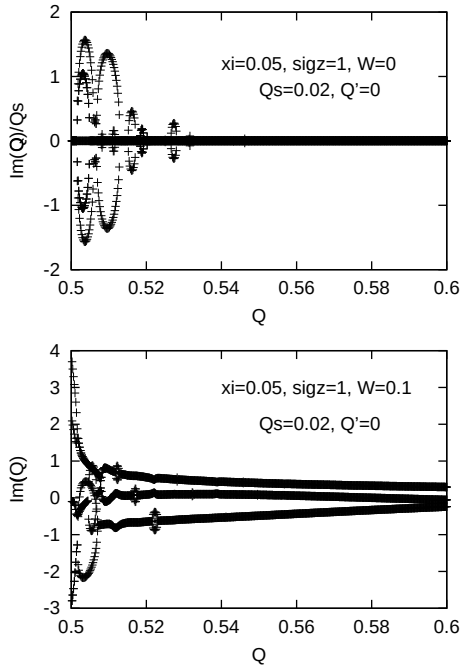

Figure 1: Variation of imaginary part of the eigenvalues depending on the betatron tune. Beam-beam parameter is chosen to be 0.05. Upper and lower pictures are for W=0 and W=0.1, respectively.

Figure 2 shows the imaginary parts as functions of the strength of the wake field and beam-beam parameter. The behavior for the wake strength is simple but that for the beam-beam parameter is complex. The beam-beam kicks depend on the longitudinal coordinate. The complex beam-beam behavior may be similar to the behavior of chromaticity for head-tail effect. Figure 3 shows the chromaticity dependence of the imaginary part of the eigenvalues.

We now discuss horizontal effect. The phase advance of beam-beam disruption is less than vertical one, because $\phi_x \approx \sqrt{\beta_y/\beta_x}\phi_y$ in ordinary colliders ($\xi_x \approx \xi_y$), while $\beta_y \ll \beta_x$. However we use an operating point slightly above a half integer horizontal tune in KEKB to get a benefit from dynamical beta effect. Horizontal effect may be therefore important though ϕ_x is small. Figure 4 shows the imaginary part of the eigenvalus of the horizontal matrix.

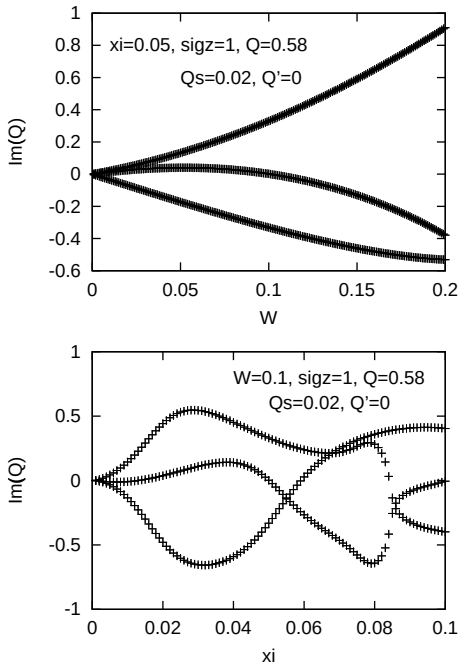

Figure 2: Dependence on the wake strength at $\xi = 0.05$ (upper) and the beam-beam parameter at W=0.1 (lower).

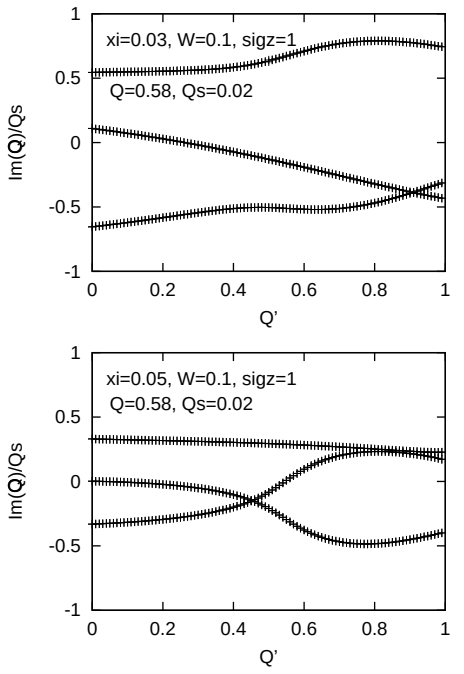

Figure 3: Chromaticity dependence. $\xi = 0.03$ (upper), $\xi = 0.05$ (lower).

We have imaginary part for $W > 0$. This means that horizontal effect should be taken care of.

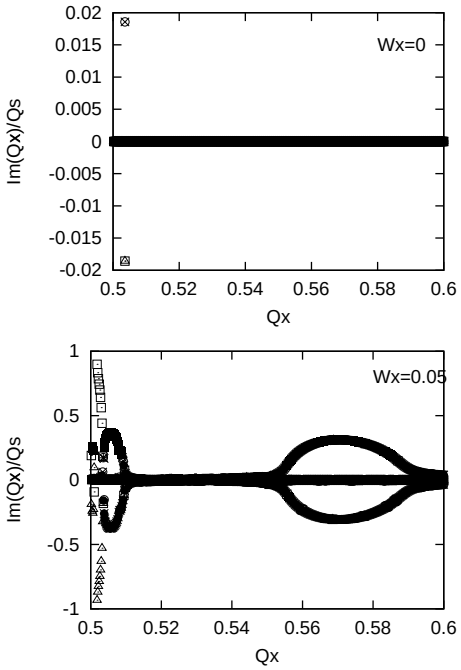

Figure 4: Dependence on horizontal tune. W=0 (upper), W=0.05 (lower). Note that the $W = 0$ case has an expanded vertical scale.

We assumed that the synchrotron tune was inverse of an integer. We extended the model to general synchrotron tune to avoid unphysical resonance behavior [5] by using a trick. We write down the transfer matrix for one synchrotron period

$$T_{syn} = T_{rev} \left(\frac{\sigma_z}{2}\right)^{\frac{1}{2\nu_s}} T_{rev} \left(-\frac{\sigma_z}{2}\right)^{\frac{1}{2\nu_s}} \qquad (25)$$

where ν_s is not an inverse of integer. We calculate the eigen value problem mathematically: i.e., in the eigen system, a noninteger power of matrix can be estimated. The collision points are assumed to be $\pm\sigma_z/2$ so that the transfer matrix is expressed by $1/2\nu_s$ power of the revolution matrices. We got results which are qualitatively consistent with the previous model.

We tried two-two particle model in which both beams are represented by two macro-particles. In this model we assumed the same sychrotron tunes for both beams. Similar results were obtained as for the one-two particle model. Further extensions are done by particle tracking simulation.

4 PARTICLE TRACKING SIMULATION USING MULTI-PARTICLE MODEL

We now proceed to a more realistic model. The beam-beam force is strongly nonlinear and the synchrotron tune is not an inverse of integer. The two beams have different

beam-beam parameters and different synchrotron and betatron tunes. Electron cloud is actully a crowd of electrons. The characteristic phase angle ϕ_e is larger than unity, and electrons are pinched by the beam force. We perform a particle tracking simulation to study the beam stability under these general conditions.

We represent the beams as a series of macro-particles (500∼1,000) with a transverse Gaussian distribution of a fixed rms size [4]. For easy visualization, we use a multiple air-bag model for the longitudinal distribution, in which the micro-bunches are distributed on concentric circles in the longitudinal phase space, characterized by the position z and the relative momentum deviation $\Delta p/p$. The interaction starts from collision between the pair of micro-bunches of the two bunches with the largest value of $z_+ + z_-$, *i.e.*, the head of the two bunches, and then continues for other micro-particles pairs at progressively smaller $z_+ + z_-$ coordinates. The collision point of a pair is $s_\pm = \pm(z_+ - z_-)/2$ from viewpoints of positron and electron beams. The coordinate should be transferred into the collision point by a transformation $D(s_\pm)$ The macro-particles are transferred around the ring using a linear transport matrix and applying a chromaticity kick.

Electron cloud is represented by a large number of macro-electrons ($\sim\ 10,000$). The interaction between positron beam and electron cloud is evaluated by solving Eqs.(1) and (2) [4]. Electron cloud is put at a fixed position in the positron ring.

Figure 5 shows the variation of maximum vertical action $J_{y,max}$ of macro-particles with and without beam-beam interaction. The electron cloud density ($\rho_e = 2 \times 10^{11} m^{-3}$) used in the simulation is less than the threshold ($\rho_{e.th} = 5 \times 10^{11} m^{-3}$). We observe the fact that a remarkable difference with and without beam-beam interaction is due to combined effect of beam-beam and beam-electron cloud interactions. There was no growth for pure beam-beam interaction without electron cloud.

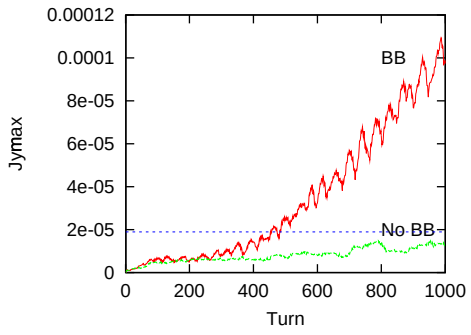

Figure 5: Combined effect of beam-beam and beam-electron cloud interactions. The two curves correspond to the variation of maximum $J_{y,max}$ of the macro-particles with and without beam-beam interaction.

Figure 6 shows the shape of the positron bunch projected onto the $y - z$ plane of the macro-particles positions after 400 and 800 turns. We can see a head-tail motion for the positron bunch experiencing both the beam-beam and the beam-electron cloud interaction.

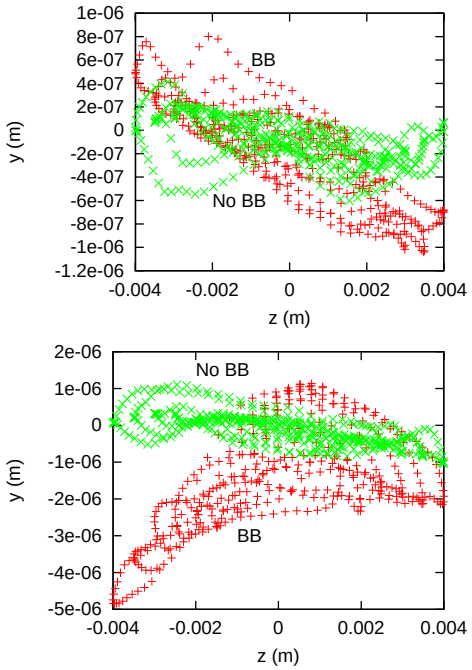

Figure 6: $y - z$ distribution of the positron bunch after 400 turns (upper) and 800 turns (lower). Different colors of the date points correspond to the bunch shapes with (red) and without (green) beam-beam interaction.

We next study effects of chromaticity and synchrotron tune spread. For a regular head-tail instability, it is well-known that chromaticity and synchrotron tune spread [6] affect its behavior. Figure 7 shows the dependence on chromaticity and synchrotron tune spread in our simulation. For the inclusion of tune spread effect, macro-particles are assumed to have a Gaussian distribution in the longitudinal phase space. These facts indicate that the chromaticity or synchrotron tune spread work to suppress the combined instability. However these effects are limited. For example, these parameters do not work well at a larger beam-beam parameter.

5 STRONG-STRONG BEAM-BEAM SIMULATION INCLUDING WAKE FIELD (PRELIMINARY)

The previous simulation is not sufficient for taking into account of nonlinearity of the beam-beam interaction, because betatron phase space location for a given syncrotron phase space location of a macro-particle is unique. Actually since there are many particles with various betatron coordinates in a region of synchrotron phase space, the beam-beam force may smear the betatron motion. To estimate the nonlinearity correctly, a strong-strong beam-beam

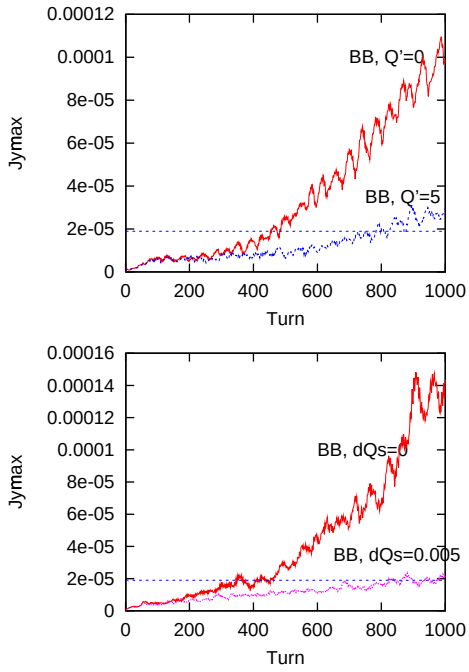

Figure 7: Dependence on chromaticity and synchrotron tune spread. Upper picture depicts evolution of J_y for $Q' = 5$ and $Q' = 0$, and lower picture depicts those for $\Delta\nu_s = 0$ and $\Delta\nu_s = 0.005$.

simulation, which treats interactions between many macro-particles, is required. Since it is complex to perform the strong-strong simulation for the both the beam-beam and beam-electron cloud effects, the beam-electron cloud interaction is approximated by an external wake field here [7]. We have already studied the beam-beam effect including wake field in two dimensional model [9], with the result that there was no remarkable effect. We now study three dimensional beam-beam system. Three dimensional beam-beam simulation is essential to study the present problem. However the three dimensional beam-beam simulation has a problem itself. The beam is divided into longitudinal slices, and slice by slice of collisions is calculated. To get a reliable result in the simulation, many longitudinal slices ($20 \sim 30$) were required depending on bunch length and beam-beam parameters. Since the calculation time scales quadratically with the number of slices, very long CPU time is required. We need to study how to integrate the three dimensional beam-beam interaction. Here a soft Gaussian approximation is used for simplification of the calculation.

A bunch is divided into N_{sl} slices which are denoted by $i = 1, N_{sl}$. We consider the collision between i-th positron slice and j-th electron slice. Beam envelope matrices for each slice are $R_{i+}(s^*)$ and $R_{j-}(s^*)$ at the design interaction point (s^*).

We propose a calculation algorithm. The algorithm has been used in weak-strong simulation [8]. We treat the collision of the two slices as collisions of positrons denoted by $a = 1, N_{i+}$ in i-th slice and j-th slice including N_{j-} electrons with an envelope R_{j-}. The role of positron bunch is exchanged for calculation of electron motion. The collision point of a-th positron and j-th electron slice is expressed by

$$s_{a+,j-} = \frac{z_{a+} - z_{j-}}{2}. \tag{26}$$

The a-th positron and j-th electron slice are transferred to the collision point $s_{a+,j-}$ according to

$$\begin{aligned} \boldsymbol{x}(s^* + s_{a+,j-}) &= D(s_{a+,j-})\boldsymbol{x}(s^*) \\ R_{j-}(s^* - s_{a+,j-}) &= D_l^{-1}(s_{a+,j-})R(s^*)D_l(s_{a+,j-}). \end{aligned} \tag{27}$$

D, which includes a dynamical variable z_{a+} of the a-th positron, is a nonlinear transformation. We take only linear part D_l for the transformation of R, while take nonlinear transformation D for $\boldsymbol{x}$. After the transformation, we calculate beam-beam interaction of the particle $\boldsymbol{x}_+$ for Gaussian beam represented by R_{j-}. We have to note that R_{j-} includes the dynamical variable z_{a+}.

This algorithm was essential to reduce the number of slices. Figure 8 shows the luminosity variation for new and old methods. The luminosity for the old method is extremely low. Increasing the number of slice for the old method, the luminosity is recovered near the level of the new method [11]. The slice number 5 is enough for the new method, while the old method requires 20-30 slices. The algorithm should be implemented in strong-strong beam-beam codes based on the Particle-In-Cell method [9, 10, 11, 12]. More details and study results will be presented elsewhere.

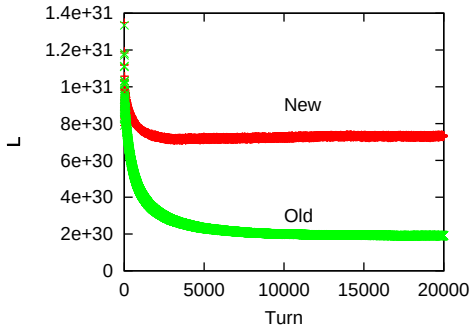

Figure 8: Luminosity variation for each turn. Bunches are divided into 5 slices. Luminosity calculated by the particle-slice algorithm is denoted by “New”, while that by slice-slice algorithm is by “Old”.

If all particles in the slices collide at a point,

$$s_{i+,j-} = \frac{z_{i+} - z_{j-}}{2}, \tag{28}$$

wrong results would be obtained yielding extremely low luminosity for a high current and long bunch length [11, 12].

We show very preliminary results of the 3-D soft Gaussian strong-strong beam-beam simulation including an external wake field.

Figure 9 shows the evolution of beam amplitudes, $\langle x_p \rangle$, $\langle y_p \rangle$, $\langle x_e \rangle$ and $\langle y_e \rangle$. We assume horizontal and vertical wake field, $W_x = 10^8 z[m^{-2}]$ and $W_y = 2 \times 10^8 z[m^{-2}]$. These strengths exceed a threshold of the vertical head-tail instability as is shown in the upper right picture. The vertical instability disappears when beam-beam interaction is included: beam-beam force suppresses the vertical head-tail instability. We found an enhancement of horizontal instability due to the beam-beam force as shown in the lower left picture. These results were unexpected from the linear theory and Gaussian simulation. We calculated the same model for sinusoidal wake fields $W_x = 2\times 10^6 \sin(213z)[m^{-2}]$ and $W_y = 1\times 10^7 \sin(570z)[m^{-2}]$ [7]. The results were similar to the Figure 9.

These behaviors are different from the linear theory and the Gaussian tracking simulation. We tried linear force for beam-beam interactions. We reduced the vertical wake field $W_y = 1.5\times 10^8 z[m^{-2}]$. There was no head-tail instability in both planes without beam-beam interaction. Figure 10 shows the evolution of beam amplitudes (upper two pictures), $y - z$ correlation (lower left) and vertical beam size (lower right). We found enhancement of the vertical instability due to the beam-beam interaction, but no effect for horizontal instability. These results are consistent with the linear theory and Gaussian simulation qualitatively.

These results should be studied further.

6 CONCLUSION

We studied combined phenomena of the beam-beam and beam-electron cloud effects using linear theory and a simulation with Gaussian approximation. In the linear theory, one-two particle model was used to describe the electron and positron beams. The electron cloud effect was approximated by a constant wake field. The beam-beam system without electron cloud effect was unstable at particular tune regions related to a synchro-beta resonance. while the combined system was always unstable regardless of the tune. The simulation with Gaussian approximation was performed to study the phenomena in general conditions. Below both thresholds of beam-beam and beam-cloud instabilities, an instability occurred due to thier combined effect in the simulation. We studied effects for the chromaticity and synchrotron tune spread. The combined phenomena may be analogous in its charercteristics to the regular head-tail effect.

We studied the phenomena using strong-strong beam-beam simulation. The results are preliminary, and should be studied further.

7 ACKNOWLEDGMENTS

This work is based on a collaboration of the authors at SLAC in the summer 2001. The authors thank E. Perevedentsev and A. Valishev for fruitful discussions. One of authors (K.O) thanks R. Ruth and Y. Cai for giving the chance of their collaboration. The author thanks F. Zimmermann for reading this manuscrit.

8 REFERENCES

[1] H. Fukuma, in this proceedings.

[2] E. A.Perevedentsev and A. A.Valishev, Phys. Rev. ST-AB, **4**, 024403 (2001); E. A. Perevedentsev, in Proc. of 1999 Part. Accel. Conf., New York, 1999, 1521 (1999); E. A. Perevedentsev, Proc. of Int. Workshop on Performance Improvement of Electron-Positron Collider Particle Factories, Tsukuba, 1999, KEK proceedings 99-24, 171 (1999).

[3] G. Rumolo and F. Zimmermann, CERN-SL-2001-0067. to be published in Proceedings of the Two-stream instability Workshop, Tsukuba (2001).

[4] K. Ohmi and F. Zimmermann, Phys. Rev. Lett., **85**, 3821 (2000).

[5] K. Oide, Private communications.

[6] P. Kernel, R. Nagaoka, J.-L. Revol, G. Besnier, EPAC 2000, Vienna (2000).

[7] K. Ohmi, F. Zimmermann, E. Perevedentsev, Phys. Rev. E **65**, 16502 (2002).

[8] K. Hirata, H. Moshammer and F. Ruggiero, Particle Accelerators, **40**, 205 (1993).

[9] K. Ohmi, Phys. Rev. E**62**, 7287 (2000).

[10] Y. Cai et. al.,Phys. Rev. ST-AB, **4**,011001 (2001).

[11] M. Tawada et. al., Proceedings of a Workshop on beam-beam effects in circular colliders, Fermilab, June 25-27, 2001, FERMILAB-Conf-01/390-T, 17 (2001).

[12] E. B.Anderson and J. T.Rogers, Proceedings of a Workshop on beam-beam effects in circular colliders, Fermilab, June 25-27, 2001, FERMILAB-Conf-01/390-T, 136 (2001).

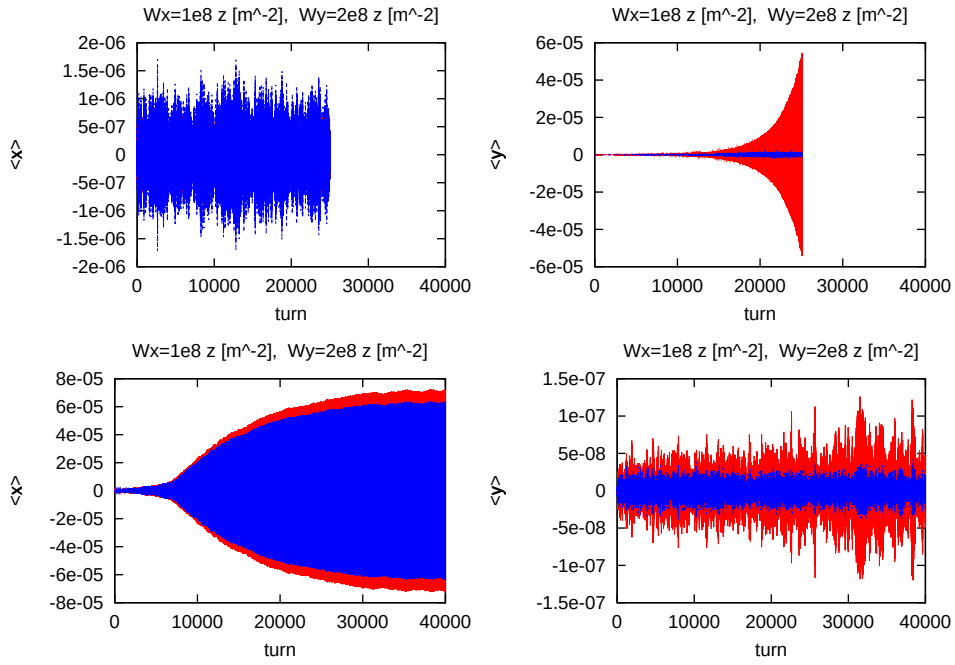

Figure 9: Evolution of beam amplitude for the strong-strong simulation including an external wake field. Red and blue curves correspond to amplitudes of positron and electron beams, respectively. Upper two pictures depict horizontal and vertical amplitudes without beam-beam interaction. Lower two pictures depict those with beam-beam interaction.

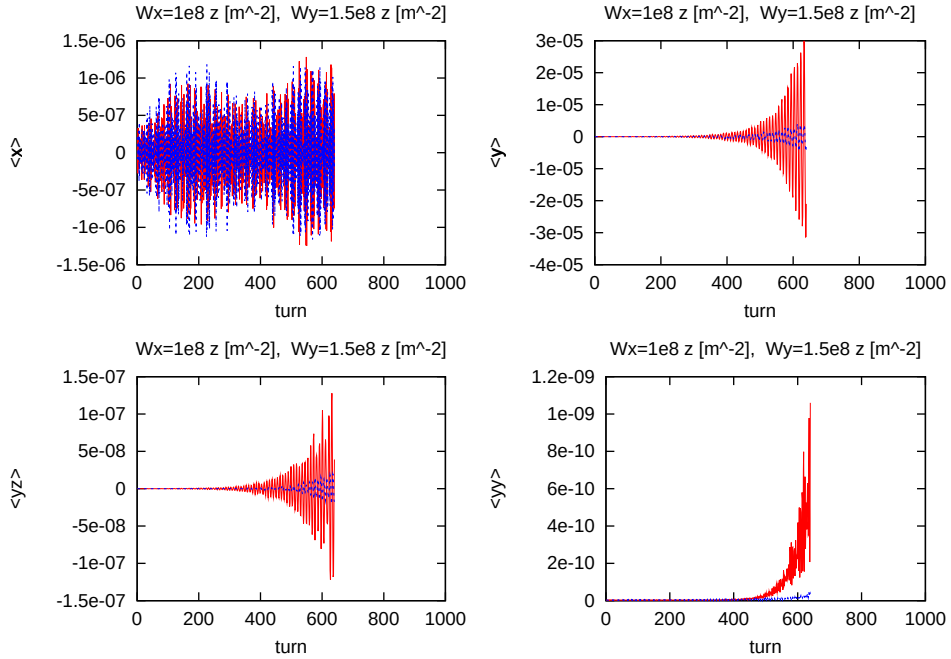

Figure 10: Evolution of beam amplitude for linear force including an external wake field. Red and blue curves correspond to amplitudes of positron and electron beams, respectively. Upper two pictures depict horizontal and vertical amplitudes with beam-beam interaction. Lower left picture depicts $y - z$ correlation $\langle yz \rangle$, and lower right depicts vertical beam size.

SIMULATION STUDY ON ECI FOR BEPC AND BEPCII*

J. Xing, Z.Y. Guo, Q. Qin, J.Q. Wang
Institute of High Energy Physics, Chinese Academy of Sciences, Beijing, 100039, P.R. China

INTRODUCTION

The Beijing Electron Positron Collidor will be upgraded to enhance the luminosity in the energy of 1.89 GeV. The machine will become a double ring (BEPCII) from a single ring. The multi-bunch electron and positron beams will circle in each ring respectively. The electron cloud instability is suspected to occur in the positron ring, and it may influence the luminosity performance of the collider. A simulation code has been developed based on similar programs, which have been used to study ECI in other laboratories. The physics model of the instability, the simulation results comparing to the observation in the BEPC experiments and simulation results on the BEPCII design study will be discussed in this paper.

PART I REVIEW OF EXPERIMENT AND SIMULATION STUDY ON BEPC

1. Instrumentation*1.1 PE detector*

Similar to the detector in the APS[2,3], a photoelectron detector was installed in the BEPC ring. It has three layers with the same diameter of 80 mm and two mesh grids in front of the detector. The outermost grid is grounded, and a bias voltage is applied to the shielded grid. The graphite-coated collector lowers the secondary electron yield and is biased with a DC voltage of +48 V with batteries. Between the detector and the support barrel mounted on an idle slot, a 1 cm annual gap exists.

The detector is mounted downstream of a dipole in the direction of positron motion, shown in Fig. 1.

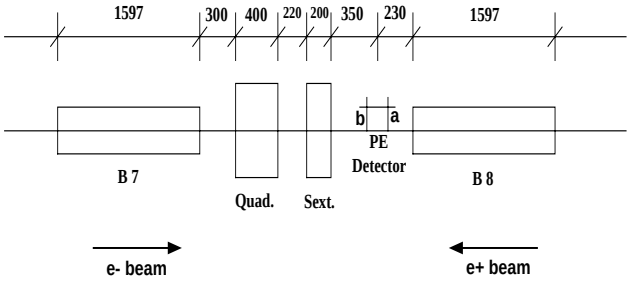

Figure 1: Position of the PE detector at the BEPC storage ring (seen from inside of the ring).

Being so close to the dipole, the PE detector has to be shielded from the magnetic field with layers of high and low permeability “mu-metal” sheets and nickel alloy sheets. After shielding, the fields at the points *a* and *b* in Fig. 1 are 9 Gauss and 0, respectively.

1.2 Apparatus setup

The detector is connected with other instruments as shown in Fig. 2. A low pass filter (LPF) is used to make sure that the signal of collector is from the electron only. The current of photoelectron is measured with the nanoampere-meter, which is connected between the resistor and ground. A temperature monitor is mounted on the detector to detect heat induced by beam-excited HOM wakefields in the annular gap between the detector and the support barrel.

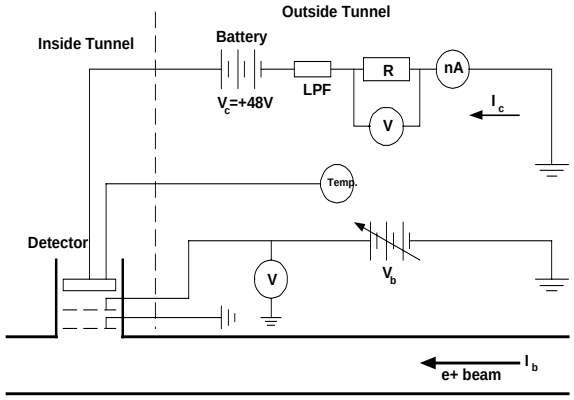

Figure 2: Setup of all apparatus in the experiment.

2 Measurements

In the following PE measurements, we apply the 150 MHz LPF to eliminate any sources of RF noise. During all the measurement, the temperature monitor displays 24±1°C with no change, which means the HOMs effect due to the annular gap between the detector and its support barrel is minimal. A bias voltage scan was made and the V_b fixed at +40V for maximum signal, as shown in Fig. 3. The derivative of the normalized I_c-V_b curve gives the photoelectron energy distribution, shown as Fig. 4.

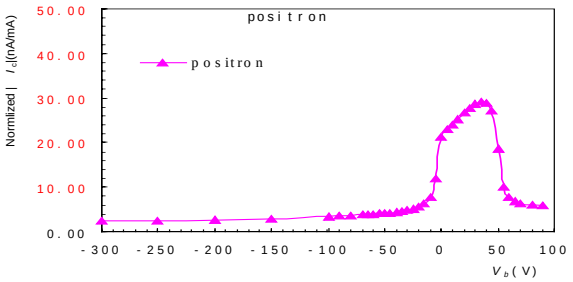

Figure 3: Detector current during bias voltage scan.

*Work supported by the Chinese National Foundation of Natural Sciences, contracts 19875063-A050501 and 19975056-A050501

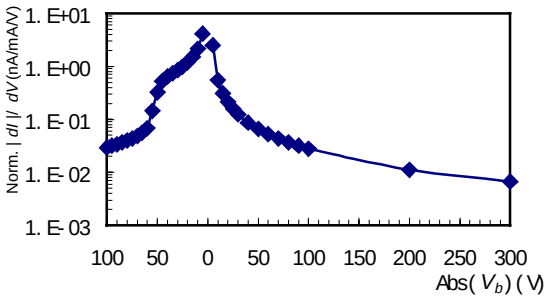

Figure 4: Photoelectron energy distribution.

2.1 Dependence on beam current

The collected electron current I_c as a function of beam current I_b is measured in the cases of single bunch and multi-bunch. Normalized by I_b, I_c is almost the same in different bunch spacing. It reads about 25nA/mA at the bunch current of 2 mA, similar to the plot in Fig. 5.

No saturation effect, in which electron generation and loss equilibrate, is found with a long bunch train and a weak bunch current, even if 40 bunches are used with the bunch current of 1 or 2 mA (I_b is 40 or 80 mA).

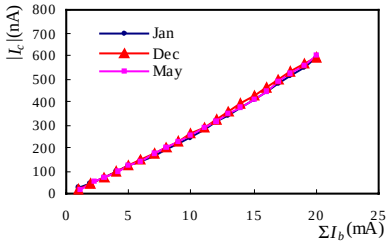

Figure 5: Collected electron current I_C as a function of beam current I_b

2.2 Secondary electron (SE) measurement

Due to the SE, a dramatic amplification of the signal is observed in the APS when the bunch spacing is 7 buckets (20 ns) [2]. But in our measurements, such an amplification is not observed as shown in Fig. 6.

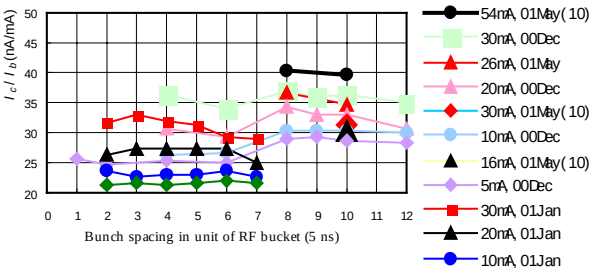

Figure 6: Normalized electron current as a function of bunch spacing and current. The legend gives beam current.

2.3 Solenoid effect

Solenoid coils winding downstream of the dipoles is a possible way to cure the PEI, like KEKB LER. In BEPC storage ring, we installed two coils on each side of the detector to observe the solenoid effect. The currents of the coils, I_s, are ±20A, generating several tens of Gauss magnetic field. Fig. 7 shows the I_c vs. I_b when solenoid has different currents.

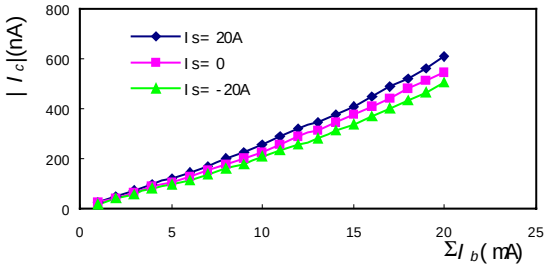

Figure 7: I_c vs. I_b with different solenoid fields.

3 Simulations

With the code developed by Dr. Y. Luo [4], the PE generation is simulated for different PE reflectivity. For a real machine, a reflectivity of 0.98 is chosen in simulation. The energy distribution of the PE is selected as 5eV±5eV. The emission yield of secondary electron is given as

$$\delta(E,\theta) = \delta_{\max} \cdot 1.11 \cdot \left(\frac{E}{E_{\max}}\right)^{-0.35} \cdot \left(1 - \exp\left[-23 \cdot \left(\frac{E}{E_{\max}}\right)^{1.35}\right]\right) / \cos\theta$$

with $\cos\theta$ distribution as the angle distribution. The energy distribution of the SE is 0±5eV, and the δ_{max} of the SE is 3 in simulation. Simulation results are shown in Fig. 8 and 9.

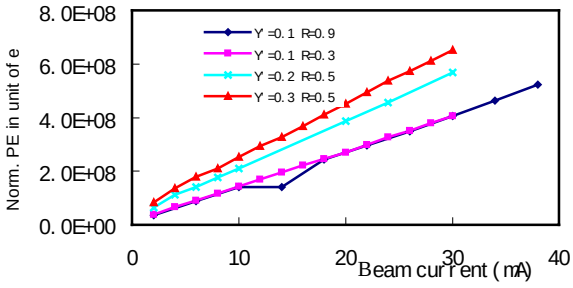

Figure 8: PE creation for different yield and reflectivity.

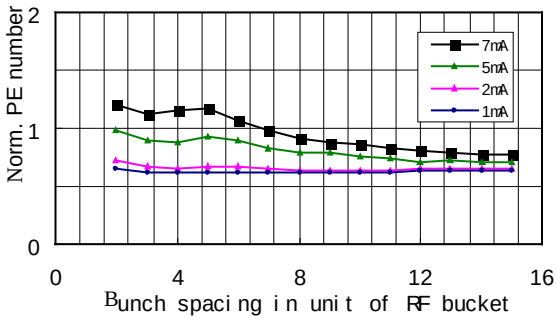

Figure 9: Simulation results on multipacting. (The legend gives bunch current.)

4 Discussions

Detailed measurements of the properties of PE cloud were carried out at the BEPC storage ring under various beam conditions. I_c varies linearly with the beam current I_b as expected. No saturation process is observed up to 40 bunches with 1 or 2 mA/bunch. We observed very weak dependence on bunch spacing, using 5 and 10 bunches

with 1 to 6 mA/bunch up to the 12-bucket spacing. No beam-induced multipacting was observed at the BEPC yet.

Two new detectors, modified as encircling the grounded grid but isolated from the retarding grid and the collector to avoid the I_c electrical leak from HOMs excited through the gap between the detector and the port, will be installed soon in the places far from dipoles. The time structure of I_c signal and the machine parameter dependences would be studied furthermore. Better shielding is necessary on the existing detector to avoid the fringe field of the dipole.

Primary simulations give some consistent results with the experiments, especially the multipacting condition and the dependences of beam parameters. More simulation studies are still under way.

PART II SIMULATION STUDY ON BEPCII

BEPCII is an upgrade project of Beijing electron-positron collider(BEPC), which will install a new inner ring based on the single-ring collider BEPC. It will provide the colliding beams of the center-mass between 1.0 GeV and 2.0 GeV and also the dedicated synchrotron radiation beam at 2.5 GeV. For the colliding beams the luminosity is optimized at 1.89 GeV with 10^{33} $cm^{-2}s^{-1}$, which is two order of magnitude of BEPC. Some parameters of BEPCII is compared with that of some other machines in table 1 [5].

Table 1: Parameters of a few storage rings

	BEPCII	KEKB	PEPII
Beam energy(GeV)	1.89	3.5	3.1
Bunch population $N_b(10^{10})$	4.84	3.3	9
Bunch spacing L_{sep}(m)	2.4	2.4	2.5
Rms bunch length s_z(m)	0.015	0.004	0.013
Rms bunch sizes $s_{x,y}$(mm)	1.18,0.15	0.42,0.06	1.4,0.2
Chamber half dimensions $h_{x,y}$(mm)	60,27	47	25
Slippage factor h (10^{-3})	22	0.18	1.3
Synchrotron tune Q_s	0.033	0.015	0.03
Circumference C(km)	0.24	3.0	2.2
Average beta function(m)	10	15	18
Parameter n_{min}	9.24	10	1
e- oscillation/bunch n_{osc} $w^o_e s_z$/(pc)	0.42	1.0	0.9
Density enhancement H_e	15	13	12
Adiabaticity A	17.4	9	8
TMCI threshold $r_e[10^{12}m^{-3}]$	22.7	0.5	1
Density ratio $r_{e,sat}/r_{e,threshold}$	0.19	4	4

1. Electron cloud Build up and Saturation

The ECLOUD programme developed by O. Bruning, G. Rumolo, F. Zimmermann of the CERN SL Division was used in the simulation study on the build up and saturation of the electron cloud on BEPCII. [6]

1.1 the photo-emission yield and the SEY

For BEPCII, The number of radiated photons per positron is about 12 photons for one dipole bending magnet. And From figure 10. , the "first strike" photons in the dipole magnet region is approximately equal to that in the field free region. And consider the effect of the antichamber, only ~1% of the radiated photons can remain inside the chamber[7][8]. Assume the electron yield per absorbed photon is 0.1, then the photonelectron yield Y_{pe} will be 0.006. Simulation result also shows that coating the inner face of the vacuum charmber with TiN will effectively reduce the number of the electrons, as shown in Fig. 11 [7].

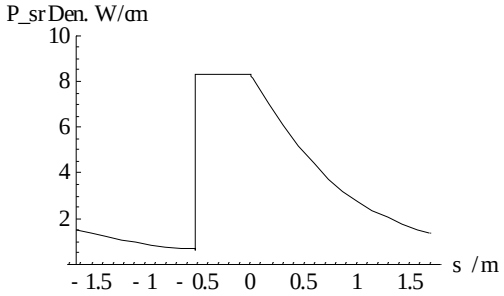

Figure10: SR power distribution along the ring(-1.6 < s < 0, means in the dipole magnet region)

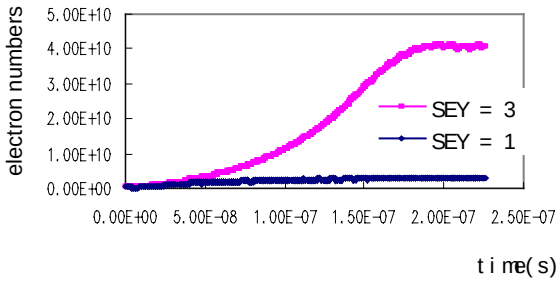

Figure11: Electron numbers with and. without TiN coating of the chamber.($Y_{e,ph}$=0.006)

1.2 The electron cloud build up and saturation

The build up and saturation of electron cloud under different conditions and possible cures were simulated, as shown in Fig.12, Fig.13, Fig. 14 and Fig.15.[9] The dipole magnets which will occupy about 25% of the whole ring, will confine many electrons to the vicinity of the pipe wall. Thus the volume density of the electrons will be reduced.[5]

The effect of the solenoid and the clearing electrode that had been successfully used to suppress the ECI were also studied for BEPCII.

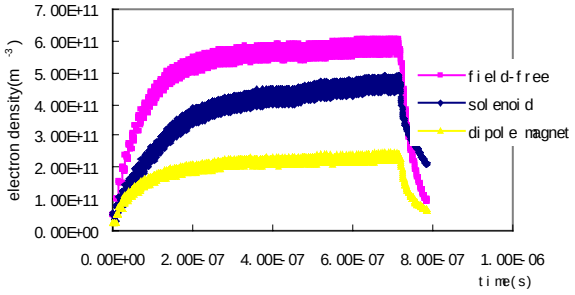

Figure 12: the average electron density of the pipe per cubic meter in the dipole magnet compared with that in the free field region with and without solenoid.

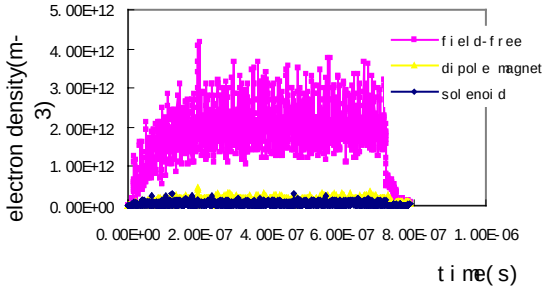

Figure 13: Electron density at the center of the pipe per cubic meter in the dipole magnet compared with that in the free field region with and without solenoid.

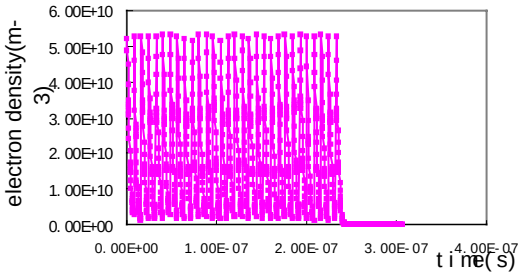

Figure 14: The average electron density of the pipe per cubic meter for a field-free region with clearing electrode (500V) vs. time.

2. Electron cloud instabilities

2.1 The coupled-bunch instability

The "turn by turn" code developed by Dr. Y. Luo was used. The rise time got from figure15 is about 0.3ms. [4]

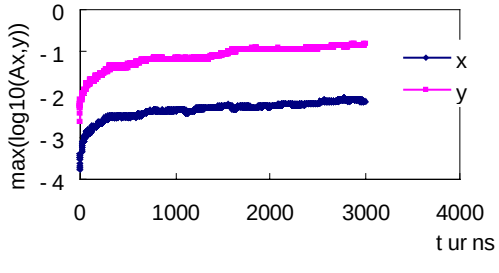

Figure.15: max($\log_{10}(A_{x,y})$) vs turns

2.2 the single-bunch instability

The **headtail** programme develeped by G. RUMOLO was used in the simulation study. [6][9]

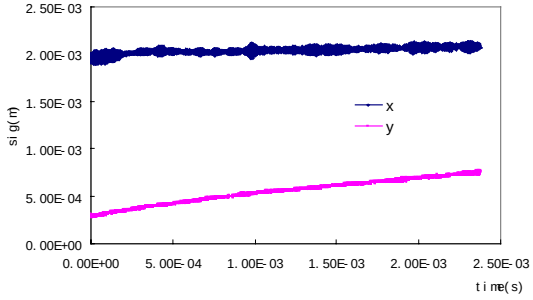

Figure 16:Sqrt(beam size) growth as a function of time in the field-free Region, assuming that the electron density is $2.0\times10^{12}/m^3$.

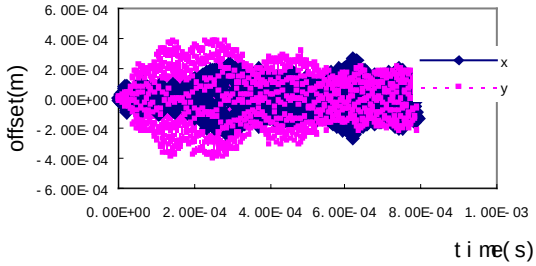

Figure 17:Simulated beam centroid motion as a function of time in the field-free region ,assume the elcetron density is $2.0\times10^{12}/m^3$.

3 Discussions

The prelimilary result shows that the instabilities caused by the ecloud will not be very serious. The very important condition is that the BEPCII will run below the TMCI threshold of the ecloud. Also it will benefit from the strong dipole magnet and other cures.

More details which will be closer to the actual conditions will be studied in the future.

ACKNOWLEDGEMENTS

We wish to thank the BEPC team for their effective work on operating the machine during the experiment. The authors would also like to thank R. Rosenberg from ANL, for his suggestion on shielding the detector.

The authors would also like to thank F. Zimmermann, G. Rumolo, K. Ohmi, L. Wang and H. Fukuma for their support.

REFERENCES

[1] Z.Y. Guo, et al, Proc. of PAC'97, 1997, EPAC'98, APAC'98, 1998.
[2] K. Harkay, R. Rosenberg, Proc. of PAC'99, 1999.
[3] R. Rosenberg, K. Harkay, NIM A 453 (2000) 507.
[4] Y. Luo, IHEP Ph.D dissertation, 2000.
[5] F. Zimmermann, PAC 2001,CERN-SL-2001-0035.
[6] F. Zimmermann, Chamonix X & XI,CERN-SL-2000-007 & 2001-003-DI;G. Rumolo et al., PRST-AB 012801(2001).
[7] M. A. Furman, G. R. Lamberson,PEP-II AP Note AP 97.27.
[8] J. Wang, BEPCII-AP-Note/2001-06.
[9] G. Rumolo, F. Zimmermann, CERN-SL-2001-041.

PLASMA MODELING OF WAKEFIELDS IN ELECTRON CLOUDS*

T. Katsouleas, A. Z. Ghalam, S. Lee,
University of Southern California (USC)
W. B. Mori, C. Huang, V. Decyk, C. Ren
University of California at Los Angeles (UCLA)

Abstract

To estimate the importance of collective fields of an electron cloud interacting with a positively charged particle beam, we apply two particle-in-cell codes from plasma physics – OSIRIS and QuickPIC. These codes have been used extensively to model the wakefields excited by positron bunches in a neutral plasma in the scheme known as the plasma wakefield accelerator (PWFA). The collective wakefields excited in the electron cloud plasma are similar. Analytic estimates and numerical solutions for the wakefields are obtained and their importance assessed. The basic approach as well as special features of the codes such as moving windows and quasi-static wakefield approximations are described.

1 INTRODUCTION

The need to understand the interaction of intense positively charged beams with the low density electron clouds they create in circular accelerators is well documented. These low density clouds constitute a non-neutral plasma which supports wakefields of the beam. The wakefields affect the beam propagation in a number of ways. They lead to focusing terms that alter the tune shift of the accelerator, longitudinal terms affecting the synchrotron motion and deflection terms that couple small offsets between the head and tail. The latter are believed to be responsible for a head–tail instability that leads to emittance blow-up and limits the beam current in many existing and planned circular accelerators.

Several simulation models have been developed for the wakes and instability of beams in electron clouds. These typically have many approximations such as neglect of the space charge of the cloud on itself, and condensation of the effect of the cloud to a single kick on the beam once per turn. Perhaps of even greater concern is the newness of the models themselves. As a result there has been little opportunity to benchmark the codes against reference codes or experimental data.

In this paper we apply some of the simulation tools we have been developing over the past decade for the study of plasma-based accelerators to the problem of wake production and beam propagation in electron clouds. Particularly relevant are recent benchmarks of these tools against a beam-driven plasma wakefield experiment at SLAC known as E-162. In that experiment, positron beams are propagated through a 1.4 meter long plasma. The physical mechanism of wakefield production; namely, the rapid drawing in of plasma electrons to the beam axis on a beam plasma frequency time-scale is nearly identical in this experiment and in the case of electron clouds in circular machines. In the remainder of this paper, we briefly review two primary simulation models we use, OSIRIS and QuickPIC, along with sample benchmarks of these codes. Then we apply them to the case of electron cloud wakefields in the SPS proton storage ring at CERN. Comparisons are made to recent models by Rumolo and Zimmerman [1]. We also examine the propagation of tilted and untilted beams through a significant length of the accelerator (40 km) in their self-consistent wakefields. The effects of the cloud wake and image forces from the wall are isolated and discussed. Finally, we comment on prospects for creating a complete high-fidelity PIC model that includes all of the relevant plasma physics contained here as well as the lattice terms and synchrotron motion of other models. Through high performance computing it may be possible to use such a model to make accurate predictions over thousands of turns. We compare analytic expressions for cloud wakefield amplitudes that we have obtained [2] and compare them to the simulations.

2 DESCRIPTION OF SIMULATION MODELS - OSIRIS AND QUICKPIC

Our primary simulation tools for beam–plasma interactions are the particle-in-cell (PIC) codes OSIRIS [3] and QuickPIC [4]. We describe each briefly here. OSIRIS is a fully self-consistent, fully relativistic, fully electromagnetic 3-D plasma PIC code. It solves Maxwell's equations on a 3-D Cartesian grid by finite difference in the time domain. The current and charge density sources for Maxwell's equations are found by depositing the positions and velocities of a collection of 10^6–10^8 charged particles on the grid. The fields are then used to update the particles' positions and velocities and the cycle is repeated. The code features a moving window (to follow a beam), is object-oriented and parallel. We have used this code to model the E-162 experiments at full scale in 3-D. This typically requires 1–10 GBytes of memory and 10^3 or more CPU hours. Such codes have proved to be highly reliable, but are obviously computationally intensive.

QuickPIC is a 3-D PIC code using a quasi-static or frozen field approximation [5]. This approximation is specifically useful for studying wakes. It requires that the beam not evolve significantly on the time scale that it takes the plasma to pass through it, or in other words, $\beta \gg \sigma_z$.

* Work supported by USDoE

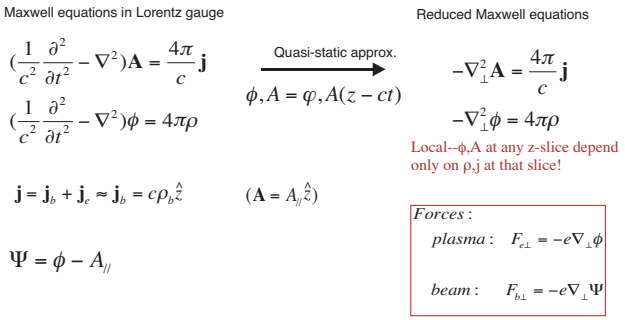

Figure 1: Quasi-static or frozen field approximation used in QuickPIC

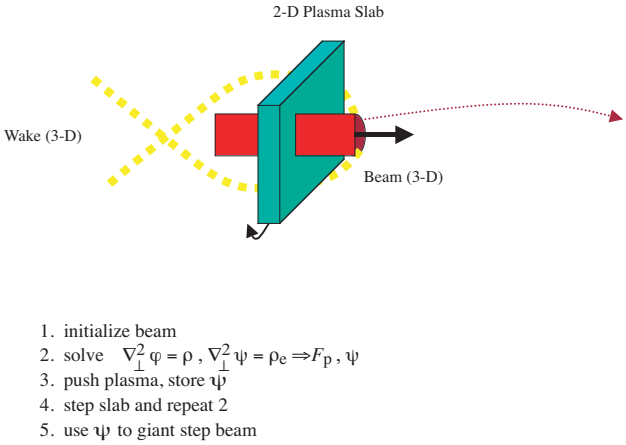

Figure 2: QuickPIC cycle. It uses a 2-D Poisson solver to calculate potentials and update particles

This is typically well satisfied. The basic equations for QuickPIC follow from the wave equations for A and ϕ in the Lorentz gauge [5] as illustrated in the box in Fig. 1.

The quasi-static approximation assumes that the wakes are functions of $z - \mathrm{ct}$ only and leads to equations for the wake potentials φ and $\Psi = \varphi - A_{\|}$ that involve only solving 2-D Poisson equations. The QuickPIC cycle is illustrated in Fig. 2. The Poisson equations are solved on a 2-D slab of plasma (using a well-established bounded 2-D PIC code BEPS as a subroutine) with conducting boundary conditions.

The wakes are stored and used to update the plasma in the slab and the slab is then pushed back a small step through the beam. After transiting the beam, the stored values of φ are used to find the force on the beam (treated as a 3-D PIC model) and it is pushed through a large step (of the order $\beta/30$). The need to solve for only a 2-D slab and the larger time steps of the 3-D push enable a time saving of 2–3 orders of magnitude. Both the 3-D outer layer and the 2-D inner layer of the code have been written in a parallel fashion to allow domain decomposition along z and y, respectively.

A comparison of QuickPIC and OSIRIS output for E-157 is shown in Fig. 3. In this experiment the wake

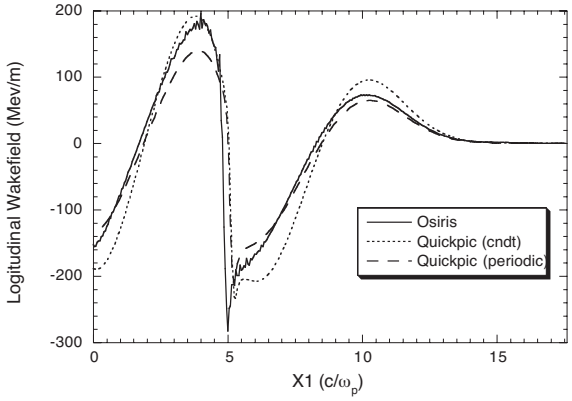

Figure 3: Wakefields for the E-157 experiment with OSIRIS and QuickPIC

Table 1: Parameters of SPS and KEKB

Variable	Symbol	SPS	KEKB
Bunch population $[10^{10}]$	N_b	10	3.3
Beam momentum [GeV/c]	p	26	3.5
Circumference [km]	C	6.9	3.0
Electron density $[10^{12}$ m$^3]$	e	1	1
rms bunch length [mm]	z	300	4
rms hor. beam size [mm]	x	3	0.4
rms vert. beam size [mm]	x	2.3	0.06

is produced by a Gaussian bunch of electrons of density 10^{15}/cm^{-3} and bunch length $\sigma_z = 0.63$ mm in a plasma of density 2×10^{14}/cm^{-3}. The agreement between the two models is reasonably good in this case. The basic QuickPIC algorithm reproduces the more exact model so long as the plasma motion is dominantly radial and the radial velocity is not relativistic, conditions that are typical also in the electron cloud regimes of interest here. Accordingly we will use QuickPIC in the simulations presented in the remainder of this paper.

Next we apply QuickPIC to the electron cloud case. We remove the background ions usually present in the plasma simulations and initialize a cloud and beam with the parameters used previously [1] for the SPS ring at CERN. The parameters are given in Table 1.

Figure 4 shows the initial beam and cloud density profiles in the X-Z plane. From this we see that cloud electrons are sucked in reaching a peak density enhancement factor of 150 at a location 1.9σ behind the beam.

The analytically expected enhancement factor at the center of the beam is given in Ref. [2] to be approximately 100 and in the simulation it is 70. The cloud response gives rise to the wakefields shown in Fig. 5.The longitudinal wake field reaches a maximum retarding field of 10 V/m near the center of the beam. This compares to the analytic expression in Ref. [2], which estimates the field at the center to be about 10 V/m.

Also for comparison we reproduce the results of Rumolo and Zimmermann [1] in Fig. 6. For identical parameters

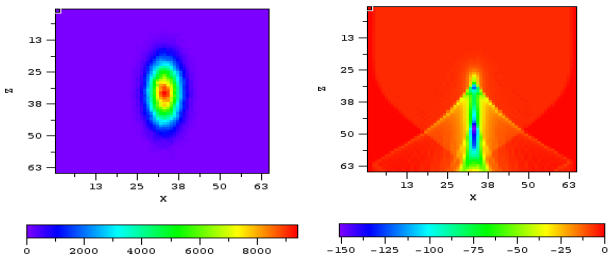

Figure 4: Initial beam and plasma density. Cloud electrons are sucked in at 1.9σ behind the beam.

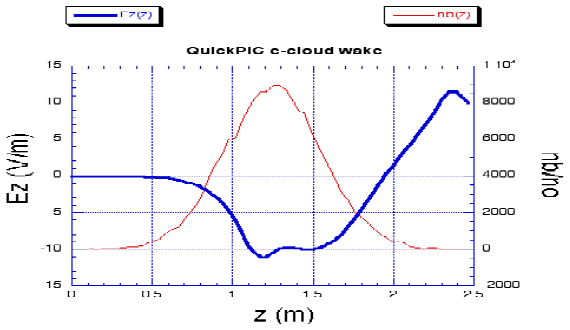

Figure 5: Longitudinal force on the beam at 1.9σ behind the beam

we see that the QuickPIC result and ECLOUD results are quite similar in the main part of the beam, but the ECLOUD result has unphysical divergences at the extreme head and tail.

In Fig. 7 we show corresponding results for the tilted beam. The beam is initially tilted by σ_r over σ_z of the bunch.

The structure of the cloud density in Fig. 7 is interesting and can be understood as follows: A compression peak is formed along the tilted axis of the beam due to the drawing in of electrons nearest the beam. Electrons from further away (nearest the pipe walls), receive their strongest kick

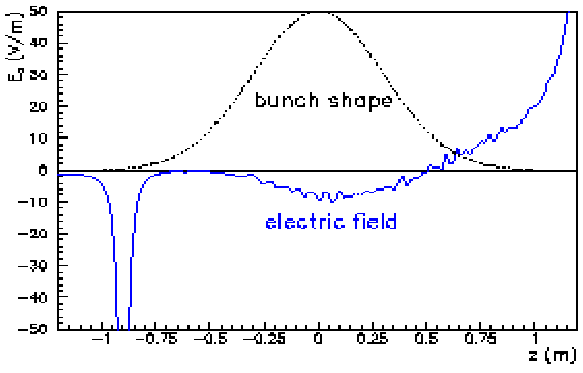

Figure 6: Longitudinal force on the beam from the electron cloud

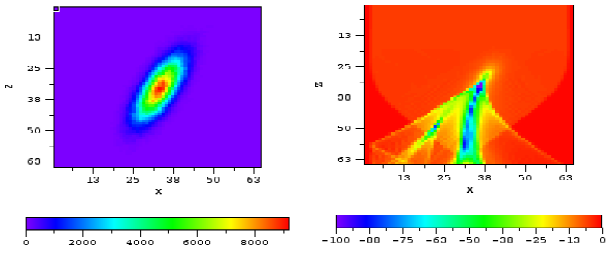

Figure 7: Initial tilted beam and plasma density. The beam is tilted σ_r over the bunch length

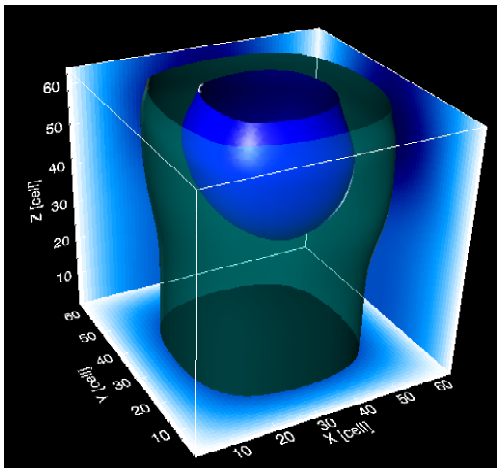

Figure 8: Wakefield potential Ψ on the beam

from the peak of the beam current (in the center of the box). By the time they arrive at the axis, they have fallen behind creating the compressions on axis at the bottom of the figure. Figure 8 shows a 3-D image of the wake potential Ψ acting on the beam. The potential at the head of the beam is attractive to the center of the pipe and is caused largely by the unperturbed cloud charge later in the beam. Later in he beam there are deflecting focusing forces coming directly from the cloud as well as from the image of the cloud in the conducting walls. We note that without the conducting boundary conditions the restoring force from the image charges would not be present.

This effect has been omitted in past work [1]. The cloud's image contributes a coherent tune shift that is larger than and in the opposite direction to the number of tune shifts caused by the image charge of the beam itself. This is because of the usual cancellation of the electric and magnetic forces between the beam and its image to order of $1/\gamma^2$. This (just as for the space charge correction to the incoherent tune shift), in the presence of the electron cloud, the tune shift due to image charges should be modified as follows:

$$\Delta\nu = A_{image} \qquad (\text{no } e_{cloud}) \tag{1}$$

$$\Delta\nu = A_{image}(1 - \eta_e\gamma^2) \qquad (\text{with } e_{cloud})\ , \tag{2}$$

where η_e is the fractional neutralization of the beam.

$$\eta_e = H_e n_c/n_b = \eta_e(z)\ , \tag{3}$$

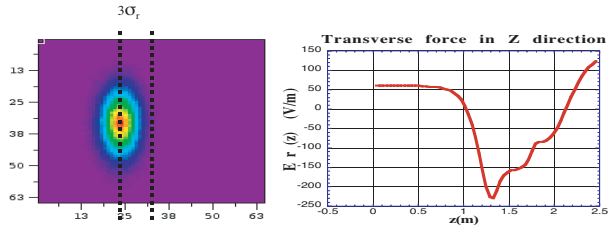

Figure 9: Right: Beam offset by $3\sigma_r$, Left: Plots of $\partial\Psi/\partial x$ at $x = 3\sigma_r$

where n_c is the cloud density before the beam and n_b is the beam density.

Note that $\Delta\nu$ varies along the bunch providing an additional mechanism for head–tail offsets to form and/or grow. Figure 9 shows simulation results for an offset beam. We next study the beam evolution in the wake potentials above. In these simulations, there is no external field (i.e., no lattice), and the emittance is artificially low thus they should be taken as cartoons to illustrate (and in some sense isolate) just the wakefield effects on propagation. Further work is needed to include the external environment of the storage ring. In these simulations the 3-D time step is 50 m. Figure 10 shows snapshots of the beam and cloud at propagation distance of $z = 0, 5, 10, 15$ and 20 km. We see the dynamic focusing of the beam by the cloud. At later times a small tail oscillations in the beam and cloud density is seen in the movies. This oscillation grows despite the fact that the beam and cloud are initially symmetric except for small numerical noise. The instability does not continue to grow in this example and saturates after 20 km of propagation. Figure 11 shows the corresponding evolution of an initially tilted beam. The tail oscillation is much more pronounced in this case.

In summary, we have applied simulation tools developed and benchmarked for plasma-based accelerator research to the problem of beam propagation in circular accelerators with low density electron clouds present. We find the wakefields compare well with analytic estimates and previous models over most conditions. We also find a new contribution to the coherent tune shift of the accelerator due to electron cloud image forces not included in previous models. We believe the combining of our quasi-static PIC models (QuickPIC) with the relevant lattice of circular accelerator models could lead to a powerful tool for predicting the onset and evolution of electron cloud instabilities. It appears that the capability for massively parallel computation with QuickPIC would enable modeling with PIC accuracy to be extended to relevant lengths (i.e., several thousand turns).

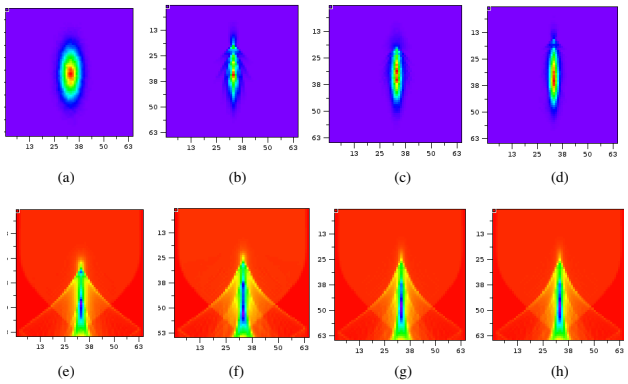

Figure 10: Snapshots of Beam (a-d) and cloud (e-h) density

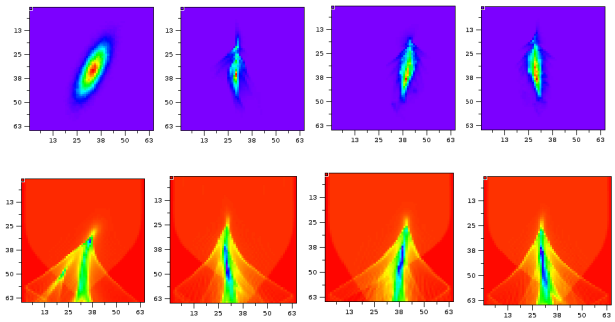

Figure 11: Corresponding Snapshots with tilted beam

3 ACKNOWLEDGEMENTS

We would like to thank Frank Zimmermann for introducing us to this problem and G. Rumolo, F. Decker, Wei Jei, C. Clayton, Bob Siemann, and the E-162 Collaboration for useful discussions. Work supported by DOE and NSF.

4 REFERENCES

[1] G. Rumolo and F. Zimmermann, Longitudinal Wake due to Electron Cloud.

[2] A.Z. Ghalam et al., in preparation.

[3] R. Hemker et al., Proc. 1999 Part. Accel. Conf. (1999).

[4] C. Choung et al., in preparation.

[5] D.H. Whittum, Phys. Plasmas, vol. 4, p. 1154, 1997.

On the Transparency of the Electron Cloud to Synchrotron Radiation

D. Kaltchev, TRIUMF, Vancouver, Canada; F. Zimmermann, CERN, Geneva, Switzerland

Abstract

We study the interaction of the synchrotron radiation, produced by a relativistic particle in a bending magnet, with the electron cloud present in the same magnet. The cloud is described as a collisionless magnetized plasma of very low, but finite temperature. Expressions are derived for the spectral intensity of synchrotron radiation far from the particle, which in absence of a cloud reduce to the Schott spectrum of radiation in vacuum.

For typical cloud parameters – a rarefied plasma, we fully neglect the refraction and only take into account the damping of the extraordinary and ordinary plasma waves at frequencies near the first electron cyclotron resonance (wave lengths $\sim$ mm) via interaction with resonance electrons. This effect would be the strongest in the hypothetic case of electron beam and electron cloud, but is found to be weaker in the realistic case of positively charged beam particle (proton, positron). In the latter case, by taking Maxwellian velocity distribution of the electrons (r.m.s. velocity $v_e = \beta_e c$) and fully neglecting the ordinary wave (factor β_e), we demonstrate that the dominant effect is coupling of π- mode of the spontaneous radiation with the extraordinary plasma wave.

1 INTRODUCTION

The goal of this paper is to study whether synchrotron radiation generated in a LHC bending magnet can significantly affect the electron cloud present within the same magnet. We consider the radiation of a relativistic particle (also called "test" particle) with rest mass M, charge $\pm Z|e|$ and energy γMc^2 $(\gamma >> 1)$ moving along the central trajectory of a bending magnet (field B_0, radius $\rho = Mc^2\beta\gamma/(Z|e|B_0)$) in presence of a non-relativistic electron plasma (electron cloud) surrounding the central trajectory. Since the length of the magnet is much larger than the formation length ρ/γ, we will assume that the whole plasma volume is illuminated by the same radiation spectrum and that the size of the electron cloud, both transversally and longitudinally with respect to the direction of propagation of the radiation, is much larger than the radiated wavelength.

Following mainly [1], in Section 2 we compute the spectral density of radiation at frequency ω, generated by the test particle as it traverses finite volume of cold electron plasma of very low density. By neglecting two-particle interactions, the test particle radiates as if it is in a free space, but the radiation decays as it propagates through the cloud.

The energy losses of the test particle are defined as the work per second done by the breaking force acting on the particle due to electromagnetic field produced by the particle itself:

$$\frac{\delta\mathcal{E}}{\delta t} = Ze(\boldsymbol{v}^{(t)} \cdot \boldsymbol{E}) \qquad (1)$$

where $\boldsymbol{v}^{(t)}$ is the test particle velocity vector; $\boldsymbol{E}$ is the field produced by the particle at its own position $\boldsymbol{r}'$ and e is the electron charge. One can think of the field $\boldsymbol{E}$ in (1) as the plane monochromatic wave which, far from the source (current density $\boldsymbol{j}^{(t)} = eZ\boldsymbol{v}^{(t)}$), coincides with the spontaneous synchrotron radiation. By neglecting all effects taking place at the plasma boundary, this wave within the plasma splits into two waves – ordinary $(-)$ and extraordinary (+) one. Propagation of the two plasma waves is described in the so called quasi-linear (geometrical optics) approximation. We realize that the geometrical optics description is not correct within several wavelengths from the source, but it can still be used approximately (as this was done in [1]).

It is also assumed that the plasma is stationary in time, i.e. it has no unstable (growing with time) modes even at the (low) frequencies near the electron cyclotron resonance.

In the limit of zero plasma density, or negligible damping of the waves at frequency ω, i.e. $k_{\pm}^{''}(\omega)L << 1$; $e^{-k_{\pm}^{''}(\omega)L} \approx 1$; where L is the length traversed by the radiation within the plasma and $k_{\pm}^{''}$ are absorption coefficients, our result should reduce to the usual formula of Schott for the spontaneous synchrotron radiation spectrum (as in vacuum).

By expanding the exponent: $e^{-k_{\pm}^{''}(\omega)L} \approx 1 - k_{\pm}^{''}(\omega)L$, the correction to the spontaneously radiated power is proportional to $-k_{+}^{''}(\omega)L$, while the absolute value $k_{+}^{''}(\omega)L$, multiplied by the spontaneously radiated power and integrated over ω and the angles, gives the total power deposited in the cloud. The latter quantity as considered in this work to be an adequate measure for the strength of interaction between synchrotron radiation and plasma.

The two cases – negative (e^-) and positive (e^+, or p^+) radiating particle

If the test particle is an electron in vacuum, a remote observer whose radius vector describes an angle θ with the

external magnetic field ($\theta < \pi/2$ means above the median plane), sees elliptically polarized spontaneous synchrotron radiation wave with electric vector $\vec{E}$ rotating in the same direction as the electron ([5]). More precisely, the projection of $\vec{E}$ on the median plane rotates in the same direction as the electron. This remains true for both an observer located above or below the median plane – the polarization changes from left- to right-, or reverse when θ crosses $\pi/2$. Thus in this case $\vec{E}$ rotates synchronously with the plasma extraordinary wave, implying stronger interaction.

If the test particle is a positron or proton, then compared to the electron case, $\vec{E}$ reverses its orientation $\vec{E} \rightarrow -\vec{E}$, but still rotates in the same direction as the test particle, i.e. opposite to the electrons of the cloud and synchronously with the ordinary wave.

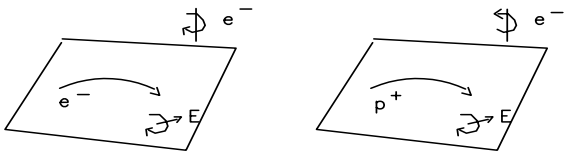

projection of E vector of rad. on the median plane rotates in the same dir. as the radiating particle

Parameters

L – propagation length of the radiation within the cloud;
B_0 – external magnetic field;
ω and $\lambda \equiv 2\pi c/\omega$ – frequency and wavelength of radiation far from the plasma;
N_0 – the number of electrons per cubic cm;
$\omega_p = \left(4\pi N e^2/m_e\right)^{1/2} = 5.64 \times 10^4 [s^{-1}] \sqrt{N_0[cm^{-3}]}$ – the electron plasma frequency;
$\Omega_e = \frac{eB_0}{m_e c} = 1.76 \times 10^7 [s^{-1}] B_0\ [Gs]$ – cyclotron frequency of the electrons;
$\Omega = \frac{ZeB_0}{Mc\gamma}$ – cyclotron frequency of the relativistic LHC particle ($\gamma >> 1$);
$n = \omega/\Omega_e$ – harmonic number;
$q = (\omega_p/\Omega_e)^2$ – density parameter;
$v_e \equiv \sqrt{< v^2 >/3}$ – the r.m.s. thermal velocity of the electrons in case of Gaussian distribution function:

$$f_e = N_0 \left(\frac{m_e}{2\pi T_e}\right)^{3/2} e^{-mv^2/2T_e}, \qquad (2)$$

where $T_e \equiv m_e v_e^2 = k_B T[K]$; $\beta_e \equiv v_e/c$ ($1/\beta_e^2 = 5.11 \times 10^5/T_e\ [eV]$);
$r_D \equiv v_e/\omega_p$ – the Debye length;
y_0 – the distance of the electronic gyro-frequency to the critical frequency of the spontaneous synchrotron radiation spectrum:

$$y_0 \equiv \frac{2\Omega_e}{3\Omega\gamma^3} = \frac{2}{3\gamma^2}\,\frac{M}{Z\,m_e}. \qquad (3)$$

For electron rings ($|Z| = 1$, $\frac{M}{m_e} = 1$), y_0 is small: $\sim \gamma^{-2}$. For protons in the LHC ($M = m_p$; $\frac{m_e}{m_p} = 5.4 \times 10^{-4}$), $y_0 << 1$ both at injection ($\gamma = 480,\ y_0 = 1/188$) and collision ($\gamma = 7462,\ y_0 = 2 \times 10^{-5}$). For heavier radiating particles (like $^{82+}_{208}Pb$ ions), with mass $M = A \times m_p$, assuming the rigidity ρH is the same as for protons, the Lorenz factor γ is multiplied by Z/A, so the y_0 values for protons are multiplied by $(A/Z)^3$. One has: at injection ($\gamma = 189, y_0 \approx 0.1$) and collision ($\gamma = 2942,\ y_0 \approx 3 \times 10^{-4}$).

Estimation of the effect

The fraction of power deposited in the cloud relative to total power radiated can be estimated in the following way. We take: $N_0 = 10^6\ cm^{-3}$, $\lambda \sim 1\ mm$, $q = 10^{-8}$, $y_0 \sim 10^{-3}$ and thickness of the plasma slab $L = 10\ m$. For Maxwellian plasma, the order of magnitude of the absorption coefficients is known: $k_+'' L \approx \frac{q}{\beta_e}\frac{L}{\lambda}$, which should be multiplied by y_0 (the center of the absorption line) and by β_e (its width) to get:

$$\frac{q}{\beta_e}\frac{L}{\lambda}\ y_0\ \beta_e\ \sim 10^{-7}.$$

2 CORRECTIONS TO THE SPONTANEOUS SYNCHROTRON RADIATION SPECTRUM CAUSED BY WAVE ABSORPTION IN THE ELECTRON CLOUD

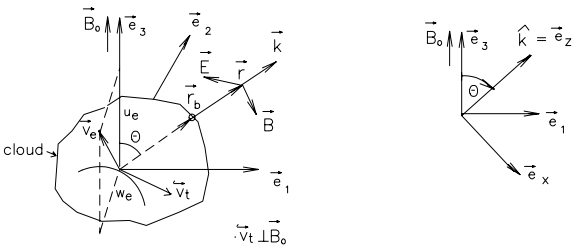

Figure 1: Left: test particle with velocity vector $\vec{v}_t \perp \vec{B}_0$ traversing electron plasma and velocity vector $\vec{v}_e$ of an electron of the plasma. Right: coordinate frame $\vec{e_x}, \vec{e_y}, \vec{e_z}$. obtained by rotation of $\vec{e_1}, \vec{e_2}, \vec{e_3}$ around the $\vec{e_2}$ axis at angle $-\theta$, so that the direction of propagation of radiation is along $\vec{e_z}$ ($\vec{k} \| \vec{e_z}$)

2.1 The self-consistent equations describing small plasma oscillations and the dispersion relation ([1], [2], [7])

We mainly follow [1], where the energy losses due to synchrotron radiation are studied for a slab of quasi-relativistic uniform electron plasma (the thermo-nuclear reactor). The electric field within the plasma $\boldsymbol{E}$, which corresponds to an external current, or a test particle current $j^{(t)}$, satisfies the

Maxwell equation:

$$rot\ rot\ \boldsymbol{E} + \frac{1}{c^2}\frac{\delta^2 \boldsymbol{E}}{\delta t^2} + \boldsymbol{j}^{(abs)} = \boldsymbol{j}^{(\mathrm{t})}, \qquad (4)$$

where the current density $\boldsymbol{j}^{(abs)}$, caused by the field $\boldsymbol{E}$, describes absorption and induced radiation within the plasma.

A test particle traversing the plasma is shown on Fig. 1. We have chosen the direction of the external field $\vec{B}_0$ to be parallel to the $\vec{e}_3$ axis and the radius vector $\vec{r}$ of the remote observer to lie in the plane $\vec{e}_1, \vec{e}_3$.

In what follows we use the relativistic form of the dielectric permittivity tensor (as in [1]; see also [8], [9]) to compute the Fourier components of the relativistic test-particle current. The same tensor, but taken in a non-relativistic approximation, ([2], [4]) will later be used to describe small oscillations of the electron plasma.

For a particle with mass of rest M and charge $q = Ze$, the relativistic tensor is:

$$\boldsymbol{Q} = -\frac{4\pi q^2}{m}\int d^3v\ f(\vec{v})\ \frac{1}{\gamma}\times$$
$$\times\left(\frac{\omega - k_\parallel u/\gamma}{w}\ \frac{\partial f}{\partial w} - \frac{k_\parallel}{\gamma}\ \frac{\partial f}{\partial u}\right)$$
$$\sum_{n=-\infty}^{n=+\infty}\frac{\boldsymbol{T}_n(\vec{v})}{\omega - (k_\parallel u/\gamma) - n\Omega}$$
$$-\frac{4\pi q^2}{m}\int d^3v\ f(\vec{v})\frac{u}{w\gamma}\left(w\frac{\partial f}{\partial u} - u\frac{\partial f}{\partial w}\right)\boldsymbol{e_3}\boldsymbol{e_3} \qquad (5)$$

$$\boldsymbol{T}_n(\vec{v}) = \begin{pmatrix} \frac{n^2w^2}{z^2}J_n^2 & \frac{inw^2}{z}J_nJ_n' & \frac{uwn}{z}J_n^2 \\ \frac{-inw^2}{z}J_nJ_n' & w^2{J'}_n^2 & -iuwJ_nJ_n' \\ \frac{uwn}{z}J_n^2 & iuwJ_nJ_n' & u^2J_n^2 \end{pmatrix}$$

with $J_n(z)$ being the Bessel function; $z \equiv k_\perp w/(\Omega\gamma)$; $\vec{k} = k_\perp\vec{e}_1 + k_\parallel\vec{e}_3$ (see Fig 1) and w and u denoting the components of the vector $\vec{v}$ transverse and parallel to $\vec{B}_0$.

Above $f(\vec{v})$ is relativistic distribution function, normalized so that $\int d^3v f(\vec{v}) = 1$. The argument $\vec{v}$ (notice an unusual notation!) denotes the particle momentum divided by the mass of rest, i.e. $\vec{v} \equiv \beta c\gamma$, with γ being the usual relativistic factor: $\gamma \equiv (1-\beta^2)^{-1/2} = (1+v^2/c^2)^{1/2}$. In the non-relativistic case ($\gamma \to 1$), $\vec{v}$ becomes the particle velocity.

By taking plane monochromatic waves $\boldsymbol{E} = \boldsymbol{E}_{\vec{k},\omega}\ e^{i(\vec{k}\cdot\vec{r})-i\omega t}$, $\boldsymbol{j}^{(t)} = \boldsymbol{j}^{(\boldsymbol{t})}_{\vec{\boldsymbol{k}},\boldsymbol{\omega}}\ e^{i(\vec{k}\cdot\vec{r})-i\omega t}$ (the size of the plasma volume is much larger than the wavelengths of interest), the Fourier-transform of (4) reads:

$$\boldsymbol{R}^{(e)}\cdot\boldsymbol{E}_{\vec{\boldsymbol{k}},\boldsymbol{\omega}} = \boldsymbol{j}^{(\boldsymbol{t})}_{\vec{\boldsymbol{k}},\boldsymbol{\omega}},$$
$$\boldsymbol{R}^{(e)} \equiv (c^2k^2 - \omega^2)\boldsymbol{I} - c^2\boldsymbol{k}\boldsymbol{k} + \boldsymbol{Q}^{(e)}. \qquad (6)$$

where $\boldsymbol{I}$ is the unity 3×3 matrix, $\boldsymbol{R}^{(e)}$ and $\boldsymbol{Q}^{(e)}$ are functions of real $\boldsymbol{k}$ and ω and $\boldsymbol{Q}^{(e)}$ is obtained from $\boldsymbol{Q}$ in (5) with substituting the electron parameters e, m_e, $\vec{v}_e$, $f(\vec{v}_e)$, Ω_e.

In the rotated coordinate frame $\vec{e_x}, \vec{e_y}, \vec{e_z}$:

$$(c^2k^2 - \omega^2)\boldsymbol{I} - c^2\boldsymbol{k}\boldsymbol{k} = -\omega^2\begin{pmatrix} 1-\mathcal{N}^2 & 0 & 0 \\ 0 & 1-\mathcal{N}^2 & 0 \\ 0 & 0 & 1 \end{pmatrix};$$

$$\mathcal{N} \equiv kc/\omega\ .$$

For a Maxwellian plasma, the non-relativistic approximation of $\boldsymbol{Q}^{(e)}$ near the first cyclotron resonance is discussed in Section 3.

The dispersion equation of small plasma oscillations is:

$$\Delta(k) \equiv \det\boldsymbol{R}^{(e)} = 0. \qquad (7)$$

For a fixed real ω, it can be shown ([1]) that in the limit of rarefied plasma $\omega_p << \omega$, the dispersion equation (7) becomes biquadratic with respect to k, so there are only two solutions for k^2, denoted here by $k_\pm^2$, corresponding to the ordinary and extraordinary waves (refraction index values $\mathcal{N}_\pm \equiv k_\pm c/\omega$). Thus we have in this limit:

$$\Delta(k) = c^4(k^2 - k_+^2)(k^2 - k_-^2). \qquad (8)$$

2.2 The field propagator

Consider a statistical ensemble (the beam) of test particles with coordinates $\vec{r'}$, velocities $\vec{v'}$. One can introduce macroscopic fluctuating-current densities $j(t,\vec{r'})$, functions of time and $\vec{r'}$. To find the field radiated at frequency ω by a current fluctuation $j(t,\vec{r'})$, one has to invert (6) and then carry out contour integration over k and spatial integration over all sources $\vec{r'}$. The result is [1]: [1]

$$\begin{aligned} \boldsymbol{E}_\omega(\boldsymbol{r}) &= \int d^3r'\ \boldsymbol{W}\cdot\boldsymbol{j}^{(t)}_\omega(\vec{r'}),\ \text{with} \\ \boldsymbol{W} &= \frac{i\omega e^{i(\omega/c)r - i(\omega/c)\hat{r}\cdot\vec{r'}}}{c^4 r(k_+^2 - k_-^2)} \\ &\quad \left(\boldsymbol{\lambda}_+^{(e)}e^{-k_+''r_b} - \boldsymbol{\lambda}_-^{(e)}e^{-k_-''r_b}\right), \\ \hat{r} &\equiv \vec{r}/r, \end{aligned} \qquad (9)$$

where the elements of the matrix $\boldsymbol{\lambda}^{(e)}$ are the cofactors of $\boldsymbol{R}^{(e)}$, i.e. $(R^{(e)})^{-1} = \boldsymbol{\lambda}^{(e)}/\Delta$ and r_b denotes a point at the plasma boundary.

The indices $+$ and $-$ appear because during the contour integration the argument k in $\lambda^{(e)}_{i,j}(k,\omega)$ is substituted with $k_\pm$, where $k_\pm$ are the two roots out of four having positive imaginary part. The factor $(k_+^2 - k_-^2)$ in the denominator appears since, according to (8), $d\Delta/dk|_{k=k_\pm} = \pm 2c^4k_\pm(k_+^2 - k_-^2) \sim \pm 2\omega c^3(k_+^2 - k_-^2)$.

In the limit $\omega_p << \omega$ (same as for (8)), it can be shown that:

$$\boldsymbol{\lambda}_+^{(e)} - \boldsymbol{\lambda}_-^{(e)} = c^2(k_+^2 - k_-^2)(\boldsymbol{I} - \hat{r}\hat{r}), \qquad (10)$$

[1] This expression for the field has the correct asymptotic at $r \to \infty$. It has been assumed valid also in the vicinity of the source $\vec{r'}$.

where in the rotated frame $\vec{e_x}, \vec{e_y}, \vec{e_z}$, shown on Figure 1:

$$(\boldsymbol{I} - \hat{\boldsymbol{r}}\hat{\boldsymbol{r}}) = \begin{pmatrix} 1 & 0 \\ 0 & 1 \end{pmatrix}.$$

If we further take $e^{-k_{\pm}^{''} r_b} \to 1$, then W reduces to the vacuum propagator.

2.3 The spectral density of radiation S_ω

The power radiated in direction $\hat{r} = \vec{r}/r$ per unit area and per unit frequency interval is [1] (the bar indicates statistical average):

$$\begin{aligned} S_\omega &= \frac{c}{8\pi^2}\int_{-\infty}^{+\infty} d\tau e^{i\omega\tau}\overline{\boldsymbol{E}^*(\vec{r},t)\cdot\boldsymbol{E}(\vec{r},t+\tau)} \\ &= \frac{c}{8\pi^2}\,\overline{\boldsymbol{E}_{-\omega}(\vec{r})\cdot\boldsymbol{E}_\omega(\vec{r})}. \end{aligned} \tag{11}$$

We substitute here (9) and notice that the only dependence on $\vec{r'}$ is in the factor $e^{i(\omega/c)\hat{r}\cdot\vec{r'}}$. S_ω therefore contains the expression:

$$\frac{\int d^3r' \int d^3r^{''} \int_{-\infty}^{+\infty} d\tau e^{i\omega\tau} e^{i(\omega/c)\hat{r}\cdot(\vec{r'}-\vec{r''})} \times}{\overline{\boldsymbol{j}^{(t),*}(\vec{r'},t)\cdot\boldsymbol{j}^{(t)}(\vec{r''},t+\tau)}}\,, \tag{12}$$

where the advance from $\vec{r'}$ to $\vec{r''}$, during time interval τ, is along the unperturbed trajectory of the test particle. The above expression (12) (as a function of real ω) is equal to the spectral density $(\boldsymbol{j}^{(t)^*}\boldsymbol{j}^{(t)})_{\vec{k}=\frac{\omega}{c}\hat{r},\omega}$ of current fluctuations for a plasma in an external magnetic field, [1], [2]. It is also called non-interacting current correlator. Thus we obtain for S_ω:

$$S_\omega = \frac{c}{8\pi^2} Sp\, \boldsymbol{W}^+ \cdot (\boldsymbol{j}^{(t)\star}\boldsymbol{j}^{(t)})_{\vec{k}=\frac{\omega}{c}\hat{r},\omega}\cdot\boldsymbol{W} \tag{13}$$

2.4 The spectral density of test particle current

The spectral density $\boldsymbol{j}^{(t)}(\vec{k}=\frac{\omega}{c}\hat{r},\omega)$, or correlator $(\boldsymbol{j}^{(t)\star}\boldsymbol{j}^{(t)})_{\vec{k}=\frac{\omega}{c}\hat{r},\omega}$, can be obtained either directly, by Fourier-expanding the unperturbed test-particle motion, or by applying the dissipation-fluctuation theorem, [1],[2]. The latter theorem states that it equals the anti-hermitian part of the tensor $\boldsymbol{Q}$ defined above, but written for an ensemble of test particles instead of electrons. Also, according to the same theorem, $\boldsymbol{Q}^{(t)}$ should be taken in the limit of vanishing particle-particle interactions, so one has to use a vanishing imaginary part $\omega \to \omega - i\varepsilon$. Correspondingly, we replace the parameters q, m, $\vec{v}$, $f(\vec{v})$, Ω in (5) with the ones describing an "ensemble" of a single test particle with charge Ze, mass Am, momentum $m\vec{v_t}$, relativistic distribution function $f(\vec{v_t'}) = \delta(\vec{v_t'} - \vec{v_t})$ and cyclotron frequency $\Omega = ZeB_0/(Amc\gamma_t)$. The result is:

$$(\boldsymbol{j}^{(t)\star}\boldsymbol{j}^{(t)})_{\vec{k}=\frac{\omega}{c}\hat{r},\omega} = 1/2[\boldsymbol{Q}^{(t)} - \boldsymbol{Q}^{(t)+}]|_{\vec{k}=\frac{\omega}{c}\hat{r},\omega} = \tag{14}$$

$$= \frac{2\pi(Ze)^2}{\gamma_t^2}\sum_{n=-\infty}^{+\infty}\delta(\omega - n\Omega)\,\boldsymbol{T}_n(\vec{v_t})|_{\vec{k}=\frac{\omega}{c}\hat{r},\omega=n\Omega},$$

where use has been made of the formal equality:

$$\lim_{\varepsilon\to 0} Im\frac{1}{\omega - i\varepsilon - n\Omega} = -\pi\delta(\omega - n\Omega). \tag{15}$$

To simplify the tensor $\boldsymbol{T}_n(\vec{v_t})$, we first notice that $u_t = 0$, hence the elements in the third row and column of $\boldsymbol{T}_n(\vec{v_t})$ are zero. The remaining 2x2 part of the tensor, transformed in the rotated coordinate frame $\vec{e_x}, \vec{e_y}, \vec{e_z}$, is

$$\begin{aligned} &\boldsymbol{T}_n(\vec{v_t})|_{\vec{k}=\frac{\omega}{c}\hat{r},\omega} \\ &= \begin{pmatrix} \frac{n^2w_t^2}{z^2}J_n^2\cos^2\theta & \frac{inw_t^2}{z}J_nJ_n'\cos\theta \\ \frac{-inw_t^2}{z}J_nJ_n'\cos\theta & w_t^2{J'}_n^2 \end{pmatrix}_{\vec{k}=\frac{\omega}{c}\hat{r},\omega} = \\ &= \begin{pmatrix} j_{x,n}^2 & ij_{x,n}j_{y,n} \\ -ij_{x,n}j_{y,n} & j_{y,n}^2 \end{pmatrix} = \vec{j_n}^*\vec{j_n}, \end{aligned}$$

where

$$\vec{j_n} \equiv \begin{pmatrix} j_{x,n} \\ ij_{y,n} \end{pmatrix}; \tag{16}$$

$$\begin{aligned} j_{x,n} &\equiv j_{\pi,n} = \frac{nw_t}{z}J_n\cos\theta = \frac{n\Omega\gamma_t}{k_\perp}J_n\cos\theta \\ &= \frac{n\Omega\gamma_t}{\omega/c}\mathrm{ctg}\;\theta J_n = c\gamma_t\;\mathrm{ctg}\;\theta\,J_n; \\ j_{y,n} &\equiv j_{\sigma,n} = w_t{J'}_n = c\beta_t\gamma_t J_n' \end{aligned} \tag{17}$$

and the argument is

$$z = \omega w_t\sin\theta/(\gamma_t c\Omega) = nw_t c\sin\theta/\gamma_t = n\beta_t\sin\theta$$

(we have replaced ω with $n\Omega$ and used that $k_\parallel = \omega\cos\theta/c$ and $k_\perp = \omega\sin\theta/c$).

We will see (the Schott formula below) that $j_{\pi,n}$ and $j_{\sigma,n}$ are actually proportional to the π and σ-component of linear polarization of the electric vector of spontaneous radiation (harmonic n). Thus the electric vector is parallel to $\vec{j_n}$ and elliptically polarized ($|j_{\pi,n}| \neq |j_{\sigma,n}|$), with direction of rotation, left- or right- as given by the signs of the components of $\vec{j_n}$. For any n, these two components have equal sign for $\theta > 0$, and opposite signs if $\theta \to \pi - \theta$, i.e. the direction of polarization of the n-th harmonic is reversed. If one fixes the frequency seen by the observer to a real positive value $\omega > 0$, then for an observer above the median plane $\Omega > 0$, which means that positive n have to be taken in the sum because of the δ-function. Below the median plane ($\theta \to \pi - \theta$), Ω is negative and hence negative n values have to be taken, which leads both $j_{\pi,n}$ and $j_{\sigma,n}$ reversing their signs.

For S_ω we get from (13), (9) and (14) :

$$\begin{aligned} r^2 S_\omega &= \frac{\omega^2(Ze)^2}{4\pi c^7\gamma_t^2}\sum_{n=-\infty}^{+\infty}\delta(\omega - n\Omega)\frac{Sp}{|k_+^2 - k_-^2|^2} \\ &\left(\boldsymbol{\lambda}_+^{(e)}e^{-k_+^{''}r_b} - \boldsymbol{\lambda}_-^{(e)}e^{-k_-^{''}r_b}\right)^+\cdot\boldsymbol{T}_n(\vec{v_t})\cdot \\ &\cdot\left(\boldsymbol{\lambda}_+^{(e)}e^{-k_+^{''}r_b} - \boldsymbol{\lambda}_-^{(e)}e^{-k_-^{''}r_b}\right) \end{aligned} \tag{18}$$

2.5 The Schott formula

Here we derive the spectral density S^0_ω of spontaneous radiation of the test particle (as in vacuum, no cloud), emitted at angle θ with respect to the external magnetic field, called the Schott formula [5].

If the size of the plasma is much smaller than the absorption depth ($k^{''}_{\pm} r_b << 1$) then, by taking into account (10), (18) becomes:

$$\begin{aligned} r^2 S^0_\omega &= \frac{\omega^2 (Ze)^2}{4\pi c^3 \gamma_t^2} \sum_{n=-\infty}^{+\infty} \delta(\omega - n\Omega)(j^2_{\pi,n} + j^2_{\sigma,n}) \\ &= \frac{\omega^2 (Ze)^2}{4\pi c^3 \gamma_t^2} \sum_{n=-\infty}^{+\infty} \delta(\omega - n\Omega)(c^2\gamma_t^2 \ \mathrm{ctg}^2\ \theta\ J^2_n(z) \\ &\quad + w_t^2 J^{'\,2}_n(z)) = \\ &= \frac{(Ze)^2 \Omega^2}{2\pi c} \sum_{n=1}^{\infty} n^2 \left(\mathrm{ctg}^2\theta J^2_n(z) + \beta_t^2 J^{'\,2}_n(z) \right) \\ &\quad \delta(\omega - n\Omega), \end{aligned} \tag{19}$$

where $z = n\beta_t \sin\theta$. The term with $n = 0$ does not contribute and the terms with n and $-n$ are equal, giving a factor 2. In (19), $r^2 S^0_\omega$ is the the energy/sec, radiated at angle θ with respect to the external magnetic field, per unit solid angle and per unit frequency interval.

2.6 Integration of the Schott spectrum over frequencies and angles

We follow the standard integration procedure ([5], [6]) to obtain the total power radiated by the test particle (from now on we omit the subscript "t"). For a highly relativistic such particle $\gamma >> 1$, $\beta \approx 1$, the radiation is concentrated near the median plane: $\theta \approx \pi/2$. The order n of the Bessel functions is therefore nearly equal to their argument: $z = n\beta \sin\theta \sim n$ and one can use the asymptotic formulas:

$$\begin{aligned} J_n(z) &= \frac{\epsilon^{1/2}}{\pi\sqrt{3}} K_{1/3}\left(\frac{n}{3}\,\varepsilon^{3/2}\right), \\ J'_n(z) &= \frac{\varepsilon}{\pi\sqrt{3}} K_{2/3}\left(\frac{n}{3}\,\varepsilon^{3/2}\right), \end{aligned} \tag{20}$$

where $\varepsilon = 1 - z^2/n^2 = 1 - \beta^2 \sin^2\theta\ << 1$. We will only need the above expressions for large harmonics $n >> 1$, where the sum over n can be replaced by an integral, which is done by the following transformation from $n,\ \theta$ to new variables y, ψ:

$$\begin{aligned} \psi &= \gamma\cos\theta; & y &= \frac{2}{3}\, n\gamma^{-3}; \\ d\psi &= \gamma\, d\cos\theta; & dy &= \frac{2}{3}\, dn\gamma^{-3} \quad (dn = 1); \\ -\gamma &< \psi < \gamma; & 0 &< y < \infty. \end{aligned}$$

Here y measures the relative distance to the critical harmonic $\frac{3}{2}\gamma^3$ (nearly equal to the spectrum maximum), while ψ measures the angle between the direction vector of propagation of the radiation and the horizontal plane (in units of $1/\gamma$). In the arguments of K, ε is expanded over the small quantities $\cos\theta$ and $\sqrt{\varepsilon}_0 \equiv 1/\gamma$ and by keeping only terms of the order of $1/\gamma^2$:

$$\begin{aligned} \varepsilon &= \varepsilon_0 \left[1 + \left(\frac{\cos\theta}{\sqrt{\varepsilon}_0} \right)^2 + \ldots \right] \approx \varepsilon_0 \left(1 + \psi^2\right) = \\ &= \frac{1}{\gamma^2}\left(1 + \psi^2\right) \\ \mathrm{ctg}\theta &\approx \cos\theta = \frac{\psi}{\gamma}. \end{aligned}$$

By substituting (20) into (19) and integrating over angles and frequencies, the total power radiated W_0 is (here $\rho = c/\Omega$):

$$\begin{aligned} &2\pi \int_0^\infty d\omega \int_0^\pi d\theta \sin\theta\ r^2 S^0_\omega(\theta) = \\ &= \frac{(Ze)^2 c}{3\pi^2\rho^2} \int_0^\pi d\theta \sin\theta \sum_{n=1}^{\infty} n^2 \\ &\left[ctg^2\theta \varepsilon K^2_{1/3}\left(\frac{n}{3}\varepsilon^{3/2}\right) + \varepsilon^2 K^2_{2/3}\left(\frac{n}{3}\varepsilon^{3/2}\right)\right] = \\ &= \frac{27}{16\,\pi^2} W_0 \int_0^\infty y^2 dy \int_{-\gamma}^{+\gamma} d\psi \\ &\left[\psi^2(1+\psi^2) K^2_{1/3}(\eta) + (1+\psi^2)^2 K^2_{2/3}(\eta)\right] = \\ &= W_0 \left(\frac{1}{8} + \frac{7}{8} \right) = W_0, \end{aligned} \tag{21}$$

where $\eta = \frac{1}{2}\ y\ (1+\psi^2)^{3/2}$ and $W_0 = \frac{2}{3}\frac{Z^2 e^2 c}{\rho^2}\gamma^4$. ($\gamma$ is replaced with infinity in the upper limit of integration over ψ, because the K functions are nonzero only for argument of the order of unity).

The frequency radiated $\omega\ (= n\Omega)$, which corresponds maximum of the spontaneous synchrotron radiation spectrum is $\simeq (3/2)\Omega\gamma^3$ meaning that the expression under the integral sign in (21), as a function of $y \equiv \frac{2}{3}\frac{\omega}{\Omega\gamma^3}$, reaches its maximum at $y \simeq 1$.

The π mode (first term) is radiated in directions above and below the median plane and becomes zero in the plane (the factor ψ^2). For the σ mode, the radiation is centered in the median plane and its total contribution is 7 times larger.

3 ESTIMATION OF THE ABSORBED POWER FOR A MAXWELLIAN CLOUD

3.1 Wave absorption at frequencies near the first cyclotron resonance

We consider a rarefied plasma $q << 1$ with electronic temperature $T_e \sim 100\ eV$ ($\beta_e \equiv \bar{v}_e/c \sim 0.01$). We assume that:

$$\left(\frac{\omega_p}{\omega}\right)^2 \frac{1}{\beta_e} = \frac{q}{n^2\beta_e} << 1 \tag{22}$$

is fulfilled for all harmonics n of $\omega = n\ \Omega_e$, even at the cyclotron resonance $n = 1$. For frequencies in the vicinity

of the first cyclotron resonance, the dielectric tensor (5) has the form ([2], [7]):

$$Q = \begin{pmatrix} -\frac{q}{4}+\sigma & \frac{iq}{4}+i\sigma & 0 \\ \frac{-iq}{4}-i\sigma & -\frac{q}{4}+\sigma & 0 \\ 0 & 0 & -q \end{pmatrix} \qquad (\sigma >> q)$$

$$\sigma = i\sqrt{\frac{\pi}{8}}\frac{\omega_p^2}{\omega^2\beta_e\cos\theta}\, w(z_1),$$
$$w(z_1) = e^{-z_1^2}\left(\frac{\cos\theta}{|\cos\theta|} + \frac{2i}{\sqrt{\pi}}\int_0^{z_1} e^{y^2}dy\right), \tag{23}$$

where $w(z)$ is the probability integral (error function of complex argument).

In more details, for Maxwellian distribution, the n-th member of the sum in (5) ($n = \pm 1 \pm 2\ldots$) is proportional to $e^{-z_n^2}$ with $z_n \equiv \frac{\omega - n|\Omega_e|}{\sqrt{2}\omega\beta_e\cos\theta}$. As ω approaches $|\Omega_e|$, the contribution to the tensor of the member (term) with $n = 1$ is the largest since $e^{-z_1^2} \sim 1$. This term is is caused by "normal Doppler effect", i.e. presence of electrons rotating in the same direction as the ω-harmonic and with velocities nearly equal to its phase velocity (for which $\omega - |\Omega_e| \approx (u/c)\,\omega\cos\theta$). For the other members of the sum, including the one with $n = -1$, produced by a harmonic rotating opposite to the electrons, $|z_n| >> 1$, so their contribution is exponentially small (their total contribution is $\sim q$). The picture is the same for higher resonances with $|\sigma_n|$ rapidly decreasing (roughly as $1/n!$).

By keeping only the resonance σ terms, the tensor Q becomes 2-dimensional and after transforming it into to frame $\vec{e_x}, \vec{e_y}, \vec{e_z}$ and substituting it into (6), one gets:

$$\boldsymbol{R}^{(e)} = \omega^2 \begin{pmatrix} \mathcal{N}^2 - 1 + \sigma\cos^2\theta & i\sigma\cos\theta \\ -i\sigma\cos\theta & \mathcal{N}^2 - 1 + \sigma \end{pmatrix}, \tag{24}$$

where

$$\mathcal{N} \equiv kc/\omega\ .$$

The determinant is ($\mathcal{N}_\pm \equiv k_\pm c/\omega$):

$$\Delta = \omega^4(\mathcal{N}^2 - \mathcal{N}_+^2)(\mathcal{N}^2 - \mathcal{N}_-^2), \tag{25}$$

where the roots are:

$$\mathcal{N}_-^2 = 1; \quad \mathcal{N}_+^2 = 1 - \sigma(1+\cos^2\theta). \tag{26}$$

As expected, in our approximation the ordinary wave propagates as in vacuum. The matrices $\lambda_\pm^{(e)}$ are computed by taking $\lambda^{(e)} \equiv (R^{(e)})^{-1}\,\Delta$ and substituting there $\mathcal{N}_\pm$ from (26). The result is:

$$\boldsymbol{\lambda}_+^{(e)} = \omega^2\sigma\begin{pmatrix} -\cos^2\theta & -i\cos\theta \\ i\cos\theta & -1 \end{pmatrix}, \tag{27}$$

$$\boldsymbol{\lambda}_-^{(e)} = \omega^2\sigma\begin{pmatrix} 1 & -i\cos\theta \\ i\cos\theta & \cos^2\theta \end{pmatrix}, \tag{28}$$

which can also be written as:

$$\boldsymbol{\lambda}_\pm^{(e)} = \vec{e}_\pm\vec{e}_\pm^{\,*}\ Sp\ \lambda_\pm^{(e)}; \qquad Sp\ \lambda_\pm^{(e)} = \mp(1+\cos^2\theta), \tag{29}$$

where the eigen-vectors are:

$$\vec{e}_+ \equiv \frac{\begin{pmatrix} -\cos\theta \\ i \end{pmatrix}}{\sqrt{1+\cos^2\theta}} \quad \vec{e}_- \equiv \frac{\begin{pmatrix} 1 \\ i\cos\theta \end{pmatrix}}{\sqrt{1+\cos^2\theta}}. \tag{30}$$

Thus the columns of $\boldsymbol{\lambda}_\pm^{(e)}$ are proportional to the components of the electric field vectors $\vec{E}_\pm$ of the two eigen-solutions called extraordinary (+) and ordinary ($-$) plasma waves. The extraordinary wave electric field vector $\vec{E}_+$ is parallel to $\vec{e}_+$ and rotates in the same direction as the electrons.

It can be shown [2], that (29) is always fulfilled for nearly transparent media (when the anti-hermitian part of $\boldsymbol{Q}$ is small compared to its hermitian part) .

One can also check directly that (10) is indeed fulfilled:

$$\frac{1}{\omega^2}\,\frac{\boldsymbol{\lambda}_+^{(e)} - \boldsymbol{\lambda}_-^{(e)}}{\mathcal{N}_+^2 - \mathcal{N}_-^2} = \frac{\boldsymbol{\lambda}_+^{(e)} - \boldsymbol{\lambda}_-^{(e)}}{c^2(k_+^2 - k_-^2)} = \begin{pmatrix} 1 & 0 \\ 0 & 1 \end{pmatrix}. \tag{31}$$

3.2 Estimation of the absorbed power

The roots $k_\pm$ and the cofactors $\boldsymbol{\lambda}_\pm$ are found in the previous section. By using some properties of $\boldsymbol{\lambda}_\pm$:

$$\boldsymbol{\lambda}_\pm.\boldsymbol{\lambda}_\mp = 0$$
$$\frac{\boldsymbol{\lambda}_+^+.\boldsymbol{\lambda}_+}{\omega^4\sigma^2} = (1+\cos^2\theta)\begin{pmatrix} \cos^2\theta & i\cos\theta \\ -i\cos\theta & 1 \end{pmatrix},$$
$$\frac{\boldsymbol{\lambda}_-^+.\boldsymbol{\lambda}_-}{\omega^4\sigma^2} = (1+\cos^2\theta)\begin{pmatrix} 1 & -i\cos\theta \\ i\cos\theta & \cos^2\theta \end{pmatrix},$$

and also the spectral density (16) of the test particle current $\vec{j_n}$, (18) is transformed as follows:

$$\begin{aligned} r^2 S_\omega =& \frac{\omega^2(Ze)^2}{4\pi c^7\gamma^2}\sum_{n=-\infty}^{+\infty}\frac{\delta(\omega - n\Omega)}{|k_+^2 - k_-^2|^2}\times \\ &\times Sp\left(\boldsymbol{\lambda}_+^+.\boldsymbol{\lambda}_+.\, e^{-2k_+^{''}r_b} + \boldsymbol{\lambda}_-^+.\boldsymbol{\lambda}_-.\, e^{-2k_-^{''}r_b}\right).\vec{j_n}^{\,*}\vec{j_n} \\ =& \frac{\omega^2(Ze)^2}{4\pi c^3\gamma^2}\sum_{n=-\infty}^{+\infty}\frac{\delta(\omega - n\Omega)}{1+\cos^2\theta}\times \\ &\times\Big[(j_{\pi,n}\cos\theta + j_{\sigma,n})^2\, e^{-2k_+^{''}r_b} \\ &+(j_{\pi,n} - j_{\sigma,n}\cos\theta)^2\, e^{-2k_-^{''}r_b}\Big] \end{aligned} \tag{32}$$

We will interpret (32), integrated over real and positive frequencies ω and angles $0 < \theta < \pi$, as the energy per second radiated by an *electron* in presence of *electron* plasma. If the beam particle and particles of the cloud has opposite sign, then the roles of ordinary extraordinary waves are reversed and correspondingly one has to exchange the indices $+$ and $-$ of $k^{''}$ in the two exponents.

With this in mind, we substitute r_b with the propagation length L within the cloud and expand the exponents $e^{-2k_{\pm}^{''}L} \approx 1-2k_{\pm}^{''}L$. This can only be done for small optical depth $k_{+}^{''}L \sim \frac{2\pi qL}{\beta_e \lambda} << 1$, which is true for $\beta_e \sim 0.01$ and the parameters in Table 1. The unity produces the spontaneous spectrum (19) while the terms $-2k_{\pm}^{''}L$ with their signs inverted yield:

$$\frac{\omega^2 (Ze)^2}{2\pi c^3 \gamma^2} \sum_{n=-\infty}^{+\infty} \frac{\delta(\omega - n\Omega)}{1+\cos^2\theta} \Big[(j_{\pi,n}\cos\theta + j_{\sigma,n})^2 \; k_{\pm}^{''} L + (j_{\pi,n} - j_{\sigma,n}\cos\theta)^2 \; k_{\mp}^{''} L \Big] \quad (33)$$

where the upper sign applies if a negatively charged beam travels through the electron cloud, and the lower sign refers to a positive beam charge as in the LHC, and

$$j_{\pi,n} = c\gamma \; ctg\; \theta \; J_n; \; j_{\sigma,n} = c\gamma J_n',$$

$$\begin{aligned} k_{+}^{''}(\omega,\theta)L =& \frac{\omega L}{2\,c} \; \mathrm{Im}\, \mathcal{N}_{+}^2 = \\ =& \frac{1}{4}\sqrt{\frac{\pi}{2}} \; \frac{\Omega_e^2}{\omega} \frac{qL}{\beta_e c} \; \frac{1+\cos^2\theta}{\cos\theta} \; \times \\ & \times \; \boldsymbol{e}^{-\left(\frac{\omega - |\Omega_e|}{\sqrt{2}\omega\beta_e \cos\theta}\right)^2} \sim \frac{qL}{\beta_e \lambda}; \end{aligned} \quad (34)$$

$$k_{-}^{''}(\omega,\theta)L \sim \frac{qL}{\lambda} \; \boldsymbol{e}^{-\left(\frac{\omega - |\Omega_e|}{\sqrt{2}\omega\beta_e \cos\theta}\right)^2}$$

$$(\text{ where } \lambda \equiv 2\pi c/\omega; \; \omega = n\Omega \approx \Omega_e).$$

Since $k_{-}^{''}$ is β_e times smaller than $k_{+}^{''}$ we only show its order of magnitude. It is easy to compute it, if the q terms in $\boldsymbol{Q}$ are kept, [2].

We choose the cyclotron frequency of the test particle to be positive for an observer above the median plane $\Omega > 0$. Since $\omega > 0$, only positive n contribute. For each n, there are two contributions – scalar products (squared) between $\vec{j}_n$ and the unit vectors $\vec{e}_+$ and $\vec{e}_-$ of the counterclockwise and clockwise rotating plasma waves. Thus the elliptically polarized synchrotron radiation wave interacts with both extraordinary and ordinary plasma modes. This is because the elliptical polarization can be decomposed into a left- and right- circular polarizations.

1) In the hypothetic case – the test particle being an electron in electron cloud, the current $\vec{j}_\omega$ has counterclockwise polarization [2] and an observer located above the median plane ($\cos\theta > 0$), sees counterclockwise rotating both beam and plasma electrons.

By setting $k_{-}^{''} = 0$ (taking only the first term), and noticing that n, $\cos\theta$, $j_{\pi,n}$ and $j_{\sigma,n}$ are all positive, we see that the contributions from σ and π modes add up (stronger absorption).

2) For a proton or positron in an electron cloud, by setting $k_{-}^{''} = 0$ (taking only the second term), the contributions from the σ and π modes partially compensate each other. The factor $1/\cos\theta$ in $k_{+}^{''}$ is canceled and both modes participate with a factor $\cos\theta \sim \gamma^{-1}$. The absorption occurs away from the median plane (zero in the plane). For this case the integration is carried out below.

We take only the second term in (33) and integrate over angles and frequencies, same as this was done for (21) (here $W_0 y_0 = \gamma\Omega_e/\rho$):

$$\begin{aligned} & 2\pi \int_0^\infty d\omega \int_0^\pi d\theta \sin\theta \times \frac{\sqrt{\pi}}{4\sqrt{2}} \; \frac{(Ze)^2 \; \Omega_e^2 \; qL}{\rho \; c \; \beta_e} \; \times \\ & \times \sum_{n=1}^{\infty} n|\cos\theta| \left(\frac{J_n}{\sin\theta} - J_n' \right)^2 \; \boldsymbol{e}^{-\left(\frac{\omega - |\Omega_e|}{\sqrt{2}\omega\beta_e \cos\theta}\right)^2} = \\ & = \frac{\sqrt{\pi}}{2\sqrt{2}} \frac{1}{3\pi^2} \left(\frac{3}{2}\right)^4 \frac{\Omega_e}{c} \; \frac{qL}{\beta_e} \; W_0 \; y_0 \; \gamma \; \times \\ & \times \int_0^\infty y dy \int_0^{+\gamma} d\psi \psi \; \times \\ & \times \left[\sqrt{1+\psi^2} K_{1/3}(\eta) \; - \frac{1+\psi^2}{\gamma} K_{2/3}(\eta) \right]^2 \boldsymbol{e}^{-\boldsymbol{z}^2} \approx \\ & \approx 0.3 \; \frac{\Omega_e}{c} \; q \; L \; W_0 \; y_0^{4/3} \; , \end{aligned} \quad (35)$$

where

$$\begin{aligned} \boldsymbol{z} &= \frac{n\,\Omega - \Omega_e}{\sqrt{2}\; n\,\Omega\; \beta_e\; \cos\theta} = \; \frac{y - y_0}{\sqrt{2}\; y \beta_e \psi/\gamma} \; = \\ &= \frac{1}{\psi\Delta} \left(1 - \frac{y_0}{y} \right), \\ \Delta &\equiv \sqrt{2}\beta_e/\gamma, \quad y_0 = \; \frac{2\Omega_e}{3\Omega\gamma^3}. \end{aligned} \quad (36)$$

Thus we have neglected the term with $K_{2/3}$, because of the factor $1/\gamma$ and have only estimated the term $K_{1/3}$ (π mode) in the following way (confirmed with direct numerical integration for γ up to 300):

$$\begin{aligned} & \int_0^\infty y dy \int_0^{+\gamma} d\psi \psi (1+\psi^2) K_{1/3}^2(\eta) \; \boldsymbol{e}^{-\boldsymbol{z}^2} \sim \\ & \sim y_0^2 \Delta \int_0^{+\gamma} d\psi \psi^2 (1+\psi^2) K_{1/3}^2(\eta_0) \approx \\ & \approx \frac{\pi}{\sqrt{3}\; 2^{1/3}} \; \Gamma(2/3) \; \Delta \; y_0^{1/3} \end{aligned} \quad (37)$$

(here $\eta_0 = \frac{y_0}{2}(1+\psi^2)^{3/2}$).
We have used the following integral:

$$\begin{aligned} & \int_{-\infty}^{+\infty} d\psi \psi^2 (1+\psi^2) K_{1/3}^2(\eta_0) = \\ & = \frac{\pi}{\sqrt{3}\; y_0} \left[\int_{y_0}^\infty K_{5/3}(x) dx + K_{2/3}(y_0) \right] \approx \\ & \approx \frac{\pi}{\sqrt{3}\; y_0} \left[\frac{3}{2} \; 2^{2/3} \; \Gamma(5/3) \; y_0^{-2/3} - 2^{-1/3} \; \Gamma(2/3) \; y_0^{-2/3} \right] = \\ & = \frac{\pi}{\sqrt{3}\; 2^{1/3}} \; \Gamma(2/3) \; y_0^{-5/3} \end{aligned} \quad (38)$$

[2] meaning that $j_{\pi,n}$ and $j_{\sigma,n}$ have the same sign, so the vector $\begin{pmatrix} x(t) \\ y(t) \end{pmatrix} = Re\; \vec{j}_\omega e^{i\omega t}$ rotates counterclockwise

$$K_\nu(y_0) \approx 2^{\nu-1}\Gamma(\nu)\, y_0^{-\nu} \quad (y_0 << 1).$$

According to (35), the fraction of deposited energy is

$$\frac{\Delta W}{W_0} \approx 0.3\, \frac{\Omega_e}{c}\, q\, L\, y_0^{4/3} \approx \frac{L}{\lambda}\, q\, y_0^{4/3}.$$

This expression scales with the beam energy as $\gamma^{-8/3}$. If the propagation length within the cloud L is fixed, it is inversely proportional to the magnetic field B_0. If L varies according to $L \sim \rho/\gamma$, then the dependence is stronger: $\sim B_0^{-2}$.

LHC parameters

The values of the density parameter q in Table 1 correspond to pessimistic (large) electron density $N_0 = 10^6\ [cm^{-3}]$ (q scales as N_0) and the propagation length within the cloud is taken to be $L \approx 10\ m$. For LHC circulating beam current $\sim 0.5\ A$, the total radiated power is $W_0 \approx 0.06$ W at injection and 3.6 kW at collision, hence the absolute deposited power per beam is negligible.

Table 1: Fraction of deposited energy with LHC parameters.

	p^+ collision	p^+ injection
γ	7460	480
B_0	83860	5390
$\omega = \Omega_e$	$1.5\ 10^{12}$	$9.5\ 10^{10}$
$\lambda[cm]$	0.1	2
Ω	$1.08\ 10^6$	$1.08\ 10^6$
y_0	$2\ 10^{-5}$	$5\ 10^{-3}$
$q\ (N_0 = 10^6\ [cm^{-3}])$	1.510^{-9}	3.510^{-7}
$\Delta W/W_0\ (L = 10\ m)$	$\sim 10^{-12}$	$\sim 10^{-8}$

4 SUMMARY AND CONCLUSIONS

An expression (corrected Schott formula) has been derived for the synchrotron radiation spectrum produced by a relativistic particle, which traverses a large (w.r.t. the wavelength) volume of magnetized plasma (electron cloud in accelerator bending magnet). We have estimated the fraction of absorbed power at frequencies near the first cyclotron resonance due to the presence of resonance electrons (Cherenkov resonance). We found that:

– the absorption would have been stronger in case of an electron traversing an electron cloud, since in such case the stronger σ mode of linear-polarization components of spontaneous radiation decays as (couples with) the extraordinary wave;

– for the realistic case of positively charged beam particle, the absorption occurs away from the median plane and is caused by coupling between the π mode and the extraordinary wave;

– for the case of LHC, both the absorbed power and the effect on the radiated spectrum are negligible.

Our estimations are based on a collisionless plasma model for the cloud, typical (LHC) density and temperature parameters, and Maxwellian velocity distribution of the electrons.

Acknowledgments: D. Kaltchev is grateful to the AP group at CERN for its hospitality, to F. Ruggiero for the support of this work, and to his former supervisor E. Perelstein.

5 REFERENCES

[1] David E. Baldwin, Ira B. Bernstein, M. P. H. Weenik, *Kinetic theory of plasma waves in magnetic field* in Advances in Plasma Physics, Vols. 3 and 4, Interscience Publishers, 1969, 1971.

[2] A.I. Achiezer, I.A. Achiezer et all, *Plasma Electrodynamics*, Pergamon Press, 1975.

[3] A.G. Sitenko, K.N. Stepanov, JITP, **31**, 642-651 (1956).

[4] Ronald C. Davidson, *Kinetic Waves and Instabilities in a Uniform Plasma*, Handbook of Plasma Physics, Eds. M.N. Rosenbluth and R.Z. Sagdeev; Volume 1: Basic Plasma Physics I, North Holland Publishing 1983.

[5] A.A. Sokolov, I.M. Ternov, *Synchrotron Radiation*, Pergamon Press, first edition in 1968.

[6] A. Hofmann, *Characteristics of synchrotron radiation*, Cern Accelerator School, CAS CERN 98-04.

[7] G. Bekefi, *Radiation processes in plasmas*, 1966.

[8] Trubnikov B.A., Dissertation, MIFI, 1958.

[9] Drummond W., Rosenbluth M.N., Phys. Fluids, **6**, 276 (1963).

Kinetic Theory of Periodic Holes in Debunched Particle Beams

J.-M. Grießmeier, H. Schamel *, Physikalisches Institut, Universität Bayreuth, D-95440 Bayreuth, Germany; Renato Fedele, Dipartimento di Scienze Fisiche, Università "Federico II" and INFN, Complesso Universitario di M.S. Angelo, I-80126 Napoli, Italy

Observations as well as numerical simulations of coasting hadron beams in circular accelerators and storage rings have revealed the excitation of long-lived coherent structures superimposed on the beam. Such beams, which are interacting with the electromagnetic fields induced by the ring environment, can develop holes (or notches) in the longitudinal distribution function and in the associated line density at thermal velocities where linear wave theory would predict strong Landau damping. It is hence a nonlinear kinetic feature of the VLASOV-POISSON system which is responsible for this ubiquitous phenomenon in beam and plasma physics.

In our contribution we report about recent progress [1-6] in the theoretical understanding of these holes, including those structures found recently at the CERN PSB [7].

We show how the VLASOV-POISSON system can be solved self-consistently in the small amplitude, steady state limit. The method, which was proposed by one of the authors earlier [8], consists first in solving the VLASOV equation in terms of the constants of motion (one of which is the single particle energy $H = \frac{mv^2}{2} + q\Phi$), from which the line density as a functional of the electrostatic potential Φ can be obtained by a velocity (momentum) integration of the distribution function. In the second step, POISSON's equation, being a second order ordinary differential equation in the resistive or purely reactive case, can be solved easily for given boundary conditions.

The analysis reveals new intrinsic modes which owe their existence to a deficiency of particles trapped in the self-sustained potential well, showing up as notches in the thermal range of the distribution function, see Fig. 1.

Several conclusions can be drawn immediately:

1) resonant (trapped) particles require a full nonlinear analysis ($\frac{q}{m}E\partial_u f_1$ is of the same order as $\frac{q}{m}E\partial_u f_0$, namely $O(\Psi)$, where $f_1 \equiv f - f_0$ and $E = -\partial_z\Phi$, f_0 is the undisturbed and f the actual distribution function), no matter how small the amplitude Ψ is;

2) the linear wave spectrum, obtained by a Landau (Keil-Schnell-Ruggiero-Vaccaro) or a van Kampen analysis, is incomplete even in the small amplitude limit and hence does not provide an appropriate basis for a general wave theory, as it is usually assumed;

3) for their existence in plasmas, holes do not require a linear instability as they can be excited nonlinearly even in linearly stable regimes due to their property of being negative energy modes [9].

* Electronic address: hans.schamel@uni-bayreuth.de

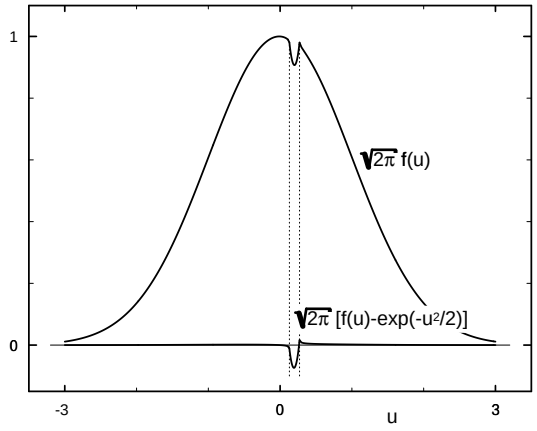

Figure 1: The distribution function $f(u)$ and its deviation from the unperturbed distribution $f_0(u)$ at potential maximum.

In beam physics, holes are reported in bunched beams, as well, and the presence of an e-cloud may provide a similar environment for a nonlinear destabilization of the beam by the negative energy concept as in plasma physics. Of interest seems to be also a non-perturbative finite amplitude analysis of holes in beams, as it was carried out in plasma physics (see [10] and the references cited therein).

Acknowledgment: This work is supported by DAAD (Deutscher Akademischer Austauschdienst) and CRUI (Conferenza dei Rettori delle Universita Italiane) within the research program "VIGONI" between the University of Bayreuth and the University Federico II of Napoli.

1 REFERENCES

[1] H. Schamel, *Phys. Rev. Lett.* **79**, 2811 (1997).
[2] H. Schamel, *Phys. Scr.* **T75**, 23 (1998).
[3] H. Schamel, in *Nonlinear and Stochastic Beam Dynamics in Accelerators: A Challenge to Theoretical and Computational Physics, Lüneburg, 1997* (DESY, Hamburg, Germany, 1998), pp. 224-235.
[4] H. Schamel and R. Fedele, in *Proceedings of the 7th European Particle Accelerator Conference, Vienna, 2000*, http://accelconf.web.cern.ch/Accelconf/e00/index.html.
[5] H. Schamel and R. Fedele, *Phys. Plasmas* **7**, 3421 (2000).
[6] J.-M. Grießmeier, H. Schamel and R. Fedele, *Phys. Rev. ST Accel. Beams* **5**, 024201 (2002).

[7] S. Koscielniak, S. Hancock and M. Lindroos, *Phys. Rev. ST Accel. Beams* **4**, 044201 (2001).
[8] H. Schamel, *Plasma Phys.* **14**, 905 (1972).
[9] J.-M. Grießmeier and H. Schamel, *Phys. Plasmas* **9**, June 2002.
[10] H. Schamel, *Phys. Rep.* **140**, 161 (1986).

Electron cloud effects in intense, ion beam linacs theory and experimental planning for heavy-ion fusion

A. W. Molvik,* R. H. Cohen,† S. M. Lund,† F.M. Bieniosek,‡ E.P. Lee,‡ L.R. Prost,‡ P.A. Seidl,‡ and Jean-Luc Vay‡
Heavy-Ion Fusion Virtual National Laboratory
(Dated: May 18, 2002)

Heavy-ion accelerators for heavy-ion inertial fusion energy (HIF) will operate at high aperture-fill factors with high beam current and long durations. (Injected currents of order 1 A and 20 μs at a few MeV for each of ~100 beams, will be compressed to the order of 100 A and 0.2 μs, reaching GeV energies in a power plant driver.) This will will be accompanied by beam ions impacting walls, liberating gas molecules and secondary electrons. Without special preparation, the ~10% electron population predicted for driver-scale experiments will affect beam transport; but wall conditioning and other mitigation techniques should result in substantial reduction. Theory and particle-in-cell simulations suggest that electrons, from ionization of residual and desorbed gas and secondary electrons from vacuum walls, will be radially trapped in the ~4 kV ion beam potential. Trapped electrons can modify the beam space charge, vacuum pressure, ion transport dynamics, and halo generation, and can potentially cause ion-electron instabilities. Within quadrupole (and dipole) magnets, the longitudinal electron velocity is limited to drift velocities ($E \times B$ and ∇B) and the electron density can vary azimuthally, radially, and longitudinally. These variations can cause centroid misalignment, emittance growth and halo growth. Diagnostics are being developed to measure the energy and flux of electrons and gas evolved from walls, and the net charge and gas density within magnetic quadrupoles. We will also measure the depth of trapping of electrons, their axial and radial transport, and the effects of electrons on the ion beam.

I. INTRODUCTION

Electron clouds have limited the performance of many positive beam rings [1–3]. We have initiated a program to determine whether they can also be dangerous in a linac. There are three main reasons for concerns with heavy-ion fusion (HIF) induction linacs: HIF injectors produce beams with line charges of ~0.2 μCoul/m resulting in several kilovolt beam potentials, which can strongly confine electrons; injected pulses have a flattop duration of ~20 μs which allows time for gas desorbed from walls by beam halo to reach the beam; and finally HIF has an economic incentive to minimize induction-core mass by fitting beam tubes tightly to the beams; how tightly may be limited by the increased generation of gas and electrons from ion bombardment of walls and reduced time for these to reach the beam.

Induction accelerators were chosen by the USA program to develop as drivers for HIF inertial fusion energy power plants because they are capable of accelerating beams currents of 10^2 to 10^4 A that are required to deliver several megajoules of energy to a target with GeV range ions [4]. In induction accelerators, the axial acceleration gaps between beam-tube arrays are surrounded by induction cores. The core mass can be reduced by reducing the diameter of the multiple beam array inside the cores, allowing smaller inner and outer core diameters for the same cross-sectional area (therefore the same volt-seconds from Faraday's Law). Reducing the beam tube diameters is beneficial because the total mass of induction cores in an inertial fusion power plant is predicted to be in the range of 10-30 $\times$ 10^6 kg, making this a major cost area [5]. HIF induction accelerators are at an early stage of development. The parameters listed in this paper represent todays concepts, which are expected to evolve.

Heavy-ion beams will be injected with about 20 μs flat top duration, and with rise and fall times of a fraction of a microsecond [5]. To maintain the flattop against space-charge driven longitudinal expansion, rapidly ramped-pulses are applied at frequent intervals to the head of the beam to slow ions there and to the tail of the beam to accelerate lagging ions. As the beams are accelerated, other ramped pulsers place a velocity tilt on them, to compress their duration and to maintain the beam current near the transport limit of magnetic quadrupoles. Minimizing the pulse duration increases the cost effectiveness of induction acceleration, providing the required volts of acceleration from a smaller volt-seconds cross-sectional area of induction cores. [New concepts are desirable for injection and low-energy transport, that would allow use of higher beam currents for shorter durations (and possibly in fewer beams) to inject the required number of ions. Such concepts would further reduce the mass of induction cores in a driver.]

The behavior of electrons in these flattopped beams will be similar to those in filled storage rings. In particular, the multipactor mechanism for electron generation and acceleration by bunched beam trains should not be present [1]. Ionization of gas is expected to be the domi-

*molvik1@llnl.gov; Lawrence Livermore National Laboratory, Livermore, CA 945500, USA
†Lawrence Livermore National Laboratory, Livermore, CA 945500, USA
‡Ernest Orlando Lawrence Berkeley National Laboratory, 1 Cyclotron Road, Berkeley, CA 94720, USA

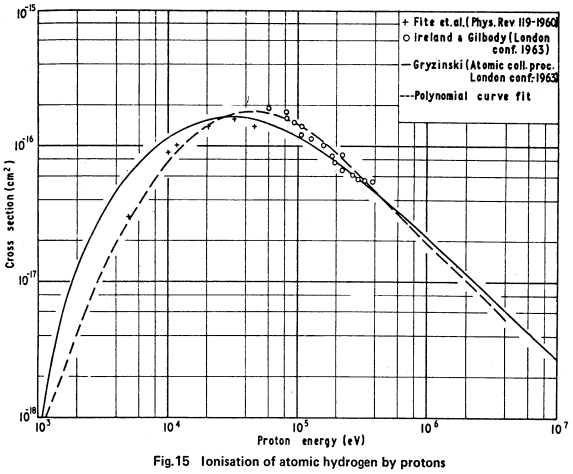

FIG. 1: The cross section for the ionization of atomic hydrogen by protons is shown as indicative of approximate ionization cross sections for typical background and adsorbed gases in vacuum systems, when heavy ion beam energies are normalized to the energy per nucleon [6].

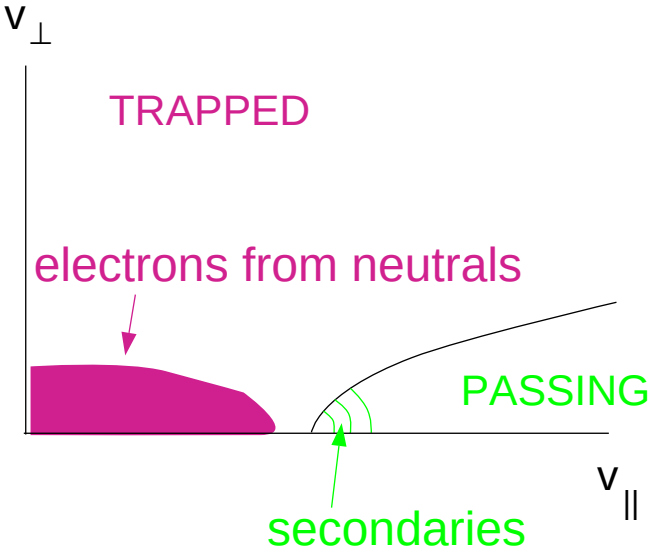

FIG. 2: (Color) Velocity space diagram of electron confinement in a magnetic field, shown at the potential peak on the beam axis. Secondary electrons from the wall are born untrapped, and can be weakly trapped by non-adiabaticity or instabilities. Electrons from the ionization of gas by collision with beam ions are born trapped, the depth of trapping depends on the radial location of the ionization event.

nant electron source term that leads to trapped electrons.

The present HIF experiments use potassium ion beams at energies of 0.5-1.8 MeV. The High-Curent Experiment (HCX) is studying coasting K^+ beams injected with 0.2-0.5 A at 1.0-1.8 MeV, these energies corresponding to 25-45 keV/nucleon. The peak beam potential will range from 2 to 4.5 kV, and the flattop duration is currently 4 μs, with rise and fall times in the range of 1 μs.

The interaction of HCX beams with gas is expected to be similar to that of a proton beam with atomic hydrogen gas, as shown in Fig. 1 [6]. The present range of energies, 25-45 keV/nucleon is near the peak cross section for ionization of background gas. Above ~200 keV/nucleon, the cross sections decrease almost linearly with beam energy. For HIF, the maximum energy needed at the target is in the range of 10-20 MeV/nucleon [7], where the cross sections are two orders of magnitude below the peak. High-energy physics accelerators typically are three to six orders of magnitude higher than this in beam energy per nucleon, with ionization cross sections nearly three to six orders of magnitude smaller than the minimum in HIF drivers.

II. THEORY - INITIAL RESULTS

We have studied the confinement of electrons by positive potential particle beams primarily within a series of quadrupole magnets. It became apparent that the electron confinement by a beam in quadrupole magnets is similar to that in our previous studies of electron confinement by magnetic-mirror confined, hot-ion plasmas [8, 9].

Electrons in a magnetic field will have a conserved magnetic moment, if they have a gyroradius which is small compared with the gradient scale length of the magnetic field. The magnetic moment is given by

$$\mu = \frac{v_\perp^2}{2B} \qquad (1)$$

where $v_\perp$ is the electron velocity perpendicular to the magnetic field of magnitude B. As a result, electrons which, at the minimum-field-strength point along a field line, have large pitch angles and/or low energies, are confined by the combination of electrostatic and magnetic fields, as shown in Fig. 2. Electrons born at the walls (secondaries) have high energy and small pitch angle at the field minimum, and so are untrapped; electrons born in the beam interior (from ionization of neutrals) are born electrostatically trapped.

This picture is only approximately correct, as electrons in a quadrupole magnetic field undergo jumps in the magnetic moment. These are negligible for field lines far from the axis. But untrapped electrons that pass moderately close to the axis can get trapped by this process and remain so for up to several hundred bounce times, ~1 μs.

In magnetic fields, high enough that the electron gyroradius is small compared with the beam and tube radii, the flow of electrons parallel to the magnetic field is at the kinetic velocity, modified by conservation of the magnetic moment, Eq. 1. The flow of electrons perpendicular to the magnetic field is restricted to the sum of the $E \times B$ and ∇B velocities. In a uniform magnetic field with no electric field, the electron orbit projection on a plane normal to B would be closed circles. An electric field or a

magnetic field gradient opens these circles, resulting in a net drift velocity. These drift velocities are given by

$$v_{E\times B} = \frac{E \times B}{B^2} \tag{2}$$

and

$$v_{\nabla B} = \frac{m}{qB^4}\left(v_{\|}^2 + \frac{v_{\perp}^2}{2}\right)\left[B \times \nabla\frac{B^2}{2}\right] \tag{3}$$

where we have included the curvature drift ($v_{\|}^2$ term) along with the usual ∇B drift ($v_{\perp}^2$ term). In drift regions between quadrupoles, electron confinement is purely by the beam potential.

Electrons generated within the beam by ionization of gas are born trapped as noted above. These will accumulate until the end of the beam pulse. This process, in conjunction with gas released from walls by ion impact, is expected to lead to a significant electron density. We expect that untrapped, secondary electrons from the wall, with trapping only from jumps in magnetic moment near the quadrupole-field nulls, will not build up to sufficiently high densities to significantly impact beam performance. However, if electron-electron instabilities reach significant levels, they could cause much greater trapping of secondary electrons.

The details of the electron transport will differ between drift and magnetic quadrupole field regions. For a flattopped beam within a drift region, we expect the electron density to equilibrate axially, and azimuthally. Radially, electrons will be confined within the birth radius. Within a quadrupole magnet, electron transport is limited to the sum of the ∇B and $E \times B$ drift velocities, directed parallel or antiparallel to the beam, depending on the quadrupole quadrant. The drift velocities are a fraction of the beam directed velocity in HCX, requiring a fraction of a microsecond to drift the 31 cm length of a quadrupole magnet. An electron may drift through multiple magnetic quadrupoles during the flattop beam duration of 4 μs.

Our present experiments also transport beams with electrostatic quadrupoles. In these, the applied electric fields dominate over the beam self fields, so no electron trapping is possible. An increase in the current of single-pass electrons during the pulse is still possible from an increase in gas density due to desorption. Approximates 1% of gas within the beam is ionized and expelled from the beam. Electrostatic quadrupole effects will not be discussed further here.

Electrons reaching a drift region rapidly free-stream to the next magnet where they either bounce back, or enter the next magnet, depending on the local drift velocity direction of that magnet. Those that bounce back to the first magnet continue to bounce until they drift azimuthally to where one of the magnets will accept them. Axial transport of electrons through a series of magnets during the flattop beam duration of 4 μs could be treated as a diffusion process.

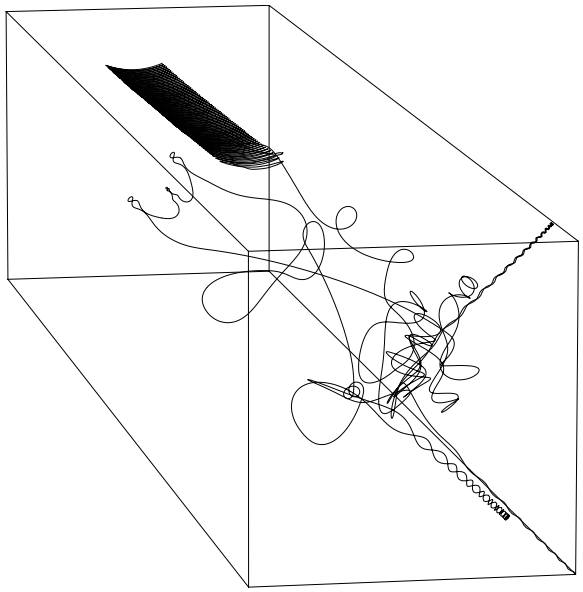

FIG. 3: 3-D plot of initially deeply trapped electron, which ∇B and $E \times B$ drifts slowly through a magnetic quadrupole, starting from the left. It is accelerated across a drift space, bounces between quadrupoles at few times, then enters the upstream (ion beam frame) quadrupole and is lost radially to the wall.

This situation is significantly changed by an acceleration gap within a drift region. It accelerates electrons backwards across an upstream (beam reference) acceleration gap, or reflects them back to the magnet from an acceleration gap at the downstream end of the magnet. Electrons that gain kinetic energy exceeding the potential trapping energy can be detrapped and deflected to the wall by an upstream magnet, Fig. 3. This is the only mechanism we have identified that will cause deeply trapped electrons to be lost before the end of the beam pulse.

The electron particle balance has two main terms, for electrons from ionization of neutrals and for those due to secondary electrons from the wall. The first term for the electron density n_e is given in terms of the neutral density within the beam n_n, the beam density n_b and velocity v_b, the ionization cross section σ, and the electron confinement time τ_e which is generally infinity during the beam flattop (i.e., the electrons remain confined radially by the beam in either drift or magnetized region unless they reach acceleration gaps where they can be accelerated to kinetic energies exceeding the potential well depth).

$$\frac{dn_e}{dt} = n_n n_b \langle \sigma v_b \rangle - \frac{n_e}{\tau_e} \tag{4}$$

where

$$n_n = \frac{2}{r_w}\langle n_{bw} v_{\perp w} \kappa_n \rangle (t - \tau_{nw}) \tag{5}$$

for a wall radius r_w, a beam density n_{bw} and velocity $v_{\perp w}$

at the wall, a gas desorption coefficient κ_n in molecules per incident beam ion, and the time of flight of gas from the wall to the beam τ_{nw}. We expect electron densities to reach several percent by the end of a 4 μs pulse in a background vacuum of 10^{-7} torr. Desorbed gas from the wall will increase electron densities further.

The trapping of secondary electrons originating at the wall radius r_w is given in terms of number of bounces that an electron is trapped Λ, the secondary emission yield κ_e, and the electron bounce time τ_{ew} which is typically 3-4 ns. We have also included a term due to photo-electrons with a coefficient κ_ν, the photons are from exitation by beam-gas collisions $\sigma_\nu v_b$, and are thought to be a small effect.

$$\frac{dn_e}{dt} = \frac{n_{bw}}{n_b}\frac{v_{\perp w}}{v_b} n_b \langle \Lambda \rangle \frac{v_b}{r_w}\kappa_e + n_n n_b \langle \sigma_\nu v_b \rangle \kappa_\nu - \frac{n_e}{\langle \Lambda \tau_{ew} \rangle} \quad (6)$$

We expect electron densities from this effect to be much less than 1%, averaged over the beam.

III. HCX FACILITY

Electron cloud experiments in HCX will be primarily performed with four pulsed magnetic quadrupoles. Each magnet has coil lengths of 31 cm, a gradient of up to 16 T/m, and a half-lattice length of 52 cm, including 4.3 cm for diagnostic access between each pair of quadrupoles. Each quadrupole has an elliptical bore with 3 × 5 cm radii at the center [10].

These provide a range of operation from transporting a small diameter beam, with an envelope radius about half that of the walls – minimizing electron and gas generation, to transporting a beam whose envelope approaches or scrapes the walls – maximizing electron and gas generation. Such a range is shown in Fig. 4. To determine limits, we will vary beam operation, until enough beam scrapes the walls to significantly change beam performance or produce electron densities approaching the beam density. Other envelope solutions (not shown) produce matched transport through the last two magnetic quadrupoles after expanding to significantly larger radius in the first magnetic quadrupole, these can produce solutions with small radii in the last two quadrupoles, but cannot attain large radius solutions there.

Before the quadrupole magnets are installed, we will begin measurements with the Gas-Electron Source Diagnostic (GESD), Fig. 5. It will be located at the end of the diagnostics tank 1.3 m beyond the end of the quadrupole transport. This drift distance will allow the beam to expand to a diameter of ∼15 cm. An entrance aperture of 0.3 × 2.5 cm allows ∼0.4% of the beam current into a box where it will impact a target at 75-88° from normal incidence. An ion gauge will measure the peak pressure rise, from which we will determine the total gas desorbed from the target. The gas pressure in the box will decay with a time constant of ∼0.5 s through pumpout holes, which is adequate for the HCX rate of 1 pulse every 10 s.

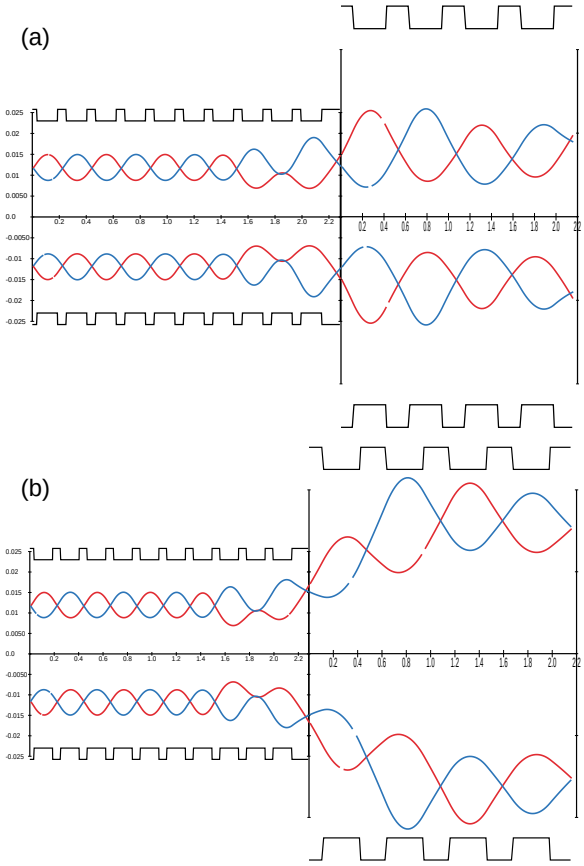

FIG. 4: (Color) Transport of a 1.0 MeV K^+ beam through 10 electrostatic quadrupoles on the left, a short drift space for diagnostics including slit scanners, followed by 4 magnetic quadrupoles. (a) A minimum radius beam is transported through the magnetic quadrupoles. (b) One of a large class of beam envelopes that approach or scrape the walls in the magnetic quadrupoles.

The target, catcher, and a surrounding grid in the GESD can be independently biased relative to the walls, to measure the current and energy of either secondary electrons or low energy secondary ions (up to a few hundred eV), and to determine the beam current to the target. At angles approaching 88°, TRIM Monte-Carlo calculations [11] predict that up to 70% of the incident ions will be reflected back out of the target, most of which will hit the ion-catcher at near normal incidence where they will stick and will not be reflected again. For 1.8 MeV beam ions incident at 88° from normal, 80% of ions scattered off the wall are at angles of less than 0.35 rad, with only 10% at angles greater than 0.5 rad. The purpose of the ion catcher is to reduce the number of ions scattered into the grid where they will produce secondary electrons, some of which will reach the target. We must keep this secondary electron current small, so that the error, in the measured beam current to the target, will be small.

The energies of desorbed molecules can also be measured – the wall beyond the ion gauge can be opened, in-

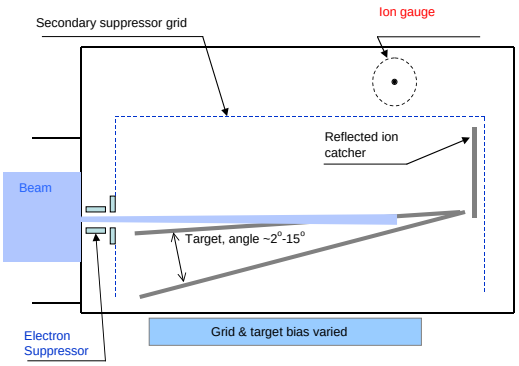

FIG. 5: (Color) The Gas-Electron Source Diagnostic (GESD) measures the number of energy of electrons and gas moelcules per incident K^+ ion. It can calibrate secondary electron measurements to beam loss and gas desorption, and can evaluate mitigation techniques.

FIG. 6: An array of collectors is shown; from left to right is (a) a flush collector, (b) a recessed collector or capacitive probe, (c) a 1-grid, and (d) a 2-grid collector.

creasing the time for gas molecules to reflect back to the gauge. Then the time of flight of molecules in the range of a few to a few hundred microseconds can be measured. This will enable us to estimate the time for gas to cross a gap between the beam and a wall, from which we can estimate the maximum beam duration that is unaffected by wall reflux. The main portion of the beam is caught in a 15 cm diameter, 23 cm long tube extending out from the beam entrance aperture. The gas from the main portion of the beam will take a few hundred microseconds to flow out and around the tube, reach the ion gauge and dominate the measurement. Time-of-flight measurements are valid only before this time. Electron (and gas) reduction techniques will be evaluated with the GESD.

We evaluated various diagnostics (Fig. 6) to measure and distinguish secondary electrons due to beam ions impinging on the wall (and to scattered ions resulting from beam ions impinging on the opposite wall), photo-electrons, ions from gas that are expelled with kinetic energy equal to the beam potential at their birth point, and untrapped electrons. A collector at the wall-potential, flush with the surface, measures the net current of all these particles, but can't distinguish between them. A second collector is recessed so that most primary and reflected beam ions can't reach it, but the other particles and electric field can; the difference between the two will be the beam current plus the secondary electron current.

Simple gridded collectors measure the remaining electron sources. A collector, shielded by 1-grid, measures the sum of the current of ions from gas plus untrapped electrons. The grid and collector are recessed so that few scattered ions reach them, since secondary electrons that reach the backside of the grid will be collected. A positive collector bias suppresses photo-electrons. A grounded collector with 2-grids, the second biased to repel electrons, measures the ionization current expelled by the beam. This directly gives the source of ions from ionization of gas. It is closely related to the source of deeply trapped electrons but includes charge exchange as well as ionization of gas. It can also be calibrated to measure the gas pressure within the beam as a function of time. The source term for expelled ions is closely related to the source term for electrons but it includes charge exchange as well as ionization. The time is skewed by the time-of-flight of the ions to the collector which is in the range of a few tenths of a microsecond for potentials of a few kV and ion masses near 20 AMU. This analyzer will also be operated in a mode to measure electron energies, as developed by the ANL group [12]. If instability levels are low, as we currently expect, the escaping electrons will have low energies of a few eV.

The escaping electron current will be especially informative during the at the end of the pulse when the confining potential of the beam decreases with the beam current. Then in Fig. 2, the loss boundary will move towards the origin, causing weakly trapped electrons that originated as secondary electrons at the wall, to be lost first. For a beam envelope that is well separated from the wall, we then expect a gap in the electron loss current until the beam potential decreases sufficiently for the much-more deeply-trapped electrons from ionized gas to be lost. Plotting the electron current versus the change in beam potential from the flat-top gives the depth-of-trapping energy distribution for electrons, and the integrated electron charge will give the accumulated trapped electron charge (per unit length and azimuth) at the end of the beam flattop. The difference between the total deeply-trapped electron charge and the integrated ion source term from the 2-grid collector provides an experimental estimate of charge-exchange versus ionization.

We plan two methods to measure the beam potential: (1) Capacitive probes, recessed with no grid, measure the electric field near the wall, from which the peak potential can be determined. (2) A gridded energy analyzer (GEA) [13, 14] measures the energy distribution of ions (from gas) that are expelled from the beam. Capacitive probes are very simple, in arrays they are used as beam-position monitors to determine the centroid, ellipticity, and perhaps the tilt of beams. The major uncertainty arises from particle and photon bombardment of the capacitive plate – the plate can be shielded from direct beam bombardment, and most scattered beam ions, by recessing it behind another electrode; however, untrapped electrons, expelled ions, and photons cannot be

prevented from bombarding the surface. Their currents, together with secondary production, add to the capacitive charging and discharging currents that occur during the rise and fall of the beam current.

The GEA consists of three grids preceding the collector: a grounded entrance grid, an ion repeller grid, and an electron repeller grid. The novel aspect of this analyzer is the requirement of biasing the ion repeller grid up to ∼5 kV. The ion-repeller precedes the electron repeller so that secondary electrons produced by reflected ions striking the back of the preceding grid will be stopped by the subsequent electron repeller grid, and so the electron repeller grid can also function as a secondary suppresser grid for the collector [13]. This arrangement can also be operated to measure photo-electrons off the collector [14]. We are also investigating the possibility of purchasing an ion energy and mass resolving analyzer from the A. F. Ioffe Physical-Technical Institute, St. Petersburg, Russia [15]. This instrument is called the Compact Ionized Particles Analyzer (CIPA), based on a similar unit developed for analyzing the flux of energetic neutral flux (to 160 keV hydrogen or 4 keV argon), resulting from energetic ions that charge-exchange on neutral atoms, in magnetic fusion experiments. It can resolve 1 AMU mass differences up to about 44 AMU.

In summary, we have listed a variety of simple instruments with which we will begin the quantitative study of the electron-cloud particle balance, the variation of electron-cloud parameters with the fill-factor of the beam in the beam tube, wall conditioning and other mitigation techniques, and – with the use of standard beam diagnostics – the effect of electrons on beam performance in HIF driver-scale beams.

Acknowledgments

We are grateful to Grant Logan for support and encouragement in this work, and to Miguel Furman for stimulating discussions connecting us to the main body of e-cloud work. This work was performed by the University of California Lawrence Livermore National Laboratory under the auspices of the U.S. Department of Energy under contract No. W-7405-ENG-48 and Lawrence Berkeley National Laboratory DE-AC03-76F00098.

[1] K. Ohmi, Phys. Rev. Lett. **75**, 1526 (1995).
[2] M. A. Furman and G. R. Lambertson, in *Proc. of the International Workshop on Multibunch Instabilities in Futhre Electron and Positron Accelerators*, edited by P. L. Roux, J. Poole, and M. Truchet (KEK Proceedings 97-17, 1997, Tsukuba, 1997), p. 170.
[3] G. Rumolo, F. Ruggiero, and F. Zimmermann, Phys. Rev. ST-AB **4**, 012801 (2001).
[4] R. O. Bangerter, Nuovo Cimento **106**, 1993 (1993).
[5] W. R. Meier, J. J. Barnard, and R. O. Bangerter, Nucl. Instr. and Meth. A **464**, 433 (2001).
[6] R. L. Freeman and E. M. Jones, Tech. Rep. CLM-R 137, Culham Laboratory, Abingdon Berkshire (1974).
[7] D. A. Callahan-Miller and M. Tabak, Nucl. Fusion **39**, 883 (1999).
[8] D. E. Baldwin, Rev. Mod. Phys. **49**, 317 (1977).
[9] R. F. Post, Nuclear Fusion **27**, 1579 (1987).
[10] A. Faltens, N. Y. Li, G. Ritchie, and D. Shuman, Proceedings of the 1999 Particle Accelerator Conference p. 3339 (1999).
[11] J. F. Zielgler, J. P. Biersack, and U. Littmark, *The Stopping and Range of Ions in Solids* (Pergaman Press, New York, 1985).
[12] R. A. Rosenberg and K. C. Harkay, Nucl. Instr. and Meth. A **453**, 507 (2000).
[13] A. W. Molvik, Rev. Sci. Instrum. **52**, 704 (1981).
[14] C. Bohm and J. Perrin, Rev. Sci. Instrum. **64**, 31 (1993).
[15] mpetrov@npd.ioffe.rssi.ru (2002), Private communication.

POSSIBLE CURES FOR ELECTRON CLOUD PROBLEMS*

R. J. Macek†
LANL, Los Alamos, NM 87545, USA

Abstract

This paper reviews and evaluates a number of methods and approaches that have been considered and/or explored at the Los Alamos PSR for mitigating the e-cloud problems. The two main approaches are (1) methods to suppress the e-cloud generation and (2) direct methods (such as damping the e-p instability) to control the adverse impact of the e-cloud on accelerator performance. In the first category, we have explored (a) suppression of the primary or "seed" electrons (reduction of losses, improved vacuum, control of the "convoy" electrons at the stripper foil, clearing fields, and suppression of secondary emission at the stripper foil), (b) reduction of electron amplification by beam-induced multipacting (TiN coatings, beam scrubbing, weak solenoids, and shaping the beam pulse), and (c) reduction of electrons that survive the gap (clearing electrodes, and reduction of beam leaking into the gap). While many of these measures suppress multipactor electrons, it is not yet demonstrated that this will cure the e-p instability at PSR. In the second category, we have had success in controlling the e-p instability by various forms of Landau damping (increasing the momentum spread by a variety of methods, multiples, skew quads and inductive inserts) and in controlling the impact on diagnostics by use of bias fields.

1 INTRODUCTION

The characteristics and impact of the electron cloud on accelerator performance can include two-stream instabilities (e.g. at the Los Alamos PSR), vacuum degradation, interference with beam diagnostics, and heat load on superconducting components in the case of LHC. Three of these, the e-p instability, vacuum pressure increases and interference with certain beam diagnostics have been observed at PSR. Most serious for PSR is the two-stream e-p instability, which was first observed at PSR late in 1985, but was not identified as such until the early 1990's [1].

At PSR the search for and development of means to mitigate the e-p instability went on in parallel with work to understand the instability and sources of electrons at a more fundamental level. The two main approaches to cures were (1) methods to suppress the e-cloud generation and (2) direct methods (such as damping the e-p instability) to control the adverse impact of the e-cloud on accelerator performance. To date, the direct methods have been more effective than most of the measures to suppress the e-cloud formation. We surmise that this is a result of suppressing electrons over just a small fraction of the ring circumference.

* Work conducted by the Los Alamos National Laboratory, which is operated by the University of California for the United States Department of Energy under contract W-7405-ENG-36.
†macek@lanl.gov

2 THE E-CLOUD IN PSR

A short summary of the present picture of the electron cloud for stable beams in PSR will aid in interpreting the results of tests of potential cures, which will be described later. We now know that electrons generated by trailing edge multipactor make up much of the electron flux ("prompt" electron signal in Figure 1) striking the wall at the end of the each passage of the bunch [2], [3]. However, electrons captured by the beam pulse from the cold (few eV) electron cloud surviving the beam-free gap between successive passages of the beam bunch ("swept" electron signal in Figure 1) are the main component in the beam neutralization averaged over the beam pulse and thus are the ones that can drive the instability. They also contribute to the "prompt" signal when they are released at the end of the beam on each turn.

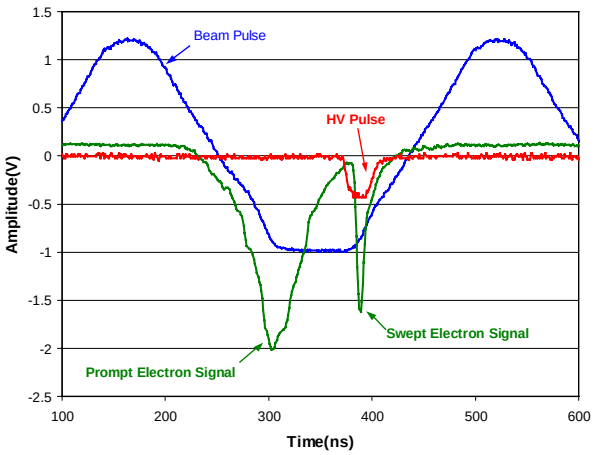

Figure 1. Signals from the electron-sweeping detector in PSR are shown in proper time relationship to the beam pulse. The "prompt" signal comes at the end of the beam pulse and the "swept" electron signal reaches the collector a few ns after the HV pulse is applied to the sweeping electrode [4]. From the swept electron signal timed at the end of the gap one obtains an average neutralization of 1-2% at the location of this detector (section 4 of PSR), which is approximately the value needed to explain the observed instability threshold curves.

The prompt electron intensity depends upon several factors including beam intensity, beam pulse shape, secondary emission yield (SEY) at the vacuum chamber surfaces, the beam losses, vacuum pressure, to name a few. Of special note is the very strong dependence on

beam intensity (stored charge in the ring) as shown in Figure 2 where both the prompt electron signal amplitude and the electrons swept out of the chamber at the end of the gap are plotted as a function of beam intensity. Features to note are the strong dependence on intensity (to approximately the 10^{th} power for the prompt and about the 7^{th} power for the electrons surviving the gap) and the saturation of the swept electron signal above ~5.5 μC/pulse. The saturation of electrons surviving the gap can be qualitatively understood as due to space charge of the electron cloud in the beam-free gap after the bunch.

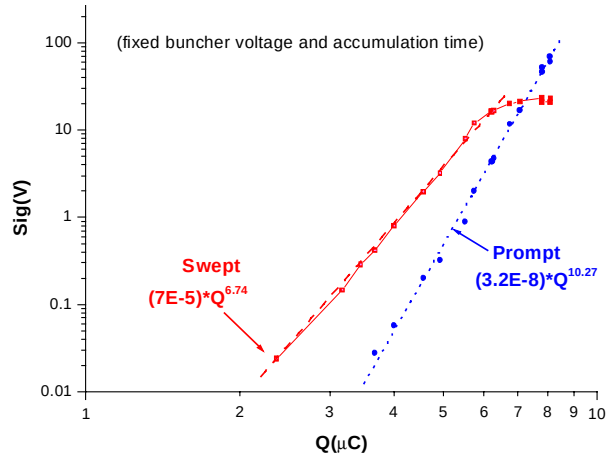

Figure 2. Prompt electron and "swept" electron (swept out of pipe at the end of the gap) signal amplitudes are plotted as a function of stored beam intensity. All other beam parameters were fixed including buncher voltage and accumulation time.

With the electron sweeper we have measured the electron survival as a function of time after the end of the beam pulse. Results are plotted in Figure 3.

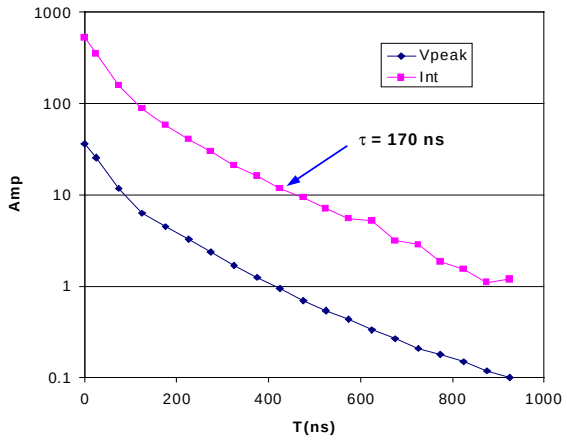

Figure 3. Electron survival plotted as a function of time after the end of the beam pulse. The origin is the end of the beam pulse. The blue diamonds are the peak amplitude (V) of the swept electron pulse while the magenta squares are the integral of the swept pulse (nVs).

An interesting feature of Figure 3 is the long exponential tail indicating that the low energy electrons in the gap can linger for quite some time. It is expected that the average electron in the gap would have an energy near the peak of the secondary emission spectra, which is around 2-5 eV. The exponential behavior in Figure 3 would result from repeated, nearly elastic collisions with the wall in a process having a relatively constant reflectivity, δ, (or, more precisely, secondary emission yield). The electron intensity as a function of time would be proportional to δ^n, where n is the number of collisions with the wall in time t and equal to t/T (T = $d\sqrt{(m_e/2E)}$ is the transit time across the pipe of diameter d). Thus, the exponential time constant for the decaying expeontential is $-T/\ln(\delta)$ and the time constant of Figure 3 implies $\delta \approx 0.5$ for electrons of 2-5 eV. This surprisingly high value of δ is reasonably consistent with recent measurements at CERN [5] for 4 eV electrons on copper. The high "reflectivity" explains the slow decay of electrons in a beam free region and survival of sufficient electrons in the gap to produce the neutralization (1-2%) needed to cause the e-p instability at PSR.

At a routine operating beam intensity of 4-5 μC/pulse, copious electron signals have been observed in PSR where ever electron diagnostics were placed including three different straight sections representing low loss and high beam loss regions and just down stream of the stripper foil. Strong electron signals were also observed on biased collection plates in both quadrupole and dipole magnets. The signal levels are much higher than can be explained by residual gas ionization and are presumed to arise from the same amplification processes (primarily trailing edge multipactor) found in straight sections.

3 CONTROL BY SUPPRESSION OF PRIMARY ELECTRONS

Reduction of the electron cloud by suppression of the primary or "seed" electrons, which are then amplified by beam-induced multipactor, is a potential remedy. At PSR the primary electrons include:

a) Electrons from beam losses where the protons hit the wall at a grazing angle and can produce as many as 100 secondary electrons per incident proton,
b) Electrons stripped from the injected H^- (two 430 keV "convoy" electrons per injected proton plus the secondary electrons from these striking an absorber),
c) Secondary electrons from foil hits by the stored beam,
d) Thermionic emission from the stripper foil, which is heated by the foil hits from the stored beam, and
e) Electrons from residual gas ionization by the beam and the multipacting electrons.

A variety of methods to suppress or control these sources and results of tests are described below.

3.1 Reduction of beam losses and better vacuum

The prompt electron flux striking the walls in a straight section has been measured as a function of local vacuum pressure and local beam losses using a special electron detector, the retarding field analyzer (RFA) developed at

ANL [6]). It has been augmented with fast electronics to provide time resolved signals similar to the prompt signal in Figure 1 [3]. Plots showing the increase in electron signal with increasing vacuum pressure and local beam losses are presented in Figures 4 and 5.

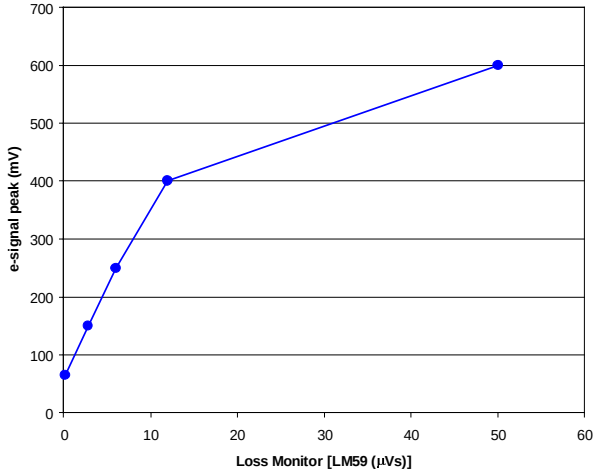

Figure 4. Prompt electron signal as a function of local losses, which were varied by use of a local closed orbit bump. All other beam parameters were held fixed. A local loss monitor placed on the wall opposite the first downstream dipole monitored beam losses. Particles produced at ~ 20° from losses in the first quadrupole just upstream of the electron detector reach the loss monitor.

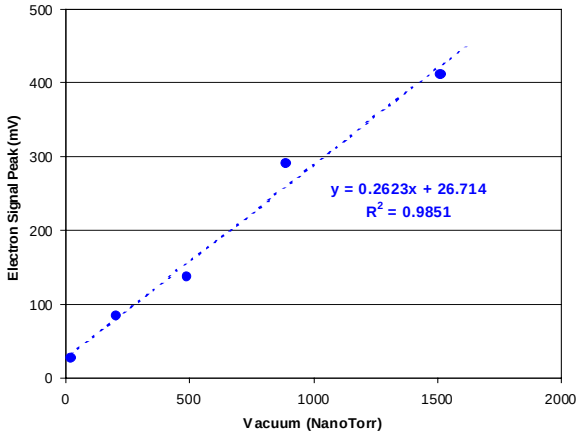

Figure 5. Prompt electron signal amplitude plotted as a function of local vacuum pressure. All other beam parameters were held fixed.

Despite the fact that the prompt electron signals vary with beam losses and residual gas pressure, global increases in losses (factors of 2-3) or vacuum pressure (more than a factor of 100) have had no effect on the instability threshold intensity curves. This long-standing puzzle can be resolved by noting the saturation of the electrons surviving the gap. These are the electrons most likely to drive the instability since they oscillate against the protons during the entire passage of the beam pulse. Thus, increases in losses or vacuum pressure will not increase the electrons driving the instability. In fact measurements of the electrons surviving the gap show absolutely no change when local losses were varied by factors of 2 to 3.

The direct H- injection upgrade of PSR [7] completed in 1998 lowered the beam losses by about a factor of 3 but did not result in an improvement in the instability threshold. In fact, it was worse as seen in the instability threshold intensity curves of Figure 6. However, after several weeks of operation at 100 μA @ 20 Hz the threshold curve returned to the historical value. This is another example of the "conditioning" effect (presumably from electron bombardment by the prompt electrons) seen on other occasions after coming back from a long shutdown where the ring was up to air for months.

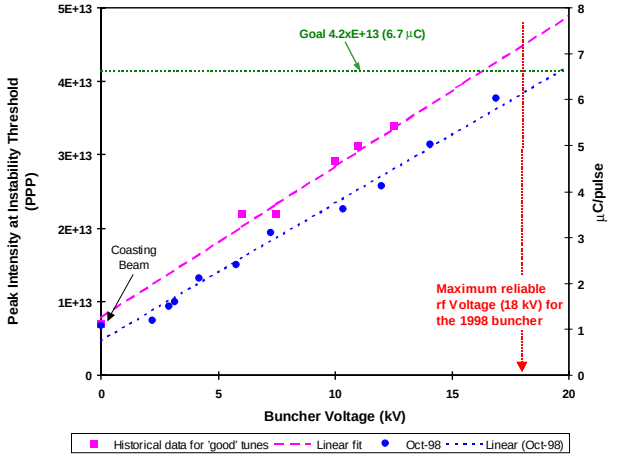

Figure 6. Instability threshold intensity plotted as a function of RF Buncher voltage. The square points are historical data for well-tuned production beams prior to the upgrade and the round points were those taken in October of 1998 during commissioning of the upgrade.

Reduction of losses and improved vacuum will reduce the prompt electron signal approximately linearly in these variables but the data in Figure 2 suggests that it could take an order of magnitude or more reduction in losses and or vacuum pressure to bring the electrons surviving the gap out of saturation and start to improve the instability threshold. Either of these options would require a major rebuild of PSR and are not practical. However, more modest improvements in combination with other measures described later could help mitigate the instability. In addition, any improvement in vacuum or reduction of losses would reduce the prompt electrons striking the wall and thus would help reduce the interference with diagnostics and reduce the vacuum pressure excursions.

3.2 Control of electrons from the stripper foil

The region of the stripper foil hosts several copious but highly localized sources of primary electrons, which were identified at the beginning of this section. Rough analytical estimates of the longitudinal motion of electrons for a typical bunched beam in PSR indicate that most will move less than 0.2 meter depending upon where they were born along the bunch. Thus the cloud density in

this region is expected to be significantly higher than elsewhere.

Since 1998 the stripper foil at PSR has been located in the fringe field of a dipole which deflects the convoy electrons onto a copper absorber ~0.15 meter downstream of the foil. These can make secondaries, which can be amplified by the trailing edge multipactor. It would be better to transport the convoy electrons to an absorber, which can be screened and biased to suppress secondaries as was done in the test described in the next section.

More efficient injection painting, which would reduce foil hits, would reduce the resulting secondary emission and heating of the foil. This was done in the direct H^- injection upgrade of 1998 where the foil hits for a given accumulation time were reduced by nearly a factor of 10. However, the increase in beam current to 100 μA required a 25% longer accumulation time, which meant that the total foil hits were reduced by a smaller factor of ~6.

Thermionic emission is a very strong function of temperature and can be a problem at the higher peak intensities. Biasing the foil with sufficient voltage to overcome the field from the beam can keep both thermionic emission and secondary emission electrons from leaving the vicinity of the foil. This was also tried in a test to be described in the next section.

3.3 Test of electron clearing devices in PSR

Clearing fields, which are strong enough to overcome the field of the beam, can be used to collect electrons from a variety of sources (e.g. beam losses, ionization, and beam losses) before they can multipactor or be captured by the beam. These were tried at PSR in conjunction with various means of controlling electrons in the vicinity of the stripper foil prior to the 1998 injection upgrade [8]. The layout of electron clearing devices in the injection section is shown in Figure 7.

The stripper foil was biased at up to 10 kV to suppress secondary and thermionic emission. The 430 keV convoy electrons and energetic knock-on electrons were deflected to a biased Faraday cup, which was behind a screen that could also be biased separately. The bias fields were configured to suppress secondaries. In addition, the drift spaces before and after the stripper foil were filled with clearing electrodes that could be biased to ± 20 kV respectively. These could be used in conjunction with DC clearing fields applied to the extraction kicker plates in sections 7 and 8, the diagnostic kicker plates in section 3 and to the striplines of three freestanding BPMs in other drift spaces.

When all of the injection devices were energized there was no reproducible effect on the instability threshold. When the other clearing fields were energized as well, there was perhaps a 10-15% increase in the instability threshold consistent with clearing 15% of the circumference of the ring. These results indicate that the injection section is not the main cause of the e-p instability and support the hypothesis that a significant electron cloud is present everywhere in the ring.

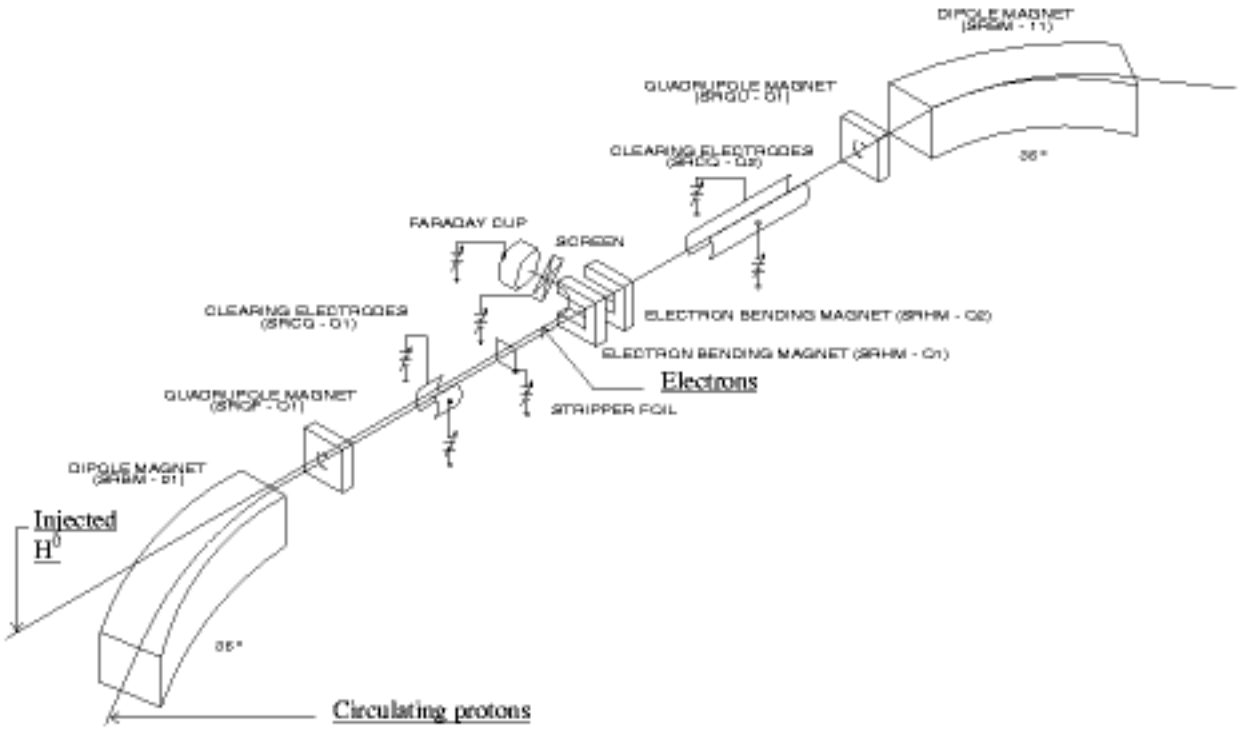

Figure 7 Layout of electron clearing devices in the injection section prior to the 1998 upgrade to direct H^- injection.

4 METHODS TO REDUCE MULTIPACTOR GAIN

Amplification by trailing edge multipactor can have a high gain, which is a strong function of secondary emission yield, but also depends strongly on beam intensity and pulse shape. Some of these features can be manipulated to reduce the multipactor gain and hence the densities of the electron cloud. At PSR we have investigated the effect of vacuum chamber coatings, beam scrubbing, weak solenoids and pulse shape for their efficacy in reducing the multipactor gain. The results of these studies are described in the following subsections.

4.1 Vacuum chamber coatings

A number of different coatings and surface treatments, TiN, C, Cr_2O_3, and TiZrV non-evaporable getter coatings, are known to influence the secondary electron yield (SEY) from electrons with energies below a few keV impinging on the surface. TiN was used to coat the aluminum chambers of the low energy ring (LER) at PEP II to suppress secondary emission. In a test of TiN at PSR (1999), a 3-meter test section of 304 stainless steel vacuum chamber was coated at SLAC using the same process as used for the LER. An identical section, which was not coated, was used for a comparison. The electron signals from the RFA in the center of the two test chambers subjected to an 8 μC/pulse beam are shown in Figure 8.

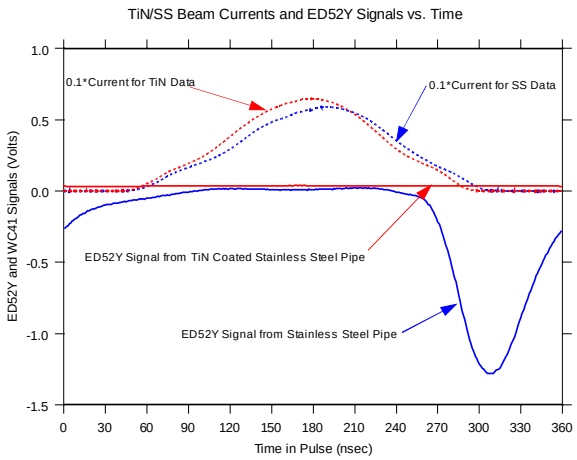

Figure 8. Electron signal from an RFA (designated as ED52Y) in the center of a 3-meter stainless steel test section (solid blue curve) compared with the much reduced (more a factor of 100) electron signal from an identical TiN coated stainless steel section (solid red curve). For reference, the corresponding beam currents are shown (dotted curves).

TiN coating was clearly effective in the reducing the prompt electron signal by a factor of 100 or more. For unstable beams, the RFA electronics were saturated in the uncoated chamber while in the coated chamber a small electron signal was observed which indicated that the detector was still working. How effective the TiN coating is in reducing the electrons surviving the gap or in improving the instability threshold remains to be tested. A definitive test would require coating a large fraction of the ring including the dipoles, which would be expensive and require a long shutdown and, therefore, unlikely to take place. However, a test using a TiN coated electron-sweeping detector in a TiN coated straight section is planned. It would measure the reduction in electrons surviving the gap. A strong reduction in these would be very encouraging for TiN coatings as a cure for the e-p instability.

4.2 Beam scrubbing

Electron bombardment is known to reduce the SEY for some technical surfaces used in accelerators. A "conditioning effect" with respect to the instability threshold curves has been observed at PSR on three occasions after a long shutdown where much of the ring was up to air for maintenance or upgrade (e.g. see the discussion in section 3.1 pertaining to Figure 6). It is presumably due to continued bombardment by the multipacting electrons, which are present even for stable beams. A more systematic study was conducted in 2000 after 4-month shutdown. Results are shown in the sequence of instability threshold curves plotted in Figure 9 below.

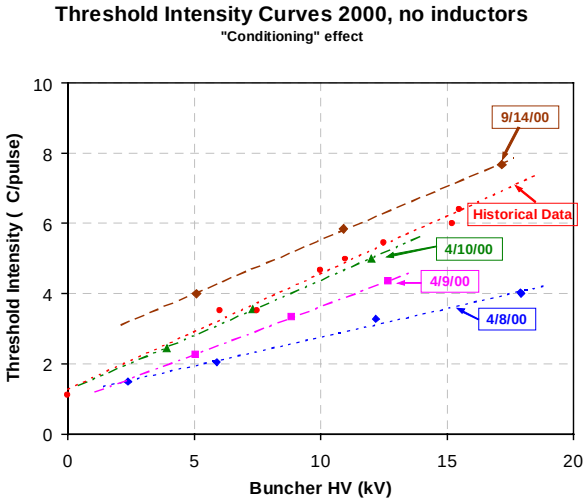

Figure 9. Instability threshold curves at various times after startup in 2000 show a "conditioning" effect.

The lowest curve in Figure 9 was taken on 4/8/00 two days after startup and shows a threshold intensity of only 4 μC/pulse at 18 kV, which is the maximum voltage that can be obtained from the RF buncher. The situation improved a day later after operating for a day at 4-5 μC/pulse. After two days of conditioning the curve about the same as the historical curve. The last curve taken 9/14/00 was obtained after about 6 weeks of routine operation at ~100 μA @ 20 Hz or 5 μC/pulse and shows a factor of two improvement in the threshold intensity at each buncher voltage compared with the lowest curve of 4/8/00.

If the conditioning effect is due to a gradual reduction in SEY then it should also reduce the prompt electrons

signal for a given beam intensity. Experimentally, it tended to diminish over course of time but because the signal is very sensitive to a number of variables, especially peak intensity, a number of corrections are needed to normalize to a given intensity. Such a detailed analysis has yet to be implemented.

4.3 Weak solenoids

Weak solenoids can reduce multipactor gain by turning back low energy electrons leaving the wall and preventing them from reaching the wall with enough energy to make more than one secondary electrons. A 0.5 meter solenoid with an RFA in the center (see Figure 10) was used for a test of the effect on prompt electrons in PSR with results which are shown in Figure 11 and 12.

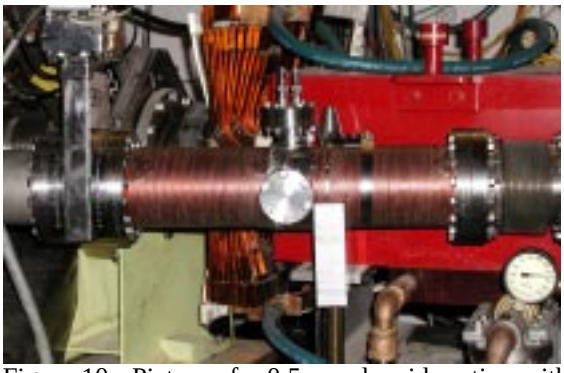

Figure 10. Picture of a 0.5 m solenoid section with an RFA in the center (installed in section 9 of PSR).

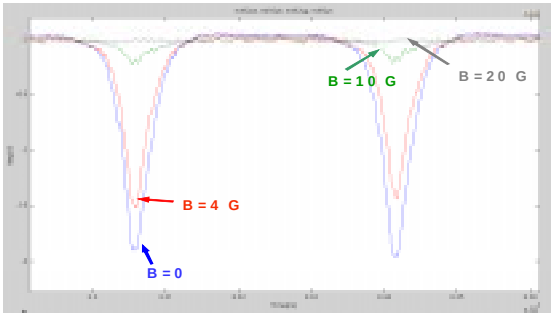

Figure 11. Prompt electron signals from the test solenoid for 3 values of the magnetic field (in Gauss). Signals are shown for two turns.

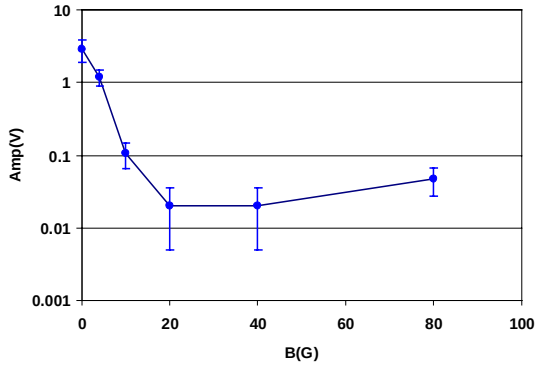

Figure 12. Curve showing the prompt electron signal from the test solenoid plotted as a function of magnetic field B (in Gauss) in the solenoid.

As can be seen in Figures 11, and 12, weak solenoid fields are effective in suppressing the prompt electrons by a factor of about 50 even in this relatively short solenoid where some electrons from the nearby straight sections (with no field) might leak in from the ends. However these measurements do not give any indication as to how many electrons remain in the pipe during the gap. Because of the solenoid field, it would difficult to use an electron sweeper to measure electrons remaining in the pipe unless the voltage could be raised to several kV. Despite the uncertainty on electrons surviving the gap, solenoids show promise for suppressing the electron cloud in a long bunch ring such as PSR. There are plans to cover about 10% of the ring circumference with solenoids as a test (in the coming run cycle) of their effect on the instability threshold in conjunction with TiN coatings in another 5% of the circumference.

4.4 Tailoring the pulse shape

Pulse shape is another parameter that has a significant influence on the prompt electron signal amplitude. This is not surprising for electrons from trailing edge multipactor, which are sensitive to the derivative of longitudinal profile of the beam pulse. Pulse shape, to the extent that it can be manipulated, becomes another variable in the overall minimization of the multipactor gain. The effect of pulse shape was studied at PSR by adjusting the rf buncher phase which produced subtle changes in shape of the trailing edge as shown in Figure 13. The prompt electron signals for these shape variations are shown in Figure 13.

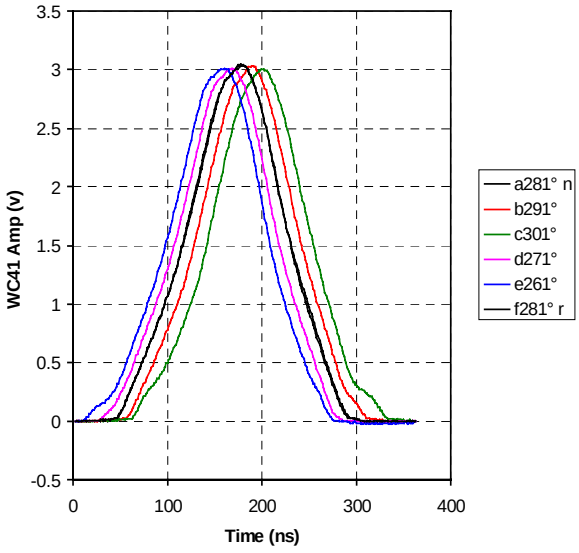

Figure 13. Effect of rf buncher phase variations on the beam pulse shape as measured with a wall current monitor (WC41).

In Figure 13 the nominal phase was 281° (trace a and a repeated run, trace f). Departures from nominal in either direction produced a shoulder on one side of the pulse or the other depending on whether the phase was increased or decreased. Increasing the phase to 301° (trace c301°) produced the largest shoulder on the trailing edge, a

situation that produced the greatest change in the prompt electron signal amplitude in Figure 14 (trace c301°).

The lowest electron amplitude is trace d271° (close to the nominal setting of 281°), which is the setting that produced the smoothest trailing edge in Figure 13 A complete study of the optimal shape has not been carried out. This is perhaps best done by first studying the effect of various shapes in simulations then checking it experimentally. We have presented just one class of pulse shape variations using the buncher phase and it indicates that one should operate without shoulders on the trailing edge, which is achieved by injecting in the center of the rf bucket. This indication is also consistent with earlier observations that the instability threshold is maximized by centering the beam in the rf bucket [9].

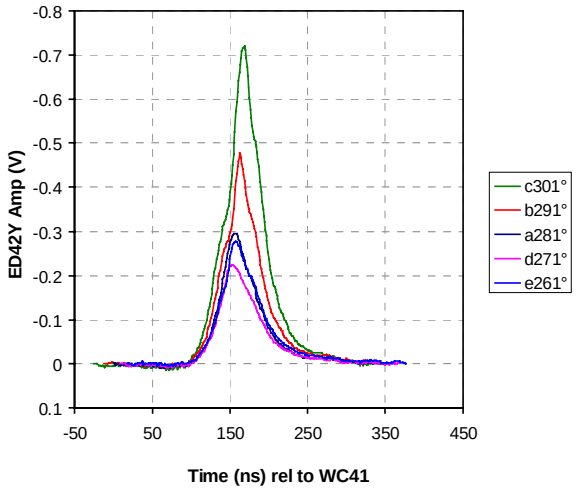

Figure 14. Effect of rf buncher phase variations on the prompt electron signal for detector ED42Y. The trace labels in the legend are keyed to the same ones as in Figure 13.

5 REDUCTION OF ELECTRONS SURVIVING THE GAP

Since the most damaging component of the electron cloud for the e-p instability is the electrons that survive the gap, reducing these would be a most effective cure.

5.1 Reduction of beam in the gap

It was once thought that beam leaking into the gap and trapping electrons was a key ingredient in the cause of the e-p instability [1]. In fact, adding beam in the gap did lower the instability threshold in experiments at PSR. Beam was added to the gap by inhibiting the chopper and injecting a number of unchopped turns in the ring. The buncher voltage at instability threshold for two fixed intensities of different bunch widths is plotted as a function of added beam in the gap in Figure 15. Adding beam to the gap increases the buncher voltage required to reach the instability threshold for fixed intensity beam. This is equivalent to lowering the threshold intensity for a fixed buncher voltage. This data shows that beam in the gap at the few percent level can affect the instability. Therefore, it is important to keep the gap quite free of beam (< 0.1%). It can be controlled by the rf system and the use of inductive inserts, which are described later in section 6.4. At PSR today, beam in the gap is typically <0.05% and is therefore not a significant factor in causing the instability.

In recent experiments with added beam in the gap both the prompt and the swept electrons increased. One expects the electrons surviving the gap to increase by the amount of beam added to the gap so as to neutralize the added protons. This was approximately what was observed.

With added beam in the gap the additional electrons surviving the gap will also be captured by the next beam pulse and then be released at the end of the pulse to contribute additional electrons to the prompt electron signal, as was also observed in these experiments. It would be informative to use an electron cloud simulation program, such as the LBNL simulation code POSINST to simulate the effect of beam in the gap for comparison with the experimental results. This would provide a better indication of the expected effects of beam in the gap than the more qualitative picture outlined above.

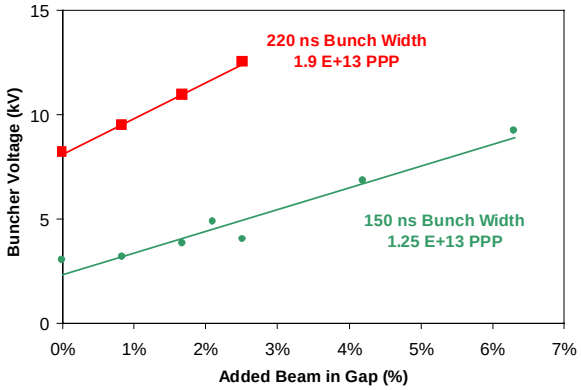

Figure 15. This graph shows the effect of added beam in the gap. The instability threshold buncher voltage is plotted as a function of added beam in the gap for two different beam intensities.

5.2 Vacuum chamber coatings and beam scrubbing

From recent measurements at CERN [5] it is now known that for Cu surfaces at least that the SEY for very low energy electrons is reduced with electron bombardment. This means that beam scrubbing or beam conditioning should reduce electrons the decay time for electrons surviving the gap, hence their number as well. This may be the cause of the conditioning effect on the instability threshold curves at PSR.

Will TiN or other coatings that reduce the SEY at the peak of the energy dependence have the same effect on low energy electrons i.e., reduce the decay time for electrons in the gap? This intriguing possibility will be checked at PSR in the near future in measurements using a TiN coated electron-sweeping detector placed in a TiN coated straight section.

6 METHODS TO DAMP THE E-P INSTABILITY

Another approach to mitigating the e-p instability is to invoke various methods of damping the instability. A number of methods have been tested at PSR in the past few years and are discussed in the subsections that follow.

6.1 Increased rf buncher voltage

Increased rf buncher voltage was the first method used to control the instability. It was observed early on that the instability threshold intensity was rather linear in rf buncher voltage as shown in Figure 14 (also see Figure 5 and 8). The linear behavior implies that the instability threshold intensity varies as the square of the momentum spread and can be understood in the coasting beam model with Landau damping if the fractional neutralization is constant [10].

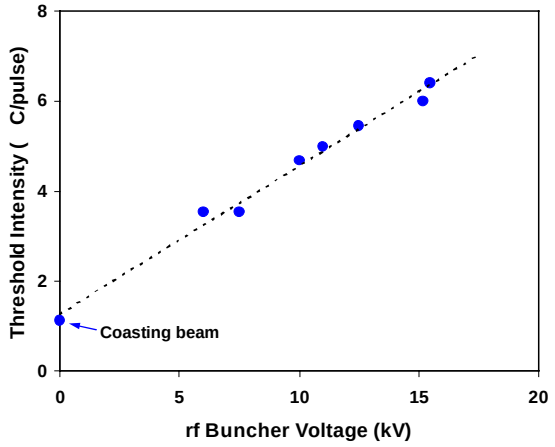

Figure 16. Instability threshold intensity as a function of rf buncher voltage. These are historical data for well-tuned production beams prior to the 1998 injection upgrade.

Because the rf buncher voltage has been our most effective control for the instability, the buncher was upgraded in 1998 to raise the reliable operating voltage from 12 kV to 18 kV in order to permit going to higher intensity. There is, however, a downside to higher momentum spread and that is increased beam losses in the ring at the higher rf voltages.

6.2 Landau damping with multipoles

Landau damping with magnetic multipoles (sextupoles and octupoles) has also been found to be effective. An example is the effect of an octupole field on the rf buncher threshold voltage for a fixed beam intensity of 5 μC/pulse as shown in Figure 17. The octupole significantly reduces the buncher voltage at the instability threshold. This is equivalent to increasing the threshold beam intensity for a fixed buncher voltage. The graph also shows the down side of using multipoles i.e., the beam losses increase as a nonlinear function of octupole excitation.

The effect of sextupoles was similar but will not be shown here. However, Figure 19 does show the beneficial effect of sextupoles to augment the benefits of inductive inserts. There is also evidence that the main effect of sextupoles on the instability is not through the change in chromaticity (effect was the same regardless of polarity) but to introduce transverse coupling. If the closed orbit is offset in a sextupole this introduces a skew quadrupole field component and, as will be shown in the next subsection, a skew quad excitation produces coupled Landau damping which is also effective in damping the instability.

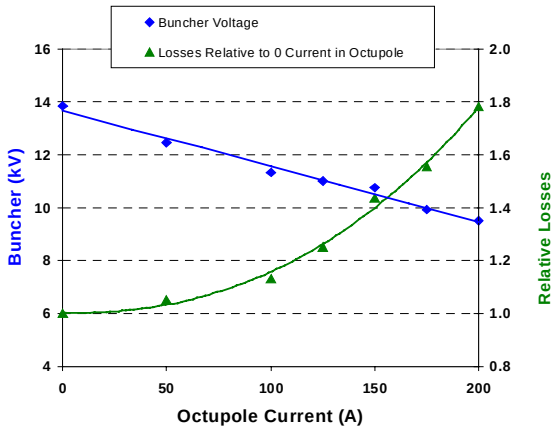

Figure 17. Instability threshold voltage (blue diamonds) plotted as a function of octupole current. Also shown are relative beam losses (green triangles) as a function of the octupole current.

6.3 Coupled Landau damping

Coupled Landau damping [11] has been tested and found effective at PSR. In these tests the operating point was tuned to be on the coupling resonance Qx-Qy = 1 and a single skew quad was weakly excited. The results are shown in Figure 18.

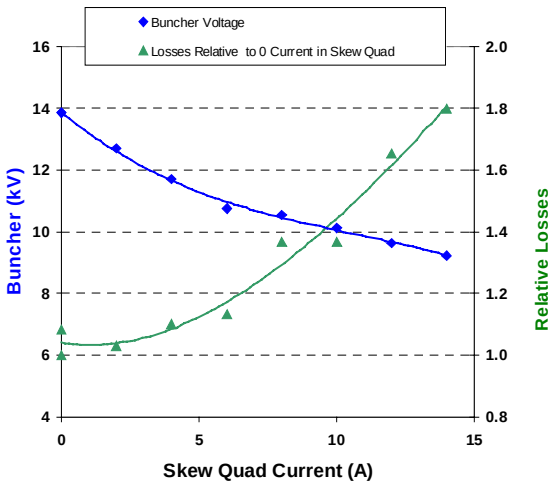

Figure 18. Instability threshold voltage (blue diamonds) plotted as a function of skew quad current. Also shown are relative beam losses (green triangles) as a function of the skew quad current.

6.4 Inductive inserts

Inductive inserts were tried in a collaborative effort with FNAL [12], [13] as part of the Short Pulse Spallation Source Enhancement Project (SPSS) at PSR. The original motivation was that passive compensation of longitudinal space charge force by the ferrite inserts would prevent beam leaking into the gap and hence would improve the instability threshold. Indeed, with the inserts the gap appears flatter and with a sharper transition between the beam and the gap. The inserts are equivalent to more rf with the harmonics which compensate the longitudinal space voltage that is proportional to the derivative the line density of the beam. Inserts would also increase the momentum spread and cause additional Landau damping by removal of the potential well distortion that depresses bucket height.

The effect of the inductive inserts on the instability threshold curves is shown in Figure 19. The instability threshold intensity improves by ~35% with inductive inserts alone. The improvement is the amount expected from the increased momentum spread of the equivalent rf. When the sextupoles were excited in the presence of the ferrite inserts, additional improvement in the threshold intensity was obtained suggesting that the improvements are approximately additive.

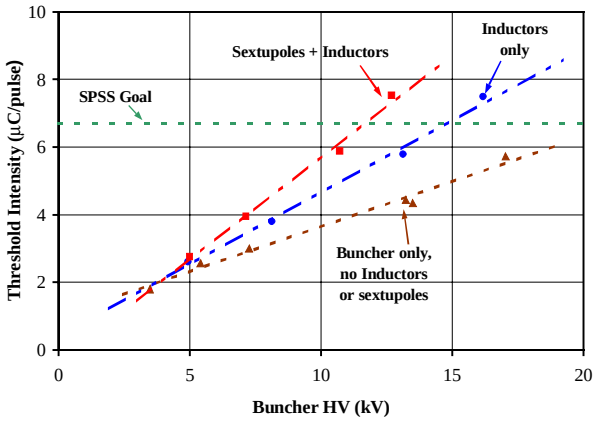

Figure 19. Graph showing the effect of inductive inserts and sextupoles on threshold intensity curves. The inductance of the inserts was 11 μH, which is the amount needed for full compensation of longitudinal space charge at PSR.

With the ferrite inserts it was also possible to increase the bunch width without affecting the instability. This helped reduce the accumulation time needed for a fixed intensity and resulted in useful savings of linac duty factor and power.

7 CONCLUSIONS

From experiment and simulations it is known that trailing edge multipactor at PSR produces a large amplification of primary electrons and, as such, is responsible for the vacuum degradation and interference with some diagnostics. Electrons, which survive the gap to be captured by the subsequent beam pulse, are the main component to average beam neutralization and are the ones expected to drive the e-p instability.

Suppression of the electron cloud by reduction of the primary or “seed” electrons (from beam losses, residual gas, and stripper foil processes) reduces the prompt electrons from the multipactor process in PSR but have not been sufficient to reduce the electrons surviving the gap. This is likely due to the saturation (at higher beam intensities) of the electrons in the gap. While presently available means to suppress the primary electrons are not sufficient to cure the instability they might be effective in combination with other methods.

TiN coatings and weak solenoids do greatly suppress the multipactor gain but it has not yet been demonstrated experimentally that they will greatly reduce the electrons surviving the gap. A test planned at PSR for the 2002 run cycle will measure the effect of TiN coatings on the electrons surviving the gap.

Beam scrubbing or conditioning is effective in reducing the prompt electron signal and in raising the instability threshold by a factor of two at PSR. Presumably, this is due to a reduction of the SEY by electron bombardment.

Bias fields to repel electrons have reduced the spurious signals on certain diagnostics affected by the electron cloud. It is anticipated that coatings such as TiN to suppress multipactor will also help these diagnostics.

Landau damping by increased rf voltage, transverse coupling, multipoles and inductive inserts have significantly raised the instability threshold but with some increase in losses. These measures along with some condition beam conditioning have allowed us to raise the stable peak intensity at PSR to 10 μC/pulse (6.3×10^{13} protons per pulse) of stored charge, which is a factor of two above the design goal of the 1998 upgrade and 50% above the SPSS project design goal.

8 ACKNOWLEDGEMENTS

Many people contributed in the past several years to the work reviewed and discussed here. I gratefully acknowledge the innumerable contributions from the other members of the PSR development team at LANL including Andrew Browman, Daniel Fitzgerald, Mike Plum, Mike Borden, Frank Merrill, Thomas Spickermann and Rod McCrady. Robert Kustom (ANL) introduced us to the RFA provided by Kathy Harkay and Richard Rosenberg and gave us much encouragement and support to resolve the instability, which he deemed a significant technical risk for the SNS project. Jim Griffin, Bill Ng and David Wildman at FNAL were collaborators on the effort to test inductive inserts. Slava Danilov, Sasha Alexandrov and David Olsen at SNS were collaborators on the test of TiN coatings. Dan Wright of SLAC coated the chambers with TiN for these tests. I also acknowledge many useful discussions with the PSR instability collaboration at LANL, LNBL, ANL, BNL, and PPPL including Tai-Sen Wang, Paul Channel, Miguel Furman, Mauro Pivi, Glen Lambertson, Kathy Harkay, Mike Blaskiewicz, Ron Davidson and Hong Qin.

9 REFERENCES

[1] D. Neuffer et al, “Observations of a Fast Transverse Instability in the PSR”, NIM A 321 (1992), p. 1-12.

[2] R. Macek et al, “New Developments on the e-p Instability at the Los Alamos Proton Storage Ring”, Proceedings of ICANS-XV, 6-9 November 2000, Tsukuba, p 229-239 (March 2001).

[3] R. Macek et al, “Electron Proton Two-Stream Instability at the PSR”, Proceedings of PAC2001, Chicago, June 18-22, 2001, p 688-692, (2001).

[4] A. Browman, private communication and T.S. Wang, et al, “The Static Electric Field of a Curved Electrode in a Beam Pipe”, PSR Technical Note 01-003 (2001). Also see R. Macek PI, LANL LDRD Progress Report, LA-13923, p 134-136, (2001).

[5] N. Hilleret et al, “A Summary of Main Experimental Results Concerning the Secondary Emission of Copper”, CERN LHC Project Report 472, August 2001.

[6] R. Rosenberg and K. Harkay, “A rudimentary electron energy analyzer for accelerator diagnostics”, NIM A 453 (2000) p507-513.

[7] D. Fitzgerald et al, “Commissioning of the Los Alamos PSR Injection Upgrade”, Proceedings of PAC99, March 29-April 2, 1999, New York, p 518-520 (1999).

[8] M. Plum, “Electron Clearing in the Los Alamos Proton Storage Ring”, Proceedings of the 1995 PAC, May 1-5, 1995 Dallas, p 3406-8, (1995).

[9] M. Plum et al, **“**Beam parameters that affect the PSR beam instability”, PSR Tech Note 97-019, (1997).

[10] R. Macek, “PSR Instability”, Buncher II Workshop, LANL, Jan 19, 1999.

[11] E. Metral, “Theory of Coupled Landau Damping", Particle Accelerators, vol. 62(3-4), p. 259, January 1999.

[12] M. A. Plum et al, “Experimental study of passive compensation of space charge at the Los Alamos National Laboratory Proton Storage Ring”, Phys. Rev. ST Accel. Beams 2, 064210 (June 1999).

[13] K.Y. Ng et al, “Recent Experience with Inductive Inserts at PSR”, Proceedings of PAC2001, Chicago June 18-22, 2001, p 704-6, (2001).

Driving the Electron-Cloud Instability by an Electron Cooler

G. Rumolo, F. Zimmermann, SL/AP, CERN, Geneva, Switzerland
O. Boine-Frankenheim, I. Hofmann, HSBP, GSI, Darmstadt, Germany

Abstract

We have studied the possibility to detune an electron cooler in order to have a high-current single bunch go through a controlled electron cloud of known density. This experiment could provide further information on the electron cloud instability, including its dependence on chromaticity, beam size, beam energy, and bunch length, and permit a calibration of the simulation code. We present simulation results for the SIS (Heavy-Ion Synchrotron) ring of GSI, equipped with electron cooler, and explore for which parameter combinations of beam intensity, bunch length, solenoid field, and electron current an instability might occur.

1 INTRODUCTION AND MOTIVATIONS

Gas ionization and/or photoemission combined with electron multiplication due to the secondary emission process on the inner side of the beam pipe may induce the build up of an electron cloud, which can significantly degrade the performance of rings operating with closely spaced proton or positron bunches. The undesired electron cloud causes pressure rise and beam instability when the parameters are pushed above certain thresholds [1].

The single-bunch instabilities driven by an electron cloud are currently studied by means of analytical approaches [2] as well as of multi-particle simulations carried out with the HEADTAIL code developed at CERN [3]. In this code, the interaction between a bunch of macro-particles and an electron cloud modeled with macro-electrons concentrated at one or more locations along the ring is simulated over successive turns. The application of the HEADTAIL to a number of existing machines where the electron cloud has been observed or to future rings where it will potentially be a limiting factor, has highlighted a series of common features of this type of instability: it appears above a certain threshold (in bunch intensity or cloud density), it gets damped by positive values of chromaticity in machines operating above transition, it is more severe for long bunches, it may be easily suppressed by weak solenoid fields present along the ring, and it is expected to be only vertical in rings where the electron cloud mainly builds up in dipole regions.

The goal of this paper is to discuss a way to benchmark the results of the code against experimental data acquired in a situation where the electron cloud is known in detail and controlled. If this were possible, the dependence of the electron cloud instability on chromaticity and/or bunch length could also be experimentally investigated and assessed. The electron cooler appears to be a very promising tool to be used for this purpose. The electron cooler generates a beam of electrons, which overlaps with the main beam circulating inside a ring (usually made of positive ions), along a small straight fraction of the whole circumference. In standard operation, the electron beam has the same mean velocity as the ion beam in order to produce its cooling by means of thermal exchange through collisions. For the experiment that we propose, we need an electron beam much slower than the ion beam (or moving in opposite direction), such that the head-tail coupling determined in the bunch by the passage through the quasi-stationary electrons can take place and moreover be produced afresh at each turn. For the set of parameters and tunability that it offers, the heavy ion synchrotron SIS at GSI-Darmstadt seems a suitable candidate to conduct this study. In Sec. II we will describe the experiment that we have conceived at the SIS in its details and discuss ranges within which parameters can be varied in order to optimize the chances of success. Section III will be devoted to the results of simulations from the adequately modified HEADTAIL code for some sample cases worked out in Sec. II. In Sec. IV conclusions are drawn.

2 EXPERIMENTAL STUDY OF THE ELECTRON CLOUD INSTABILITY AT THE SIS

To understand the single bunch instabilities due to the electron cloud and the dependence on bunch length and chromaticity, the use of an electron cooler at the GSI heavy ion synchrotron SIS could provide definite experimental answers. The idea is to generate through the cooler a controlled electron cloud, very well localized and with known features, whose effects on the beam could then be easily monitored and analyzed. Contrary to what happens in a cooling process, an electron beam used for simulating an electron cloud must be strongly detuned with respect to the high energy ion beam. A list of essential simulation parameters for the electron cooler experiment are summarized in Table I.

Protons or D^+ ions are preferred in this experiment because of their light masses. The reason why the choice would rather fall on D^+ ions than on protons lies in the fact that a high current D^+ beam can be produced much more easily from the GSI ion sources. Through multi-turn injec-

tion into the SIS, intensities up to 1 to 2 $\times 10^{11}$ D^+/beam or about 10^{10} protons/beam can be achieved. The factor 10 to 20 in current compared with the factor 2 in particle masses obviously renders the option of using a D^+ beam more attractive. Such a beam can be accelerated up to 2 GeV/u inside the SIS. It can be split into 4 bunches with an intensity of 2.5 to 5 $\times 10^{10}$ ions each and 5 to 10 m long (in total), as is required for the accelerating process, or the 4 bunches can be optionally merged into one single bunch 10 to 20 m long. Maximum detuning of the electron beam with respect to the ion beam can be achieved by tuning the electron beam on the ions at injection energy (10 MeV/u). This means that we can dispose of an electron beam having relativistic factors $\beta_{\rm e} = 0.145$ and $\gamma_{\rm e} = 1.106$, whereas the ions have $\gamma_{\rm e} = 3.129$ after acceleration. Because of the non-negligible longitudinal motion of the electrons, a modification to the ordinary HEADTAIL code has been implemented to take into account a "sliding" effect: each bunch slice sees mostly the previously deformed electron cloud but also a small fraction of newly generated electrons in substitution of those collected to the anode in the Δt between two subsequent slices.

The electrons in the cooler are guided by a solenoid field, whose minimum intensity (known as Brillouin field [4]) is proportional to the square root of the electron current density (and therefore to the electron volume density, too),

$$B = \sqrt{\frac{2{\rm m_e} I_{\rm e} \gamma_{\rm e}}{\epsilon_0 {\rm e} \beta_{\rm e} {\rm c} (\pi r_{be}^2)}} \ , \qquad (1)$$

where $I_{\rm e}$ is the electron current and r_{be} is the radius of the cross section of the electron beam. Available electron currents at the SIS cooler are in the range 0.35–1.5 A. Currents are easy to relate to the electron volume densities via

$$n_{\rm e} = \frac{I_{\rm e}}{(\pi r_{be}^2) {\rm e} \beta_{\rm e} {\rm c}} \ .$$

The radius of the cross section of the electron beam r_{be} can be equal to the radius of the cathode ($r_c = 1.27$ cm), or can be expanded by a factor as large as $\sqrt{3}$ (namely a factor 3 in the cross section) [4]. Maximum density is obtained with maximum current and minimum cross section expansion ($I_{\rm e} = 1.75$ A, $r_{be} = r_c$). These values yield $n_{\rm e}^{\rm max} = 4.25 \times 10^{14}$ m^{-3}. As the electron cooler stretches only over $\Delta s_{\rm cool} = 3$ m out of $C = 216$ m ring length, the simulated density integrates the potential effect of an electron cloud uniformly distributed along the ring and having reduced equivalent density $n_{\rm e}^{\rm max-eq} = n_{\rm e}^{\rm max} \frac{\Delta s_{\rm cool}}{C} = 6 \times 10^{12}$ m^{-3}. Unfortunately the high density also requires a quite strong solenoid field to be confined, which can be evaluated using Eq. (1): $B^{\rm max} = 9.5$ mT. Strong solenoid fields are not desirable in this context, because they are known to have a stabilizing action and therefore push the instability thresholds higher [5], making the regime in which we are interested more difficult to reach. Minimum solenoid field is associated with minimum current and maximum cross section expansion ($I_{\rm e} = 0.35$ A, $r_{be} = \sqrt{3} r_c$): $B^{\rm min} = 2.6$ mT. Densities corresponding to this value are $n_{\rm e}^{\rm min} = 3.3 \times 10^{13}$ m^{-3} and $n_{\rm e}^{\rm min-eq} = 5 \times 10^{11}$ m^{-3}. In the simulations described in the next Section an intermediate case with $n_{\rm e} = 10^{12}$ and $B = 6.7$ mT will be examined.

Table 1: SIS parameters used for the simulations.

Circumference	216 m
Relativistic γ	3.129
Number of bunches	1 to 4
Bunch population (N_b)	2.5×10^{10} to 10^{11} D^+
Emittances ($\epsilon_{x,y}$)	$3.75/1.25$ μm
Tunes ($Q_{x,y,s}$)	4.308/3.29/4.8$\times 10^{-4}$
Bunch rms-length (σ_z)	1.25 m to 5 m
Beta's at the cooler ($\beta_{x,y}$)	7.67/8.12 m
Alpha's at the cooler ($\alpha_{x,y}$)	-0.66/-0.28
Dispersion at the cooler ($D_{x,y}$)	2.08/0 m
Mom. compaction (α)	0.0356
Rms-energy spread ($\delta p/p_0$)	5.2 to 21×10^{-4}
Chromaticities ($\xi_{x,y}$)	corrected
Cooler length ($\Delta L_{\rm cool}$)	3 m
Cooler cathode radius (r_c)	1.27 cm
Electron current (I_e)	0.35 to 1.5 A
Electron relat. $\beta_{\rm e}$	0.145

3 SIMULATION OF THE TWO-STREAM INSTABILITY INDUCED BY THE ELECTRON BEAM IN THE COOLER

The code HEADTAIL has been used to simulate the effect of the electrons from a cooler on the D^+ ions of a bunch circulating in the SIS. For this purpose two major modifications of the original code were needed. First, a solenoid field acting on the electrons has been added. Recent studies on the wake functions due to the electron cloud have shown that a solenoid field can lower by one or two orders of magnitude the trailing field induced by a displaced bunch head as the rest of the bunch goes through an electron cloud [3, 5]. Therefore the presence of a solenoid, which is necessary in the cooler to keep the electron stream confined, is expected to play an important role that should not be neglected in a realistic study. Second, the electrons in the cooler, even if they are slow with respect to the ions in the beam, have a high longitudinal velocity (about 0.145c), which causes a small fraction of electrons to be lost to the anode during the bunch slice passage time Δt_{sl} and to be replaced by newly incoming electrons. In most cases, this is a significant effect since we can easily check that for the short bunches ($\approx$ 5 m), when we come to the very end of the bunch, between 1/3 and 1/2 of the electrons have been regenerated during the bunch passage and thus do not carry any memory of the bunch head. This effect becomes worse yet for

longer bunches. In quantitative terms, we could say that the longitudinal motion of the electrons introduces a sort of *interaction length* above which any possible coupling along the bunch disappears: $\Delta l_{int} = \Delta L_{\rm cool}(\beta_i/\beta_e - 1)$. SIS numbers yield $\Delta l_{int} \approx 18$ m, which means that in the case of the single long bunch in the machine head and tail are not coupled by the cooler (the wake field has a shorter range than the whole bunch longitudinal extension). In the code, we require that after N_{sl} slices only a fraction $f = (1 + \Delta L_b/\Delta L_{\rm cool})\beta_e/\beta_i$ of the N_{me} macroelectrons must have memory. The effect can be achieved if at each slice $N_{me}/(f \times N_{sl})$ electrons are regenerated anew.

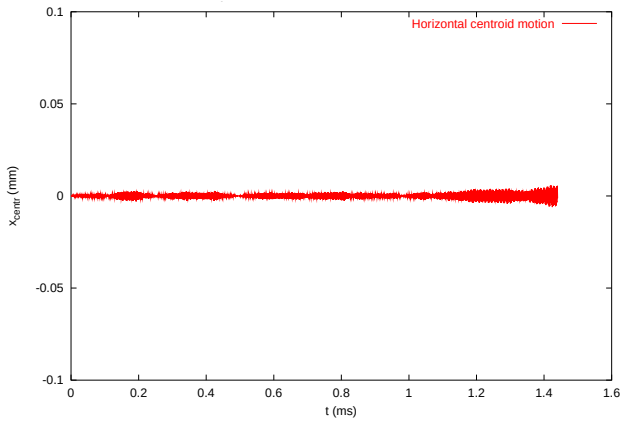

Figure 1: Horizontal centroid motion of an SIS bunch when the cooler parameters are $n_e = 10^{12}$ m^{-3} and $B = 6.7$ mT.

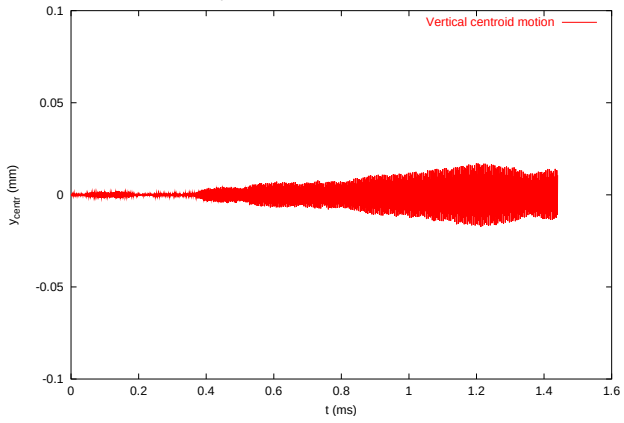

Figure 2: Vertical centroid motion of an SIS bunch when the cooler parameters are $n_e = 10^{12}$ m^{-3} and $B = 6.7$ mT.

Both the solenoid field and the interaction length tend to have a stabilizing effect on the beam.
Results from HEADTAIL simulations show that using the sets of nominal parameters as found in the previous section, the bunch never becomes unstable because of the cooler. For instance, Figs. 1 and 2 show the centroid motion for the intermediate case $n_e = 10^{12}$ m^{-3} and solenoid field $B = 6.7$ mT (4 bunches in the SIS). The single bunch does not exhibit any significant unstable dipole oscillation over 2000 turns. Figures 3 and 4 show that also the bunch rms-sizes remain stable over 2000 turns.

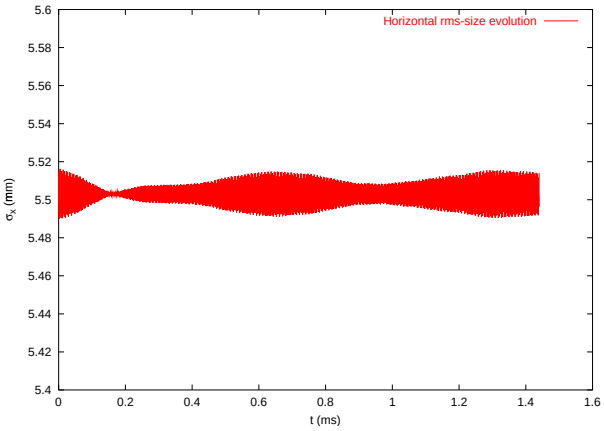

Figure 3: Horizontal rms-size evolution of an SIS bunch when the cooler parameters are $n_e = 10^{12}$ m^{-3} and $B = 6.7$ mT.

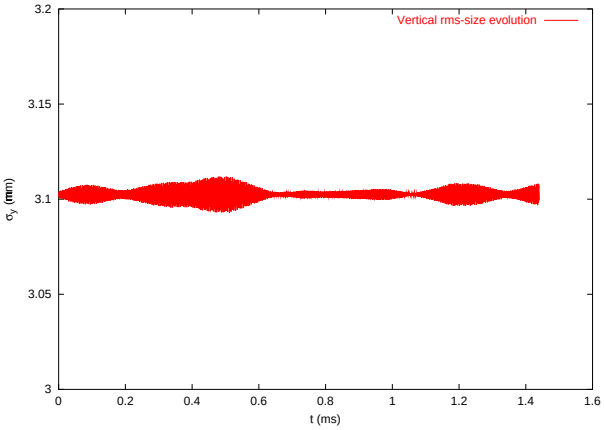

Figure 4: Vertical rms-size evolution of an SIS bunch when the cooler parameters are $n_e = 10^{12}$ m^{-3} and $B = 6.7$ mT.

If we move parameters away from the nominal setting, we can easily cross the stability boundary. As examples of instability driven by the electron cooler we present:

- 4 bunches configuration, solenoid field about 0.01 T, electron beam density $n_e = 6 \times 10^{13}$ m^{-3}, which is about a factor 10 higher than thought to be achievable at the SIS cooler. Horizontal and vertical emittance growths relative to this case are plotted in Figs. 5 and 6.

- Single bunch configuration, electron beam density $n_e = 10^{12}$ m^{-3}, solenoid field $B = 0.67$ mT, namely ten times lower than required to keep the electron beam stable in the SIS cooler. Horizontal and vertical centroid motions are plotted in Figs. 7 and 8, and relative emittance blow-ups in Figs. 9 and 10.

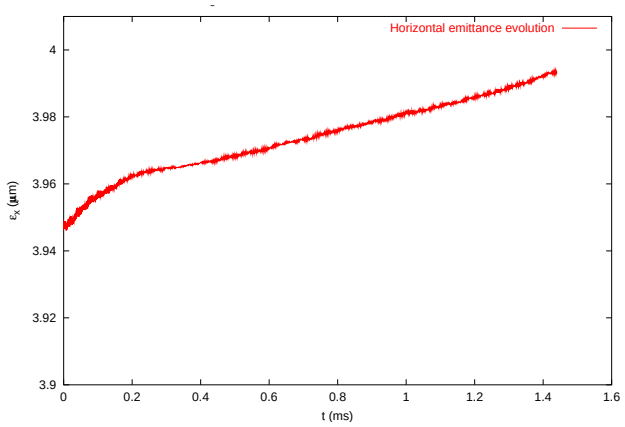

Figure 5: Emittance growth of an SIS bunch when the cooler parameters are $n_e = 6\times10^{13}$ m^{-3} and $B = 9.5$ mT.

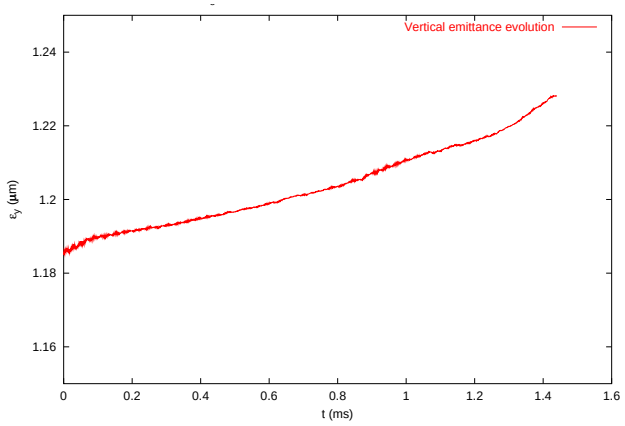

Figure 6: Emittance growth of an SIS bunch when the cooler parameters are $n_e = 6\times10^{13}$ m^{-3} and $B = 9.5$ mT.

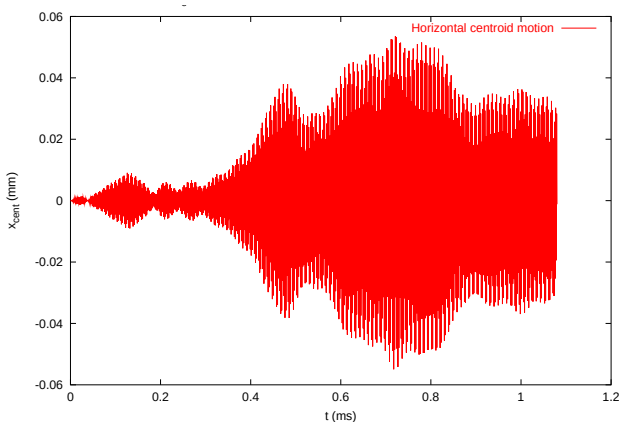

Figure 7: Horizontal centroid motion of an SIS bunch (single bunch configuration) when the cooler parameters are $n_e = 10^{12}$ m^{-3} and $B = 0.67$ mT.

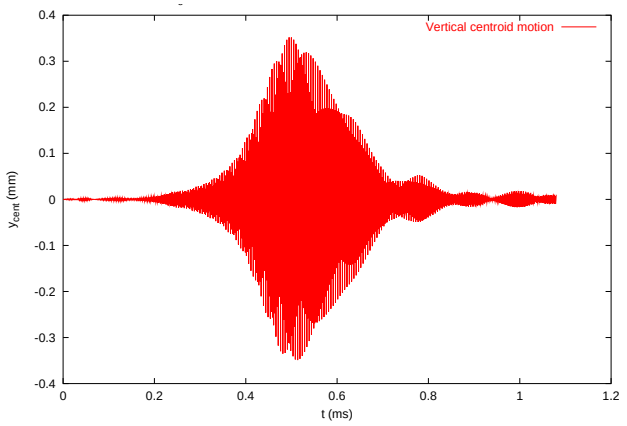

Figure 8: Vertical centroid motion of an SIS bunch (single bunch configuration) when the cooler parameters are $n_e = 10^{12}$ m^{-3} and $B = 0.67$ mT.

4 CONCLUSIONS AND OUTLOOK

In conclusion, we have studied possible beam-machine configurations which would allow us to excite an instability on a proton or ion beam by means of the electron cooler. The feasibility of this experiment would provide an invaluable tool to benchmark simulation outputs from the electron cloud instability codes against real data obtained under controlled conditions.

Simulations carried out using the parameters for the SIS synchrotron indicate that the instability cannot be driven in this particular ring under standard working conditions. Possible solutions would be to push the current to higher values and/or have a transversely smaller beam at the cooler section and/or decrease Q_s. Another possibility to be explored is the excitation of a regular head-tail instability instead of a TMCI by setting the chromaticity to appropriate positive values (as we are below transition).

Simulations have anyway proven that by pushing the parameters sufficiently above some SIS thresholds, the strong head-tail instability can be triggered. This means that the use of machines other than the SIS should be taken into consideration, where a more favourable ratio between cooler section and ring circumference and/or higher proton currents could be available. Presently, the idea of using the ESR at GSI in isochronous mode (bunches are longitudinally frozen) appears especially promising. Work and inter-lab activity is underway to study in detail this and diverse further proposed options (use of the CERN-AD or the e-cooler at the FNAL).

5 ACKNOWLEDGEMENTS

The authors would like to thank F. Ruggiero, G. Arduini, D. Schulte, E. Metràl, M. Giovannozzi, D. Möhl, M. Chanel, M. Blaskiewicz, A. Burov for helpful discussion and information.

6 REFERENCES

[1] G. Rumolo, F. Ruggiero and F. Zimmermann, Phys. Rev. ST Accel. Beams, **4**, 012801 (2001).

[2] K. Ohmi,, F. Zimmermann ans E. Perevedentsev, Phys. Rev. E **65** (2002) 016502

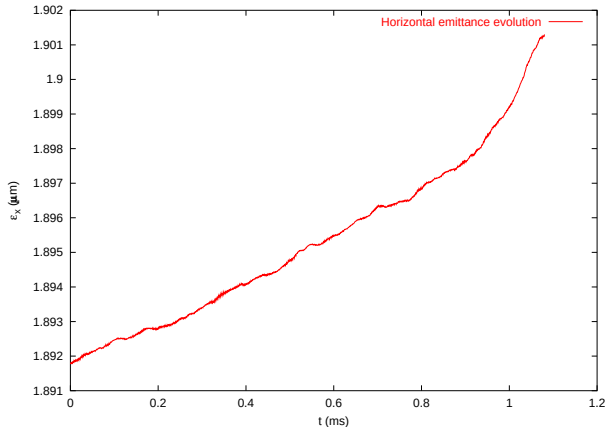

Figure 9: Emittance growth of an SIS bunch (single bunch configuration) when the cooler parameters are $n_e = 10^{12}$ m^{-3} and $B = 0.67$ mT.

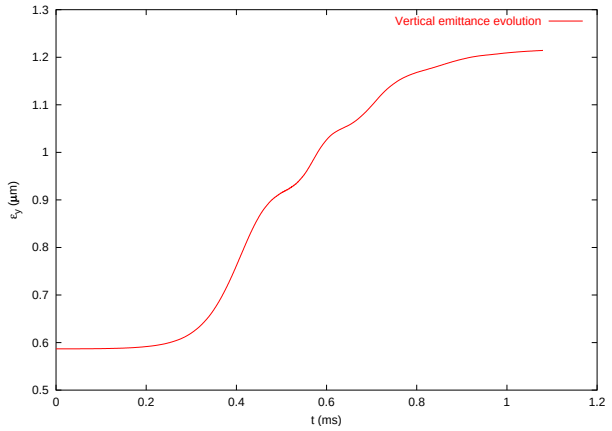

Figure 10: Emittance growth of an SIS bunch (single bunch configuration) when the cooler parameters are $n_e = 10^{12}$ m^{-3} and $B = 0.67$ mT.

[3] G. Rumolo and F. Zimmermann, “Electron Cloud Simulations: Beam Instabilities and Wake Fields”, elsewhere in these proceedings.

[4] L. Groening, “Untersuchungen zur Elektronenkuehlung und Rekombination hochgeladener Ionen am Schwerionen-Synchrotron SIS” PhD thesis, GSI-Report DISS. 98-15 Dezember 1998.

[5] G. Rumolo and F. Zimmermann, “Contributions of the SL-AP Group to the Two-stream Instabilities Workshop”, CERN SL-2001-067 (2001).

RF TEST BENCHES FOR ELECTRON CLOUD STUDIES

F. Caspers, J-M. Laurent, U.Iriso Ariz, A. Mostacci
CERN, Geneva, Switzerland

Abstract

In the framework of the CERN program on the electron cloud effects, two laboratory Radio Frequency (RF) set-ups have been built to study and characterize the phenomena by complementing one to the other. The first consists in a coaxial test stand with a 100 mm diameter vacuum chamber forming the outer conductor and 6 wires cage-aerial-type as the inner conductor. In order to simulate the bunched beam, this test stand is powered with short pulses. The available field strength in a travelling wave mode allows triggering electron multipacting in stainless steel surfaces, but not in chambers treated to reduce the secondary emission yield. Thus, upgrades in the bench set-up have been pursued: instead of dumping the pulsed power into a load, it is re-circulated in a multiple frequency ring resonator. For this purpose, we designed a directional coupler with several kV DC isolation, very low transmission losses and a bandwidth of 4 octaves.
In the second set-up, multipacting is produced in a resonator consisting in a coaxial wave guide (1.5 m long) shunted at both ends: the inner conductor diameter is 32 mm while the outer conductor diameter amounts to 100 mm. Due to the standing wave configuration, high electromagnetic fields are stored inside the set-up, and multipacting is 'one point type'. This is rather different than the one taking place in accelerators, but electron surface bombardment is large enough to produce and characterize the scrubbing effect. An overview of the present status of both set-ups is given here, highlighting the latest improvements and results.

1. THE TRAVELING WAVE MULTIWIRE CHAMBER

1.1. Introduction: the need of a Ring Resonator

Multipacting is an electron multiplication resonance, which develops in RF devices when a periodic field strength is maintained between two opposite surfaces and if energy and resonant conditions for electron kinetics are met. Such conditions will show up in the Large Hadron Collider (LHC). The bunched proton beam will provide the periodic electric field; an electron cloud may develop leading to vacuum breakdown by a fast pressure increase and potentially ending in important degradation in beam performance and/or excessive liquid helium consumption.
In order to study those phenomena in a laboratory, a bench test set-up [1] was built where six wires are inserted in a circular vacuum chamber and submitted to RF pulses simulating the Transverse Electro-Magnetic (TEM) field produced by a bunched beam (Fig. 1). That travelling wave (TW) coaxial structure is powered by a wideband power amplifier* driven from a pulse generator. The output is connected to a RF load, which absorbs the transmitted power and prevents undesirable reflections. Two probes have been installed to collect the electrons, one placed on top of the chamber and the second one is the pick-up shown in Fig. 1.

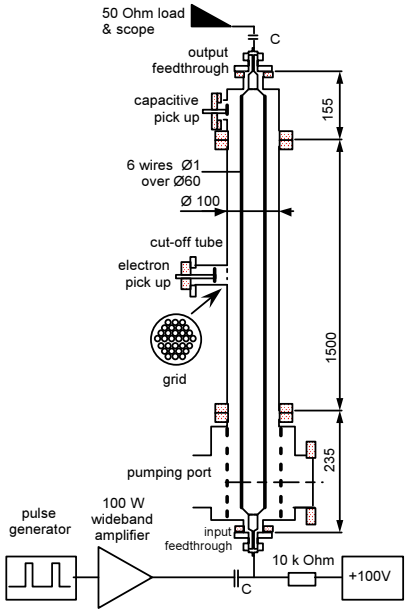

Figure 1. TW multi-wire chamber. The pulses coming from the signal generator are amplified up to 100 V by the wideband power amplifier. The pulse, biased to ensure a positive voltage, travels along the six wires inside the chamber. The 50 Ω RF load on the top avoids undesirable reflections. The capacitors on top and bottom isolate the DC currents inside the chamber. Lengths are given in mm.

The achievable electric field strength is mainly limited by the output power of the wideband amplifier. On the 50 Ω load, the initial (i.e. before improvements) output voltage, V_{IN}, is limited to 100 V (baseline-peak), which corresponds to multipacting electron energy E^{in}_{e} = 75 eV, according to both simulations and measurements in [1]. To trigger multipacting, the Secondary Emission Yield (SEY) has to be greater than 1.3 [2]. A typical characteristic for baked-out stainless steel surfaces is shown in Fig. 2, from where it is clear that 75 eV is sufficient to trigger multipacting. The SEY behaviour

* 'Amplifier research, Model 100W1000, 1-1000 MHz, 100 W.

for “treated” chambers is similar as what is shown in Fig. 2 for bake-out stainless steel, except that the minimum multipacting energy is pushed further. On top of that, this energy increases also after that the material has been exposed to a certain electron dose. For materials common in accelerator technology, the minimum multipacting energy can be moved up to the 200 eV range. Therefore it is desirable to reach higher multipacting energies in the bench test stand.

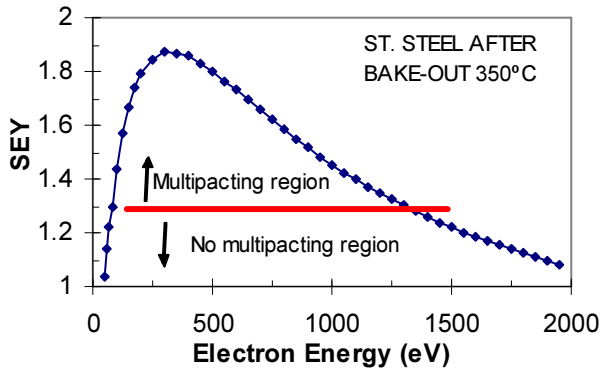

Figure 2. Secondary Emission Yield (SEY) for stainless steel after bake-out (data measured by Y. Bojko, CERN-LEP-VAC, 1996). Multipacting occurs only when the SEY is above the horizontal line (i.e. SEY greater than 1.3).

A possible way to increase the voltage V_{IN} (without changing the amplifier), is to re-inject a fraction of the output power into the system, similarly to what is proposed in [3]. Such a re-circulating scheme is called Ring Resonator (RR) and allows a much more efficient use of the amplifier output power.

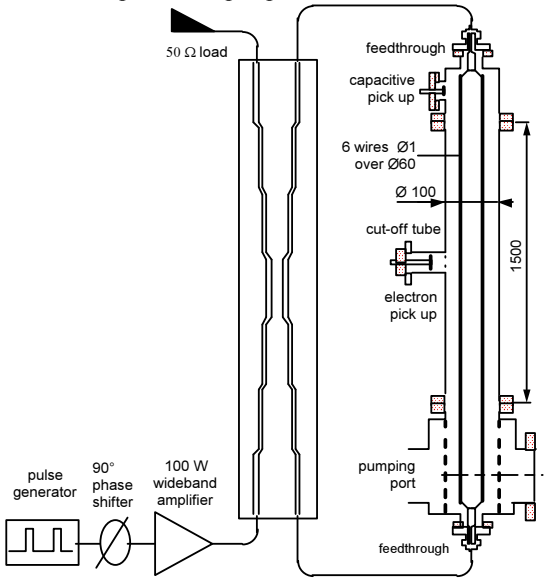

Figure 3. Ring resonator outline. Pulses from the signal generator are amplified in the power amplifier, and introduced in the wideband directional coupler. Part of the pulse is dumped at the end of one arm of the coupler to the RF load, while the other arm sends the induced signal to the chamber. When leaving the chamber, the pulse enters again in the coupler, where it is added to the next pulse delivered by the amplifier. The phase shifter compensates the 90º phase offset produced by the coupler. On top of the chamber there is a button probe, which will be used to evaluate the power enhancement effect of the RR.

The conceptual scheme is shown in Fig. 3: the pulse coming from the chamber and the pulse coming from the amplifier are superimposed by means of a directional coupler. The RF pulses coming from the signal generator are amplified in the power amplifier, and then introduced in the wideband directional coupler. Part of the pulse power is dumped to the RF load, while another part enters into the chamber. When leaving the chamber, the pulse again goes through the coupler, where it is added to the next pulse delivered by the amplifier. The 90° phase shifter between the signal generator and the power amplifier, compensates the 90 deg. offset introduced by the coupler.
The RR has stringent requirements: low reflection from the Travelling Wave transmission line and a RF coupler designed “ad hoc”. The final goal is to get a gain for the incident power around 8 or 9 dB (sec. 1.2), i.e. nearly 10 times the amplifier output power. In the following we report about the necessary steps to build the RR: improvements on the TW chamber (sec. 1.3) and design and test of the coupler (sec. 1.4). Achieved performances are given as well (sec. 1.5).

1.2. Loop power gain

In a RR, the (maximum) power gain (G) is given by [4]

$$G = \left[\frac{C}{1 - 10^{-\alpha/20}\sqrt{1-C^2}} \right] \qquad (1)$$

where C is the voltage coupling factor of the coupler and α is the one-way attenuation in the ring (in dB). Figure 4 sketches the power gain as a function of the attenuation for different values of C. To get a useful gain (G ~8-9 dB), a possible choice is α ~0.5 dB and C ~10 dB (circle in Fig. 4). Those conditions have to be maintained up to a maximum frequency f_{MAX} given by the relative bandwidth of the coupler (i.e. BW=20 from previous experience) and by the minimum working frequency, f_{MIN}=30MHz (corresponding to the 25 ns bunch spacing of LHC plus a “contingency margin”): $f_{MAX} = BW * f_{MIN} = 600$ MHz. The one way attenuation α depends mainly on the reflection coefficient and the transmission losses in the TW chamber (sec. 1.3), while the voltage coupling factor is a specification of the coupler (sec. 1.4).

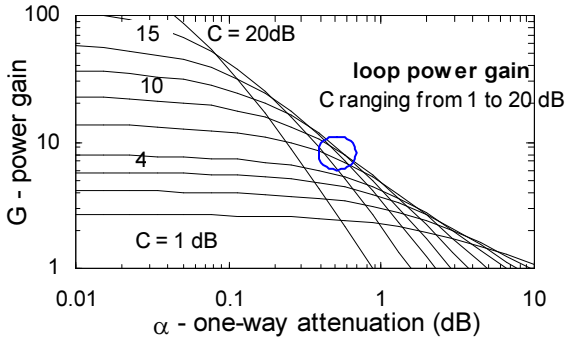

Figure 4. Power gain in the ring resonator (G) as a function of the attenuation in the ring (α) and the voltage coupling factor C. The circle marks a possible choice of parameters: α~0.5dB and C~10dB to get a power gain G between 8 and 9 dB.

1.3. Improvements to the original chamber

Reducing the one way attenuation (α) requires acting both on the transmission losses of the six wires in the (circular) vacuum chamber and on the impedance matching among cables, feedthroughs and the coaxial structure (i.e. reducing reflections). The frequency response of the initial set-up has been measured with a Vector Network Analyzer (HP8753D), as shown in Fig. 5 (transmission coefficient versus frequency) and Fig. 6 (characteristic impedance (Z_{line}) along the structure). These plots compare the initial situation (dotted lines) to the improved one (solid lines). The initial transmission coefficient is plotted in Fig. 5 (dotted line) showing that it has to be further reduced (at least up to f_{MAX}). Using the time domain option (step mode) of the instrument, the reflection coefficient Γ can be measured as a function of the position along the coaxial line. Then from

$$Z_{line} = Z_0 \frac{1+\Gamma}{1-\Gamma}, \qquad (2)$$

one gets Z_{line} along the transmission line, as shown in Fig. 6. Ideally, the characteristic impedance should be 50 Ω all along the path, in order to avoid reflections. The dotted line (original status) indicates impedance mismatches at the feedthrough locations as well as along the wire (minor effect). The transition pieces, joining the wires to the feedthroughs, have been electrically and mechanically redesigned (Fig. 7 is a sketch of the relevant geometry). The joint is made of Cu and the Cu-Be transition star has been gold plated in order to reduce its contact resistance and to improve the welding properties. The diameter of the different parts of the joint is chosen according to

$$Z = 60 \ln\left(D_{ext} / D_{\text{int}} \right), \qquad (3)$$

while their heights (h) are such that $h \cong D_{ext}/9$ in order to provide a smooth RF transition [4]. On one side of the chamber, the six Cu wires are crimped and welded on the transition stars arms, while on the other side they are fixed by clamps. The diameter of the circle formed by the six wires (60 mm in our case) has been optimised following experimental results (no analytical approach is available). Special feedthroughs, taken from the LEP Standing Wave Cavities (LEP SWC), have been also used for UHV performance and mechanically robustness in order to resist the mechanical tension of the wires.

All these improvements produced the effect seen in figures 5 and 6 (solid lines). The transmission coefficient is now within the correct limits (0.5 dB at 600 MHz), since the impedance is close to 50 Ω all along the line, except at the unavoidable transition between the 6 wires structure and feedthroughs. Anyway, according to the measurements, this residual mismatch causes no significant losses in α.

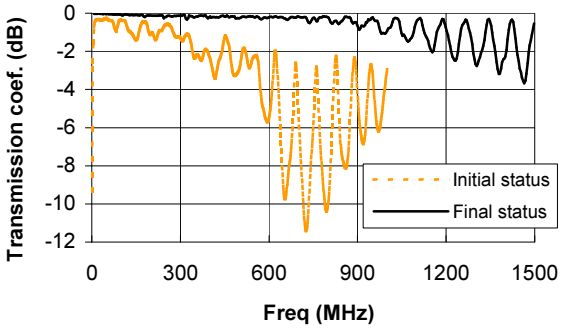

Figure 5. Transmission coefficient of the TW chamber before (dotted orange line) and after (solid black line) the improvements described in sec. 1.3. The transmission coefficient is within desired limits: 0.5 dB up to 600 MHz.

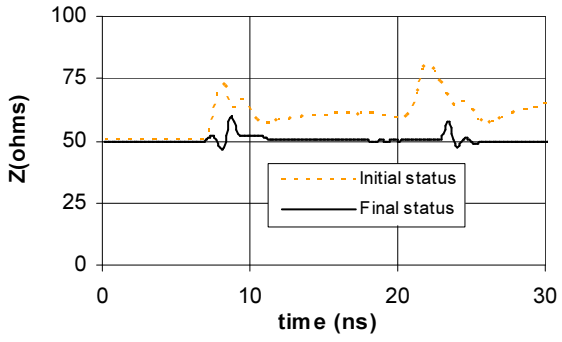

Figure 6. Characteristic impedance along the chamber before (dotted orange line, upper trace) and after (solid black line) the improvements described in sec. 1.3. Eventually, the impedance along the line is everywhere close to 50 Ω except for the unavoidable residual mismatches after the feedthroughs (transition from the feedthroughs to the 6 wire structure), which do not affect significantly the transmission coefficient.

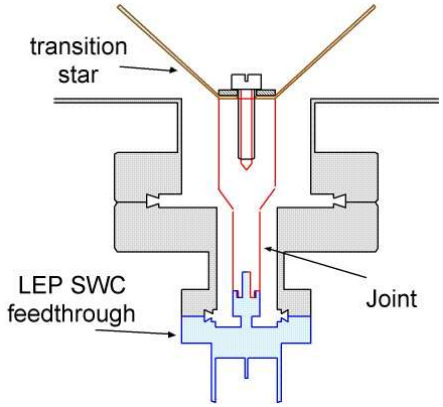

Figure 7. Bottom part of the chamber, where we can see the transition pieces between the feedthroughs and the six wires. The joint is made of Cu, while the transition star is made on Cu-Be. The transition star has six arms, corresponding to the six inner wires, but only two of them are drawn here.

1.4. Coupler design.

As stated above, the coupler should have a voltage coupling factor C =10 dB in the whole frequency range. On top of that, the coupler must stand DC isolation up to 1 kV between the strip-lines and ground (according to multipacting simulations). The lowest working frequency (f_L) is fixed by the spacing between the RF pulses. Since the aim is to simulate LHC bunches, where the bunch spacing can go up to ΔT=50 ns, the lowest relevant frequency is $f_L = 1/\Delta T$=20 MHz (with reduced performances). The upper frequency limit (f_{MAX}) is set to 600 MHz as explained in sec. 1.2. The λ/4 symmetric 9 sections coupler described in [5] accomplishes our requirements. Since the central frequency is 300 MHz, each section is λ/4=25 cm, which implies a coupler length ~2.25 m (see Fig. 8). Due to the non standard specifications, the coupler has been built "ad hoc" using copper strips 0.3 mm thick (to reduce ohmic losses) and bending them as shown in Fig. 8 (right picture). Such a "U-like shape" is repeated for each section, varying its characteristic lengths: *x, w, u, l*, and *s*. The dimensions of the shielding box are chosen according to the cut-off frequency of the high order propagating mode (i.e. 1 GHz for our structure).

The voltage coupling factor depends on the characteristic impedance for the odd and even TEM propagating modes (Z_{odd} and Z_{even}). The free design parameters are the geometrical dimensions (defined in Fig. 8): they are carefully determined to meet the required value of Z_{odd} and Z_{even} for each section [6]. For a given geometry (i.e. a set of values for *x, w, u, l*, and *s*) the odd and even impedances are first computed with *SuperFish*, a 2-D electrostatic computer code wide used in RF accelerating cavities [7], and then measured on a special test stand. This procedure has been then repeated for each section.

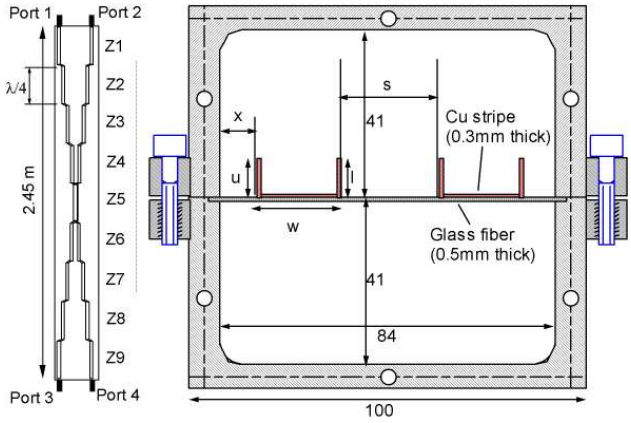

Figure 8. Top view (left picture) and cross section (right picture) of the coupler. The left side shows the layout of the coupler with the nine sections (referred as Z_i with $i=1,\ldots,9$). Since the coupler is symmetrical, $Z_j=Z_{10-j}$ ($j=1,\ldots,4$).The right picture shows the copper stripes parameters (*w, u* and *l*) and their positions (*x* and *s*) that change for each section to have the appropriate values of the impedance. All distances are given in mm.

The *SuperFish* simulation works as follows. The two strips are (numerically) excited both with a voltage $+V$ (even mode) or one with $+V$ and the other with $-V$ (odd mode). The code computes the energy stored inside the box for each excitation (U_{odd} and U_{even}). Following the analogy with electric circuits [8], one gets:

$$Z_{odd} = \frac{2 \cdot V^2}{c \cdot U_{odd}} \qquad (4)$$

and

$$Z_{even} = \frac{V^2}{c \cdot 2 \cdot U_{even}}, \qquad (5)$$

where c is the velocity of light.

Each section is then tested in a dedicated coupler 50 cm long but with exactly the same cross section dimensions (the only ones important for Z_{odd} and Z_{even}). The impedance of both modes in the whole coupler are shown in Fig. 9, where the ideal (or theoretical) impedance values found in [9] are marked with red crosses. In Fig. 9, Z_{odd} and Z_{even} are measured connecting the VNA to ports 1 and 2 (Fig. 8, left) through a hybrid coupler to give a phase offset: 0 degrees for even mode measurement, 180 degrees for the odd mode measurement. The time domain (step mode) reflection data are then converted to impedance data using Eq. (2). After half of the structure, the previous data are not longer valid because of multiple reflections and the same measurement has been done from ports 3 and 4 (Fig. 8, left): the results are very similar (minor tolerances).

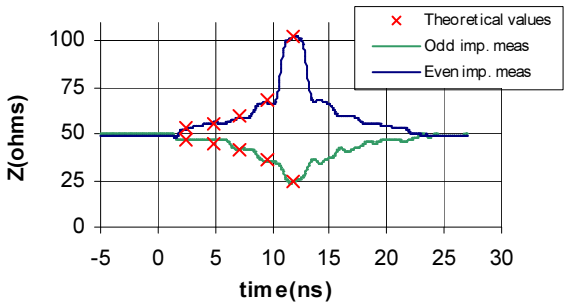

Figure 9. Z_{odd} and Z_{even} measured in the final coupler as a function of the time (i.e. position along the line). After half of the structure, measurements are not longer valid because of the measuring reflections.

Figure 10 shows the behaviour of C as a function of the frequency for three cases: the ideal one (corresponding exactly to the theoretical impedance values given in [9]), the calculated behaviour of C from Z_{odd} and Z_{even} measured for each section separately and the measurement on the whole coupler. Concerning the blue curve of Fig. 10, the coupling factor has been computed with SERENADE, while the violet curve is the transmission between ports 1 and 2 of the coupler: Actually, the coupler working range is from f_{MIN}=20 MHz up to f_{MAX}=530 MHz (instead of 30 - 600 MHz): the effects of this difference are negligible in the final RR working. The ripple in C is sensible to small variations of the characteristic impedance of each section.

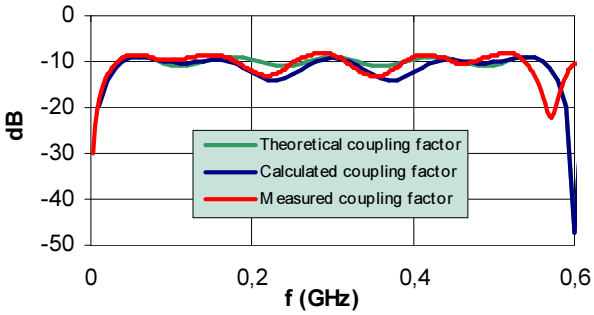

Figure 10. Coupling factor of the final coupler. The ripple of the measured coupling factor (violet line) is reasonably close to both theoretical (light blue line) and calculated (blue line) behaviour in the relevant frequency range (20 to 530 MHz, as explained in the text).

1.5. Final Ring Resonator

The final layout of the RR is shown in Fig. 3. In order to see the power enhancement effect of the Ring Resonator, we measure the transmission between a button probe located on top of the chamber and the bottom connection of the chamber. Figure 11 compares the signals seen using the RR (black line) compared to the signal in the original TW chamber (orange line). The power enhancement occurs only at particular frequencies which are integer multiples of $f_R = 1/T_R$, being T_R the round trip time in the RR. The round trip time depends also on the length of the connecting cables and was chosen to be 25 ns, according to the nominal LHC bunch spacing. Figure 11 shows a value of f_R close to 40 MHz. The difference between the orange line (measured directly to the chamber) and the black curve (measured using the RR) shows a minimum gain at $(n*f_R)$ of 6 dB, where n is a natural number.

To compensate the 90° phase offset intrinsically given by the coupler, the pulse has been "pre-distorted" with a phase shifter placed just after the source (see Fig. 3). The phase shifter enhances also the amplitude of the signal actually sent into the RR. The plot in Fig. 12 shows a gaussian unitary pulse before (orange line) and after (blue line) a 90° phase shift, as in an ideal 90° phase shifter. The amplitude of the phase shifted pulse varies from -0.65 to +0.65. Assuming that the amplifier output voltage swing is ±1 (after normalisation), the "bipolar-like" signal is amplified by 2/1.3=1.53, i.e. 3.7 dB. Thus the total power enhancement is 6+3.7=9.7 dB.

Thus the available amplitude of the TW pulses can be at least 3 times bigger, which allow to produce multipacting electrons of roughly 200 eV. At this energy, typically the SEY is bigger than 1.3 (multipacting threshold) and close to its maximum (SEY_{max}).

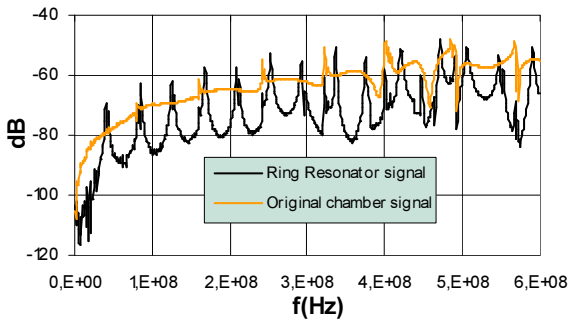

Figure 11. Amplitude of the signal seen in a button pick-up on the top of the chamber as a function of the frequency with the effect of the RR (black line) compared with the original chamber (orange line). In this plot, the maximum peaks frequency rate for the RR set-up is slightly larger than 40 MHz due to cables length.

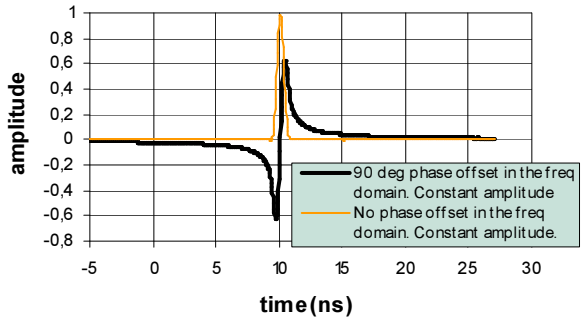

Figure 12. Effect of a 90° phase shift on a gaussian pulse. The plot shows a gaussian unit pulse before (blue line) and after (orange line) a 90° phase shift, as in an ideal phase shifter. The curves are obtained measuring with VNA (time domain, pulse mode) the transmission through a cable between port 1 and port2.

2. THE STANDING WAVES SINGLE CONDUCTOR COAXIAL CHAMBER

2.1. Introduction: motivation for a Standing Waves single conductor coaxial chamber

In an accelerator, the emitted electrons from one side of the wall cross the chamber to impact the other side of the chamber (two points multipacting). As seen in sec. 1, this can be simulated by a TW structure, but the electric field available is limited. In order to reach higher electric fields, a Standing Wave (SW) single conductor coaxial chamber has been developed and used to test multipacting. Since in a SW configuration electric field is confined inside the resonator, the electron energy and bombardment dose can be high enough to simulate accelerator conditions. Not only fully treated surface can be tested, but also the study of samples is suitable. Nevertheless, this set-up does not satisfactorily simulate the multipacting in an accelerator: in a SW configuration (due to RF sinusoidal field) the outgoing electrons from one wall may hit again the same surface after one or several complete RF cycles (one point multipacting) [10].

There are several reasons to study this effect. In fact, multipacting currents can absorb RF energy and produce breakdown in high power components, such as couplers or RF accelerator cavities (superconducting or not). It is useful to compare different surface treatments or different materials, providing a 'calibration' for numerical simulations.

2.2. Experimental set-up

The SW single conductor coaxial chamber is nothing else than a coaxial resonator: a 1.5 m long coaxial line shunted at both ends (with an inner diameter is 32 mm and an outer one of 100 mm). The upper end holds two adjustable magnetic couplers: one, critically coupled, for feeding RF power and the second one, weekly coupled, to measure in transmission mode the resonance frequency and the quality factor Q. The lower plane is perforated (towards the vacuum pump) in order to allow the vacuum pumping of the resonator. A typical operational vacuum pressure is 5 10^{-8} mbar. An electron pick-up is placed in the middle of the resonator where the electric field is maximum (in the fundamental mode) and thus where most of the electrons are produced (see Fig. 13). The pick-up layout depends on the actual measurement and two typical ones are discussed below.

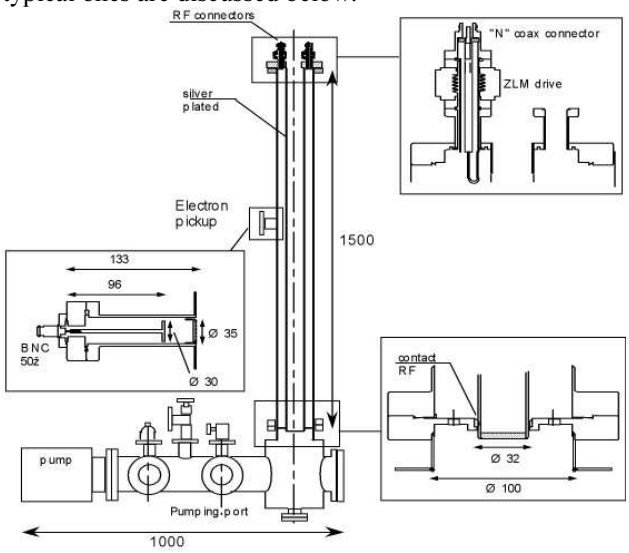

Figure 13. Layout of the coaxial resonator with details of top and bottom parts. The inner conductor is silver plated to increase its conductance, and the electron pick-up is placed in the middle of the resonator where the electric field is maximum. The upper end holds the two adjustable magnetic couplers, while the lower end is perforated to allow the vacuum pumping of the resonator. Lengths are given in mm.

The resonator is operated in the fundamental TEM mode, at a resonant frequency f_0 (f_0=98.7 MHz); a drift of f_0 (±0.1 % variation) has been observed and it is mainly due to temperature, which varies with the dissipated power in the structure. As confirmed by simulations [11], multipacting is one point type and takes places in the inner surface of the outer conductor. The outer conductor is made of stainless steel while the inner conductor is silver-plated in order to improve its conductance: the field is higher there and the silver plating increases the quality factor Q of the resonator. Q_{load} is the ratio between the energy stored in the resonator and the power losses:

$$Q_{load} = \frac{f_0 W}{P_p}, \quad (6)$$

where W is the total stored energy and P_p is the power lost in the resonator, including the external coupling system (losses due to feeding couplers, transmitter, etc). For this set-up, Q_{load} has been computed from the voltage measured at the output coupler as a function of the frequency:

$$Q_{load} = \frac{f_0}{f_2 - f_1} \quad (7)$$

where f_0 corresponds to an output voltage of V_{max}, and f_2 and f_1 are the frequencies at which $V=V_{max}/\sqrt{2}$ (3 dB points). Usually when feeding power into a resonator from a RF source, part of it goes into the resonator and part of it is lost in the coupling circuit. The so called "critical coupling" is when all power goes to the resonator and no reflection occurs [12]. One can reach a condition close to critical coupling by modifying the coupling circuit (to minimise reflections). Assuming critical coupling, the Q of the resonator is twice the Q_{load} measured from the coupling circuit (in our case $Q=2*Q_{load}=760$).

The magnetic coupling loops are mounted on two manual drives, which allow adjustment of their active area. The RF power is fed to the resonant resonator via the input coupling loop. Its positioning allows to change the input coupling and obtain critical coupling (i.e. minimizing the reflected measured signal). The output loop is, instead, adjusted to observe a small signal from the electromagnetic field stored in the resonator. Both loops are placed where the magnetic field is maximum.

2.3. Electric field calibration

The maximum amplitude of the electric field inside the chamber is measured from the power stored in the resonator. The signal generator produces the input signal, which then is amplified by a 50 dB amplifier (see Fig. 14). A power meter measures the incident power to and the reflected power from the resonator.

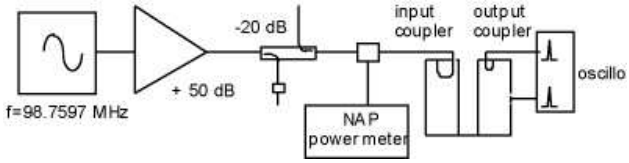

Figure 14. Layout used to measure the power inside the resonator, and thus, calculate the electric field. The signal generator sends the RF sinusoidal signal, which then is amplified (50 dB) by the power amplifier and finally introduced to the resonator via the input coupler. The power meter measures the incident and reflected power, while the power stored in the resonator is measured with the output coupler.

The voltage difference between the inner and outer conductor is given by [13]

$$u = \sqrt{P_{inside} \cdot Q_{load} \cdot Z \cdot (4/\pi)} \quad (8)$$

where P_{inside} is measured, and Z is the characteristic impedance calculated using Eq. (3).

In an infinitely long coaxial line, the electric field produced by a inner conductor with linear charge density λ is:

$$E(r) = \frac{\lambda}{2\pi\varepsilon_0 r} \quad (9)$$

being ε_0 the vacuum dielectric constant. Analogous to what is seen in Eq. (8), the potential u can be calculated as:

$$u = \frac{\lambda}{2\pi\varepsilon_0} \ln(R_{ext}/R_{int}), \quad (10)$$

with R_{ext} the internal radius of the outer conductor, and R_{int} the radius of the inner conductor.

Comparing eqs. (8, 10) and then using Eq. (9), one gets the electric field in terms of the power measured inside the resonator, i.e.

$$E(r = R_{ext}) = \frac{\sqrt{Q_{load} \cdot Z \cdot (4/\pi)}}{R_{ext} \cdot \ln(R_{ext}/R_{int})} \cdot \sqrt{P_{inside}} \quad (11)$$

This expression for the electric field is used to set the multipacting threshold of the material under study.

According to [14], the electric field that accelerates multipacting electrons in an accelerator (circular) beam pipe is

$$E = \frac{q_b}{2\pi\varepsilon_0 r_{pipe} (c \cdot \Delta t_b)} \quad (12)$$

where q_b is the bunch charge, r_{pipe} is the pipe radius and Δt_b the bunch spacing. For example, assuming for the CERN-SPS a circular beam pipe, the expected electric field in the SPS and the field actually got in the bench set-up have the same order of magnitude of roughly 10^4 V/m, i.e. P_{inside}=10 W (10^{11} protons, 2.5cm pipe radius and 1 ns bunch length). Thus also the electron bombardment dose in the bench set-up is close to the SPS one, validating this method to test different surface treatments.

2.4. Multipacting signatures

The SW coaxial chamber allows the detection of multipacting in two different ways. Typical signatures are the sudden pressure rise, and the collection electron current at the pick up. By amplitude and frequency modulation of the input signal, it is also possible to determine how multipacting affects the resonant conditions.

2.4.1. Pressure rise

Due to Electron Stimulated Desorption (ESD), when multipacting takes place, the vacuum pressure rises depending on the electric field amplitude. The pressure is measured by a Penning vacuum gauge located on the pumping stand (Fig. 13). Thus varying the electric field amplitude, the pressure growth can be controlled, as shown in Fig. 15, where the time evolution of the pressure can be seen. The pressure increases (depending on the electric field inside) up to a factor of 8, close to the values found in accelerators [15].

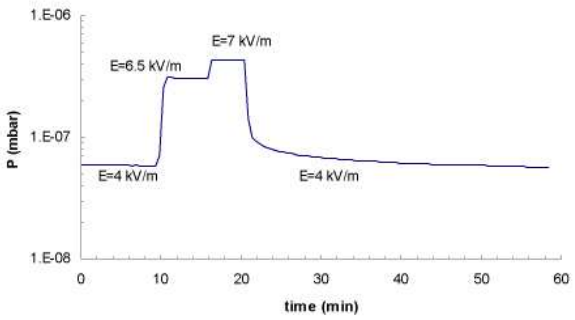

Figure 15. Pressure behaviour varying the electric field amplitude in the resonator. The working pressure is 5 10^{-8} mbar, but when multipacting is triggered (t=10min) the pressure suddenly increases, up to a stable value. Increasing the electric field, the pressure still increases.

2.4.2. Electron current

The multipacting electrons can be detected by the positively biased pick-up where they induce a negative signal. Varying the power in the resonator around the multipacting threshold, allows the detection of the beginning of multipacting. This threshold is usually given in terms of electric field, using Eq. (11). The electron current measured on the pick up can be also modulated by varying the amplitude of the incident power with the signal generator. This effect is shown in Fig. 16, where the incident signal was 10% modulated in amplitude around the multipacting level at a frequency of 10 Hz. For electric field amplitudes lower than the multipacting threshold, no electron current is collected, but when multipacting is active, the electron current increases when increasing the input power (i.e. the electric field in the resonator). For each input power level, the electron current is limited presumably by space charge effects.

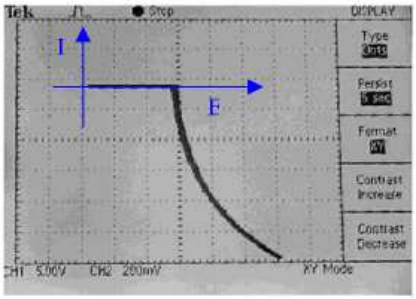

Figure 16. Electron current versus electric field (10% modulation at 10 Hz of the resonator input signal). The amplitude modulation is done using the signal generator. When multipacting takes place, electron current is detected on the pick-up. For electric field below the multipacting level, no electron current is collected.

The threshold changes depending on the material inside the resonator, as it will be seen in sec. 2.4. A surprising effect was detected by modulating the amplitude of the electric field with at increasing frequencies. Figure 17 was recorded in the same conditions as Fig. 16, (10% amplitude modulation) but the frequency of the amplitude modulation was much faster: 100 Hz. This hysteresis cycle shows that, at least for this set-up, it is easier to maintain multipacting than to trigger it.

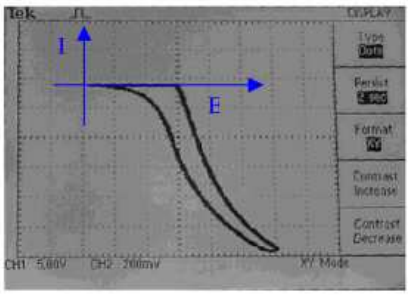

Figure 17. Electron current versus electric field (10% modulation at 100 Hz of the resonator input signal). Hysteresis cycle for the electron current is detected: triggering multipacting when there are electrons inside the resonator is easier than triggering it when there are no electrons.

2.4.3. Set-up detuning

By modulating the input power and recording the amplitude of the reflected and transmitted signals, it is possible to detect the onset of multipacting. Figure 18 shows the outline of the measurement set-up: the RF generator is operated in amplitude modulation mode, with a typical modulation index of 10%. A bi-directional coupler permits the measurement of the input power and of the reflected signal. The field amplitude inside the resonator is measured by the output coupler. The biased pickup and the electrometer allow to measure the electron current at the resonator wall. Those signals are recorded by an oscilloscope.

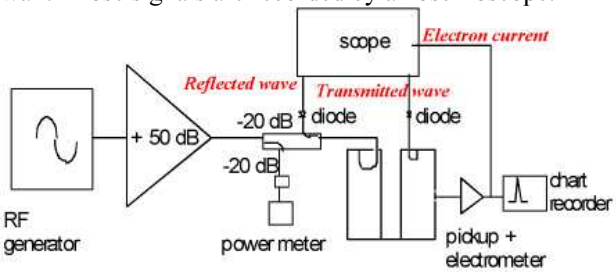

Figure 18. Layout for the measurement of the reflected and transmitted wave. After being amplified by the 50 dB power amplifier, a –20dB directional coupler is placed between the resonator and the power amplifier. This directional coupler permits to measure the incident wave and the reflected wave produced in the resonator. The transmitted wave is measured with the output coupler, the electron current is collected by the biased pick-up and amplified by the electrometer.

Typical results are shown in Fig. 19: the time evolution of the transmitted and reflected signal, as well as the electron current are recorded while modulating amplitude without using the diodes of Fig. 18. During multipacting, the space charge due to electrons detunes the resonator and the resonant conditions are no longer fulfilled. Thus, when multipacting is triggered, transmission levels off (top trace) and reflection increases (middle trace), which is evidenced by the electron current in the pick-up (bottom trace).

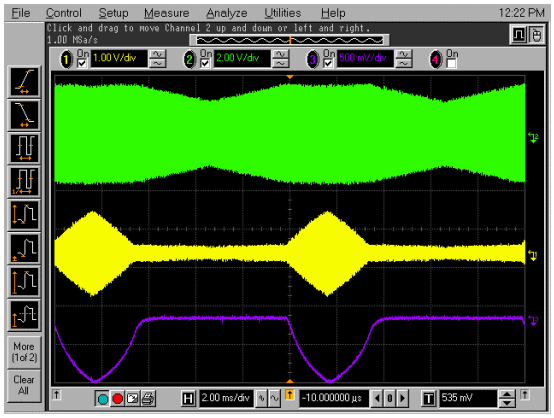

Figure 19. Time evolution of the transmitted signal (top), reflected signal (centre), and electron current (bottom), while modulating amplitude (10%). When the electric field exceeds the multipacting level, transmission becomes flat, reflection increases and electron current is collected.

2.5. Scrubbing effect for different materials

The present layout allows the comparison of multipacting level for different samples introduced in the resonator (operated in the fundamental mode). The maximum electric field is in the centre of the resonator, where the electron pick-up and the sample are located. If the multipacting level of the sample is lower than the one of stainless steel, multipacting is first produced on the sample, and then on the other parts of the resonator. In the following, we discuss measurement of multipacting level in stainless steel sample as well as ferrite and amorphous carbon (a-C).

Two different pick-up configurations are used: one to study the behaviour of the whole chamber, and one for samples of different material (Fig. 20). In the first case, the pick-up is located behind a grid of the same material as the vacuum chamber. The grid is actually a part of the outer conductor surface. Multipacting takes place on the grid, and the electrons leaving its surface pass through its holes and are collected in the electrode behind the grid. In the second pick-up configuration, the sample is supported by the pick-up itself and becomes part of the vacuum chamber wall. Hence, electrons outgoing the sample surface come back to the collector producing an electron current. In both cases, during continuous exposure, the electron dose is estimated by time integration of the pick-up current.

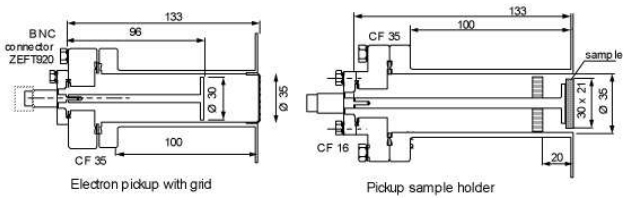

Figure 20. Pickups used to measure multipacting level of the whole chamber (left) and of samples of different materials (right). The grid used on the left pick-up is part of the outer conductor surface wall. Electrons emitted from the surface pass through the holes of the grid and reach the pick-up surface collector. On the other hand, the pick-up sample (right) forms part of the wall chamber surface and it acts also as the electron collector. Electrons emitted by the sample reach again the collector surface.

2.5.1. Scrubbing effect for stainless steel

The first step is to measure the multipacting level for the stainless steel, that is, the minimum electric field amplitude (E_0^{ss}) that will trigger the electron cloud inside the chamber. Therefore a stainless steel grid has been placed in front of the pick-up (Fig. 20) and whenever the field magnitude of E_0^{ss} is reached, the electron avalanche starts in the grid and in the surrounding area.

The minimum electric field E_0^{ss} to trigger multipacting varies after dose exposures. In Fig. 21, the electron current is plotted versus the electric field inside the resonator after 3 different electron exposures, and the multipacting level is set as the electric field corresponding to a measurable electron current. Multipacting level of "as received" stainless steel is 5.8 kV/m, but it increases with the electron dose (scrubbing effect).

This effect is well known (but not yet completely understood) as “RF conditioning” in RF devices [10]. Generally, the SEY decreases with the exposed dose [16], and thus, larger electric field amplitudes are required to trigger multipacting.

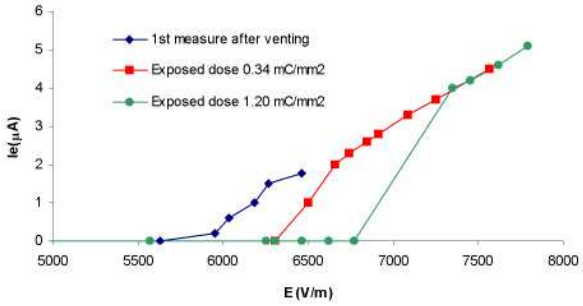

Figure 21. Electron current versus electric field amplitude for stainless steel. After different dose exposures, bigger electric field is required to trigger multipacting (scrubbing effect).

2.5.2. Scrubbing effect for ferrite sample

In the framework of the studies of the longitudinal beam coupling impedance in the LHC injection kicker model [17], it is important to evaluate the multipacting level for the ferrite used in the kicker yoke. Figure 22 shows again the current in the pick-up as a function of the resonator field: the multipacting level for ferrite is close to 1.8 kV/m, and there is no noticeable scrubbing effect (at least for this kind of ferrite) in the measured dose range (0-0.18 mC/mm^2). Actually, two multipacting levels are detected: the first one (1.8 kV/m) is due to the ferrite, while the second one (5.5 kV/m) corresponds to stainless steel. Therefore it is evident that multipacting is produced first on the vertical centre of the resonator (where the ferrite is placed) and then in the other parts. It is worth noting that the multipacting level for stainless steel is slightly lower than the previous value found for stainless steel alone (5.8 kV/m) because it is easier to trigger the multipacting if there are already electrons in the resonator (similarly to the hysteresis effect mentioned in sec. 2.3).

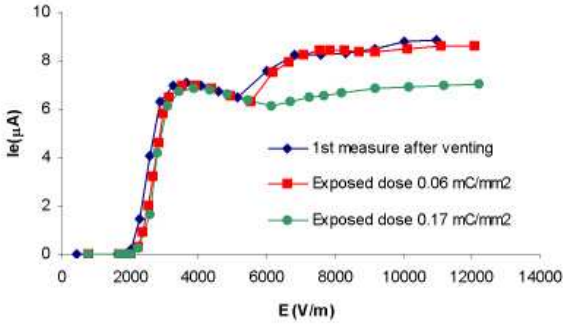

Figure 22. Electron current versus electric field amplitude for a ferrite sample. Two multipacting levels can be seen in this plot: the first one (at ~2 kV/m) corresponding to the ferrite sample, the second one (~5 kV/m) corresponding to the stainless steel chamber.

2.4.3. Scrubbing effect for a-C sample†

Other tests have been carried out on samples of Diamond type amorphous carbon (a-C), known as DLC (Diamond Like-Carbon). Such a material may be an interesting coating against multipacting since it has very good mechanical properties and it is very easy to prepare [18]. Actually a sample of a-C H-terminated diamond has been tested.

Figure 23 is analogous to Fig. 21 and 22. It shows a value of $E_0^{a\text{-}C} \cong 4.5$ kV/m independently of the exposed electron dose, which is lower than the value for stainless steel even just after venting ($E_0^{ss} = 5.8$ kV/m).

† Sample provided by Joan Esteve, from the Applied Physics Department of the Universitat de Barcelona.

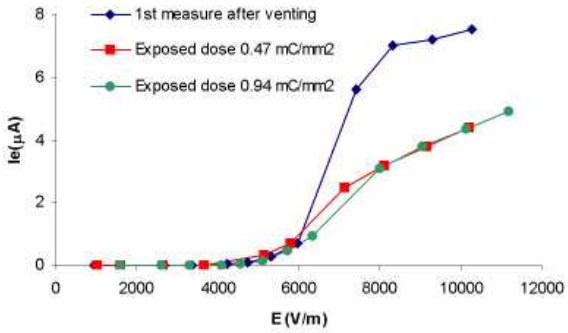

Figure 23. Electron current versus electric field amplitude for an a-C sample. No scrubbing effect is detected for this sample. However, for electric fields above its multipacting level, the electron current collected is much lower after the first electron dose, since electrons remove the first contaminated layer of the sample.

This behaviour is explained in [19] by the low electron affinity at the surface, which is mainly responsible for the high SEY from H-terminated diamond samples. Despite the fact that $E_0^{a\text{-}C}$ does not decrease with the exposed dose, Fig. 23 shows anyway a reduction of the SEY which can be seen in terms of the collected current after the first dose: for a given value of the electric field (above the multipacting level), the electron current is significantly lower after the first dose due to the removing of the first contamination layer. The latter effect can be even probably even greater because of the rapid decrease in the yield from H-terminated diamond due to electron impingement [19]. Anyway a rigorous prove is not possible with this set-up, since part of the electron current is due to multipacting in the stainless steel. However, this material is not a good candidate to decrease multipacting due to its low multipacting level "as received", and due to the weak scrubbing effect detected.

2.5.4. Scrubbing effect for a Non Evaporable Getter (NEG) coating

In a getter coated beam pipe one expects the electron cloud build-up to be strongly decreased. In the framework of the studies of the electron cloud in the SPS, a NEG (TiZrV) coated vacuum chamber has been tested in this set-up, as planned in [20]. Coating the whole inner surface of the outer conductor (including the grid) avoids the effect of two multipacting levels taking place at the same time inside the resonator (as occurred for ferrite and a-C samples).

When NEG is not activated (i.e. heated at 200ºC for 24 hours), there is a clear electron cloud build up and a consistent scrubbing effect. Figure 24 shows this effect in the same way as Fig. 21. However, when activated, there is no electron signature inside the resonator (no electron current, no changes in transmitted and/or

reflected waves), but the pressure increase is nevertheless not negligible. Thus such a pressure increase can not be explained by electron multipacting, but it may be due to some thermal effect or other RF breakdown mechanism.

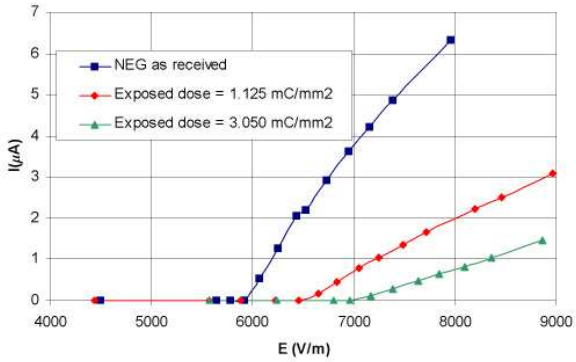

Figure 24. Electron current versus amplitude of the electric field for a non activated NEG coating in a vacuum chamber. With the exposed dose, the electron current decreases and multipacting level increases, evidencing the scrubbing effect for a non activated NEG.

Figure 25 clearly shows that transmission and pressure rise are not correlated. It should be mentioned that NEG usually reaches pressures around 10^{-11} mbar after activation; such low pressures were not obtained when the measurement took place (see Fig. 25), possibly indicating a non proper activation process.

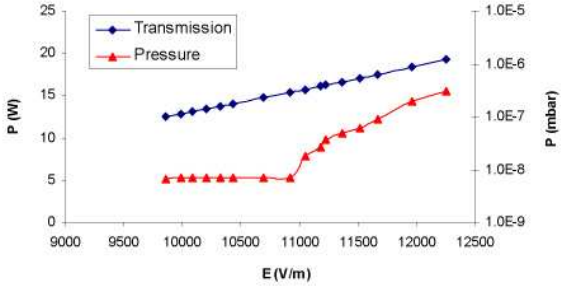

Figure 25. Transmitted power and pressure inside the resonator versus electric field amplitude for an activated NEG coating inside the resonator. After activation, the NEG coating does not show any multipacting signatures. Only a pressure increase, likely not due to multipacting since no electron current and no limitation in transmission signal are detected.

2.6. Conclusions

The coaxial resonator set-up allows the production of high electric fields and the generation of the high electron doses needed to properly study the behaviour of materials submitted to multipacting and thus it is a suitable test bench for electron cloud studies. We have demonstrated qualitatively how the resonator changes its resonant conditions when multipacting takes place. The resonator detunes while electron current is detected on the pick-up: transmitted signal levels off and reflected signal increases suddenly. The appearance of the hysteresis cycle in the collected electron current after proper modulation of the input power, shows that the effect continues at electric fields lower than needed to start it.

It is possible to measure the onset of multipacting and its variations with the exposed dose of electrons, which makes it an effective tool to study the scrubbing effect for different samples. No scrubbing effect was evidenced in ferrite (at least in the applied dose range), while for a-C the scrubbing effect cannot be identified by the multipacting level but only in the collected electron current at higher electric fields. For stainless steel, scrubbing effect has been shown clearly. Also a NEG (TiZrV) coated vacuum chamber has been tested in this set-up. After activation, preliminary results do not show any evidence of electron multipacting (no electron current, no changes in transmitted and/or reflected signal are detected) but only a pressure rise. The reason can be found in a thermal effect or other form of RF breakdown due to the high power introduced in the set-up, but further studies are needed to explain this effect.

In the framework of the electron cloud program carried out at CERN, a computer code is going to be developed to simulate multipacting in this set-up. Checking simulation results with measurements in the laboratory will be a useful tool to understand this phenomenon. Further surface treatments (TiN and ArGD) are going to be tested as coatings against multipacting in this set-up, which is becoming a useful test bench for electron cloud studies.

3. REFERENCES

[1]. M. Pivi. Beam induced electron multipacting in the LHC. PhD Thesis. CERN – University of Torino. Geneva, May 2000.

[2]. F. Ruggiero et al. Beam-induced electron cloud in the LHC and posible remedies. Geneva-CERN. In: 6th European Particle Accelerator Conference, Stockholm, Sweden, Jun 1998 - IOP, 1999. - pp.359-361

[3]. H.H. Braun et al., The CLIC RF power source: a novel scheme of two beam acceleration for e± Linear colliders, CERN Clic Note 864 (unpublished).

[4]. Matthaei, GL; Young; L and Jones, EMT. Microwave filters, impedance-matching networks and coupling structures. Ed. by Artech house books, section 14.05.

[5]. Zinke and Brunswig. Hochfrequenztechnik I. Ed. Auflage.

[6]. Harlan Howe, JR. Stripline circuit design. Ed. by Artech house, Inc. Ch 5.

[7]. A. Lombardi, private communications.

[8]. Zinke, O. and Brunswig, H. Lehrbuch der Hochfrequenztechnik. Chap. 3. New York 1973.

[9]. Cristal, E.G. and Young, L. IEEE Transaction on microwave theory and techniques. Pg 544-558, September 1965.
[10]. H. Padammsee, T. Hays and J. Knobloch. RF Superconductivity for accelerators. Ed. Wiley Interscience publications.
[11]. O. Brüning, F. Caspers, J.-M. Laurent, M. Morvillo, and F. Ruggiero. Multipacting tests with magnetic field for the LHC beam screen. LHC project report 187, June 1998.
[12]. CAS - RF engineering for particle accelerators. April 1991, Oxford, UK. Proceedings edited in Geneva 1992, CERN.
[13]. F. Caspers private communications.
[14]. U. Iriso et al. Improvements on the Traveling Wave chamber for multipacting simulations. Vac. Tech. Note, 01-17. November 2001.
[15]. G.Arduini et al. Electron cloud: observations with LHC-type beams in the SPS. Presented in EPAC 2000, Vienna, Austria. June 2000.
[16]. N.Hilleret et al. Electron cloud and beam scrubbing in the LHC. Presented at PAC 1999, New York City, NY, USA. April 1999. Ed. by Luccio, A and MacKay, W W - IEEE Computer Society Press, Piscataway, NJ, 1999.
[17]. F. Caspers, C. Gonzalez, H. Tsutsui and M. D'yachkov. Impedance measurements on the LHC injection kicker prototype. LHC project note, March 2000.
[18]. J. Esteve, F.J. Pino, J.L. Andújar. Obtención de recubrimientos de carbono amorfo tipo diamante. Presented in TRATERMAT 2000, Barcelona, Spain. June 2000.
[19]. A. Shih, J. Yater, C. Hor, R. Abrams. Secondary electron emission studies. Applied Surface Science 111 (1997), 251-258.
[20]. Conceptual design review of the room temperature parts of the beam vacuum system for the long straight sections for the LHC. Engineering report. LHC project document, March 2002.

4. ACKNOWLEDGMENTS

P. Griessen supplied the feedthroughs from the SWC-LEP; H.Kos and D. Collet machined precisely the pieces we were looking for; A. Lombardi gave the idea and help with using *Superfish*; C. Deibele (Oak Ridge National Laboratories, US) substantially helped with the calculations of the coupling factor with *SERENADE*; J. Esteve and the Applied Physics Department from the Universitat de Barcelona provided the a-C samples. Eventually, many thanks to all the LHC/VAC group for their support; and F. Ruggiero, G. Rumolo and F. Zimmermann for their encouragements.

FUTURE ELECTRON CLOUD STUDIES AT CERN AND PLANS IN THE ACCELERATOR PHYSICS GROUP

F. Ruggiero, CERN, Geneva, Switzerland

Abstract

I sketch future plans for electron cloud studies at CERN, discussing input parameters and reliability of simulations performed in the Accelerator Physics group.

1 INTRODUCTION

Our priority is to study electron cloud effects and cures for LHC, SPS, and PS. The following is a list of relevant future activities that I will shortly discuss:

- Input parameters: do we need more laboratory measurements?
- Simulations of electron-cloud build up and heat load
- Simulations of electron-cloud instabilities
- Scrubbing scenarios and possible other cures
- Benchmark simulation codes by machine experiments
- Benchmark simulation codes by multipacting tests
- New physics and different approaches for our simulation codes: magnetron effect and plasma approach?

2 INPUT PARAMETERS: DO WE NEED MORE LAB MEASUREMENTS?

Input parameters required for electron cloud simulations include:

- Beam and machine parameters
  - bunch population and bunch train pattern
  - vacuum chamber geometry and bunch dimensions (σ_x, σ_y, and σ_z)
  - machine energy, tunes, chromaticities
  - linear and nonlinear optics (β-functions, beam offsets, detuning with amplitude, etc.)
  - machine impedance (wakefields, trapped modes)
- Primary electron sources
  - residual gas pressure and ionization cross section
  - beam losses
  - photon flux
- Surface properties vs electron and photon(?) scrubbing dose
  - surface reflectivity vs photon energy and incidence angle
  - energy spectrum of reflected photons vs angle of reflection
  - photoelectron yield
  - SEY vs primary electron energy and incidence angle
  - energy spectrum of secondary electrons

We need reliable input parameters for our simulations and therefore *we strongly encourage:*

- further reflectivity measurements
- further SEY measurements in the laboratory and in-situ, for Cu and SS
- an experimental scrubbing test in *cold LHC conditions*

We need *certified and representative* experimental data, possibly with recommended fits agreed by experts at CERN and in other laboratories, for the SEY at low energy and at high energy including reflected and re-diffused electrons.

3 SIMULATIONS OF ELECTRON CLOUD BUILD-UP, HEAT LOAD, SCRUBBING TIME

- definition of a threshold current (10% of saturation?)
- scaling of threshold current with bunch spacing
- scaling of threshold current with bunch dimensions
- stripe location (with 25 vs 50 ns bunch spacing?)
- role of satellite bunches $\Longrightarrow$ SPS machine experiment
- simulations of heat load in COLDEX and WAMPAC
- simulations of scrubbing time $\Longrightarrow$ SPS scrubbing test
- documentation of ECLOUD and HEADTAIL codes
- systematic comparison of predictions by different codes $\Longrightarrow$ standardization of input-output format across different labs?

4 SIMULATIONS OF ELECTRON CLOUD INSTABILITITES

- explore plasma approach and include image charges from electron cloud $\Longrightarrow$ add boundary to the code HEADTAIL, use module from plasma code by Tom Katsouleas and set up collaboration with USC
- confirm explanation of PS horizontal instability by combined function magnets. Include sextupole field? Understand PEP-II results.
- Include linear coupling and check stabilizing effect $\Longrightarrow$ test in the PS/SPS
- systematic comparison of simulated and measured instability growth rates
- simulate spectrum of multi-bunch instabilities $\Longrightarrow$ compare with SPS measurements and results by Su su Win at KEK
- use improved SPS impedance model (from measured coherent tune shifts and spectra of high order head-tail modes) and use it in simulation with space charge and electron cloud impedance

- is there a discrepancy between electron cloud wake-fields computed at CERN and elsewhere? Why spikes are absent from KEK results?

5 BENCHMARKING SIMULATION CODES BY MULTIPACTING TESTS

- repeat multipacting tests with realistic LHC-like RF pulse trains
- simulate results
- test and simulate stripes in a dipole field?
- test and simulate trapping in a quadrupole field?
- compare with results of other codes (e.g. Lanfa Wang at KEK)

6 OTHER SIMULATIONS

- electron cloud and trapped modes $\Longrightarrow$ implication for LHC collimation? Heat load in experimental chambers?
- study very high intensity regime proposed by Sam Heifets for PEP-II upgrade $\Longrightarrow$ 5 ns bunch spacing for LHC upgrade?
- simulations for CLIC damping rings

7 ACKNOWLEDGMENTS

Many of the ideas sketched here have been triggered by contributions to the ECLOUD'02 workshop [1]. In particular, I would like to thank Frank Zimmermann for several useful discussions and hints.

8 REFERENCES

[1] Proc. of the Mini-Workshop on 'Electron-Cloud Simulations for Proton and Positron Beams' (ECLOUD'02), CERN, 15–18 April 2002, edited by G. Rumolo and F. Zimmermann, CERN Yellow Report 2002-001, and `http://slap.cern.ch/collective/ecloud02/`.

SUMMARY OF SESSION I, EXPERIMENTAL OBSERVATIONS AT EXISTING ACCELERATORS AND CONCERNS FOR FUTURE MACHINES

Robert J. Macek†, LANL, Los Alamos, NM 87545, USA

Abstract

This report briefly summarizes the first session (I) at the mini-workshop, ECLOUD'02, held at CERN, 15-18 April 2002. As the title indicates, this session focused on experimental observations at existing accelerators and concerns for future machines. Observations were reported from KEKB, PEP-II, SPS, and PSR and design issues involving the electron cloud were presented for SNS, Linear Collider Damping Rings and the LHC. These represent a good sample of the broad spectrum of accelerator types impacted by electron cloud effects (ECE).

1 AGENDA

The list of presentations included:

0. F. Ruggiero (CERN) – *Welcome and Goals of the Workshop*.
1. H. Fukuma (KEK) – *Electron Cloud Effects at KEKB*.
2. F. J. Decker (SLAC) – *Electron Cloud Effects at PEP-II*.
3. K. Cornelis (CERN) – *Electron Cloud Instability at the SPS*.
4. M. Jimenez (CERN) – *Electron-Cloud Observations in the SPS.*
5. J. Wei (BNL) – *Electron Cloud Effects in High-Intensity Proton Machines.*
6. A. Wolsky (LBNL) – *Electron Cloud in Linear Collider Damping Ring*.
7. F. Zimmermann (CERN) – *Electron Cloud in the LHC*.

2 GENERAL COMMENTS

Ruggerio, in his opening remarks, set the tone for the workshop and listed the following guiding goals and expectations:

- Benchmark simulations against beam observations and against each other
- Determine which simulation approaches best represent reality
- Document the present understanding and determine the important open questions
- Develop a program for future research and development
- Strengthen and expand international collaborations for this work

This session contributed to these goals by discussing many of the beam observations and outlining the key concerns for major new or proposed machines. In addition, a number of comparisons to simulations were made.

In discussing experimental observations and their interpretation, a good starting point is a reasonably comprehensive itemization of the various observed or anticipated electron cloud effects (ECE). Such a listing or categorization of ECE and many of the machines where they have been observed (in parentheses) or, in the case of proposed machines [in square brackets], are at risk from the particular ECE includes:

- Beam induced multipacting
  - Resonant (APS, KEKB, PS, SPS), [LHC]
  - Trailing-edge multipactor (PSR), [SNS, JHF]
- Vacuum degradation i.e., electron-stimulated gas desorption, is perhaps the most common indication of beam induced multipactor or intense electron cloud formation
- Transverse coupled bunch instability from the electron cloud wake (APS, B factories, PS, SPS), [LHC]
- Transverse single bunch (head-tail) instability; emittance blowup (APS, B factories, PS, SPS)
- Transverse coasting beam or long bunch, two-stream instabilities (e-p) (ISR, PSR, AGSB), [SNS, JHF]
- Tune shifts (KEKB, AGS Booster) and tune spread are undoubtedly present at some level whenever an electron cloud is formed
- Heat load on vacuum chamber walls (SPS) is a major concern for the cold bore of [LHC]
- Cloud-induced noise or spurious signals in beam diagnostics (e.g., wire scanners, electrostatic pickups, ionization profile monitors) (PSR, PS, SPS, KEK-PS)
- Electrons trapped in distributed ion pump leakage field (CESR)
- Electrical breakdown or discharge in high voltage systems such as strip line kickers or unshielded rf gaps (possibly seen at PSR)

Longitudinal effects have not been specifically identified nor included in most theoretically treatments or analyses. They are undoubtedly present at some level, as noted by Ruggerio.

The sources of primary electrons are essential inputs to the simulations and vary across the spectrum of accelerators. Photoelectrons from synchrotron radiation are well understood and are undoubtedly the dominant source at positron rings and the anticipated source at LHC. For proton rings, the situation is less clear-cut and

†macek@lanl.gov

subject to greater uncertainty and ambiguity. At PSR significant primary electrons originate at the stripper foil (convoy electrons from the stripping process, secondary emission from foil hits by the stored beam, and even thermionic emission caused by beam heating of the foil) and from proton beam losses. Residual gas ionization is another source. When the electron cloud buildup can saturate before encountering a long gap, as seems to be the case for long bunch trains in a number of machines (e.g. the SPS), the exact source strength is less important than in smaller rings such as PSR or SNS.

3 REVIEW OF PRESENTATIONS

3.1 Electron Cloud Effects at KEKB

Fukuma reviewed experience with ECE at the KEKB low energy ring (LER), which included observations of emittance growth, instability mode spectra and growth times, tune shifts and luminosity degradation both with and without solenoids. In the absence of mitigation, emittance growth and luminosity degradation greatly limited facility performance. Solenoids, which now cover 95% of the straight sections (~70% of the ring circumference), were most beneficial in suppressing the electron cloud effects and have resulted in a good improvement in the KEKB luminosity.

Beam blowup in the LER at KEKB was eliminated after the last (5^{th}) installment of solenoids. The tune shift along the train (from the electron cloud), which seems to be a good measure of the cloud density, was reduced by at least 40% after the 4^{th} installment of solenoids. The growth rate of the coupled bunch instability was reduced by a factor of two after the 4^{th} installment of solenoids. Mode spectra from simulations of the electron cloud induced coupled bunch instability (solenoids off) are in general agreement with observations for the vertical plane but not for the horizontal plane, if the photoelectrons are produced mainly at an illumination point of the synchrotron radiation. However, if the photoelectrons are produced uniformly over the surface of the vacuum chamber, then the simulated mode spectra are consistent with observations for both planes.

3.2 Electron Cloud Effects at PEP-II

Deckers reported that, despite an antechamber and TiN coatings in the LER arcs, significant ECE are observed at PEP-II. These include vacuum degradation, growth of beam size, and reduction of both luminosity and beam lifetime at high current. Solenoids, which now cover 95% of the drift spaces, have reduced multipacting as detected by vacuum pressure readings but have not eliminated the electron cloud and resulting performance degradation at the highest intensities.

Creative operational measures have been invoked to maximize luminosity in the presence of the electron cloud including:

- Minimizing emittance growth by optimizing the number of bunches and bunch spacing,
- Use of gaps between trains (mini-gaps) to clear the electron cloud, and
- Use of a ramp in bunch current after the ion gap to avoid losing HER bunches.

While good progress has been made to reduce the ECE with solenoids and creative operational measures, a number of puzzling or controversial issues remain. For example, the beam size blows up in the horizontal plane in experiments while simulations show it in the vertical. Also the variability in the instability thresholds from day to day is unexplained. The bottom line for PEP-II is that despite the lingering ECE effects, the solenoids and operational measures have permitted operation at up to 1750 mA in the LER without severe degradation of luminosity.

3.3 Electron Cloud Instability at the SPS

Cornelis presented persuasive evidence (beam position centroid measurements) for a fast (growth time ~ 50 turns) coupled bunch instability of low order in the horizontal plane and a single bunch (head-tail) instability in the vertical plane induced by the electron cloud. The later has a growth time that depends on intensity starting from ~ 500 turns just above threshold and going to ~ 100 turns at twice threshold intensity. The horizontal instability is amenable to control by the existing transverse feedback system. The cloud, as evidenced by observations detailed in the talk by Jimenez, develops first in the dipoles. This helps explain the difference in behavior of the instabilities in the two planes.

In the analysis by Cornelis, a bunch experiences a horizontal force from the horizontally constrained cloud in the dipoles proportional to its horizontal displacement. This system can be described as a set of coupled oscillators for the various bunches and can lead to the coupled bunch instability. In the vertical plane, the electrons are free to move toward the center of the bunch and can even be trapped inside the bunch producing the conditions that can produce a head-tail coupling and resulting instability. The equivalent impedance in the vertical has been measured by following the betatron phase evolution of head and tail over one synchrotron period after a vertical kick. Calculations (using a wake field approach) and measurements for the first bunch in the train and one residing in the cloud were in reasonable agreement after adjusting (shortening) the range of the wake for the bunching sitting in the cloud.

3.4 Electron Cloud Observations at the SPS

Jimenez reviewed an extensive program of systematic experimental observations pertaining to the electron cloud in the SPS for LHC-type beam (bunch spacing of 25 ns). This program was launched after large vacuum pressure increases, anomalous signals (baseline shift) on electrostatic pickups, and beam instabilities were observed the first time high-intensity bunches were

injected under LHC conditions. Pressure rises indicated that the electron cloud appears in the dipoles at a significantly lower threshold than in the straight sections, which was confirmed in 2001 with new strip detectors placed in a special test dipole in the ring.

The novel strip detector was developed to detect the presence of the electron cloud impinging on the chamber walls in a dipole field and to measure the horizontal spatial distribution of the cloud. Simulations predicted there would be two peaks or strips in the cloud distribution (in a dipole) above the threshold for multipacting. These were subsequently observed in the strip detector and studied as a function of dipole field, bunch spacing and filling pattern.

A unique setup was deployed in the ring to provide in-situ measurements of the secondary emission yield (SEY) of Cu samples exposed to the beam induced electron cloud. These demonstrated the effect of beam scrubbing and showed a significant reduction in SEY as a function of integrated beam time under LHC conditions. The peak SEY went from 2.4 to 1.6 after 90 hours of integrated beam time. Beam scrubbing was also indicated by the decrease in pressure rise ($\Delta P/P$) from multipacting, which decreased linearly by a factor of ~40 over a period of ~60 hours of integrated LHC-type beam time.

Since the main concern for LHC is the heat load on the cold bore, a pick up calorimeter has been developed and calibrated. It will be used to measure the heat load in the SPS and extrapolate to LHC conditions. Future work will also include improved measurements of the spatial distribution of the cloud to firm up the location of the pumping slots in the LHC beam screens.

3.5 ECE in High Intensity Proton Machines

Jie Wei reviewed the current understanding of ECE in high intensity proton machines with emphasis on the effects most relevant to long-bunch accumulator rings, in particular, the existing PSR and implications for the SNS ring now under construction. He reported that another machine (RHIC) should be added to the growing list of accelerators where ECE is observed. There is now evidence for beam-induced multipactor from the newly commissioned RHIC where a strong vacuum pressure rise was observed when the bunch spacing was halved during high intensity gold beam injection. In addition, the fast instability observed for debunched coasting beams at the AGS Booster is thought to be the two-stream e-p instability.

In long-bunch accumulator rings the trailing edge multipactor mechanism, a nonresonant amplification process, prevails as contrasted with the resonant variety found in short bunch rings such as SPS or LHC or the positron rings. Trailing edge multipactor also differs in that the electron cloud buildup typically does not saturate as it does in a long train of bunches common in other rings where ECE is observed. The sources of primary electrons also differ. In PSR and SNS the stripper foil has several mechanisms for generating electrons including the several hundred keV electrons stripped from H^- (the so called “convoy” electrons), secondary emission and knock on electrons from foil hits by the stored beam and even thermionic emission from the foil. Continual proton losses from foil hits and other mechanisms or in collimators can generate many primary electrons per lost proton. The convoy electrons, if not properly collected, can also cause localized heat damage to the wall.

The most serious ECE for PSR and SNS is no doubt the two-stream e-p instability from coupled oscillations of the electron cloud and the proton beam. Enhanced Landau damping by higher rf voltage, multipoles, X,Y coupling and inductive inserts have been helpful in significantly raising the instability at PSR. Reduction of the primary electrons by lower vacuum, lower beam losses, clearing fields, collection of the convoy electrons and bias on the stripper foil reduce the prompt electron signal (largely due to trailing edge multipactor) at the end of each bunch passage but have little effect on the instability threshold because the electrons driving the instability are mainly those that survive the gap to be captured by the next pulse. Measurements of these with the electron sweeping detector at PSR show a saturation characteristic which can explain why variations of prompt electron have little effect on the instability. A larger reduction in the primary sources is probably needed to bring the electrons surviving the gap out of saturation. TiN coatings and weak solenoids have made large reductions in the prompt or multipactor electrons in a small test section in PSR. This is a potential cure but it has not been shown experimentally that this will be sufficient to greatly reduce the electrons surviving the gap. Combinations of methods may be needed to adequately suppress the electron cloud generation in SNS.

The SNS ring design has incorporated many measures to suppress electron production. Fractional beam losses will be kept low; the ring vacuum will be an order of magnitude better (~ 5 nTorr) than PSR, electrons at the stripper foil will be collected and backscatter suppressed, the vacuum chambers will be coated with TiN to suppress multipactor, and a beam-in-gap kicker will be deployed to keep the gap free of beam (10^{-4}level). Landau damping will be enhanced by a large momentum acceptance and sextupole families, use of momentum painting and high RF voltage. Space is also reserved for a possible wide band damper system.

3.6 Electron Cloud in Linear Collider Damping Ring

Wolsky discussed work to estimate the instabilities driven by the electron cloud in both the NLC and TESLA positron damping rings. He began with a comparison of parameters for the damping rings and currently operating positron storage rings of roughly comparable parameters. These comparisons alone raise the specter of ECE for future linear collider damping rings.

Simplified analytical models were used for rough estimates of thresholds and growth rates of the single

bunch and coupled bunch modes. In these the cloud buildup was assumed to reach saturation with a density given by the neutralization condition. The wake field from the cloud was estimated from a broad-band resonator model with different parameters for short-range and long range wakes. Growth rates were estimated by standard theory. As a check the models were also applied to some existing positron rings with reasonable results. The analytical long range wake field for the NLC compared favorably to the results of POSINST simulations.

The main conclusion from this work was that the NLC and TESLA damping rings could, indeed, encounter performance-limiting ECE. More detailed studies with simulations are warranted and possible countermeasures such as TiN coatings need to be investigated.

3.7 Electron Cloud in the LHC

Zimmermann wrapped up the session with review of the latest estimates of ECE at LHC. For some time the main concerns have been the heat loads on the beam screen inside the superconducting magnets and through the pumping slots, although beam instability at injection could be a problem as well as vacuum pressure and gas desorption in the interaction regions.

For LHC the dominant source of primary electrons is the photo-electrons from synchrotron radiation from the 7 TeV proton beam. Parametric studies of the electron cloud buildup and resulting heat load in various ring components have been carried by computer simulation (ECLOUD). The cloud buildup and heat load are sensitive to a number of parameters including the maximum secondary emission yield (δ_{max}), photon reflectivity, bunch intensity, bunch spacing and inclusion of elastic electron reflection. It also depends on the type of magnetic field. Dipole fields had the lowest heat load while drifts were highest with quads in between.

In order to achieve the LHC design bunch intensity (1.1×10^{11} proton/bunch) at a bunch spacing of 25 ns within the planned cooling capacity, δ_{max} must be brought down to ~1.1. Measurements at CERN of δ_{max} (for Cu) as a function of electron bombardment dose indicate this can be achieved at a dose of 0.01 C/mm^2. The present strategy is to use beam scrubbing during commissioning to reduce δ_{max} to 1.1. Other features of the LHC recipe for dealing with ECE are to use a sawtooth chamber in the arc dipoles to reduce photon reflections and coat all warm section with non evaporable getter material (TiZrV), which has a low SEY and is quite stable. Finally, there are backup solutions of larger bunch spacing and the use of satellite bunches.

Estimates of the threshold cloud density for the single bunch transverse mode coupling instability (TMCI) are below the saturation electron cloud densities for LHC and SPS. The heat load in LHC could set a tighter tolerance, but, TMCI could still be a problem especially at injection.

4 CONCLUSIONS

Electron cloud effects, such as beam induced multipacting, vacuum degradation, instabilities and interference with diagnostics, are now observed at many high intensity machines and are a serious technical risk for new machines e.g. LHC, SNS and future linear colliders. Heat load on the cold bore of LHC is another important ECE. For the high intensity accumulator rings, the “convoy" electrons from the H^- injection stripping process can cause local heat damage to the wall if not dealt with in a adequate fashion.

Significant progress has been made both to understand ECE at a fundamental level and to mitigate the adverse impact on accelerator design and operation. While there has been good progress, the problem is far from being resolved. The quantitative agreement between simulated results and measurements remains uneven, and the predictive power of the available tools does not appear to be sufficient to extrapolate with high confidence the present results to future machines with higher beam intensity. A significant part of the problem for proton machines is the level of uncertainty and ambiguity on the input parameters associated with the primary electrons and the SEY, which must be determined experimentally or by other analyses. More work is clearly needed.

SUMMARY SESSION II, OBSERVATIONS, LABORATORY MEASUREMENTS, MODELLING

O. Gröbner, M. Jimenez , CERN, Geneva, Switzerland

1 REVIEW OF RECENT OBSERVATIONS

An extensive review of recent observations and of new diagnostics has been presented for the following machines: PS, RHIC, PSR, APS, and SPS.

It is very significant to note that some "old" machines show electron cloud related effects when they are operated with new or with upgraded beam parameters.

This is not only the case for the PS and the SPS at CERN but most recently also for RHIC. Rather satisfactory agreement exists between models and observations increasing the confidence in the predictive power of simulation codes.

2 MODELLING

The modelling of the e-cloud build-up, heat load measurements using calorimeters, observations of pressure rises and the evolution of the secondary electron yield as a function of beam scrubbing have been addressed in several presentations during this session. There has been a remarkable progress in this field, the most noteworthy being the better description and parameterisation of the low energy secondary electrons (reflected electrons) (see talks by N.H., M.F., I.C.). Introducing these new input data in the codes shows that e-cloud build-up and heat load are indeed very sensitive to the very low energy part in the distribution. Since low energy electrons are notoriously difficult to measure as they are affected by very low magnetic and electric fields, it will be a challenge to obtain data, which can be used reliably for a real machine.

Complimentary measurements of the secondary electron yield *in situ* and in laboratory systems give confidence in the models used in the simulation codes.

3 DISCUSSIONS

A very interesting observation in the SPS has been the appearance of multipacting electron stripes in the dipoles. From the subsequent discussions it was not clear whether the horizontal position of these stripes are reproduced reliably by simulation codes. A follow-up on this question is necessary and has direct implications for the urgent decision on LHC beam screen slots.

The important question of generation and the apparently rather long survival time of electrons e.g. during bunch gaps in the PSR has been raised.

How can thresholds be defined for observable effects and used for benchmarking of simulation codes: multipactor electron signals, vacuum pressure rise, beam stability, emittance growth,.

Many machines (SPS and LHC) strongly rely on beam conditioning (scrubbing) of the surface. There seems to be consensus that more work has to be done to better understand the process. How closely is the evolution of the secondary electron yield and of the pressure rise linked together? Is it possible to relate one to the other?

For the cryogenic system of the LHC the important question remains whether beam scrubbing depends on temperature and whether room temperature results can be used for a cryogenic system

A point, which should not be overlooked, is the close relation between heat load (P) and dose rate (D):

$$D(C/s/mm^2) = \frac{P(W/m)}{F(mm^2/m) < E >}$$

For the LHC beam screen the surface which needs to be scrubbed: F~5 10^4 mm^2/m. N. Hilleret et.al. find 10^{-2} C/mm^2 for a well-scrubbed Cu surface with <1.3 for δmax. Operating the LHC within the cryogenic budget of P = 0.5 W/m and assuming a mean electron cloud energy <E> ~ 100 eV, one finds that it should take only about 30 hours to accumulate this dose.

From this simple argument one may conclude that in case the heat load is limiting the operation of the LHC, scrubbing should go fast. Conversely, if heat load is not a problem, there should be no problem and scrubbing is not an issue.

The analogous argument also applies to vacuum scrubbing, i.e. the reduction of the electron stimulated desorption yield of the surface. Most recent results from the SPS have indeed confirmed the fast clean-up of the vacuum system due to the multipacting electrons.

A detailed scenario should be worked out for the LHC to show the various options which can be followed to achieve δmax below 1.3 : bunch intensity & spacing,

filling patterns, absence of synchrotron radiation and hence no photo electrons for beam energies < 2 TeV.

At CERN, the valuable possibility exists to use the SPS as a test bed for the LHC. With the installation of the COLDEX system, the cryogenic aspects can be tested. For this important program substantial beam time will need to be allocated, which are not foreseen in the present schedule.

The possible use of microwave power either as a diagnostic tool, as a means to enhance the surface conditioning or even as a remedy to suppress the electron cloud has been suggested and has been discussed at some length.

Concerning the surprising results from RHIC, it should not be overlooked that the LHC ion beams may show a similar behaviour, not necessarily in the LHC ring but perhaps in one of the pre-injector machines. Are there similarities between RHIC and LEIR, which could produce similar pressure rises?

A very attractive means to eliminate or to reduce the electron cloud will be the use of NEG-films in addition to the more conventional TiN coatings, which both have a low secondary electron yield. For those regions in the LHC, which can be baked and hence the getter film activated *in situ* (long straights and experimental vacuum chambers) this solution has been adopted. Further studies and a comparison of the relative merits of such surface coating should be encouraged.

Summary of Session III*

M. A. Furman†, LBNL, Berkeley, CA 94720, USA

Abstract

This is a summary of the talks presented in Session III ("Simulations of Electron-Cloud Build Up") of the *Mini-Workshop on Electron-Cloud Simulations for Proton and Positron Beams ECLOUD-02*, held at CERN, 15–18 April 2002.

1 CONTRIBUTIONS

The talks presented in Session III, with speakers' names underlined, were:

1. *Adiabatic Theory of Electron Oscillations and its Application to SIS-100/200*, P. Zenkevich, N. Mustafin and O. Boine-Frankenheim.
2. *Electron-Cloud Simulations: Build Up and Related Effects*, G. Rumolo and F. Zimmermann.
3. *3D Simulation of Photoelectron Cloud in KEKB LER*, L. F. Wang, H. Fukuma, K. Ohmi, S. Kurokawa, K. Oide and F. Zimmermann.
4. *A Simulation Study of the Electron Cloud in the Experimental Regions of the LHC*, A. Rossi, G. Rumolo and F. Zimmermann.
5. *Qualitative Analysis of Electron Cloud Effects in the NLC Damping Ring*, S. Heifets.
6. *Electron Cloud Updated Simulation Results for the PSR, and Recent Results for the SNS*, M. Pivi and M. A. Furman.

2 SUMMARIES

Adiabatic Theory of Electron Oscillations and its Application to SIS-100/200. The SIS machines are synchrotrons being designed at GSI to store U_{238}^{+28} ions. SIS-100 will have an energy of 100 MeV/u with four bunches, while SIS-200 will have an energy of 1000 MeV/u. The subject of this paper is to study the motion of electrons trapped by the ion beam. The only source of electrons considered is ionization of residual gas. The electron line density, λ_e, is assumed to be uniform. The ion line density $\lambda_i(\tau)$, on the other hand, is a function of the normalized time $\tau = t/T$, where $t =$ time and $T =$ revolution period (or bunch period if more than one bunch). The normalized net line density function is

$$F(\tau) = \frac{Z_i\lambda_i(\tau) - \lambda_e}{Z_i\langle\lambda_i\rangle} \qquad (1)$$

where Z_i is the ion charge. The scale of $F(\tau)$ is set by the neutralization factor $\eta = N_e/N_iZ_i$, where N_e and N_i are the total number of electrons and ions, respectively. The investigation was carried out for 4 assumed shapes of $F(\tau)$. In all cases, a gap is assumed between bunches. In the gap the ion density is assumed to be uniform and is characterized by a leak parameter $\chi =$ (ion density in gap)/(ion density at center of the beam). The transverse density of the ions and the electrons is assumed to be round-Gaussian, both of the same σ. For small amplitudes, the transverse equation of motion of an individual electron in the combined field of the ions and electron cloud can be linearized leading to Hill's equation in which $F(\tau)$ plays the role of the periodic focusing function. This equation is analyzed by standard transfer-matrix techniques, leading to linear instability for certain values of χ. If the electrons are stable, they form a core within the ion beam. Large-amplitude electron motion was also investigated. In this case, the heating of the electrons is assumed to be due to ion-electron Coulomb scattering. An electron is assumed to be lost if its energy exceeds the net beam potential (it is assumed to be absorbed at the vacuum-chamber walls with unit probability). This analysis leads to very small equilibrium values of η for both SIS-100 and SIS-200 under nominal conditions. Future plans call for code improvements, using the Monte Carlo method, and additional sources of electrons.

Electron-Cloud Simulations: Build Up and Related Effects. The CERN electron-cloud simulation code ECLOUD models the build up of an electron cloud in the vacuum chamber under the influence of a charged bunched beam. The primary sources of electrons are photoemission off the chamber walls, and residual gas ionization. The model also takes into account secondary emission by electrons striking the chamber walls, including elastic reflection. Direct and image (surface) forces on the electrons are considered, both from the beam and from the space charge of the electron cloud. These forces are applied to the electrons by an appropriate time discretization, both within a bunch and in the gaps between bunches. Longitudinal ($\mathbf{E} \times \mathbf{B}$) forces are also included. Besides field-free regions, the code can describe the electron cloud in several magnetic field configurations. Standard cases are dipole, quadrupole and solenoid fields, although any field can be considered if specified in analytic form. The secondary emission yield (SEY) has been modeled by fits to experimental data, including the reflected component. The code has been applied to describe various electron-cloud effects (ECEs) such as the electron density build-up and related phenomena such as electron energy spectra, heat load on the LHC beam screen, spatial patterns of the electron

* Work supported by the US DOE under contract DE-AC03-76SF00098.

† mafurman@lbl.gov

cloud, electron flux at pick-up buttons, multi-bunch instability growth rates, electron trapping by magnetic fields, and electron-cloud build up for electron beams. Results for the electron-cloud build up and heat load (for LHC) are sensitive to the parametrization of secondary emission and photoemission. Important are also the beam and electron image charges, the electron space charge, and magnetic fields, even if they are only a few Gauss. The simulated electron-cloud build up is in good agreement with observations for the CERN SPS, the CERN PS and the KEKB LER. An interesting disagreement between measurements and simulations pertains to the exact position of the two "vertical stripes" (locations of peak electron density) in an SPS dipole. The simulated separation between the stripes is about a factor ~ 2 larger than observed for a bunch population of 8×10^{10}. In recent developments, the code has been applied to study the electron cloud in KEKB LER quadrupole magnets, predicting the trapping of electrons for very long times. The code has also been applied to the case of electron (rather than positron) beams, in which case an electron cloud is seen to develop, although at lesser intensity than for positron beams.

3D Simulation of Photoelectron Cloud in KEKB LER. A 3-dimensional particle-in-cell (PIC) simulation code, PICEC3, has been developed to study the photoelectron cloud, including all space-charge effects. The code uses an irregular mesh in order to adequately represent the shape of the vacuum chamber. This irregular mesh requires a modification of the conventional algorithm to assign the charge of any given macroparticle to the nodes of the cell that contains it. Besides field-free regions, the code can be applied to any magnetic field configuration. The code includes models for photoemission and secondary emission, and has been applied to study the instabilities in the KEKB LER. Results show that a solenoidal field is very effective in confining the photoelectrons near the vacuum chamber wall, thereby creating a beneficial charge-free region in the vicinity of the beam. The more uniform the solenoid field, the more effective the confinement. A comparison with C-yoke magnets shows that solenoids are more effective at electron trapping. Multipacting can occur in a field-free region and in a dipole magnet. The code has been applied to quadrupole and sextupole magnets, for which a serious electron trapping phenomenon has been found during the train gap. The mechanism is analogous to the magnetic bottle confinement of plasmas. In order for the trapping to get started, the adiabatic condition of the electron motion in a magnetic field must be broken. This happens for sufficiently short bunches, in which case the electrons get a substantial impulse kick. The condition on the bunch length is $\sigma_z < 2\pi mc/eB$, where B is the field at the mirror point of the trapped electron trajectory. In practical units, this condition reads σ_z [mm] $< 10.7/B$ [T]. For KEKB conditions, the simulated trapping time in a quadrupole is $\sim 10^5$ ns. This long confinement time may cause multibunch instabilities. Simulation results on the trapping mechanisms agree well with theoretical analysis. The code has so far been applied to cylindrical vacuum chamber geometry and round gaussian beams, but the extension to more complicated cases is in progress.

A Simulation Study of the Electron Cloud in the Experimental Regions of the LHC. The vacuum chamber in the experimental regions of the LHC will be at room temperature and will have complicated geometry in order to accommodate the detectors (ATLAS, CMS-TOTEM, LHCb and ALICE) and the two coexisting beams. The baseline design calls for coating the chamber with TiZrV, a getter material that possesses the virtues of effective pumping after activation at 200 C, low SEY, and good stability *vis-à-vis* exposure to air. The primary motivation for these electron cloud studies is to determine the residual gas pressure and composition, of critical importance for the acceptable detector background level. Also important is the contribution of these warm sections to the electron-cloud effects on the beams. As opposed to the arcs, where the basic criterion on the SEY is the maximum tolerable heat deposition from the electron cloud, in the experimental regions the basic criterion on the SEY is the maximum tolerable gas pressure, particularly from electron-stimulated desorption (ESD). Depending on the exact location, the chamber radius varies in these regions from 22 to 200 mm. Since the electron-cloud simulation tool used does not at present allow for the modeling of two counter-circulating beams, the assumption was made that the ECEs could be bracketed by studying two extreme cases with the conventional (single-beam) simulation, namely: (a) bunch spacing has the nominal value ($s_b = 7.48$ m) but bunch intensity is twice the nominal value ($2N_b = 2.1 \times 10^{11}$), and (b) bunch spacing is $s_b/2$ but bunch intensity is N_b. In the real machine, these two cases obtain at discrete points along the chamber whenever the distance from the IP is an integer or half-integer multiple of s_b, respectively. Besides ESD, photon-stimulated desorption (PSD) was also taken into account (ion-stimulated desorption was considered and found to be negligible). Assuming peak SEY values of 1.1 or 1.4 and a calculated photon flux of 10^{16} γ/m/s, the simulation code yields the electron flux and energy spectrum at the chamber walls for a given radius. These results, combined with measured values of the PSD and ESD for TiZrV, yield the local pressure of H_2, CH_4, CO and CO_2. It was found that ESD is the main source of gas. In order to sharpen the quantitative predictive ability of the code, the simulations have been repeated for the SPS and compared with pickup electron signals and pressure rise measurements (in this case the main source of electrons is residual gas ionization). For a 72-bunch train at 26 GeV and $N_b = 8.3 \times 10^8$, the measured pickup signal in a field-free section matches the simulations for a pressure of 200 nT and a peak SEY=1.6. Similar tests have been carried out for other bunch-train patterns. Further benchmarks will be carried out, including tests in a special section of chamber coated with TiZrV.

Qualitative Analysis of Electron Cloud Effects in the NLC Damping Ring. The motivation of this work is to try to obtain analytic estimates of the electron-cloud density and magnitude of the resultant wake in order to interpret numerical results from simulations and allow parameter scaling without additional lengthy calculations. In this approach the beam is assumed to be non-dynamical hence unperturbable by the cloud. The analysis is developed for a quasi steady state equilibrium, defined by the condition $\kappa \ll 1$, where κ is given by

$$\kappa = \frac{N_b r_e s_b}{b^2} \tag{2}$$

Here N_b and s_b are the bunch population and spacing, respectively, r_e is the classical radius of the electron, and b is the vacuum chamber radius. The condition $\kappa = 1$ defines the beam-induced multipacting resonance condition [1], corresponding to the equality of the bunch spacing (in time units) and the traversal time of an electron across a chamber diameter under the impulse of a single bunch passage. The limit $\kappa = 0$ at fixed N_b and b corresponds effectively to a coasting beam, hence only a static electron cloud can develop in this limit. The condition $0 < \kappa \ll 1$ corresponds to a regime in which the beam and the electron cloud (or, at least, most of the electrons in the cloud) are weakly coupled hence an analytic approach may be fruitful. In the high-current limit of a bunched beam, $\kappa \gg 1$, the electrons cross the chamber so quickly under the action of a single bunch that an electron cloud in the usual sense is not well defined.

As a first approximation, the electron cloud distribution is computed in steady state for a coasting beam in a cylindrical chamber of radius large compared with the transverse beam dimensions. The electrons move in the combined potential of the beam and the space charge of the cloud. The requirement of zero radial electric field at the wall yields an average electron-cloud density

$$n_0 = \frac{N_b}{\pi b^2 s_b}\,, \tag{3}$$

corresponding to the average beam neutralization condition. The charge distribution is given by a Boltzmann form, $n(r) \propto \exp(-U(r)/T)$ where U is the self-consistent beam-cloud potential and T is a temperature. For a bunched beam with $\kappa \ll 1$, an electron takes, on average κ^{-1} bunch passages to cross the chamber. Since this is a large number, its motion can be taken to be sensibly random. Thermalization of the electrons takes place within some distance from the beam. Even if the linear bounce frequency of an electron within a bunch is $\gg$ bunch frequency, such electrons can still be described by the Boltzmann distribution due to randomness of the electron motion. Assuming that an electron that hits the chamber wall is absorbed, equating the average energy gain from a bunch-electron kick with the average energy lost by an electron hitting the wall defines the cloud temperature T in steady state. This calculation also yields the energy spectrum of the electrons hitting the wall. Photoelectrons and secondary electrons are attracted towards the beam. These newly-generated electrons produce jets that may have higher density than the average n_0. The calculation shows that these jets significantly increase the cloud density near the chamber center. Once saturation level is achieved, which takes a few bunch passages, the newly-generated photoelectrons and secondary electrons are repelled by the potential and are sent back to the chamber wall. This implies that the level of the density at saturation is fairly independent of the photoelectron and secondary yield. Multipacting does not change the temperature much but rather affects the distribution of electrons only in the vicinity of the wall. This explains why the average density of the cloud is close to that given by the beam neutrality condition. The analysis also yields the long-range wake and the corresponding linear growth rate of coupled-bunch instability.

This qualitative analysis for $\kappa \ll 1$ was applied to the NLC Main Damping Ring, for which $\kappa = 0.28$. Good general agreement is found with available simulations.

Electron Cloud Updated Simulation Results for the PSR, and Recent Results for the SNS. The LBNL electron-cloud code POSINST, which was initially developed to study the ECE in the PEP-II positron beam starting in 1995, has been recently applied to the electron-cloud instability seen at the Proton Storage Ring (PSR) ring at LANL, and to the storage ring of the Spallation Neutron Source (SNS), presently under construction at ORNL. The physical model embodied by this code is similar to that of the code ECLOUD, described above. However, the secondary emission process is somewhat different. An improved, complete, model for this process, including detailed descriptions of the three main components of the emission spectrum (true secondary, rediffused and backscattered electrons) has been recently included in the code. The code has been benchmarked against measurements at the PSR obtained by means of dedicated electron probes which measure the flux, time structure, and energy spectrum of the electrons striking the chamber walls. The PSR contains a single proton bunch of full length ~ 60 m and energy 1.735 GeV in a stainless steel chamber of 5 cm radius and 90 m ring circumference. The simulations show very clear trailing-edge beam-induced multipacting (BIM), in good agreement with measurements. This effect was clearly seen in a digital simulated movie of the electron cloud build up and dissipation during two bunch passages. The electrons that are present in the chamber during the beam gap typically have low energy; they are captured adiabatically by the beam during the passage of its leading edge, and released with equally low energy towards the end of the trailing edge. These electrons, therefore, do not contribute to trailing-edge BIM. However, the electrons that are generated from stray protons hitting the chamber *during* the bunch passage, especially those produced near the peak of the bunch current, are captured non-adiabatically

and are released at high energy soon after the passage of the peak of the bunch, and contribute strongly to trailing-edge BIM. This phenomenon leads to a strong sensitivity of the electron-wall current (and hence the electron distribution) to the longitudinal profile of the bunch. The time-energy joint electron spectrum is in good qualitative agreement with measurements, although the quantitative agreement is within a factor ~ 2, assuming a peak SEY value of 2. Preliminary simulations for the SNS show that an average electron line density of ~ 150 nC/m may be reached in a field-free region, leading to a significant tune shift due to beam neutralization. Due to an unexpectedly large electron multiplication during the passage of the SNS beam, simulations have have so far used a low number of seed macroparticles per bunch passage, leading to poor statistics for peak SEY values above 1.3. The code will soon be improved to deal with this problem.

3 ACKNOWLEDGMENTS

I am grateful to G. Rumolo for his effective job as the Scientific Secretary of Session III, and to F. Zimmermann for organizing such an informative workshop.

4 REFERENCES

[1] O. Gröbner, "Bunch-Induced Multipactoring," Proc. 10th Intl. Accel. Conf., Serpukhov, 1977, p. 277.

Summary of Session IV: Simulations of Electron-Cloud Instabilities

F. Zimmermann, CERN, Geneva, Switzerland

Abstract

I summarize the session IV of the ECLOUD'02 worskhop, which was devoted to the simulation of electron-cloud instabilities.

1 INTRODUCTION

In Session IV, 10 presentations were given:

- *Simulation of Emittance Growth due to Electron Cloud in the PEP-II Positron Ring* by Y. Cai (SLAC),
- *Electron Cloud Simulations: Beam Instabilities and Wake Fields* by G. Rumolo (CERN),
- *Study for ep Instability in JAERI-KEK Joint Project* by T. Toyama (KEK),
- *Study for ep Instability in High Intensity Proton Rings* by K. Ohmi (KEK),
- *Head-Tail Instability Caused by Electron Cloud* by E. Perevedentsev (INP),
- *Wake Field of the e-Cloud and its Effect on the Upgrade of PEP-II* by S. Heifets (SLAC),
- *Electron Cloud in the PSR and SNS* by M. Blaskiewicz (BNL),
- *Effect of Electron Cloud on the Bunch Oscillations in KEKB LER* by S. S. Win (KEK),
- *Study of Electron Cloud Effect in JLC Damping Ring* by K. Ohmi (KEK), and
- *Effect of Bunch Length, Chromaticity, and Linear Coupling on the Transverse Mode-Coupling Instability due to Electron Cloud* by E. Metral (CERN).

In the following, I discuss the session highlights and some unresolved questions.

2 TALKS

2.1 Electron Cloud Simulations for PEP-II (Y. Cai)

Y. Cai presented the results of a micro-bunch simulation, which uses a model first described in Ref. [1]. He also included radiation damping for the centroid motion of each bunch slice (or micro-bunch). The deflection of the electrons is computed by assuming a constant transverse size of each bunch particle. The inverse force is obtained from the action-reaction principle. Using PEP-II LER parameters, he observed a clear threshold in the electron cloud density beyond which the vertical beam size rapidly increases. Above threshold the beam-size growth time is of the order of the synchrotron period (40 turns). The threshold coincides with the threshold of the transverse mode-coupling instability. This is evidenced by computing the Fourier spectrum of the beam dipole motion: the threshold of beam-size growth corresponds to the merger of the $l = -1$ and $l = 0$ head-tail modes. An experimental measurement at PEP-II showed a similar signature of mode coupling as obtained in the simulation. The simulated threshold for the horizontal blow up is about two times higher.

The measured spectrum resembles the spectrum simulated for a density of $\rho_e = 10^{11}$ m^{-3}, which is about half the saturated density found in electron build-up simulations and only 20% of the estimated threshold density. Indeed, this value corresponds to only 1% of the average neutralization density, which is attributed to the effectiveness of the solenoid windings.

Using the independently simulated electron density $\rho_e = 2 \times 10^{11}$ m^{-3} and a build-up time constant of 50 ns, Y. Cai studied the beam size increase along a bunch train and found a 30% blow up, roughly consistent with observations at PEP-II and KEKB.

The effect of chromaticity was explored for a density of $\rho_e = 8 \times 10^{11}$ m^{-3}, *i.e.*, well above the TMCI threshold of 5×10^{11} m^{-3}. A positive chromaticity had no significant effect, while for negative chromaticity both horizontal and vertical beam sizes increased strongly. This may be consistent with observations. However, the actual electron density in PEP-II seems to be below the threshold.

In this context it is interesting that the simulation shows a significant growth of the beam size also at lower currents (below the threshold). The reason for this beam-size increase is not yet explained. So far the effect of chromaticity in this regime, *i.e.*, below the TMCI threshold, has not been investigated. Such a study would help in unravelling the origin of the blow up, and in contriving a cure.

A second unresolved mystery is that in the simulation the vertical blow up is much stronger than the horizontal, whereas in reality the horizontal emittance blow up is larger.

2.2 Beam Instabilities and Wake Fields (G. Rumolo)

G. Rumolo described the HEADTAIL code developed at CERN for the simulation of single-bunch instabilities driven by the electron cloud. The code includes fully 3-

dimensional beam motion, a PIC module for computing the electric fields of the beam and the electrons, the option of nonzero chromaticity, external magnetic fields, detuning with amplitude, arbitrary initial electron distributions (*e.g.*, two vertical stripes), conventional a wake field, proton space charge, beam-beam collision, and synchrotron oscillations. For the computation of space charge, the interaction with the electron cloud, and the conventional wake field, the macroparticles constituting the bunch are temporarily assigned to a number of longitudinal slices, for each of which the interaction is calculated successively. The linear space-charge force is modelled by an additional rotation in transverse phase space around the center of the associated local beam slice. The instability simulation is performed over many turns (several synchrotron periods). The code can also compute the transverse wake field, by displacing a single slice transversely, and calculating the force on later parts of the bunch. The longitudinal wake field is obtained by identifying the longitudinal slice position with time.

The simulation reveals the electron phase space, and in particular the pronounced pinching of electrons at the center of the bunch during its passage. An additional broadband impedance and a space-charge tune spread have a strong impact on the dynamics of the single-bunch instability simulated for the LHC beam in the SPS. The vertical emittance growth can be suppressed by a large chromaticity $Q'_y \geq 10$ (or $\xi_y \geq 0.4$). The inclusion of the proton space-charge force qualitatively changes the character of the instability, converting an otherwise smooth blow up into violent oscillations along the bunch.

The simulated transverse wake fields depend on the position of the displaced source slice. This is easily understood from the electron pinch and from the variation of the electron oscillation frequency along a Gaussian bunch. The wake fields also differ strongly whether one computes the field on axis or the field averaged over the transverse beam distribution. A dipole field suppresses the horizontal wake and also lowers the vertical. The longitudinal wake field was shown to be insignificant for the SPS.

Simulations were also performed for KEKB. A strong dipole motion inside the bunch is visible for the vertical plane only. This is due to the flatness of the bunch, and it is consistent with observations. A chromatcity of $\xi_y = 0.35$ cures this instability.

A detailed comparison of KEKB simulation results using the HEADTAIL code and the PIC module of K. Ohmi's PEI code has shown a good agreement in the emittance growth for several different chromaticities. The results also appear to be consistent with experimental observations [4], both exhibiting a similarly beneficial effect of positive chromaticity.

The KEKB solenoids with a field of 30 G do not much affect the single-bunch instability, because the cyclotron period is much longer than the bunch length. However, simulations have shown that for the longer bunches in the SPS a 100-G solenoid suppresses the electron pinch and also couples the wakes excited in the two transverse planes.

2.3 Electron-Cloud Build-Up and Instability for High-Intensity Proton Rings and in particular for the JAERI-KEK Joint Project (T. Toyama, K. Ohmi)

The JKJ project comprises two high-intensity proton rings accelerating to 3 GeV and to 50 GeV, respectively. The electron-cloud effects observed at the LANL PSR and BNL AGS have motivated a study of e-p instability for JKJ.

Simulations of electron-cloud build up were performed for various machines and the saturated electron densities were compared with instability thresholds predicted by a dispersion relation. This dispersion relation was obtained by approximating the single-bunch wake field by a resonator (derived from a simulation), and then evoking a coasting beam approximation, which included Landau damping due to the slippage factor and the beam energy spread. As an independent cross check, the instability growth rates were directly simulated by micro-bunch tracking.

The results suggest that the JKJ rings should operate below the instability threshold. The PSR is found to be unstable, while the ISIS ring (UK) is predicted to be stable, both in good agreement with observations.

The secondary emission yield of various materials was measured in the laboratory before and after sputtering the surface with Argon ions. The sputtering reduces the yield of all materials. The isotropic graphite had the lowest yield in either case. The TiN film presumably contained carbon and oxygen impurities.

In a dedicated experiment at the KEK PS electron-cloud signals were detected on pick ups with a high-impedance termination. The signal showed a clear baseline drift during the passage of a bunch train, which depended strongly on the number of bunches. A bias voltage or a weak solenoid field strongly affected the signal, which indicates that electrons are at the origin of the shift.

Simulations of the electron-cloud build up are roughly consistent with the measurement and also show that the simulation result critically changes when elastically reflected electrons are taken into account.

More studies are planned, for example, the simulations for JKJ will be repeated using a more realistic model, which includes the elastically scattered electrons, the measured secondary emission yields, and also the electron space charge.

2.4 Head-Tail Instability caused by Electron Cloud (E. Perevedentsev)

E. Perevedentsev presented a comprehensive treatment of the combined head-tail and TMCI instability driven by the electron cloud. The wake field due to the electron cloud may be parametrized either by a broadband resonator or by

a Struve function. The latter can further be approximated by a J_1 Bessel function.

He then applied a standard mode coupling analysis to the electron cloud instability in KEKB and in the CERN SPS. The coupling matrix was limited to 3 radial moides and truncated at azimutahl modes $-5 \leq l \leq 4$. The convergence was checked by extending the order of truncation. Next, the tune variation along the bunch due to the electron pinch was included in the TMCI calculation. It was found that this pinch is stabilizing, in accordinace with earlier studies by V. Danilov for conventional wake fields [3].

Most importantly, in the write-up for these proceedings, E. Perevedentsev generalized the mode coupling theory to the case of a wake field $W(z, z')$, depending on the longitudinal coordinates z and z' of the source and test particle, respectively. This describes the electron cloud more appropriately than a conventional wake $W(z - z')$, since the electron distribution changes during the bunch passage. The generalized wake field can be computed by simulations.

Also a simple feedback with resistive and reactive components was introduced. An analysis for the conventional wake field shows that a large chromaticity can suppress the instability. For a chromatic phase shift of $\chi \sim 2$ all lower-order modes are stable in KEKB and in the SPS, which both correspond to the case of a 'long bunch', defined by a number of oscillations along the bunch which is equal to 1 or larger.

An optimum stabilization may be reached by a judicious combination of moderate chromaticity and choice of feedback phase.

E. Perevedentsev finally considered the coasting beam limit. Treating the cases of low-order modes and modes near the resonant frequency he derived somewhat different stability conditions. In positron rings, high-order instability modes are rapidly damped by a diffusion process arising from the synchrotron-radiation quantum fluctuation.

Assuming saturation, the threshold current scales in proportion to the bunch spacing. On the other hand, in the short bunch limit, the threshold current scales as the square root of the bunch spacing.

The generalized wake concept provides us with an extremely powerful tool for more accurately analysing the electron-cloud head-tail instability.

2.5 Electron Cloud at High Beam Current: PEP-II Upgrade (S. Heifets)

The presentation by S. Heifets discussed the prospect of obtaining even higher beam currents at PEP-II, without aggravating the electron-cloud effects. This is motivated by a proposed upgrade which should increase the PEP-II luminosity by more than an order of magnitude, with a stored beam current up to 18 A. S. Heifets introduced two paramaters characterizing the electron-cloud build up: κ and ζ, defined by

$$\kappa = \frac{2N_b r_e s_b}{b^2} \tag{1}$$

and

$$\zeta = \frac{s_b}{b}\sqrt{\frac{2E_0}{mc^2}}\,. \tag{2}$$

The former describes the distance traversed by an electron which is near the wall when a bunch passes by until the arrival of the next bunch in units of the beam-pipe radius. It is 2 times the multipacting parameter considered by O. Grobner [2]. The second parameter describes the distance travelled by a secondary electron emitted with energy E_0 over a time corresponding to the bunch spacing s_b, again in units of the beam-pipe radius. The expectation is that for high values of κ and low ζ the center of the beam pipe is almost free of electrons, and there will be no electron-cloud instability. S. Heifets confirmed this by a simplified simulation study. This parameter regime exactly corresponds to that of an upgraded PEP-II, envsioning closely spaced bunches (small s_b) and high bunch charges (large N_b).

In these conditions, the cloud density is no longer set by the condition of neutrality, but by an equality of the electron space-charge potential and the initial energy E_0. This means that the electron density will be much lower than naively expected. However, inside dipole fields the electron density might grow to larger values.

For certain intermediate beam currents, the simulation showed an increase of the electron-cloud density for every other bunch, which may explain why the PEP-II luminosity was observed to alternate periodically from bunch to bunch.

At low current, the wake field is determined by electrons in the vicinity of the beam. An additional effect is the asymmetry introduced by the jet of primary photoelectrons or by an ante-chamber. The estimated change in equilibrium beam energy due to the static dipolar force is small. At high current the bunch-to-bunch wake field arises from the asymmetry of the secondary electrons caused by a transverse bunch offset. An explicit formula for $\zeta \ll 1$ was given. The azimuthal harmonic $m = 2$ of the electron cloud generates a contribution to the tune shift which is equal and of opposite sign in the two transverse planes. The primary jets of photoelectrons cause a variation of tune shift and orbit distortion along the bunch. The head-tail instability can be treated using the Satoh-Chin formalism, by a proper choice of the rang of the coupling matrix. The instability may be stabilized if the number of head-tail oscillations along the bunch is large.

2.6 Electron Clouds in the PSR and SNS (M. Blaskiewicz)

M. Blaskiewicz discussed electron-cloud effects in the PSR and SNS, first considering the electron cloud generation and then the beam stabiilty. A remarkable plot from the PSR (Fig. 1 in the talk) shows the threshold rf voltage as a function of beam charge. Two curves for 30% different bunch lengths were almost identical. It appears difficult to explain this independence of bunch length by common instability models.

Primary electrons are assumed to be generated by losses and gas ionization. Secondary electrons are parametrized in the usual way, *i.e.*, using the Seiler formula. A rough estimate is a generation rate of 200 electrons per lost proton and 0.1% loss, resulting in 2×10^8 primary electrons per meter and turn.

In a simple coasting beam model, where space charge is assumed to be the dominant contribution to the tune shift, the threshold bunch current should scale as the third power of the bunch length (note the striking difference to the observed independence!). The focus of the simulations has thus been the scaling with the bunch length and the modelling of a realistic electron cloud.

The simulation model used is essentially 1-dimensional, describing only the vertical motion of protons and electrons. The forces between proton beam and electrons are approximated, so that they are correct in the limits of small and large amplitudes. The electron cloud is represented by a small number (20–200) of macroparticles, the beam by 2×10^6 macroparticles, and space-charge kicks are applied about 10 times per betatron oscillation. Many parameters were varied in the simulations. Electron densities of 1 nC/m led to a rapid instability with beam loss. Smaller densities could give rise to persistent oscillations at a finite amplitude. The simulated threshold densities and threshold rf voltages differ from the observation in the PSR by factors of about 0.2 and 1.5. The origin of the additional damping is unclear.

Complementary to the simulation, an eigenmode analysis was performed, where the rf voltage was approximated by a square potential. Again the threshold rf voltage varies strongly with bunch length. The eigenmode analysis was benchmarked against a coasting beam calculation. The results are sensitive to tails in the momentum distribution.

The same eigenmode analysis was applied to the 2-MW SNS and an electron density of 2 nC/m, corresponding to fairly large values of secondary emission yield and electron reflectivity. The threshold predicted for the SNS looks acceptable.

A convergence test of the eigenmode analysis required many modes in order to reproduce the known beam breakup limit, and showed that the coasting beam dispersion relation gives a good estimate for the threshold.

2.7 *Coupled Bunch Instability in KEKB LER (S.S. Win)*

S.S. Win presented measurements and simulation results for the spectrum and growth rates of multi-bunch instabilities driven by the electron cloud in KEKB.

Multibunch mode spectra and instability growth rates were measured with solenoids on and off. At beam currents approaching 1 A, the instability growth rates, measured after deactivating the transverse feedback, are of the order of 500 μs. With solenoids off the spectra show a strong peak near mode number 800 (out of about 1300) and two smaller peaks around 1100 and 150 (and a fourth peak at 350 in the horizontal plane). On the other hand, when the solenoids are turned on, only low-order modes near 0 are excited.

Good agreement between simulated mode spectra and measurements was achieved, by assuming — in the case without solenoids — that the photoelectrons are generated uniformly around the chamber wall and not concentrated at the primary illumination point. The case with solenoids also shows a good agreement, but is insensitive to details of the initial electron distribution. If one assumes a solenoid field of about 10 G, the simulated horizontal growth rate agrees with the measurement, and the simulated vertical growth rate is about 50% higher.

2.8 *Electron Cloud in the JLC Damping Ring (K. Ohmi)*

K. Ohmi studied the electron cloud phenomenon in two versions of the JLC damping ring, which differ by the bunch spacing (1.4 ns and 2.8 ns, respectively).

He first studied the electron cloud build up. The photon absorption efficiency of the antechamber was estimated at 80% based on an experiment at KEKB. The simulated cloud densities in saturation at the center of the chamber then are 8×10^{12} m^{-3} and 3×10^{12} m^{-3}.

The simulated growth rate of the coupled bunch instability was found to be 26 μs (20 turns) or 130 μs (100 turns), for the two bunch spacings.

The single-bunch wake field was computed analytically and by a macroparticle simulation. The coasting beam instability threshold was then used to estimate the threshold electron density. For a synchrotron tune of $\nu_s = 0.01$, it is about half the density simulated for the 1.4-ns spacing. Some ambiguity remains in the choice of the wake quality factor, Q, and the enhancement factor due to the electron pinch, K.

K. Ohmi concluded that a further reduction in the electron density by a factor 5–10 will be needed. Clearly, the electron cloud would favor the larger bunch spacing, where the conditions appear considerably more relaxed.

Finally, results were also presented for DAFNE. The average electron density for present beam conditions is estimated at 6×10^{11} m^{-3}, which is 3 times less than the predicted single-bunch instability threshold. Since the design current of DAFNE is 5 times higher than the present value, the instability might be observed in the future.

2.9 *Effect of Bunch Length, Chromaticity and Linear Coupling (E. Metral)*

E. Metral analysed the electron cloud instability by adapting the transverse mode-coupling theory. He approximated the wake field by a resonator. The strong dependence of the electron-cloud wake-field parameters on bunch length, transverse beam size, and bunch current were taken into account.

The model was applied to the CERN SPS, and it was shown that for the 2001 beam parameters, a strong sensitiv-

ity to chromaticity and bunch length is expected in agreement with the observations. For short bunches ($\sigma \leq 15$ cm) or high chromaticities ($\xi_y > 0.8$) the LHC beam in the SPS is expected to be stable up to nominal intensity.

In the SPS, most of the electrons reside in dipole fields, where the horizontal single-bunch wake vanishes, since the electrons here only move vertically. Therefore, linear coupling can share the growth rate between the two planes, and increase the instability rise time by a factor of two. It is foreseen to test this stabilization scheme in 2002.

3 OPEN QUESTIONS AND FUTURE STUDIES

One burning question concerns the missing physics input that could explain why the blow up in PEP-II preferentially occurs in the horizontal plane and not in the vertical as simulated. Another question is the character of the PEP-II instability below the simulated TMCI threshold.

It is not enirely clear if the observed electron cloud effects in PEP-II are consistent with simulations or not, given the installation of antechambers and extensive TiN surface coating. A comprehensive comparison would be most valuable for the accelerator-physics community.

Experimental and simulation studies should further be advanced, in order to explore the high-intensity 'blow-out' regime contemplated for the PEP-II upgrade.

The striking fact that the measured threshold rf voltage in the PSR is nearly independent of the bunch length still calls for an explanation.

A highlight of this session is the generalized TMCI theory including pinch effect and time-dependent wake field. The new theory should be applied and benchmarked against simulations and experiments.

A small mystery is why the (photo?)-electrons in KEKB seem to be generated so uniformly around the chamber wall.

Additional refined studies may be necessary for a reliable prediction of electron cloud effects in future high-intensity proton rings and in future linear colliders, though a promising start has been made and the preliminary results are encouraging.

The stabilization of the electron-cloud instability by linear coupling should be tested experimentally.

4 ACKNOWLEDGEMENT

I thank T. Raubenheimer, the session chairman, and A. Wolsky, who gave the summary talk, for inspiring discussions.

5 REFERENCES

[1] K. Ohmi and F. Zimmermann, PRL 85, 3821 (2000).

[2] O. Gröbner, HEACC'77, Protvino (1977).

[3] V.V. Danilov, PRST-AB 1, 041301 (1998).

[4] H. Fukuma, these proceedings.

SUMMARY SESSION V: COMPARISONS AND PLASMA APPROACHES

R. Aßmann, CERN, Geneva, Switzerland
T. Katsouleas, University Southern California, CA, USA

1 PRESENTATIONS

The talks in session V covered a wide range of topics:

1. Electron cloud instability.
2. Instabilities with concurrent beam-beam and electron cloud.
3. Plasma wakefields and plasma modelling for electron cloud.
4. Synchrotron radiation effects on electron clouds.
5. Theory of holes in particle beams.
6. Vlasov-Poisson equations for proper non-linear description.
7. Experimental, simulation, and theoretical results for the PS, SPS, BEPC, BEPCII, SLAC plasma experiments, Heavy Ion Fusion.

The session illustrated that the modelling and understanding of the electron cloud is an area with a large scope of issues and interests, bringing together a wide range of diverse expertise. In the following we summarize the main results presented.

Electron build-up and instability: Comparison between observation and numerical simulations for the CERN PS (G. Rumolo et al) G. Rumolo presented that and electron cloud build up and instability can be observed in the PS. Simulations aimed at understanding the observations, especially the observed and unexpected horizontal instability. He showed that the detailed magnetic configuration is an important input to simulations. Including the combined function magnets into the model, a strong horizontal wake function can indeed be predicted. He presented results on the electron cloud density in saturation, versus different beam intensities. It is not understood why the equilibrium cloud density decreases with increasing beam population.

Combined phenomenon of the beam-beam and the beam-electron effects (K. Ohmi et al) K. Ohmi showed theory and simulation results for e^+e^- colliders that indicate that the concurrent effects from beam-beam and electron cloud can lower the instability threshold significantly. This complex phenomenon should exist, though the predictions from linear theory and strong-strong simulation with a soft Gaussian model disagree. Further work is required for a more detailed understanding, including the effect from strong Landau damping due to beam-beam.

Simulation study on electron cloud instability for BEPC and its upgrade plan BEPCII (J. Xing et al) J. Xing reported that a photo electron detector has been installed in the BEPC ring. Electron production is observed with this monitor, however, without any saturation in electron density, if the beam intensity is increased. This is consistent with simulations of electron production for different yields, reflectivities, and beam currents. Electron cloud is a potential concern for the two ring upgrade BEPCII, where it could limit the maximum intensity in the positron ring. BEPCII will have more bunch intensity than KEK-B with the same bunch spacing and lower beam energy (1.9 GeV). J. Xing showed that the electron cloud seems not to be a serious problem for BEPCII, possibly because it will be below the TMCI threshold of the electron cloud volume density.

Plasma modelling of wakefields in electron clouds (T. Katsouleas et al) T. Katsouleas presented experimental results from plasma wakefield acceleration experiments and the corresponding simulations. He demonstrated the advanced state of plasma simulation (both 3D and 2D), visible from the excellent agreement of simulation with observation. Applying these tools to the SPS parameters he found good agreement in the predicted longitudinal wakefield with results from F. Zimmermann and G. Rumolo, however, without some unphysical artefacts in the beginning and end of the bunch. He also raised the point of the image charge tune shift due to the electron cloud itself that had so far not been included correctly into simulations. He concluded that it is possible to build a powerful tool that combines the best of plasma and accelerator tools.

On the transparency of the electron cloud to synchrotron radiation (D. Kaltchev) D. Kaltchev analyzed the effect of synchrotron radiation on the electron cloud. He concluded that there is a negligible effect for LHC parameters.

Kinetic theory of periodic holes in debunched particle beams (H. Schamel et al) H. Schamel discussed the appropriate theoretical treatment of plasmas. He questioned the "standard wave concept in plasma theory" that small amplitude waves can be predicted by a linearized theory and that non-linear effects become important only for larger amplitudes. Based on experimental results he demonstrated for electro-static phase space structures that nonlinearity starts from the onset, even at infinitesimal amplitudes. This is adequately described by a solution of the Vlasov-Poisson system with a potential method.

Electron cloud effects in intense ion beam linacs; theory and experimental planning for heavy ion fusion (M. Furman) M. Furman presented the plans for a fusion power plant, relying on 100-200 simultaneous heavy ion, singly ionized beams. The energy would be 1-4 GeV with an energy of several MJ. There is a concern that the electron cloud could affect the focusing of the beams which must overlap with a small spot size in the fusion point. Studies have started and extensive instrumentation has been proposed for electron detection in the test facility HCX.

2 MAJOR QUESTIONS RAISED FOR FURTHER WORK

- What is the explanation for lower equilibrium e-cloud density with higher beam intensity, as predicted from simulations for the PS?
- Why do the linear and Gaussian beam-beam approximations for beam-beam with electron cloud give somewhat different results? What is the tune dependence of the effect?
- Can one do meaningful experiments on this effect at PEP-2 (maybe explaining the difference between horizontal and vertical observation in PEP-2)?
- What is the expected combined effect of beam-beam and electron cloud in proton-proton colliders like the the LHC?
- Can the build-up of the electron cloud be integrated into the plasma modelling codes, instead of staring from an existing electron cloud density?
- Can the effect of damping and diffusion be included into the theory of holes?
- Can the fringe fields be included into electron cloud simulations to maybe explain the differences in horizontal and vertical observations in PEP-2 (similar to the effect of combined function magnets in the PS)?

SUMMARY REPORT OF SESSION VI

W. Chou, Fermilab, Batavia, IL 60510, USA
O. Brüning, M. Giovannozzi, E. Metral, CERN, Geneva, Switzerland

Abstract

This report gives a brief review of the presentations in Session VI of the Ecloud'02 Workshop and summarizes the major points during the discussions. Some points (e.g., the critical mass phenomenon) are not conclusive and even controversial. But it has been agreed that further investigations are warranted.

1 REVIEW OF TALKS

The topic of Session VI in the Ecloud'02 workshop is *"Discussions of future studies, collaborations and possible solutions."* Half of the session is devoted to presentations, another half to discussions. This report will focus on the latter.

There are six presentations:

- R. Macek, *Possible cures to the e-cloud problem.*
- G. Rumolo, *Driving the electron-cloud instability by an electron cooler.*
- U. Iriso Ariz, *RF test benches for electron-cloud studies.*
- F. Caspers, *Stealth clearing electrodes.*
- F. Ruggiero, *Future electron-cloud studies at CERN.*
- E. Perevedentsev, *Beam-beam and transverse impedance model.*

Macek gives an extensive list of possible cures to the e-cloud effects (ECE). Among them, the most interesting ones are those that have been proved to be either effective or ineffective. For example, the PSR has found three effective cures: beam scrubbing, inductive inserts and sextupoles. The inductive insert is a new idea that was originally suggested for compensating space charge effects. It works well for giving a "cleaner" gap (i.e., reduced population of electrons in the gap) and, thus, raises the e-p instability threshold. The effectiveness of the sextupoles comes with a pleasant surprise. Because the e-p instability in the PSR is in the vertical direction, these sextupoles give a skew quadrupole field, which couples the x and y motion that helps stabilize the beam. The PSR has also tried TiN coating, solenoids and a better vacuum. Although these measures greatly reduce the prompt electrons, they show no effect on the threshold. On the other hand, however, KEK-B and PEP-II have both found TiN coating and solenoids useful in suppressing ECE.

Rumolo proposes to carry out an e-cloud experiment in the GSI cooler ring. Iriso Ariz has built two rf stands that can be used for bench test of ECE. Caspers introduces a clearing electrode that was used in the CERN Antiproton Accumulator. A special design makes it invisible to the beam. Ruggiero gives a comprehensive work list of future ECE study at CERN. Perevedentsev introduces an analytical model that takes into account both beam-beam and coupling impedance of the machine.

2 SUMMARY OF DISCUSSIONS

2.1 "Critical Mass" Phenomenon

During the discussion, attempts are made to identify a few key parameters that are most crucial for studying ECE. One seems to be the volume density of the particles. Table 1 lists the machine parameters obtained from a survey during this workshop. First take a look at the existing (or existed) proton machines. Six machines have reported observations of ECE. They are: ISR, CERN PS (CPS), SPS with LHC beams, SPS with fixed target beams, PSR, and RHIC in proton operations. The parameters listed in the table are the ones when a machine starts to observe ECE before taking any curing measures. As a comparison, the parameters of the ISIS are also listed, which never sees this effect. The energy (E), protons per bunch (N_b), and r.m.s. beam sizes (σ_x, σ_y and σ_z) are drastically different in the six machines. Nonetheless, the particle volume density of these machines when reaching the e-cloud threshold takes a remarkably similar value: about $(0.2 \pm 0.1) \times 10^8$ /mm^3. By contrast, this number of the ISIS is much lower (0.006). We call this a "critical mass" phenomenon. This is solely an empirical observation. But it may not a pure coincidence. Different explanations exist and further investigation is warranted. To the very least, one may use this critical value to judge how likely or unlikely ECE could become a problem for a machine under design or under construction. For example, from Table 1 one may say that the SNS and JHF 50-GeV Ring should pay more attention to the e-cloud problem than the JHF 3-GeV Ring or the Fermilab Proton Driver.

The "critical mass" of positron machines is in a rather different regime. Three machines (APS, KEK-B and PEP-II) have observed ECE. The onset values of the particle volume density are more than three orders of magnitude higher than that of the proton machines. Moreover, unlike proton machines, these values are not close to each other. One hand waving explanation is that, the mechanism of the primary electron generation in positron machines is very different from that in proton machines (see Section 2.2). Furthermore, some positron machines have antechambers, some don't. This could be the reason for different critical mass values. On the other hand, the low volume density of the DAΦNE may explain why it does not see ECE.

2.2 Comments on Primary Electrons

One difference between proton and positron machines concerning ECE is the source of the primary electrons. For proton machines, it is believed that the primary electrons come from proton losses and the stripping foil (in the case of H^- injection), whereas for positron machines, it is photoemission. Ionization (i.e., vacuum) is not considered to be important in this process.

However, reducing primary electrons does not seem to be helpful. ECE is mainly due to secondary electron yield from the wall. Someone even claims that, one primary electron is enough to cause ECE.

2.3 A Puzzle

From the PEP-II experience, the solenoid is an effective way to suppress ECE. When only 8% of the machine was equipped with solenoids, there was already a significant increase in beam intensity. The more solenoids are in place, the higher the beam current is. Now more than 70% of the machine has solenoids. However, The PSR experience is quite different. When 15% of the machine was equipped with clearing electrodes, there was no effect on the beam.

2.4 DC vs. AC Operations

By far, all ECE that have been observed are either in DC machines (accumulators and storage rings) or AC machines in DC operation (i.e., on flat top or flat bottom). No ECE has been reported in AC machines during ramping. (The SPS does see electron clouds during ramping. But it does no harm to the beam.)

This fact has important implication in choosing between two types of high intensity proton machines: linac-based or synchrotron-based, if the latter is indeed immune to ECE.

2.5 Collaborations

Two collaborations have been formed at the workshop:

- Comparison of measurements on e-cloud generation. Three labs will compare their results. The point-of-contacts are: F. Ruggiero at CERN, F-J. Decker at SLAC, and S. Kato at KEK.
- Development of a reliable theory: Three people will work together on this. A. Chao on a non-perturbative method, M. Furman on e-cloud build-up, and S. Heifets on beam dynamics.

2.6 Code Benchmarking

There are a number of codes that have been written for simulating ECE. An incomplete list is as follows:

- E-cloud build-up codes: LBL (M. Furman), CERN (F. Zimmermann), KEK (K. Ohmi, L. Wang), LANL (T. Wang).
- Instability codes: CERN (G. Rumolo), KEK (K. Ohmi, L. Wang), SLAC/LBL (Y. Cai), BNL (M. Blaskiewicz), USC (T. Katsouleas), PPPL (H. Qin), LANL (T. Wang).

It is important that these codes are benchmarked so that the results can be compared with each other. The workshop asks F. Zimmermann to coordinate this work.

3 CONCLUSIONS

Significant progresses have been made on the ECE study in the past several years, including simulations, bench measurements and machine experiments. However, lack of a reliable theory remains to be a problem in this field. Several empirical observations discussed at this workshop (e.g., the critical mass phenomenon, AC *vs.* DC) cannot be explained or overruled without a deeper understanding of this effect. The collaborations formed at the workshop provide a useful environment to further the study.

Table 1: Particle Volume Density in Proton and Positron Machines
(Note: Existing machines with * have not observed ECE)

Machine	E (GeV)	N_b	σ_x (mm)	σ_y (mm)	σ_z (mm)	$N_b / (\sigma_x\sigma_y\sigma_z)$ (10^8 / mm^3)
Proton, existing (or existed)						
ISR	30	1×10^{14}	12.5	2.5	236,000	0.14
CPS	26	4×10^{10}	1.6	1.2	750	0.28
SPS (LHC beam)	26	3×10^{10}	2.2	2.2	300	0.21
SPS (fixed target beam)	100	5×10^{9}	2	1	190	0.13
PSR	0.8	3×10^{13}	10	10	19,500	0.15
RHIC	25	1×10^{11}	3	3	1,125	0.10
ISIS (*)	0.07	1.25×10^{13}	38	38	15,000	0.006
Proton, under construction						
SNS	1	2×10^{14}	15	15	30,000	0.30
JHF (3-GeV Ring)	3	4.15×10^{13}	19	19	27,500	0.04
JHF (50-GeV Ring)	50	4.15×10^{13}	11	11	20,500	0.17
LHC	7000	$1.1x10^{11}$	0.3	0.3	77	159
Proton Driver proposal						
Fermilab 8-GeV Proton Driver	0.6	3×10^{11}	23	13	300	0.033
Positron, existing						
APS	7	5×10^{10}	0.2	0.02	10	12,500
KEK-B	3.5	2.2×10^{10}	0.5	0.05	6	1,470
PEP-II	3.1	5×10^{10}	0.7	0.1	12	600
DAΦNE(*)	0.55	4×10^{10}	2	0.063	24	132